



*metals*

# News Trends in Powder Metallurgy

## Microstructures, Properties, Durability

---

Edited by

Eric Hug and Guy Dirras

Printed Edition of the Special Issue Published in *Metals*

# **News Trends in Powder Metallurgy: Microstructures, Properties, Durability**



# **News Trends in Powder Metallurgy: Microstructures, Properties, Durability**

Editors

**Eric Hug**

**Guy Dirras**

MDPI • Basel • Beijing • Wuhan • Barcelona • Belgrade • Manchester • Tokyo • Cluj • Tianjin



*Editors*

Eric Hug  
Normandy University  
France

Guy Dirras  
Université Paris  
France

*Editorial Office*

MDPI  
St. Alban-Anlage 66  
4052 Basel, Switzerland

This is a reprint of articles from the Special Issue published online in the open access journal *Metals* (ISSN 2075-4701) (available at: [https://www.mdpi.com/journal/metals/special\\_issues/powder\\_metallurgy](https://www.mdpi.com/journal/metals/special_issues/powder_metallurgy)).

For citation purposes, cite each article independently as indicated on the article page online and as indicated below:

|  |
|--|
| LastName, A.A.; LastName, B.B.; LastName, C.C. Article Title. <i>Journal Name</i> <b>Year</b> , <i>Volume Number</i> , Page Range. |
|--|

**ISBN 978-3-0365-1782-7 (Hbk)**

**ISBN 978-3-0365-1781-0 (PDF)**

© 2021 by the authors. Articles in this book are Open Access and distributed under the Creative Commons Attribution (CC BY) license, which allows users to download, copy and build upon published articles, as long as the author and publisher are properly credited, which ensures maximum dissemination and a wider impact of our publications.

The book as a whole is distributed by MDPI under the terms and conditions of the Creative Commons license CC BY-NC-ND.

# Contents

## **Eric Hug and Guy Dirras**

News Trends in Powder Metallurgy: Microstructures, Properties, Durability

Reprinted from: *Metals* **2021**, *11*, 1216, doi:10.3390/met11081216 . . . . . 1

## **Bhupendra Sharma, Guy Dirras and Kei Ameyama**

Harmonic Structure Design: A Strategy for Outstanding Mechanical Properties in Structural Materials

Reprinted from: *Metals* **2020**, *10*, 1615, doi:10.3390/met10121615 . . . . . 5

## **Benjamin Guennec, Takayuki Ishiguri, Mie Ota Kawabata, Shoichi Kikuchi, Akira Ueno and Kei Ameyama**

Investigation on the Durability of Ti-6Al-4V Alloy Designed in a Harmonic Structure via Powder Metallurgy: Fatigue Behavior and Specimen Size Parameter Issue

Reprinted from: *Metals* **2020**, *10*, 636, doi:10.3390/met10050636 . . . . . 21

## **Benoît Fer, David Tingaud, Azziz Hocini, Yulin Hao, Eric Leroy, Frédéric Prima and Guy Dirras**

Powder Metallurgy Processing and Mechanical Properties of Controlled Ti-24Nb-4Zr-8Sn Heterogeneous Microstructures

Reprinted from: *Metals* **2020**, *10*, 1626, doi:10.3390/met10121626 . . . . . 43

## **Yang Song, Zhe Zhang, Hantuo Ma, Masashi Nakatani, Mie Ota Kawabata and Kei Ameyama**

Ratcheting-Fatigue Behavior of Harmonic-Structure-Designed SUS316L Stainless Steel

Reprinted from: *Metals* **2021**, *11*, 477, doi:10.3390/met11030477 . . . . . 63

## **Lucía García de la Cruz, Mayerling Martínez Celis, Clément Keller and Eric Hug**

Exploring the Strain Hardening Mechanisms of Ultrafine Grained Nickel Processed by Spark Plasma Sintering

Reprinted from: *Metals* **2021**, *11*, 65, doi:10.3390/met11010065 . . . . . 75

## **Jean-Philippe Monchoux, Alain Couret, Lise Durand, Thomas Voisin, Zofia Trzaska and Marc Thomas**

Elaboration of Metallic Materials by SPS: Processing, Microstructures, Properties, and Shaping

Reprinted from: *Metals* **2021**, *11*, 322, doi:10.3390/met11020322 . . . . . 93

## **Sarah Dine, Elodie Bernard, Nathalie Herlin, Christian Grisolia, David Tingaud and Dominique Vrel**

SHS Synthesis, SPS Densification and Mechanical Properties of Nanometric Tungsten

Reprinted from: *Metals* **2021**, *11*, 252, doi:10.3390/met11020252 . . . . . 113

## **Mathias Moser, Sylvain Lorand, Florian Bussiere, Frédéric Demoisson, Hervé Couque and Frédéric Bernard**

Influence of Carbon Diffusion and the Presence of Oxygen on the Microstructure of Molybdenum Powders Densified by SPS

Reprinted from: *Metals* **2020**, *10*, 948, doi:10.3390/met10070948 . . . . . 129

## **Awais Ikram, Muhammad Awais, Richard Sheridan, Allan Walton, Spomenka Kobe,**

## **Franci Pušavec and Kristina Žužek Rožman**

Spark Plasma Sintering as an Effective Texturing Tool for Reprocessing Recycled HDDR Nd-Fe-B Magnets with Lossless Coercivity

Reprinted from: *Metals* **2020**, *10*, 418, doi:10.3390/met10030418 . . . . . 147

|   |     |
|---|-----|
| <b>Ntebogeng F. Mogale and Wallace R. Matizamhuka</b><br>Spark Plasma Sintering of Titanium Aluminides: A Progress Review on Processing,<br>Structure-Property Relations, Alloy Development and Challenges<br>Reprinted from: <i>Metals</i> <b>2020</b> , <i>10</i> , 1080, doi:10.3390/met10081080 . . . . .   | 165 |
| <b>Foad Naimi, Jean-Claude Niepce, Mostapha Ariane, Cyril Cayron, José Calapez,<br/>Jean-Marie Gentzittel and Frédéric Bernard</b><br>Joining of Oxide Dispersion-Strengthened Steel Using Spark Plasma Sintering<br>Reprinted from: <i>Metals</i> <b>2020</b> , <i>10</i> , 1040, doi:10.3390/met10081040 . . . . .  | 189 |
| <b>Jorge Sergio Téllez-Martínez, Luis Olmos, Víctor Manuel Solorio-García,<br/>Héctor Javier Vergara-Hernández, Jorge Chávez and Dante Arteaga</b><br>Processing and Characterization of Bilayer Materials by Solid State Sintering for<br>Orthopedic Applications<br>Reprinted from: <i>Metals</i> <b>2021</b> , <i>11</i> , 207, doi:10.3390/met11020207 . . . . .              | 199 |
| <b>Jesús E. González, Gabriela de Armas, Jeidy Negrin, Ana M. Beltrán, Paloma Trueba,<br/>Francisco J. Gotor, Eduardo Peón and Yadir Torres</b><br>Influence of Successive Chemical and Thermochemical Treatments on Surface Features of<br>Ti6Al4V Samples Manufactured by SLM<br>Reprinted from: <i>Metals</i> <b>2021</b> , <i>11</i> , 313, doi:10.3390/met11020313 . . . . . | 215 |

Editorial

# News Trends in Powder Metallurgy: Microstructures, Properties, Durability

Eric Hug <sup>1,\*</sup> and Guy Dirras <sup>2,\*</sup>

<sup>1</sup> CRISMAT Laboratory, UMR 6508, Normandy University, 6 Boulevard Marechal Juin, CEDEX 4, 14050 Caen, France

<sup>2</sup> LSPM Laboratory, CNRS-UPR 3407, Sorbonne Paris Nord University, 99 Avenue Jean Baptiste Clément, 93430 Villetaneuse, France

\* Correspondence: eric.hug@ensicaen.fr (E.H.); dirras@lspm.cnrs.fr (G.D.)

## 1. Context and Scope of the Special Issue

Compared with traditional casting or plastic deformation processes, powder metallurgy-based methods are versatile routes for producing in-demand microstructures of various types. Centimeter-sized, fully dense, coarse-grained, ultrafine-grained, nanostructured, and heterogeneous-controlled structure (architected) materials can indeed be processed in respect to the bottom-up approach through techniques of fast sintering (SPS, microwave sintering...) and the emerging additive manufacturing such as by powder bed fusion (PBF), leading to an original microstructure design. Consequently, the mechanical and physical properties of the alloys, and their durability, are profoundly modified, thus broadening the application range.

In this Special Issue, we have initially proposed to interested authors to contribute to the following topics:

- Toward new microstructures: analysis, properties, and stability;
- Powder properties, nanostructuring, mechanical alloying, and aging;
- Unconventional sintering processes: SPS, microwave, etc.;
- Additive manufacturing by powder bed melting processes;
- Mechanical properties: fatigue, creep, plasticity mechanisms;
- Physical properties: magnetism, electrical conduction;
- Damage, fracture, and effect of the environment: oxidation, electrochemical corrosion.

Finally, a review of the scientific advances in this field have been carried out through a selection of 13 original research papers (progress reviews and articles) on the impact of the microstructure on the mechanical and functional properties of metallic alloys obtained by sintering (SPS) and additive manufacturing (PBF) routes.

## 2. Presentation of the Contributions

From the point of view of traditional metallurgy, mechanical resistance and ductility are antagonist properties. Therefore, the quest for methodologies and concepts that are susceptible to make them coexist are of great interest. To this end, and among others, the idea of a harmonic structure, first introduced by Prof. Ameyama, has been proven to be of prime interest for addressing the dual problem of improving both the strength and the ductility and other fatigue properties of metallic materials. Four main contributions to this Special Issue by Bhupendra et al. [1], Guennec et al. [2], Fer et al. [3], and Song et al. [4] illustrate the incredible potential of the concept which can be indeed applied to various metallic materials and alloys.

Nevertheless, the microstructural mechanisms at the origin of the coexistence between ductility and mechanical resistance of heterogeneous structures of harmonic types are not yet well understood, particularly in terms of synergy between the different structural entities (shell and core). This understanding begins with identifying the unique plasticity

**Citation:** Hug, E.; Dirras, G. News Trends in Powder Metallurgy: Microstructures, Properties, Durability. *Metals* **2021**, *11*, 1216. <https://doi.org/10.3390/met11081216>

Received: 28 July 2021

Accepted: 28 July 2021

Published: 30 July 2021

**Publisher's Note:** MDPI stays neutral with regard to jurisdictional claims in published maps and institutional affiliations.



**Copyright:** © 2021 by the authors. Licensee MDPI, Basel, Switzerland. This article is an open access article distributed under the terms and conditions of the Creative Commons Attribution (CC BY) license (<https://creativecommons.org/licenses/by/4.0/>).

mechanisms of the coarse grains of the core and the ultra-fine grains of the shell. In this Special Issue, a first answer is provided by Garcia de la Cruz et al. [5]. In their study, the authors discuss the work hardening mechanisms of UFG nickel, interestingly considering samples with grain sizes ranging from 0.82 to 25  $\mu\text{m}$ . While a lower strain hardening capability is observed with decreasing grain size, samples in the submicrometric range display the three distinct stages of strain hardening representative of face-centered cubic metals, with a short second stage and the third stage beginning soon after yielding.

Again, in terms of properties (mechanical or physical), and considering durability issues, metallic structures could not be conceived without optimizing the microstructure, which we know has a colossal influence on the subsequent properties, and therefore on the performances. The review by Monchoux et al. [6] provides an overview of the link between process, microstructures, and properties of metallic alloys elaborated by SPS. In this Special Issue, these aspects are also approached and presented systematically by Moser et al. through two studies that focus on the importance of densification on the mechanical properties of tungsten which are made ductile via nanostructuring and densification after SPS, by Dine et al. [7], as well as on the influence of impurities such as oxygen and carbon on SPS-processed Molybdenum. [8]. Finally, considering sustainability, metal recycling is a hot topic. Ikram et al. [9] demonstrate how SPS can be effective with recycled metal powders for obtaining Nd-Fe-B permanent magnets with magnetic properties equivalent to those elaborated using pristine powder.

If it was still needed to convince of the versatility of the processes for the development of products and parts with great added value, based on powder metallurgy routes (in particular spark plasma sintering and additive manufacturing), the reader would find some essential data in this Special Issue. First, a detailed review on titanium aluminides having the potential of substituting nickel-based superalloys (NBSAs) in the aerospace industries is discussed by Mogale et al. [10]. Then, this article further reviews published works on phase constituents, microstructures, alloy developments, and mechanical properties of TiAl alloys produced by SPS. Finally, an overview of challenges as far as the implementation of TiAl in industries of interest is highlighted.

In the same vein, assembly processes to produce structural or functionalized structural materials (or parts to be functionalized later) can become real challenges. Powder metallurgy and SPS make it possible to meet these challenges. Three studies presented in this Special Issue deal with these aspects. First, Naimi et al. [11] propose to use SPS sintering of ODS steels to overcome the difficulties with joining oxide dispersion-strengthened (ODS) steels using traditional welding routes. Then, in the work of Tellez-Martinez et al. [12], ingeniously, a new processing route is proposed to produce graded porous materials by placing particles of Ti6Al4V with different sizes in different configurations to obtain bilayer samples that can be used as bone implants. It is concluded that the proposed elaboration way can produce materials with specific and graded characteristics, with the radial configuration being the most promising for biomedical applications. Finally, mastering the texturing of surfaces is an important issue, in particular for the chemical or biological functionalization of medical implants, which constitutes a societal issue of great importance for which new material solutions are sought. In this quest, additive manufacturing and, in particular, powder bed processes are of particular interest. In this perspective, Gonzales et al. [13] present an original approach for texturing Ti6Al4V samples obtained by SLM subjected to successive treatments: acid etching, chemical oxidation in hydrogen peroxide solution, and thermochemical processing. The effect of temperature and time of acid etching on the surface roughness, morphology, topography, and chemical and phase composition after the thermochemical treatment was studied. These surfaces are expected to generate greater levels of bioactivity and high biomechanics fixation of implants, as well as better resistance to fatigue.

**Acknowledgments:** As guest editors of this Special Issue, we hope that the present selected papers will be useful to researchers working in the area of powder metallurgy. We would like to thank the authors for their contributions to this Special Issue, and all of the reviewers for their efforts in ensuring high-quality publications. We would also thank to the Metals editorial assistants for their support during the preparation of this volume. Finally, we would especially thank Natalie Sun, managing Editor of Metals, for offering us the opportunity to work on this project, and for guiding us through the editorial set-up.

**Conflicts of Interest:** The authors declare no conflict of interest.

## References

1. Sharma, B.; Dirras, G.; Ameyama, K. Harmonic Structure Design: A Strategy for Outstanding Mechanical Properties in Structural Materials. *Metals* **2020**, *10*, 1615. [[CrossRef](#)]
2. Guennec, B.; Ishiguri, T.; Kawabata, M.O.; Kikuchi, S.; Ueno, A.; Ameyama, K. Investigation on the Durability of Ti-6Al-4V Alloy Designed in a Harmonic Structure via Powder Metallurgy: Fatigue Behavior and Specimen Size Parameter Issue. *Metals* **2020**, *10*, 636. [[CrossRef](#)]
3. Fer, B.; Tingaud, D.; Hocini, A.; Hao, Y.; Leroy, E.; Prima, F.; Dirras, G. Powder Metallurgy Processing and Mechanical Properties of Controlled Ti-24Nb-4Zr-8Sn Heterogeneous Microstructures. *Metals* **2020**, *10*, 1626. [[CrossRef](#)]
4. Song, Y.; Zhang, Z.; Ma, H.; Nakatani, M.; Kawabata, M.O.; Ameyama, K. Ratcheting-Fatigue Behavior of Harmonic-Structure-Designed SUS316L Stainless Steel. *Metals* **2021**, *11*, 477. [[CrossRef](#)]
5. De La Cruz, L.G.; Celis, M.M.; Keller, C.; Hug, E. Exploring the Strain Hardening Mechanisms of Ultrafine Grained Nickel Processed by Spark Plasma Sintering. *Metals* **2020**, *11*, 65. [[CrossRef](#)]
6. Monchoux, J.P.; Couret, A.; Durand, L.; Voisin, T.; Trzaska, Z.; Thomas, M. Elaboration of Metallic Materials by SPS: Processing, Microstructures, Properties, and Shaping. *Metals* **2021**, *11*, 322. [[CrossRef](#)]
7. Dine, S.; Bernard, E.; Herlin, N.; Grisolia, C.; Tingaud, D.; Vrel, D. SHS Synthesis, SPS Densification and Mechanical Properties of Nanometric Tungsten. *Metals* **2021**, *11*, 252. [[CrossRef](#)]
8. Moser, M.; Lorand, S.; Bussiere, F.; Demoisson, F.; Couque, H.; Bernard, F. Influence of Carbon Diffusion and the Presence of Oxygen on the Microstructure of Molybdenum Powders Densified by SPS. *Metals* **2020**, *10*, 948. [[CrossRef](#)]
9. Ikram, A.; Awais, M.; Sheridan, R.; Walton, A.; Kobe, S.; Pušavec, F.; Rožman, K. Spark Plasma Sintering as an Effective Texturing Tool for Reprocessing Recycled HDDR Nd-Fe-B Magnets with Lossless Coercivity. *Metals* **2020**, *10*, 418. [[CrossRef](#)]
10. Mogale, N.F.; Matizanhuka, W.R. Spark Plasma Sintering of Titanium Aluminides: A Progress Review on Processing, Structure-Property Relations, Alloy Development and Challenges. *Metals* **2020**, *10*, 1080. [[CrossRef](#)]
11. Naimi, F.; Niepce, J.C.; Ariane, M.; Cayron, C.; Calapez, J.; Gentzittel, J.M.; Bernard, F. Joining of Oxide Dispersion-Strengthened Steel Using Spark Plasma Sintering. *Metals* **2020**, *10*, 1040. [[CrossRef](#)]
12. Téllez-Martínez, J.S.; Olmos, L.; Solorio-García, V.M.; Vergara-Hernández, H.J.; Chávez, J.; Arteaga, D. Processing and Characterization of Bilayer Materials by Solid State Sintering for Orthopedic Applications. *Metals* **2021**, *11*, 207. [[CrossRef](#)]
13. González, J.; Armas, G.; Negrin, J.; Beltrán, A.; Trueba, P.; Gotor, F.; Peón, E.; Torres, Y. Influence of Successive Chemical and Thermochemical Treatments on Surface Features of Ti6Al4V Samples Manufactured by SLM. *Metals* **2021**, *11*, 313. [[CrossRef](#)]



Review

# Harmonic Structure Design: A Strategy for Outstanding Mechanical Properties in Structural Materials

Bhupendra Sharma <sup>1,\*</sup>, Guy Dirras <sup>2</sup> and Kei Ameyama <sup>3</sup>

<sup>1</sup> Department of Mechanical Engineering, Research Organization of Science and Technology, Ritsumeikan University, 1-1-1 Noji-Higashi, Kusatsu 525-8577, Shiga, Japan

<sup>2</sup> Université Sorbonne Paris Nord, LSPM-CNRS, 99 Avenue Jean-Baptiste Clément, 93430 Villetaneuse, France; dirras@univ-paris13.fr

<sup>3</sup> Faculty of Science and Engineering, Ritsumeikan University, 1-1-1 Noji-Higashi, Kusatsu 525-8577, Shiga, Japan; ameyama@se.ritsumei.ac.jp

\* Correspondence: bhupen@fc.ritsumei.ac.jp; Tel.: +81-80-7793-0128

Received: 6 October 2020; Accepted: 28 November 2020; Published: 1 December 2020

**Abstract:** Structured heterogeneous materials are ubiquitous in a biological system and are now adopted in structural engineering to achieve tailor-made properties in metallic materials. The present paper is an overview of the unique network type heterogeneous structure called Harmonic Structure (HS) consisting of a continuous three-dimensional network of strong ultrafine-grained (shell) skeleton filled with islands of soft coarse-grained (core) zones. The HS microstructure is realized by the strategic processing method involving severe plastic deformation (SPD) of micron-sized metallic powder particles and their subsequent sintering. The microstructure and properties of HS-designed materials can be controlled by altering a fraction of core and shell zones by controlling mechanical milling and sintering conditions depending on the inherent characteristics of a material. The HS-designed metallic materials exhibit an exceptional combination of high strength and ductility, resulting from optimized hierarchical features in the microstructure matrix. The experimental and numerical results demonstrate that the continuous network of gradient structure in addition to the large degree of microstructural heterogeneity leads to obvious mechanical incompatibility and strain partitioning, during plastic deformation. Therefore, in contrast to the conventional homogeneous (homo) structured materials, synergy effects, such as synergy strengthening, can be obtained in HS-designed materials. This review highlights recent developments in HS-structured materials as well as identifies further challenges and opportunities.

**Keywords:** powder metallurgy; harmonic structure; severe plastic deformation; strength-ductility; structural characteristics

---

## 1. Introduction

Metallic materials are significantly crucial for manufacturing industry and structural applications. Metals with an optimized balance of higher strength and ductility are in demand for many industrial applications. Unfortunately, strength and ductility are antinomies in conventional homogeneous materials. Over many years, ultrafine-grained (UFG) metallic materials proved to be attractive structural materials due to higher strength [1–3], especially when compared to their coarse-grained (CG) counterparts. However, the drawback of homo UFG materials is typically a poor elongation due to the lack of sustained strain hardening rate in the early stage of deformation [4,5]. A major challenge, therefore, is to engineer novel microstructures to obtain materials with high synergetic strength and ductility. Therefore, recently, new fabrication and subsequent processing approaches were introduced to achieve overall as well as nano-scale microstructural control via grain engineering. One can now

create ultrafine-grained homo and heterostructures in metallic materials. The strength and ductility trade-off became a primary challenge in developing high-performance metallic materials.

There have been several successful research studies to achieve high strength while retaining reasonable ductility through solid solution strengthening, precipitation strengthening, transformation hardening, dispersion hardening, etc., by incorporating multiple phases in alloys with several elements, as well as developing composites [6–10]. In addition, several techniques were used to refine the microstructures and improve the mechanical properties through grain refinement by several means, for example; severe plastic deformation, thermo-mechanical treatments, friction stir processing, etc. These techniques use the interruption in the dislocations' motion, but still make a dislocation activity possible to ensure some ductility. It was also reported that using a combination of the above-mentioned approaches, i.e., compositional change and thermomechanical treatment can be used to achieve balanced mechanical properties [11,12]. The focus of this review is, however, on single-phase metallic materials, such as; pure metals (Ti and Ni) or solid solutions (SUS316L) based on principal elements.

## 2. The Strength–Ductility Behavior of Homo- and Hetero-Structured Materials

For the conventional UFG homo metallic materials, the slope of the engineering stress–strain curve after the yield point, i.e., during work hardening, is remarkably lower than that of the counterpart materials with comparatively coarse grains. Figure 1 depicts a schematic drawing of a true stress–true strain diagram of conventional homo-structured metallic materials. It is well known that, during the tensile deformation, the localized reduction in the cross-sectional area of the tensile specimen, i.e., necking, occurs when the rate of strain hardening is lower than the flow stress of the material. It can be expressed as  $d\sigma/d\varepsilon \leq \sigma$  ( $\sigma$  is the true stress and  $\varepsilon$  is the true strain).

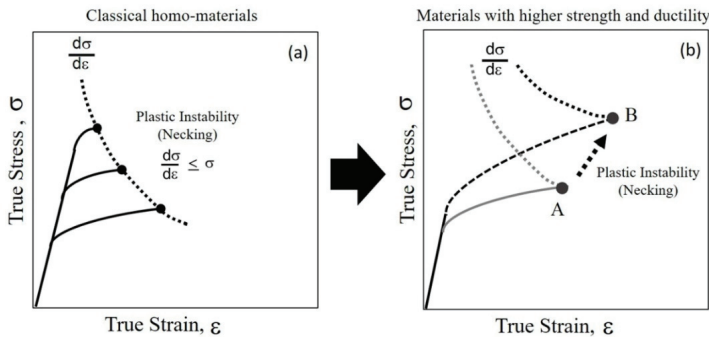


**Figure 1.** Schematic illustrations of true stress–true strain curves in; (a) materials with conventional homogeneous microstructure, and (b) advanced materials with a combination of higher strength and ductility.

In general, high strength but poor ductility of the metallic materials with microstructural homogeneity and fine grains is due to the poor strain hardening capabilities (Figure 1a). However, by introducing heterogeneities in the microstructure matrix, the strain hardening rate  $d\sigma/d\varepsilon$  of the metallic materials can be improved while preventing the inequality conditions (Figure 1b). In other words, a good combination of superior strength and ductility can be achieved when a larger strain hardening rate is achieved. In addition, at the same time, deformation localization should be suppressed to obtain further elongation.

To address this strength–ductility trade-off issue, heterogeneous structures with large microstructural heterogeneities were introduced in metallic materials [3,13–16], such as bimodal structure [17], gradient structure [18–20], gradient nano-twined structure [21], nano-laminae structure [22], and heterogeneous laminae structure [13]. Such heterogeneous-designed structures were prepared via developing modern processing techniques without changing the composition,

which includes surface grinding or rolling, severe plastic deformation, and electrodeposition. The resulting structured heterogeneous materials exhibit excellent mechanical properties.

Many pieces of research are being conducted on hetero-structured materials owing to their controllable and superior mechanical properties that are unattainable in the conventional homogeneous-structured materials. Therefore, structured heterogeneous materials are quickly emerging as a major materials research area, which also presents renewed concepts of materials science that challenged our traditional perceptions and impressions. In this review paper, we primarily focus on the microstructural heterogeneities in the metallic materials. Compared to conventional homo materials, hetero-structured metallic materials contain heterogeneous regions that contrast in their constitutive properties. It was reported that structured heterogeneous materials are advantageous properties owing to the synergetic effects occurring from the interactivity and pairing between structural contrasting. For example, the trade-off in strength and ductility can be alleviated or controlled [13–15]. This intended structural contrasting induces heterogeneous plastic deformation, and the fine-scale constituents stipulate exorbitant strain gradients. As a result, higher strain hardening and consequently uniform tensile ductility at high flow stresses can be achieved. However, the realization of heterogeneous design together with their microstructure and properties control is limited by multiple complex processing steps. Nevertheless, their properties are limited to the uni- or bidirectional (anisotropic characteristics).

Recently, Ameyama et al. proposed a novel concept of “harmonic structure” (HS) design, consisting of a specific spatial distribution of ultra-fine grains (UFG) and coarse grains (CG), that is, the CG areas (core) surrounded by three-dimensionally (3D) continuously connected network of UFG areas (shell) [23–31]. Owing to its unique topological 3D gradient structure, the harmonic-structured materials were reported to exhibit high work hardening that extends to higher strain regions, leading to delay in the initiation of plastic instability. Consequently, a good combination of high strength and high ductility can be achieved [29–31].

In the present review, an overview of the basics of harmonic structure design and highlighting recent developments in harmonic structured materials is presented, as well as identifying perspectives and future challenges and opportunities.

### 3. Concept of Harmonic Structure Design and Processing Considerations

From the above points, the harmonic structure (HS) design can be a candidate material design, which combines high strength with high ductility at the same time. Figure 2 demonstrates a concept of the HS design. The HS material is composed of a shell/core bimodal particle unit. A harmonic structure designed material is produced by the sintering of the particle units. In contrast to a homo-UFG material, HS material has a heterogeneous microstructure consisting of controlled and uniquely arranged fine and coarse grains with a particular topological distribution in a network. That is, the HS can be visualized as homogeneous on large scale but heterogeneous on a small scale, as shown in Figure 2.

During fabrication processing, it is crucial to control and optimize the characteristics of the shell/core regions, such as; volume fraction, grain size, morphology, and topology. These characteristics may strongly influence the properties of the HS materials. The physical properties of the HS materials can be affected by the grain size distribution and grain gradients and morphology of the shell/core regions. To control these factors in the as-fabricated HS compacts, it is necessary but challenging to invent efficient processing methods. In this regard, the unique three-dimensional network-type microstructure of the HS materials adds considerable complexity to processing. In addition to the wide range of multiple variables, the type of material, i.e., the behavior of a particular class of materials, also affects the microstructure of the as-fabricated HS compacts. However, in general, by varying these parameters, HS microstructure was developed in various metals and alloys. To achieve a tailor-made HS microstructure design, the following efficient and feasible processing method, based on powder metallurgy processing, was developed.

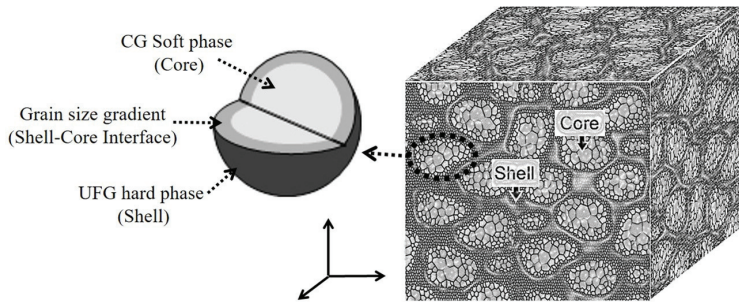


Figure 2. Concept of the harmonic structure (HS) design.

3.1. Mechanical Milling Process (MM Process)

The MM process involves mechanical milling (i.e., ball milling, high-pressure gas milling, etc.) of Plasma Rotating Electrode Processed (PREP) powder of metallic powder and their subsequent sintering. As shown in Figure 3a, powder with a bimodal grain size distribution, i.e., SPD powder surface with fine grains (shell), and comparatively less deformed (or undeformed) powder interior (core), can be fabricated by the MM process. The MM processed powder surface becomes the three-dimensional shell network structure after sintering. As depicted in the schematic diagram of Figure 3a, the depth of plastic deformation, at the powder surface, can be changed by changing the mechanical milling time. Consequently, it is feasible to achieve a tailor-made microstructure with predetermined shell/core fractions. However, it is to be noted that the deformation at the surface and respective microstructure evolution depends on the type of initial material.

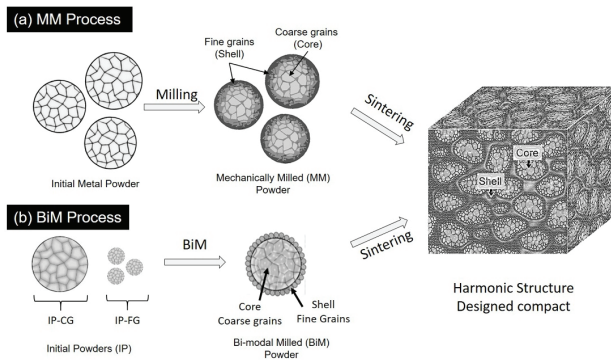


Figure 3. Fabrication processes of the harmonic structure materials; (a) Mechanical Milling (MM) and (b) Bimodal Milling (BiM) process.

3.2. Bimodal Milling Process (BiM Process)

The BiM process involves milling initial powders of coarse-grained large-sized (IP-CG) and comparatively fine-grained small-sized (IP-FG) powders, wherein the powder fractions and milling time are chosen depending on the desired fractions and grain size of shell/core, respectively [32]. The hierarchical distribution of fine/coarse-grains can be achieved due to repeated coating of plastically deformed IP-FG to the IP-CG powder, during milling. A schematic diagram illustrating the BiM powder metallurgy-based processing approach is demonstrated in Figure 3b. As depicted in the schematic diagram of Figure 3b, the fraction of a tailor-made microstructure with desired shell/core fractions can be achieved either by varying the fractions of IP-FG and IP-CG powders, and/or varying milling time.

The selection of a specific fabrication process was based on many factors such as the type of material, powder particles size, the susceptibility of the material with milling media, the permitted level of contamination from the milling vial and balls, and malleability and work hardening characteristics of the materials being processed [27]. For example, the soft materials can be flattened, i.e., might form flakes, during the severe milling process. Therefore, the BiM processing approach can be utilized to achieve a high shell fraction in a short time milling. On the other hand, less ductile materials can be processed through the MM process.

#### 4. Microstructure of BiM and MM Processed Powders

The effect of controlled milling through BiM and MM processes on the morphology and microstructure of SUS316L alloys powders is shown in Figure 4. In the BiM process, IP-FG (powder particle size  $\sim 7 \mu\text{m}$ ) and IP-CG (powder particle size  $\sim 142 \mu\text{m}$ ) powders were mixed in a 3:2 ratio, respectively, and BiM processed for 36 and 360 ks (Figure 4a,b). On the other hand, in the MM process, the PREP alloy powder of SUS316L IP-CG was milled for 108 and 540 ks.

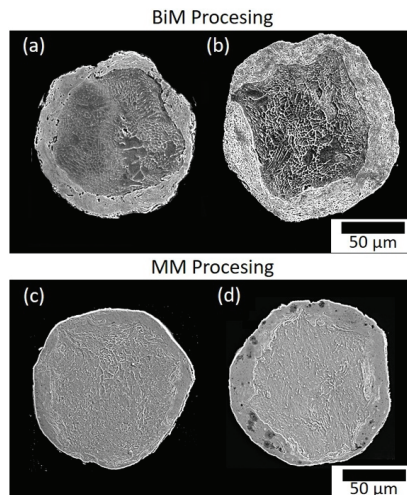


**Figure 4.** SEM images of SUS316L powders cross-section after BiM and MM processing. (a) BiM 36 ks, (b) BiM 360 ks, (c) MM 108 ks, and (d) MM 540 ks.

It is evident that the overall morphology of the spherical shape of the powder does not change as a result of both MM and BiM processing. However, it is to be noted that a highly deformed zone (shell) is formed at the surface, whereas the inner regions (Core) of the powder remain approximately undeformed or partially deformed, depending on the milling conditions. It is interesting to note that the high fraction of shell could be achieved in a shorter time of BiM processing compared to the MM processing. In contrast to the MM powder, the outer surface of BiM powder is composed of several layers of fine powder particles.

Therefore, it can be predicted that the shell evolution mechanism in both BiM and MM process is different. It was reported that the powder particle size of BiM powders increases with BiM processing time, whereas in the case of the MM process, the MM powder particle size remains approximately similar to the starting powder. Therefore, it can be assumed that the surface irregularity of the BiM powder is primarily due to the repeated coating of SPD fine powder to the surface of coarse powder, during milling. On the other hand, the surface irregularity in MM powder is owing to the surface deformation of the starting powder particles. However, it can be ensured that both MM and BiM powders show a bimodal microstructure wherein the center of powder is coarse-grained, whereas

the surface composed of SPD sub-micron-sized grains. Similar morphological changes were also reported wherein it was observed that the increase in milling time leads to the formation of the severely deformed layer, consisting of nano-crystallites, near the surface of the powders [33–37]. Moreover, it must be realized that a gradient of the degree of deformation exists in both BiM and MM processed powders, and the severity of the accumulated plastic strain decreases from the particle surface towards the center of the particles.

In particular, the successful application of the new BiM process to achieve controlled deformation in the variety of materials is of important technological interest, which is a feasible, energy-efficient, and cost-effective process, particularly, for industrial-scale production. The effectiveness of the BiM process to create a controlled microstructure at shell and core is owing to the fine and coarse powders, respectively. It must be pointed out that the finer powder particles make the milling process easier, and grain refinement occurs in a shorter time when compared to coarse powder particles. Therefore, in contrast to the prolonged milling in the MM process, significantly shorter milling might result in the development of a large shell fraction with nano grain formation. It naturally follows that one can build a hierarchical microstructure with controlled fractions of shell/core zones by varying amounts of IP-FG and IP-CG powders, and/or milling time. Optimizing such hierarchical grained zones and their fractions for a better synergy of superior strength and ductility, in an as-sintered bulk compact, calls for modern fabrication approaches for precise microstructure control. Hence, it would be appealing to analogize the designs of BiM- and MM-processed SUS316L compacts for a better interpretation and rationalization of the synergistic effects of various combinations of structural contrasts.

Figure 5 shows TEM micrographs near the shell region of the mechanically milled pure titanium powder with enlarged areas of selected rectangular areas indicated as A, B, and C. It could be observed that near to the surface, equiaxed grains (<20 nm) were observed whereas a layer of elongated grains was seen in the inner zones of the milled powder. The grain subdivision and rotation of those elongated grains led to the formation of equiaxed nano-grain structure in milled powder [30,33,37–41].

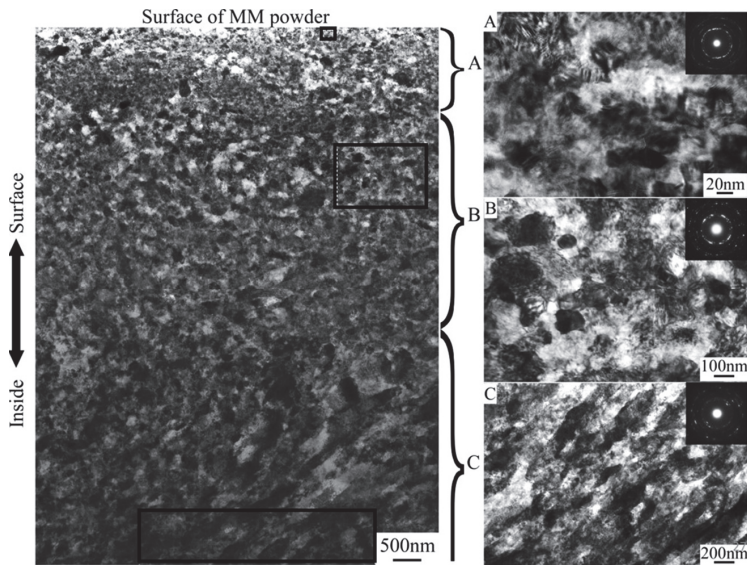


**Figure 5.** TEM micrographs of the shell area of milled pure Ti powder. Enlargement of rectangular areas of (A), (B) and (C) are separately presented.

## 5. Microstructure of Harmonic Structure Designed Compacts

The milled powders via the BiM and MM process were sintered at 1173 and 1223 K temperatures, respectively, to prepare bulk compacts. Recently, spark plasma sintering (SPS) was utilized extensively for the consolidation of powders due to fast sintering together with avoidance of significant grain growth even at high-temperature operations. The microstructures of the H-structured compacts (MM and BiM) SUS316L compacts are shown in Figure 6.

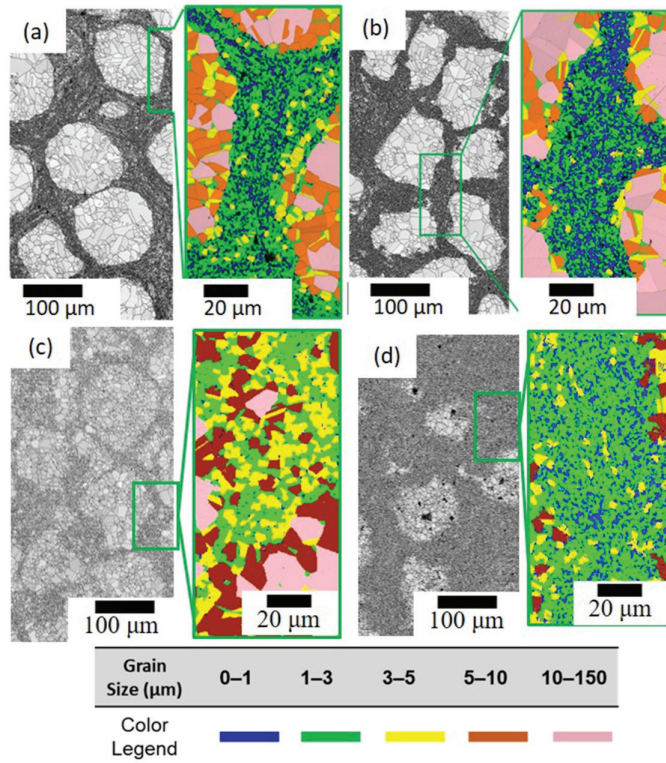


**Figure 6.** EBSD image quality maps of BiM (a,b), and MM compacts (c,d) of SUS316L. (a) BiM 36 ks, (b) BiM 180 ks, (c) MM 216 ks, and (d) MM 540 ks. The corresponding enlarged grain size images of the shell–core interface are separately shown (the grain size legend is presented at the bottom).

As shown in Figure 6a,b, the BiM compacts exhibited a network-type arrangement of bimodal grains wherein the coarse grains ( $d > 5.0 \mu\text{m}$ ) were surrounded by comparatively finer grains ( $d \leq 5.0 \mu\text{m}$ ). Particularly, it is to be noted that the well-defined and dense shell network could be achieved even after a short time (36 ks) of BiM processing (Figure 6c). The grain size contrast of the shell and core could be observed in the enlarged Electron Backscatter Diffraction (EBSD) grain size images. It should be noted that the core grains are not remarkably deformed even after a long milling time (180 ks). Therefore, it can be envisaged that the shell area of BiM compacts mainly developed due to the coating and frequent plastic deformation of fine particles to the surface of coarse particles, during milling. However, the spherical shape of the core gradually deformed with milling time, suggesting that the prolonged milling leads to the partial deformation of the outer core area. Therefore, it can be envisaged that increasing milling time leads to effective plastic deformation of fine powder, which in turn increases the fraction of fine shell grains ( $< 3 \mu\text{m}$ ), which was obvious in the shell grain size

distribution through the color-coded grain size distribution map of BiM compacts. Also, in the case of MM compacts (Figure 6c,d), a harmonic structure was achieved. However, substantial damage apparent to the core area was noticed after a long period of milling (540 ks). In addition, most notable was that even after prolonged milling up to 540 ks, the large fractions of shell grains were in the range of 3–5  $\mu\text{m}$ , which is significantly larger than that of the BiM-processed specimens. Finally, it would be worth emphasizing that, in comparison to the MM process, the BiM approach is highly efficient in achieving ultra-fine shell grains in a shorter period.

## 6. Mechanical Properties of Harmonic Structure-Designed Compacts

Figure 7 shows the representative engineering stress–strain curves of harmonic structured compacts of SUS316L developed by BiM and MM approaches. All of the HS materials that were examined indicated high strength, high ductility, and high tensile toughness at the same time. That is to say, regardless of the fabrication process, the HS compacts of SUS316L had a good combination of strength and elongation compared to the conventional counterparts developed and/or processed by different methods, such as; casting, powder metallurgy, selective laser melting, and thermomechanically treated compacts of SUS316L alloy (Figure 8) [42–61]. In general, it was reported that the conventional homo-structured compacts of SUS316L exhibited significant strength–ductility trade-off owing to the grain size strengthening effect [42–61]. However, in contrast, as shown in Figure 7, the improvement in the strength of harmonic structured SUS316L compacts were accompanied by a nominal ductility loss. The improvement in strength and nominal ductility loss can be attributed to grain boundary strengthening caused by grain refinement in the shell and higher shell fraction. Particularly, the reduction in ductility is associated with a higher shell fraction, as shown in Figure 6. Plastic deformation in most metallic materials was commonly mediated by the dislocation slip [26,27]. The increased fractions of fine-grained shell from a certain level suppressed the dislocation initiation and slip phenomena, and increased the prospect of dislocation annihilation at boundaries by thermally activated cross slip and climb, which in turn leads to ductility loss [28,29]. The most noticeable was the synergy of high strength and ductility of harmonic-structured BiM compacts, which was achieved in an efficient time compared to that achieved by MM processing. As can be seen, the improvement in mechanical properties by efficient BiM processing was encouraging, which may lead to the synergetic strength–ductility combination by introducing an optimized fraction of the shell network. In the present case, the optimized grain size and shell fractions were approximately 2  $\mu\text{m}$  and 30%, respectively [32].

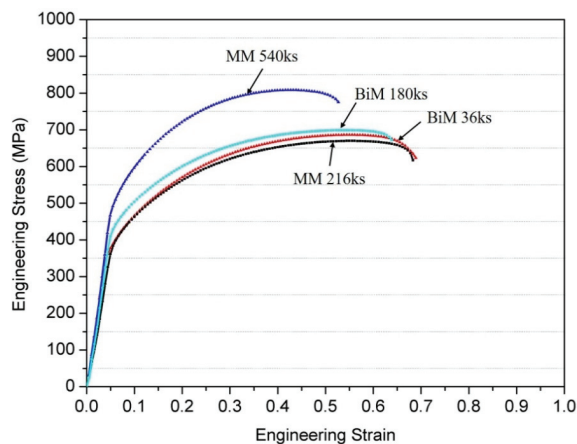


**Figure 7.** Tensile engineering stress–strain curves of harmonic structured SUS316L compacts developed through BiM and MM processes.

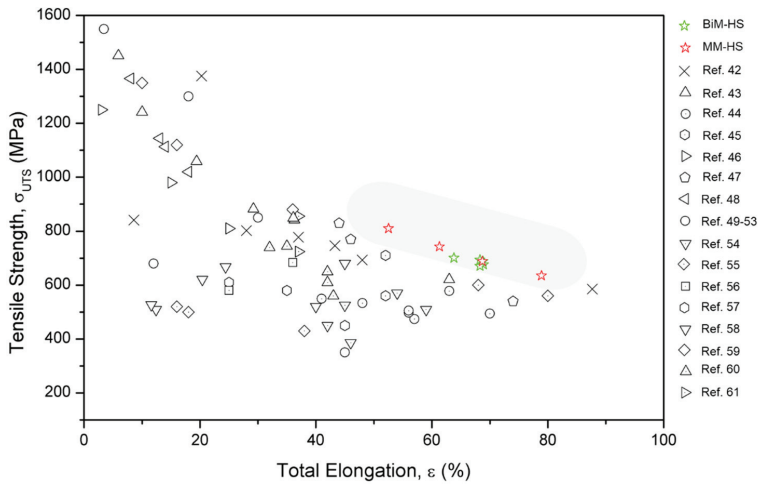


**Figure 8.** Ultimate tensile strength versus total elongation chart for HS SUS316L compacts, and their comparison with SUS316L counterparts produced by various methods [42–61].

## 7. Mechanism of the Outstanding Mechanical Properties

### 7.1. Stress Concentration Effects

Figure 9 shows the microstructure of conventional homogeneous-structured (homo) and harmonic-structured pure Ti compacts after 10% cold rolling. EBSD Kernel Average Misorientation (KAM) images show that, in contrast to the homo Ti with significant KAM values in the matrix, slight KAM value increased especially in the shell region. Since the increase in the KAM value strongly related to the dislocation storage, it suggests that deformation took place in the shell and shell/core interface regions.

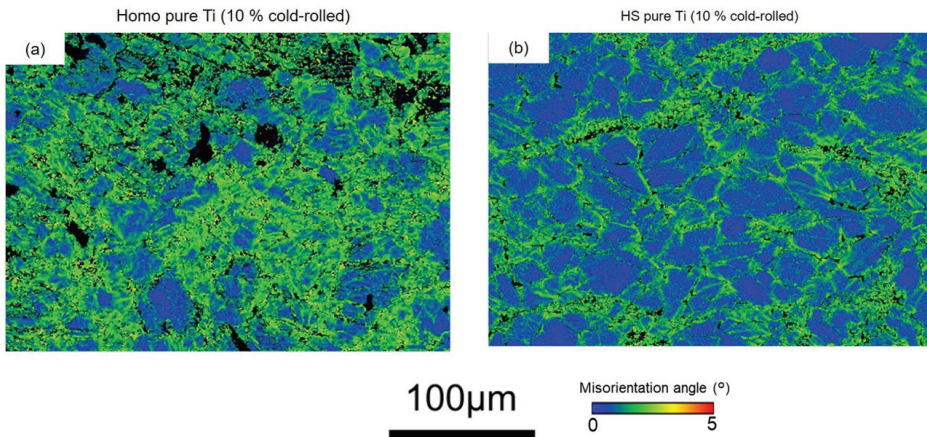


**Figure 9.** KAM image of; (a) homo and (b) HS structured pure Ti compacts.

As reported by Ameyama et al. [35] using ECCI (Electron Channeling Contrast Image) of Figure 10a: shell area and Figure 10b core area, it can be seen that dislocations were mainly in the shell grains, whereas the core dislocations were cell-like, and comparatively not highly dense

(Figure 10). These results were quite consistent with the KAM distribution observed for pure Ti (Figure 9). The higher dislocation density in the shell region was evidence of stress concentration in the shell. Therefore, it was confirmed that during the early stage of deformation, the shell and its network can be an effective dislocation source. It is to be noted that such a “dislocation-source network” structure is a unique characteristic of the HS materials. Consequently, a large strain hardening rate and higher uniform elongation can be achieved in the HS materials. Interestingly, despite the soft core regions, the hard shell deforms before the core in the early stage of deformation. Such a stress concentration effect was also predicted by a multi-scale-FEM simulation (Figure 11) [62]. From the numerical simulation, the UFG shell regions are the high-stress concentration areas, while the CG core region did not show evidence of accumulation of any significant stress concentration.

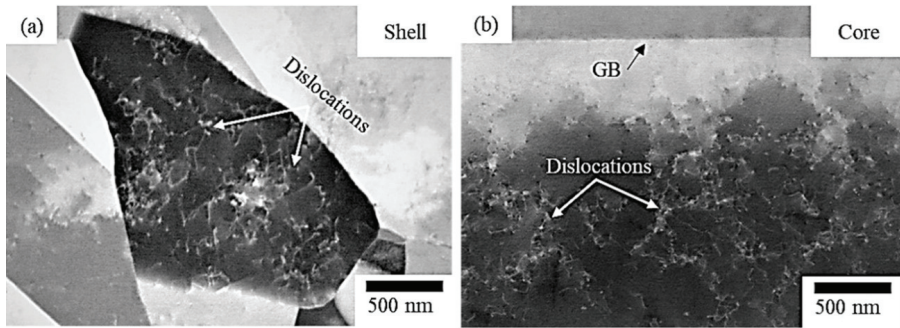


Figure 10. ECCI of pure Ni HS after 5% tensile deformation. (a): shell and (b): core.

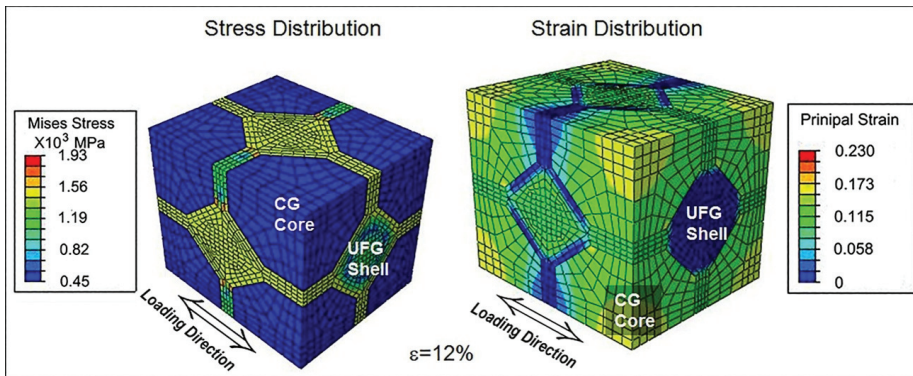


Figure 11. Numerical simulation (FEM) results of HS pure Ti illustrating the stress and strain distribution after ~12% tensile deformation [62].

### 7.2. Strain Dispersion Effects

It was also reported that the mutual constraints of the unstable UFG area and the comparatively stable CG area made the deformation processing captive and lead to a different stress level [63]. The geometrically necessary dislocations (GNDs) emerged due to the geometrical constraints of soft (core) and hard (shell) areas in the HS specimens’ need to accommodate the strain gradient areas; if not, the voids and overlaps may occur between the grain boundaries [64]. As a consequence of the interaction and amassing of dislocations, extraordinary work hardening occurs.

As shown in the numerical simulation results of strain distribution (Figure 11), higher strain concentration was seen in the shell zones aligned parallel to the tensile axis. In contrast, no evidence

of accumulated strain concentration was seen in the shell zones aligned perpendicular to the tensile deformation axis [62]. However, interestingly, accumulated strain concentration successively increased from the shell to core. Consecutively, the highest accumulated strain was observed at the center of the core.

In general, the early necking of fine-grained materials is due to high-stress concentration. The crack propagation is hard to block with fine grains owing to suppressed dislocation initiation and slip phenomenon [1,65]. However, when the well-bonded, tri-directional network of hierarchical microstructure was stressed, the fast strain localization tendency of the fine-grained shell can be effectively constrained by the stable coarse-grained core through the interfaces [66]. In addition, the strain partitioning between incompatible shell and core areas may also play a crucial role in alleviating the strain localization [62,67,68]. Such behavior may suggest that the complete shell network structure plays a crucial role in the uniform strain dispersion, and thus, deformation localization is prevented.

## 8. Fracture Behavior of HS Materials

The superior strength–ductility combination of pure HS materials can be attributed to the three-dimensional topological distribution of connected-type hard shell regions. In particular, the higher toughness can be associated with topology-driven diversion of crack propagation paths as well as an obstacle in their growth and propagation due to the soft core regions [69]. To analyze the fatigue crack propagation and growth mechanism, Kikuchi et al. [70] and Osaki et al. [71] investigated the effect of grain size on fatigue crack propagation in HS pure Ti. It was reported that the fatigue crack propagation and growth resistance of HS Ti were significantly reduced for a high-stress ratio as compared to the counterpart with homogeneous coarse-grained microstructure. Nukui et al. [72] found that the fatigue strength is increased because the resistance of the material to the initiation of fatigue cracks was improved by the grain refinement at the shell. The beginning of fatigue cracks was also observed in the coarse grains core in harmonic-structured designed materials, including CP titanium [72], Ti–6Al–4V alloys [73,74], and austenitic stainless steel [75,76]. However, in alloys, it can be attributed to both the network topology and strain-induced phase transformations, for example;  $\alpha$ -fcc to  $\epsilon$ -hcp in CCM [28]. However, further exhaustive studies should be carried out to confirm the fracture behavior of different metallic materials.

## 9. Perspectives of HS Materials and Future Challenges

Harmonic structure–designed materials are emerging structural materials that are becoming an attractive research field. The area of hetero-structured materials was extensively studied. However, in particular, harmonic structure–designed materials are in their infancy, requiring intense studies both in terms of characterization methods, scientific modeling tools, and fabrication approaches.

A complete clarification of the underlying mechanism and availability of any consolidated model regarding the excellent strengthening of HS materials is still a matter of pursuit. Some efforts were made to annotate this direction through experimental documentation as well as theoretical techniques [77–80]. In particular, owing to the unique 3D connected type microstructural design of harmonic-structured materials, rigorous efforts are required to decipher the mechanism of strengthening completely.

In addition, it should be mentioned that development and microstructure controlling of all the customized microstructures, including harmonic structure, are relatively laborious to produce and are not comprehensive. The microstructure control at micro- as well as macro-scale and repeatability in performances are another great challenge. To this aspect, further efforts are required to develop a consolidated design concept and mechanistic approach for harmonic structure–designed materials.

The technological and engineering affairs need to be addressed by both theoretical models and experiments to quantify the correlation between structural heterogeneity and mechanical performance, which is crucial for the development of harmonic structure materials with efficient design and optimized mechanical performance.

## 10. Conclusions

In this review, a relatively new concept of harmonic structure materials has been introduced, and its basic concept, mechanical performance, and advantages along with present development status and perspectives are discussed. The harmonic structure (HS)-designed metallic materials can be successfully produced by efficient powder metallurgy approaches, such as mechanical milling and bimodal milling (BiM). In contrast to the significant strength–ductility trade-off issues of conventional homogeneous-structured materials, harmonic-structured materials exhibit a superior combination of high synergetic strength and ductility. The superior tensile strength of the HS materials is owing to its unique network-type arrangement of the UFG grains (shell), which provides higher strain hardening due to the stress concentration effect, whereas the superior ductility of the HS materials is attributed to the soft core regions. The results suggested that the higher ductility of the HS materials was due to strain dispersion effects. In other words, microstructural singularity in harmonic structure design plays a crucial role in achieving an outstanding combination of strength and ductility.

**Author Contributions:** Conceptualization, B.S., G.D., K.A.; methodology, B.S.; formal analysis, B.S.; investigation, B.S.; writing—original draft preparation, B.S.; writing—review and editing, B.S., G.D., K.A.; supervision, K.A.; project administration, B.S., G.D., K.A.; funding acquisition, B.S., G.D., K.A. All authors have read and agreed to the published version of the manuscript.

**Funding:** This work was supported by the Japan Society for The Promotion of Science (JSPS) Grants-in-Aid for Scientific Research (KAKENHI) Grant Numbers 20K15064 and JP18H05256. This support is gratefully appreciated. The support by the French National Research Agency in the framework of the ANR 14-CE07-0003 “HighS-Ti” program is highly acknowledged.

**Conflicts of Interest:** The authors declare no conflict of interest.

## References

1. Meyers, M.A.; Mishra, A.; Benson, D.J. Mechanical properties of nanocrystalline materials. *Prog. Mater. Sci.* **2006**, *51*, 427–556. [[CrossRef](#)]
2. Khan, H.; Farrokh, B.; Takacs, L. Compressive properties of Cu with different grain sizes: Sub-micron to nanometer realm. *J. Mater. Sci.* **2008**, *43*, 3305–3313. [[CrossRef](#)]
3. Ma, E.; Zhu, T. Towards strength—Ductility synergy through the design of heterogeneous nanostructures in metals. *Mater. Today* **2017**, *20*, 323–331. [[CrossRef](#)]
4. Saito, Y.; Utsunomiya, H.; Tsuji, N.; Sakai, T. Novel ultra-high straining process for bulk materials—Development of the accumulative roll-bonding (ARB) process. *Acta Mater.* **1999**, *47*, 579–583. [[CrossRef](#)]
5. Estrin, Y.; Vinogradov, A. Extreme grain refinement by severe plastic deformation: A wealth of challenging science. *Acta Mater.* **2013**, *61*, 782–817. [[CrossRef](#)]
6. Manzoni, A.M.; Glatzel, U. New multiphase compositionally complex alloys driven by the high entropy alloy approach. *Mater. Charact.* **2019**, *147*, 512–532. [[CrossRef](#)]
7. Kumar, K.; Van Swygenhoven, H.; Suresh, S. Mechanical behavior of nanocrystalline metals and alloys. The Golden Jubilee Issue—Selected topics in Materials Science and Engineering: Past, Present and Future, edited by S. Suresh. *Acta Mater.* **2003**, *51*, 5743–5774. [[CrossRef](#)]
8. Zhao, Y.H.; Lavernia, E.J.; Whang, S.H. *Nanostructured Metals and Alloys*; Woodhead Publishing: Cambridge, UK, 2011; pp. 375–376.
9. Hofinger, M.; Turk, C.; Ognianov, M.; Leitner, H.; Schnitzer, R. Precipitation reactions in a Cu-Ni-Al medium carbon alloyed dual hardening steel. *Mater. Charact.* **2020**, *160*, 110126. [[CrossRef](#)]
10. Wegst, U.G.K.; Bai, H.; Saiz, E.; Tomsia, A.P.; Ritchie, R.O. Bioinspired structural materials. *Nat. Mater.* **2015**, *14*, 23–36. [[CrossRef](#)]
11. Gwalani, B.; Soni, V.; Lee, M.; Mantri, S.; Ren, Y.; Banerjee, R. Optimizing the coupled effects of Hall-Petch and precipitation strengthening in a Al 0.3 CoCrFeNi high entropy alloy. *Mater. Des.* **2017**, *121*, 254–260. [[CrossRef](#)]

12. Cheng, H.; Wang, H.Y.; Xie, Y.C.; Tang, Q.H.; Dai, P.Q. Controllable fabrication of a carbide-containing FeCoCrNiMn high-entropy alloy: Microstructure and mechanical properties. *Mater. Sci. Technol.* **2017**, *33*, 2032–2039. [[CrossRef](#)]
13. Wu, X.; Yang, M.; Yuan, F.; Wu, G.; Wei, Y.; Huang, X.; Zhu, Y. Heterogeneous lamella structure unites ultrafine-grain strength with coarse-grain ductility. *Proc. Natl. Acad. Sci. USA* **2015**, *112*, 14501–14505. [[CrossRef](#)] [[PubMed](#)]
14. Embury, D.; Bouaziz, O. Steel-based composites: Diving forces and Classifications. *Annu. Rev. Mater. Res.* **2010**, *40*, 213–241. [[CrossRef](#)]
15. Wu, X.; Zhu, Y.T. Heterogeneous materials: A new class of materials with unprecedented mechanical properties. *Mater. Res. Lett.* **2017**, *5*, 527–532. [[CrossRef](#)]
16. Lu, K. Stabilizing nanostructures in metals using grain and twin boundary architectures. *Nat. Rev. Mater.* **2016**, *1*, 16019. [[CrossRef](#)]
17. Wang, Y.; Chen, M.; Zhou, F.; Ma, E. High tensile ductility in a nanostructured metal. *Nat. Cell Biol.* **2002**, *419*, 912–915. [[CrossRef](#)]
18. Fang, T.H.; Li, W.L.; Tao, N.R.; Lu, K. Revealing Extraordinary Intrinsic Tensile Plasticity in Gradient Nano-Grained Copper. *Science* **2011**, *331*, 1587–1590. [[CrossRef](#)]
19. Wu, X.; Jiang, P.; Chen, L.; Yuan, F.; Zhu, Y.T. Extraordinary strain hardening by gradient structure. *Proc. Natl. Acad. Sci. USA* **2014**, *111*, 7197–7201. [[CrossRef](#)]
20. Thevamaran, R.; Lawal, O.; Yazdi, S.; Jeon, S.-J.; Lee, J.-H.; Thomas, E.L. Dynamic creation and evolution of gradient nanostructure in single-crystal metallic microcubes. *Science* **2016**, *354*, 312–316. [[CrossRef](#)]
21. Cheng, Z.; Zhou, H.; Lu, Q.; Gao, H.; Lu, L. Extra strengthening and work hardening in gradient nanotwinned metals. *Science* **2018**, *362*, eaau1925. [[CrossRef](#)]
22. Liu, X.C.; Zhang, H.; Lu, K. Strain-Induced Ultrahard and Ultrastable Nanolaminated Structure in Nickel. *Science* **2013**, *342*, 337–340. [[CrossRef](#)] [[PubMed](#)]
23. Zhang, Z.; Vajpai, S.K.; Orlov, D.; Ameyama, K. Improvement of mechanical properties in SUS304L steel through the control of bimodal microstructure characteristics. *Mater. Sci. Eng. A* **2014**, *598*, 106–113. [[CrossRef](#)]
24. Vajpai, S.K.; Ota, M.; Watanabe, T.; Maeda, R.; Sekiguchi, T.; Kusaka, T.; Ameyama, K. The Development of High Performance Ti-6Al-4V Alloy via a Unique Microstructural Design with Bimodal Grain Size Distribution. *Met. Mater. Trans. A* **2015**, *46*, 903–914. [[CrossRef](#)]
25. Sharma, B.; Nagano, K.; Kawabata, M.; Ameyama, K. Microstructure and mechanical properties of hetero-designed Ti-25Nb-25Zr alloy fabricated by powder metallurgy route. *Lett. Mater.* **2019**, *9*, 511–516. [[CrossRef](#)]
26. Ota, M.; Vajpai, S.K.; Imao, R.; Kurokawa, K.; Ameyama, K. Application of High Pressure Gas Jet Mill Process to Fabricate High Performance Harmonic Structure Designed Pure Titanium. *Mater. Trans.* **2015**, *56*, 154–159. [[CrossRef](#)]
27. Vajpai, S.K.; Ota, M.; Zhang, Z.; Ameyama, K. Three-dimensionally gradient harmonic structure design: An integrated approach for high performance structural materials. *Mater. Res. Lett.* **2016**, *4*, 191–197. [[CrossRef](#)]
28. Vajpai, S.K.; Sawangrat, C.; Yamaguchi, O.; Ciuca, O.P.; Ameyama, K. Effect of bimodal harmonic structure design on the deformation behavior and mechanical properties of Co-Cr-Mo alloy. *Mater. Sci. Eng. C* **2016**, *58*, 1008–1015. [[CrossRef](#)]
29. Fujiwara, H.; Oda, E.; Ameyama, K. Mechanical Milling Process as Severe Plastic Deformation Method. *Tetsu-to-Hagane* **2008**, *94*, 608–615. [[CrossRef](#)]
30. Ameyama, K.; Horikawa, N.; Kawabata, M. Unique Mechanical Properties of Harmonic Structure Designed Materials. *Tetsu-to-Hagane* **2019**, *105*, 124–126. [[CrossRef](#)]
31. Fujiwara, H.; Inomoto, H.; Sanada, R.; Ameyama, K. Nano-ferrite formation and strain-induced-ferrite transformation in an SUS316L austenitic stainless steel. *Scr. Mater.* **2001**, *44*, 2039–2042. [[CrossRef](#)]
32. Yagi, K.; Sharma, B.; Kawabata, M.; Ameyama, K. Fabrication of SUS316L Harmonic Structure Compacts by Bi-Modal Milling Process. *J. Jpn. Soc. Powder Powder Met.* **2020**, *67*, 239–244. [[CrossRef](#)]
33. Nagata, M.; Horikawa, N.; Kawabata, M.; Ameyama, K. Effects of Microstructure on Mechanical Properties of Harmonic Structure Designed Pure Ni. *Mater. Trans.* **2019**, *60*, 1914–1920. [[CrossRef](#)]
34. Sawangrat, C.; Yamaguchi, O.; Vajpai, S.K.; Ameyama, K. Application of Harmonic Structure Design to Biomedical Co-Cr-Mo Alloy for Improved Mechanical Properties. *Mater. Trans.* **2014**, *55*, 99–105. [[CrossRef](#)]

35. Ameyama, K.; Kawabata, M.; Sharma, B. ISOPE-I-19-101. In Proceedings of the 29th International Ocean and Polar Engineering Conference, Honolulu, HI, USA, 16–21 June 2019; ISBN 978-1-880653-85-2.
36. Sawangrat, C.; Kato, S.; Orlov, D.; Ameyama, K. Harmonic-structured copper: Performance and proof of fabrication concept based on severe plastic deformation of powders. *J. Mater. Sci.* **2014**, *49*, 6579–6585. [[CrossRef](#)]
37. Fujiwara, H.; Akada, R.; Noro, A.; Yoshita, Y.; Ameyama, K. Enhanced Mechanical Properties of Nano/Meso Hybrid Structure Materials Produced by Hot Roll Sintering Process. *Mater. Trans.* **2008**, *49*, 90–96. [[CrossRef](#)]
38. Fujiwara, H.; Inomoto, H.; Ameyama, K. Formation of ( $\alpha + \gamma$ ) Nano-duplex Structure by Severe Plastic Deformation in a SUS316L Stainless Steel. *Tetsu-to-Hagane* **2005**, *91*, 839–845. [[CrossRef](#)]
39. Mohamed, F.A. A dislocation model for the minimum grain size obtainable by milling. *Acta Mater.* **2003**, *51*, 4107–4119. [[CrossRef](#)]
40. Chaubey, A.K.; Scudino, S.; Khoshkhou, M.S.; Prashanth, K.G.; Mukhopadhyay, N.K.; Mishra, B.; Eckert, J. Synthesis and Characterization of Nanocrystalline Mg-7.4%Al Powders Produced by Mechanical Alloying. *Metals* **2013**, *3*, 58–68. [[CrossRef](#)]
41. Oda, E.; Fujiwara, H.; Ameyama, K. Nano Grain Formation in Tungsten by Severe Plastic Deformation-Mechanical Milling Process. *Mater. Trans.* **2008**, *49*, 54–57. [[CrossRef](#)]
42. Zheng, R.; Zhang, Z.; Nakatani, M.; Ota, M.; Chen, X.; Ma, C.; Ameyama, K. Enhanced ductility in harmonic structure designed SUS316L produced by high energy ball milling and hot isostatic sintering. *Mater. Sci. Eng. A* **2016**, *674*, 212–220. [[CrossRef](#)]
43. Li, J.; Cao, Y.; Gao, B.; Li, Y.; Zhu, Y.T. Superior strength and ductility of 316L stainless steel with heterogeneous lamella structure. *J. Mater. Sci.* **2018**, *53*, 10442–10456. [[CrossRef](#)]
44. Chen, X.; Li, J.; Cheng, X.; Wang, H.; Huang, Z. Effect of heat treatment on microstructure, mechanical and corrosion properties of austenitic stainless steel 316L using arc additive manufacturing. *Mater. Sci. Eng. A* **2018**, *715*, 307–314. [[CrossRef](#)]
45. Yin, Y.; Sun, J.; Guo, J.; Kan, X.; Yang, D. Mechanism of high yield strength and yield ratio of 316 L stainless steel by additive manufacturing. *Mater. Sci. Eng. A* **2019**, *744*, 773–777. [[CrossRef](#)]
46. Long, Q.; Lu, J.; Fang, T. Microstructure and mechanical properties of AISI 316L steel with an inverse gradient nanostructure fabricated by electro-magnetic induction heating. *Mater. Sci. Eng. A* **2019**, *751*, 42–50. [[CrossRef](#)]
47. Lu, K.; Yan, F.; Wang, H.; Tao, N. Strengthening austenitic steels by using nanotwinned austenitic grains. *Scr. Mater.* **2012**, *66*, 878–883. [[CrossRef](#)]
48. Xiong, L.; You, Z.; Lu, L. Enhancing fracture toughness of nanotwinned austenitic steel by thermal annealing. *Scr. Mater.* **2016**, *119*, 55–59. [[CrossRef](#)]
49. Chen, X.; Lu, J.; Lu, L.; Lu, K. Tensile properties of a nanocrystalline 316L austenitic stainless steel. *Scr. Mater.* **2005**, *52*, 1039–1044. [[CrossRef](#)]
50. Wang, Y.; Huang, C.; Wang, M.; Li, Y.; Zhu, Y. Quantifying the synergetic strengthening in gradient material. *Scr. Mater.* **2018**, *150*, 22–25. [[CrossRef](#)]
51. Ueno, H.; Kakihata, K.; Kaneko, Y.; Hashimoto, S.; Vinogradov, A. Enhanced fatigue properties of nanostructured austenitic SUS 316L stainless steel. *Acta Mater.* **2011**, *59*, 7060–7069. [[CrossRef](#)]
52. Poling, W.A. Grain Size Effects in Micro-Tensile Testing of Austenitic Stainless Steel. Master's Thesis, Colorado School of Mines, Golden, CO, USA, 2012.
53. Vinogradov, A.; Yasnikov, I.; Matsuyama, H.; Uchida, M.; Kaneko, Y.; Estrin, Y. Controlling strength and ductility: Dislocation-based model of necking instability and its verification for ultrafine grain 316L steel. *Acta Mater.* **2016**, *106*, 295–303. [[CrossRef](#)]
54. Zhong, Y.; Rannar, L.E.; Liu, L.; Koptuyug, A.; Wikman, S.; Olsen, J.; Cui, D.; Shen, Z. Additive manufacturing of 316L stainless steel by electron beam melting for nuclear fusion applications. *J. Nucl. Mater.* **2017**, *486*, 234–245. [[CrossRef](#)]
55. Röttger, A.; Geenen, K.; Windmann, M.; Binner, F.; Theisen, W. Comparison of microstructure and mechanical properties of 316L austenitic steel processed by selective laser melting with hot-isostatic pressed and cast material. *Mater. Sci. Eng. A* **2016**, *678*, 365–376. [[CrossRef](#)]
56. Casati, R.; Lemke, J.; Vedani, M. Microstructure and Fracture Behavior of 316L Austenitic Stainless Steel Produced by Selective Laser Melting. *J. Mater. Sci. Technol.* **2016**, *32*, 738–744. [[CrossRef](#)]

57. Bartolomeu, F.; Buciumeanu, M.; Pinto, E.; Alves, N.; Carvalho, O.; Silva, F.; Miranda, G. 316L stainless steel mechanical and tribological behavior—A comparison between selective laser melting, hot pressing and conventional casting. *Addit. Manuf.* **2017**, *16*, 81–89. [[CrossRef](#)]
58. Suryawanshi, J.; Prashanth, K.; Ramamurty, U. Mechanical behavior of selective laser melted 316L stainless steel. *Mater. Sci. Eng. A* **2017**, *696*, 113–121. [[CrossRef](#)]
59. Wang, S.; Li, J.; Cao, Y.; Gao, B.; Mao, Q.; Li, Y. Thermal stability and tensile property of 316L stainless steel with heterogeneous lamella structure. *Vacuum* **2018**, *152*, 261–264. [[CrossRef](#)]
60. Ma, M.; Wang, Z.; Zeng, X. A comparison on metallurgical behaviors of 316L stainless steel by selective laser melting and laser cladding deposition. *Mater. Sci. Eng. A* **2017**, *685*, 265–273. [[CrossRef](#)]
61. Peng, P.; Wang, K.-S.; Wang, W.; Han, P.; Zhang, T.; Liu, Q.; Zhang, S.; Wang, H.; Qiao, K.; Liu, J. Relationship between microstructure and mechanical properties of friction stir processed AISI 316L steel produced by selective laser melting. *Mater. Charact.* **2020**, *163*, 110283. [[CrossRef](#)]
62. Vajpai, S.K.; Yu, H.; Ota, M.; Watanabe, I.; Dirras, G.; Ameyama, K. Three-Dimensionally Gradient and Periodic Harmonic Structure for High Performance Advanced Structural Materials. *Mater. Trans.* **2016**, *57*, 1424–1432. [[CrossRef](#)]
63. Yang, X.; Zhang, J.; Gong, Y.; Nakatani, M.; Sharma, B.; Ameyama, K.; Zhu, X. A superior strength-ductility combination in gradient structured Cu-Al-Zn alloys with proper stacking fault energy and processing time. *Mater. Sci. Eng. A* **2020**, *789*, 139619. [[CrossRef](#)]
64. Kundu, A.; Field, D.P. Influence of plastic deformation heterogeneity on development of geometrically necessary dislocation density in dual phase steel. *Mater. Sci. Eng. A* **2016**, *667*, 435–443. [[CrossRef](#)]
65. Yang, M.; Pan, Y.; Yuan, F.; Zhu, Y.; Wu, X. Back stress strengthening and strain hardening in gradient structure. *Mater. Res. Lett.* **2016**, *4*, 145–151. [[CrossRef](#)]
66. Lu, K. Making strong nanomaterials ductile with gradients. *Science* **2014**, *345*, 1455–1456. [[CrossRef](#)] [[PubMed](#)]
67. Zheng, R.; Liu, M.; Zhang, Z.; Ameyama, K.; Ma, C. Towards strength-ductility synergy through hierarchical microstructure design in an austenitic stainless steel. *Scr. Mater.* **2019**, *169*, 76–81. [[CrossRef](#)]
68. Fan, G.; Geng, L.; Wu, H.; Miao, K.; Cui, X.; Kang, H.; Wang, T.; Xie, H.; Xiao, T. Improving the tensile ductility of metal matrix composites by laminated structure: A coupled X-ray tomography and digital image correlation study. *Scr. Mater.* **2017**, *135*, 63–67. [[CrossRef](#)]
69. Ueno, A.; Fujiwara, H.; Rifai, M.; Zhang, Z.; Ameyama, K. Fractographical Analysis on Fracture Mechanism of Stainless Steel Having Harmonic Microstructure. *J. Soc. Mater. Sci. Jpn.* **2012**, *61*, 686–691. [[CrossRef](#)]
70. Kikuchi, S.; Mori, T.; Kubozono, H.; Nakai, Y.; Kawabata, M.O.; Ameyama, K. Evaluation of near-threshold fatigue crack propagation in harmonic-structured CP titanium with a bimodal grain size distribution. *Eng. Fract. Mech.* **2017**, *181*, 77–86. [[CrossRef](#)]
71. Osaki, K.; Kikuchi, S.; Nakai, Y.; Kawabata, M.O.; Ameyama, K. The effects of thermo-mechanical processing on fatigue crack propagation in commercially pure titanium with a harmonic structure. *Mater. Sci. Eng. A* **2020**, *773*, 138892. [[CrossRef](#)]
72. Nukui, Y.; Kubozono, H.; Kikuchi, S.; Nakai, Y.; Ueno, A.; Kawabata, M.O.; Ameyama, K. Fractographic analysis of fatigue crack initiation and propagation in CP titanium with a bimodal harmonic structure. *Mater. Sci. Eng. A* **2018**, *716*, 228–234. [[CrossRef](#)]
73. Kikuchi, S.; Takemura, K.; Ueno, A.; Ameyama, K. Evaluation of the 4-points bending fatigue properties of Ti-6Al-4V alloy with harmonic structure created by mechanical milling and spark plasma sintering. *J. Soc. Mater. Sci. Jpn.* **2015**, *64*, 880–886. [[CrossRef](#)]
74. Kikuchi, S.; Kubozono, H.; Nukui, Y.; Nakai, Y.; Ueno, A.; Kawabata, M.O.; Ameyama, K. Statistical fatigue properties and small fatigue crack propagation in bimodal harmonic structured Ti-6Al-4V alloy under four-point bending. *Mater. Sci. Eng. A* **2018**, *711*, 29–36. [[CrossRef](#)]
75. Kikuchi, S.; Nakatsuka, Y.; Nakai, Y.; Nakatani, M.; Kawabata, M.O.; Ameyama, K. Evaluation of Fatigue Properties under Four-point Bending and Fatigue Crack Propagation in Austenitic Stainless Steel with a Bimodal Harmonic Structure. *Frattura ed Integrità Strutturale* **2019**, *13*, 545–553. [[CrossRef](#)]
76. Kikuchi, S.; Nukui, Y.; Nakatsuka, Y.; Nakai, Y.; Nakatani, M.; Kawabata, M.O.; Ameyama, K. Effect of bimodal harmonic structure on fatigue properties of austenitic stainless steel under axial loading. *Int. J. Fatigue* **2019**, *127*, 222–228. [[CrossRef](#)]

77. Wang, X.; Cazes, F.; Li, J.; Hocini, A.; Ameyama, K.; Dirras, G. A 3D crystal plasticity model of monotonic and cyclic simple shear deformation for commercial-purity polycrystalline Ti with a harmonic structure. *Mech. Mater.* **2019**, *128*, 117–128. [[CrossRef](#)]
78. Liu, J.; Dirras, G.; Ameyama, K.; Cazes, F.; Ota, M. A three-dimensional multi-scale polycrystalline plasticity model coupled with damage for pure Ti with harmonic structure design. *Int. J. Plast.* **2018**, *100*, 192–207. [[CrossRef](#)]
79. Dirras, G.; Tingaud, D.; Ueda, D.; Hocini, A.; Ameyama, K. Dynamic Hall-Petch versus grain-size gradient effects on the mechanical behavior under simple shear loading of  $\beta$ -titanium Ti-25Nb-25Zr alloys. *Mater. Lett.* **2017**, *206*, 214–216. [[CrossRef](#)]
80. Momprou, F.; Tingaud, D.; Chang, Y.; Gault, B.; Dirras, G. Conventional vs. harmonic-structured  $\beta$ -Ti-25Nb-25Zr alloys: A comparative study of deformation mechanisms. *Acta Mater.* **2018**, *161*, 420–430. [[CrossRef](#)]

**Publisher’s Note:** MDPI stays neutral with regard to jurisdictional claims in published maps and institutional affiliations.



© 2020 by the authors. Licensee MDPI, Basel, Switzerland. This article is an open access article distributed under the terms and conditions of the Creative Commons Attribution (CC BY) license (<http://creativecommons.org/licenses/by/4.0/>).



Article

# Investigation on the Durability of Ti-6Al-4V Alloy Designed in a Harmonic Structure via Powder Metallurgy: Fatigue Behavior and Specimen Size Parameter Issue

Benjamin Guennec <sup>1,\*</sup>, Takayuki Ishiguri <sup>2</sup>, Mie Ota Kawabata <sup>3</sup>, Shoichi Kikuchi <sup>4</sup>, Akira Ueno <sup>3</sup> and Kei Ameyama <sup>3</sup>

<sup>1</sup> Department of Mechanical System Engineering, Faculty of Engineering, Toyama Prefectural University, Kurokawa 5180, Imizu, Toyama 959-0398, Japan

<sup>2</sup> Lead Frame Business Unit, Mitsui High-tec Inc., 965-1 Oaza Nakaizumi, Nogata, Fukuoka 822-0011, Japan; takayuki-ishiguri@mitsui-high-tec.com

<sup>3</sup> Department of Mechanical Engineering, Faculty of Science and Engineering, Ritsumeikan University, 1-1-1 Noji-higashi, Kusatsu, Shiga 525-8577, Japan; mie-ota@fc.ritsumei.ac.jp (M.O.K.); ueno01@fc.ritsumei.ac.jp (A.U.); ameyama@se.ritsumei.ac.jp (K.A.)

<sup>4</sup> Department of Mechanical Engineering, Faculty of Engineering, Shizuoka University, 3-5-1 Johoku, Naka-ku, Hamamatsu, Shizuoka 432-8561, Japan; kikuchi.shoichi@shizuoka.ac.jp

\* Correspondence: bguennec@pu-toyama.ac.jp; Tel.: +81-766-56-7500

Received: 28 April 2020; Accepted: 10 May 2020; Published: 14 May 2020

**Abstract:** In the present work, the four-point bending loading fatigue properties of a heterogeneously distributed grain size microstructure consolidated from Ti-6Al-4V alloy powder are studied. The microstructure involved here, a so-called “harmonic structure”, possesses quasi-spherical large grain regions (“cores”) embedded in a continuous fine grain region (“shell”). Unlike the previous reports dealing with this issue, the effect of the specimen size on the fatigue characteristics is also probed, since two distinct specimen configurations are considered. Furthermore, the obtained experimental data are compared with the corresponding fatigue results derived from homogeneous coarse grain counterparts. Contrary to homogeneous structure material, discrepancies on both the fatigue strength and the fatigue crack initiation aspects are found for the harmonic structure material. Consequently, the present work aims to clarify the underlining phenomena involved in the specimen size effect detected for Ti-6Al-4V designed in the harmonic structure. A less active interface surface between the core and the shell combined with a wider critical volume in the large size specimen should be the main reasons of the fatigue strength discrepancy.

**Keywords:** fatigue; titanium alloy; bimodal structure; size effect; EBSD investigation; fatigue crack growth

## 1. Introduction

As the mechanical properties of metallic materials are highly influenced by their microstructures, advanced material processes have been developed to acquire superior strengths. Among them, the grain refinement of polycrystalline metallic materials is an effective way to increase yield stress [1–3]. Nevertheless, fine-grained structural materials also lead to a critical loss of ductility. To reach both high strength and high ductility simultaneously, numerous microstructural designs have been proposed lately [4–11]. The most common strategy to achieve such superior mechanical properties consists in the design of bimodal grain size structures, possessing coarse and fine grains. Such structures are reported to enhance the back-stress hardening of metallic materials [11]. Fabrication of

such heterogeneous microstructures can be controlled by several techniques, such as severe plastic deformation processes [8,11,12] or the recently developed cold spray additive manufacturing [13].

Another process for the creation of heterogeneous structure materials is given by the flexibility of the powder metallurgy route. Taking advantage of this characteristic, a peculiar bimodal structure having approximately spherical coarse grain regions (hereafter referred as the “cores”) surrounded by a continuous fine grain network (denoted as “shell”) has been developed [14–19]. This so-called “harmonic structure”, obtained from spark plasma sintering (SPS), enhances the tensile strength of Ti-based materials [14–21] compared with homogeneous grain size counterparts without significant loss of ductility. Nevertheless, tensile properties are not sufficient to assess the reliability of harmonic structured compounds for structural purposes. Indeed, the investigation of the fatigue behavior is one of the crucial aspects to probe before attempting any application as structural material. Therefore, several works have already been carried out to estimate the properties of materials tailored into harmonic structures under cyclic loading [20–27]. An increase of the fatigue endurance is reported, in line with the static tensile strength, despite the decrease of the fatigue stress intensity factor threshold. However, these reports involved miniature sized specimens (specimen thickness of 1 mm) due to the limited diameter of initial sintered compacts considered. Therefore, it is interesting to undertake investigation on the fatigue behavior of harmonic structured materials based on thicker specimens to acquire a refined image of its behavior from a macroscopic viewpoint, as examination of the specimen size effect on the fatigue properties of material presenting bimodal microstructure is very scarce.

In the present work, the four-point bending fatigue aspects of Ti-6Al-4V designed in a harmonic structure have been investigated using two specimen size configurations. In particular, the present report involves fatigue tests performed with the specimens’ size following the ISO 22214 Standard, which is significantly larger than the one accepted in our previous work [20]. The experimental results will be compared with the fatigue behavior derived from miniaturized sized specimens, accepting a configuration similar to [20]. Furthermore, the effect of the harmonic structure itself is also examined, since homogeneous coarse grains microstructure material is involved in this work, for both specimen size configurations. The experimental results highlight a significant influence of the specimen size on the fatigue strength of Ti-6Al-4V designed in a harmonic structure, whereas homogeneous material shows a similar fatigue strength for both size configurations. In addition, noticeable differences on the fatigue crack initiation mechanisms are observed. Regardless of the size of the specimen, the fatigue crack propagation path in the harmonic structure material is indifferent of the location of the shell and core regions. In this study, a series of electron backscatter diffraction (EBSD) data acquisitions are undertaken to assess the geometrically necessary dislocations (GNDs) accumulation in the fatigued harmonic material, revealing an effect of the specimen size. Based on these experimental results, coupled to the introduction of a simplified model for comparison of the interface activity between the shell and the cores, the main reasons for the size effect arisen in the present report can be grasped.

## 2. Experimental Procedure

### 2.1. Material Processing

Even though the material processing is following the same procedure already described elsewhere [21], this section will sum up the main processing stages. Raw material is 186  $\mu\text{m}$ -particle diameter Ti-6Al-4V powder, prepared by a plasma rotating electrode process (PREP). The material inside the initial powder presents an acicular microstructure, which is a typical characteristic of  $\alpha'$  martensitic transformation induced by PREP rapid cooling, with an average hardness of 326 Hv [17]. The chemical composition of this powder is introduced in Table 1. This powder is subjected to mechanical milling (MM) for 90 ks in an argon atmosphere, to generate a several tens micron-thick layer of fine grains from the powder surface, resulting in 397 and 369 Hv average hardness values inside the fine grain layer and powder center region, respectively [17]. The obtained powder is then consolidated by SPS at 1123 K for 1.8 ks in a vacuum to obtain the MM material. For the sake of

comparison, sintered samples from the as-received initial powder (IP) are considered, leading to IP material. The sintered compacts of MM and IP materials consist of a cylindrical geometry with a 50 mm diameter and a height of 11 mm. Post SPS examination indicates a relative density of 99.9% of the compacts, which suggests a limited number of pores inside the examined materials, as already reported [14]. The compacts are large enough to be able to cut off every needed specimen from the same compact for each material. In other words, only one compact for each material has been sintered to provide all required specimens.

**Table 1.** Chemical composition of the Ti-6Al-4V plasma rotating electrode process (PREP) powder (mass %).

| Al        | V         | Fe        | H     | N           | O           | C      | Ti   |
|-----------|-----------|-----------|-------|-------------|-------------|--------|------|
| 6.24~6.37 | 4.10~4.15 | 0.10~0.13 | 0.002 | 0.005~0.006 | 0.108~0.116 | 0.0024 | Bal. |

## 2.2. Mechanical Testing Procedure

The uniaxial tensile properties of both the MM and IP materials have been investigated through AG-X plus a tensile testing machine (Shimadzu Corp., Kyoto, Japan). To this end, tensile specimens accepting the dimensions depicted in Figure 1a are subjected to crosshead displacement control tests at an initial strain rate of  $5.6 \times 10^{-4} \text{ s}^{-1}$ . The strain measurement is assured by two strain gauges attached on opposite surfaces to each other to optimize the recording accuracy.

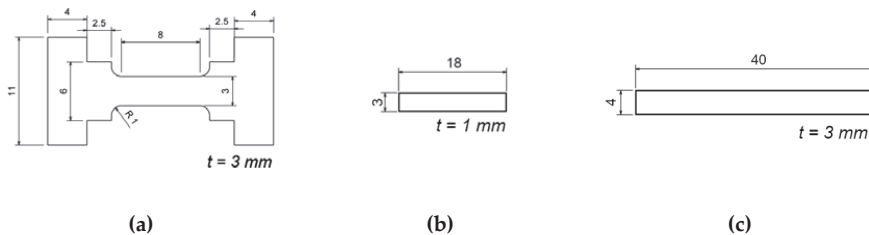


**Figure 1.** Shapes and dimensions of the specimens. (a) Tensile specimen; (b) fatigue miniature size (MS) specimen; and (c) fatigue standard size (SS) specimen.

The fatigue characteristics of the investigated compounds are conducted as follows. Load-controlled fatigue tests under four-point bending loading have been performed using two distinct specimen sizes:

- The miniature size (hereafter denoted MS) specimen with length, width and thickness dimensions of 18, 3 and 1 mm, respectively (see Figure 1b). To this end, an electro-dynamic fatigue testing machine using a 9514-AN/SD actuator (EMIC Corp., Tokyo, Japan), operating at a loading frequency of 10 Hz, is considered. The frame geometry of the four-point bending loading adopts an inner span of 5 mm and an outer span of 15 mm. Such a configuration is identical to the one accepted in our previous work [20].
- The standard size (SS) specimen, presenting the length, width and thickness values of 40, 4 and 3mm, respectively (see Figure 1c). The dedicated frame possesses inner and outer spans of 10 and 30 mm, respectively, in accordance with the ISO 22214 Standard. To this end, a servo-hydraulic fatigue testing machine (SMH201, SAGINOMIYA, Tokyo, Japan), accepting a loading frequency of 20 Hz, has been used.

Regardless of the specimen size, small chamfers have been introduced by #2000 grinding paper on the edges of every fatigue specimen to relieve the stress concentration there. The tensile surface of the fatigue specimens is finished by 1  $\mu\text{m}$  alumina suspension buffing. All fatigue tests have been carried out in air and at room temperature environment, considering a stress ratio  $R (= \sigma_{\min}/\sigma_{\max})$  of 0.1. Fatigue tests were terminated at  $10^7$  cycles for unbroken specimens.

### 2.3. Analysis Tools

Observations of the fracture and the tensile surfaces of the failed specimens were carried out using a SU6600 SEM (Hitachi, Tokyo, Japan), equipped with an HKL NordlyF camera for EBSD acquisition, with AZtec 3.1 software (Oxford Instrument, Abington, UK) for data processing. A critical angle of  $5^\circ$  has been accepted to define grain boundaries in the present work. Some investigations included in this work involve kernel average misorientation (KAM) analysis to determine the local lattice rotation, based on the orientation of the fifth nearest neighbor pixels, with a distance between two neighbors (i.e. step size) of  $0.25 \mu\text{m}$ . The same microscope is also equipped with an energy dispersive X-ray spectrometry (EDS) device for chemical composition analysis. Every fatigue strength regression showed in *S-N* diagrams in the present work is obtained by the JSMS-SD-11-08 standard [28].

## 3. Experimental Results

### 3.1. Characterization of the Materials' Microstructure

The microstructures of the obtained compacts were investigated prior to the mechanical testing campaign by the EBSD technique, over a surface of  $500 \mu\text{m} \times 400 \mu\text{m}$  regions. The experimental results are displayed through grain size (GS) maps in Figure 2, where the black lines highlight high angle boundaries having a misorientation angle higher than  $15^\circ$ . One example of the microstructure found from the IP material is shown in Figure 2a, where a large predominance (approximately 80%) of acicular large grains, appearing in red color, is found. The remaining consists of some fine grains, presumably induced by a thin layer of such grain at the initial powder surface. According to these experimental results, the average grain size in the IP material is  $11.6 \mu\text{m}$ .

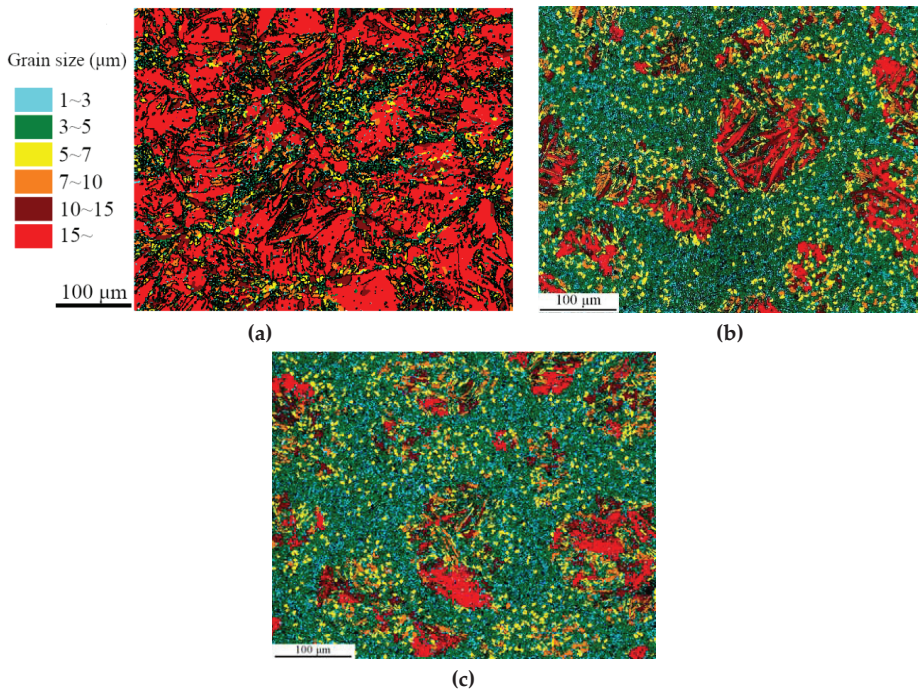


**Figure 2.** Microstructure characterization of the investigated materials displayed in the form of grain size and high angle boundaries maps. (a) IP material; (b) MM material in the inner region; and (c) MM material in the outer region of the sintered compact. Step size of  $0.25 \mu\text{m}$ .

The corresponding microstructure characterization for the MM material has been undertaken at two different spots of the sintered compact. Indeed, since the present report manipulates a sintered compact having larger dimensions than the previous reports [20,21], a temperature gradient throughout the compact may arise in the SPS process. In such a case, the microstructure of the MM material should reveal significant discrepancies depending on its relative position in the compact. Therefore, Figure 2b,c present examples of the microstructures found in the MM material in the inner and outer regions of the sintered compact. These regions are located at a maximum distance of 3 mm from the center and the edge of the sintered compact, respectively. For both GS maps, MM material consists of coarse grains regions accepting mainly acicular geometry, surrounded by a continuous network of fine equiaxed grains. Consequently, the MM material highlights a harmonic structure.

In addition, the Figure 2b,c outlines the absence of significant microstructure differences. Grain possessing an equivalent diameter larger than 5  $\mu\text{m}$  is denoted as “coarse” (and referred to as “fine” in the opposite case), and a refined analysis of the MM material’s microstructures in the inner and outer regions is given in Table 2, based on two distinct EBSD acquisitions. The numerical results highlight very close figures, in both regions, which assure similar microstructures of the MM material throughout the entire compact.

**Table 2.** Microstructure of mechanical milling (MM) material in the inner and outer regions of the sintered compact.

| Position in Compact                          | Inner Region | Outer Region |
|--|--------------|--------------|
| Areal fraction of coarse grains (%)          | 31           | 32           |
| Average coarse grain size ( $\mu\text{m}$ )  | 7.1          | 7.1          |
| Overall average grain size ( $\mu\text{m}$ ) | 4.3          | 4.3          |

### 3.2. Tensile Tests Results

Static mechanical properties on average values, based on nominal stress calculation, are listed in Table 3. One can note that MM material highlights both a larger ultimate tensile strength  $\sigma_{\text{UTS}}$  and elongation at fracture  $\delta$  than IP counterpart. This trend, which has been reported for material designed in a harmonic structure [14–19], is usually induced by the ability to reach larger elongation before emergence of necking phenomenon. To reconfirm this feature, an example of the true stress–true strain curve is presented in Figure 3 for each material investigated. The MM material shows both superior yield stress and enhanced capability to deform uniformly. This combination results in a higher tensile strength than the IP counterpart, in addition with a postponed necking phenomenon.

**Table 3.** Average mechanical properties of the MM and initial powder (IP) materials based on nominal stress–strain curve.

| Material | Tensile strength $\sigma_{\text{UTS}}$ (MPa) | Yield Stress at 0.2% Offset $\sigma_y$ (MPa) | Reduction of Area $\varphi$ (%) | Elongation at Fracture (%) |
|----------|--|--|---------------------------------|----------------------------|
| IP       | 1092   | 984  | 34.0                            | 22.7                       |
| MM       | 1124   | 1089   | 33.3                            | 23.3                       |

It is noteworthy that the tensile strength levels obtained in the present investigation from both the IP and MM materials are significantly larger than in our previous study [20], outlining a gap of approximately 150 MPa. Indeed, the microstructure observed in this previous report revealed significantly larger grain sizes, with an overall average grain size of 26.3 and 16.9  $\mu\text{m}$  for IP and MM materials, respectively. Thus, the higher tensile strength reported in the present work is likely caused by the finer microstructures.

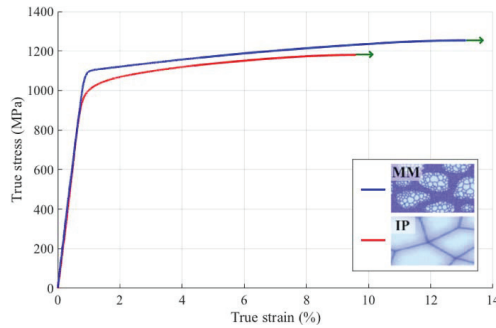


**Figure 3.** Example of the true stress–true strain curves from the IP and MM materials. Green arrows underline the beginning of necking phenomenon.

### 3.3. Fatigue Tests Results

#### 3.3.1. Fundamental Fatigue Strength from the MS Configuration

Firstly, let us focus on the fatigue test results related to the MS configuration only. The corresponding fatigue strength results are depicted in the form of an *S-N* curve, in Figure 4a. According to the *S-N* diagram, IP and MM compounds show equivalent strength in the  $N_f < 10^6$  cycles region, whereas the MM material highlights a slight increase of fatigue strength compared to its IP counterpart for the  $N_f > 10^6$  cycles region. Therefore, the fatigue endurance at  $10^7$  cycles of the MM material ( $738 \pm 15$  MPa) is higher than the IP one ( $683 \pm 14$  MPa). A similar trend has been reported in our previous work dedicated to Ti-6Al-4V alloy [20], as emphasized in Figure 4a. The fatigue strength offset between data from [20] and reported in the present study is caused by the tensile strength discrepancy of the investigated materials, as mentioned in Section 3.2.

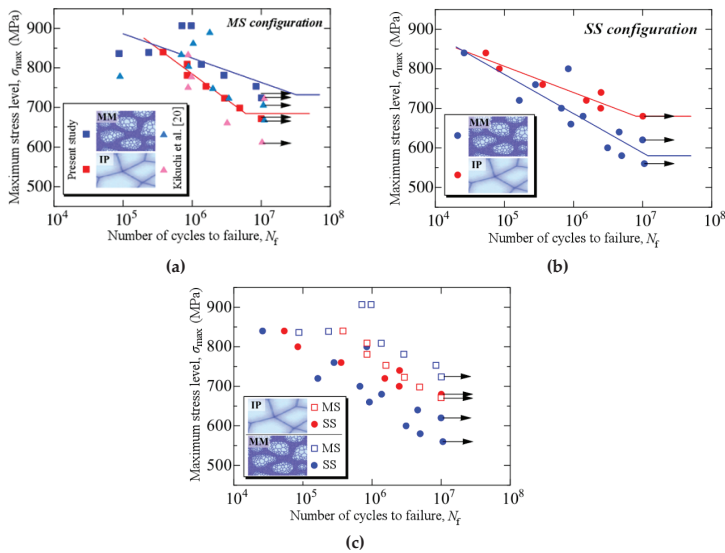


**Figure 4.** Fatigue data obtained from IP and MM materials in the form of *S-N* diagrams. (a) Case of MS configuration only and comparison with experimental results from our previous work, data from [20]; (b) case of SS configuration only; and (c) entire collected data in the same diagram. Arrows indicate run-out tests.

### 3.3.2. S-N Characteristics from SS Specimens

The *S-N* diagram comparing the fatigue strength measured in the SS configuration for both the IP and MM materials is presented in Figure 4b. One can note that the fatigue strength is almost equivalent in the  $N_f < 2 \times 10^5$  cycles region, in a way rather similar to the results found in Section 3.3.1 for the MS configuration. However, in a clearly opposite trend to the MS configuration, the MM compound shows a distinct decrease of fatigue strength in the  $N_f > 2 \times 10^5$  cycles region, compared to its IP counterpart. This decrease is particularly visible in the region of the  $10^6 < N_f < 10^7$  cycles, where several specimens made of the MM material highlight fatigue failure at low stress levels ranging from 580 to 640 MPa. It results in a  $570 \pm 10$  MPa fatigue endurance for the MM material, significantly lower than the  $680 \pm 20$  MPa one found for the IP counterpart. Therefore, the experimental data obtained from the SS configuration are in discrepancy with the data collected from the MS configuration.

In order to better grasp the situation here from a strictly fatigue strength viewpoint, Figure 4c gathers the *S-N* data obtained in the present study from both specimen size configurations in the same diagram. On the one hand, even though a slight discrepancy is found from the IP material fatigue strengths from the MS and SS configurations in the limited fatigue region, the fatigue endurances at  $10^7$  cycles are similar. Thus, no significant specimen size effect on the fatigue properties of Ti-6Al-4V in the IP structure is detected here. On the other hand, the MM material highlights a clear specimen size effect, where the fatigue endurance decreased from  $738 \pm 15$  to  $570 \pm 10$  MPa for the MS to SS configurations, respectively.

### 3.3.3. Fatigue Crack Initiation Features

In the case of the MS configuration, the typical features of micrographs focused on the fatigue crack initiation region are depicted in Figure 5. In a way similar to the observations carried out in our previous work [20] involving only experiments on the MS configuration, the IP compound showed a crack initiation at the specimen's tensile surface revealing clear facets, as depicted in Figure 5a. Due to the size of facets observed, the crack nucleated from acicular coarse grains of the structure. For the MM material, the fatigue crack initiation has occurred at three different possible positions underlined by white ellipses in Figure 5b–d: (i) at the tensile surface (Figure 5b); (ii) showing facets in contact with the surface (Figure 5c); and (iii) inside the specimen body (Figure 5d). In accordance to the related micrographs, regardless the position of the crack initiation region, one can detect clear facets. According to our previous work, such facets are certainly caused by the basal slip in the  $\alpha$ -phase grain [20]. Due to the size of the formed facets at the initiation site, cracks are certainly nucleated inside a core of the harmonic structure, in agreement with our previous work [20]. An analysis of the occurrences of these three nucleation patterns is depicted in the form of an *S-N* diagram, in Figure 5e. Clearly, the distinct patterns are well distributed over the *S-N* diagram. Thus, rather than an effect of the fatigue loading level or fatigue life region, the pattern occurrence is presumably governed by the intrinsic local resistance against fatigue crack nucleation of the specimen. Several literature reports [29–32] have underlined similar fatigue strengths from interior and surface-induced crack mechanisms in Ti-6Al-4V alloy, in line with the experimental results found in the present work.

Let us now introduce the fatigue crack initiation features observed in the SS configuration. Two nucleation patterns were found for the IP material, as depicted in Figure 6a,b. In Figure 6a, the nucleation site takes place at the specimen's tensile surface, whereas the interior induced initiation is shown in Figure 6b. Regardless of the position of the initiation, similar facets to the one depicted in Figure 5 can be observed, thus reasonably induced by the same basal slip mechanism discussed earlier in this section. In the case of the MM material, four distinct fatigue crack initiation modes have been identified and relevant micrographs are presented in Figure 6c–f. In Figure 6c, the crack initiation takes place close to the chamfer of the specimen. However, an orthogonal viewpoint of the fracture surface is not suitable to observe the nucleation site. Thus, a tilted micrograph taken in the orientation highlighted by the black arrow is introduced as an inset of Figure 6c, where facets similar to Figure 5d are found. The size of the facets, probably induced by the basal slip mechanism, suggests that the

initiation is nucleated from the core of the harmonic structure, in a way similar to the MM material in the MS configuration. On the other hand, Figure 6d underlines intergranular crack initiation, which occurred from a core in regard to the size of the intergranular facets thus formed. For a unique specimen case, the crack was nucleated far from the tensile surface, as depicted in Figure 6e, where pores can be observed (see inset). These kinds of defects are certainly induced by SPS processing, leading to the fatigue crack nucleation. Furthermore, occurrences of cracks induced by inclusions, located certainly in the shell of the MM material, were found. Indeed, Figure 6f shows a typical example of a fatigue crack initiation site, where an inclusion has been detected by the means of an EDS analysis carried out in the white-squared region highlighted on the micrograph. Local high concentrations of Ca, Mg and O chemical elements are detected, in this particular case. Some other inclusions also present Si atoms. Since titanium alloys are known to be relatively clean compounds [30,33], such foreign atoms in Ti-6Al-4V alloy are certainly induced by a contamination of the powder previous to SPS processing. Furthermore, the IP counterpart is not prone to such a fatigue crack initiation phenomenon, leading to the suggestion that the mechanical milling process likely causes this contamination.

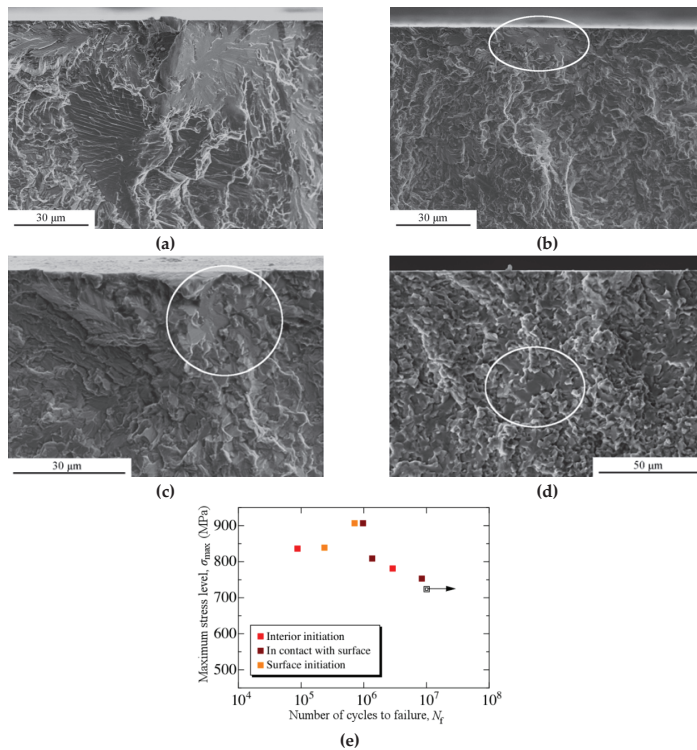


**Figure 5.** Typical fatigue crack initiation features in the MS configuration. The white ellipse highlights the crack initiation site. (a) Intragranular facets at the tensile surface for IP material ( $\sigma_{max} = 753$  MPa,  $N_f = 1.59 \times 10^6$  cycles); (b) facets at the tensile surface for MM material ( $\sigma_{max} = 907$  MPa,  $N_f = 7.14 \times 10^5$  cycles); (c) facets in contact with the tensile surface for MM material ( $\sigma_{max} = 907$  MPa,  $N_f = 9.71 \times 10^5$  cycles); (d) interior-induced initiation feature with formation of facets for MM material ( $\sigma_{max} = 836$  MPa,  $N_f = 8.76 \times 10^4$  cycles); and (e) fatigue crack initiation phenomenon occurrence for MM material in the form of an S-N diagram.

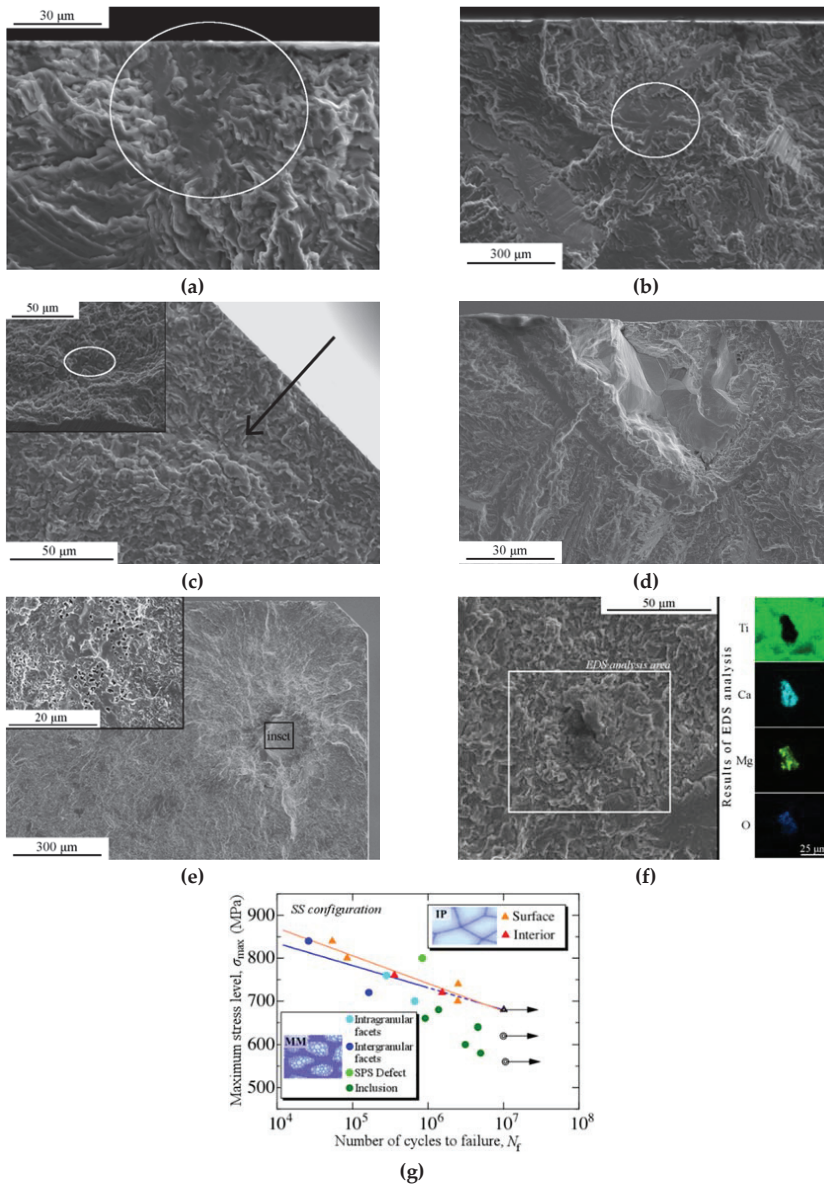


**Figure 6.** Typical fatigue crack initiation features found in SS configuration, for IP material (a,b) and MM material (c–f). The white ellipse highlights the initiation site. (a) Initiation at the tensile surface with facets ( $\sigma_{\max} = 700$  MPa,  $N_f = 2.48 \times 10^6$  cycles); and (b) interior-induced initiation with facets ( $\sigma_{\max} = 720$  MPa,  $N_f = 1.54 \times 10^6$  cycles); (c) intragranular initiation mechanism from a core forming facets ( $\sigma_{\max} = 700$  MPa,  $N_f = 6.65 \times 10^5$  cycles); (d) intergranular initiation from a core ( $\sigma_{\max} = 840$  MPa,  $N_f = 2.61 \times 10^4$  cycles); (e) initiation from pore defects ( $\sigma_{\max} = 800$  MPa,  $N_f = 8.40 \times 10^5$  cycles); (f) initiation from an inclusion detected by EDS analysis ( $\sigma_{\max} = 660$  MPa,  $N_f = 9.18 \times 10^5$  cycles); and (g) fatigue crack initiation phenomenon occurrence in the form of an S-N diagram, where the regression in blue excludes fatigue data from inclusion-induced nucleation phenomenon.

### 3.3.4. Fatigue Crack Propagation Aspects in the MM Material

In the case of the MM material, typical features of the fatigue crack propagation zone are depicted in Figure 7a,b, corresponding to the MS and SS specimen configurations, respectively. One can notice formation of apparent dark zones in the fatigue crack propagation region, regardless of the specimen size. The most preminent zones are highlighted by white-dotted ellipses in Figure 7a,b. In order to clarify the nature of these zones, a refined analysis of the region highlighted by a solid ellipse in Figure 7b will be carried out. A high magnification micrograph of the corresponding zone is shown in Figure 7c.

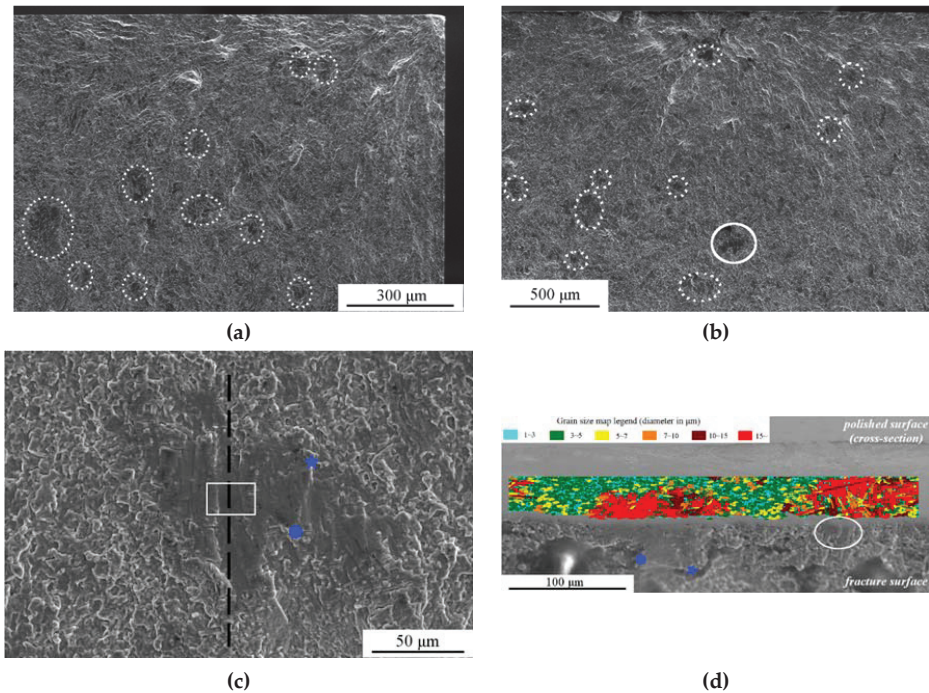


**Figure 7.** Analysis of the fatigue crack propagation features in MM material. (a) Overview of the fatigue crack propagation region, MS configuration ( $\sigma_{\max} = 781$  MPa,  $N_f = 2.89 \times 10^6$  cycles); (b) overview of the fatigue crack propagation region, SS configuration ( $\sigma_{\max} = 680$  MPa,  $N_f = 1.38 \times 10^6$  cycles); (c) high magnification micrograph of the dark zone highlighted by a solid white ellipse in (b); and (d) after  $90^\circ$  clockwise rotation, acquisition results from the electron backscatter diffraction (EBSD) technique in the form of a grain size map showing the microstructure beneath the dark zone analyzed. Blue dots in (c,d) indicate the same locations before and after rotation.

The specimen has been grinded along the vertical black broken line displayed in Figure 7c, and then the newly created surface was finished by oxide polishing suspension (OPS). The prepared surface is then subjected to an EBSD analysis to monitor the microstructure beneath the dark zone pattern. Acquisition results thus obtained are depicted in Figure 7d, where the specimen orientation has been rotated to  $90^\circ$  clockwise and tilted at an angle of  $70^\circ$ , showing the prepared cross-section surface and the fracture surface on the upper and lower sides of the micrograph, respectively. In order to understand more easily the respective locations on the fracture surfaces depicted in Figure 7c,d, two distinct location spots in both photographs have been highlighted by two reference points appearing in blue color.

The results from the EBSD analysis conducted on the prepared surface are presented in the form of a GS map, in Figure 7d. This map underlines the presence of the coarse grain structure beneath the investigated dark zone. This analysis demonstrates that the dark zone is induced by the fatigue crack propagation through the core of the MM material. Furthermore, on the right-hand side of the same map, one can also point out another coarse grain region beneath the fracture surface. Even though a dark zone as large as the initially investigated one cannot be observed on the fracture surface, a tiny region that depicts similar features is also highlighted by a white ellipse. The reason for the size discrepancy between these two zones observed on the fracture surface results from the relative locations of the crack path and the two cores. Indeed, the crack path almost gets through the center of the core in the initial studied region, whereas the crack path propagates only close to the outer region of the core located at the right-hand side of the EBSD analyzed region. Therefore, these experimental results demonstrate that the fatigue crack path is unaffected by the microstructure features of the harmonic structure, at least in locations far from the fatigue crack initiation site. Similar behaviors for Ti-based materials designed in a harmonic structure have been recently reported in [34,35].

### 3.3.5. Characterization of the Fatigue Behavior of MM Material by Local Misorientation Analysis

The Section 3.3.2 emphasized distinct fatigue resistance levels of the MM material depending on its specimen size configuration, i.e., MS or SS specimens. This fatigue behavior discrepancy is mandatory to clarify. To this end, this section aims at identifying possible divergences between one individual specimen of each size (MS and SS) prone to the same stress level  $\sigma_{\max} = 780$  MPa. According to the *S-N* regression curves introduced in Figure 4a,b, the respective fatigue lives  $N_f$  for the MS and SS configurations are  $5.0 \times 10^6$  and  $9.0 \times 10^4$  cycles, respectively. Since both values are remarkably distinct to each other, the present discussion will consider four arbitrary fatigue stages of 0% (initial state), 5%, 20% and 60% of the respective fatigue lives  $N_f$ .

For each specimen considered, prior to testing, the tensile surface was finished by OPS to obtain an observation condition suitable for EBSD data acquisition. Then, EBSD analyses were performed at every fatigue stage described earlier in this section at the same peculiar location prone to the maximum bending moment. To ensure meaningful data processing, the lattice rotation over a region covering roughly ten cores and its surrounding shell network has been probed. EBSD data results are presented in the form of KAM maps in Figure 8. Figure 8a–d depicts the KAM maps for the SS specimen at 0%, 5%, 20% and 60% of  $N_f$ , respectively. In a similar trend to the results observed from harmonic materials prone to uniaxial tension tests, the lattice misorientation increases in the shell network [22,36,37]. Furthermore, Figure 8e,f displays the corresponding KAM maps for the MS specimen at the initial stage and at 60% of  $N_f$ , respectively. Even though the lattice rotation shows a similar trend to the SS specimen, the shell network in Figure 8f presents a KAM value at 60% of  $N_f$  significantly larger in the MS configuration than the SS one, in accordance with the color scale.

To further discuss these collected data, the present analysis considers the KAM average value, as a hint of the concentration of GNDs [38–41]. The average KAM value is calculated on the basis of KAM distribution considering classes width of  $0.05^\circ$  over the  $0^\circ$  to  $5^\circ$  range. The obtained values, for both the MS and SS specimen size configurations, are presented through bar diagrams in Figure 9. First, let us introduce in Figure 9a the KAM average values obtained from the whole analyzed surface (i.e., the entire surface shown in Figure 8). Whereas the SS specimen shows a slight increase of the KAM average value at approximately  $0.86^\circ$  after 5%  $N_f$  and then keeps almost constant up to 60%  $N_f$ , the analyzed surface from the MS specimen emphasized a steady increase of the KAM average value from approximately  $0.85^\circ$  to  $0.99^\circ$ . Since the core regions are concentrating high KAM values, such data processing is obviously dependent on the core fraction in the considered areas. Furthermore, in accordance with Figure 8, a change of lattice misorientation occurs essentially in the shell of the harmonic structure. Thus, KAM average values were also investigated in one selected shell location for each specimen size configuration, highlighted by a white square in Figure 8a,e, for the SS and MS configuration, respectively. The corresponding results are shown in a bar diagram in Figure 9b. In an

analogous trend to Figure 9a, the collected data from the shell location emphasized a clear increase of the KAM average value in the MS specimen, whereas the increasing trend in the SS configuration is rather limited, reaching a saturation level after only 5%  $N_f$  stage. This discrepancy suggests that the MM material designed in a harmonic structure does not undergo the same hardening behavior under cyclic loading in the MS and SS configurations. Further discussions will be elaborated in Section 4.4.

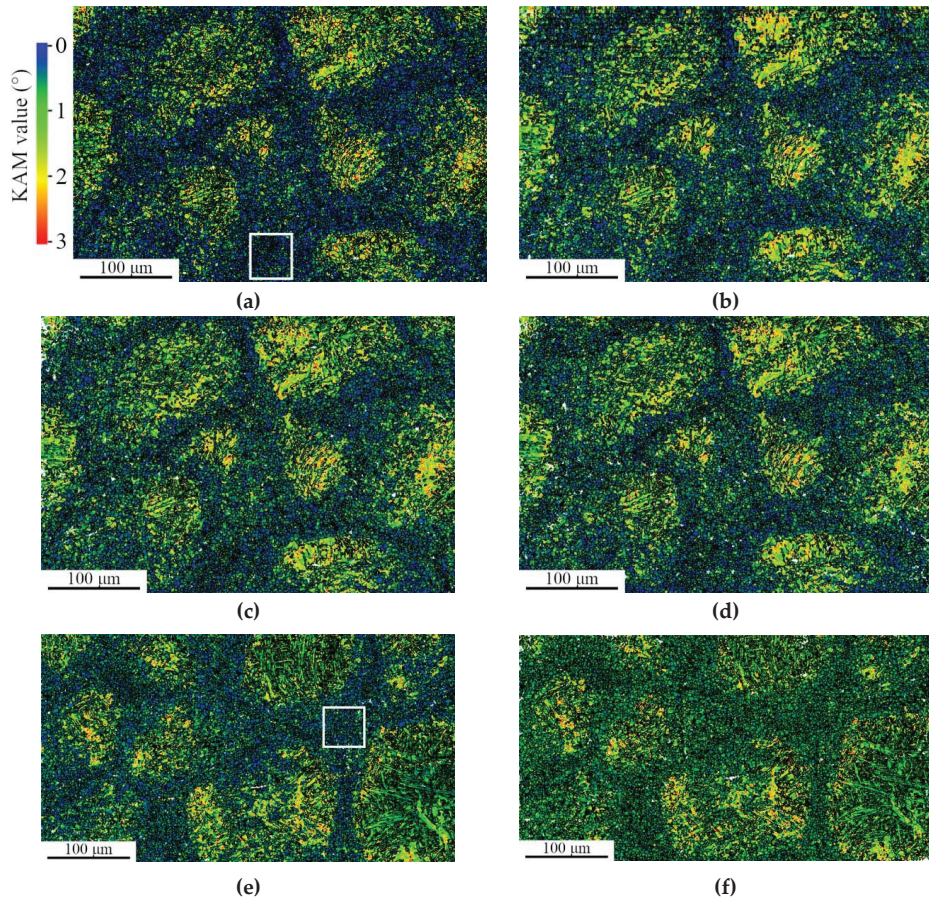


**Figure 8.** Kernel average misorientation (KAM) maps obtained from the fatigue specimen on the tensile surface, MM material. Results from the SS configuration at initial state (0%  $N_f$ ) and 5%  $N_f$ , 20%  $N_f$  and 60%  $N_f$  are displayed in (a–d), respectively. Results from MS configuration at initial state and 60%  $N_f$  are included in (e,f), respectively. Step size of 0.25  $\mu\text{m}$ . Color range from blue (0°) to red (3° and higher).

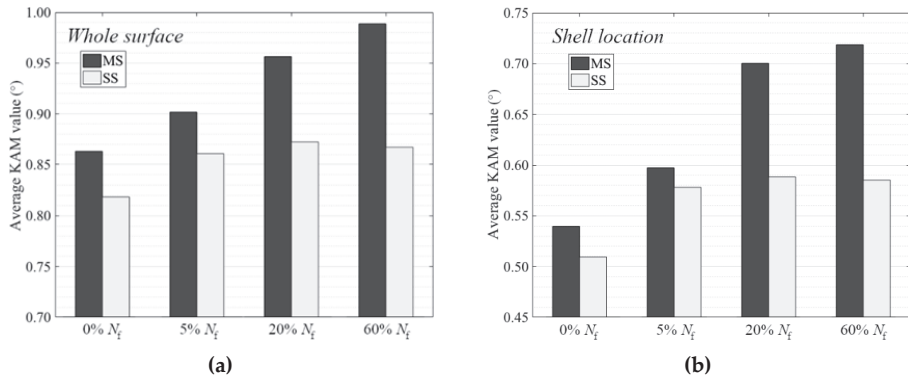


**Figure 9.** Comparison of the KAM average values in both MS and SS specimen configurations on the whole surface and in the shell location, in (a,b), respectively. “Whole surface” is dealing with the analysis of the entire surface shown in Figure 8; “shell location” is corresponding to the data inside the white-squared zone outlined in Figure 8a,e.

**4. Discussion**

The present discussion will further analyze some remaining interrogations relative to the fatigue behavior of Ti-6Al-4V designed in a harmonic structure. Therefore, these questions will be addressed in the following Sections 4.1–4.4.

*4.1. Why the Inclusion Induced Initiation Mechanism Occurs Exclusively in the  $10^6 \sim 10^7$  Cycles Region?*

In order to answer to this question, a refined analysis of the inclusion-induced fatigue fracture needs to be carried out, from fracture surface observations. Consequently, several critical aspects relating to these inclusions, such as its depth from the tensile surface  $d_{inc}$  or its projected size on the fracture surface  $area^{1/2}$  have been listed in Table 4. In this table, the stress range at the inclusion site  $\Delta\sigma_{at}$  takes into consideration the bending stress gradient. According to the numerical values introduced in Table 4, one can undertake the calculation of the stress intensity factor induced by the inclusion  $\Delta K_{inc}$ , accepting the following Equation (1), proposed by Murakami and Endo [42].

$$\Delta K_{inc} = 0.5 \cdot \Delta\sigma_{at} \sqrt{\pi \cdot area^{1/2}} \tag{1}$$

**Table 4.** Characteristics of inclusions generating fatigue crack initiation phenomenon (MM material, SS configuration).

| Number of Cycles to Failure $N_f$ (Cycles) | Depth of Inclusion $d_{inc}$ ( $\mu\text{m}$ ) | Stress Range at Inclusion $\Delta\sigma_{at}$ (MPa) | Projected Size of Inclusion $area^{1/2}$ ( $\mu\text{m}$ ) |
|--|--|---|--|
| $9.18 \times 10^5$                         | 100  | 553   | 22.6   |
| $1.38 \times 10^6$                         | 141  | 553   | 17.4   |
| $4.99 \times 10^6$                         | 84   | 492   | 18.3   |
| $3.12 \times 10^6$                         | 149  | 485   | 18.3   |
| $4.58 \times 10^6$                         | 72   | 547   | 12.4   |

The obtained results are displayed in Figure 10, where  $\Delta K_{inc}$  is represented in the y-axis, as a function of the number of cycles to failure, with  $N_f$  as the x-axis. One can see that the fatigue life tends to increase when the stress intensity factor range induced by the inclusion decreases. In accordance with the experimental results from [21,24], this diagram also indicates the values of the effective stress intensity factor range threshold  $\Delta K_{eff,th} = 2.9 \text{ MPa}\sqrt{\text{m}}$  for long cracks in the MM material prone to the same stress ratio of  $R = 0.1$ . Obviously, the stress intensity factor range induced

by inclusions  $\Delta K_{inc}$  takes place in the region lower than the threshold one for long cracks. Fatigue failure induced by small-size inclusion requires numerous stressing cycles to generate a propagating crack, as usually discussed in literature reports dealing with very high cycle fatigue regime [43,44]. In particular, experimental results similar to Figure 10 have been highlighted for high strength steels investigated in very high cycle regime [45,46]. Thus, due to the size of the involved inclusions, the related fatigue crack nucleation can reasonably occur only in the vicinity of the high cycle fatigue region limit ( $N_f \sim 10^7$  cycles).

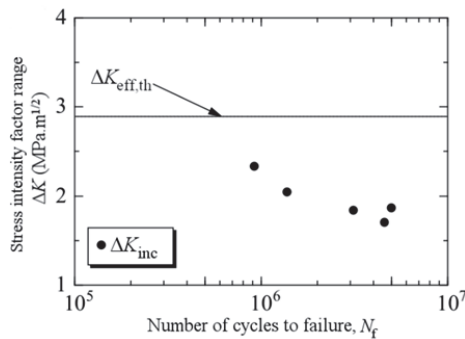


**Figure 10.** Relationship between stress intensity factor ranges induced by inclusions  $\Delta K_{inc}$  and fatigue life, in comparison with effective threshold value for long cracks  $\Delta K_{eff,th}$  of MM material.

#### 4.2. Why the MS Configuration did not Show Any Inclusion-Induced Fatigue Rupture?

Unlike the SS configuration, none of the MM material specimen fatigued in the MS one was prone to inclusion-induced crack nucleation. This observation is certainly induced by the difference of critical volume between the specimen size configurations investigated here.

Indeed, it is well known that defects in the microstructure of a metallic part have a higher probability to be found in large size specimens than in small size ones. According to Table 4, the inclusion-induced crack nucleation happened at a maximum depth of approximately 150  $\mu\text{m}$  in the SS configuration. Considering the nominal specimen thickness of 3 mm, the local stress level at 150  $\mu\text{m}$  depth corresponds to 90% of the maximum one. Therefore, let us consider a specimen critical volume with a threshold level of 90% of the maximum stress in the rest of the present report. Denoting the critical volume height of the SS configuration  $h_{SS} = 150 \mu\text{m}$ , the reciprocal critical volume height for MS configuration becomes  $h_{MS} = 50 \mu\text{m}$ . In regard to the inclusion projected size  $area^{1/2}$  ranging from 12.4 to 22.6  $\mu\text{m}$  (see Table 4), it seems unlikely that such inclusions were formed in a 50  $\mu\text{m}$  thick layer. Besides, one can note the limited number of MS specimens ruptured in the  $N_f = 10^6 \sim 10^7$  cycles region, decreasing statistically the probability of the occurrence of inclusion-induced initiation in the present work. From these viewpoints, the absence of inclusion-induced fatigue crack initiations can be reasonably grasped.

#### 4.3. Why the Fatigue Nucleation Site Tends to Move from a Surface-Induced to an Interior-Induced Pattern When Transitioning from the MS to SS Configuration?

According to the literature, the transition of the surface- to interior-induced fatigue crack initiation pattern in Ti-alloys depends on various parameters, such as the material microstructure [30] or the stress ratio [32,33,47]. In addition to these parameters, the type of fatigue loading has undoubtedly an influence on the fatigue crack initiation site, since bending loading induces a stress gradient with a maximum value at the tensile surface, whereas no-stress gradient axial loading should favor the interior-induced mechanism.

The transition from the MS to SS configuration goes hand in hand with a notable change of the stress gradient exerted on the specimen, leading to an increase of the critical volume's height, as already

discussed in Section 4.2. Thus, it is reasonable to observe more interior-induced nucleation occurrences in the SS configuration, regardless of the microstructure of the studied materials. Furthermore, the surface to interior transition is more distinct in the case of the MM material, since the critical volume's height  $h_{SS}$  becomes larger than the core diameter value. Therefore, the crack is way more likely to initiate from the "second row" of the core regions from the tensile surface, as schematically illustrated in Figure 11. This second row of cores offers a significantly larger number of potential fatigue crack initiation sites inside the specimen, resulting in the heavy interior-induced fatigue crack nucleation trend observed for the MM material in SS configuration.

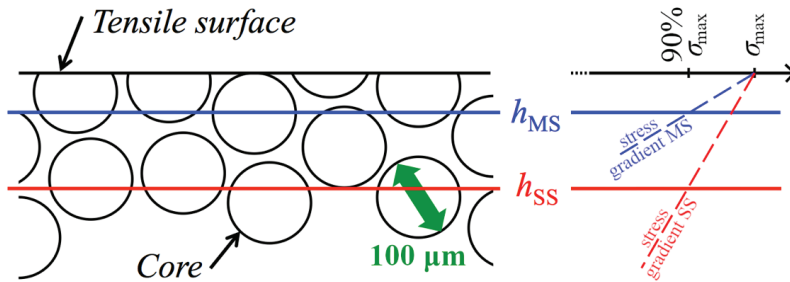


**Figure 11.** Schematic 2D illustration of the harmonic structure prone to two different critical volume heights  $h_{MS}$  and  $h_{SS}$ , corresponding to the MS and SS configurations, respectively.

In addition to the stress gradient induced by the fatigue loading type, Adachi et al. [29] have proposed a mechanism taking into consideration the influence of compressive residual stress induced by the localized plastic deformation due to the tension-tension fatigue loading for Ti-alloys. Similar discussions have been evocated in [33,48] to discuss the transition from surface- to interior-induced crack initiation trend. Even though the authors cannot assure that this phenomenon is at stake here, it may contribute to the interior-induced initiation pattern observed in the present report.

#### 4.4. Putting Aside the Inclusion-Induced Ruptures, Why MM Material did not Show Equivalent Fatigue Strength in MS and SS Configurations?

Since contamination of the powder during the mechanical milling process generates the inclusions found in the MM material, this feature is not intrinsically caused by the harmonic structure itself. However, even though fatigue failure data induced by inclusions is taken aside, Figure 12 underlines a fatigue strength in the MS configuration 100 MPa higher than the SS configuration's one. As a consequence, the present work demonstrated an effect of the specimen size on the fatigue strength of the Ti-6Al-4V material designed in a harmonic structure.

Further investigations on the behavior of the MM material have been undertaken through KAM analysis from a series of EBSD data acquisitions, as introduced in Section 3.3.5. Both configurations underlined an increase of the KAM values in the shell network of the harmonic structure. Nevertheless, the increasing trend was notably more distinct in the MS configuration compared with the SS one. This significant increase of the average KAM value in the shell network in the MS configuration is interpreted as an intense accumulation of GNDs there, i.e., a hint of back-stress hardening.

Indeed, heterogeneous structured materials in general are usually said to enhance the back-stress hardening in comparison with homogeneous counterparts. This feature of heterogeneous materials was noted a long time ago in a study by Ashby [49], which pointed out the essential role of GNDs to mitigate the voids and overlaps between neighboring grains having different mechanical properties. Such a trend has been experimentally reported lately for harmonic structured materials. Park et al. [50] compared the back-stress levels in homogeneous and harmonic structured SUS 304L stainless steel derived from the strain partitioning method. The heterogeneous harmonic material showed a significantly larger back-stress component than the homogeneous counterpart. From another viewpoint, several

analyses based on the finite element method (FEM) have been conducted. Yu et al. [51] reported that most of the stress is distributed on the shell, whereas most of the strain is concentrated in the core of the harmonic structure. Similar conclusions have been drawn from another FEM analysis conducted by Wang et al. [52] simulating monotonic and cyclic shear loading, leading to the conclusion that “the shell regions form a thin but hard skeleton enveloping the multicrystalline soft core region.” Mompioni et al. [37] have performed TEM observations on harmonic  $\beta$ -titanium alloy, leading to the following behavior: (i) at low strain, the soft core tends to yield first, resulting in formation of slip bands there; (ii) these slip bands eventually extend up to the hard shell, which activate dislocation sources from GBs in highly constrained grains in the shell; (iii) such sources generate an accumulation of dislocations in the form of piles-up or tangles, inducing an increase of the GND density in the shell. It should be noted that similar dislocation nucleation in the hard phase of an heterogeneous Ti-6242Si alloy has been reported [53]. This mechanism hardens the shell network of the harmonic structure, allowing it to bear the majority of the external load in the process. Analogous behavior is reported more generally in the heterogeneous structure materials [9].

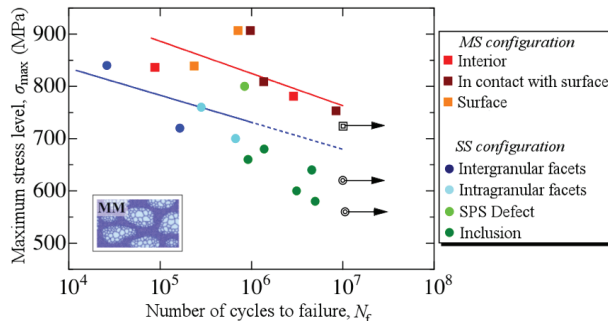


**Figure 12.** Occurrences of the different fatigue crack initiation features for MM material in MS and SS configurations. The red line denotes the regression for the MS configuration, whereas the corresponding regression for the SS configuration in blue excludes fatigue data from inclusion-induced crack nucleation phenomenon.

As pointed out in Section 3.3.5, experimental results from the average KAM values suggest that the size of the specimen impacts the ability of the MM material to generate GNDs in the shell. Which feature could reasonably suppress the GNDs accumulation in the SS configuration? According to the previous TEM observations [37], the interface between the hard and soft regions fundamentally contributes in the back-stress hardening of harmonic materials. Therefore, the present work proposes a simplified model for assessment of the active interface in both the MS and SS configurations. This model is based on the following assumptions:

- MM material consists of an “assembly” of  $u = 150 \mu\text{m}$  edge length cubic pattern, where the core takes place in a  $r_c = 50 \mu\text{m}$ -radius spherical region at its center (i.e., the region outside the sphere corresponds to the shell region). It leads to a harmonic structured material having a core areal fraction of 35%, close to the actual value in the MM material investigated here, as written in Table 2.
- The active interface takes place only inside the critical volume region, i.e., for a depth lower than  $h_{MS}$  and  $h_{SS}$  for the MS and SS configurations, respectively. Since the bending stress is maximum in this region, core grains inside the critical volume are very likely to yield there, generating the GNDs accumulation at the core interface.
- A core region generates an active interface only if its center is inside the critical volume region. Indeed, it is reasonable to consider that a sufficient volume of the core region is needed to cause dislocation pile-ups and tangles at the interface between the core and shell regions. For the sake

of simplicity, the authors propose that this sufficient core volume threshold is half of the total core region, resulting in this third assumption.

Based on these assumptions, a 2D illustration of the model is displayed in Figure 13, where the active interface is highlighted in purple color. Accordingly, the active interface length  $L_i$  depends on the relative locations of the core region and the tensile surface. Therefore, let us consider that  $c$  is the distance between the tensile surface and the center of the core region. Furthermore, introduce  $\alpha$ ,  $\beta$  and  $\beta'$  angles defined as  $\sin \alpha = c/r_c$ ,  $\sin \beta = (h_{SS}-c)/r_c$  and  $\sin \beta' = (h_{MS}-c)/r_c$ , as shown in Figure 13a,b. As  $h_{SS}$  is larger than the diameter of the core region, the active interface length is  $(L_i)_{SS} = r_c(\pi + 2\alpha)$  for  $0 < c \leq r_c$ ,  $(L_i)_{SS} = 2\pi r_c$  for  $r_c \leq c \leq 2r_c$  and  $(L_i)_{SS} = r_c(\pi + 2\beta)$  for  $2r_c \leq c < 3r_c$ . In the case of the MS configuration,  $(L_i)_{MS} = 2r_c(\alpha + \beta')$  for  $0 \leq c \leq r_c$ . After noticing that critical volume heights  $h_{SS}$  and  $h_{MS}$  correspond to  $3r_c$  and  $r_c$  values respectively, the collected interface length function traces are plotted in Figure 13c,d for the SS and MS configurations, respectively. Comparing the average values of the obtained functions  $\overline{(L_i)_{SS}}$  and  $\overline{(L_i)_{MS}}$ , and taking into consideration the critical volume discrepancy between the MS and SS configurations, the active length interface indexes, denoted  $(i_L)_{MS}$  and  $(i_L)_{SS}$ , are defined by Equations (2) and (3) for the MS and SS configurations, respectively.

$$(i_L)_{MS} = \frac{\overline{(L_i)_{MS}}}{h_{MS}} \quad (2)$$

$$(i_L)_{SS} = \frac{\overline{(L_i)_{SS}}}{h_{SS}} \quad (3)$$

Developing the Equations (2) and (3) results in the following numerical values:  $(i_L)_{MS} = 2(\pi - 2)$  and  $(i_L)_{SS} = 2(3\pi - 2)/9$ . Therefore, the active length interface index in MS configuration is nearly 40% higher than the one derived from SS configuration. One can also carry out a similar approach involving the spherical interface surface in a 3D viewpoint, in substitution to the length in the 2D one. The corresponding activated interface surface  $S_i$  functions are represented in Figure 13e,f for the MS and SS configurations, respectively. In a way comparable to Equations (2) and (3), let us define the active surface interface indexes  $(i_S)_{MS}$  and  $(i_S)_{SS}$  by the ratios of the activated surface average values over the critical surfaces in both configurations involved, i.e.,  $u \times h_{MS}$  and  $u \times h_{SS}$  for MS and SS, respectively. Numerical applications of these two surface indexes gives  $(i_S)_{MS} = 2\pi/3$  and  $(i_S)_{SS} = 10\pi/27$ , which emphasize a value 80% larger for MS configuration. The index gaps reported from activated lengths and surfaces viewpoints are induced by two features: (i) the very narrow critical volume height  $h_{MS}$ , which tends to maximize the active interface fraction for MS configuration, and (ii) the low fraction of the core region in the investigated MM material, which increases the distance between each core region and decreases the active interface index for the SS configuration.

Even though this model consists in a simplified overview of the interaction at the interface between the core and shell regions, it draws the main reasons for the lower ability of the shell region at the specimen surface to generate GNDs in the SS configuration, in agreement with the experimental results discussed in Section 3.3.5 outlining a low saturation level value of KAM in shell region. As reported for other heterogeneous structure materials [54,55], and in accordance with theoretical discussion by Ashby [49], insufficient GNDs accumulation leads to strain localization phenomenon. In the case of the harmonic structure, Park et al. [50] outlined that strain localization may take place inside grains of the core region, in line with the fatigue crack initiation site observed in Figure 6. Such strain localization phenomenon is very likely to generate early fatigue crack nucleation.

Lastly, as discussed in Section 4.3, the larger critical height in the SS configuration than the MS one results in a subsequent larger amount of core region locations in the critical volume. Since accumulation of GNDs is very limited in the SS configuration, each new core region inside the critical volume can be considered as a “weak point”, where the crack can potentially initiate, due to strain localization phenomenon. Therefore, the decreasing fatigue strength of the MM material in the SS configuration, highlighted by the S-N curves in Figure 12, is caused by the combination of two features: (i) the limited

GNDs accumulation resulting in possible strain localization phenomenon inside the core regions, and (ii) the larger amount of core regions inside the critical volume, which highly increases the probability of an early fatigue crack nucleation.

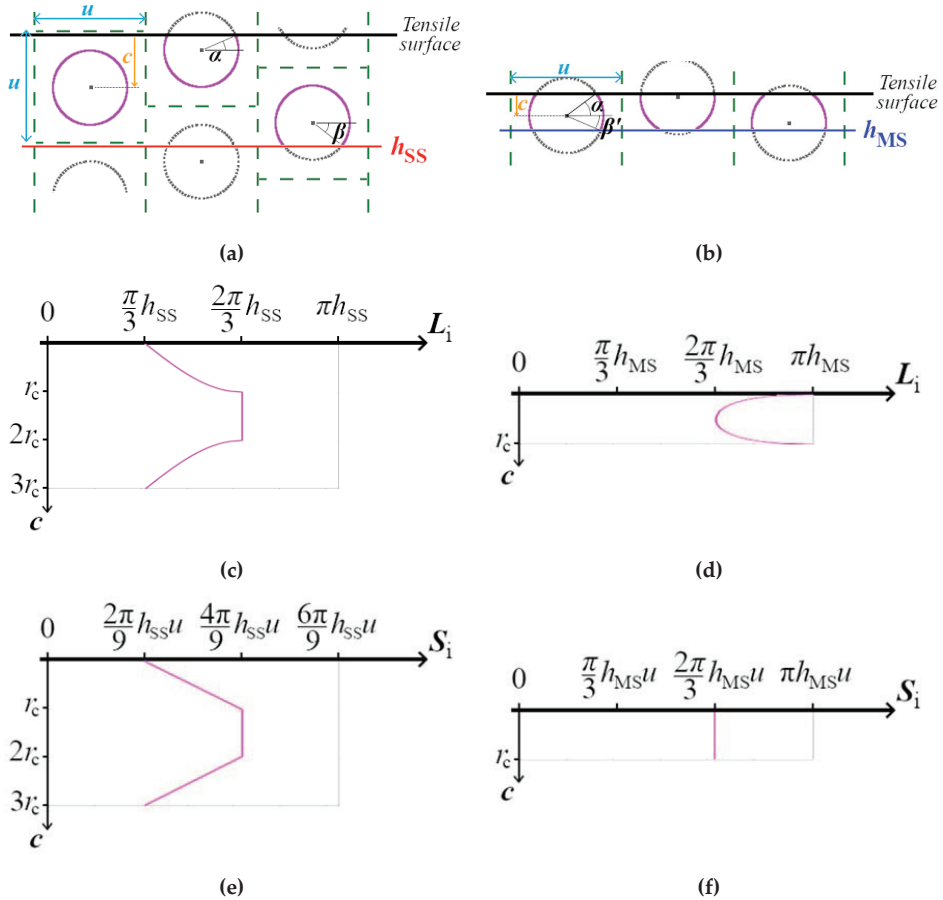


**Figure 13.** Schematic illustration for active interface calculation based on the proposed model. The active interface between the shell and cores is highlighted in purple color for the SS and MS configurations in (a,b), respectively. Corresponding active interface length functions  $L_i$  are represented in (c,d), whereas active interface surface functions  $S_i$  are depicted in (e,f), for the SS and MS configurations, respectively.

### 5. Conclusions

In the present investigation, the four-point bending fatigue properties of Ti-6Al-4V alloy designed in a bimodal harmonic structure (MM material) have been investigated. Unlike the previous reports dealing with this issue, the present work investigates the fatigue properties using the standard specimen (SS) configuration to better grasp the reliability of macroscopic parts. Furthermore, fatigue properties of the miniature specimen (MS) size configuration were also carried out, for the sake of comparison with previous experimental results. Lastly, fatigue data from homogeneous coarse grain IP material were collected to assess the impact of the harmonic microstructure on the mechanical characteristics. The main findings of the present report are summarized below:

1. Analysis of the microstructure of 50 mm diameter sintered compact made from powder prone to mechanical milling revealed a harmonic microstructure, without significant discrepancies throughout the entire compact.
2. Fatigue test results obtained from the MS configuration underlined fatigue endurance at  $10^7$  cycles of  $738 \pm 15$  MPa, distinctly higher than the IP one of  $683 \pm 14$  MPa. This trend is similar to results found in our previous work. An opposite situation is reported for fatigue tests accepting the SS configuration, where fatigue endurances at  $10^7$  cycles are  $570 \pm 10$  and  $680 \pm 20$  MPa, for the MM and IP materials, respectively.
3. Excepting the case of the MM material in the SS configuration, fatigue crack nucleation of both IP and MM materials revealed facets, presumably induced by the basal slip of  $\alpha$ -Ti grains. More particularly, the crack nucleates at the core region of the MM material in the MS configuration. However, the MM material highlighted other initiation features in the SS configuration, since inclusion-induced nucleation from the shell is found exclusively in the  $N_f > 10^6$  region. According to the chemical compositions of the involved inclusions, they are likely caused by powder contamination during the mechanical milling process.
4. A simplified model has been proposed to assess the activity between the core and shell regions, which outlined a significantly larger active interface fraction in the MS configuration than the SS one. Such a trend is in line with the more distinct increase of GNDs accumulation in the shell in the MS configuration, according to KAM analysis. GNDs accumulation mechanism mitigated, heterogeneous structure materials cannot keep their cohesion, leading to the generation of a local zone prone to considerable strain concentration, usually referred to as strain localization phenomenon.
5. The fatigue strength loss observed in the MM material for the SS configuration, in comparison with the MS one, should be induced by two main reasons: mitigated GNDs accumulation resulting in strain localization in core regions; coupled to a larger critical volume increasing notably the number of cores vulnerable to generate early fatigue crack nucleation.

Even though further analyses should be undertaken to refine our comprehension on the effect of the specimen size on the fatigue properties of harmonic structure materials, experimental results of the present work urge us to consider possible effects of the specimen size on various mechanical properties of such heterogeneous structure materials. In accordance with the simplified model, fatigue performance from harmonic structure materials with a large shell areal fraction should be altered, if the smallest dimension of the critical volume is out of the same order as the core/shell unit size. On the contrary, the fatigue strength of harmonic structure materials possessing a low shell areal fraction should hardly be affected, due to the limited influence of the critical volume size on the active interface between the core and shell regions. Lastly, it should be noted that future investigations on harmonic structured materials should pay additional attention on the material fabrication processing in order to keep such compounds as clean as possible. Refined examinations dealing with the fatigue behavior on such advanced tailored materials are at this cost.

**Author Contributions:** Conceptualization, K.A. and A.U.; methodology, B.G., S.K. and A.U.; software, B.G.; validation, B.G. and A.U.; formal analysis, B.G.; investigation, T.I., B.G., S.K. and A.U.; resources, K.A. and M.O.K.; data curation, B.G.; writing—original draft preparation, B.G.; writing—review and editing, S.K., A.U. and K.A.; visualization, B.G.; supervision, A.U., S.K. and B.G.; project administration, A.U., S.K. and B.G.; funding acquisition, K.A. All authors have read and agreed to the published version of the manuscript.

**Funding:** This work was supported by the French national research agency in the framework of ANR 14-CE07-0003 “HighS-Ti” program. This study is carried out with the aid of JSPS Grant-in-Aid for Scientific Research JP18H05256 and JP19H02024, along with The Light Metal Educational Foundation, Inc.

**Acknowledgments:** Authors would like to thank Takuya Nobori and Hirota Kuwahara (Graduate school of Mechanical Science and Engineering, Ritsumeikan University) for their kind helps in mechanical testing operations. A warm thank is dedicated to Guy Dirras (Université Paris 13, France) for our communications on various subjects dealing with this manuscript.

**Conflicts of Interest:** The authors declare no conflict of interest.

## References

- Hall, E.O. The deformation and ageing of mild steel: III Discussion of results. *Proc. Phys. Soc. B* **1951**, *64*, 747–752. [[CrossRef](#)]
- Petch, N.J. The cleavage strength of polycrystals. *J. Iron Steel Inst.* **1953**, *174*, 25–28.
- Tsuji, N.; Ito, Y.; Saito, Y.; Minamino, Y. Strength and ductility of ultrafine grained aluminum and iron produced by ARB and annealing. *Scr. Mater.* **2002**, *47*, 893. [[CrossRef](#)]
- Ma, E. Instabilities and ductility of nanocrystalline and ultrafine-grained metals. *Scr. Mater.* **2003**, *49*, 663–668. [[CrossRef](#)]
- Morita, T.; Hatsuoka, K.; Iizuka, T.; Kawasaki, K. Straightening of Ti-6Al-4V by short-time duplex heat treatment. *Mater. Trans.* **2005**, *46*, 1681–1686. [[CrossRef](#)]
- Szabo, P.J.; Field, D.P.; Joni, B.; Horky, J.; Ungar, T. Bimodal grain size distribution enhances strength and ductility simultaneously in a low-carbon low alloy steel. *Metall. Mater. Trans. A* **2015**, *46*, 1948–1957. [[CrossRef](#)]
- Terada, D.; Inoue, M.; Kitahara, H.; Tsuji, N. Change in mechanical and microstructure of ARB processed Ti during annealing. *Mater. Trans.* **2008**, *49*, 41–46. [[CrossRef](#)]
- Wang, Y.; Chen, M.; Zhou, F.; Ma, E. High tensile ductility in a nanostructured metal. *Nature* **2002**, *419*, 912–915. [[CrossRef](#)]
- Ma, E.; Zhu, T. Towards strength-ductility synergy through the design of heterogeneous nanostructures in metals. *Mater. Today* **2017**, *20*, 323–331. [[CrossRef](#)]
- Fang, T.H.; Li, W.L.; Tao, N.R.; Lu, K. Revealing extraordinary intrinsic tensile plasticity in gradient nano-grained copper. *Science* **2011**, *331*, 1587–1590. [[CrossRef](#)]
- Wu, X.; Yang, M.; Yuan, F.; Wu, G.; Wei, Y.; Huang, X.; Zhu, Y. Heterogeneous lamella structure unites ultrafine-grain strength with coarse-grain ductility. *Proc. Natl. Acad. Sci. USA* **2015**, *112*, 14501–14505. [[CrossRef](#)] [[PubMed](#)]
- Wu, X.; Jiang, P.; Chen, L.; Yuan, F.; Zhu, Y. Extraordinary strain hardening by gradient structure. *Proc. Natl. Acad. Sci. USA* **2014**, *111*, 7197–7201. [[CrossRef](#)] [[PubMed](#)]
- Bagherifard, S.; Astaraee, A.H.; Locati, M.; Nawaz, A.; Monti, S.; Kodas, J.; Singh, R.; Guagliano, M. Design and analysis of additive manufactures bimodal structures obtained by cold spray deposition. *Addit. Manuf.* **2020**, *33*, 101131.
- Sekiguchi, T.; Ono, K.; Fujiwara, H.; Ameyama, K. New microstructure design for commercially pure titanium with outstanding mechanical properties by mechanical milling and hot roll sintering. *Mater. Trans.* **2010**, *51*, 39–45. [[CrossRef](#)]
- Fujiwara, H.; Sekiguchi, T.; Ameyama, K. Mechanical properties of pure titanium and Ti-6Al-4V alloys with a new tailored nano/meso hybrid microstructure. *Int. J. Mater. Res.* **2009**, *100*, 796. [[CrossRef](#)]
- Kikuchi, S.; Nakamura, Y.; Ueno, A.; Ameyama, K. Low temperature nitriding of commercially pure titanium with harmonic structure. *Mater. Trans.* **2015**, *56*, 1807–1813. [[CrossRef](#)]
- Vajpai, S.K.; Ota, M.; Watanabe, T.; Maeda, R.; Sekiguchi, T.; Kusaka, T.; Ameyama, K. The development of high performance Ti-6Al-4V alloy via a unique microstructural design with bimodal grain size distribution. *Mater. Metall. Mater. Trans. A* **2015**, *46*, 903–914. [[CrossRef](#)]
- Ota, M.; Vajpai, S.K.; Imao, R.; Kurokawa, K.; Ameyama, K. Application of high pressure gas jet mill process to fabricate high performance harmonic structure designed pure titanium. *Mater. Trans.* **2015**, *56*, 154–159. [[CrossRef](#)]
- Vajpai, S.K.; Ota, M.; Zhang, Z.; Ameyama, K. Three-dimensionally gradient harmonic structure design: An integrated approach for high performance structural materials. *Mater. Res. Lett.* **2016**, *4*, 191–197. [[CrossRef](#)]
- Kikuchi, S.; Hayami, Y.; Ishiguri, T.; Guennec, B.; Ueno, A.; Ota, M.; Ameyama, K. Effect of bimodal grain size distribution on fatigue properties of Ti-6Al-4V alloy with harmonic structure under four-point bending. *Mater. Sci. Eng. A* **2017**, *687*, 269–275. [[CrossRef](#)]
- Kikuchi, S.; Imai, T.; Kubozono, H.; Nakai, Y.; Ota, M.; Ueno, A.; Ameyama, K. Effect of harmonic structure design with bimodal grain size distribution on near-threshold fatigue crack propagation in Ti-6Al-4V alloy. *Int. J. Fatigue* **2016**, *92*, 616–622. [[CrossRef](#)]

22. Zhang, Z.; Ma, H.; Zheng, R.; Hu, Q.; Nakatani, M.; Ota, M.; Chen, G.; Chen, X.; Ma, C.; Ameyama, K. Fatigue behavior of a harmonic structure designed austenitic stainless steel under uniaxial stress loading. *Mater. Sci. Eng. A* **2017**, *707*, 287–294. [[CrossRef](#)]
23. Kikuchi, S.; Mori, T.; Kubozono, H.; Nakai, Y.; Kawabata, M.; Ameyama, K. Evaluation of near-threshold fatigue crack propagation in harmonic-structured CP Titanium with a bimodal grain size distribution. *Eng. Fract. Mech.* **2017**, *181*, 77–86. [[CrossRef](#)]
24. Kikuchi, S.; Imai, T.; Kubozono, H.; Nakai, Y.; Ueno, A.; Ameyama, K. Evaluation of near-threshold fatigue crack propagation in Ti-6Al-4V alloy with harmonic structure created by mechanical milling and spark plasma sintering. *Frat. Ed Integr. Strutt.* **2015**, *34*, 261–270. [[CrossRef](#)]
25. Kikuchi, S.; Nakatsuka, Y.; Nakai, Y.; Nakatani, M.; Kawabata, M.; Ameyama, K. Evaluation of fatigue properties under four-point bending and fatigue crack propagation in austenitic stainless steel with a bimodal harmonic structure. *Frat. Ed Integr. Strutt.* **2019**, *48*, 545–553. [[CrossRef](#)]
26. Kikuchi, S.; Nukui, Y.; Nakatsuka, Y.; Nakai, Y.; Nakatani, M.; Kawabata, M.; Ameyama, K. Effect of bimodal harmonic structure on fatigue properties of austenitic stainless steel under axial loading. *Int. J. Fatigue* **2019**, *127*, 222–228. [[CrossRef](#)]
27. Osaki, K.; Kikuchi, S.; Nakai, Y.; Kawabata, M.; Ameyama, K. The effects of thermo-mechanical processing on fatigue crack propagation in commercially pure titanium with a harmonic structure. *Mater. Sci. Eng. A* **2020**, *773*, 13892. [[CrossRef](#)]
28. JSMS Committee on Fatigue of Materials; JSMS Committee on Reliability Engineering. Standard Evaluation Method of Fatigue Reliability for Metallic Materials—Standard Regression Method of S-N Curves. JSMS-SD-11-08. *J. Soc. Mater. Sci. Jpn.* **2005**. [[CrossRef](#)]
29. Adachi, S.; Wagner, L.; Lutjering, G. Influence of microstructure and mean stress on fatigue strength of Ti-6Al4V. In Proceedings of the Fifth International Conference on Titanium, Munich, Germany, 10–14 September 1984; pp. 2139–2146.
30. Zuo, J.H.; Wang, Z.G.; Han, E.H. Effect of microstructure on ultra-high cycle fatigue behavior of Ti-6Al-4V. *Mater. Sci. Eng. A* **2008**, *473*, 147–152. [[CrossRef](#)]
31. Golden, P.J.; John, R.; Porter, W.J., III. Variability in room temperature fatigue life of alpha + beta processed Ti-6Al-4V. *Int. J. Fatigue* **2009**, *31*, 1764–1770. [[CrossRef](#)]
32. Liu, X.; Sun, C.; Hong, Y. Effects of stress ratio on high-cycle and very-high-cycle fatigue behavior of a Ti-6Al-4V. *Mater. Sci. Eng. A* **2015**, *622*, 228–235. [[CrossRef](#)]
33. Tokaji, K.; Kariya, H. Mean stress dependence of fatigue strength and subsurface crack initiation in Ti-15Mo5Zr-3Al. *Mater. Sci. Eng. A* **2000**, *281*, 268–274. [[CrossRef](#)]
34. Kikuchi, S.; Kubozono, H.; Nukui, Y.; Nakai, Y.; Ueno, A.; Kawabata, M.; Ameyama, K. Statistical fatigue properties and small fatigue crack propagation in bimodal harmonic structured Ti-6Al-4V alloy under four point bending. *Mater. Sci. Eng. A* **2018**, *711*, 29–36. [[CrossRef](#)]
35. Nukui, Y.; Kubozono, H.; Kikuchi, S.; Nakai, Y.; Ueno, A.; Kawabata, M.; Ameyama, K. Fractographic analysis of fatigue crack initiation and propagation in CP titanium with a bimodal harmonic structure. *Mater. Sci. Eng. A* **2018**, *716*, 228–234. [[CrossRef](#)]
36. Dirras, G.; Ueda, D.; Hocini, A.; Tingaud, D.; Ameyama, K. Cyclic shear behavior of conventional and harmonic structure-designed Ti-25Nb-25Zr  $\beta$ -titanium alloy: Back-stress hardening and twinning inhibition. *Scr. Mater.* **2017**, *138*, 44–47. [[CrossRef](#)]
37. Momprou, F.; Tingaud, D.; Chang, Y.; Gault, B.; Dirras, G. Conventional vs Harmonic-structured  $\beta$ -Ti-25Nb-25Zr alloys: A comparative study of deformation mechanisms. *Acta Mater.* **2018**, *161*, 420–430. [[CrossRef](#)]
38. Calcagnotto, M.; Ponge, D.; Demir, E.; Raabe, D. Orientation gradients and geometrically necessary dislocations in ultrafine grained dual-phase steels studied by 2D and 3D EBSD. *Mater. Sci. Eng. A* **2010**, *527*, 2738–2746. [[CrossRef](#)]
39. Allain-Bonasso, N.; Wagner, F.; Berbenni, S.; Field, D.P. A study of the heterogeneity of plastic deformation in IF steel by EBSD. *Mater. Sci. Eng. A* **2010**, *548*, 56–63. [[CrossRef](#)]
40. He, W.; Ma, W.; Pantleon, W. Microstructure of individual grains in cold-rolled aluminum from orientation inhomogeneities resolved by electron backscattering diffraction. *Mater. Sci. Eng. A* **2008**, *494*, 21–27. [[CrossRef](#)]

41. Britton, T.B.; Biroscas, S.; Preuss, M.; Wilkinson, A.J. Electron backscatter diffraction study of dislocation content of a macrozone in hot-rolled Ti-6Al-4V alloy. *Scr. Mater.* **2010**, *62*, 639. [[CrossRef](#)]
42. Murakami, Y.; Endo, M. Effects of defects, inclusions and inhomogeneities on fatigue strength. *Int. J. Fatigue* **1994**, *16*, 163–182. [[CrossRef](#)]
43. Chapetti, M.D.; Tagawa, T.; Miyata, T. Ultra-long cycle fatigue of high-strength carbon steels part I: Review and analysis of the mechanism of failure. *Mater. Sci. Eng. A* **2003**, *356*, 227–235. [[CrossRef](#)]
44. Sakai, T.; Nakagawa, A.; Oguma, N.; Nakamura, Y.; Ueno, A.; Kikuchi, S.; Sakaida, A. A review on fatigue fracture modes of structural metallic materials in very high cycle regime. *Int. J. Fatigue* **2016**, *93*, 339–351. [[CrossRef](#)]
45. Sakai, T.; Takeda, M.; Tanaka, N.; Kanemitsu, M.; Oguma, N.; Shiozawa, K. S-N property and fractography of high carbon chromium bearing steel over ultra wide life region under rotating bending. *Trans. Jpn. Soc. Mech. Eng. Ser. A* **2001**, *67*, 1805–1812. (In Japanese) [[CrossRef](#)]
46. Shiozawa, K.; Morii, Y.; Nishino, S.; Lu, L. Subsurface crack initiation and propagation mechanism in high-strength steel in a very high cycle fatigue regime. *Int. J. Fatigue* **2006**, *28*, 1521–1532. [[CrossRef](#)]
47. Shiozawa, K.; Kuroda, Y.; Nishino, S. Effect of the stress ratio on subsurface fatigue crack initiation behavior of beta-type titanium alloy. *Trans. Jpn. Soc. Mech. Eng. A* **1998**, *64*, 2528–2535. (In Japanese) [[CrossRef](#)]
48. Li, S.; Xiong, B.; Hui, S.; Ye, W.; Yu, Y. Comparison of the fatigue and fracture of Ti-6Al-2Zr-1Mo-1V with lamellar and bimodal microstructures. *Mater. Sci. Eng. A* **2007**, *460*, 140–145. [[CrossRef](#)]
49. Ashby, M.F. The deformation of plastically non-homogeneous materials. *Philos. Mag. Ser.* **1970**, *21*, 399–424. [[CrossRef](#)]
50. Park, H.K.; Ameyama, K.; Yoo, J.; Hwang, H.; Kim, H.S. Additional hardening in harmonic structured materials by strain partitioning and back stress. *Mater. Res. Lett.* **2018**, *6*, 261–267. [[CrossRef](#)]
51. Yu, H.; Watanabe, I.; Ameyama, K. Deformation behavior analysis of harmonic structure materials by multi-scale finite element analysis. *Adv. Mater. Res.* **2015**, *108*, 853–857. [[CrossRef](#)]
52. Wang, X.; Cazes, F.; Li, J.; Hocini, A.; Ameyama, K.; Dirras, G. A 3D crystal plasticity model of monotonic and cyclic simple shear deformation for commercial-purity Ti with a harmonic structure. *Mech. Mater.* **2019**, *128*, 117–128. [[CrossRef](#)]
53. Joseph, S.; Bantounas, I.; Lindley, T.C.; Dye, D. Slip transfer and deformation structures resulting from the low cycle fatigue of near-alpha titanium alloy Ti-6242Si. *Int. J. Plast.* **2018**, *100*, 90–103. [[CrossRef](#)]
54. Zhang, Y.; Topping, T.D.; Yang, H.; Lavernia, E.J.; Schoenung, J.M.; Nutt, S.R. Micro-strain evolution and toughening mechanisms in a trimodal Al-based metal matrix composite. *Metall. Mater. Trans. A* **2015**, *46*, 1196–1204. [[CrossRef](#)]
55. Zan, Y.N.; Zhou, Y.T.; Liu, Z.Y.; Ma, G.N.; Wang, D.; Wang, Q.Z.; Wang, W.G.; Xiao, B.L.; Ma, Z.Y. Enhancing strength and ductility synergy through heterogeneous structure design in nanoscale Al<sub>2</sub>O<sub>3</sub> particulate reinforced Al composites. *Mater. Des.* **2019**, *166*, 10762–10769. [[CrossRef](#)]



© 2020 by the authors. Licensee MDPI, Basel, Switzerland. This article is an open access article distributed under the terms and conditions of the Creative Commons Attribution (CC BY) license (<http://creativecommons.org/licenses/by/4.0/>).

Article

# Powder Metallurgy Processing and Mechanical Properties of Controlled Ti-24Nb-4Zr-8Sn Heterogeneous Microstructures

Benoît Fer <sup>1,2,\*</sup>, David Tingaud <sup>1</sup>, Azziz Hocini <sup>1</sup>, Yulin Hao <sup>3</sup>, Eric Leroy <sup>4</sup>, Frédéric Prima <sup>2</sup> and Guy Dirras <sup>1</sup>

<sup>1</sup> Université Sorbonne Paris Nord, Laboratoire de Sciences des Procédés et des Matériaux, CNRS, UPR 3407, 93430 Villetaneuse, France; david.tingaud@univ-paris13.fr (D.T.); hocini@univ-paris13.fr (A.H.); dirras@univ-paris13.fr (G.D.)

<sup>2</sup> PSL University, Chimie ParisTech, CNRS, Institut de Recherche de Chimie Paris, 75005 Paris, France; frederic.prima@chimieparistech.psl.eu

<sup>3</sup> Shi-Changxu Innovation Center for Advanced Materials, Institute of Metal Research, Chinese Academy of Sciences, Shenyang 110016, China; ylhao@imr.ac.cn

<sup>4</sup> Université Paris Est Créteil, CNRS, ICMPE, UMR 7182, 2 rue Henri Dunant, 94320 Thiais, France; leroy@icmpe.cnrs.fr

\* Correspondence: benoit.fer@lspm.cnrs.fr; Tel.: +33-648218555

Received: 7 November 2020; Accepted: 1 December 2020; Published: 4 December 2020

**Abstract:** This paper gives some insights into the fabrication process of a heterogeneous structured  $\beta$ -metastable type Ti-24Nb-4Zr-8Sn alloy, and the associated mechanical properties optimization of this biocompatible and low elastic modulus material. The powder metallurgy processing route includes both low energy mechanical ball milling (BM) of spherical and pre-alloyed powder particles and their densification by Spark Plasma Sintering (SPS). It results in a heterogeneous microstructure which is composed of a homogeneous 3D network of  $\beta$  coarse grain regions called “core” and  $\alpha/\beta$  dual phase ultra-fine grain regions called “shell.” However, it is possible to significantly modify the microstructural features of the alloy—including  $\alpha$  phase and shell volume fractions—by playing with the main fabrication parameters. A focus on the role of the ball milling time is first presented and discussed. Then, the mechanical behavior via shear tests performed on selected microstructures is described and discussed in relation to the microstructure and the probable underlying deformation mechanism(s).

**Keywords:** heterogeneous microstructure; titanium alloy; powder metallurgy; mechanical properties

## 1. Introduction

$\beta$ -metastable titanium alloys are widely used among titanium alloys in aerospace and biomedical application domains. These alloys contain enough  $\beta$ -stabilizer chemical elements (Mo, V, Nb . . . ) to retain metastable  $\beta$  phase at ambient temperature after water quenching from the  $\beta$  phase stability field. Because of the metastability of the  $\beta$  phase, it is possible to reach various microstructures according to the fabrication process or thermo-mechanical treatments and therefore it gives birth to a wide range of mechanical properties [1].

In this study, we focus on Ti-24Nb-4Zr-8Sn (wt%, thereafter called Ti-2448). The weight fraction of niobium in the alloy is high enough to classify it as a  $\beta$ -metastable type alloy. Zirconium and tin are considered as neutral chemical elements. This alloy is of high interest for biomedical applications because:

- Ti-2448 is only composed of non-cytotoxic chemical elements [2].
- Its Young modulus is lower than the one of the other  $\beta$  or  $\alpha + \beta$  titanium alloys, and significantly lower than the Young's modulus of stainless steel or Cr-Co-based alloys generally used in

biomedical applications. Values of Young's modulus around 40 to 50 GPa are quoted for Ti-2448 in multiple studies [3–5].

As a result, it is possible to significantly reduce “stress-shielding” effects which usually occur when the Young's modulus of the implant material is drastically superior to the Young's modulus of human cortical bone. In that case, all mechanical stresses applied on the implanted bone are undertaken by the implant instead of the surrounding bone, which may finally induce bone resorption—according to Wolff's law [6]. This phenomenon has been, for example, studied using a comparison between Ti-2448 and TA6V by Qu et al. on porcine models, resulting in improved results with Ti-2448 implants [7].

Moreover, depending on its initial microstructure, Ti-2448 may benefit from a super-elastic mechanical behavior. Super-elastic alloys are attractive for biomedical application fields, as they allow a better integration of the implant in its new environment. This elastic behavior is due to the stress-induced  $\beta$  to  $\alpha'$  phase transformation, which is reversible and occurs during the first stage of deformation. It allows high values of reversible elastic strain. Stress-induced  $\beta$  to  $\alpha'$  phase transformation in Ti-2448 has been studied several times [8,9]. Besides, twinning may occur when Ti-2448 is plastically deformed. Nevertheless, the exact nature of twins in the deformed microstructure and the full sequence of deformation in conventional Ti-2448 are not completely understood [10–12].

In order to limit implant replacement surgery, yield strength and fatigue strength are critical cursors to be maximized for orthopedic alloys. Several strategies may be followed to improve yield strength of Ti-2448 [13,14]. Processes based on the precipitation of a second phase of the microstructure (usually  $\alpha$  phase in  $\beta$ -metastable titanium alloys which is related to  $\omega$  phase precipitation at low temperature [15,16]) are efficient to significantly improve strength of the  $\beta$ -metastable alloys [17]. Other hardening strategies are based on the chemical design of the alloy. Using Bo-Md diagrams, it is possible to control the deformation mode of the alloys [18], and to induce transformation-induced plasticity (TRIP) or twinning-induced plasticity (TWIP) effects [19,20]. Grain refinement could also be used as a hardening strategy, by the development of ultrafine-grained (UFG) structures, which can be obtained via severe plastic deformation or powder metallurgy processing routes. However, these structures generally suffer from a significant lack of ductility [21]. To face the problems of ductility losses, heterogeneous grain structures have been elaborated on several studies, and they have proved to be an efficient way to maximize the strength-ductility synergy of different materials [22–24].

One particular heterogeneous microstructure is the so-called harmonic structure, which is composed of an interconnected and homogeneous 3D network of fine grains regions called “shell” and coarse grain regions called “core.” The fabrication process of harmonic microstructure is based on powder metallurgy, including low energy mechanical ball milling (BM) and sintering (spark plasma, hot isostatic pressing) of pre-alloyed and spherical shaped powder particles [25–28]. Although a range of titanium powders have been consolidated using SPS/FAST [29–31], a very few attempts have been published in literature to fabricate Ti-2448 via powder metallurgy route. On the one hand, sintering of Ti-2448 has been made from elemental powder particles by Li et al. [32] but the sintered material could not achieve full density. Metal Injection Molding of pre-alloyed Ti-2448 particles was achieved by Kafkas et al. [33]. The results are promising despite the precipitation of  $Ti_3C$  carbides along the grain boundaries. Additive manufacturing (including both Electron Beam Melting and Selective Laser Melting) was also successfully applied on Ti-2448 [34–36]. On the other hand, the elaboration process of harmonic microstructures has been successfully performed on several materials, including steel [27,37], CP  $\alpha$  titanium and  $\alpha + \beta$  TA6V alloy [25] and  $\beta$ -stable Ti-25Nb-25Zr alloy [38]. In many cases, it results in an improvement of both yield strength and ultimate tensile strength almost without a ductility loss, even when deformation modes switch from mechanical twinning to dislocation glide [39].

In this work, the effect of heterogeneous grain structures and precipitation hardened structures are combined by processing a specific dual-phase harmonic microstructure based on the Ti-2448 alloy. Heterogeneous structured Ti-2448 samples with various microstructural features (including  $\alpha$  precipitates volume fraction, core and shell fraction, grain sizes) have been fabricated via the control

of mechanical BM parameters. The link between the resulting microstructures and the mechanical behavior of the alloy is further discussed.

## 2. Materials and Methods

Ti-2448 spherical shaped powder particles which have been argon atomized at the Institute of Metal Research (IMR) from the Chinese Academy of Sciences have been used as raw materials for this study. A sieving stage has been performed after gas atomization to sort powder particles according to their size. For this work, powder particles whose diameter is in the range 100–160  $\mu\text{m}$  have been chosen, as they allow a good balance between core and shell in the final heterogeneous microstructures. Mechanical BM has been performed by the use of a Pulverisette 7 premium line planetary ball mill (FRITSCH, Idar-Oberstein, Germany), using both jar and 10 mm diameter balls made of steel. No significant iron or carbon contamination was detected after BM in a steel environment. Rotational speed of the mill was fixed at 200 rpm, using a ball-to-powder ratio (BPR, weight ratio) of 2:1. BM time is the varying parameter of the study (0 h, 12 h, 25 h, 50 h, and 100 h). Names of the as-processed samples are the following: IP (for initial powder) when the starting powder was directly sintered, BM 12 h for a BM time of 12 h, BM 25 h for a BM time of 25 h, etc. For the consolidation step, Spark Plasma Sintering (SPS) was performed using Dr. Sinter 515 S Syntex (Fuji Electronic Industrial co., Tsurugashima, Japan) setup belonging to the “Plateforme de Frittage Île-de-France” (Thiais, France). Cylindrical samples whose diameter is 20 mm and height are 2 mm were fabricated under argon atmosphere, and sintering parameters were fixed and chosen in order to ensure complete densification of the powder. Therefore, a sintering temperature of 800 °C and a compressive pressure of 100 MPa were applied for 30 min. Heating rate is 50 °C/min. For illustration purposes, a typical sintering cycle is displayed on Figure 3.

The microstructural characterization of the samples was performed using a scanning electron microscope SUPRA 40VP (ZEISS, Jena, Germany), equipped with a field-emission gun and an Electron BackScatter Diffraction (EBSD) acquisition system. Chemical analysis was performed using Wavelength Dispersion Spectroscopy (WDS) or Energy Dispersive Spectroscopy (EDS) techniques on an electron probe microanalyser SX100 (CAMECA, Gennevilliers, France). The WDS analyses were recorded at a voltage of 15 kV and an electric current of 40 nA. For EBSD acquisition 400  $\mu\text{m}^2$  or 800  $\mu\text{m}^2$  zones have been analyzed most of the time, with a respective step size of 0.25  $\mu\text{m}$  or 0.5  $\mu\text{m}$ . Both  $\beta$  and  $\alpha$  phase data have been used to index patterns using OimDC NORDIF software (version VS2005, EDAX, Weiterstadt, Germany). OIM Analysis software (version 5.3, EDAX, Weiterstadt, Germany) was used to analyze EBSD data. X-ray diffraction (XRD) measurements were acquired using a diffractometer Equinox 1000 (INEL, Ardenay, France) with a copper ( $\lambda = 0.1540$  nm) or cobalt ( $\lambda = 0.1789$  nm) monochromatic radiation. Data from the cobalt radiation diffractometer are converted to data which would have been collected using a copper experimental setup in order to ensure coherency of the results. Phase identification was based on Match software database. Density measurements were performed using Archimedes' principle in o-xylene liquid.

Mechanical properties were investigated via simple shear tests, using a home-made shear setup mounted on an MTS M20 testing machine (MTS Systems Corporation, Eden Prairie, MN, USA). The load capacity of the shearing device is 100 kN. Rectangular samples whose thickness is in the range 1.6–1.8 mm and width in the range 16–17 mm were cut along the radial direction of the cylindrical pads which are obtained after SPS. They are settled between two jaws, including one of them which is fixed and the other one which is moving vertically to shear the sample. The sheared volume is similar for every mechanical test. The deformation is followed directly on the sample, by using a video extensometer and computing the variation of the shear angle between a black line drawn on the surface of the sample and its initial horizontal position. These tests were performed at room temperature, at a shear strain rate of  $10^{-3}$  s $^{-1}$ .

### 3. Results and Discussion

#### 3.1. Powder Metallurgy Processing Route

The fabrication process is based on powder metallurgy. The powder particles which have been used for this study have been obtained via argon atomization of a cylindrical pre-alloyed Ti-2448 alloy ingot. The initial morphology of the powder particles is shown in Figure 1a. They are mostly of spherical shape and their diameters are in the range 100–160  $\mu\text{m}$ . The largest particles are surrounded by satellite particles which have not been shown to play any role during the process. Moreover, each powder particle is composed of single polycrystalline  $\beta$  phase, as it can be seen in the Inverse Pole Figure (IPF) map of a selected representative powder particle (Figure 1b) or on the X-ray diffraction pattern (XRD) of the initial powder (IP on Figure 2e). The average grain size in a representative initial powder particle is 15  $\mu\text{m}$  (Figure 1b).

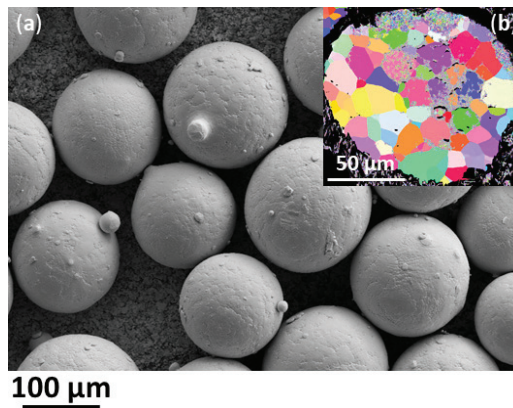


**Figure 1.** Characterization of initial powder particles (a) Scanning Electron Microscope (SEM) secondary electron image of the powder, (b) Inverse Pole Figure (IPF) image of a selected powder particle highlighting its microstructure.

The first stage of the fabrication process of this dual phase heterogeneously structured Ti-2448 is the mechanical planetary BM of the powder. Low energy parameters are selected for BM, as the objective of this stage is to induce superficial plastic deformation on the powder particles without affecting the core.

Figure 2 displays the morphology of the powder particles after BM for different BM times. The effect of BM on the morphology of powder particles is clear from a BM time of 12 h after which powder particles have lost their spherical shape. For a longer BM time (25 h and 50 h), some particles are severely affected by BM and are indicated by white arrows on Figure 2b–d. Furthermore, after BM for 100 h, fragmentation of some particles occurs: the fragments are indicated by red arrows on Figure 2d. XRD patterns are also plotted in Figure 2e for powders after BM. The results confirm the high plastic deformation which is induced on powder particles during BM stage. Indeed, a significant broadening of the  $\beta$  phase peaks—especially the main  $\beta$  {110} peak—takes place when increasing the BM time. Inset in Figure 2e plots the evolution of the full width at half maximum (FWHM) of the main {110} peak. A global increase in the FWHM occurs, but it is worth noting that the increase is not linear. A clear broadening of the peak is noted after a BM of 12 h. The evolution is then smoother between 12 h and 50 h, before increasing again for a BM time of 100 h. It means that plastic deformation of the powder is very high at that last BM level. Moreover, we can clearly observe the appearance of an additional peak in the XRD pattern of the 50 h—BM and 100 h—BM powders, which is indicated by a black star on Figure 2e and could be indexed as hexagonal or orthorhombic titanium

phase. However, because mechanical BM is not supposed to induce the precipitation of hexagonal  $\alpha$  phase in the powder, it is possible that reversible stress-induced martensitic transformation  $\beta$  to  $\alpha''$  occurs during BM. Incomplete reversion of this transformation (because  $\alpha''$  precipitates may be trapped by dislocations or other deformation traces) might explain the presence of this extra peak [12]. Nevertheless, the thermo-elastic behavior of the orthorhombic martensitic phase allows the complete reversion of it when heated at a moderate temperature, as it is the case during the first stage of sintering. As a result, this extra phase might not have a significant impact on the processing route.

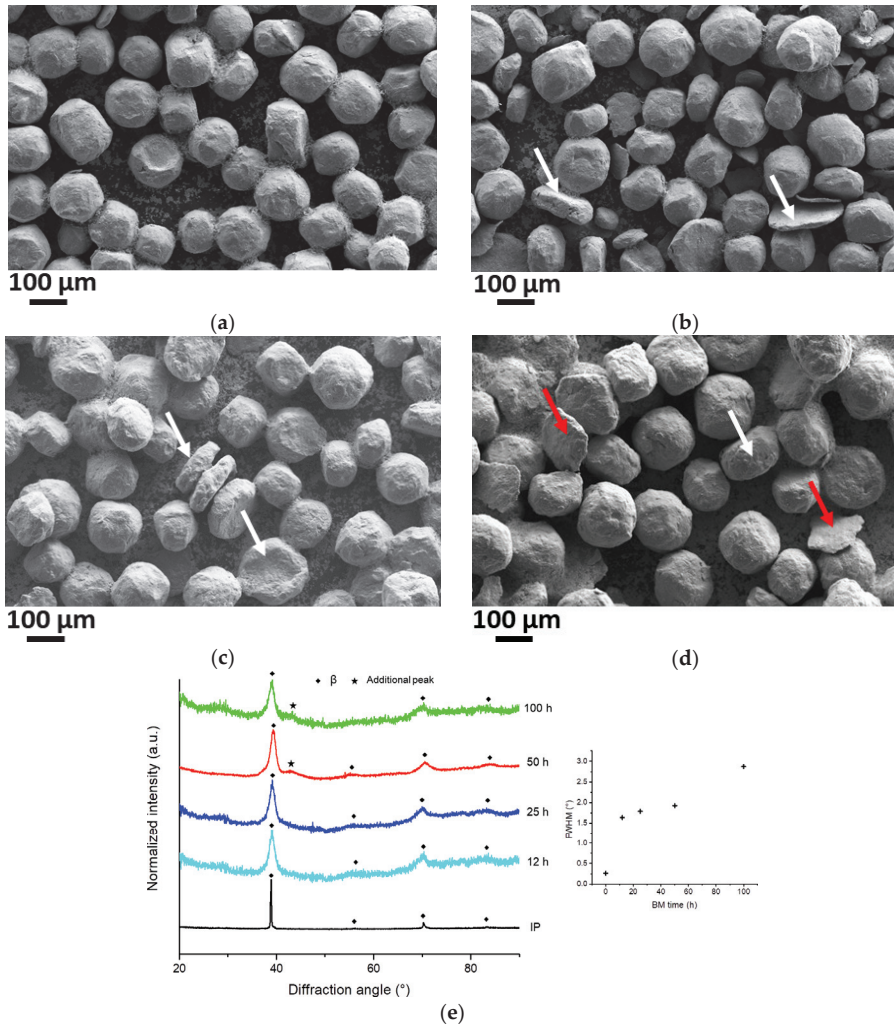


**Figure 2.** Characterization of ball-milled powders (a) SEM secondary electrons image after 12 h ball milling (BM) (b) after 25 h BM (c) after 50 h BM and (d) after 100 h BM. (e) X-ray diffraction (XRD) results of Ti-2448 powders after BM, including diffractograms for each BM time and the corresponding evolution of the full width at half maximum (FWHM) of the main  $\{110\}$   $\beta$  phase peak.

All samples have been sintered using the same SPS cycle, so that only BM time has been modified between samples during the whole fabrication process. Figure 3 is a comparative plot of the SPS

responses of IP, BM 12 h, and BM 50 h. It shows the evolution against time of the temperature, pressure, and derivative of the displacement of the piston during sintering of the three samples. This last parameter is useful to follow the densification of the samples during SPS, which takes place in two steps. The first one is associated with cold compaction of the powders, at ambient temperature once the pressure is applied. The second one occurs when the temperature reaches the beginning of sintering temperature. That time is indicated with arrows for each sample on Figure 3 and is associated with the effective sintering of the material. As we can see, BM affects the sintering reactivity of the powders, as the sintering temperatures are not the same for each sample. The longer the BM time is, the lower the sintering temperatures are. It means that the sintering reactivity of the powder particles has been increased by mechanical BM via storing mechanical energy in the material and increasing the density of structural defects in it. Therefore, diffusion phenomena are favored during sintering which consequently occurs at a slightly lower temperature.

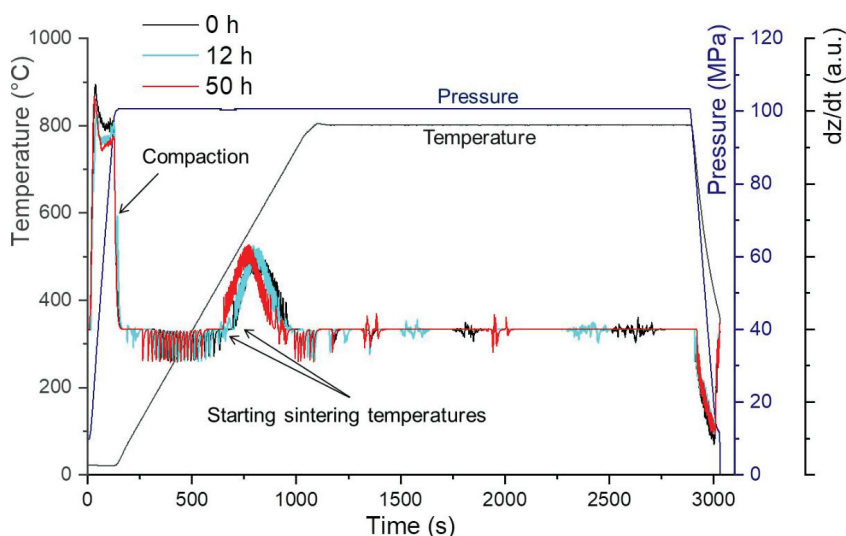


**Figure 3.** Spark Plasma Sintering (SPS) cycle showing the evolution against time of temperature, pressure and the derivative of the displacement of the piston of IP, BM 12 h, and BM 50 h.

The SPS stage has two main goals: the first one is to obtain dense materials and the second one is to allow recrystallization of the heavily deformed surface of powders, whose volume is directly connected to the BM time (Figure 2e). This recrystallization is therefore the key phenomenon to induce the formation of the fine grain region called “shell.”

### 3.2. Microstructural Features of the As-Sintered Samples

The fabrication process—which includes both BM and SPS—has resulted in dense samples with a relative density of 100%. For each processed sample, the density is measured via Archimede’s method and compared with the theoretical density of the material. The theoretical density of single  $\beta$ -phase Ti-2448 has been calculated using XRD data of an as-sintered single-phase IP sample. The cell parameter of the single phase  $\beta$ -BCC structure, which has been computed via Rietveld refinement of the XRD results, is 3.300 Å and the corresponding calculated theoretical density of a full  $\beta$  Ti-2448 structure is 5.44 g/cm<sup>3</sup>. This value is confirmed in literature by Li et al., who have found a close value of 5.46 g/cm<sup>3</sup> [32].

Illustrations of a typical heterogeneous microstructure, which is obtained at the end of the processing route, are given in Figure 4. As it is illustrated, the as-sintered microstructures are heterogeneous and bimodal:

- Firstly, they contain two populations of  $\beta$  phase grains homogeneously dispersed in the whole volume of the sample. The first one consists in fine grains—with an average grain size of about 4 to 5  $\mu\text{m}$  depending on the sample—and is located at every zone where plastic deformation occurs during BM. It constitutes the “shell” of the harmonic structure. The other one is made of coarse grains—the average grain size in the core against BM time is plotted for every sample on Figure 7b—and is formed in the core of the powder particles, where no plastic deformation was produced by the BM stage. It constitutes the “core” of the harmonic structure. The presence of fine  $\beta$  grains is clearly observed on the close-up views of Figure 4. The shell region may also be separated into the outer—consisted of micron-wide  $\beta$  grains—and inner shell consisted of grains about hundreds of nanometers wide.
- Secondly, they are bimodal from a chemical point of view, as they contain  $\alpha$  phase precipitates near the shell. In most samples, the core is exclusively consisted of  $\beta$  phase and no  $\alpha$  phase has been detected (except for BM 100 h). As we can see in Figure 4b, the average grain size of  $\alpha$  precipitates is 1  $\mu\text{m}$  and they are located at the  $\beta$  grain boundaries in the shell vicinity. They benefit from the excess of energy due to grain boundaries to precipitate during sintering.

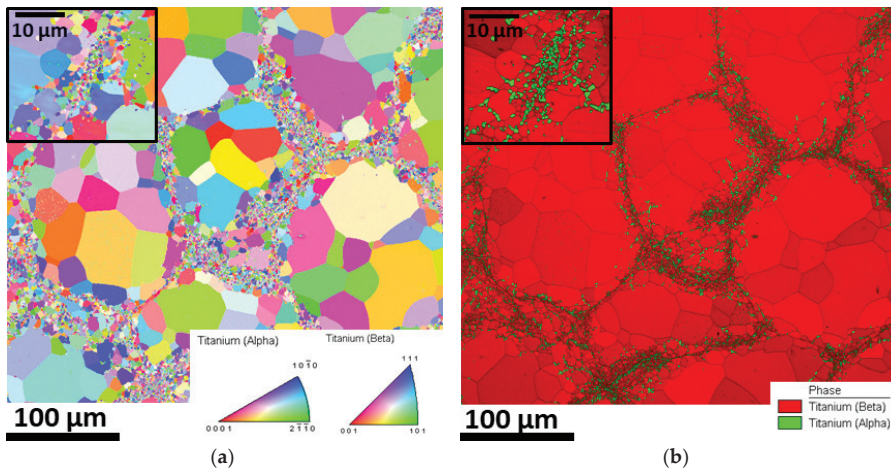


**Figure 4.** The microstructural characterization of BM 25 h. (a) 400  $\mu\text{m}^2$  IPF image and a close-up view of the shell region framed in black (b) corresponding phase image and a close-up view of the shell framed in black.

However, chemical composition of the alloy at this stage of the fabrication process could also be the cause of  $\alpha$  phase precipitation. Figure 5 shows WDS maps of chemical elements repartition in the harmonic microstructure of BM 50 h sample. The shell which is composed of both  $\alpha$  and  $\beta$  phases is enriched in titanium (Figure 5b) and depleted in niobium (Figure 5c), which is a  $\beta$ -stabilizer chemical element. Besides, Figure 5d clearly shows a local enrichment in oxygen in the shell vicinity, which probably enhances local  $\alpha$  phase precipitation. Oxygen is indeed a strong  $\alpha$ -stabilizer chemical element [40,41]. The oxygen contamination probably occurs during the mechanical BM stage, as the longer BM is processed, the higher the oxygen content in the alloy is.

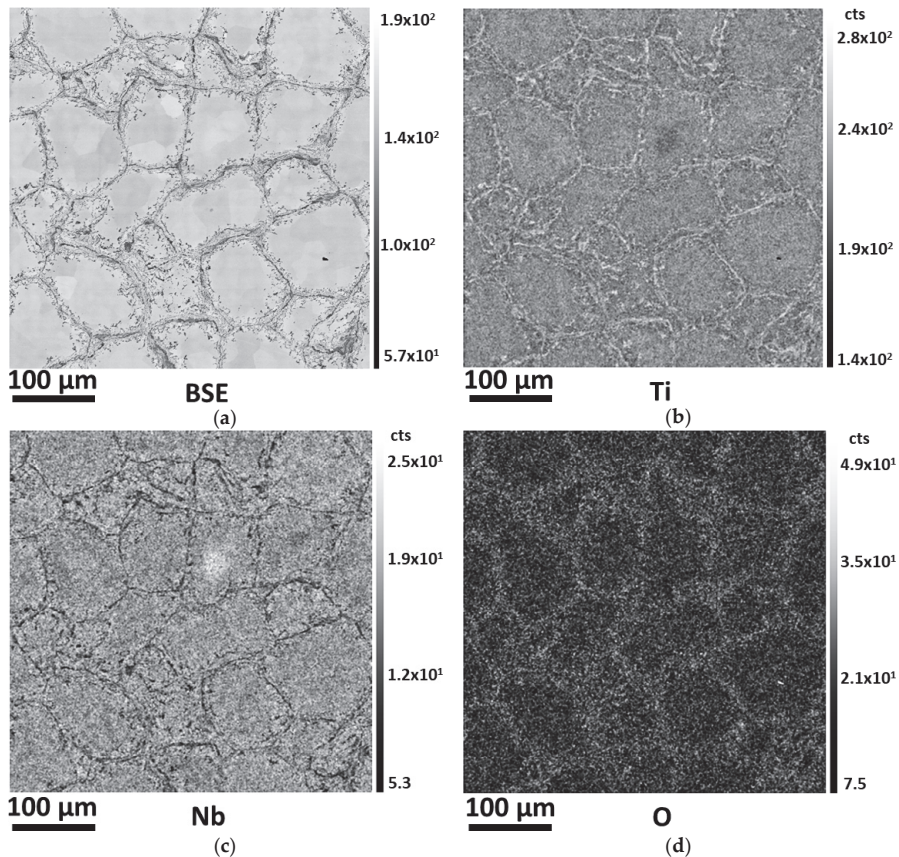


**Figure 5.** Chemical mapping of a BM 50 h sample. (a) Back-scattered electron image and corresponding (b) Ti repartition map, (c) Nb repartition map, and (d) O repartition map.

This investigation shows that it is possible to modify the microstructural features of the harmonic microstructures by playing with the processing parameters. The focus was made on the influence of BM time on the final microstructures. BM is indeed of primary importance in the fabrication process: it must be low energetic to avoid fracture of powder particles and high enough to induce local plastic deformation on the surface of the powder particles. Figure 6 shows IPF and grain size maps of 5 different samples fabricated using various BM times of 0 h, 12 h, 25 h, 50 h, and 100 h. Grains are considered to belong to the shell when their diameter is less than 10 μm. The other grains are considered to belong to the core of the microstructure. All the parameters which have been calculated, including shell surface fraction,  $\alpha$  phase surface fraction and grain sizes in the core and in the shell are evaluated thanks to EBSD data. Note that an average grain size in the shell has been calculated for both  $\beta$  and  $\alpha$  phases. The main microstructural features of the as-sintered samples are summarized in Table 1.

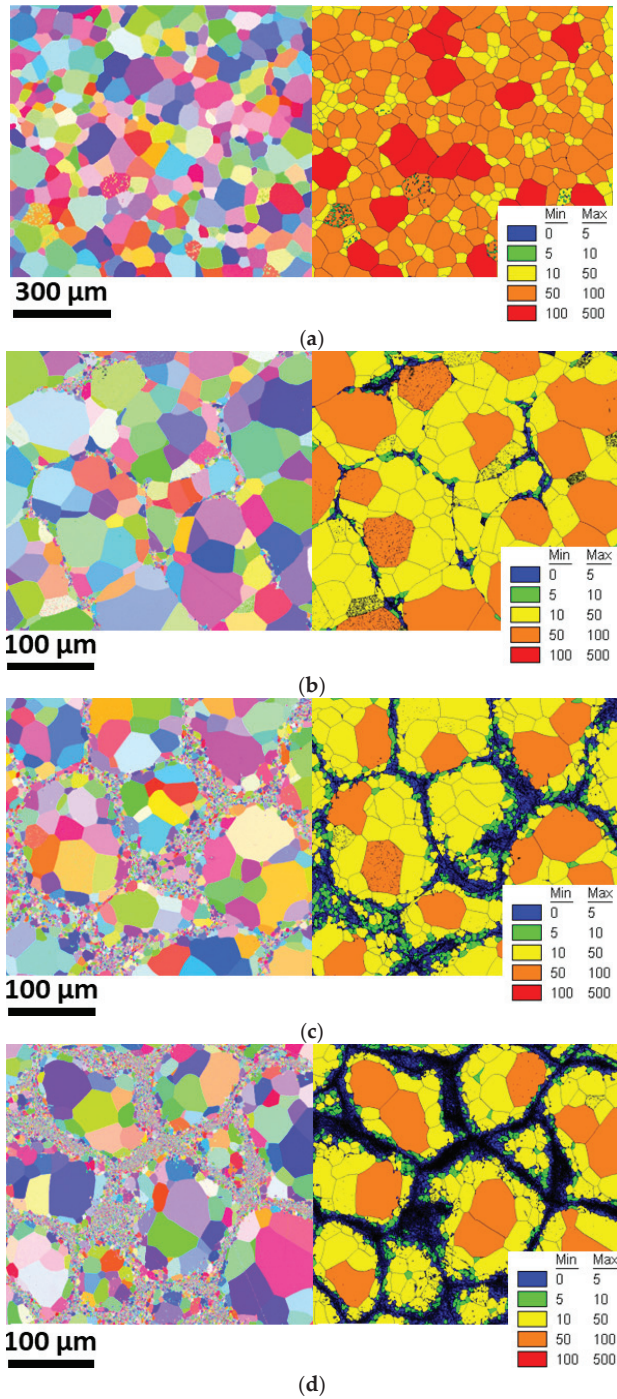
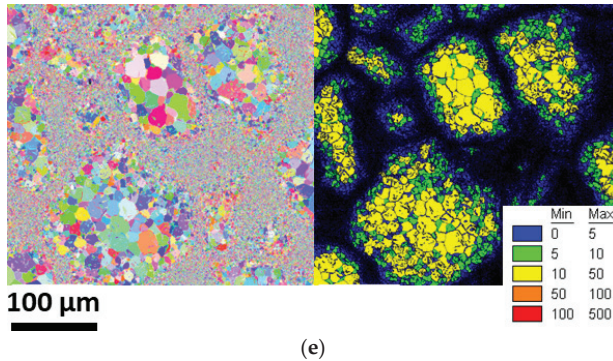


Figure 6. Cont.



**Figure 6.** IPF and grain size maps of as-sintered samples (a) IP (no BM), (b) BM 12 h, (c) BM 25 h, (d) BM 50 h, and (e) BM 100 h. Black lines are drawn as a representation of grain boundaries on grain size maps. Small grains areas appear thus in black, especially in the shell of (d,e).

**Table 1.** Microstructural features. A cross X is marked when the sample is not concerned by the microstructural feature.

| Name of the Sample | Surface Fraction of the Shell (%) | $\alpha$ Phase Fraction (%) | Average $\beta$ Grain Size of the Core ( $\mu\text{m}$ ) | Average $\beta$ Grain Size of the Shell ( $\mu\text{m}$ ) | Average $\alpha$ Grain Size of the Shell ( $\mu\text{m}$ ) |
|--------------------|-----------------------------------|-----------------------------|--|---|--|
| IP                 | X                                 | 0                           | 73.7   | X   | X  |
| BM 12 h            | 6.6                               | 2.0                         | 50.2   | 5.2   | 1.0  |
| BM 25 h            | 23.7                              | 4.4                         | 40.2   | 4.1   | 1.1  |
| BM 50 h            | 32.1                              | 12.7                        | 39.7   | 3.4   | 1.1  |
| BM 100 h           | 77.2                              | 39.2                        | 19.1   | 3.8   | 1.2  |

From the above data, it is obvious that BM time plays a key role on the shell volume fraction by modifying its width. The longer mechanical BM is processed, the wider the shell region is. The evolution of shell and  $\alpha$  phase fractions are plotted versus BM time on Figure 7a and indeed, the shell fraction increases from 6.6% for BM 12 h to 77.2% for a BM 100 h. In return,  $\alpha$  phase fraction also increases from 2.0% (for BM 12 h) to 39.2% (for BM 100 h) with BM time. This result could be expected as  $\alpha$  phase precipitates on grain boundaries in the shell vicinity. Moreover, as it was said earlier, a long BM stage implies a significant oxygen enrichment of the material, which could favor  $\alpha$  phase precipitation. Besides, the evolution of the grain size in the core versus BM time is also plotted on Figure 7b. The average grain size in the core slightly decreases when BM time increases. This decrease is notably obvious for BM 100 h, which has an average grain size in the core of about 20  $\mu\text{m}$ , close to the average value of the initial grain size in the powder particles.

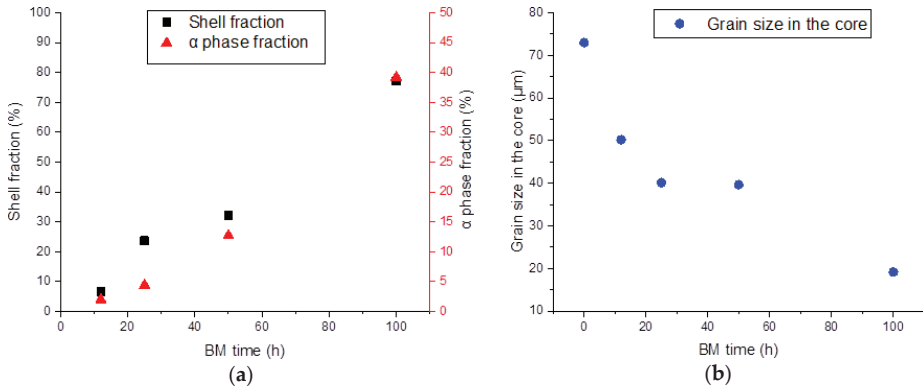


**Figure 7.** Evolution of (a) both shell fraction and  $\alpha$  phase fraction against BM time and (b) average grain sizes in the core against BM time.

To explain the unusual decrease of grain size in the core with BM time, a particular observation is pointed out for BM 100 h. Indeed, intergranular  $\alpha$  phase has precipitated inside the core of this microstructure, which has not been observed for samples processed with a lower BM time. That is probably why  $\beta$  grain growth in the core during SPS is limited for BM 100 h and the average value of grain size in the core is low for this sample.

A comparison of XRD results for all samples is shown on Figure 8. For every BM time,  $\beta$  phase peaks are detected on diffractograms. For BM 25 h, BM 50 h, and BM 100 h, additional  $\alpha$  peaks are detected and the intensity of these peaks increases with BM time. It confirms the fact that more and more  $\alpha$  phase is contained in the samples when BM time is increased. For BM 12 h, the volume fraction of  $\alpha$  phase is too low to be detected on XRD, whereas 2.2% of  $\alpha$  phase has been detected thanks to EBSD data. No other unindexed peak is detected on diffractograms.

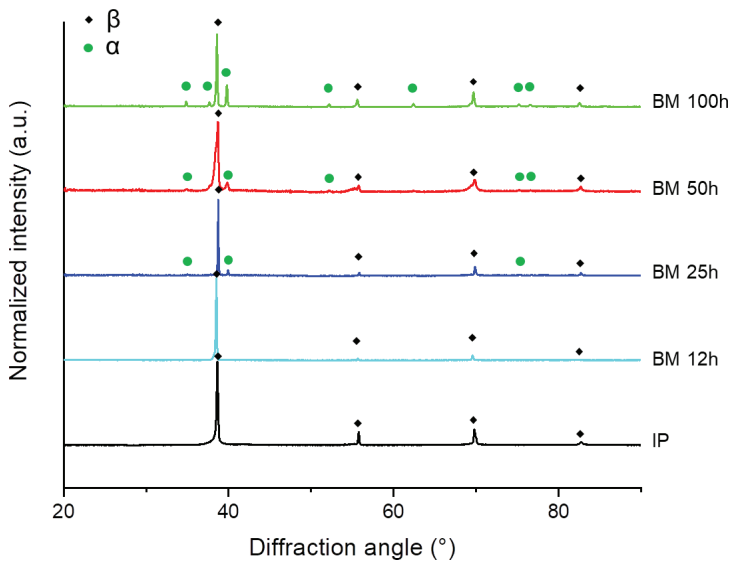


**Figure 8.** XRD results showing an increase in  $\alpha$  phase peak intensities with BM time.

### 3.3. Mechanical Properties of the As-Sintered Ti-2448 Samples

The samples introduced in the previous part of the study have been mechanically tested using room temperature simple shear tests. Equivalent Von-Mises tensile stress and strain have been computed as:  $\sigma = \tau \times \sqrt{3}$  and  $\varepsilon = \gamma / \sqrt{3}$ , where  $\tau$  and  $\gamma$  are respectively the shear stress and the shear strain. Figure 9a shows the equivalent tensile true stress-true strain curves of the simple shear tested samples. The corresponding strain hardening rate evolution against true strain is presented in the insert as Figure 9b.

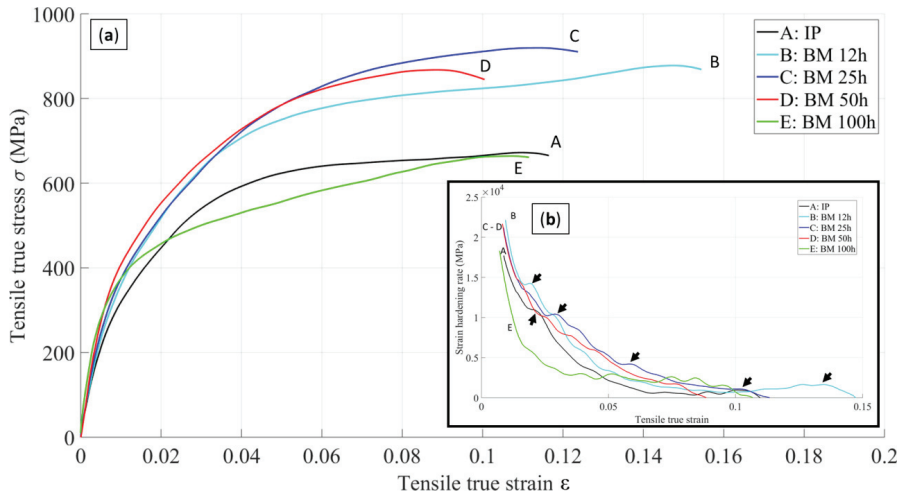


**Figure 9.** (a) Tensile curves and (b) corresponding strain-hardening rate versus true tensile strain curves. Curves are indexed with letters for clarity: A for the conventional microstructure IP, B for BM 12 h, C for BM 25 h, D for BM 50 h, and E for BM 100 h.

The mechanical tests have confirmed the high interest of heterogeneous microstructure for a better mechanical performance of materials and processing such heterogeneous materials is promising in order to increase the strength-ductility compromise of Ti-2448. Indeed, when compared with the conventional microstructure IP, both BM 12 h, BM 25 h, and BM 50 h curves reach a higher ultimate tensile stress while keeping comparable values of ductility and the heterogeneity of the microstructure contributes to the global increase of the flow stress. Only BM 100 h whose microstructure is mainly consisted of sub-micrometric  $\alpha$  and  $\beta$  grains (about 70%) reaches a lower ultimate tensile stress value than IP.

At low strain values, i.e. until 2%, heterogeneous microstructures reach higher stress values than the conventional one. However, from this first threshold point, BM 100 h differentiates from the other heterogeneous samples by starting a stationary regime where the increase of the flow stress is quite linear. Then, BM 12 h, BM 25 h and BM 50 h display a similar mechanical behavior until 4% strain, which is characterized by several strain hardening rate rebounds—defined as local minima followed by brief increases of the curve. Most of them are marked with black arrows on Figure 9b. The IP sample also benefits from a similar strain hardening rate rebound (also identified with a black arrow on Figure 9b). From this strain value of 4%, BM 12 h tends to soften, whereas both BM 25 h and BM 50 h keep hardening. At the same time, strain hardening rate of BM 100 h tends to stabilize at about 2.5 GPa, between strain values of 4 to 10%; however, stress levels which are reached by this sample are lower than every other sample. Finally, above 6% strain, BM 25 h keeps hardening with a last strain hardening rate rebound, whereas BM 12 h and BM 50 h do not. Yet, it is interesting to note

that for BM 12 h, a strain hardening increase starts from a strain of 10% and keeps going until 14%. It could be the cause of the higher true strain, which is finally reached by BM 12 h.

To explain the differences between shear behaviors, a first series of observations may be made on the elastic domains. Figure 10 is a comparative plot of experimentally and theoretically calculated Young's moduli of the samples. Error bars are calculated thanks to the data of the two mechanical tests which have been performed for each sample and the error on stress and strain measurements. The experimentally calculated modulus corresponds to the slope of the experimental curves whereas the theoretical Young's modulus is calculated using a rule of mixture considering both  $\alpha$  and  $\beta$  phase fractions and respective Young's moduli. A clear increase of Young's modulus of the samples with BM time is observed, which fits the evolution of the calculated Young's modulus. The evolution of the Young's modulus may be associated with the fact that  $\alpha$  phase volume fraction increases when BM time increases. As Young's modulus variations are due to the strength of chemical bonds between atoms, the change in chemistry of the alloy induces a change in the Young's modulus of the alloy. It increases when  $\alpha$  phase fraction increases but keeps a rather low value of around 50 GPa for a BM time of 50 h. By interpolating the experimental curve, it may therefore be possible to control the elastic modulus of the as-processed material by controlling BM time. In any case, it remains close to the Young's modulus of human bones (around 30 GPa for cortical human bones) and fulfills one of the requirements for biomedical and orthopedic implants.

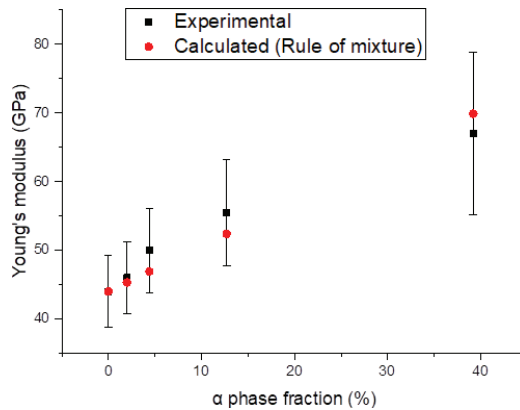


**Figure 10.** Evolution of Young's modulus (experimentally and theoretically calculated) against the  $\alpha$  phase fraction.

Apart from the increase of the Young's modulus with BM time, another global observation could help explaining the differences between the tensile curves of the samples. Indeed, for every sample except BM 100 h, the plots display wide elastic to plastic transition domains. Several hypotheses could be made to explain this unusual behavior. Firstly, it could be linked with the stress-induced martensitic phase transformation which may occur during straining of Ti-2448. For  $\langle 110 \rangle_{\beta}$  Ti-2448 single crystals, the stress-induced  $\beta$  to  $\alpha''$  phase transformation takes place at a constant stress and is thus characterized by a plateau on the stress-strain curve [10,11,42]. However, for isotropic polycrystals, the stress-induced transformation might occur together with other deformation mechanisms of  $\beta$  phase and be characterized by a nonlinear elastic domain and a wide elastic to plastic transition zone [8,43,44]. Besides, Ti-2448 is also liable to deform via  $\{332\} \langle 113 \rangle_{\beta}$  mechanical twinning [10–12,45], and this deformation mechanism could be the cause of the nonlinear elastic domain of the alloy. Finally, it could be linked with the heterogeneity of the as-processed microstructures. There is indeed a significant mechanical contrast between core and shell regions in the harmonic structure.

In order to get a better understanding of the mechanical behavior of every sample, three different mechanical characteristics have been calculated using experimental data: the conventional yield stress at 0.2% offset, a chosen 1% plastic strain offset (due to the difficulty of finding a linear part of the elastic domain from Figure 9) and finally the ultimate tensile stress (UTS). If the stress-induced phase transformation actually takes place during straining, the 0.2% plastic strain yield stress could also be interpreted as the stress required to induce the martensitic transformation of the  $\beta$  phase. They are plotted against BM time on Figure 11. It shows a global increase of the characteristic stresses when increasing BM time until BM 50 h is reached. BM 12 h, BM 25 h, and BM 50 h have a close 1% offset stress. For BM 100 h, both yield stress and ultimate tensile stress are lower than the one of the other samples.

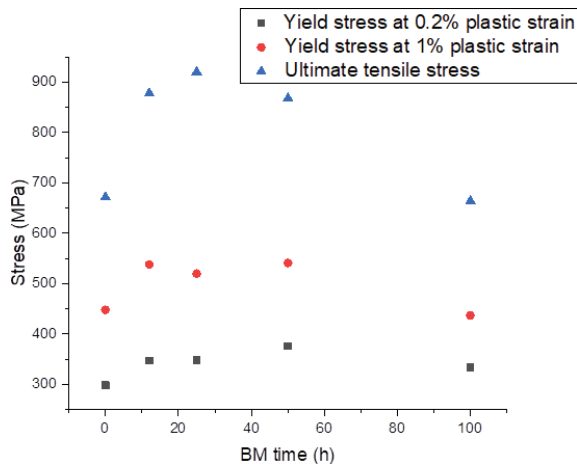


**Figure 11.** Evolution of yield stresses (at 0.2% and 1% plastic strain) and ultimate tensile stress against BM time.

These characteristic values (Figure 11) could be compared with the one in literature, especially those when Ti-2448 is processed by powder metallurgy. Kafkas et al. found UTS values of 650 to 720 MPa for Ti-2448 processed with Metal Injection Molding with coarse grain sizes and carbides precipitates [33]. When Ti-2448 is sintered using elemental powders by Li et al., UTS reaches 750 to 900 MPa according to the microstructure features [32]. Ti-2448 processed with Selective Laser Melting also display similar values of UTS, from 840 to 950 MPa with a heterogeneous microstructure in Yang et al.'s work to 665 MPa in Zhang et al.'s study. This last value may be improved by thermo-mechanical treatments [35,36]. In our work, UTS value which is reached by IP sample is comparable to UTS values of as-processed samples in literature, whereas heterogeneous samples have UTS values close to the ones of samples whose microstructure seems to be optimized.

The shear results also suggest a surprising behavior of BM 100 h. Indeed, the mechanical curve of BM 100 h is completely opposed to what would be expected based on the Hall-Petch relationship. Yet, the Hall-Petch relationship is mainly used for single phase pure metals and alloys whose grains are micron-wide. It is not the case here and consequently it could be an explanation of the differences which are observed between the experimental data and those expected by respect of the Hall-Petch relationship. Besides, the hypothesis which is made here is that  $\beta$  to  $\alpha''$  stress-induced martensitic transformation occurs during shear deformation of IP, BM 12 h, BM 25 h, and BM 50 h. However, both the drastic decrease of grain sizes and the notable increase of the fraction of  $\alpha$  precipitates could have inhibited the TRIP and/or TWIP phenomena for BM 100 h. For IP, the stress-induced phase transformation occurs early, but it is delayed when the shell and  $\alpha$  fraction are increased in BM 12 h,

BM 25 h, and BM 50 h. On the contrary, the BM 100 h material behaves like ultra-fine grain materials (UFG). Indeed, strain hardening rate curve of BM 100 h is characteristic of the behavior of UFG materials: strain hardening rate is high at the beginning of plastic deformation, but its decrease is very sharp once the second stage of plastic deformation is reached. This behavior is usually associated with a significant lack of ductility [46,47]. Fracture surface of BM 100 h is by the way characteristic of a brittle material.

The other samples—including IP, BM 12 h, BM 25 h, and BM 50 h—display local minima (followed by either a plateau or an increase) and fluctuations of the strain hardening rate. For IP, the local minimum of the strain hardening rate is followed by a plateau, whereas for heterogeneous ones (BM 12 h, BM 25 h, and BM 50 h), local minima are followed by a short increase of the strain hardening rate. These have been associated in the literature with the activation of a secondary deformation mechanism, which could be twinning or phase transformation [38,48]. However, no twin or martensite traces have been observed for the corresponding deformed post-mortem microstructures, and even for the post-mortem IP conventional microstructure, which is more susceptible to benefit from TRIP and/or TWIP deformation mechanisms. More investigations, including in situ tensile tests and/or cyclic mechanical tests, must be carried out for a better understanding of the global deformation mechanism. Other studies have associated the appearance of fluctuations in strain hardening rate curves with the formation of deformation gradients inside the microstructure [49]. Indeed, in heterogeneous and harmonic structures, the presence of both fine and coarse grains inside the microstructure induces hardness gradients in the microstructure. Coarse grains are easier to deform and start plastic deformation earlier than fine grains regions. Consequently, deformation gradients are formed at the core-shell interfaces which must be accommodated by geometrically necessary dislocations (GNDs). Piling up of GNDs at the core-shell interfaces results in high back stresses acting against the propagation of newly formed dislocations: it is a form of kinematic hardening contributing to the global work hardening of the alloy [50–52]. Fluctuations of the strain hardening rate of BM 12 h, BM 25 h, and BM 50 h might be the signatures of this kind of deformation mechanism.

The differences in mechanical behavior between samples are also illustrated by the characterization of the post-mortem deformed microstructures which has been carried out using XRD, microscopy, and EBSD. Figure 12 presents post-mortem optical images of the deformed surface of BM 12 h, BM 25 h, BM 50 h, and BM 100 h, whereas Figure 12e presents a SEM secondary electrons close-up view of the deformation bands on IP. Deformation marks are visible on the surface of the samples. For IP and BM 12 h, a very high number of marks is clearly identified. The number of these bands decreases with BM time (and consequently with shell and  $\alpha$  precipitates fraction). Indeed, for BM 25 h and BM 50 h, only a few bands are visible, and no trace is identified for BM 100 h. EBSD investigation has shown that these bands are not twins, even if some similar deformation features have been identified as mechanical twins in recent studies [11,12]. Therefore, it may be slip bands. These slip bands are straight and parallel in some grains, whereas in others, they intersect and overlap. It means that several gliding systems are successively activated. Moreover, cross-slip of dislocations also occurs, because of the wavy shape of these deformation traces. Their intersection shows shearing effects (clearly visible on Figure 12e), which could give us information about the timing of the appearance of these bands during deformation. The progressive disappearance of deformation marks with BM time confirms the fact that a change in deformation mechanism of Ti-2448 occurs when it is heterogeneously processed.

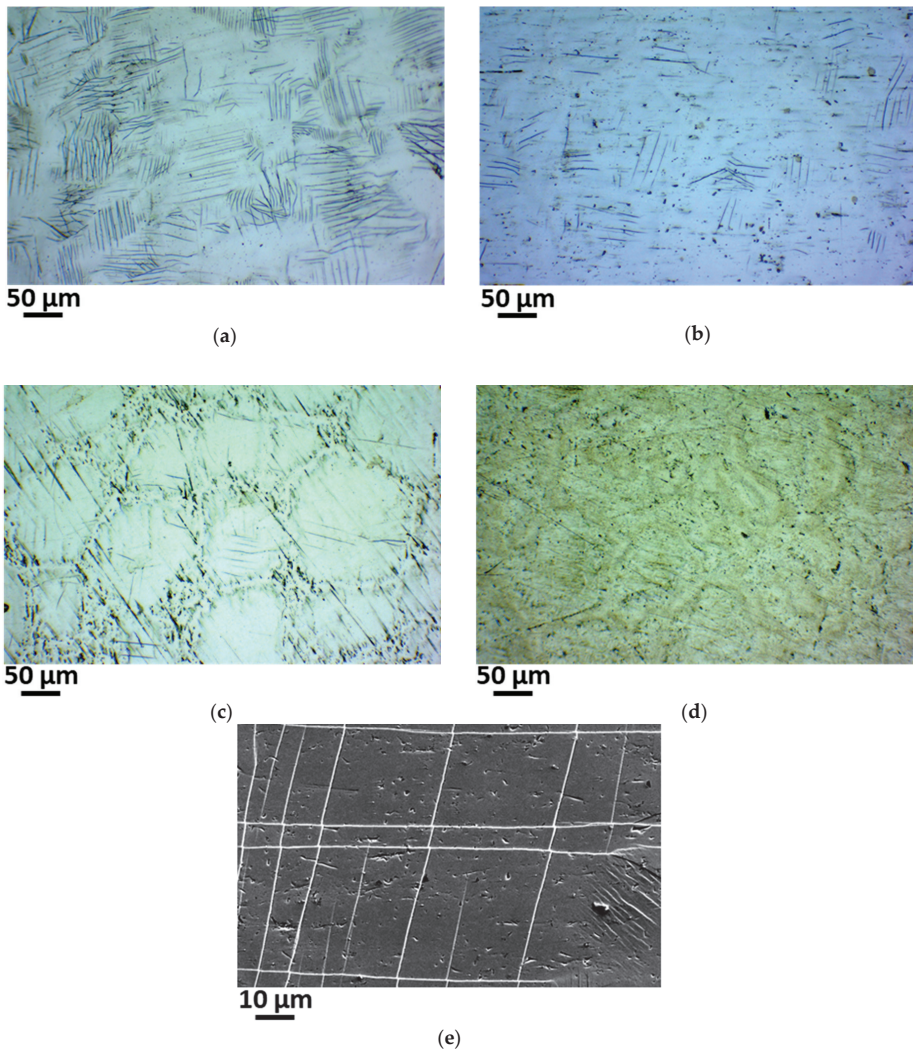


**Figure 12.** Optical images of the surface of the samples after simple shear (a) BM 12 h, (b) BM 25 h, (c) BM 50 h, (d) BM 100 h, and (e) SEM secondary electrons image of deformation bands on the surface of the IP sample.

#### 4. Conclusions

This study has highlighted different mechanical responses of Ti-2448 samples according to the powder metallurgy processing route. These differences may reasonably be figured out. Indeed, several microstructural features have been modified by playing with the processing parameters, including grain sizes in both core and shell, chemical concentrations, and  $\alpha$  phase precipitation. Most of these features have been shown to play a role in the deformation mechanism of  $\beta$ -metastable titanium alloys. The chemical composition of the alloy, and most particularly the oxygen content, is indeed of primary importance on the stress-induced  $\beta$  to  $\alpha'$  phase transformation [53]. Grain sizes also influence the appearance of phase transformation and mechanical twinning in the deformation sequence of

$\beta$ -metastable alloys [54,55]. Finally, precipitation of  $\alpha$  and/or  $\omega$  phases also significantly influences the mechanical behavior of Ti-2448 [43,56].

**Author Contributions:** Conceptualization, D.T. and G.D.; investigation, B.F., A.H. and E.L.; methodology, B.F., D.T. and Y.H.; resources, Y.H. and F.P.; supervision, D.T., F.P. and G.D.; writing—original draft, B.F.; writing—review & editing, F.P. and G.D. All authors have read and agreed to the published version of the manuscript.

**Funding:** This research received no external funding.

**Conflicts of Interest:** The authors declare no conflict of interest.

## References

- Banerjee, D.; Williams, J.C. Perspectives on Titanium Science and Technology. *Acta Mater.* **2013**, *61*, 844–879. [CrossRef]
- Steinemann, S.G. Metal implants and surface reactions. *Injury* **1996**, *27*, S/C16–S/C22. [CrossRef]
- Hao, Y.L.; Li, S.J.; Sun, S.Y.; Zheng, C.Y.; Yang, R. Elastic deformation behaviour of Ti–24Nb–4Zr–7.9Sn for biomedical applications. *Acta Biomater.* **2007**, *3*, 277–286. [CrossRef] [PubMed]
- Zhang, Y.W.; Li, S.J.; Obbard, E.G.; Wang, H.; Wang, S.C.; Hao, Y.L.; Yang, R. Elastic properties of Ti–24Nb–4Zr–8Sn single crystals with bcc crystal structure. *Acta Mater.* **2011**, *59*, 3081–3090. [CrossRef]
- Hao, Y.L.; Li, S.J.; Sun, S.Y.; Yang, R. Effect of Zr and Sn on Young's modulus and superelasticity of Ti–Nb-based alloys. *Mater. Sci. Eng. A* **2006**, *441*, 112–118. [CrossRef]
- Arifin, A.; Sulong, A.B.; Muhamad, N.; Syarif, J.; Ramli, M.I. Material processing of hydroxyapatite and titanium alloy (HA/Ti) composite as implant materials using powder metallurgy: A review. *Mater. Des.* **2014**, *55*, 165–175. [CrossRef]
- Qu, Y.; Zheng, S.; Dong, R.; Kang, M.; Zhou, H.; Zhao, D.; Zhao, J. Ti-24Nb-4Zr-8Sn Alloy Pedicle Screw Improves Internal Vertebral Fixation by Reducing Stress-Shielding Effects in a Porcine Model. Available online: <https://www.hindawi.com/journals/bmri/2018/8639648/> (accessed on 23 March 2020).
- Yang, Y.; Castany, P.; Cornen, M.; Prima, F.; Li, S.J.; Hao, Y.L.; Gloriant, T. Characterization of the martensitic transformation in the superelastic Ti–24Nb–4Zr–8Sn alloy by in situ synchrotron X-ray diffraction and dynamic mechanical analysis. *Acta Mater.* **2015**, *88*, 25–33. [CrossRef]
- Yang, Y.; Castany, P.; Cornen, M.; Thibon, I.; Prima, F.; Gloriant, T. Texture investigation of the superelastic Ti–24Nb–4Zr–8Sn alloy. *J. Alloys Compd.* **2014**, *591*, 85–90. [CrossRef]
- Yao, T.; Du, K.; Wang, H.; Huang, Z.; Li, C.; Li, L.; Hao, Y.; Yang, R.; Ye, H. In situ scanning and transmission electron microscopy investigation on plastic deformation in a metastable  $\beta$  titanium alloy. *Acta Mater.* **2017**, *133*, 21–29. [CrossRef]
- Yang, Y.; Castany, P.; Bertrand, E.; Cornen, M.; Lin, J.X.; Gloriant, T. Stress release-induced interfacial twin boundary  $\omega$  phase formation in a  $\beta$  type Ti-based single crystal displaying stress-induced  $\alpha''$  martensitic transformation. *Acta Mater.* **2018**, *149*, 97–107. [CrossRef]
- Liang, Q.; Kloenne, Z.; Zheng, Y.; Wang, D.; Antonov, S.; Gao, Y.; Hao, Y.; Yang, R.; Wang, Y.; Fraser, H.L. The role of nano-scaled structural non-uniformities on deformation twinning and stress-induced transformation in a cold rolled multifunctional  $\beta$ -titanium alloy. *Scr. Mater.* **2020**, *177*, 181–185. [CrossRef]
- Li, S.J.; Jia, M.T.; Prima, F.; Hao, Y.L.; Yang, R. Improvements in nonlinear elasticity and strength by grain refinement in a titanium alloy with high oxygen content. *Scr. Mater.* **2011**, *64*, 1015–1018. [CrossRef]
- Zhang, S.Q.; Li, S.J.; Jia, M.T.; Prima, F.; Chen, L.J.; Hao, Y.L.; Yang, R. Low-cycle fatigue properties of a titanium alloy exhibiting nonlinear elastic deformation behavior. *Acta Mater.* **2011**, *59*, 4690–4699. [CrossRef]
- Prima, F.; Vermaut, P.; Texier, G.; Ansel, D.; Gloriant, T. Evidence of  $\alpha$ -nanophase heterogeneous nucleation from  $\omega$  particles in a  $\beta$ -metastable Ti-based alloy by high-resolution electron microscopy. *Scr. Mater.* **2006**, *54*, 645–648. [CrossRef]
- Zheng, Y.; Williams, R.E.A.; Sosa, J.M.; Wang, Y.; Banerjee, R.; Fraser, H.L. The role of the  $\omega$  phase on the non-classical precipitation of the  $\alpha$  phase in metastable  $\beta$ -titanium alloys. *Scr. Mater.* **2016**, *111*, 81–84. [CrossRef]
- Li, C.; Chen, J.; Li, W.; Ren, Y.J.; He, J.J.; Song, Z.X. Effect of heat treatment variations on the microstructure evolution and mechanical properties in a  $\beta$  metastable Ti alloy. *J. Alloys Compd.* **2016**, *684*, 466–473. [CrossRef]

18. Abdel-Hady, M.; Hinoshita, K.; Morinaga, M. General approach to phase stability and elastic properties of  $\beta$ -type Ti-alloys using electronic parameters. *Scr. Mater.* **2006**, *55*, 477–480. [[CrossRef](#)]
19. Lai, M.J.; Tasan, C.C.; Raabe, D. On the mechanism of {332} twinning in metastable  $\beta$  titanium alloys. *Acta Mater.* **2016**, *111*, 173–186. [[CrossRef](#)]
20. Marteleur, M.; Sun, F.; Gloriant, T.; Vermaut, P.; Jacques, P.J.; Prima, F. On the design of new  $\beta$ -metastable titanium alloys with improved work hardening rate thanks to simultaneous TRIP and TWIP effects. *Scr. Mater.* **2012**, *66*, 749–752. [[CrossRef](#)]
21. Li, Z.; Zheng, B.; Wang, Y.; Topping, T.; Zhou, Y.; Valiev, R.Z.; Shan, A.; Lavernia, E.J. Ultrafine-grained Ti–Nb–Ta–Zr alloy produced by ECAP at room temperature. *J. Mater. Sci.* **2014**, *49*, 6656–6666. [[CrossRef](#)]
22. Shin, S.; Zhu, C.; Zhang, C.; Vecchio, K.S. Extraordinary strength-ductility synergy in a heterogeneous-structured  $\beta$ -Ti alloy through microstructural optimization. *Mater. Res. Lett.* **2019**, *7*, 467–473. [[CrossRef](#)]
23. Lu, K. Making strong nanomaterials ductile with gradients. *Science* **2014**, *345*, 1455–1456. [[CrossRef](#)] [[PubMed](#)]
24. Yang, M.; Yan, D.; Yuan, F.; Jiang, P.; Ma, E.; Wu, X. Dynamically reinforced heterogeneous grain structure prolongs ductility in a medium-entropy alloy with gigapascal yield strength. *Proc. Natl. Acad. Sci. USA* **2018**, *115*, 7224–7229. [[CrossRef](#)]
25. Vajpai, S.K.; Ota, M.; Zhang, Z.; Ameyama, K. Three-dimensionally gradient harmonic structure design: An integrated approach for high performance structural materials. *Mater. Res. Lett.* **2016**, *4*, 191–197. [[CrossRef](#)]
26. Vajpai, S.K.; Sawangrat, C.; Yamaguchi, O.; Ciucu, O.P.; Ameyama, K. Effect of bimodal harmonic structure design on the deformation behaviour and mechanical properties of Co–Cr–Mo alloy. *Mater. Sci. Eng. C* **2016**, *58*, 1008–1015. [[CrossRef](#)] [[PubMed](#)]
27. Zhang, Z.; Vajpai, S.K.; Orlov, D.; Ameyama, K. Improvement of mechanical properties in SUS304L steel through the control of bimodal microstructure characteristics. *Mater. Sci. Eng. A* **2014**, *598*, 106–113. [[CrossRef](#)]
28. Kikuchi, S.; Hayami, Y.; Ishiguri, T.; Guennec, B.; Ueno, A.; Ota, M.; Ameyama, K. Effect of bimodal grain size distribution on fatigue properties of Ti–6Al–4V alloy with harmonic structure under four-point bending. *Mater. Sci. Eng. A* **2017**, *687*, 269–275. [[CrossRef](#)]
29. Weston, N.S.; Derguti, F.; Tudball, A.; Jackson, M. Spark plasma sintering of commercial and development titanium alloy powders. *J. Mater. Sci.* **2015**, *50*, 4860–4878. [[CrossRef](#)]
30. Weston, N.S.; Jackson, M. FAST-forged Titanium Alloy Swarf: A Solid-State Closed-Loop Recycling Approach for Aerospace Machining Waste. *Metals* **2020**, *10*, 296. [[CrossRef](#)]
31. Bodunrin, M.O.; Chown, L.H.; Omotoyinbo, J.A. Development of low-cost titanium alloys: A chronicle of challenges and opportunities. *Mater. Today Proc.* **2020**, S2214785320317685. [[CrossRef](#)]
32. Li, X.; Ye, S.; Yuan, X.; Yu, P. Fabrication of biomedical Ti–24Nb–4Zr–8Sn alloy with high strength and low elastic modulus by powder metallurgy. *J. Alloys Compd.* **2019**, *772*, 968–977. [[CrossRef](#)]
33. Kafkas, F.; Ebel, T. Metallurgical and mechanical properties of Ti–24Nb–4Zr–8Sn alloy fabricated by metal injection molding. *J. Alloys Compd.* **2014**, *617*, 359–366. [[CrossRef](#)]
34. Liu, Y.; Li, S.; Hou, W.; Wang, S.; Hao, Y.; Yang, R.; Sercombe, T.B.; Zhang, L.-C. Electron Beam Melted Beta-type Ti–24Nb–4Zr–8Sn Porous Structures with High Strength-to-Modulus Ratio. *J. Mater. Sci. Technol.* **2016**, *32*, 505–508. [[CrossRef](#)]
35. Yang, C.L.; Zhang, Z.J.; Li, S.J.; Liu, Y.J.; Sercombe, T.B.; Hou, W.T.; Zhang, P.; Zhu, Y.K.; Hao, Y.L.; Zhang, Z.F.; et al. Simultaneous improvement in strength and plasticity of Ti–24Nb–4Zr–8Sn manufactured by selective laser melting. *Mater. Des.* **2018**, *157*, 52–59. [[CrossRef](#)]
36. Zhang, L.C.; Klemm, D.; Eckert, J.; Hao, Y.L.; Sercombe, T.B. Manufacture by selective laser melting and mechanical behavior of a biomedical Ti–24Nb–4Zr–8Sn alloy. *Scr. Mater.* **2011**, *65*, 21–24. [[CrossRef](#)]
37. Zheng, R.; Zhang, Z.; Nakatani, M.; Ota, M.; Chen, X.; Ma, C.; Ameyama, K. Enhanced ductility in harmonic structure designed SUS316L produced by high energy ball milling and hot isostatic sintering. *Mater. Sci. Eng. A* **2016**, *674*, 212–220. [[CrossRef](#)]
38. Dirras, G.; Ueda, D.; Hocini, A.; Tingaud, D.; Ameyama, K. Cyclic shear behavior of conventional and harmonic structure-designed Ti–25Nb–25Zr  $\beta$ -titanium alloy: Back-stress hardening and twinning inhibition. *Scr. Mater.* **2017**, *138*, 44–47. [[CrossRef](#)]

39. Momprou, F.; Tingaud, D.; Chang, Y.; Gault, B.; Dirras, G. Conventional vs harmonic-structured  $\beta$ -Ti-25Nb-25Zr alloys: A comparative study of deformation mechanisms. *Acta Mater.* **2018**, *161*, 420–430. [[CrossRef](#)]
40. Combres, Y. *Propriétés Du Titane Et De Ses Alliages*; Techniques de l'ingénieur: Paris, France, 2010.
41. Chou, K.; Marquis, E.A. Oxygen effects on  $\omega$  and  $\alpha$  phase transformations in a metastable  $\beta$  Ti–Nb alloy. *Acta Mater.* **2019**, *181*, 367–376. [[CrossRef](#)]
42. Yao, T.; Du, K.; Wang, H.; Qi, L.; He, S.; Hao, Y.; Yang, R.; Ye, H. Reversible twin boundary migration between  $\alpha''$  martensites in a Ti–Nb–Zr–Sn alloy. *Mater. Sci. Eng. A* **2017**, *688*, 169–173. [[CrossRef](#)]
43. Sun, F.; Hao, Y.L.; Zhang, J.Y.; Prima, F. Contribution of nano-sized lamellar microstructure on recoverable strain of Ti–24Nb–4Zr–7.9Sn titanium alloy. *Mater. Sci. Eng. A* **2011**, *528*, 7811–7815. [[CrossRef](#)]
44. Hao, Y.L.; Zhang, Z.B.; Li, S.J.; Yang, R. Microstructure and mechanical behavior of a Ti–24Nb–4Zr–8Sn alloy processed by warm swaging and warm rolling. *Acta Mater.* **2012**, *60*, 2169–2177. [[CrossRef](#)]
45. Yang, Y.; Castany, P.; Hao, Y.L.; Gloriant, T. Plastic deformation via hierarchical nano-sized martensitic twinning in the metastable  $\beta$  Ti–24Nb–4Zr–8Sn alloy. *Acta Mater.* **2020**, *194*, 27–39. [[CrossRef](#)]
46. Shumilin, S.E.; Janecek, M.; Isaev, N.V.; Homola, P.; Kral, R. Low Temperature Plasticity of an Ultrafine-Grained Al–3Mg Alloy Prepared by Accumulative Roll Bonding. *Adv. Eng. Mater.* **2012**, *14*, 35–38. [[CrossRef](#)]
47. Krasilnikov, N.; Lojkowski, W.; Pakiel, Z.; Valiev, R. Tensile strength and ductility of ultra-fine-grained nickel processed by severe plastic deformation. *Mater. Sci. Eng. A* **2005**, *397*, 330–337. [[CrossRef](#)]
48. Ueda, D.; Dirras, G.; Hocini, A.; Tingaud, D.; Ameyama, K.; Langlois, P.; Vrel, D.; Trzaska, Z. Data on processing of Ti–25Nb–25Zr  $\beta$ -titanium alloys via powder metallurgy route: Methodology, microstructure and mechanical properties. *Data Brief* **2018**, *17*, 703–708. [[CrossRef](#)]
49. Jiang, F.; Zhao, C.; Liang, D.; Zhu, W.; Zhang, Y.; Pan, S.; Ren, F. In-situ formed heterogeneous grain structure in spark-plasma-sintered CoCrFeMnNi high-entropy alloy overcomes the strength-ductility trade-off. *Mater. Sci. Eng. A* **2020**, *771*, 138625. [[CrossRef](#)]
50. Wu, X.; Zhu, Y. Heterogeneous materials: A new class of materials with unprecedented mechanical properties. *Mater. Res. Lett.* **2017**, *5*, 527–532. [[CrossRef](#)]
51. Wang, Y.F.; Wang, M.S.; Fang, X.T.; Guo, F.J.; Liu, H.Q.; Scattergood, R.O.; Huang, C.X.; Zhu, Y.T. Extra strengthening in a coarse/ultrafine grained laminate: Role of gradient interfaces. *Int. J. Plast.* **2019**, *123*, 196–207. [[CrossRef](#)]
52. Yang, M.; Pan, Y.; Yuan, F.; Zhu, Y.; Wu, X. Back stress strengthening and strain hardening in gradient structure. *Mater. Res. Lett.* **2016**, *4*, 145–151. [[CrossRef](#)]
53. Obbard, E.G.; Hao, Y.L.; Talling, R.J.; Li, S.J.; Zhang, Y.W.; Dye, D.; Yang, R. The effect of oxygen on  $\alpha''$  martensite and superelasticity in Ti–24Nb–4Zr–8Sn. *Acta Mater.* **2011**, *59*, 112–125. [[CrossRef](#)]
54. Bhattacharjee, A.; Bhargava, S.; Varma, V.K.; Kamat, S.V.; Gogia, A.K. Effect of  $\beta$  grain size on stress induced martensitic transformation in  $\beta$  solution treated Ti–10V–2Fe–3Al alloy. *Scr. Mater.* **2005**, *53*, 195–200. [[CrossRef](#)]
55. Danard, Y.; Sun, F.; Gloriant, T.; Freiherr Von Thüngen, I.; Piellard, M.; Prima, F. The Influence of Twinning on the Strain–Hardenability in TRIP/TWIP Titanium Alloys: Role of Solute–Solution Strengthening. *Front. Mater.* **2020**, *7*. [[CrossRef](#)]
56. Coakley, J.; Rahman, K.M.; Vorontsov, V.A.; Ohnuma, M.; Dye, D. Effect of precipitation on mechanical properties in the  $\beta$ -Ti alloy Ti–24Nb–4Zr–8Sn. *Mater. Sci. Eng. A* **2016**, *655*, 399–407. [[CrossRef](#)]

**Publisher's Note:** MDPI stays neutral with regard to jurisdictional claims in published maps and institutional affiliations.



© 2020 by the authors. Licensee MDPI, Basel, Switzerland. This article is an open access article distributed under the terms and conditions of the Creative Commons Attribution (CC BY) license (<http://creativecommons.org/licenses/by/4.0/>).



Article

# Ratcheting-Fatigue Behavior of Harmonic-Structure-Designed SUS316L Stainless Steel

Yang Song <sup>1</sup>, Zhe Zhang <sup>2,3,\*</sup>, Hantuoma Ma <sup>2</sup>, Masashi Nakatani <sup>4</sup>, Mie Ota Kawabata <sup>4</sup> and Kei Ameyama <sup>4</sup>

- <sup>1</sup> Tianjin Key Laboratory for Advanced Mechatronic System Design and Intelligent Control, National Demonstration Center for Experimental Mechanical and Electrical Engineering Education, School of Mechanical Engineering, Tianjin University of Technology, Tianjin 300384, China; songyang2661@sina.com
- <sup>2</sup> School of Chemical Engineering and Technology, Tianjin University, Tianjin 300350, China; hantuoma@hotmail.com
- <sup>3</sup> Tianjin Key Laboratory of Chemical Process Safety and Equipment Technology, Tianjin 300350, China
- <sup>4</sup> Department of Mechanical Engineering, Faculty of Science and Engineering, Ritsumeikan University, Shiga 525-8577, Japan; rm005034@ed.ritsumei.ac.jp (M.N.); mie-ota@fc.ritsumei.ac.jp (M.O.K.); ameyama@se.ritsumei.ac.jp (K.A.)
- \* Correspondence: zhe.zhang@tju.edu.cn

**Abstract:** Stainless steels with harmonic-structure design have a great balance of high strength and high ductility. Therefore, it is imperative to investigate their fatigue properties for engineering applications. In the present work, the harmonic-structured SUS316L stainless steels were fabricated by mechanical milling (MM) and subsequent hot isostatic pressing (HIP) process. A series of ratcheting-fatigue tests were performed on the harmonic-structured SUS316L steels under stress-control mode at room temperature. Effects of grain structure and stress-loading conditions on ratcheting behavior and fatigue life were investigated. Results showed that grain size and applied mean stress had a significant influence on ratcheting-strain accumulation and fatigue life. Owing to the ultrafine grained structure, tensile strength of the harmonic-structured SUS316L steels could be enhanced, which restrained the ratcheting-strain accumulation, resulting in a prolonged fatigue life. A higher mean stress caused a faster ratcheting-strain accumulation, which led to the deterioration of fatigue life. Moreover, a modified model based on Smith–Watson–Topper (SWT) criterion predicted the ratcheting-fatigue life of the harmonic-structured SUS316L steels well. Most of the fatigue-life points were located in the 5 times error band.

**Citation:** Song, Y.; Zhang, Z.; Ma, H.; Nakatani, M.; Kawabata, M.O.; Ameyama, K. Ratcheting-Fatigue Behavior of Harmonic-Structure-Designed SUS316L Stainless Steel. *Metals* **2021**, *11*, 477. <https://doi.org/10.3390/met11030477>

Academic Editor: Eric Hug

Received: 25 January 2021

Accepted: 5 March 2021

Published: 13 March 2021

**Publisher's Note:** MDPI stays neutral with regard to jurisdictional claims in published maps and institutional affiliations.



**Copyright:** © 2021 by the authors. Licensee MDPI, Basel, Switzerland. This article is an open access article distributed under the terms and conditions of the Creative Commons Attribution (CC BY) license (<https://creativecommons.org/licenses/by/4.0/>).

**Keywords:** stainless steel; harmonic structure; ratcheting; fatigue; fatigue-life prediction

## 1. Introduction

Austenitic stainless steels have excellent mechanical properties and corrosion resistance, and are often used as structural materials in petrochemical equipment, nuclear equipment, and medical equipment [1–3]. Therefore, it is imperative to realize high strength and high ductility in stainless steels for structural safety. Usually, these types of equipment are often subjected to cyclic loading in service. Thus, cyclic deformation and fatigue properties of stainless steels need to be considered [4–6].

In recent years, structural materials with heterogenous microstructures have been proposed to achieve excellent mechanical properties and good fatigue resistance [7–15]. Mechanical properties and deformation mechanisms of some typical heterogenous microstructures, such as gradient nanograined (GNG) structure [9–11], lamellar structure [12–14], hierarchical and laminated grains and twins structure [15], and harmonic structure [16,17], have been investigated. As indicated in Figure 1a, the conventional bimodal structure has an irregular coarse grain (CG) and ultrafine grain (UFG) distribution. By contrast, harmonic structure has a regular bimodal grain-size distribution, whereas UFG structure (shell) exhibits a three-dimensional, continuously connected network structure (Figure 1b).

The regular network structure could relieve strain localization during tensile deformation, which causes an extra strain hardening. Therefore, the harmonic-structure-designed materials exhibit a superior strength–ductility synergy [18–23].

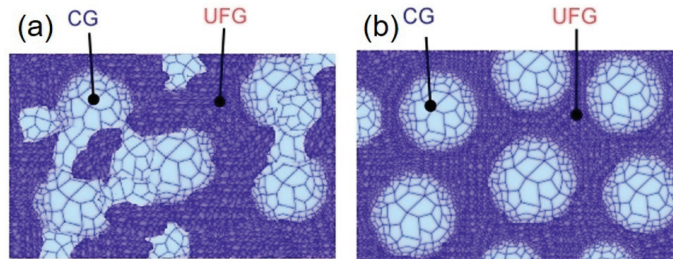


**Figure 1.** Schematic of (a) bimodal structure and (b) harmonic structure.

For engineering applications in service, the cyclic response and fatigue properties of heterogenous-structured stainless steels have been studied in the past decades. GNG SUS316L steels demonstrated a superior balance of high strength and large uniform elongation, as well as good fatigue resistance. Due to the increased tensile strength by GNG surface layer, high-cycle fatigue resistance could be improved in GNG steels compared to CG or UFG steels. By contrast, it is remarkable that abnormal grain coarsening could suppress surface roughening and fatigue cracking. Thus, low-cycle fatigue resistance was also improved in GNG materials [9,10]. It was found that lamellar structure impeded fatigue-crack growth, which restrained fatigue-crack growth rates [13,14]. Therefore, the lamellar-structured steels also demonstrated good fatigue resistance. Furthermore, the steels with hierarchical and laminated grains and twins also induced a friction stress that acted on the crack surface and decelerated fatigue-crack opening and growth [15]. The high-cycle fatigue properties and fatigue-crack growth behavior of harmonic-structured SUS316L steels have been investigated [24,25]. Fatigue limits of the harmonic-structure SUS316L steels were higher than that of the CG SUS316L steels, which was related to the enhanced tensile strength [24]. As expected, the UFG structure had worse crack-growth resistance than the CG structure. Therefore, the harmonic-structured 316L steels had higher fatigue-crack growth rates and a lower threshold stress intensity factor range for crack growth ( $\Delta K_{th}$ ) compared to the homogeneous CG SUS316L steels. Fatigue cracks tended to propagate along UFG network structure in harmonic-structured SUS316L steels [25,26].

As mentioned, stainless steels are often used as structural materials in thin-wall piping systems, which are often subjected to cyclic loading and alternating temperature or internal pressure, especially during start/stop operation. Therefore, pipelines are subjected to an asymmetric stress cycling, which can cause an accumulation of plastic strain known as ratcheting strain [27–31]. For example, in the early 1990s, the ratcheting-fatigue behavior of nuclear pipes and its detrimental effect on the nuclear-reactor structure were contained in the American ITER design code and ASME NB 32xx code [27]. As reported, mean stress had a much higher influence on ratcheting-strain accumulation than stress amplitude or stress-loading rate. Therefore, the effects of mean stress on ratcheting strain and low-cycle fatigue life were investigated in stainless steels. In general, a larger mean stress induced a rapid -train accumulation, resulting in deterioration of fatigue life. Moreover, many stress-based criteria have been proposed to correct the effect of mean stress on fatigue-life prediction in the past decades, such as the Goodman criterion, Gerber criterion, Smith–Watson–Topper (SWT) criterion, and so on. It also has been reported that the models based on the SWT criterion possessed a higher prediction accuracy for ratcheting-fatigue life of steels subjected to asymmetrical stress cyclic loading [4,28]. However, comprehensive understanding of ratcheting behavior and fatigue-life prediction for harmonic-structured stainless steels still remains unclear.

In the present work, the ratcheting-fatigue properties of the harmonic-structured SUS316L steels were investigated. The effect of grain structure and applied mean stress on ratcheting strain and fatigue life are revealed. Moreover, a modified model based on the SWT criterion is proposed for the prediction of fatigue life of harmonic-structured SUS316L steels.

## 2. Materials and Experiments

SUS316L stainless steels with a harmonic-structure topology were fabricated using horizontal ball-milling and hot isostatic pressing (HIP) processes. The chemical composition of the SUS316L gas-atomized powders is shown in Table 1. The powder features, mechanical milling, and sintering process were introduced in our previous study [32]. In the present work, gas-atomized SUS316L steel powders were milled at room temperature for 10 h and 30 h. The compacts were sintered from initial powders and milled powders using a hot isostatic pressing (HIP) process with a pressure of 200 MPa at 900 °C for 4 h. The compact sintered from initial powders was denoted as the MM0h compact. The compacts sintered from milled powders for 10 h and 30 h were denoted as the MM10h compact and the MM30h compact, respectively. The grain structures of sintered compacts are shown in Figure 2. It can be seen in Figure 2a that the MM0h compact had a partial harmonic structure, which was attributed to an irregular initial powder size ranging from 1 µm to 20 µm. As indicated in Figure 2b,c, it was seen that the volume fraction of ultrafine grains increased as the mechanical milling time increased from 10 h to 30 h, resulting in a reduced grain size. Moreover, a continuous UFG network structure was observed, which indicated that a harmonic structure was produced in the compacts sintered from milled powders. Grain size and its volume fraction of sintered compacts are presented in Table 2. As indicated in Table 3, both yield strength (YS) and ultimate tensile strength (UTS) were enhanced with decreasing grain size [32].

**Table 1.** Chemical composition of SUS316L gas-atomized powders (mass%).

| C     | Si  | Mn   | P     | S     | Ni    | Cr    | Mo   | Fe   |
|-------|-----|------|-------|-------|-------|-------|------|------|
| 0.018 | 0.9 | 1.07 | 0.032 | 0.017 | 12.44 | 17.31 | 2.11 | Bal. |

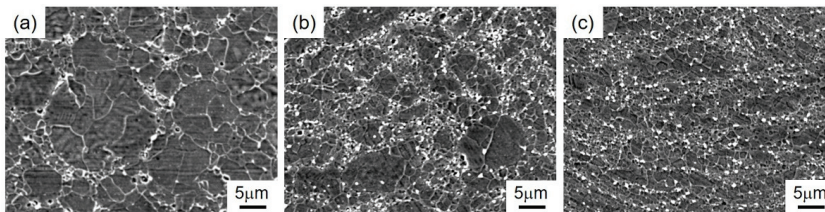


**Figure 2.** Microstructure of sintered SUS316L compacts: (a) MM0h compact; (b) MM10h compact; (c) MM30h compact.

**Table 2.** Grain size of harmonic-structured SUS316L compacts.

| Materials | Core Grain Size (CG), mm | Core Fraction | Shell Grain Size (UFG), mm | Shell Fraction |
|-----------|--------------------------|---------------|----------------------------|----------------|
| MM0h      | 3.94                     | 86.7%         | 1.28                       | 13.3%          |
| MM10h     | 1.84                     | 73.5%         | 0.64                       | 26.5%          |
| MM30h     | 1.16                     | 45.5%         | 0.42                       | 54.5%          |

**Table 3.** Loading conditions and fatigue life of ratcheting-fatigue tests for harmonic-structured SUS316L steels.

| Materials | Mean Stress $\sigma_m$ (MPa) | Stress Amplitude $\sigma_a$ (MPa) | Stress Rate (MPa/s) | Fatigue Life $N_f$ (Cycles) |
|-----------|------------------------------|-----------------------------------|---------------------|-----------------------------|
| MM0h      | 300                          | 300                               | 300                 | 29,774                      |
|           | 400                          |                                   |                     | 14,440                      |
|           | 450                          |                                   |                     | 432                         |
| MM10h     | 400                          | 300                               | 300                 | 17,854                      |
|           | 450                          |                                   |                     | 14,666                      |
| MM30h     | 400                          | 300                               | 300                 | 41,227                      |
|           | 450                          |                                   |                     | 18,599                      |

Figure 3 shows the setup of the ratcheting-fatigue test. As shown in Figure 3a, fatigue tests were conducted with an in-situ fatigue-testing machine (IBTC-5000, CARE, Tianjin, China) under stress-control mode at room temperature. A triangle waveform stress loading with a constant loading rate 300 MPa/s was carried out. In order to prevent buckling of the specimen, the stress ratio  $R$  was more than zero. Displacement of gauge area was recorded by a noncontact CCD camera (Figure 3c). The typical stress–strain response is shown in Figure 3b. The dimensions of specimens for the ratcheting fatigue tests are shown in Figure 3b. The specimens were ground using a 5000 grit SiC paper before fatigue tests. The ratcheting strain ( $\epsilon_r$ ) is defined as:

$$\epsilon_r = \frac{1}{2}(\epsilon_{max} + \epsilon_{min}) \tag{1}$$

where  $\epsilon_{max}$  and  $\epsilon_{min}$  are demoted as the maximum strain and minimum strain in each cycle, respectively. The loading conditions of ratcheting fatigue tests and observed fatigue life are listed in Table 3. Some high-cycle fatigue data of the harmonic-structured 316 L steels from our previous study were obtained [24]. These data were also used to analyze the fatigue-life-prediction model of harmonic-structured 316 L steels. Grain structure and fatigue fracture surface were examined by field emission-scanning electron microscopy (FE-SEM, SU4800, Tokyo, Japan) at 15 kV.

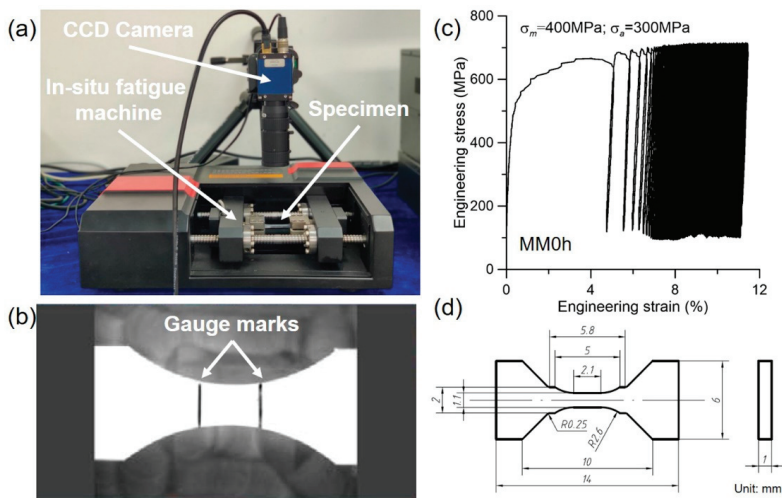


**Figure 3.** (a) Experiment setup; (b) typical stress–strain response; (c) displacement of gauge area measurement; (d) dimensions of specimen for ratcheting-fatigue test.

### 3. Results and Discussion

#### 3.1. Effects of Grain Structure on Ratcheting-Fatigue Behavior of Harmonic-Structured SUS316L Steels

Figure 4 summarizes the effects of grain structure on ratcheting strain and fatigue life of the harmonic-structured SUS316L steels. As shown in Figure 4a,b, the ratcheting-fatigue tests of the harmonic structured SUS316L steels with different grain sizes were performed under the same loading condition ( $\sigma_m = 400$  MPa,  $\sigma_a = 300$  MPa). It is noted that the grain structure had a great influence on both ratcheting strain and fatigue life. Figure 4b shows the ratcheting strain versus  $N/N_f$ . It can be seen in Figure 4b that the ratcheting strain accumulated rapidly in the early stage of cyclic deformation. The ratcheting strain of MM0h compact was approximately 10.6% at  $0.1N_f$ . By contrast, the values were approximately 4.2% and 2.5% for the MM10h compact and the MM30h compact, respectively. It is noteworthy that the ratcheting strain decreased with decreasing grain size. Subsequently, the increment of ratcheting strains was stable between  $0.1N_f$  and  $0.8N_f$ . At the final stage, the ratcheting strain increased rapidly to failure as  $N/N_f$  was over than 0.8. Moreover, the number of cycles to failure for the MM0h compact was 14,440 cycles, while the values for the MM10h compact and the MM30h compact were 17,854 cycles and 41,227 cycles, respectively. It was indicated that the harmonic-structured SUS316L steel with lower grain size possessed a longer fatigue life. A similar tendency was also observed in the results shown in Figure 4c,d at  $\sigma_m = 450$  MPa,  $\sigma_a = 300$  MPa.

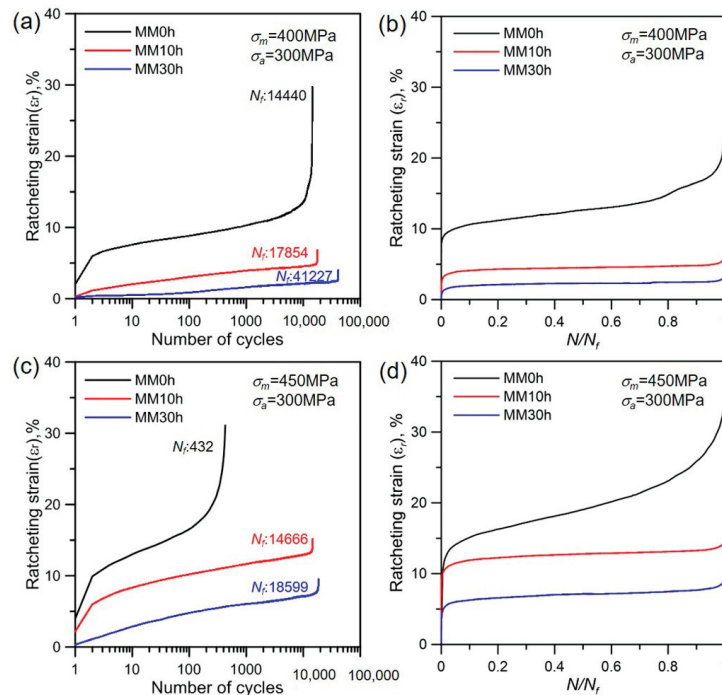


**Figure 4.** Effects of grain structure on fatigue life (a,c) and ratcheting strain (b,d) of harmonic-structured SUS316L steels: (a,b)  $\sigma_m = 400$  MPa,  $\sigma_a = 300$  MPa; (c,d)  $\sigma_m = 450$  MPa,  $\sigma_a = 300$  MPa.

As indicated in Figure 4, the variation of ratcheting strain could be divided into three stages, which appeared to be creep strain. It is known that creep strain is caused by microvoid formation and grain boundary sliding. However, the mechanism of ratcheting strain is different. Specifically, ratcheting strain is thought to be related to the progressive

development of plastic deformation. Active dislocations decrease in the early stage of cyclic deformation, which leads to a rapid ratcheting strain accumulation. The dislocation structure becomes stable in the following stage, resulting in a stable ratcheting-strain rate. At the last stage, due to microcracks or main fatigue-crack growth, the true stress level increases, resulting in an accelerated ratcheting-strain rate [33].

Owing to the shell region in harmonic-structured SUS316L steels, the strength increases with increasing shell volume fraction. Moreover, the ratcheting strain is determined by accumulative plastic deformation. Therefore, it can be seen in Figure 4 that the ratcheting strains were restrained in the MM10h compact and the MM30h compact compared to the MM0h compact. A lower strength produced a higher plastic strain under the same stress level. The ratcheting strain obviously was produced in the first stage of cyclic deformation, and decreased with increasing strength of materials. Moreover, the ratcheting-strain rates of the harmonic-structured SUS316L steels were nearly stable in the secondary stage, which may indicate that the dislocation structure in the harmonic structure was stable under stress cycling [33].

The morphology of ratcheting-fatigue fracture surfaces of the harmonic-structured SUS316L steels are presented in Figure 5. It can be seen in Figure 5a that an obvious necking was observed in the ratcheting-fractured MM0h compact. This indicates that a large plastic deformation occurred before the fatigue fracture. In contrast, the fracture surface area of the MM10h compact and the MM30h compact was larger than that of the MM0h compact. As grain size decreased, the necking became insignificant. Therefore, this also showed that the accumulative plastic deformation became lower as the grain size decreased. Moreover, it can be seen in Figure 5 that the crack initiated from the specimen surface in the harmonic-structured SUS316L steels subjected to ratcheting-fatigue tests.

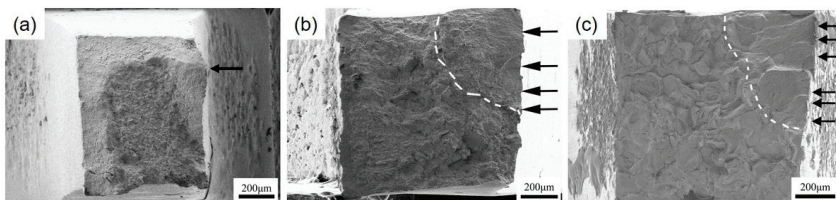


**Figure 5.** Morphology of ratcheting-fatigue fracture surface of harmonic-structured SUS316L steels: (a) MM0h compact; (b) MM10h compact; (c) MM30h compact.

As shown in Figures 4 and 5, the fatigue life was prolonged as the grain size decreased. It has been reported that ratcheting strain is produced from accumulative plastic deformation, which has detrimental effects on the fatigue life of materials [31]. In the present work, it is worthy to note that the ratcheting strain could be restrained in the harmonic-structured SUS316L steels due to their enhanced strength, which has great benefits for fatigue life. Therefore, it is thought that the harmonic-structure design could improve fatigue resistance under asymmetric stress cycling.

### 3.2. Effects of Mean Stress on Ratcheting-Fatigue Behavior of Harmonic Structured SUS316L Steels

As mentioned, the ratcheting strain increases with the increase of mean stress, which also affects fatigue life [29–31]. Therefore, the ratcheting behavior and fatigue life of the harmonic-structured SUS316L steels under the same stress amplitude ( $\sigma_a = 300$  MPa) but different mean stresses are presented in Figure 6. The results of ratcheting strain versus  $N/N_f$  for MM0h compact, MM10h compact, and MM30h compact are shown in Figure 6b,d,f, respectively. As expected, an increased mean stress level brought about a higher ratcheting strain for harmonic-structured SUS316L steels. It can be seen from Figure 6b that the ratcheting-strain rate of the MM0h compact was nearly zero in the secondary stage at  $\sigma_m = 300$  MPa. In contrast, the stable ratcheting-strain rate increased

at high stress levels. Both the ratcheting strain and ratcheting-strain rate increased as the mean stress increased from 300 MPa to 450 MPa. As indicated in Figure 6d,f, the higher mean stress also induced the higher ratcheting strain for the MM10h compact and the MM30h compact. However, the variation in the ratcheting-strain rate in the stable region was not significant.

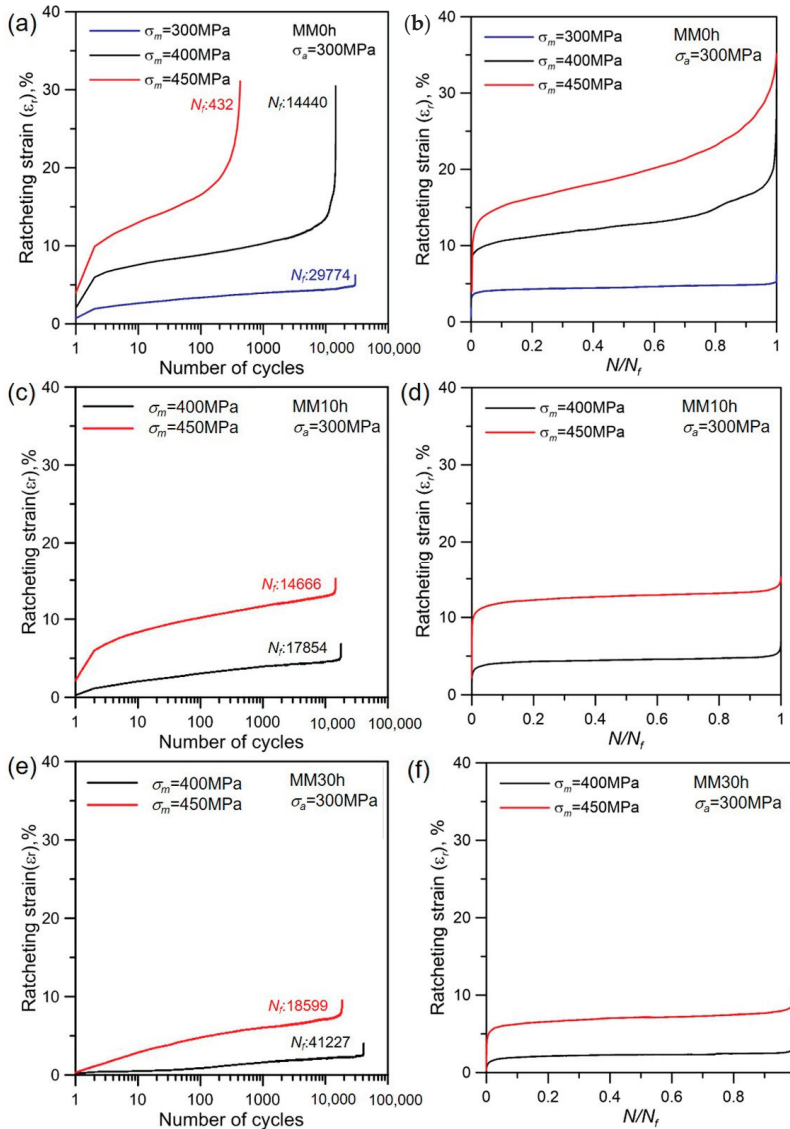


**Figure 6.** Effects of mean stress on fatigue life (a,c,e) and ratcheting strain (b,d,f) of harmonic-structured SUS316L steels: (a,b) MM0h compacts; (c,d) MM10h compacts; (e,f) MM30h compacts.

As expected, the increased mean stress produced a higher stress level, which promoted ratcheting-strain accumulation. The rapidly accumulative ratcheting strain was harmful for fatigue life. As indicated in Figure 6, the mean stress also played an important role in

the ratcheting-fatigue life of harmonic-structured SUS316L steels subjected to asymmetric stress cycling. As the applied mean stress increased, the fatigue life decreased gradually. Therefore, the effects of mean stress on fatigue life need to be considered in fatigue-life prediction.

### 3.3. Ratcheting-Fatigue-Life Prediction of Harmonic-Structured SUS316L Steels

In the past decades, Basquin's equation has been used as a classical fatigue-life-prediction model for fully reversed cyclic stress loading, as given in Equation (2) [28]:

$$\sigma_a = \sigma'_f (2N_f)^b \quad (2)$$

where  $\sigma_a$  and  $N_f$  are the stress amplitude and fatigue life, respectively.  $\sigma'_f$  is the fatigue strength coefficient, and  $b$  is the fatigue exponent. However, if the mean stress is not zero, ratcheting strain could appear, which is harmful for fatigue life. Therefore, equivalent stress amplitude ( $\sigma_a^{eq}$ ) has been proposed in many modified models for considering mean stress effects. As mentioned, the modified model based on the SWT criterion showed a higher prediction accuracy for ratcheting-fatigue life of materials performed under asymmetrical cyclic stress loading, as given in Equation (3):

$$\sigma_a^{eq} = \sqrt{\sigma_{max}\sigma_a} = \sigma_a \sqrt{1 + \frac{\sigma_m}{\sigma_a}} = \sigma'_f (2N_f)^b \quad (3)$$

where  $\sigma_{max}$ ,  $\sigma_m$ , and  $\sigma_a$  are ultimate tensile strength, mean stress, and stress amplitude, respectively. In our previous work, a part of fatigue lives of harmonic-structured SUS316L steels were obtained under pulsating cyclic stress loading [24]. Although both mean stress and stress amplitude were changed in these experiments, the fatigue-life data can also be used to fit the parameters of the SWT fatigue-life-prediction model. Therefore, all fatigue life data under asymmetric stress cycling were used to analyze the fatigue life of the harmonic-structured SUS316L steels.

Figure 7 shows the relationship between equivalent stress amplitude based on the SWT criterion and fatigue life. Overall, the fatigue-life deviation of harmonic-structured SUS316L steels was significant. The fatigue life decreased with an increase of equivalent stress amplitude. Compared with the CG bulk SUS316L steels, the harmonic-structured SUS316L steels had a higher fatigue strength. The fatigue strength coefficient  $\sigma'_f$  and fatigue exponent  $b$  in the SWT model are shown in Table 4. As indicated in Table 4, no appreciable influence of grain structure on  $\sigma'_f$  and  $b$  was observed. Figure 8 shows the comparison between the observed and predicted fatigue life determined from parameters of the SWT model for the MM0h compact. Due to the large deviation in fatigue life, it is seen in Figure 8a that the fatigue lives of MM0h compacts were almost located in the 5 times error band. However, as shown in Figure 8b,c, the fatigue lives of the MM10h and MM30h compacts could not be predicted well using the same parameters of the MM0h compacts. Therefore, this indicated that the deviation of the fatigue life of harmonic-structured SUS316L steels was significant, and fatigue life was influenced significantly by grain structure. The parameters for the MM0h compacts were not suitable for the MM10h and MM30h compacts.

**Table 4.** Tensile strength and SWT parameters of harmonic-structured SUS316L steels.

| Materials | Yield Strength $\sigma_s$ (MPa) | Ultimate Tensile Strength $\sigma_{UTS}$ (MPa) | Fatigue Strength Coefficient $\sigma'_f$ | Fatigue Exponent $b$ |
|-----------|---------------------------------|--|--|----------------------|
| MM0h      | 512                             | 721  | 681                                      | −0.046               |
| MM10h     | 580                             | 776  | 891                                      | −0.069               |
| MM30h     | 675                             | 794  | 735                                      | −0.041               |
| Bulk [24] | 315                             | 607  | 499                                      | −0.073               |

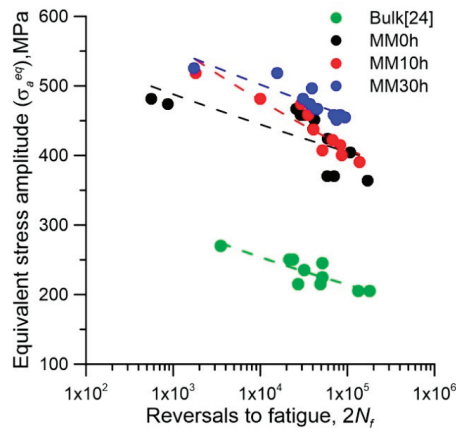


Figure 7. The dependence of the fatigue life ( $2N_f$ ) on the equivalent stress amplitude ( $\sigma_a^{eq}$ ) of harmonic-structured 316LN steels.

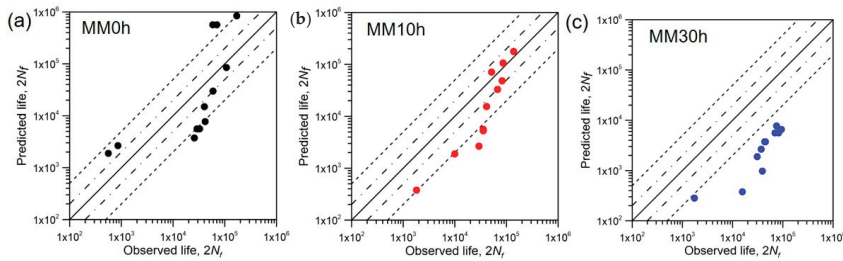


Figure 8. Comparison between observed life and predicted life based on the SWT fatigue-life-prediction model of harmonic-structured SUS316L steels: (a) MM0h compacts; (b) MM10h compacts; (c) MM30h compacts.

As mentioned, the strength of harmonic-structured SUS316L steels increased with increasing shell volume fraction, which also enhanced the fatigue resistance. Therefore, the strength variation caused by different grain sizes needs to be considered in fatigue-life prediction. To improve the response of grain structure on fatigue-life prediction of harmonic-structured SUS316L steels, a modified equivalent stress amplitude for the SWT criterion is proposed in Equation (4):

$$\sigma_a^{eq*} = \sigma_a^{eq} \left( 1 - \frac{\sigma_u^* - \sigma_{u, MM0h}}{\sigma_{u, MM0h}} \right) \tag{4}$$

where  $\sigma_a^{eq}$  and  $\sigma_a^{eq*}$  are the as-reserved equivalent stress amplitude determined by the SWT equation and the modified equivalent stress amplitude of the MM10h or MM30h compacts.  $\sigma_u^*$  is the ultimate tensile strength of the MM10h compact or the MM30h compact.  $\sigma_{u, MM0h}$  is the ultimate tensile strength of the MM0h compact. Therefore, by introducing the effect of the enhanced ultimate tensile strength into the SWT criterion, the fatigue-life-prediction model for the harmonic-structured SUS316L steels under asymmetric stress cycling is proposed in Equation (5). The same parameters  $\sigma_f'$  and  $b$  for MM0h compacts are also used in the modified model:

$$\sigma_a^{eq*} = \sigma_a^{eq} \left( 1 - \frac{\sigma_u^* - \sigma_{u, MM0h}}{\sigma_{u, MM0h}} \right) = \sigma_f' (2N_f)^b \tag{5}$$

The comparison between observed fatigue life and predicted fatigue life determined by the modified model based on the SWT criterion is presented in Figure 9. As indicated in Figure 9b,c, most of the fatigue-life points of the harmonic-structured SUS316L steels were located in the 5 times error band. The predicted results for the MM10h compacts and MM30h compacts by the modified model was better than that predicted by the as-received SWT fatigue-life-prediction model.

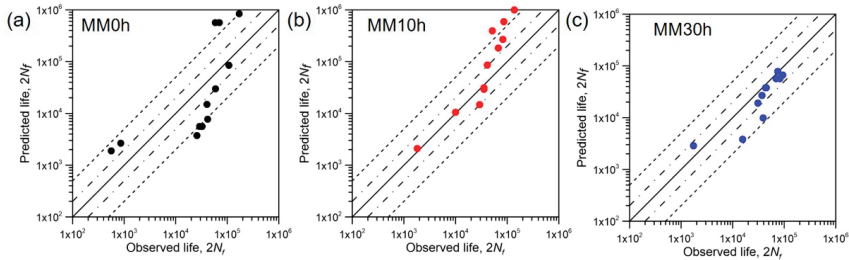


**Figure 9.** Comparison between observed life and predicted life based on the modified SWT fatigue-life-prediction model of harmonic-structured SUS316L steels: (a) MM0h compacts; (b) MM10h compacts; (c) MM30h compacts.

#### 4. Conclusions

In the present work, the ratcheting-fatigue behavior of harmonic-structured SUS316L stainless steels was investigated under asymmetrical stress cycling at room temperature. The effects of grain structure and mean stress on ratcheting strain and fatigue life were analyzed. The main conclusions are summarized as follows:

- (1) The ratcheting behavior of the harmonic-structured SUS316L steels subjected to under asymmetrical stress cycling was significant. The ratcheting strain was produced rapidly in the early stage of cyclic deformation, and became stable in the following stage. Finally, it increased near fatigue failure. The ratcheting-strain accumulation was highly influenced by grain structure and mean stress level. A lower grain size or higher mean stress tended to induce a higher ratcheting strain. The increased shell volume fraction enhanced the strength of materials, which restrained the ratcheting-strain accumulation under the same stress level.
- (2) The ratcheting strain had detrimental effects on the fatigue life of the harmonic-structured SUS316L steels. A rapid ratcheting-strain accumulation caused a shorter fatigue life. As the shell volume fraction increased or mean stress decreased, the ratcheting strain was restricted, which prolonged the fatigue life.
- (3) A proposed fatigue-life model based on the SWT criterion was employed to predict the fatigue life of the harmonic-structured SUS316L steels under asymmetrical stress cycling. The variation of ultimate tensile strength induced by grain refinement was considered in the modified fatigue-life-prediction model, which showed good predicting accuracy. Most of the fatigue-life points were located in the 5 times error band.
- (4) Compared with homogeneous CG materials, the harmonic-structure-designed materials had a good balance of high strength and high ductility. Meanwhile, the method also had great benefits for improving fatigue resistance under asymmetrical stress cycling.

**Author Contributions:** Conceptualization, Z.Z. and K.A.; methodology, Z.Z.; software, Y.S.; validation, Z.Z.; formal analysis, Z.Z.; investigation, Z.Z.; resources, Y.S., H.M. and M.N.; data curation, Y.S. and H.M.; writing—original draft preparation, Y.S.; writing—review and editing, Z.Z. and M.O.K.; visualization, Z.Z.; supervision, Z.Z. and K.A.; project administration, Z.Z., M.O.K. and K.A.; funding acquisition, Z.Z. All authors have read and agreed to the published version of the manuscript.

**Funding:** This work was partially supported by the National Key Research and Development Program of China (2018YFC0808600), and the National Natural Science Foundation of China (52075368, 51605325).

**Institutional Review Board Statement:** Not applicable.

**Informed Consent Statement:** Not applicable.

**Data Availability Statement:** Data is contained within the article.

**Acknowledgments:** The authors would like to thank Xu Chen and Chao Zhang (School of Chemical Engineering and Technology, Tianjin University) for their kind help in mechanical testing and modification of the fatigue-life-prediction model.

**Conflicts of Interest:** The authors declare no conflict of interest.

## References

- Kikuchi, S.; Nukui, Y.; Nakatsuka, Y.; Nakai, Y.; Nakatani, M.; Kawabata, M.O.; Ameyama, K. Effect of bimodal harmonic structure on fatigue properties of austenitic stainless steel under axial loading. *Int. J. Fatigue* **2019**, *127*, 222–228. [[CrossRef](#)]
- Chadha, K.; Tian, Y.; Spray, J.G.; Aranas, C. Effect of Annealing Heat Treatment on the Microstructural Evolution and Mechanical Properties of Hot Isostatic Pressed 316L Stainless Steel Fabricated by Laser Powder Bed Fusion. *Metals* **2020**, *10*, 753. [[CrossRef](#)]
- Zheng, R.; Liu, M.; Zhang, Z.; Ameyama, K.; Ma, C. Towards strength-ductility synergy through hierarchical micro-structure design in an austenitic stainless steel. *Scr. Mater.* **2019**, *169*, 76–81. [[CrossRef](#)]
- Yuan, X.; Yu, W.; Fu, S.; Yu, D.; Chen, X. Effect of mean stress and ratcheting strain on the low cycle fatigue behavior of a wrought 316LN stainless steel. *Mater. Sci. Eng. A* **2016**, *677*, 193–202. [[CrossRef](#)]
- Li, B.; Zheng, Y.; Shi, S.; Zhang, Z.; Chen, X. Cyclic deformation behavior and failure mechanism of S32205 duplex stainless steel under torsional fatigue loadings. *Mater. Sci. Eng. A* **2020**, *786*, 139443. [[CrossRef](#)]
- Li, B.; Zheng, Y.; Shi, S.; Zhang, Z.; Chen, X. Cyclic deformation and cracking behavior of 316LN stainless steel under thermomechanical and isothermal fatigue loadings. *Mater. Sci. Eng. A* **2020**, *773*, 138866. [[CrossRef](#)]
- Ueno, H.; Kakihata, K.; Kaneko, Y.; Hashimoto, S.; Vinogradov, A. Enhanced fatigue properties of nanostructured austenitic SUS 316L stainless steel. *Acta Mater.* **2011**, *59*, 7060–7069. [[CrossRef](#)]
- Ovid'ko, I.; Valiev, R.; Zhu, Y. Review on superior strength and enhanced ductility of metallic nanomaterials. *Prog. Mater. Sci.* **2018**, *94*, 462–540. [[CrossRef](#)]
- Lei, Y.; Wang, Z.; Xu, J.; Lu, K. Simultaneous enhancement of stress- and strain-controlled fatigue properties in 316L stainless steel with gradient nanostructure. *Acta Mater.* **2019**, *168*, 133–142. [[CrossRef](#)]
- Pan, Q.; Lu, L. Improved fatigue resistance of gradient nanogained metallic materials: Suppress strain localization and damage accumulation. *Scr. Mater.* **2020**, *187*, 301–306. [[CrossRef](#)]
- Pan, Q.; Long, J.; Jing, L.; Tao, N.; Lu, L. Cyclic strain amplitude-dependent fatigue mechanism of gradient nanogained Cu. *Acta Mater.* **2020**, *196*, 252–260. [[CrossRef](#)]
- Mine, Y.; Katashima, S.; Ding, R.; Bowen, P.; Takashima, K. Fatigue crack growth behaviour in single-colony lamellar structure of Ti–6Al–4V. *Scr. Mater.* **2019**, *165*, 107–111. [[CrossRef](#)]
- Chakraborti, P.; Mitra, M. Room temperature low cycle fatigue behaviour of two high strength lamellar duplex ferrite/martensite (DFM) steels. *Int. J. Fatigue* **2005**, *27*, 511–518. [[CrossRef](#)]
- Nalla, R.K.; Boyce, B.L.; Campbell, J.P.; Peters, J.O.; Ritchie, R.O. Influence of microstructure on high-cycle fatigue of Ti–6Al–4V: Bimodal vs. Lamellar structures. *Metall. Mater. Trans. A* **2002**, *31A*, 899–918. [[CrossRef](#)]
- Koyama, M.; Zhang, Z.; Wang, M.; Ponge, D.; Raabe, D.; Tsuzaki, K.; Noguchi, H.; Tسان, C.C. Bone-like crack re-sistance in hierarchical metastable nanolaminate steels. *Science* **2017**, *355*, 1055–1057. [[CrossRef](#)] [[PubMed](#)]
- Orlov, D.; Ameyama, K. Critical Assessment 37: Harmonic structure materials—Idea, status and perspectives. *Mater. Sci. Tech-Lond.* **2020**, *36*, 517–526. [[CrossRef](#)]
- Wu, X.; Zhu, Y. Heterogeneous materials: A new class of materials with unprecedented mechanical properties. *Mater. Res. Lett.* **2017**, *5*, 527–532. [[CrossRef](#)]
- Zhang, Z.; Vajpai, S.K.; Orlov, D.; Ameyama, K. Improvement of mechanical properties in SUS304L steel through the control of bimodal microstructure characteristics. *Mater. Sci. Eng. A* **2014**, *598*, 106–113. [[CrossRef](#)]
- Zhang, Z.; Orlov, D.; Vajpai, S.K.; Tong, B.; Ameyama, K. Importance of Bimodal Structure Topology in the Control of Mechanical Properties of a Stainless Steel. *Adv. Eng. Mater.* **2014**, *17*, 791–795. [[CrossRef](#)]
- Vajpai, S.K.; Ota, M.; Watanabe, T.; Maeda, R.; Sekiguchi, T.; Kusaka, T.; Ameyama, K. The Development of High Performance Ti–6Al–4V Alloy via a Unique Microstructural Design with Bimodal Grain Size Distribution. *Met. Mater. Trans. A* **2015**, *46*, 903–914. [[CrossRef](#)]
- Vajpai, S.K.; Sawangrat, C.; Yamaguchi, O.; Ciucu, O.P.; Ameyama, K. Effect of bimodal harmonic structure design on the deformation behavior and mechanical properties of Co–Cr–Mo alloy. *Mater. Sci. Eng. C* **2016**, *58*, 1008–1015. [[CrossRef](#)] [[PubMed](#)]

22. Li, G.; Liu, M.; Lyu, S.; Nakatani, M.; Zheng, R.; Ma, C.; Li, Q.; Ameyama, K. Simultaneously enhanced strength and strain hardening capacity in FeMnCoCr high-entropy alloy via harmonic structure design. *Scr. Mater.* **2021**, *191*, 196–201. [[CrossRef](#)]
23. Dirras, G.; Ueda, D.; Hocini, A.; Tingaud, D.; Ameyama, K. Cyclic shear behavior of conventional and harmonic structure-designed Ti-25Nb-25Zr  $\beta$ -titanium alloy: Back-stress hardening and twinning inhibition. *Scr. Mater.* **2017**, *138*, 44–47. [[CrossRef](#)]
24. Zhang, Z.; Ma, H.; Zheng, R.; Hu, Q.; Nakatani, M.; Ota, M.; Chen, G.; Chen, X.; Ma, C.; Ameyama, K. Fatigue behavior of a harmonic structure designed austenitic stainless steel under uniaxial stress loading. *Mater. Sci. Eng. A* **2017**, *707*, 287–294. [[CrossRef](#)]
25. Zhou, G.; Ma, H.; Zhang, Z.; Sun, J.; Wang, X.; Zeng, P.; Zheng, R.; Chen, X.; Ameyama, K. Fatigue crack growth behavior in a harmonic structure designed austenitic stainless steel. *Mater. Sci. Eng. A* **2019**, *758*, 121–129. [[CrossRef](#)]
26. Kikuchi, S.; Mori, T.; Kubozono, H.; Nakai, Y.; Kawabata, M.O.; Ameyama, K. Evaluation of near-threshold fatigue crack propagation in harmonic-structured CP titanium with a bimodal grain size distribution. *Eng. Fract. Mech.* **2017**, *181*, 77–86. [[CrossRef](#)]
27. Kang, G. Ratcheting: Recent progresses in phenomenon observation, constitutive modeling and application. *Int. J. Fatigue* **2008**, *30*, 1448–1472. [[CrossRef](#)]
28. Lim, C.-B.; Kim, K.; Seong, J. Ratcheting and fatigue behavior of a copper alloy under uniaxial cyclic loading with mean stress. *Int. J. Fatigue* **2009**, *31*, 501–507. [[CrossRef](#)]
29. Lin, Y.; Chen, X.-M.; Chen, G. Uniaxial ratcheting and low-cycle fatigue failure behaviors of AZ91D magnesium alloy under cyclic tension deformation. *J. Alloy. Compd.* **2011**, *509*, 6838–6843. [[CrossRef](#)]
30. Paul, S.K.; Sivaprasad, S.; Dhar, S.; Tarafder, S. Ratcheting and low cycle fatigue behavior of SA333 steel and their life prediction. *J. Nucl. Mater.* **2010**, *401*, 17–24. [[CrossRef](#)]
31. Xia, Z.; Kujawski, D.; Ellyin, F. Effect of mean stress and ratcheting strain on fatigue life of steel. *Int. J. Fatigue* **1996**, *18*, 335–341. [[CrossRef](#)]
32. Zheng, R.; Zhang, Z.; Nakatani, M.; Ota, M.; Chen, X.; Ma, C.; Ameyama, K. Enhanced ductility in harmonic structure designed SUS316L produced by high energy ball milling and hot isostatic sintering. *Mater. Sci. Eng. A* **2016**, *674*, 212–220. [[CrossRef](#)]
33. Gaudin, C.; Feaugas, X. Cyclic creep process in AISI 316L stainless steel in terms of dislocation patterns and internal stresses. *Acta Mater.* **2004**, *52*, 3097–3110. [[CrossRef](#)]

Article

# Exploring the Strain Hardening Mechanisms of Ultrafine Grained Nickel Processed by Spark Plasma Sintering

Lucía García de la Cruz <sup>1</sup>, Mayerling Martinez Celis <sup>1</sup>, Clément Keller <sup>2</sup> and Eric Hug <sup>1,\*</sup>

<sup>1</sup> Laboratoire CRISMAT, UNICAEN, Normandie University, CNRS, 6 Bvd du Maréchal Juin, 14050 Caen, France; lucia.garcia9@um.es (L.G.d.l.C.); mayerling.martinez@ensicaen.fr (M.M.C.)

<sup>2</sup> Groupe de Physique des Matériaux, CNRS-UMR6634, Université de Rouen, INSA de Rouen, Avenue de l'Université, 76800 Saint-Etienne du Rouvray, France; clement.keller@insa-rouen.fr

\* Correspondence: eric.hug@ensicaen.fr

**Abstract:** Ultrafine grained (UFG) materials in the bigger grain size range (0.5–1)  $\mu\text{m}$  display a good combination of strength and ductility, unlike smaller size UFG and nanostructured metals, which usually exhibit high strength but low ductility. Such difference can be attributed to a change in plasticity mechanisms that modifies their strain hardening capability. The purpose of this work is to investigate the work hardening mechanisms of UFG nickel considering samples with grain sizes ranging from 0.82 to 25  $\mu\text{m}$ . Specimens processed combining ball milling and spark plasma sintering were subjected to monotonous tensile testing up to fracture. Then, microstructural observations of the deformed state of the samples were carried out by electron backscattered diffraction and transmission electron microscopy. A lower strain hardening capability is observed with decreasing grain size. Samples in the submicrometric range display the three characteristic stages of strain hardening with a short second stage and the third stage beginning soon after yielding. Microstructural observations display a low fraction of low angle grain boundaries and dislocation density for the sample with  $d = 0.82 \mu\text{m}$ , suggesting changes in plasticity mechanisms early in the UFG range.

**Keywords:** nickel; spark plasma sintering; ultrafine grained microstructure; plasticity mechanisms; deformed state; dislocation structures

**Citation:** García de la Cruz, L.; Celis, M.M.; Keller, C.; Hug, E. Exploring the Strain Hardening Mechanisms of Ultrafine Grained Nickel Processed by Spark Plasma Sintering. *Metals* **2021**, *11*, 65. <https://doi.org/10.3390/met11010065>

Received: 9 December 2020

Accepted: 28 December 2020

Published: 30 December 2020

**Publisher's Note:** MDPI stays neutral with regard to jurisdictional claims in published maps and institutional affiliations.



**Copyright:** © 2020 by the authors. Licensee MDPI, Basel, Switzerland. This article is an open access article distributed under the terms and conditions of the Creative Commons Attribution (CC BY) license (<https://creativecommons.org/licenses/by/4.0/>).

## 1. Introduction

Ultrafine grained (UFG) metals (with an average grain diameter  $d = 0.1\text{--}1 \mu\text{m}$ ), situated between nanostructured metals (NsM) ( $d < 0.1 \mu\text{m}$ ) and coarse grained (CG) materials display intriguing mechanical properties and plasticity mechanisms [1–6]. In CG polycrystals plastic deformation is controlled by dislocation dynamics, where dislocation sources can be found in grain boundaries and the grain core [7]. Meanwhile, in UFG/NsM metals, grain boundaries have been reported to be exclusively the dislocation sources and sinks, limiting their mean free path and consequently modifying their mechanical properties and hardening behavior [8,9]. The investigation of strain hardening in UFG/NsM metals is not straightforward for different reasons. The low ductility often displayed by such materials [10–12], with fracture or heterogeneous deformation after yielding, renders the study of the plasticity mechanisms and the determination of the classical stages of strain hardening challenging. In addition, the use of nonstandard tensile specimens [6,13,14] can generate confusing results if not analyzed correctly. F. Dalla Torre et al. [15] succeeded in the investigation of the evolution of the strain hardening rate and the hardening stages of two nanostructured Ni samples processed by electrodeposition ( $d = 21 \pm 9 \text{ nm}$ ) and by high pressure torsion ( $d = 105 \pm 69 \text{ nm}$ ). Both samples displayed a lower hardening rate than CG Ni, characterized by a steep decrease in the beginning of plastic deformation, and no transition between the first and second stages of work hardening. The reduced strain hardening capability has been explained in terms of a lower ability of the specimens to accumulate dislocations, which act as obstacles to dislocation glide. It has been reported [8,9]

that in the UFG/NsM regime, dislocation storage is lessened by dynamic recovery and annihilation of dislocations at grain boundaries. Considering the continuous decrease in hardening rate with increasing strain for NsM, some authors consider that the third stage is directly reached whereas others suggest that no correlation exists between the hardening stages in conventional polycrystals and in NsM/UFG materials [15,16]. To help clarify these different positions, studies addressing the microstructure of NsM/UFG materials after tensile deformation are needed.

Despite the large bibliography concerning the mechanical properties of NsM and the smaller grain size range of UFG metals developed in the last three decades [17–24], information concerning strain hardening of larger grain sized UFG metals (also called submicrometric metals) is still lacking. The study of such samples could bring light to the transition, in terms of plasticity mechanisms, between conventional CG metals and NsM. Investigations on the mechanical properties of UFG copper [25], aluminum [26] and austenitic stainless steel [27] display an intriguing transition of tensile deformation behavior in samples with grain sizes in the range 0.4–4  $\mu\text{m}$ . In this face centered cubic metals, a Lüders-type deformation, preceded in some cases by a yield drop, was observed in the beginning of plastic deformation. Moreover, the yield strength of specimens displaying the Lüders-type deformation was reported higher than the expected value from the Hall–Petch relation for aluminum by Yu et al. [26]. It was shown that such deviation corresponds to inhomogeneous yielding associated with a lack of mobile dislocations in the smaller grains of the UFG microstructures in the beginning of plastic deformation. This feature has also been observed by the authors in a previous article dedicated to the mechanical properties assessment of UFG Ni polycrystals [28]. The persistence of the deviation in UFG Ni, at a lower extent, at higher deformation states, suggests changes in the strain hardening mechanisms.

A large bibliography is available for pure Ni, often used as model material to investigate different properties such as diffusivity, mechanical strength, resistivity, etc. [29–33]. The lack of complex phases, precipitates or other structural features simplifies the study of such properties enabling the investigation of the effect of single parameters (grain size for instance). Thus, Ni was chosen as a starting point to understanding plastic deformation in UFG materials that are more complex.

This paper aims to study the evolution of strain hardening mechanisms for samples with grain sizes in the range 0.82–25  $\mu\text{m}$  and to contribute to the knowledge of plastic deformation in the UFG range. Uniaxial tensile testing up to fracture was performed using standardized specimens and the obtained results analyzed focusing in strain hardening. Finally, electron backscattered diffraction (EBSD) and transition electron microscopy (TEM) were used to examine microstructures deformed at fracture and investigate dislocation accumulation and structures, shedding light on the hardening mechanisms.

## 2. Materials and Methods

### 2.1. Sample Synthesis and Characterization

Powder metallurgy was chosen for the synthesis of the specimens, combining high energy ball milling (BM) and consolidation by spark plasma sintering (SPS), to produce specific fine grained (FG) and UFG microstructures. High purity nickel powder (>99.8%) was used as the starting material, with Fe 100 ppm, C 200–600 ppm, O 1000 ppm and S 10 ppm as the main impurities. To produce FG/UFG samples the as-received powder was modified by BM in a Fritsch planetary pulverisette 7, using WC vials (80 mL) and grinding balls (5 mm in diameter). A ball to powder ratio was fixed to 10:1 and anhydrous methanol was used as a process control agent. To avoid oxidation of the powders, vials were filled with high purity argon. Rotation speed and milling time were selected to produce highly deformed UFG powders with different characteristics, to process specimens with distinct microstructures after sintering. The synthesis parameters and grain size for each sample are displayed in Table 1. More information concerning the impact of BM parameters in the microstructure of consolidated samples can be found elsewhere [28].

**Table 1.** Synthesis parameters of the samples (BM: ball milling).

| Sample | Grain Size ( $\mu\text{m}$ ) | $\rho_{\text{rel}}$ (%) | Type of Powder | BM Time (h) | BM Speed (rpm) | Amount of Methanol (%) | Sintering Temperature (K) |
|--------|------------------------------|-------------------------|----------------|-------------|----------------|------------------------|---------------------------|
| 1      | $0.82 \pm 0.67$              | 98.5                    | BM             | 10          | 350            | 66.7                   | 1023                      |
| 2      | $1.11 \pm 0.84$              | 99.5                    | BM             | 3           | 350            | 16.7                   | 1023                      |
| 3      | $1.39 \pm 1.11$              | 99.3                    | BM             | 3           | 300            | 66.7                   | 1023                      |
| 4      | $4.0 \pm 2.4$                | 97.6                    | As-received    | –           | –              | –                      | 1023                      |
| 5      | $25 \pm 17$                  | 98.7                    | As-received    | –           | –              | –                      | 1273                      |

The powders were sintered by SPS with a FCT System GmbH, HD25 SPS apparatus (Figure 1a left), under medium dynamic vacuum (0.5 mbar), using graphite dies, punches and foils (Figure 1a right). To limit grain growth, the sintering temperature was set to 1023 K, with a heating rate of 100 K/min by continuous current. The heating cycle was accompanied by a uniaxial pressure cycle throughout the sintering process, with a maximum value of 75 MPa. Maximum pressure and temperature were maintained for 10 min to ensure high density. Four disc-like specimens were processed using this program, with a diameter of approximately 50 mm and a thickness of 6 mm, to extract tensile specimens for mechanical testing (Figure 1b). To assess the impact of grain size on strain hardening mechanisms, an extra sample with a grain size in the CG range was produced from the as-received powder using the same sintering conditions, with the exception of temperature, 1273 K (Table 1). To confirm good homogeneity, hardness maps of the surface were performed in all samples. The density of the bulk samples was determined by an immersion densitometry method, with a mass accuracy of 1 mg.

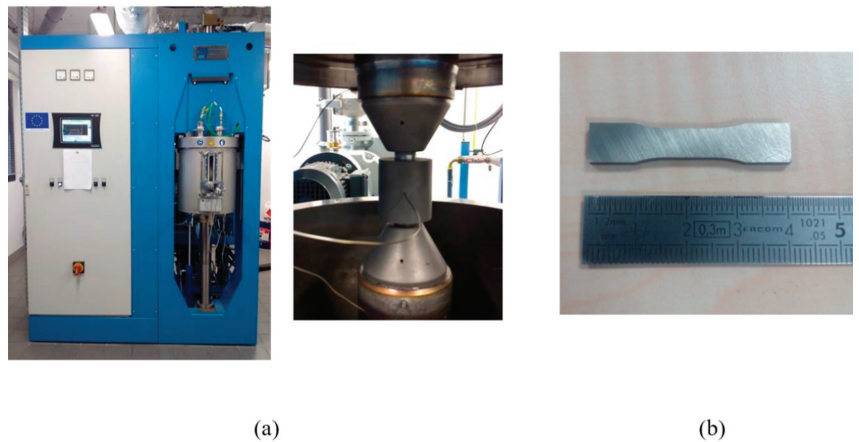


**Figure 1.** FCT System GmbH, HD25 SPS apparatus (left) and sintering set-up (right) (a). The metallic wire positioned in a hole in the die is a thermocouple used to control the sintering temperature. Tensile specimen extracted from a 50 mm sintered disc (b).

## 2.2. Microstructure Analysis and Mechanical Properties

The microstructure of the sintered samples was investigated in the initial state and the deformed state at fracture by means of EBSD. Prior to measurements, samples were mechanically polished with SiC paper and electropolished using a solution of perchloric acid, 2-butoxyethanol and ethanol at a voltage of 24 V, for an optimal surface condition. The EBSD acquisition system used was a QUANTAX EBSD (Bruker, Berlin, Germany) mounted on a Zeiss Supra 55. An operating voltage of 15 kV, aperture size of 60  $\mu\text{m}$  and a working distance (WD) of 14.5–16.5 mm were the acquisition parameters. For each sample, at least 1000 grains were covered using a step size ensuring more than 4 points per grain

along a given direction. Data was analyzed with the TSL OIM 6 × 64 Analysis™ v 6.2 software (EDAX, Ametek Inc., Berwyn, PA USA) to estimate average grain size, grain boundary character distribution (GBCD), grain orientation, grain orientation spread (GOS) and Kernel average misorientation (KAM) of the sintered specimens. A misorientation angle of 2–15° [34] was chosen to define low angle grain boundaries (LAGBs), and Brandon's criterion [35] was used to determine coincidence site lattice (CSL) fractions, calculated on a length basis. Basic clean-up was performed before each analysis to eliminate artifacts. In addition, TEM observations of dislocation structures were performed on selected samples with a JEOL 2010 at an operating voltage of 200 kV. To this aim, specimens were prepared from 3 mm discs mechanically polished down to approximately 100 µm and then electropolished using a solution of 17% perchloric acid in ethanol by the twin jet method in a Tenupol 5.

The influence of grain size in the UFG range on the strain hardening mechanisms was investigated using uniaxial tensile testing up to fracture. Dog-bone tensile samples with a gauge length of 11 mm and a thickness of 1 mm were extracted from the 50 mm discs (Figure 1b), using electrical discharge machining to avoid sample damage. More information concerning the dimensions of the tensile specimens and their position in the sintered sample can be found elsewhere [36,37]. Prior to testing the surfaces of the specimens were carefully polished with a diamond suspension of 6 µm to remove the roughness induced by the machining and to eliminate any contamination in the near surface area. A Zwick device with a load cell of 50 kN maximum capability was used for uniaxial tensile testing at room temperature. The strain rate was set to  $10^{-3} \text{ s}^{-1}$ , and the deformation was recorded with the ARAMIS® software (Mentel Co., Ltd., Bangkok, Thailand) by measuring displacement fields using digital image correlation. The stress-strain measurements reported in the following paragraphs correspond to the average value from three different samples.

### 3. Results and Discussion

#### 3.1. Strain Hardening in FG and UFG Ni

To investigate the influence of grain size in the FG/UFG range on the mechanisms of plasticity, five samples were prepared with grain sizes ranging from 0.82 to 25 µm. The synthesis parameters (Table 1) were selected to produce specimens with a small fraction of low angle grain boundaries (LAGBs) and a high fraction of  $\Sigma 3$  grain boundaries, and random high angle boundaries (HABs) [28]. The high relative density for all samples (Table 1) confirms the good consolidation of powders by SPS. In addition, specimens show overall low internal stress in the initial state, quantitatively estimated from a grain orientation spread (GOS) below 1° [28,38].

The respective true stress ( $\sigma$ )/true strain ( $\epsilon$ ) curves are plotted in Figure 2. Regardless the grain size, all samples display high strength and ductility in tensile deformation, with the best combination found for sample 1 ( $d = 0.82 \text{ }\mu\text{m}$ ).

As discussed in our previous work [28,37], samples 1 ( $d = 0.82 \text{ }\mu\text{m}$ ) and 2 ( $d = 1.11 \text{ }\mu\text{m}$ ), display an unusual Lüders-type plateau in the beginning of plastic deformation. The origin of this phenomenon seems to be an inhomogeneous yielding associated with a microstructure displaying grains of different sizes, which present specific deformation behaviors. The lack of mobile dislocations in the smallest grains of the UFG microstructures increases the yielding strength, followed by a Lüders-type deformation before homogeneous deformation begins. Despite the differences in grain size, covering three ranges, CG, FG and UFG, all samples display considerable strain hardening after yielding. However, if the ratio of maximum stress over yield stress is considered, bigger grain size samples display higher ratios with a value of seven observed for sample 5 ( $d = 25 \text{ }\mu\text{m}$ ), against a ratio of two displayed by sample 1 ( $d = 0.82 \text{ }\mu\text{m}$ ).

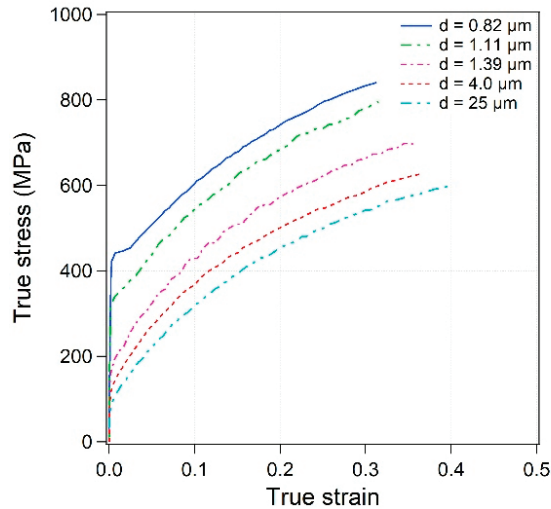


**Figure 2.** True stress–true strain tensile curves for Ni samples 1–5 processed by spark plasma sintering (SPS).

The evolution of the strain hardening rate  $\theta = \left(\frac{d\sigma}{d\varepsilon}\right)$ , with true stress normalized by yield strength ( $\sigma_y$ ) is plotted in Figure 3. At low flow stress, a strong decrease in the hardening rate can be observed, which evolves towards a more stabilized hardening rate, irrespective of the sample. However, a clear difference can be observed between UFG and FG/CG samples. Samples 3–5 display the same hardening behavior at the beginning of plastic deformation, a steep decrease in  $\theta$  followed by a smoother decrease. Then, for  $\sigma/\sigma_y = 2$ , hardening rates diverge as sample 5 ( $d = 25 \mu\text{m}$ ) displays a higher hardening capability than samples 3 ( $d = 1.39 \mu\text{m}$ ) and 4 ( $d = 4.0 \mu\text{m}$ ). Samples 1 ( $d = 0.82 \mu\text{m}$ ) and 2 ( $d = 1.11 \mu\text{m}$ ) display, on the other hand, a much steeper decrease of  $\theta$  in the beginning of plastic deformation followed by a much lower strain hardening rate, compared to the FG/CG counterparts. The lower hardening capability assessed for the UFG samples in this study, is in agreement with the tendency observed by F. Dalla Torre et al. [15]. Nevertheless, the transition to a more stabilized decrease in  $\theta$  for UFG, contrasting with their observations on nanocrystalline Ni, suggests different hardening mechanisms in our samples.

Work hardening in polycrystals can be divided into three stages that are related to different plasticity mechanisms that can be investigated by physical models [39]. Using the Mecking–Kocks model, the relation between flow stress ( $\sigma$ ) and total dislocation density ( $\rho$ ) can be expressed as [40–42]:

$$\sigma = \alpha\mu bM\sqrt{\rho}, \quad (1)$$

where  $\alpha$  is a coefficient that depends on the type of interaction between dislocations and their configuration,  $\mu$  is the shear modulus,  $b$  is the norm of the Burgers vector and  $M$  is the Taylor factor [43,44]. Furthermore, for monophasic and recrystallized face centered cubic metals, the evolution of  $\rho$  with deformation can be described by the following equation [40,45,46]:

$$\frac{d\rho}{d\varepsilon} = \frac{M\sqrt{\rho}}{\beta b} + \frac{k_s M}{bd} - \frac{2MPy_a \rho}{b}. \quad (2)$$

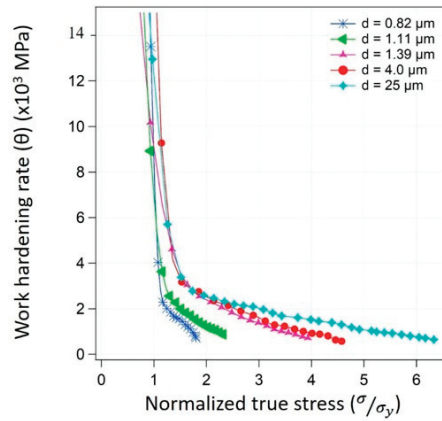


**Figure 3.** Evolution of the work hardening rate ( $\theta = \left(\frac{d\sigma}{d\varepsilon}\right)$ ), determined from tensile testing to failure at a strain rate of  $10^{-3} \text{ s}^{-1}$ , with true stress normalized by yield strength for Ni samples prepared by SPS with different grain sizes. The average grain size of the samples is indicated in a color scale for each figure.

The first term of the right-hand side of Equation (2) concerns the accumulation of mobile dislocations, where  $\beta$  represents the ratio between the dislocation mean free path ( $\Lambda$ ) and the near neighbor dislocation spacing ( $l_d$ ):  $\beta = \frac{\Lambda}{l_d}$ , and the other parameters have their usual meaning. The dislocation mean free path is the distance travelled by a dislocation before being stopped by crystalline defects (i.e., other dislocations, precipitates and grain boundaries) and becomes stored [47]. The second term accounts for the generation of geometrically necessary dislocations (GNDs) at grain boundaries [46,48], where  $k_g$  represents a geometric factor that depends on the morphology of grains. Finally, the last term corresponds to dislocation annihilation that results from generalized cross-slip. The probability of annihilation is represented by  $P$  and  $y_a$  symbolizes the distance of annihilation of two dislocations by cross-slip [46,48]. If Equations (1) and (2) are combined the following expression is obtained:

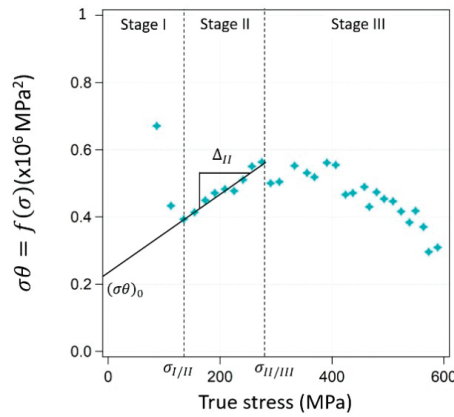
$$\sigma \cdot \theta = \sigma \frac{d\sigma}{d\varepsilon} = \frac{\alpha\mu M^2}{2\beta} \sigma + \frac{\alpha^2 \mu^2 b M^3 k_g}{2d} - \frac{\alpha\mu M P y_a \sigma^2}{b} \tag{3}$$

The low probability of dislocation annihilation in the beginning of strain hardening makes the last term in Equation (3) negligible throughout stages I and II. Thus, the study of the transition between hardening stages can be performed from the evolution of the product  $\sigma \cdot \theta$  as it displays clear slope changes. Stage I is characterized by a steep decrease in  $\sigma \cdot \theta$  and is characterized by non-homogeneous deformation with a gradual elastic to plastic transition, which depends on grain orientation and size. Planar/single slip is the main deformation mechanism and the elevated hardening rate is due to deformation incompatibility between grains. Then, a linear part of increasing  $\sigma \cdot \theta$  represents stage II, which is characterized by multiple slip, beginning of cross-slip and the formation of dense dislocation structures, including tangles, dislocation walls and cells [49]. Assuming the Mecking–Kocks model and the approximation of low probability of dislocation annihilation, stage II can be investigated as dependent on two terms [50]:

$$\sigma \cdot \theta = \frac{\alpha\mu M^2}{2\beta} \sigma + \frac{\alpha^2 \mu^2 b M^3 k_g}{2d} = \Delta_{II} \sigma + (\sigma\theta)_0 \tag{4}$$

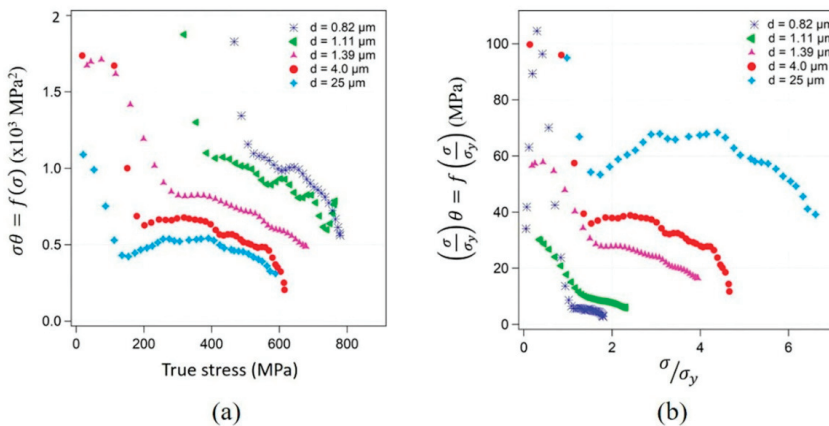
The first one ( $\Delta_{II}$ ), known as the latent hardening rate, is related to the accumulation and interaction between dislocations. The second one ( $(\sigma\theta)_0$ ) corresponds, for a polycrystal

of a pure single-phase metal, to the contribution of grain boundaries, through GNDs, to strain hardening. The contribution of  $(\sigma\theta)_0$  to strain hardening increases when the microstructure is refined. Both terms can be obtained from the fraction of the plots of  $\sigma\cdot\theta$  as a function of stress situated between the transition stress from stage I to stage III ( $\sigma_{I/III}$ ) and the one from stage II to III ( $\sigma_{II/III}$ ). A linear fit of this section gives  $\Delta_{II}$  as the slope and  $(\sigma\theta)_0$  as the origin intercept (Figure 4). Once linearity is lost, stage III of strain hardening begins, where cross-slip is generally occurring and dislocation annihilation predominantly takes place.



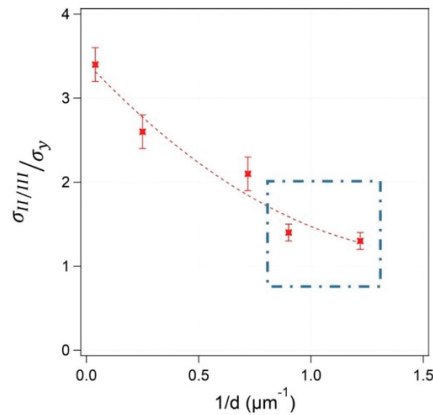
**Figure 4.** Example of the evolution of the  $\sigma\cdot\theta$  product with stress for polycrystalline Ni ( $d = 25 \mu\text{m}$ ), displaying the three stages of strain hardening, the transition stresses  $\sigma_{I/II}$  and  $\sigma_{II/III}$ ,  $\Delta_{II}$  and  $(\sigma\theta)_0$ .

Figure 5a displays the evolution of  $\sigma\cdot\theta$  with stress for the sintered samples. A strong effect of grain size on  $\sigma_{I/II}$  is observed, arising from the difference in  $\sigma_y$  between individual samples. When normalizing stress by  $\sigma_y$  (Figure 5b), the transition took place at a value of  $\sigma/\sigma_y$  close to 1.5 independently of the grain size.



**Figure 5.** Evolution of the  $\sigma\cdot\theta$  product with stress for the Ni samples processed by SPS with different grain sizes (a) and the same curves after normalization of stress by yield strength  $\sigma_y$  (b). The average grain size of the samples is indicated in a color scale for each figure.

The transition stress from stage II to stage III ( $\sigma_{II/III}$ ), normalized by yield strength decreased with decreasing grain size (Figure 6). The stress necessary for the transition to stage III for CG nickel (sample 5) was 3.5 times its yield strength, whereas for the two UFG samples (framed in blue) the transition took place shortly after the initial yield stress. The faster transition from stage II to stage III in UFG samples suggests different hardening mechanisms compared to CG specimens.



**Figure 6.** Evolution of the transition stress from work hardening stage II to stage III ( $\sigma_{II/III}$ ) normalized by yield strength as a function of  $1/d$  for the five sintered samples. The two UFG samples are framed in blue.

The evolution of  $\Delta_{II}$  with grain size is plotted in Figure 7a. Despite the important scattering of experimental values, resulting from noisy data, a decrease of the latent hardening rate with decreasing grain size can be observed, approaching zero for the smallest grain sizes. The latent hardening rate is related to the rate in which mobile dislocations are stored within the grain from the interaction with the dislocation density that is already stored [43]. In the second work hardening stage, dislocations store by rearranging into low energy structures such as dislocation cells. The faster transition to stage III in UFG specimens suggests that generalized cross-slip and annihilation of dislocations takes place in the beginning of plastic deformation, reducing the possibility of dislocation interaction and reorganization. A decrease in  $\Delta_{II}$  implies a decrease of the interaction coefficient,  $\alpha$ , and/or an increase of the parameter  $\beta$  (Equation (4)). A lower  $\alpha$  suggests low dislocation interaction and organization. A higher  $\beta$  entails an increase in  $\Lambda$  and/or a decrease in  $l_d$ , thus, a lower possibility of interaction between dislocations. The evolution of  $(\sigma\theta)_0$  as a function of the inverse value of grain size is displayed in Figure 7b. A linear trend can be depicted, where the parameter  $(\sigma\theta)_0$  increases with decreasing grain size. The value of  $k_g$  can be determined from the slope:

$$(\sigma\theta)_0 = \frac{\alpha^2 \mu^2 b M^3 k_g}{2} \cdot \frac{1}{d}. \quad (5)$$

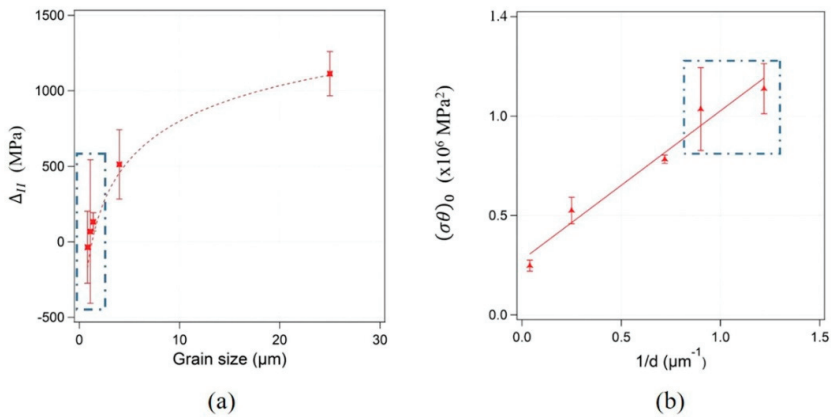


**Figure 7.** Evolution of the latent hardening rate ( $\Delta_{II}$ ) in stage II of strain hardening as a function of grain size (a) for the five sintered samples. Evolution of  $(\sigma\theta)_0$  as a function of  $1/d$  for the five sintered samples (b). The two UFG samples are framed in blue.

Considering the value of  $\alpha$  estimated for polycrystals in [45],  $\alpha = 0.45$ , the obtained value of  $k_g$  in this study was  $0.15 \pm 0.02$ , which was in good agreement with the experimental value obtained in [45] for polycrystalline nickel,  $k_g = 0.20$ . Thus, the Mecking–Kocks model applies to the study of the plasticity mechanisms in this work [51]. Given that  $(\sigma\theta)_0$  is related to the contribution of grain boundaries to strain hardening, these results suggest that for UFG samples, the hardening mechanisms mainly take place at grain boundaries. In consequence, when grain size decreases, dislocation interaction with grain boundaries becomes the main hardening mechanism.

### 3.2. Investigation of the Deformed State at Fracture by EBSD and TEM Observations

Previous conclusions issued from the Mecking–Kocks model suggest a change in strain hardening mechanisms with grain refinement. Dislocation accumulation through cell formation would be present in the core of the grain for coarse grain specimens. Whereas in UFG samples, hardening would be mainly related to interactions between dislocations and grain boundaries. To explore this possibility, the deformed state at fracture was investigated by means of EBSD.

Figure 8 displays a global outlook of the deformed microstructures from the inverse pole figure (IPF) taking the tensile stress direction as reference. The good quality of the data was ensured by an indexation rate above 88% for all samples. A preferred crystallographic orientation is observed where grains rotate so that a  $\langle 111 \rangle$  or  $\langle 100 \rangle$  axis tends to become parallel to the tensile axis, which is the expected behavior for highly deformed face centered cubic (FCC) metals [52,53]. In addition, elongation of grains following the tensile stress axis can be observed, leading to an increase in the grain boundary area. This phenomenon is more present for samples 4 and 5 depicting higher grain size (Figure 8c,d) and almost negligible for sample 1, with the smallest grain size (Figure 8a). The area increase requires a high fraction of dislocations storing in the grain boundaries, which accounts for a significant part of the strain hardening energy [54]. The difference in elongation to fracture ( $\varepsilon_f$ ) could explain such a difference as  $\varepsilon_f = 49\% \pm 3\%$  for sample 4 ( $d = 4 \mu\text{m}$ ) and  $\varepsilon_f = 39\% \pm 3\%$  for sample 1 [28]. Nevertheless, Q.H. Bui et al. [33] reported a similar result for samples of CG and UFG Ni deformed in compression at the same level of deformation.

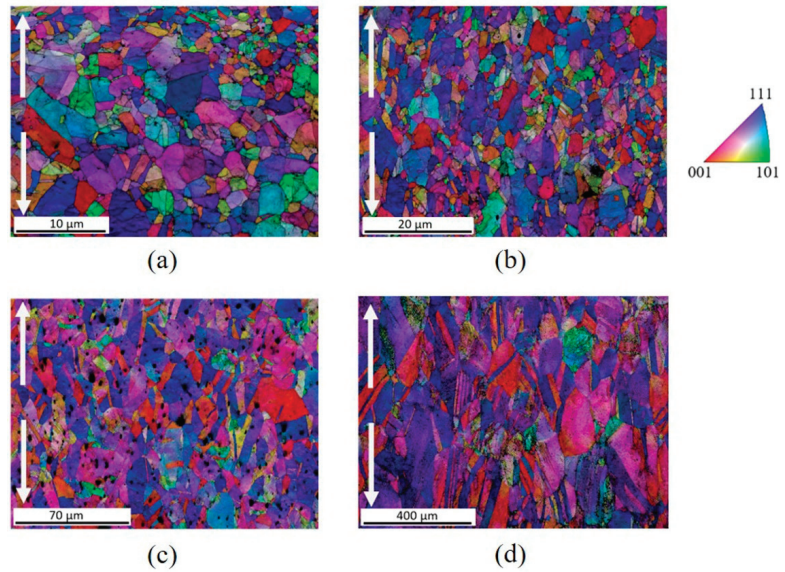


**Figure 8.** Superposition of inverse pole figure (IPF) + image quality (IQ) cartography for samples 1 ( $d = 0.82 \mu\text{m}$ ) (a), 3 ( $d = 1.39 \mu\text{m}$ ) (b), 4 ( $d = 4.0 \mu\text{m}$ ) (c) and 5 ( $d = 25 \mu\text{m}$ ) (d) with the tensile stress direction as reference, for fractured samples. White arrows indicate the tensile direction.

A change in the GBCD is also observed after deformation (Table 2), where a decrease in the  $\Sigma 3$  grain boundary density was accompanied by an important increase in the LAGB density. The lower fraction of  $\Sigma 3$  grain boundaries can be explained as the outcome of gliding dislocations interacting with pre-existing twin boundaries (a particular case of  $\Sigma 3$  grain boundaries), resulting in the accumulation of the slip dislocations in such boundaries. This can be achieved by dissociation of slip dislocations into partials under high stress [55,56]. Gubicza et al. [57] observed the same phenomenon for UFG Ni prepared by SPS from nanopowders deformed by the compression test. The higher fraction of LAGBs is the outcome of the arrangement of dislocations into subgrain boundaries at high levels of deformation [58].

**Table 2.** Grain boundary character distribution (GBCD) of samples in the initial state and deformed at fracture.

| Sample | Grain Size ( $\mu\text{m}$ ) | Initial State [28] |            |       |       | Deformed at Fracture |            |       |       |
|--------|------------------------------|--------------------|------------|-------|-------|----------------------|------------|-------|-------|
|        |                              | LAGBs              | $\Sigma 3$ | CSL   | HABs  | LAGBs                | $\Sigma 3$ | CSL   | HABs  |
| 1      | $0.82 \pm 0.67$              | 0.036              | 0.495      | 0.056 | 0.413 | 0.057                | 0.388      | 0.047 | 0.508 |
| 2      | $1.11 \pm 0.84$              | 0.04               | 0.456      | 0.044 | 0.46  | 0.133                | 0.246      | 0.056 | 0.565 |
| 3      | $1.39 \pm 1.11$              | 0.023              | 0.535      | 0.057 | 0.385 | 0.093                | 0.336      | 0.044 | 0.527 |
| 4      | $4.0 \pm 2.4$                | 0.02               | 0.526      | 0.046 | 0.408 | 0.383                | 0.202      | 0.036 | 0.379 |
| 5      | $25 \pm 17$                  | 0.02               | 0.616      | 0.037 | 0.327 | 0.73                 | 0.088      | 0.022 | 0.16  |

Table 2 shows that bigger grain size entailed a sharper decrease in  $\Sigma 3$  grain boundaries and a stronger increase of LAGBs. The probability of reducing the fraction of  $\Sigma 3$  grain boundaries was thus higher for samples with grain sizes in the CG regime. The considerable difference in the fraction of LAGBs for fractured samples 4 and 5, compared to samples 1–3, can be related to the short strain hardening stage II in UFG samples. In this second stage, dislocations reorganize into lower energy structures to accommodate deformation. They evolve with increasing strain from tangled dislocations to dislocation cells due to a multiple slip, which enables the multiplication of dislocations. In stage III, cross-slip is

generalized and dislocation cells are the predominant dislocation arrangement. For higher deformation levels, the misorientation across dislocation walls increases, which results in the development of subgrains from the original dislocation cells [59], ultimately forming LAGBs [54]. The fast occurrence of stage III in the UFG samples hinders the formation dislocation cells and their evolution to LAGBs.

EBSD is also useful in the investigation of the misorientations within grains, as this can be related to the presence of dislocations [29,38]. Figure 9 displays GOS cartographies of samples 1 ( $d = 0.82 \mu\text{m}$ ) (a), 3 ( $d = 1.39 \mu\text{m}$ ) (b) and 4 ( $d = 4 \mu\text{m}$ ) (c), calculated for the initial state (left) and the deformed state at fracture (right). The average GOS value increased for all samples from  $0.6^\circ$ , in the initial state, to around  $2^\circ$ , in fractured samples, with the smallest value corresponding to sample 1 ( $\text{GOS} = 1.7^\circ \pm 0.9^\circ$ ). Nevertheless, the distribution of the GOS value highly depended on grain size. For instance, the fraction of grains with a  $\text{GOS} < 2^\circ$  for sample 5 ( $d = 25 \mu\text{m}$ ) was 2.9%, whereas sample 1 ( $d = 0.82 \mu\text{m}$ ) exhibited a fraction of 29.8%.

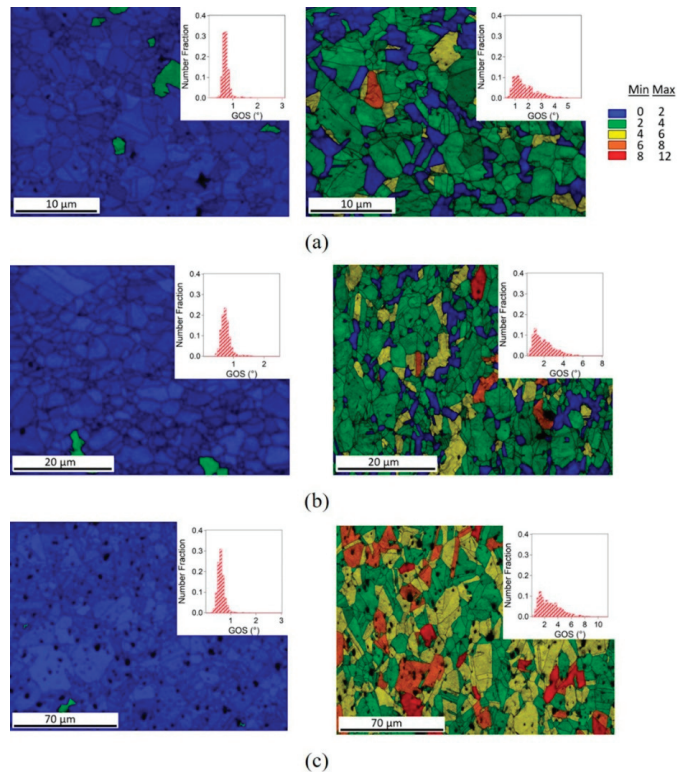


**Figure 9.** Grain orientation spread (GOS) + IQ map of samples 1 ( $d = 0.82 \mu\text{m}$ ) (a), 3 ( $d = 1.39 \mu\text{m}$ ) (b) and 4 ( $d = 4.0 \mu\text{m}$ ) (c) at the initial state (left) and deformed state at fracture (right). Color legend represents the orientation spread in degrees. Inserts display the distribution of GOS values for each state and sample.

To investigate the correlation between grain size and orientation spread, the EBSD data for sample 1 at fracture ( $d = 0.82 \mu\text{m}$ ) was divided into two groups, based on the GOS value. The first group included grains that display a  $\text{GOS} < 2^\circ$  and the second group grains with  $\text{GOS} > 2^\circ$ . The measured average grain sizes of each partition were  $d = 0.54 \pm 0.38 \mu\text{m}$  and  $d = 1.39 \pm 0.84 \mu\text{m}$ , respectively. These results indicate that deformed grains in the UFG regime display less orientation spread and thus exhibited a lower level of deformation [60].

This difference in deformation capability offers an explanation to the heterogeneous deformation (Lüders-type plateau) at the beginning of plastic deformation. In addition, Figure 9 shows that at higher deformation levels, despite the macroscopic homogeneous deformation displayed in Figure 2, the deformation at a microscopic scale is heterogeneous and dependent on grain size. The same analysis was performed in samples 2 and 3, and a similar trend was observed concerning the grains in the UFG regime. The fraction of grains that displayed a GOS  $< 1^\circ$  (considered as non-deformed grains) was less than 3% for all samples.

GOS cartographies offer a general view of deformation considering averaged values for each grain. Nevertheless, different deformation levels are present on a microscale inside the grains, where dislocations are frequently distributed in a heterogeneous manner, alternating regions of high and low local dislocation density. KAM cartographies can be employed for a local description of the presence of misorientations within a grain [61]. The first neighbor KAM cartographies of samples 1 ( $d = 0.82 \mu\text{m}$ ) (a), 3 ( $d = 1.39 \mu\text{m}$ ) (b) and 4 ( $d = 4 \mu\text{m}$ ) (c) are displayed in Figure 10. In the deformed state in sample 4 (Figure 10c right), it is noticeable that high misorientations (above  $1^\circ$ ) are present at grain boundaries and in the bulk of grains. In addition, the average KAM value in this sample increased from  $0.7^\circ$  in the initial state to  $1.4^\circ$  deformed at fracture, as expected for deformed samples [62]. With grain refinement, lower misorientations are observed and are mostly located at grain boundaries (Figure 10a,b right). The generalized higher dislocation density at grain boundaries is in agreement with the model developed by Meyers and Ashworth based on a different deformation behavior between the inside of grains and their boundaries [63]. Deformation incompatibility between grains develops a stress concentration at grain boundaries, which entails the activation of supplementary slip systems as compared to the core of the grain [7]. Hence, regions closer to the grain boundaries will strain harden faster. This effect is particularly noticeable in the UFG grains, which display low misorientations in the core of grains. These observations are in agreement with the results obtained in the previous section and suggest hardening mechanisms mainly related to interactions between dislocations and grain boundaries. Samples 1–3 display no significant change in the average KAM value between the initial state and the deformed state.

To complete these observations, TEM observations were performed at fracture for two samples, representing the FG and the UFG range. Figure 11 displays bright field TEM images of sample 4 ( $d = 4.0 \mu\text{m}$ ). Grains divided by geometrical dislocation cells (or subgrains) can be observed with different misorientations as depicted in Figure 11a for a single grain observed using a diffraction vector  $\vec{g} = [1\bar{1}1]$ . The high density of dislocations in the cell walls and cores can be observed in Figure 11b, where a grain boundary is displayed edge-on. The average size of the dislocation cells was estimated as  $0.53 \pm 0.18 \mu\text{m}$ , from 28 cells in different grains. This value, rather independent of grain size, is in agreement with the value of  $0.35\text{--}0.55 \mu\text{m}$  observed in CG nickel [64] for a high plastic strain. The features of the deformed microstructure correspond to those expected for highly deformed nickel, characterized by high dislocation density and dislocation cells [65].

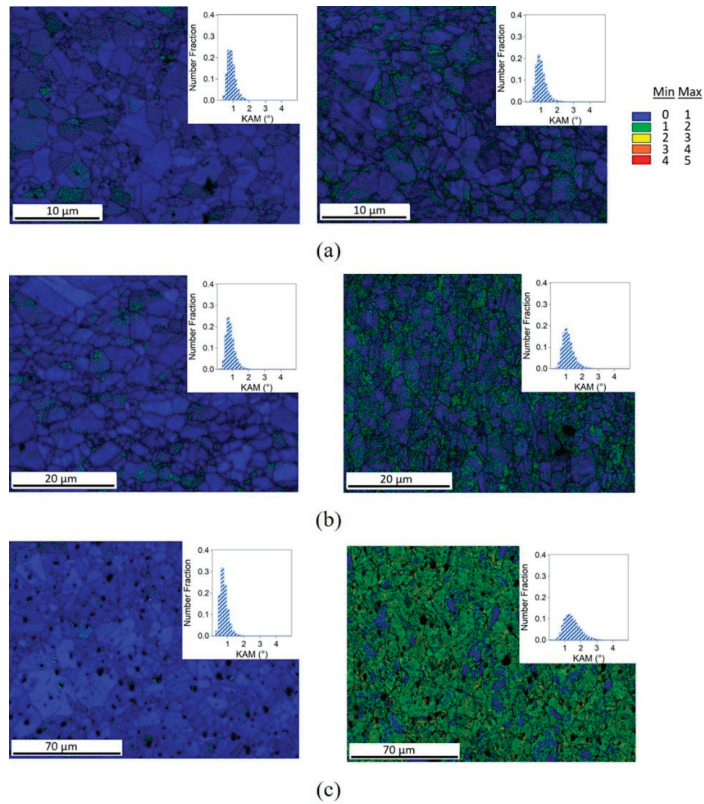


**Figure 10.** First neighbor kernel average misorientation (KAM)+IQ cartographies of samples 1 ( $d = 0.82 \mu\text{m}$ ) (a), 3 ( $d = 1.39 \mu\text{m}$ ) (b) and 4 ( $d = 4 \mu\text{m}$ ) (c) in the initial state (left) and for fractured samples (right). Color legend represents the kernel average misorientation in degrees. Inserts display the distribution of first neighbor KAM values for each state and sample.

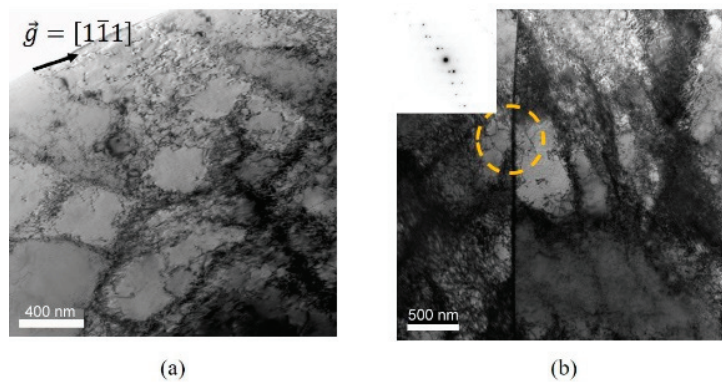


**Figure 11.** TEM images of grains of fractured sample 4 ( $d = 4.0 \mu\text{m}$ ), containing dislocation cells. Accumulation of geometric dislocation cells of similar size in a single grain ( $\vec{g} = [1\bar{1}1]$ ) (a) and contiguous grains displaying dislocation cells with a high density of dislocations (b).

Concerning the UFG regime, the deformed state of sample 1 ( $d = 0.82 \mu\text{m}$ ) displays a much different appearance (Figure 12). Figure 12a shows an overview of small equiaxed grains with a lower dislocation density inside grains, compared with sample 4 ( $d = 4.0 \mu\text{m}$ ) (Figure 11). Moreover, dislocations tend to accumulate preferably close to grain boundaries. The lack of dislocation walls, tangles or cells indicates low misorientation (as seen in EBSD) and hardening mechanisms related mainly to the interaction between individual dislocations. A decrease in the interactions between dislocations and dense dislocation structures implies a decrease in the value of  $\alpha$  and thus of  $\Delta_{II}$ . Small size dislocation cells were rarely found in the deformed microstructure (Figure 12b). Given the grain size ( $d = 0.82 \mu\text{m}$ ), which approaches the cell size in CG Ni, the few dislocation cells observed display in all cases a smaller size than those observed in FG specimens. Nevertheless, TEM observations show that dislocation cells are not a characteristic feature of the deformed state of UFG Ni. These results are in agreement with the EBSD analyses, and with the strain hardening behavior of UFG samples. The lower density of dislocations and the lack of dislocation substructures hinder the hardening capability of UFG specimens and has a major impact in their strain hardening mechanisms.

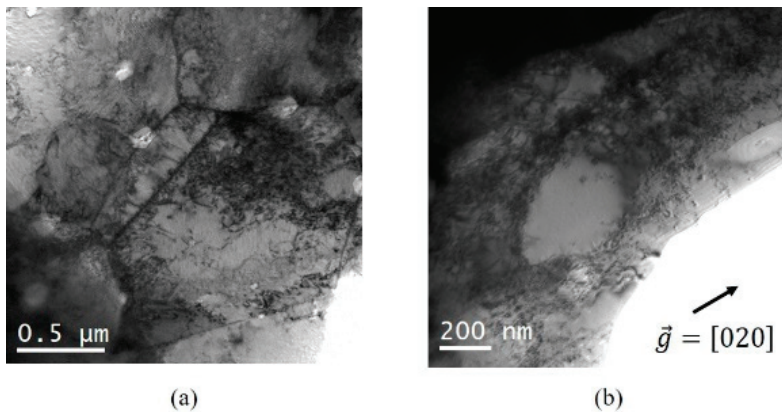


**Figure 12.** TEM images of sample 1 ( $d = 0.82 \mu\text{m}$ ) deformed up to fracture. Grains with different contrasts possibly due to a high density of dislocations (a) and a nanometric dislocation cell ( $\vec{g} = [020]$ ) (b).

#### 4. Conclusions

Changes in the plasticity mechanisms were investigated in Ni samples obtained by SPS with grain sizes ranging from  $0.82$  to  $25 \mu\text{m}$ , through tensile testing up to fracture and microstructural observations. The main results obtained in this study can be summarized as follows:

- Considerable strain hardening is displayed by all samples, including those with grain sizes in the UFG regime, although a decrease in the strain hardening capacity is observed with decreasing grain size.
- The three stages characteristic of plastic deformation in CG specimens were identified in the UFG samples. Considering the normalized stress  $\sigma/\sigma_y$ , the transition stress from stage I to II was similar in all samples, whereas a very short stage II was displayed by the UFG samples, entering in stage III just after initial yielding.
- A decrease of  $\Delta_{II}$  with decreasing grain size was observed suggesting low accumulation and interaction between dislocations in UFG specimens. In addition, the increase of  $(\sigma\theta)_0$  with  $1/d$  indicate a high contribution of dislocation interaction with grain boundaries to the strain hardening of such samples.

- Microstructural observations performed by EBSD showed fewer changes in the microstructure, such as changes in morphology or low formation of LAGBs, in samples with grain sizes in the UFG range.
- Misorientation cartographies (GOS and KAM), suggest low deformation of small size grains with low values of GOS and KAM, and preferred accumulation of dislocations close to grain boundaries.
- TEM observations of the deformed state of UFG samples ( $d = 0.82 \mu\text{m}$ ) showed low dislocation density heterogeneously distributed, and lack of well-defined dislocation cells.

From these results, we could conclude that with grain refinement in the UFG regime, dislocation storage was lessened by generalized cross-slip mechanisms and dislocation annihilation starting just after yielding, hindering the formation of organized dislocation structures in the grain core. Hardening is thus mainly mediated by dislocation interactions with grain boundaries, for grain sizes below  $d = 1.11 \mu\text{m}$ , which enable good ductility contrary to deformation mechanism such as grain sliding, observed in smaller size UFG and NsM metals.

**Author Contributions:** Conceptualization, L.G.d.I.C. and E.H.; methodology, L.G.d.I.C., M.M.C. and E.H.; validation, E.H. and C.K.; formal analysis, L.G.d.I.C., C.K. and E.H.; investigation, all authors; writing—original draft preparation, L.G.d.I.C.; writing—review and editing, all authors; supervision, E.H.; project administration, E.H. All authors have read and agreed to the published version of the manuscript.

**Funding:** This research received no external funding.

**Institutional Review Board Statement:** Not applicable.

**Informed Consent Statement:** Not applicable.

**Data Availability Statement:** The data presented in this study are available on request from the corresponding author.

**Conflicts of Interest:** The authors declare no conflict of interest.

## Glossary

### Abbreviations

|       |                                       |
|-------|---------------------------------------|
| BM    | Ball milling                          |
| CG    | Coarse grained                        |
| CSL   | Coincidence site lattice              |
| EBSD  | Electron backscatter diffraction      |
| FCC   | Face centered cubic                   |
| FG    | Fine grained                          |
| GBCD  | Grain boundary character distribution |
| GNDs  | Geometrically necessary dislocations  |
| GOS   | Grain orientation spread              |
| HABs  | High angle boundaries                 |
| IQ    | Image quality                         |
| IPF   | Inverse pole figure                   |
| KAM   | Kernel average misorientation         |
| LAGBs | Low angle grain boundaries            |
| NsM   | Nanostructured materials              |
| SPS   | Spark plasma sintering                |
| TEM   | Transmission electron microscopy      |
| UFG   | Ultrafine grained                     |

## Abbreviations

### Symbols

|                    |   |
|--------------------|---|
| $\alpha$           | Parameter of dislocation interaction and configuration            |
| $b$                | Norm of the Burgers vector  |
| $\beta$            | Parameter that relates $\Lambda$ and $l_d$ .                      |
| $d$                | Grain size  |
| $\Delta_{II}$      | Latent hardening rate   |
| $\varepsilon$      | True strain   |
| $\varepsilon_f$    | Elongation to failure   |
| $\vec{g}$          | Diffraction vector  |
| $\theta$           | Work hardening rate   |
| $k_g$              | Geometric factor related to grain morphology                      |
| $l_d$              | Average distance between dislocations                             |
| $\Lambda$          | Average distance traveled by a dislocation                        |
| $M$                | Taylor factor   |
| $P$                | Probability of dislocation annihilation                           |
| $\rho$             | Total dislocation density   |
| $\rho_{rel}$       | Relative density  |
| $\sigma$           | True stress   |
| $\sigma_y$         | Yield strength  |
| $\sigma_{I/II}$    | Stress of transition between hardening stages I and II.           |
| $\sigma_{II/III}$  | Stress of transition between hardening stages II and III.         |
| $y_a$              | Dislocation annihilation distance                                 |
| $(\sigma\theta)_0$ | Parameter of contribution of grain boundaries to strain hardening |

## References

- Lu, L.; Yongfeng, S.; Chen, X.; Qian, L.; Lu, K. Ultrahigh Strength and High Electrical Conductivity in Copper. *Science* **2004**, *304*, 422–426. [[CrossRef](#)] [[PubMed](#)]
- Zhu, K.N.; Godfrey, A.; Hansen, N.; Zhang, X.D. Microstructure and Mechanical Strength of Near- and Sub-Micrometre Grain Size Copper Prepared by Spark Plasma Sintering. *Mater. Des.* **2017**, *117*, 95–103. [[CrossRef](#)]
- Gu, C.; Lian, J.; Jiang, Z.; Jiang, Q. Enhanced Tensile Ductility in an Electrodeposited Nanocrystalline Ni. *Scr. Mater.* **2006**, *54*, 579–584. [[CrossRef](#)]
- Dhal, A.; Panigrahi, S.K.; Shunmugam, M.S. Achieving Excellent Microformability in Aluminum by Engineering a Unique Ultrafine-Grained Microstructure. *Sci. Rep.* **2019**, *9*, 10683. [[CrossRef](#)] [[PubMed](#)]
- Le, G.M.; Godfrey, A.; Hansen, N.; Liu, W.; Winther, G.; Huang, X. Influence of Grain Size in the Near-Micrometre Regime on the Deformation Microstructure in Aluminium. *Acta Mater.* **2013**, *61*, 7072–7086. [[CrossRef](#)]
- Zhu, Y.T.; Wu, X.L. Ductility and Plasticity of Nanostructured Metals: Differences and Issues. *Mater. Today Nano* **2018**, *2*, 15–20. [[CrossRef](#)]
- Ashby, M.F. The Deformation of Plastically Non-Homogeneous Materials. *Philos. Mag.* **1970**, *21*, 399–424. [[CrossRef](#)]
- Cheng, S.; Spencer, J.A.; Milligan, W.W. Strength and Tension/Compression Asymmetry in Nanostructured and Ultrafine-Grain Metals. *Acta Mater.* **2003**, *51*, 4505–4518. [[CrossRef](#)]
- Hayes, R.W.; Witkin, D.; Zhou, F.; Lavernia, E.J. Deformation and Activation Volumes of Cryomilled Ultrafine-Grained Aluminum. *Acta Mater.* **2004**, *52*, 4259–4271. [[CrossRef](#)]
- Kumar, K.S.; Suresh, S.; Chisholm, M.F.; Horton, J.A.; Wang, P. Deformation of Electrodeposited Nanocrystalline Nickel. *Acta Mater.* **2003**, *51*, 387–405. [[CrossRef](#)]
- Ma, E. Instabilities and Ductility of Nanocrystalline and Ultrafine-Grained Metals. *Scr. Mater.* **2003**, *49*, 663–668. [[CrossRef](#)]
- Krasilnikov, N.; Lojkowski, W.; Pakiela, Z.; Valiev, R. Tensile Strength and Ductility of Ultra-Fine-Grained Nickel Processed by Severe Plastic Deformation. *Mater. Sci. Eng. A* **2005**, *397*, 330–337. [[CrossRef](#)]
- Samigullina, A.A.; Nazarov, A.A.; Mulyukov, R.R.; Tsarenko, Y.V.; Rubanik, V.V. Effect of Ultrasonic Treatment on the Strength and Ductility of Bulk Nanostructured Nickel Processed by Equal-Channel Angular Pressing. *Rev. Adv. Mater. Sci.* **2014**, *39*, 48–53. [[CrossRef](#)]
- Dalla Torre, F.; Van Swygenhoven, H.; Victoria, M. Nanocrystalline Electrodeposited Ni: Microstructure and Tensile Properties. *Acta Mater.* **2002**, *50*, 3957–3970. [[CrossRef](#)]
- Dalla Torre, F.; Spatig, P.; Schaublin, R.; Victoria, M. Deformation Behaviour and Microstructure of Nanocrystalline Electrodeposited and High Pressure Torsioned Nickel. *Acta Mater.* **2005**, *53*, 2337–2349. [[CrossRef](#)]
- Meyers, M.A.; Mishra, A.; Benson, D.J. Mechanical Properties of Nanocrystalline Materials. *Prog. Mater. Sci.* **2006**, *51*, 427–556. [[CrossRef](#)]
- Erb, U. Electrodeposited Nanocrystals: Synthesis, Properties and Industrial Applications. *Nanostruct. Mater.* **1995**, *6*, 533–538. [[CrossRef](#)]

18. Valiev, R.Z.; Islamgaliev, R.K.; Alexandrov, I.V. Bulk Nanostructured Materials from Severe Plastic Deformation. *Prog. Mater. Sci.* **2000**, *45*, 103–189. [[CrossRef](#)]
19. Barry, A.H.; Dirras, G.; Schoenstein, F.; Tétard, F.; Jouini, N. Microstructure and Mechanical Properties of Bulk Highly Faulted Fcc/Hcp Nanostructured Cobalt Microstructures. *Mater. Charact.* **2014**, *91*, 26–33. [[CrossRef](#)]
20. Ebrahimi, F.; Bourne, G.R.; Kelly, M.S.; Matthews, T.E. Mechanical Properties of Nanocrystalline Nickel Produced by Electrodeposition. *Nanostruct. Mater.* **1999**, *11*, 343–350. [[CrossRef](#)]
21. Valiev, R.Z.; Langdon, T.G. The Art and Science of Tailoring Materials by Nanostructuring for Advanced Properties Using SPD Techniques. *Adv. Eng. Mater.* **2010**, *12*, 677–691. [[CrossRef](#)]
22. Gleiter, H. Materials with Ultrafine Microstructures: Retrospectives and Perspectives. *Nanostruct. Mater.* **1992**, *1*, 1–19. [[CrossRef](#)]
23. Gleiter, H. Nanostructured Materials: Basic Concepts and Microstructure. *Acta Mater.* **2000**, *48*, 1–29. [[CrossRef](#)]
24. Estrin, Y.; Vinogradov, A. Extreme Grain Refinement by Severe Plastic Deformation: A Wealth of Challenging Science. *Acta Mater.* **2013**, *61*, 782–817. [[CrossRef](#)]
25. Tian, Y.Z.; Gao, S.; Zhao, L.J.; Lu, S.; Pippin, R.; Zhang, Z.F.; Tsuji, N. Remarkable Transitions of Yield Behavior and Lüders Deformation in Pure Cu by Changing Grain Sizes. *Scr. Mater.* **2018**, *142*, 88–91. [[CrossRef](#)]
26. Yu, C.Y.; Kao, P.W.; Chang, C.P. Transition of Tensile Deformation Behaviors in Ultrafine-Grained Aluminum. *Acta Mater.* **2005**, *53*, 4019–4028. [[CrossRef](#)]
27. Gao, S.; Bai, Y.; Zheng, R.; Tian, Y.; Mao, W.; Shibata, A.; Tsuji, N. Mechanism of Huge Lüders-Type Deformation in Ultrafine Grained Austenitic Stainless Steel. *Scr. Mater.* **2019**, *159*, 28–32. [[CrossRef](#)]
28. García de la Cruz, L.; Martínez, M.; Keller, C.; Hug, E. Achieving Good Tensile Properties in Ultrafine Grained Nickel by Spark Plasma Sintering. *Mater. Sci. Eng. A* **2020**, *772*, 138770. [[CrossRef](#)]
29. Jin, Y.; Lin, B.; Bernacki, M.; Rohrer, G.S.; Rollett, A.D.; Bozzolo, N. Annealing Twin Development during Recrystallization and Grain Growth in Pure Nickel. *Mater. Sci. Eng. A* **2014**, *597*, 295–303. [[CrossRef](#)]
30. García de la Cruz, L.; Domenges, B.; Divinski, S.V.; Wilde, G.; Hug, E. Ultrafast Atomic Diffusion Paths in Fine-Grained Nickel Obtained by Spark Plasma Sintering. *Met. Mat. Trans. A* **2020**, *51*, 3425–3434. [[CrossRef](#)]
31. Song, J.-M.; Lee, J.-S. Self-Assembled Nanostructured Resistive Switching Memory Devices Fabricated by Templated Bottom-up Growth. *Sci. Rep.* **2016**, *6*, 18967. [[CrossRef](#)] [[PubMed](#)]
32. Cabibbo, M. Grain Refinement and Hardness Saturation in Pure Nickel Subjected to a Sequence of ECAP and HPT. *Metall. Ital.* **2015**, *9*, 37–48.
33. Bui, Q.H.; Dirras, G.; Ramtani, S.; Gubicza, J. On the Strengthening Behavior of Ultrafine-Grained Nickel Processed from Nanopowders. *Mater. Sci. Eng. A* **2010**, *527*, 3227–3235. [[CrossRef](#)]
34. Randle, V. The Coincidence Site Lattice and the ‘Sigma Enigma’. *Mater. Charact.* **2001**, *47*, 411–416. [[CrossRef](#)]
35. King, A.H.; Shekhar, S. What Does It Mean to Be Special? The Significance and Application of the Brandon Criterion. *J. Mater. Sci.* **2006**, *41*, 7675–7682. [[CrossRef](#)]
36. de la Cruz, L.G.; Flipon, B.; Keller, C.; Martínez, M.; Hug, E. Nanostructuring of Metals via Spark Plasma Sintering Using Activated Powder Obtained by Ball-Milling: Impact on the Strain-Hardening Mechanisms. In Proceedings of the AIP Conference Proceedings 1896, Dublin, Ireland, 26–28 April 2017; Volume 1896, p. 200002. [[CrossRef](#)]
37. García de la Cruz, L. Ultrafine Grained Nickel Processed by Powder Metallurgy: Microstructure, Mechanical Properties and Thermal Stability. Ph.D. Thesis, Normandie Université, Caen, France, 2019.
38. Sitarama Raju, K.; Ghanashyam Krishna, M.; Padmanabhan, K.A.; Subramanya Sarma, V.; Gurao, N.P.; Wilde, G. Microstructure Evolution and Hardness Variation during Annealing of Equal Channel Angular Pressed Ultra-Fine Grained Nickel Subjected to 12 Passes. *J. Mater. Sci.* **2011**, *46*, 2662–2671. [[CrossRef](#)]
39. Feaugas, X.; Haddou, H. Grain-Size Effects on Tensile Behavior of Nickel and AISI 316L Stainless Steel. *Metall. Mater. Trans. A* **2003**, *34*, 2329–2340. [[CrossRef](#)]
40. Kocks, U.F.; Mecking, H. Physics and Phenomenology of Strain Hardening: The FCC Case. *Prog. Mater. Sci.* **2003**, *48*, 171–273. [[CrossRef](#)]
41. Mecking, H.; Kocks, U.F. Kinetics of Flow and Strain-Hardening. *Acta Metall.* **1981**, *29*, 1865–1875. [[CrossRef](#)]
42. Kuhlmann-Wilsdorf, D. Theory of Plastic Deformation: Properties of Low Energy Dislocation Structures. *Mater. Sci. Eng. A* **1989**, *113*, 1–41. [[CrossRef](#)]
43. Kubin, L.; Devincere, B.; Hoc, T. Modeling Dislocation Storage Rates and Mean Free Paths in Face-Centered Cubic Crystals. *Acta Mater.* **2008**, *56*, 6040–6049. [[CrossRef](#)]
44. Jordan, L.; Swanger, W.H. The Properties of Pure Nickel. *Bur. Standards. J. Res.* **1930**, *10*, 6028.
45. Narutani, T.; Takamura, J. Grain-Size Strengthening in Terms of Dislocation Density Measured by Resistivity. *Acta Metall. Mater.* **1991**, *39*, 2037–2049. [[CrossRef](#)]
46. Keller, C. Etude Expérimentale Des Transitions Volume/Surface Des Propriétés Mécaniques Du Nickel Polycristallin de Haute Pureté. Ph.D. Thesis, Université de Caen Basse-Normandie, Caen, France, 2009.
47. Devincere, B.; Hoc, T.; Kubin, L. Dislocation Mean Free Paths and Strain Hardening of Crystals. *Science* **2008**, *320*, 1745–1748. [[CrossRef](#)]
48. Dubos, P.A. Influence de La Température et Du Trajet de Chargement Sur Les Transitions Volume/Surface Des Métaux Cubiques à Faces Centrées. Ph.D. Thesis, Université de Caen Basse-Normandie, Caen, France, 2013.

49. Hansen, N.; Huang, X. Microstructure and Flow Stress of Polycrystals and Single Crystals. *Acta Mater.* **1998**, *46*, 1827–1836. [[CrossRef](#)]
50. Hug, E.; Keller, C. Intrinsic Effects Due to the Reduction of Thickness on the Mechanical Behavior of Nickel Polycrystals. *Metall. Mater. Trans. A* **2010**, *41A*, 2498–2506. [[CrossRef](#)]
51. Estrin, Y.; Mecking, H. A Unified Phenomenological Description of Work Hardening and Creep Based on One-Parameter Models. *Acta Metall.* **1984**, *32*, 57–70. [[CrossRef](#)]
52. Jensen, D.J.; Thompson, A.W.; Hansen, N. The Role of Grain Size and Strain in Work Hardening and Texture Development. *Metall. Trans. A* **1989**, *20*, 2803–2810. [[CrossRef](#)]
53. Taylor, G.I. Plastic Strain in Metals. *J. Inst. Met.* **1938**, *62*, 307–324.
54. Humphreys, F.J.; Hatherly, M. *Recrystallization and Related Annealing Phenomena*, 2nd ed.; Elsevier: Oxford, UK, 2004.
55. Rémy, L. The Interaction between Slip and Twinning Systems and the Influence of Twinning on the Mechanical Behavior of Fcc Metals and Alloys. *Metall. Trans. A* **1981**, *12*, 387–408. [[CrossRef](#)]
56. Yamakov, V.; Wolf, D.; Phillpot, S.R.; Gleiter, H. Dislocation–Dislocation and Dislocation–Twin Reactions in Nanocrystalline Al by Molecular Dynamics Simulation. *Acta Mater.* **2003**, *51*, 4135–4147. [[CrossRef](#)]
57. Gubicza, J.; Bui, H.-Q.; Fella, F.; Dirras, G.F. Microstructure and Mechanical Behavior of Ultrafine-Grained Ni Processed by Different Powder Metallurgy Methods. *J. Mater. Res.* **2009**, *24*, 217–226. [[CrossRef](#)]
58. Brewer, L.N.; Field, D.P.; Merriman, C.C. Mapping and Assessing Plastic Deformation Using EBSD. In *Electron Backscatter Diffraction in Materials Science*; Springer Science & Business Media: Berlin/Heidelberg, Germany, 2009.
59. Kuhlmann-Wilsdorf, D.; Hansen, N. Geometrically Necessary, Incidental and Subgrain Boundaries. *Scr. Metall. Mater.* **1991**, *25*, 1557–1562. [[CrossRef](#)]
60. Field, D.P.; Bradford, L.T.; Nowell, M.; Lillo, T.M. The Role of Annealing Twins during Recrystallization of Cu. *Acta Mater.* **2007**, *55*, 4233–4241. [[CrossRef](#)]
61. Schwartz, A.J.; Kumar, M.; Adams, E. *Backscatter Diffraction in Materials Science*; Field, D.P., Adams, B.L., Kumar, M., Schwartz, A.J., Eds.; Springer US: Boston, MA, USA, 2000.
62. Sakakibara, Y.; Kubushiro, K. Stress Evaluation at the Maximum Strained State by EBSD and Several Residual Stress Measurements for Plastic Deformed Austenitic. *World J. Mech.* **2017**, *7*, 195–210. [[CrossRef](#)]
63. Fu, H.-H.; Benson, D.J.; Meyers, M.A. Analytical and Computational Description of Effect of Grain Size on Yield Stress of Metals. *Acta Mater.* **2001**, *49*, 2567–2582. [[CrossRef](#)]
64. Feaugas, X.; Haddou, H. Effects of Grain Size on Dislocation Organization and Internal Stresses Developed under Tensile Loading in Fcc Metals. *Philos. Mag.* **2007**, *87*, 989–1018. [[CrossRef](#)]
65. Keller, C.; Hug, E.; Retoux, R.; Feaugas, X. TEM Study of Dislocation Patterns in Near-Surface and Core Regions of Deformed Nickel Polycrystals with Few Grains across the Cross Section. *Mech. Mater.* **2010**, *42*, 44–54. [[CrossRef](#)]

Review

# Elaboration of Metallic Materials by SPS: Processing, Microstructures, Properties, and Shaping

Jean-Philippe Monchoux<sup>1,2,\*</sup>, Alain Couret<sup>1,2</sup>, Lise Durand<sup>1,2</sup>, Thomas Voisin<sup>3</sup>, Zofia Trzaska<sup>4,5</sup> and Marc Thomas<sup>6</sup>

<sup>1</sup> Centre d'Elaboration de Matériaux et d'Etudes Structurales, Centre National de la Recherche Scientifique, Unité Propre de Recherche 8011, 29 rue J. Marvig, BP 94347, CEDEX 4, 31055 Toulouse, France; alain.couret@cemes.fr (A.C.); lise.durand@cemes.fr (L.D.)

<sup>2</sup> Université Toulouse III—Paul Sabatier, 118 Route de Narbonne, CEDEX 9, 31062 Toulouse, France

<sup>3</sup> Lawrence Livermore National Laboratory, 7000 East Av., Livermore, CA 94550, USA; voisin2@llnl.gov

<sup>4</sup> Institut de Chimie et des Matériaux Paris-Est, Unité Mixte de Recherche 7182, 2-8, rue Henri Dunant, 94320 Thiais, France; zofia.trzaska@univ-paris13.fr

<sup>5</sup> Université Sorbonne Paris Nord, 99, Avenue Jean-Baptiste Clément, 93430 Villetaneuse, France

<sup>6</sup> ONERA—The French Aerospace Lab, Department of Materials and Structures, Université Paris-Saclay, 29 Avenue de la Division Leclerc, BP 72, 92322 Châtillon CEDEX, France; marc.thomas@onera.fr

\* Correspondence: monchoux@cemes.fr

**Abstract:** After a few decades of increasing interest, spark plasma sintering (SPS) has now become a mature powder metallurgy technique, which allows assessing its performances toward fabricating enhanced materials. Here, the case of metals and alloys will be presented. The main advantage of SPS lies in its rapid heating capability enabled by the application of high intensity electric currents to a metallic powder. This presents numerous advantages balanced by some limitations that will be addressed in this review. The first section will be devoted to sintering issues, with an emphasis on the effect of the electric current on the densification mechanisms. Then, typical as-SPS microstructures and properties will be presented. In some cases, they will be compared with that of materials processed by conventional techniques. As such, examples of nanostructured materials, intermetallics, metallic glasses, and high entropy alloys, will be presented. Finally, the implementation of SPS as a technique to manufacture complex, near-net shape industrial parts will be discussed.

**Keywords:** SPS; metals; TiAl; microstructure; mechanical properties; shaping

**Citation:** Monchoux, J.-P.; Couret, A.; Durand, L.; Voisin, T.; Trzaska, Z.; Thomas, M. Elaboration of Metallic Materials by SPS: Processing, Microstructures, Properties, and Shaping. *Metals* **2021**, *11*, 322. <https://doi.org/10.3390/met11020322>

Academic Editor: Eric Hug

Received: 18 January 2021

Accepted: 7 February 2021

Published: 12 February 2021

**Publisher's Note:** MDPI stays neutral with regard to jurisdictional claims in published maps and institutional affiliations.



**Copyright:** © 2021 by the authors. Licensee MDPI, Basel, Switzerland. This article is an open access article distributed under the terms and conditions of the Creative Commons Attribution (CC BY) license (<https://creativecommons.org/licenses/by/4.0/>).

## 1. Introduction

Spark plasma sintering (SPS) has become a widely used processing technique for a broad class of materials, including ceramics, metals, and polymers. Consequently, significant improvements were achieved since the review conducted by Orru et al. [1] in 2009, allowing SPS to reach pre-industrialization. Early on, the ability of SPS to rapidly process many different materials with improved microstructures and properties was attributed to electricity-induced phenomena, such as the occurrence of sparks or plasma at the powder particle interfaces (which the process was named after), the involvement of electromigration, electroplasticity, and so on. However, after two decades of investigations, it is now possible to discuss more accurately these early hypotheses, and to establish more firmly its physical principles.

In this chapter, we will concentrate on the case of the metallic materials. Regarding potential electrical effects, these materials exhibit the particularity of a high electric conductivity. Therefore, they have been particularly the subject of investigation of electrically-induced effects. We will present studies devoted to these questions, but also, more generally, to the densification mechanisms and kinetics. Then, we will present the original microstructures, which can be achieved, characterized often by nanostructure, and we will present results showing the relation between the microstructures obtained by

SPS and those predicted by the equilibrium phase diagram. This will lead us to make a review of materials, which have been the subject of particular interest regarding their processing by SPS: intermetallics, nanostructured materials, metallic glasses, and high entropy alloys. Then, because processing of parts in complex geometries is becoming a major issue, we will deal with the necessary steps involved to achieve this goal: thermo-mechanical modeling, upscaling, and shaping.

## 2. Overview of the SPS Process

SPS technology consists in densifying powders by applying high electric current pulses under mechanical pressure. This results in rapid heating and compaction of the powder into fully dense materials. As shown in the reviews of Orru et al. [1] and of Munir et al. [2], the principle of the SPS originates in 1922. The ideas of local heating at the particle contacts was proposed in 1945, and the hypothesis of vaporization of superficial oxide layers by dielectric breakdown was formulated in the 1950s. The term *spark sintering* appeared in 1965, and Inoue enriched these concepts by describing phenomena, such as electric discharge, ionization, or local melting, and developed devices based on the use of high frequency electric currents. The works of Inoue lead to the development of Be-based materials for missiles at the Lockheed Corporation at the end of the 1960s. However, the extensive spreading of the current-assisted sintering technologies occurred at the beginning of the 1990s, when the Sumitomo Coal Mining company developed the so-called *spark plasma sintering* technology, based on patents of the 1960s. Since then, the number of works devoted to the SPS approach has increased very rapidly. For example, an analysis of the number of articles published per year containing the keywords “spark plasma sintering” is given in Figure 1. It shows an impressive increase in publications since the first time this term was encountered in literature, in 1994. Among this production, an analysis of the review of Orru et al. in 2009 [1] shows that the studies on metallic systems represent  $\approx 15\%$  of the total, a proportion probably stable over time.

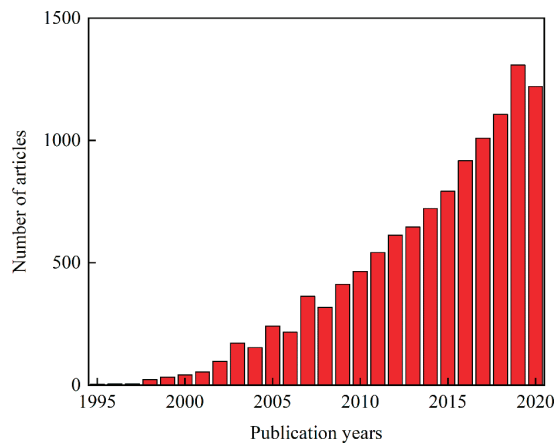


**Figure 1.** Number of articles per year related to spark plasma sintering (SPS) technology (source: Web of Science).

A simplified schematic of the powder sintering setup as found in most commercial SPS machines is depicted in Figure 2. The powder is filled inside a graphite mold, generally made of graphite, consisting in a cylindrical container closed by two compression electrodes, and this assembly is introduced into an evacuated chamber. As a high pressure (typically around 100 MPa) and a high intensity current are applied through the pistons, the entire setup, including the powder if conductive, rapidly heats up by Joule effect. In fact, because the heat production occurs internally, high heating rates can be achieved

(typically 50–1000 °C/min, depending on the setup, material, and intensities). As a result, short processing times (5–60 min) can be achieved. Figure 3 gives an example of a typical processing cycle for TiAl disks 36 mm in diameter and 8 mm thick. It can be seen, in this example, that the current intensity reached 3000 A. Because the temperature is usually not measured at the sample but either on the external surface of the die or inside one of the electrodes, a few cm away from the sample, a temperature gradient between the measure and the sample exists. In this case, corrections can be applied based on experimental calibrations or simulations. This will be discussed in Section 5.

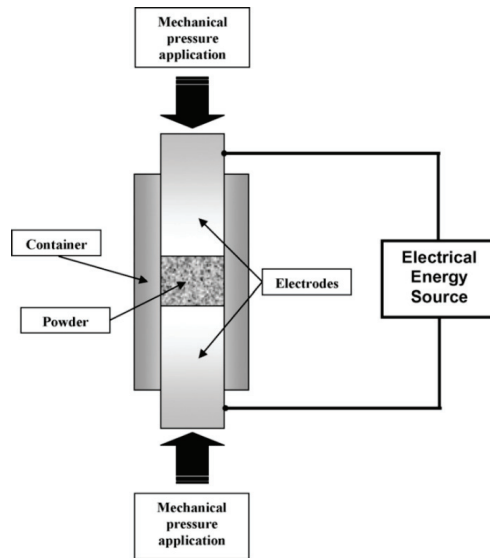


Figure 2. Schematic representation of the SPS process [1]. Reproduced with permission from *Materials Science and Engineering: R*, published by Elsevier, 2009.

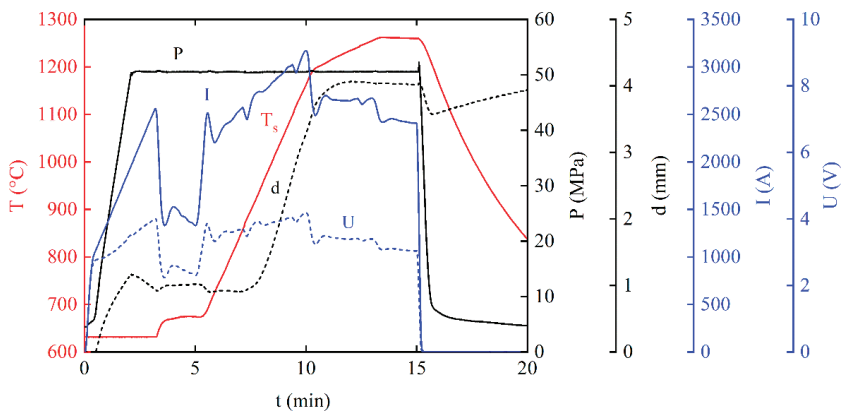


Figure 3. Evolution of the SPS parameters during the processing of a metallic TiAl alloy, in the case of a 36 mm sample (T<sub>s</sub>: corrected sample temperature, P: applied mechanical pressure, I: intensity, U: voltage and d: sample thickness reduction).

### 3. Densification Mechanisms and Kinetics

It has been suggested that the high intensity electric current applied upon processing could intrinsically influence the sintering kinetics and the densification mechanisms [1–3]. We present here the main efforts dedicated to verifying this hypothesis.

#### 3.1. Microscopic Densification Mechanisms

Several mechanisms that can be induced by the high-intensity electrical current during SPS can be classified as follow: (i) dielectric breakdown of the oxide layers at the surface of the powder particles. (ii) Arcs and plasma generation between powder particles. (iii) Local overheating due to a current density increase at the contact between powder particles. (iv) Activation of electromigration and electroplasticity.

Mechanisms (i) and (ii) have been first proposed by Tokita [3]. Breakdowns of superficial oxide layers, mechanism (i), were reported in many studies [4–7], but without providing convincing experimental evidences. Arcing, as in mechanism (ii), has been on the contrary more clearly observed between adjacent Cu powder particles 550  $\mu\text{m}$  in diameter (Figure 4) [8]. However, in this work the applied pressure was very low, which did not reproduce the conditions encountered during an actual SPS cycle. Detection of arcs by emission spectroscopy has been attempted by two teams. Plasma was reported in a W powder for applied voltages  $>50$  V by Saunders et al. [9]. Conversely, Hulbert et al. [10] concluded to the absence of plasma in various metallic powders (Al, Mg, Zn) for voltages  $\approx 1$ –2 V, which are closer to that observed in typical SPS experiments. Even though spark and/or plasma events may still happen at the onset of sintering, the heavy plastic deformation of the interparticle contact regions due to the applied high pressure may too quickly remove the geometrical singularities at the origin of electric current intensification and arcing.

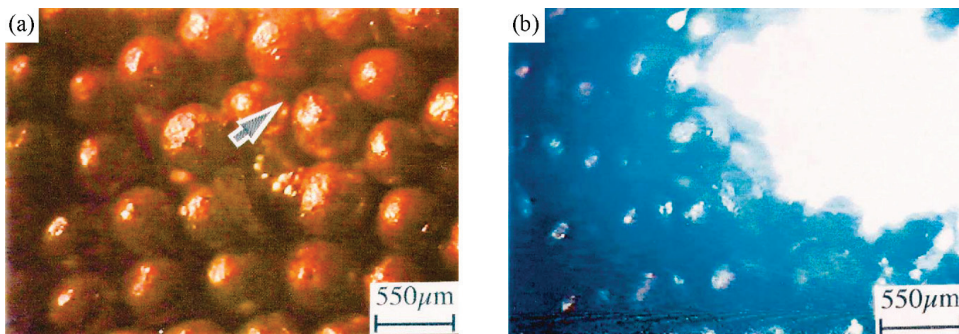


**Figure 4.** (a) Cu powder particles 550  $\mu\text{m}$  in diameter. (b) Generation of an electric arc by a current pulse of 6700  $\text{A}/\text{cm}^2$  during 100 ms, at the location indicated by an arrow in Figure (a) [8]. Reproduced with permission from *Materials Science and Engineering: A*, published by Elsevier, 2003.

Local Joule overheating at the contacts between powder particles, mechanism (iii) has mainly been investigated theoretically. In the early works, very elevated local current densities, leading to local high overheating at the contacts (up to 10,000  $^{\circ}\text{C}$ ), were computationally calculated [8,11]. The main limitation of these simulations is that they did not consider heat conduction within the particles, which was later shown to play a major role [12–16]. Even though more recent simulations predict local current densities as high as  $\approx 5 \times 10^4$   $\text{A}/\text{cm}^2$  at the contacts between particles [15–17], it has been shown that, for regular-size powder particles ( $\approx 100$   $\mu\text{m}$ ), the temperature homogenization by heat conduction takes only milliseconds, which was not compatible with stabilization of “hot spots” at the particle contacts [15,16]. Few experimental works with FeAl [18] and metallic glasses [19] concluded local overheating, but clear and direct evidence could not be

provided. Therefore, the formation of “hot spots” at the regions of contact between powder particles due to local electrical current concentrations is still debated in the literature.

Finally, the activation of metallurgical effects by electric currents, mechanisms (iv), has been considered, because the high current densities in the particles contact regions ( $\approx 5 \times 10^4 \text{ A/cm}^2$ ) are near or above the activation threshold for electroplasticity ( $10^3\text{--}10^6 \text{ A/cm}^2$ ) [20–22] and electromigration ( $10^2\text{--}10^3 \text{ A/cm}^2$ ) [2]. For example, model experiments with 3 mm Cu spheres in contact with Cu plates showed enhanced growth rates of the sphere-plate contact zones with currents  $\approx 5 \times 10^2 \text{ A/cm}^2$  [17]. This effect, which could account for increase in densification rate of metallic powders by the current, was interpreted by electromigration phenomena. However, another interpretation can also be proposed. When the size of the powder particle increases, and reaches millimeters and above, the thermal equilibration of the powder particles takes longer time [12,13], and hot spots can therefore be stabilized in the contact regions. Consequently, the local increase of the temperature can lead to acceleration of plastic deformation by creep. Other experimental investigations have been performed by focused ion beam and transmission electron microscopy (TEM) in the contact regions between powder particles in TiAl [23] and Ni [24]. It has been shown that the elementary deformation mechanisms were dislocation glide and climb, followed by dislocations recovery and recrystallization. For example, Figure 5 shows TEM images of a thin foil extracted in the contact region between two Ni powder particles [24]. High dislocation densities, and recovery walls, can be observed. This suggests that the observed mechanisms, which are those classically involved in power-law creep, are not significantly modified by the electric current.

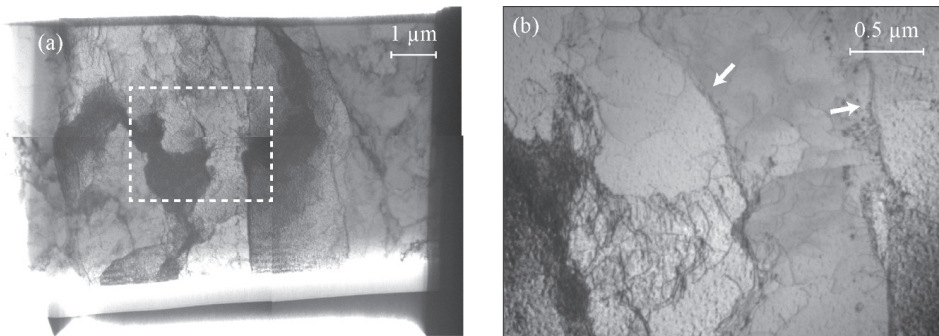


**Figure 5.** (a) TEM thin foil extracted from the contact region between two particles during densification of a Ni powder by SPS. (b) Zoom-in corresponding to the white dashed rectangle in (a) showing the presence of dislocations wall associated to dislocation recovery mechanisms [24]. Reproduced with permission from *Metallurgical and Materials Transactions: A*, published by Springer Nature, 2018.

### 3.2. Influence of High Intensity Currents on Powder Densification Kinetics

The effect of high intensity currents on the metallic powder densification at macroscopic scale has been the subject of several studies that gave contradictory results. For example, Figure 6 shows that when increased currents are applied to a Ni powder, by use of devices forcing all of the current to flow through the sample (setup 2), the final density of the sample is about 5% higher than that obtained in current-insulated experiments (setup 3), keeping the other parameters (temperature, pressure, dwell time, etc.) identical [25]. Similarly, Aleksandrova et al. [26] observed a density increase of Cu specimens when applying currents of  $1000 \text{ A/cm}^2$ , compared with experiments without current. On the contrary, a comparison between SPS and hot pressing with Cu [27] and TiAl [28] powders highlighted similar densification kinetics (density as a function of time) independently of the process employed.

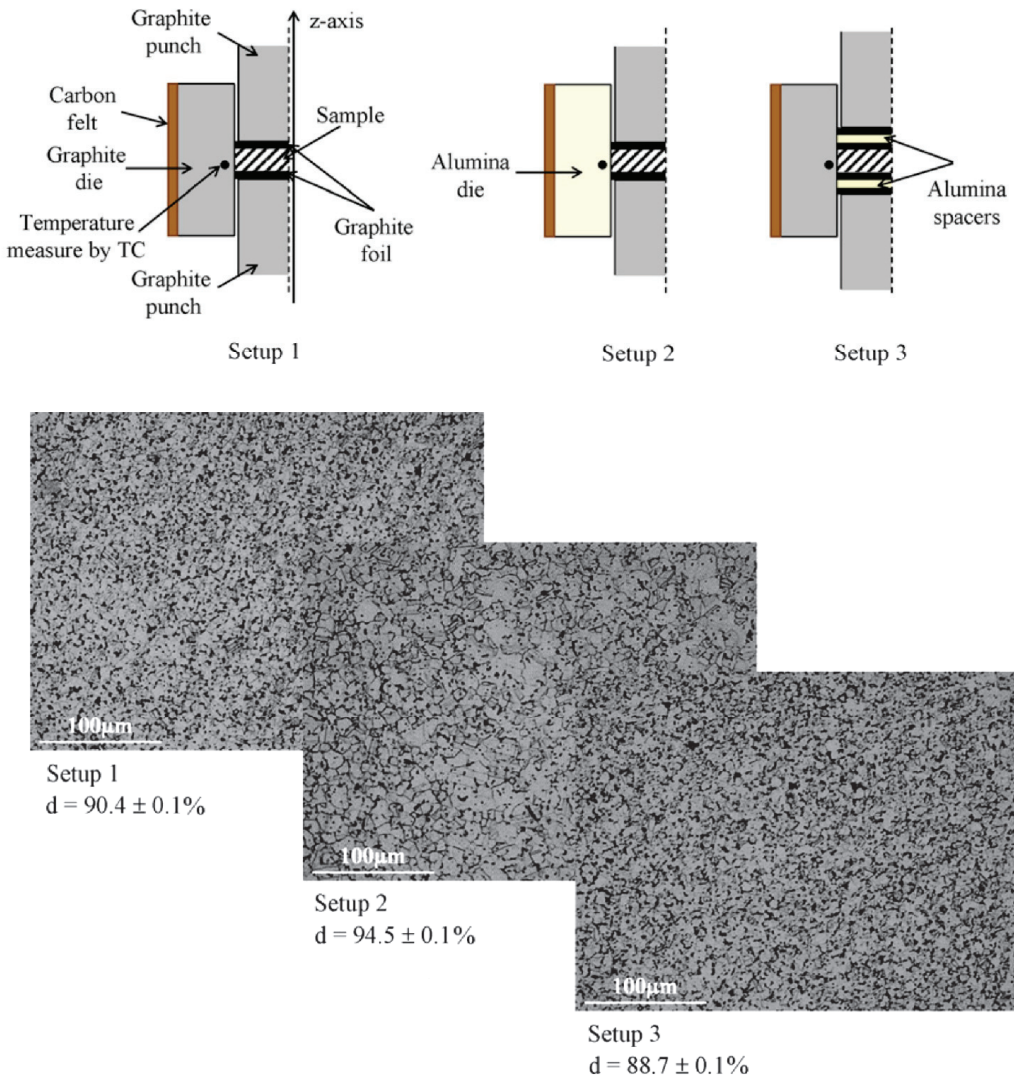


**Figure 6.** Relative density  $d$  of a Ni powder submitted to normal SPS conditions (setup 1), and to conditions where all of the SPS current flows through the sample (setup 2) and where the sample is electrically insulated (setup 3). Note in particular the difference in relative density  $d$  between samples processed using setup 2 ( $d = 94.5\%$ ) and setup 3 ( $d = 88.7\%$ ), showing an increase of sample relative density of about 5% due to the electric current [25]. Reproduced with permission from *Journal of Alloys and Compounds*, published by Elsevier, 2010.

### 3.3. Conclusions

What the investigations reported in this section agree on is that it is not possible to definitively conclude on the role of high intensity electric currents on the densification mechanisms and kinetics besides providing an effective heat source. Macroscopic effects are at most moderate [26], limited [25] or inexistent [27,28]. Moreover, at the microscopic scale, with the noticeable exception of the study of Yanagisawa et al. [8], no evident phenomena have been experimentally detected. The densification mechanisms are consequently similar to those classically involved in densification theories: deformation of the powder particles

by power-law creep involving dislocations glide and climb, followed by recovery and recrystallization [23,24]. Therefore, it can reasonably be stated that the densification of metallic powders by SPS experiments is not governed by electrical effects. As such, the process can be adequately modeled using Norton law constitutive relations, as will be detailed in Section 5.

#### 4. As-SPS Microstructure and Mechanical Properties

As a powder metallurgy technique, the SPS primarily purpose is to densify powders to obtain bulk metallic materials of controlled density. However, because the sintering takes place at high temperatures, it is also possible to optimize the microstructures. In many cases, this results in improved mechanical properties. Moreover, the rapid densification capability of the SPS technique allows obtain nanostructured or metastable materials by using very short thermal cycles. Another important advantage of the SPS technique is the microstructure homogeneity, which is generally more satisfactory than with other techniques, such as casting for example. However, the distribution of the electric current during SPS is often heterogeneous throughout the samples, which causes temperature gradients, especially for large samples, resulting in possible microstructure variations. Therefore, a significant effort has been dedicated to model the temperature fields in samples and molds toward optimizing the temperature distribution in large specimens, as will be discussed in Section 5. These microstructures heterogeneities are nevertheless less pronounced than with casting, because in this latter case solidification leads to many structural defects: cracks, porosities, contaminations, segregations and so on. Moreover, the problem of temperature heterogeneity in large parts tends to be mastered, by adapting the geometry of the molds, or by developing the so-called “hybrid” SPS technology, which provides additional heat sources leading to decrease of the temperature gradients within the parts. Therefore, the SPS shows now a high potential for developing advanced materials, for parts of increasing dimensions. This section is thus dedicated to discuss selected studies that best illustrate the potential of SPS to tune microstructures and improve the resulting mechanical properties.

##### 4.1. Equilibrium Microstructures

Because of the rapidity of the SPS technique, it is anticipated that the phases and microstructures of metallic alloys can differ from those at equilibrium as predicted by the phase diagrams. This point has been investigated in the case of TiAl alloys, for which processing by conventional techniques in suitable fields of the binary phase diagram lead to well referenced near  $\gamma$ , duplex, and lamellar microstructures [29]. It has been shown that, in the case of the simplest TiAl-based GE alloy (Ti-Al<sub>48</sub>-Cr<sub>2</sub>-Nb<sub>2</sub>), manufacturing by SPS leads to an accurate correspondence with the binary phase diagram (Figure 7 [30]). Each microstructure exhibits a specific mechanical response to uniaxial tension at room temperature and uniaxial tensile creep testing at high temperature. This provides the opportunity to find a microstructure with an optimized balance between room temperature ductility and high temperature properties. Unfortunately, such a compromise cannot be reached with the Ti-Al<sub>48</sub>-Cr<sub>2</sub>-Nb<sub>2</sub> composition as show in Figure 7. The duplex microstructure offering the best ductility exhibits high creep deformation rate and limited lifetime (Figure 7d,f). However, because the obtained microstructures were those predicted by the phase diagrams, it was possible to design materials of more complicated chemistries and microstructures, based on theoretically predicted phase diagrams, to improve the mechanical properties [30,31]. Thus, the beneficial roles of W on the creep resistance, through reduction of the diffusion rates, and that of B on the limitation of grain growth, through grain boundary pinning on TiB<sub>2</sub> precipitates, have been investigated. This resulted in the so-called IRIS alloy, of Ti-48Al-2W-0.1B composition, which strength at high temperature was higher than alloys elaborated by other techniques (Figure 8 [32,33]).

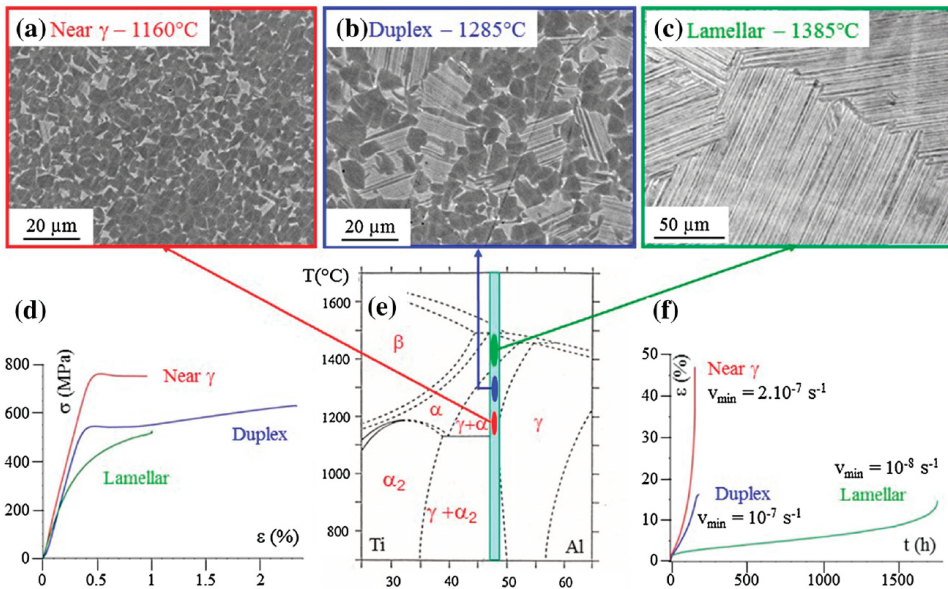


**Figure 7.** (a–c) Near  $\gamma$ , duplex, and lamellar microstructure of the Ti-Al<sub>48</sub>-Cr<sub>2</sub>-Nb<sub>2</sub> alloy obtained by elaboration by SPS, compared with the binary phase diagram of this alloy (e). Mechanical properties in tension at room temperature (d) and in creep (700 °C—300 MPa) (f) of the corresponding materials [30]. Reproduced with permission from *Journal of the Minerals, Metals and Materials Society*, published by Springer Nature, 2017.

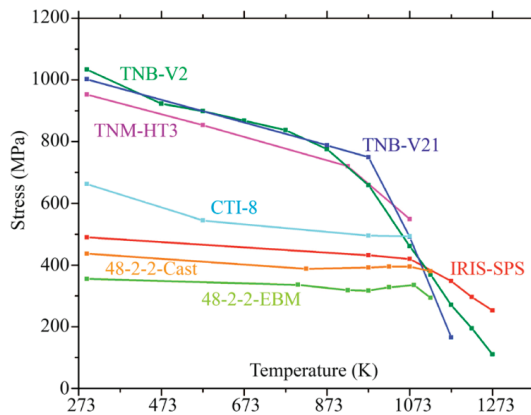


**Figure 8.** Variation of the yield stress as a function of temperature of the TiAl IRIS alloy elaborated by SPS, compared with that of alloys elaborated by other techniques (TNM-HT3: forging, TNB-V2, TNB-V21 and CTI-8: extrusion, 48-2-2: casting, 48-2-2-EBM: electron beam melting) [33]. Reproduced with permission from *Metallurgical and Materials Transactions: A*, published by Springer Nature, 2016.

4.2. Nanostructured Materials

Limiting the grain coarsening during manufacturing is one of the main advantages of SPS. Densification can occur fast enough for samples to be held at high temperature over short period of time, typically in the order of minutes. Therefore, nanostructured materials can be obtained with potentially original mechanical properties.

Various nanostructured metals and alloys were obtained by SPS using nanopowders such as Cu [34], TiNi [35], Al [7,36], and W [37]. For example, in the case of Al, the use of

appropriate SPS parameters allows to keep an extremely fine microstructure, the average grain size being in the order of 50 nm [7]. In addition, using nanopowders [38–42], or micrometric mechanically activated powders [43–45], nanostructured Ni materials have successfully been obtained. In particular, these routes allowed elaboration of nanomaterials exhibiting very high-accumulated strains during cyclic tests [38], as well as significantly enhanced strength (Figure 9) [43]. However, in the case of nanopowders, oxides at the surface of the powder particles were found to affect the cohesion of the material [42], leading to low ductility in compression [39] and tension [41]. Incidentally, these results indicate that a removal of the superficial oxide layers by electric arcs and/or plasma, as proposed in several studies [4–7], does not seem to operate. Finally, original harmonic microstructures consisting in nanograins surrounding large grains could be stabilized with  $\beta$ -Ti due to the rapidity of the SPS process (Figure 10) [46–49]. These materials exhibited enhanced resistance under monotonic sollicitation [46,47] and fatigue [48,49].

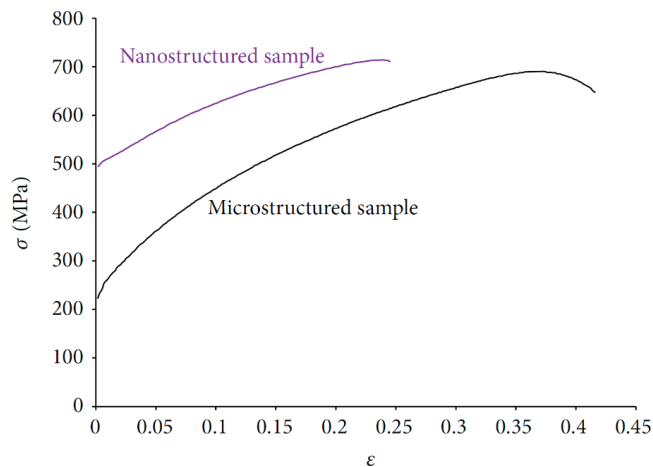


**Figure 9.** Tensile curves of micro- and nanostructured Ni materials elaborated by SPS [43]. Reproduced with permission from *Journal of Nanomaterials*, published by Hindawi, 2013.

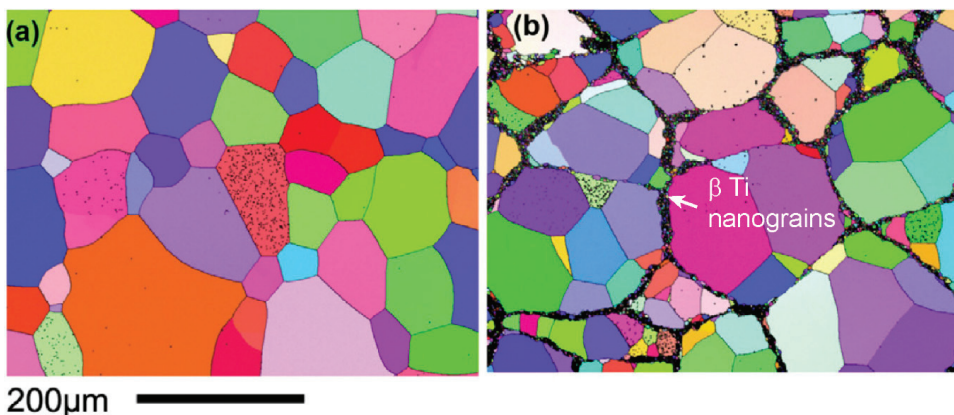


**Figure 10.** SEM electron back-scattered diffraction inverse pole figure maps of the  $\beta$ -Ti phase comparing the coarse grain microstructure of a material conventionally processed (a), to the harmonic microstructure, consisting of large grains surrounded by nanograins, of a material processed by SPS (b) [48]. Reproduced with permission from *Scripta Materialia*, published by Elsevier, 2017.

#### 4.3. Metallic Glasses

The SPS technique has shown a high potential for developing amorphous metallic materials. This is first the consequence that the pre-alloyed powders can be prepared by atomization, the very fast cooling rates of the liquid alloy droplets ( $10^5$ – $10^8$  °C/s) [50] during the atomization process, favoring solidification in amorphous state. Therefore, the atomization route has been successfully employed since the late 1970s [51]. Then, to avoid devitrification during processing of the amorphous powder at high temperature, the SPS method is particularly interesting in reason of its rapidity. As such, many metallic glasses have been developed as recently reviewed by Perrière et al. [52]. However, in some cases with Zr-based metallic glasses, devitrification was observed at the powder particle contacts at the early stages of densification, a phenomenon that was interpreted by local overheating effects [19,53]. Such devitrification effects can be detrimental for the development of metallic glasses by SPS, and need now to be better controlled.

#### 4.4. High Entropy Alloys

The use of the SPS for developing high entropy alloys (HEA) results from the better homogeneity obtained by this technique as compared to casting, and also from the very fine microstructures, which can be achieved. However, sintering of elemental powders is most of the time not possible, because of incomplete reaction at the end of the elaboration. Therefore, mechanical alloying (MA) is frequently employed before elaboration by SPS. Surprisingly, there were only few attempts so far to investigate the gas atomization technique [54,55] despite the wide use of this technique to produce pre-alloyed powders. Therefore, the works reported below only refer to materials obtained by SPS after MA.

For example, the MA + SPS route allowed to obtain  $\text{Co}_{25}\text{Ni}_{25}\text{Fe}_{25}\text{Al}_{7.5}\text{Cu}_{17.5}$  alloys exhibiting strength more than eight times higher than materials elaborated by arc melting [56],  $\text{Ni}_{1.5}\text{Co}_{1.5}\text{CrFeTi}_{0.5}$  alloys exhibiting very good combination of strength and ductility [57], and other high-strength alloys (e.g.,  $\text{AlCoCrCuFe}$  and  $\text{NiCoCrCuFe}$  [58],  $\text{Al}_{0.75}\text{FeNiCrCo}$  [59],  $\text{Ni}_{1.5}\text{CoCuFeCr}_{0.5}$  [60]). In all of these cases, the interest of the SPS was the preservation of the nanostructure. In addition, the possibility to mix different powders by SPS allowed obtaining self-lubricating  $\text{CoCrFeNi}$ -(Ag,  $\text{BaF}_2/\text{CaF}_2$ ) composites that can reach friction coefficients below 0.26 [61].

In these studies, the rapid densification by SPS allowed retaining nanostructures, which partially explains the high strength. Note that the potential powder contamination during MA by the milling medium or the environment can be overcome by developing suitable methodologies [62]. The main disadvantage of MA remains the long process time. For that, powder gas atomization appears more suited as it has demonstrated successful obtention of several pre-alloyed powders with metals of very different melting points, such as Al, Ti, Re, and W [63].

#### 4.5. Conclusions

The examples shown in this part demonstrate that the SPS allows elaborating materials with elevated mechanical properties. Moreover, the microstructures can be accurately predicted provided that the theoretical phase diagram is known. Therefore, it has been attempted, in some cases, to manufacture parts of larger sizes and of increased geometrical complexity. This is the subject of the next section.

### 5. Towards Elaboration of Complex Parts

Beside manufacturing materials, it has been demonstrated that the SPS technique was also efficient for shaping. However, it has to be underlined that, if some achievements look impressive, the development of shaping by SPS is not straightforward. Because the processing occurs by submitting a powder to a uniaxial pressure at high temperature, many constraints have to be considered: the electrodes move in only one direction, the volume occupied by the parts evolves due to densification of the powder, the temperature is not homogeneous within the material, and so on. Therefore, it has been proved useful to first

develop predictive modeling strategies, based on multi-physics finite element methods coupling the various physical parameters of the technique (electric fields, temperature gradients, stress distribution). After these modeling studies, it is generally necessary to develop suitable SPS cycles for parts of large dimensions. Due to energy limitations, most laboratory SPS equipment have a limit in maximum sample size that is, even though material dependent, usually around 5 cm in diameter for a couple cm in thickness. Finally, shaping of small or large specimen is attempted, using specially designed molds. This is this last part, which is by far the most critical, and different approaches have been proposed.

### 5.1. Modeling of the SPS Process

Modeling the SPS process is a complex task that requires accounting for several physics at once. The case of conducting metallic materials has been considered in the following references: [64–79]. As depicted by Achenani et al. [78], the ongoing modeling effort can be divided in two categories: thermoelectric coupling to simulate temperature gradients in fully-dense, static conditions [64–67,70,74,76,78,79], and stress distribution calculations to model the densification kinetics [28,68,69,71–73,75,77].

#### 5.1.1. Thermoelectric Coupling

Knowing the temperature distribution in SPS samples during processing is key to control the temperature gradients and ensure full densification and homogeneous microstructures. However, the temperature fields within the samples and molds are complex, because they result from two main contributions. The first one is the heat generated by the Joule effect under the influence of the high intensity electric current. The current distribution being non-uniform, the heat production exhibits also high variations within the sample/mold assembly. The second is the cooling, by heat radiation from the external surfaces and by heat transfer towards the water-cooled electrodes (note that exothermic or endothermic reactions within the samples are here not considered.) Because the influence of these contributions on the resulting temperature fields can be difficult to anticipate, modeling has proved very useful. Thus, the finite element method (FEM) has been widely employed to predict the temperature fields within the sample/molds assembly. Equations coupling the contributions of heat production by Joule effect and of heat conduction are solved, which are generally of the following forms:

$$\nabla \times \nabla(V) = 0, \quad (1)$$

$$\nabla \times (-k\nabla T) + \rho c_p \left( \frac{\partial T}{\partial t} \right) = Q, \quad (2)$$

$$Q = \sigma(\nabla V)^2, \quad (3)$$

where  $V$ : electric potential,  $k$ : thermal conductivity,  $\rho$ : density,  $c_p$ : thermal capacity,  $\sigma$ : electrical conductivity,  $T$ : temperature and  $t$ : time. Using this approach, Anselmi-Tamburini et al. [80] showed that the current density profile across the sample and mold is significantly non-uniform and highly depending on the electrical conductivity of the sample (Figure 11a,b). Consequently, the temperature field is also non-uniform within the molds and the samples (Figure 11c). However, the shape of the thermal gradient cannot be deduced in a straightforward manner from the current density profile, and modeling proves here quite useful. By comparing insulating and conducting materials, Vanmeensel et al. [67] concluded that the amplitude of the temperature gradient was more elevated in the latter case (Figure 12). Similar simulations were developed and experimentally validated for TiAl alloys by Voisin et al. [74]. As discussed in Section 4.1, Ti-Al<sub>48</sub>-Cr<sub>2</sub>-Nb<sub>2</sub> undergoes a microstructure transition from duplex to lamellar at 1335 °C. This was used as an indicator of the local temperature to validate FEM models predictions. It was thus shown that the predicted temperature gradients in TiAl samples was depending on the geometry of the setup, in quantitative agreement with experimental metallographic observations (Figure 13). In particular, the use of elongated molds allowed to move away from each

other the hot spots created at the extremities of the molds, and consequently to lower the temperature gradients in the parts.

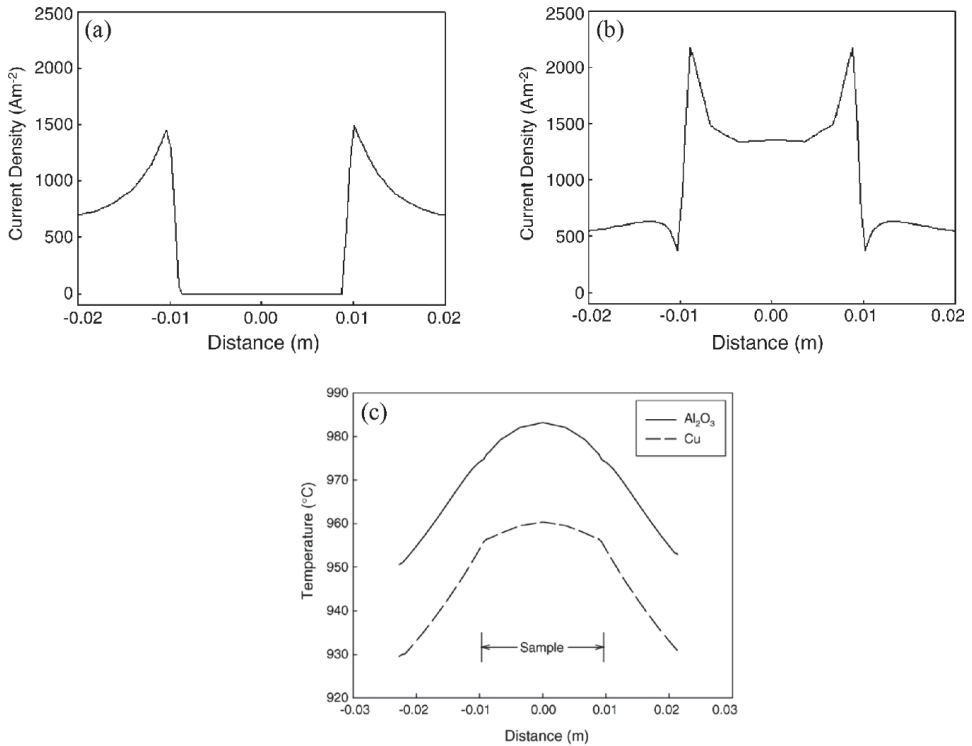


**Figure 11.** Radial current density distribution for non-conducting and conducting materials (applied voltage: 5V): Al<sub>2</sub>O<sub>3</sub> (a) and Cu (b). Temperature distribution for Al<sub>2</sub>O<sub>3</sub> and Cu (constant current applied: 1000 A) (c). In all cases, the profile is passing through the center of the samples and though the graphite molds surrounding them [80]. Reproduced with permission from *Materials Science and Engineering: A*, published by Elsevier, 2005.

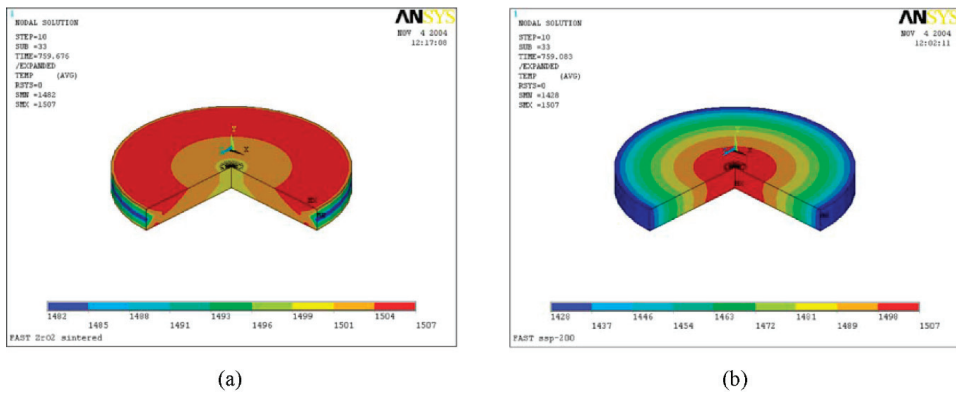


**Figure 12.** Temperature distribution in insulating ZrO<sub>2</sub> (a) and conducting TiN (b) samples during holding at 1500 °C [67]. Reproduced with permission from *Acta Materialia*, published by Elsevier, 2005.

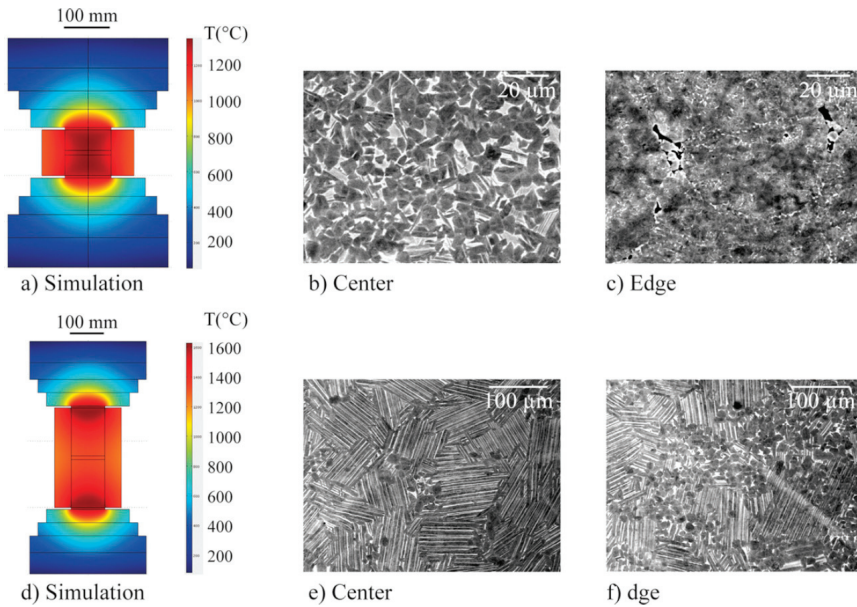


**Figure 13.** FEM simulations of two SPS setups, compared with metallographic observations of the center and edge of TiAl samples. For setup (a), the microstructure of the center is duplex (b), and that of the edge is near- $\gamma$  with some remaining porosities (c). This indicates a temperature gradient between the center and the edge of the sample of about 100 °C, in reasonable agreement with the FEM modeling (a), which predict a gradient of 125 °C. For setup (d), the FEM simulation predicts a temperature gradient between center and edge of the samples of 30 °C. The corresponding microstructures are near lamellar at the center (e) and duplex at the edge (f), indicating a thermal gradient of 25–50 °C, close to the simulations [74]. Reproduced with permission from *Journal of Materials Processing Technology*, published by Elsevier, 2013.

In summary, the temperature distribution throughout samples during SPS can be accurately predicted with FEM. Indeed, it is a necessary tool for designing molds that minimize thermal gradients and increase the microstructure homogeneity while limiting more expensive and time-consuming experimental testing.

### 5.1.2. Modeling of Densification Kinetics

There are two ways to model the densification of porous materials: a micromechanical approach based on analytical calculations [81,82] or continuum mechanics derivations [83,84]. The interest of the micromechanical approach is its simplicity, but its limitation is that the model is highly idealized (random dense packing of equal spheres [81]), and can therefore describe too roughly the actual geometrical features of the problem (e.g., powder particles sizes distributed over granulometry ranges). Moreover, the expressions are discontinuous for a density  $D$  of 0.9. Despite these shortcomings, it proved to be reasonably accurate. However, to increase results precision, more complex models based on continuum mechanics have been developed notably by Abouaf and Olevsky.

One common input to these calculations is the material constitutive law. For metals, the constitutive laws are most of the time of the following form (Norton relation):

$$\dot{\epsilon} = A_0 \exp \left[ -\frac{Q}{RT} \right] \sigma^n, \quad (4)$$

where  $\dot{\epsilon}$ : deformation rate,  $\sigma$ : stress,  $Q$ : activation energy,  $n$ : stress exponent,  $A_0$ : material constant,  $R$ : gas constant and  $T$ : temperature. Using micromechanical or continuum mechanics models, simulations of the densification kinetics have been successfully performed for TiAl [28,73,85], ZrC [86], Ni [77], Fe and Al [87], and Ti-6Al-4V [88]. An example of such

calculations applied to TiAl is shown in Figure 14, in the case of a continuum mechanics model. It can be seen that the calculated densification kinetics reproduces the experimental one with an accuracy better than 5%. Therefore, the models seem to be reasonably accurate.

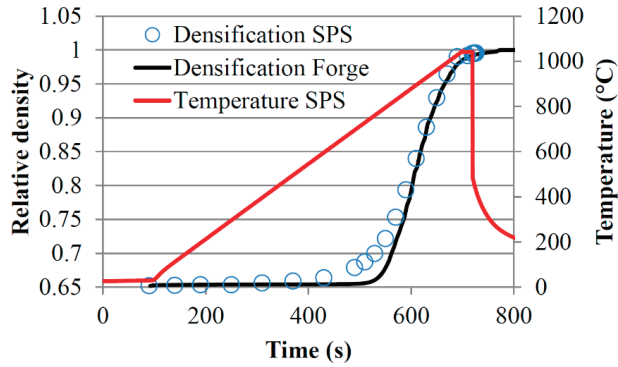


**Figure 14.** Densification kinetics by SPS of a TiAl alloy, compared with modeling by Forge software and continuum mechanics, using constitutive relations of bulk TiAl [85]. Reproduced with permission from *Intermetallics*, published by Elsevier, 2017.

However, these calculations are very sensitive to the material stress exponent [28]. For example, Figure 15a shows constitutive relations for a recrystallized TiAl powder, in which the activation parameters have been experimentally determined:  $n = 1.9$ , and  $Q = 308$  kJ/mol [28]. This law agrees with literature data for bulk TiAl and well captures the SPS kinetics (Figure 15b). However, if  $n$  is changed to 3 for a same  $Q$  ( $= 308$  kJ/mol) for example, the constitutive relations obtained are still in reasonable agreement with the literature data (Figure 15a), but the model prediction is no longer in phase with the experiment (Figure 15b). Therefore, it appears that the models used to predict the SPS densification behavior are very sensitive to the material parameters, which are difficult to accurately determine. Moreover, as can be seen in Figure 15a, the constitutive relations from literature are significantly scattered, and making proper choices of  $n$  and  $Q$  can be difficult. Therefore, the determination of the material constants has to be carefully carried out.

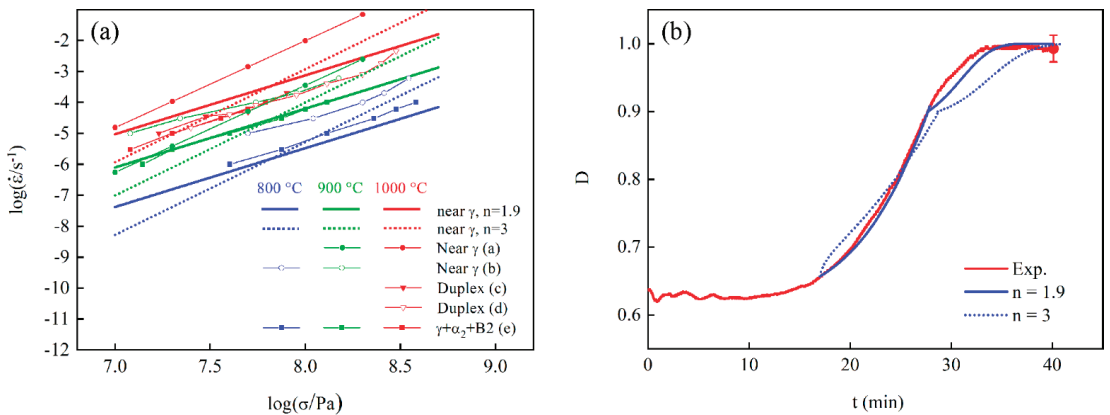


**Figure 15.** (a) Norton laws of a near  $\gamma$  TiAl alloy, taking  $n = 1.9$  and  $n = 3$ , the activation energy being identical ( $Q = 308$  kJ/mol). Comparison with literature data of alloys of similar near- $\gamma$  and duplex microstructures ((a): [85], (b): [89], (c): [90], (d): [91], (e): [92]). (b) Densification curves of TiAl ( $D$ : relative density,  $t$ : time) calculated using  $n = 1.9$  [28], and  $n = 3$ , compared with experiment.

### 5.2. Up-Scaling

Manufacturing big parts is an important issue, to obtain pieces of dimensions suitable for industrial applications. Sintering of metallic disks up to 350 mm in diameter has been reported [93], but a limited number of studies have been published to date. Early works report on processing of large specimens constituted of the following materials: Al [94], Ti (Figure 16) [95], TiAl [74,96]. One of the main difficulties, when processing parts of large dimensions is the presence of thermal and hence microstructure gradients in the materials, which are amplified with respect to those existing in small size samples. Therefore, the geometry of the molds needs to be optimized to homogenize the temperature distribution as previously discussed in Section 5.1.1 by using predictive FEM simulations. Another method is emerging with hybrid SPS machines. Since the temperature gradients are caused by a difference in current density between the center and the edges of the samples, a complimentary external furnace is added to heat the entire mold, thus limiting the temperature gradients. Unfortunately, it seems that no work on this promising approach has been published to date.



**Figure 16.** Ti composite part of large dimensions (20 cm in diameter), elaborated by SPS [95]. Reproduced with permission from *Materials Science and Engineering: A*, published by Elsevier, 2016.

### 5.3. Complex Shaping

Finally, shaping of parts of complex geometries is also an important issue, because this would allow to avoid or to limit machining, which can be difficult or even impossible, depending on the material. An early study reported the sintering of WC/Co/Ni screws for extrusion machines by SPS [93]. Unfortunately, little information is provided concerning the methodology. Later on, a method based on the deformation of an interface between a metallic powder and using sacrificial powders transmitting the pressure to the component has allowed forming 3 cm long CoNiCrAlY turbine blades (Figure 17) [97]. Finally, studies have reported on the development of parts in TiAl and NbSi reproducing the shape of turbine blades of aircraft engines, constituted of elongated and massive portions, as long as 10 cm (Figure 18) [30,32,98]. Here, the main challenge lied in compacting regions of different thicknesses such as encountered in this case between the elongated and massive portions. This was overcome by using separate plungers [98].

### 5.4. Conclusions

The development of simulations of thermoelectric coupling and of densification kinetics proved to be key to optimizing the processing of complex parts. This enabled up-scaling laboratory proof-of-concept to full-size components. Near-net shaping complex, full-scale parts has been successfully demonstrated, opening the doors to a wide range of possibilities, notably for materials hard to obtain with conventional manufacturing techniques.

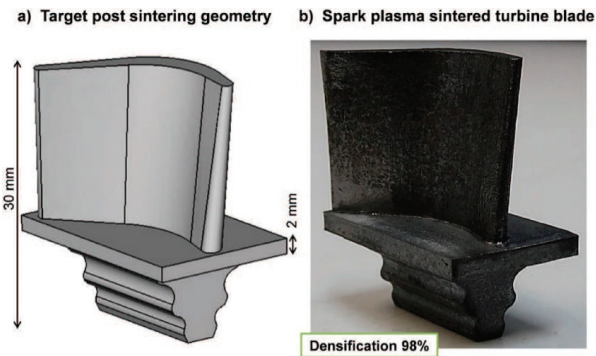


**Figure 17.** Example of turbine blade in CoNiCrAlY obtained by the deformed interfaces method. (a) Target shape. (b) Complex part obtained by SPS [97]. Reproduced with permission from *Powder Technology*, published by Elsevier, 2017.

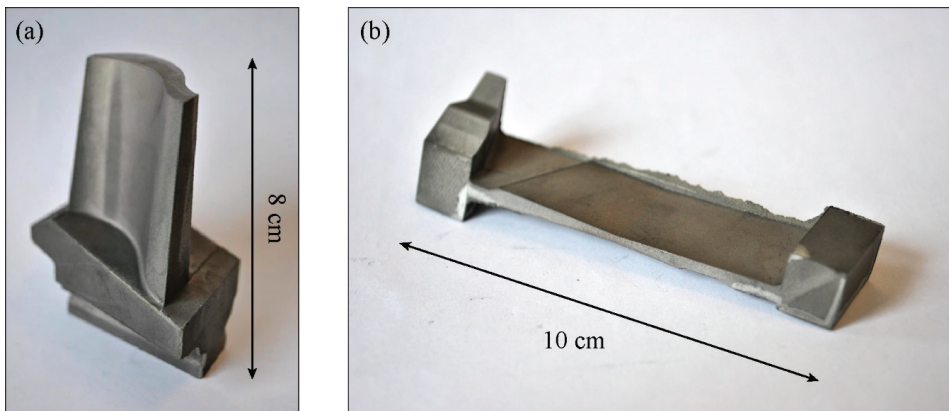


**Figure 18.** Turbine blade preforms in TiAl (a) 8 cm in height [32], and (b) 10 cm long [98], shaped by SPS. Reproduced with permission from *Advanced Engineering Materials*, published by John Wiley and Sons, 2015, and from *Springer eBook*, published by Springer Nature, 2019.

However, the challenge is now to implement these approaches in industrial processes, and to develop integrated production sectors. For this purpose, two critical steps can be identified: production of high quality powders, and automation of the SPS process. If satisfactory answers are given to these questions, the SPS technology could potentially experience a large development, because of the elevated properties reached in many cases by the elaborated materials. Therefore, the development of SPS-based processes deserves now increased industrial efforts.

### 6. General Conclusions

Over the past two decades, SPS has emerged as a technique of choice for producing innovative materials with optimized microstructures and properties, and for shaping complex parts. Despite the absence of demonstrated current-induced effects, the rapid heating by Joule effect allowing short densification cycles appears very efficient at retaining fine, homogeneous microstructures. Design of equilibrium or metastable microstructures can be controlled, depending on the alloy and on the processing conditions. As a result, a wide range of materials can be obtained with improved mechanical properties such as

nanostructured materials, intermetallics, metallic glasses, and high entropy alloys. Moving forward, introducing SPS to new industrial chains will require stepping toward more automated processes, allowing production of parts in larger quantities.

**Author Contributions:** Methodology, J.-P.M., Z.T., T.V.; software, L.D., T.V.; investigation, J.-P.M., Z.T., T.V.; writing—original draft preparation, J.-P.M.; writing—review and editing, J.-P.M., A.C., L.D., T.V., Z.T., M.T.; supervision, A.C., M.T.; project administration, A.C.; funding acquisition, A.C. All authors have read and agreed to the published version of the manuscript.

**Funding:** This research was funded by Agence Nationale de la Recherche, grant numbers MF2-ANR-2011-PBS09-020 and IRIS-ANR-08-MAPR-0018. T. Voisin was supported by the Laboratory Directed Research and Development (LDRD) program (21-LW-027) at Lawrence Livermore National Laboratory. T. Voisin’s work was performed under the auspices of the U.S. Department of Energy by Lawrence Livermore National Laboratory under contract no. DE-AC52-07NA27344.

**Institutional Review Board Statement:** Not applicable.

**Informed Consent Statement:** Not applicable.

**Data Availability Statement:** Data is contained within the article.

**Acknowledgments:** SPS experiments were performed using the Sumitomo 2080 SPS machine of the Plateforme Nationale de Frittage Flash du CNRS, Paul Sabatier University, Toulouse, France.

**Conflicts of Interest:** The authors declare no conflict of interest. The funders had no role in the design of the study; in the collection, analyses, or interpretation of data; in the writing of the manuscript, or in the decision to publish the results.

## References

- Orru, R.; Licheri, R.; Locci, A.M.; Cincotti, A.; Cao, G. Consolidation/synthesis of materials by electric current activated/assisted sintering. *Mater. Sci. Eng. R Rep.* **2009**, *63*, 127–287. [\[CrossRef\]](#)
- Munir, Z.A.; Anselmi-Tamburini, U.; Ohyanagi, M. The effect of electric field and pressure on the synthesis and consolidation of materials: A review of the spark plasma sintering method. *J. Mater. Sci.* **2006**, *41*, 763–777. [\[CrossRef\]](#)
- Tokita, M. Development of large-size ceramic/metal bulk FGM fabricated by spark plasma sintering. *Mater. Sci. Forum* **1999**, *308–311*, 83–88. [\[CrossRef\]](#)
- Omori, M. Sintering, consolidation, reaction and crystal growth by the spark plasma system (SPS). *Mater. Sci. Eng. A* **2000**, *287*, 183–188. [\[CrossRef\]](#)
- Okazaki, K. Electro-discharge consolidation applied to nanocrystalline and RSP/MA powders. *Mater. Sci. Eng. A* **2000**, *287*, 189–197. [\[CrossRef\]](#)
- Groza, J.R.; Zavaliangos, A. Sintering activation by external electrical field. *Mater. Sci. Eng. A* **2000**, *287*, 171–177. [\[CrossRef\]](#)
- Ye, J.; Ajdelsztajn, L.; Schoenung, J.M. Bulk nanocrystalline aluminum 5083 alloy fabricated by a novel technique: Cryomilling and spark plasma sintering. *Metall. Mater. Trans. A* **2006**, *37*, 2569–2579. [\[CrossRef\]](#)
- Yanagisawa, O.; Kuramoto, H.; Matsugi, K.; Komatsu, M. Observation of particle behavior in copper powder compact during pulsed electric discharge. *Mat. Sci. Eng. A* **2003**, *350*, 184–189. [\[CrossRef\]](#)
- Saunders, T.; Grasso, S.; Reece, M.J. Plasma formation during electric discharge (50 V) through conductive powder compacts. *J. Eur. Ceram. Soc.* **2015**, *35*, 871–877. [\[CrossRef\]](#)
- Hulbert, D.M.; Anders, A.; Andersson, J.; Lavernia, E.J.; Mukherjee, A.K. A discussion on the absence of plasma in spark plasma sintering. *Scripta Mater.* **2009**, *60*, 835–838. [\[CrossRef\]](#)
- Song, X.; Liu, X.; Zhang, J. Neck Formation and Self-Adjusting Mechanism of Neck Growth of Conducting Powders in Spark Plasma Sintering. *J. Am. Ceram. Soc.* **2006**, *89*, 494–500. [\[CrossRef\]](#)
- Xiong, Y.; Liu, D.; Li, Y.; Zheng, B.; Haines, C.; Paras, J.; Martin, D.; Kapoor, D.; Lavernia, E.J.; Schoenung, J.M. Spark plasma sintering of cryomilled nanocrystalline Al alloy—Part I: Microstructure evolution. *Metall. Mater. Trans. A* **2012**, *43*, 327–339. [\[CrossRef\]](#)
- Diouf, J.S.; Fedrizzi, A.; Molinari, A. A fractographic and microstructural analysis of the neck regions of coarse copper particles consolidated by SPS. *Powder Tech.* **2013**, *221*, 220–227. [\[CrossRef\]](#)
- Trapp, J.; Kieback, B. Temperature distribution in metallic powder particles during initial stage of field-activated sintering. *J. Am. Ceram. Soc.* **2015**, *98*, 3547–3552. [\[CrossRef\]](#)
- Collard, C.; Trzaska, Z.; Durand, L.; Chaix, J.M.; Monchoux, J.P. Theoretical and experimental investigations of local overheating at particle contacts in spark plasma sintering. *Powder Tech.* **2017**, *321*, 458–470. [\[CrossRef\]](#)
- Trzaska, Z.; Collard, C.; Durand, L.; Couret, A.; Chaix, J.M.; Fantozzi, G.; Monchoux, J.P. SPS microscopic mechanisms of metallic systems: Experiments and simulations. *J. Am. Ceram. Soc.* **2019**, *102*, 654–661.

17. Frei, J.M.; Anselmi-Tamburini, U.; Munir, Z.A. Current effects on neck growth in the sintering of copper spheres to copper plates by the pulsed electric current method. *J. Appl. Phys.* **2007**, *101*, 114914. [[CrossRef](#)]
18. Ji, G.; Grosdidier, T.; Bozzolo, N.; Launois, S. The mechanisms of microstructure formation in a nanostructured oxide dispersion strengthened FeAl alloy obtained by spark plasma sintering. *Intermetallics* **2007**, *15*, 108–118. [[CrossRef](#)]
19. Nowak, S.; Perrière, L.; Dembinski, L.; Tusseau-Nenez, S.; Champion, Y. Approach of the spark plasma sintering mechanism in Zr<sub>57</sub>Cu<sub>20</sub>Al<sub>10</sub>Ni<sub>8</sub>Ti<sub>5</sub> metallic glass. *J. Alloy. Compd.* **2011**, *509*, 1011–1019. [[CrossRef](#)]
20. Sprecher, A.F.; Mannan, S.L.; Conrad, H. On the mechanisms for the electroplastic effect in metals. *Acta Metall.* **1986**, *34*, 1145–1162. [[CrossRef](#)]
21. Conrad, H.; Sprecher, A.F.; Cao, W.D.; Lu, X.P. Electroplasticity—The effect of electricity on the mechanical properties of metals. *JOM* **1990**, *42*, 28–33. [[CrossRef](#)]
22. Guan, L.; Tang, G.; Chu, P.K. Recent advances and challenges in electroplastic manufacturing processing of metals. *J. Mater. Res.* **2010**, *25*, 1215–1224. [[CrossRef](#)]
23. Trzaska, Z.; Couret, A.; Monchoux, J.P. Spark plasma sintering mechanisms at the necks between TiAl powder particles. *Acta Mater.* **2016**, *118*, 100–108. [[CrossRef](#)]
24. Trzaska, Z.; Cours, R.; Monchoux, J.P. Densification of Ni and TiAl by SPS: Kinetics and microscopic mechanisms. *Metall. Mater. Trans. A* **2018**, *49*, 4849–4859. [[CrossRef](#)]
25. Minier, L.; Le Gallet, S.; Grin, Y.; Bernard, F. Influence of the current flow on the SPS sintering of a Ni powder. *J. Alloys. Compd.* **2010**, *508*, 412–418. [[CrossRef](#)]
26. Aleksandrova, E.V.; Ilyina, A.M.; Grigoryev, E.G.; Olevsky, E.A. Contribution of electric current into densification kinetics during spark plasma sintering of conductive powder. *J. Am. Ceram. Soc.* **2015**, *98*, 3509–3517. [[CrossRef](#)]
27. Collet, R.; Le Gallet, S.; Naimi, F.; Charlot, F.; Bonnefont, G.; Fantozzi, G.; Chaix, J.M.; Bernard, F. Effect of current on the sintering of pre-oxidized copper powders by SPS. *J. Alloy. Compd.* **2017**, *692*, 478–484.
28. Trzaska, Z.; Bonnefont, G.; Fantozzi, G.; Monchoux, J.P. Comparison of densification kinetics of a TiAl powder by spark plasma sintering and hot pressing. *Acta Mater.* **2017**, *135*, 1–13. [[CrossRef](#)]
29. Bewlay, B.P.; Nag, S.; Suzuki, A.; Weimer, M.J. TiAl alloys in commercial aircraft engines. *Mater. High Temp.* **2016**, *33*, 549–559. [[CrossRef](#)]
30. Couret, A.; Voisin, T.; Thomas, M.; Monchoux, J.P. Development of a TiAl alloy by spark plasma sintering. *JOM* **2017**, *69*, 2576–2582. [[CrossRef](#)]
31. Voisin, T.; Monchoux, J.P.; Perrut, M.; Couret, A. Obtaining of a fine near-lamellar microstructure in TiAl alloys by Spark Plasma Sintering. *Intermetallics* **2016**, *71*, 88–97. [[CrossRef](#)]
32. Voisin, T.; Monchoux, J.P.; Durand, L.; Karnatak, N.; Thomas, M.; Couret, A. An innovative way to produce-TiAl blades: Spark plasma sintering. *Adv. Eng. Mater.* **2015**, *17*, 1408–1413. [[CrossRef](#)]
33. Voisin, T.; Monchoux, J.P.; Thomas, M.; Deshayes, C.; Couret, A. Mechanical properties of the TiAl IRIS alloy. *Metall. Mater. Trans. A* **2016**, *47*, 6097–6108. [[CrossRef](#)]
34. Zhang, Z.; Wang, F.; Lee, S.; Liu, Y.; Cheng, J.; Liang, Y. Microstructure characteristic, mechanical properties and sintering mechanism of nanocrystalline copper obtained by SPS process. *Mat. Sci. Eng. A* **2009**, *523*, 134–138. [[CrossRef](#)]
35. Shearwood, C.; Fu, Y.; Yu, L.; Khor, K. Spark plasma sintering of TiNi nano-powder. *Scripta Mater.* **2005**, *52*, 455–460. [[CrossRef](#)]
36. Kellogg, F.; McWilliams, B.; Sietins, J.; Giri, A.; Cho, K. Comparison of SPS processing behavior between as atomized and cryomilled aluminum alloy 5083 powder. *Metall. Mater. Trans A* **2017**, *48*, 5492–5499. [[CrossRef](#)]
37. El-Atwania, O.; Quach, D.V.; Efe, M.; Cantwell, P.R.; Heim, B.; Schultz, B.; Stach, E.A.; Groza, J.R.; Allain, J.P. Multimodal grain size distribution and high hardness in fine grained tungsten fabricated by spark plasma sintering. *Mat. Sci. Eng. A* **2011**, *528*, 5670–5677. [[CrossRef](#)]
38. Dirras, G.; Bouvier, S.; Gubicza, J.; Hasni, B.; Szilagy, T. Mechanical characteristics under monotonic and cyclic simple shear of spark plasma sintered ultrafine-grained nickel. *Mat. Sci. Eng. A* **2009**, *526*, 201–210. [[CrossRef](#)]
39. Bui, Q.H.; Dirras, G.; Ramtani, S.; Gubicza, J. On the strengthening behavior of ultrafine-grained nickel processed from nanopowders. *Mat. Sci. Eng. A* **2010**, *527*, 3227–3235. [[CrossRef](#)]
40. Dutel, G.D.; Tingaud, D.; Langlois, P.; Dirras, G. Nickel with multimodal grain size distribution achieved by SPS: Microstructure and mechanical properties. *J. Mater. Sci.* **2012**, *47*, 7926–7931. [[CrossRef](#)]
41. Farbaniec, L.; Dirras, G.; Krawczynska, A.; Mompou, F.; Couque, H.; Naimi, F.; Bernard, F.; Tingaud, D. Powder metallurgy processing and deformation characteristics of bulk multimodal nickel. *Mater. Charac.* **2014**, *94*, 126–137. [[CrossRef](#)]
42. Tingaud, D.; Jenei, P.; Krawczynska, A.; Mompou, F.; Gubicza, J.; Dirras, G. Investigation of deformation micro-mechanisms in nickel consolidated from a bimodal powder by spark plasma sintering. *Mater. Charac.* **2015**, *99*, 118–127. [[CrossRef](#)]
43. Naimi, F.; Minier, L.; Le Gallet, S.; Couque, H.; Bernard, F. Dense nanostructured nickel produced by SPS from mechanically activated powders: Enhancement of mechanical properties. *J. Nanomater.* **2013**, *2013*, 674843. [[CrossRef](#)]
44. García de la Cruz, L.; Flipon, B.; Keller, C.; Martinez, M.; Hug, E. Nanostructuring of metals via spark plasma sintering using activated powder obtained by ball-milling: Impact on the strain-hardening mechanisms. *AIP Conf. Proc.* **2017**, *1896*, 200002.
45. García de la Cruz, L.; Martinez, M.; Keller, C.; Hug, E. Achieving good tensile properties in ultrafine grained nickel by spark plasma sintering. *Mat. Sci. Eng. A* **2020**, *772*, 138770. [[CrossRef](#)]

46. Vajpai, S.K.; Yu, H.; Ota, M.; Watanabe, I.; Dirras, G.; Ameyama, K. Three-dimensionally gradient and periodic harmonic structure for high performance advanced structural materials. *Mater. Trans.* **2016**, *57*, 1424–1432. [[CrossRef](#)]
47. Dirras, G.; Tingaud, D.; Ueda, D.; Hocini, A.; Ameyama, K. Dynamic Hall-Petch versus grain-size gradient effects on the mechanical behavior under simple shear loading of  $\beta$ -titanium Ti-25Nb-25Zr alloys. *Mater. Lett.* **2017**, *206*, 214–216. [[CrossRef](#)]
48. Dirras, G.; Ueda, D.; Hocini, A.; Tingaud, D.; Ameyama, K. Cyclic shear behavior of conventional and harmonic structure-designed Ti-25Nb-25Zr  $\beta$ -titanium alloy: Back-stress hardening and twinning inhibition. *Scripta Mater.* **2017**, *138*, 44–47. [[CrossRef](#)]
49. Ueda, D.; Dirras, G.; Hocini, A.; Tingaud, D.; Ameyama, K.; Langlois, P.; Vrel, D.; Trzaska, Z. Data on processing of Ti-25Nb-25Zr  $\beta$ -titanium alloys via powder metallurgy route: Methodology, microstructure and mechanical properties. *Data Brief* **2018**, *17*, 703–708. [[CrossRef](#)]
50. Charpentier, M. Hétérogénéités Héritées de la Solidification et Formation des Microstructures Dans L’alliage Ti48Al2Cr2Nb. Contribution au Développement des Alliages Intermétalliques de Base  $\gamma$ -TiAl. Ph.D. Thesis, Ecole des Mines, Nancy, France, 2003.
51. Miller, S.A.; Murphy, R.J. A gas-water atomization process for producing amorphous powders. *Scripta Metall.* **1979**, *13*, 673–676. [[CrossRef](#)]
52. Perrière, L.; Champion, Y.; Bernard, F. Spark plasma sintering of metallic glasses. In *Spark Plasma Sintering of Materials*; Cavaliere, P., Ed.; Springer: Cham, Switzerland, 2019; pp. 291–335.
53. Perrière, L.; Thai, M.T.; Tusseau-Nenez, S.; Blétry, M.; Champion, Y. Spark plasma sintering of a Zr-based metallic glass. *Adv. Eng. Mater.* **2011**, *13*, 581–586. [[CrossRef](#)]
54. Liu, Y.; Wang, J.S.; Fang, Q.H.; Liu, B.; Wu, Y.; Chen, S.Q. Preparation of superfine-grained high entropy alloy by spark plasma sintering gas atomized powder. *Intermetallics* **2016**, *68*, 16–22. [[CrossRef](#)]
55. Zhou, P.F.; Xiao, D.H.; Wu, Z.; Song, M. Microstructure and mechanical properties of AlCoCrFeNi high entropy alloys produced by spark plasma sintering. *Mater. Res. Express* **2019**, *6*, 0865e7. [[CrossRef](#)]
56. Fu, Z.; Chen, W.; Wen, H.; Zhang, D.; Chen, Z.; Zheng, B.; Zhou, Y.; Lavernia, E.J. Microstructure and strengthening mechanism in an fcc structured single-phase nanocrystalline Co<sub>25</sub>Ni<sub>25</sub>Fe<sub>25</sub>Al<sub>7.5</sub>Cu<sub>17.5</sub> high-entropy alloy. *Acta Mater.* **2016**, *107*, 59–71. [[CrossRef](#)]
57. Moravcik, I.; Cizek, J.; Zapletal, J.; Kovacova, Z.; Vesely, J.; Minarik, P.; Kitzmantel, M.; Neubauer, E.; Dlouhy, I. Microstructure and mechanical properties of Ni<sub>1.5</sub>Co<sub>1.5</sub>CrFeTi<sub>0.5</sub> high entropy alloy fabricated by mechanical alloying and spark plasma sintering. *Mater. Des.* **2017**, *119*, 141–150. [[CrossRef](#)]
58. Praveen, S.; Murty, B.S.; Kottada, R.S. Alloying behavior in multi-component AlCoCrCuFe and NiCoCrCuFe high entropy alloys. *Mater. Sci. Eng. A* **2012**, *534*, 83–89. [[CrossRef](#)]
59. Chen, Z.; Chen, W.; Wu, B.; Cao, X.; Liu, L.; Fu, Z. Effects of Co and Ti on microstructure and mechanical behaviour of Al<sub>0.75</sub>FeNiCrCo high entropy alloy prepared by mechanical alloying and spark plasma sintering. *Mater. Sci. Eng. A* **2015**, *648*, 217–224. [[CrossRef](#)]
60. Wang, P.; Cai, H.; Cheng, X. Effect of Ni/Cr ratio on phase, microstructure and mechanical properties of Ni<sub>x</sub>CoCuFeCr<sub>2-x</sub> (x = 1.0, 1.2, 1.5, 1.8 mol) high entropy alloys. *J. Alloy. Compd.* **2016**, *662*, 20–31. [[CrossRef](#)]
61. Zhang, A.; Han, J.; Su, B.; Meng, J. A novel CoCrFeNi high entropy alloy matrix selflubricating composite. *J. Alloy. Compd.* **2017**, *725*, 700–710. [[CrossRef](#)]
62. Suryanarayana, C. Mechanical alloying and milling. *Prog. Mater. Sci.* **2001**, *46*, 1–184. [[CrossRef](#)]
63. Jabbar, H.; Couret, A.; Durand, L.; Monchoux, J.P. Identification of microstructural mechanisms during densification of a TiAl alloy by spark plasma sintering. *J. Alloy. Compd.* **2011**, *509*, 9826–9835. [[CrossRef](#)]
64. Yucheng, W.; Zhengyi, F. Study of temperature field in spark plasma sintering. *Mater. Sci. Eng. B* **2002**, *90*, 34–37. [[CrossRef](#)]
65. Matsugi, K.; Kuramoto, H.; Hatayama, T.; Yanagisawa, O. Temperature distribution at steady state under constant current discharge in spark sintering process of Ti and Al<sub>2</sub>O<sub>3</sub> powders. *J. Mater. Process. Tech.* **2004**, *146*, 274–281. [[CrossRef](#)]
66. Zavaliangos, A.; Zhang, J.; Krammer, M.; Groza, J.R. Temperature evolution during field activated sintering. *Mater. Sci. Eng. A* **2004**, *379*, 218–228. [[CrossRef](#)]
67. Vanmeensel, K.; Laptov, A.; Hennicke, J.; Vleugels, J.; Van der Biest, O. Modelling of the temperature distribution during field assisted sintering. *Acta Mater.* **2005**, *53*, 4379–4388. [[CrossRef](#)]
68. Wang, X.; Casolco, S.R.; Xu, G.; Garay, J.E. Finite element modeling of electric current activated sintering: The effect of coupled electrical potential, temperature and stress. *Acta Mater.* **2007**, *55*, 3611–3622. [[CrossRef](#)]
69. McWilliams, B.; Zavaliangos, A. Multi-phenomena simulation of electric field assisted sintering. *J. Mater. Sci.* **2008**, *43*, 5031–5035. [[CrossRef](#)]
70. Molénat, G.; Durand, L.; Galy, J.; Couret, A. Temperature control in spark plasma sintering: An FEM approach. *J. Metallurgy* **2010**, 145431. [[CrossRef](#)]
71. Muñoz, S.; Anselmi-Tamburini, U. Temperature and stress fields evolution during spark plasma sintering processes. *J. Mater. Sci.* **2010**, *45*, 6528–6539. [[CrossRef](#)]
72. Song, Y.; Li, Y.; Zhou, Z.; Lai, Y.; Ye, Y. A multi-field, coupled FEM model for one-step forming process of spark plasma sintering considering local densification of powder material. *J. Mater. Sci.* **2011**, *46*, 5645–5656. [[CrossRef](#)]
73. Mondalek, P.; Silva, L.; Bellet, M. A numerical model for powder densification by SPS technique. *Adv. Eng. Mater.* **2011**, *13*, 587–593. [[CrossRef](#)]

74. Voisin, T.; Durand, L.; Karnatak, N.; Le Gallet, S.; Thomas, M.; Le Berre, Y.; Castagné, J.F.; Couret, A. Temperature control during Spark Plasma Sintering and application to up-scaling and complex shaping. *J. Mater. Proc. Tech.* **2013**, *213*, 269–278. [[CrossRef](#)]
75. Wolff, C.; Mercier, S.; Couque, H.; Molinari, A. Modeling of conventional hot compaction and spark plasma sintering based on modified micromechanical models of porous materials. *Mech. Mater.* **2012**, *49*, 72–91. [[CrossRef](#)]
76. Pavia, A.; Durand, L.; Ajustron, F.; Bley, V.; Chevallier, G.; Peigney, A.; Estournès, C. Electro-thermal measurements and finite element method simulations of a spark plasma sintering device. *J. Mater. Process. Tech.* **2013**, *213*, 1327–1336. [[CrossRef](#)]
77. Wolff, C.; Mercier, S.; Couque, H.; Molinari, A.; Bernard, F.; Naimi, F. Thermal-electrical-mechanical simulation of the nickel densification by Spark Plasma Sintering. Comparison with experiments. *Mech. Mater.* **2016**, *100*, 126–147. [[CrossRef](#)]
78. Achenani, Y.; Saâdaoui, M.; Cheddadi, A.; Bonnefont, G.; Fantozzi, G. Finite element modeling of spark plasma sintering: Application to the reduction of temperature inhomogeneities, case of alumina. *Mater. Des.* **2017**, *116*, 504–514. [[CrossRef](#)]
79. Manière, C.; Pavia, A.; Durand, L.; Chevallier, G.; Afanga, K.; Estournès, C. Finite-element modeling of the electro-thermal contacts in the spark plasma sintering process. *J. Eur. Ceram. Soc.* **2016**, *36*, 741–748. [[CrossRef](#)]
80. Anselmi-Tamburini, U.; Gennari, S.; Garay, J.E.; Munir, Z.A. Fundamental investigations on the spark plasma sintering/synthesis process: II. Modeling of current and temperature distributions. *Mater. Sci. Eng. A* **2005**, *394*, 139–148. [[CrossRef](#)]
81. Arzt, E.; Ashby, M.F.; Easterling, K.E. Practical applications of hot-isostatic pressing dia-grams: Four case studies. *Metall. Trans. A* **1983**, *14*, 211–221. [[CrossRef](#)]
82. Helle, A.S.; Easterling, K.E.; Ashby, M.F. Hot-isostatic pressing diagrams: New develop-ments. *Acta Metall.* **1985**, *33*, 2163–2174. [[CrossRef](#)]
83. Abouaf, M. Modélisation de la Compaction de Poudres Métalliques Frittées—Approche par la Mécanique des Milieux Continus. Ph.D. Thesis, Institut National Polytechnique, Grenoble, France, 1985.
84. Olevsky, E.A. Theory of sintering: From discrete to continuum. *Mat. Sci. Eng. R* **1998**, *23*, 41–100. [[CrossRef](#)]
85. Martins, D.; Grumbach, F.; Manière, C.; Sallot, P.; Mocellin, K.; Bellet, M.; Estournès, C. In-situ creep law determination for modeling spark plasma sintering of TiAl 48-2-2 powder. *Intermetallics* **2017**, *86*, 147–155. [[CrossRef](#)]
86. Wei, X.; Back, C.; Izhevyanov, O.; Khasanov, O.L.; Haines, C.D.; Olevsky, E.A. Spark plasma sintering of commercial zirconium carbide powders: Densification behavior and mechanical properties. *Materials* **2015**, *8*, 6043–6061. [[CrossRef](#)]
87. Manière, C.; Durand, L.; Chevallier, G.; Estournès, C. A spark plasma sintering densification modeling approach: From polymer, metals to ceramics. *J. Mater. Sci.* **2018**, *53*, 7869–7876. [[CrossRef](#)]
88. Manière, C.; Kus, U.; Durand, L.; Mainguy, R.; Huez, J.; Delagnes, D.; Estournès, C. Identification of the Norton-Green compaction model for the prediction of the Ti-6Al-4V densification during the spark plasma sintering process. *Adv. Eng. Mater.* **2016**, *18*, 1720–1727. [[CrossRef](#)]
89. Sun, J.; He, Y.H.; Wu, J.S. Characterization of low-temperature superplasticity in a thermomechanically processed TiAl based alloy. *Mat. Sci. Eng. A* **2002**, *329–331*, 885–890. [[CrossRef](#)]
90. Sun, J.; Wu, J.S.; He, Y.H. Superplastic properties of a TiAl based alloy with a duplex microstructure. *Mater. Sci.* **2000**, *35*, 4919–4922. [[CrossRef](#)]
91. Cheng, S.C.; Wolfenstine, J.; Sherby, O.D. Superplastic behavior of 2-phase titanium aluminides. *Metall. Trans. A* **1992**, *23*, 1509–1513. [[CrossRef](#)]
92. Nieh, T.G.; Hsiung, L.M.; Wadsworth, J. Superplastic behavior of a powder metallurgy TiAl alloy with a metastable microstructure. *Intermetallics* **1999**, *7*, 163–170. [[CrossRef](#)]
93. Tokita, M. The potential of spark plasma sintering (SPS) method for the fabrication on an industrial scale of functionally graded materials. *Adv. Sci. Tech.* **2010**, *63*, 322–331. [[CrossRef](#)]
94. Sweet, G.A.; Brochu, M.; Hexemer, R.L.; Donaldson, I.W.; Bishop, D.P. Microstructure and mechanical properties of air atomized aluminum powder consolidated via spark plasma sintering. *Mater. Sci. Eng. A* **2014**, *608*, 273–282. [[CrossRef](#)]
95. Lagos, M.A.; Agote, V.; Atxaga, G.; Adarraga, O.; Pambaguian, L. Fabrication and characterisation of Titanium Matrix Composites obtained using a combination of Self propagating High temperature Synthesis and Spark Plasma Sintering. *Mater. Sci. Eng. A* **2016**, *655*, 44–49. [[CrossRef](#)]
96. Naanani, S.; Hantcherli, M.; Hor, A.; Mabru, C.; Monchoux, J.P.; Couret, A. Study of the low cyclic behaviour of the IRIS alloy at high temperature. *MATEC Web Conf.* **2018**, *165*, 06007. [[CrossRef](#)]
97. Manière, C.; Nigito, E.; Durand, L.; Weibel, A.; Beynet, Y.; Estournès, C. Spark plasma sintering and complex shapes: The deformed interfaces approach. *Powder Tech.* **2017**, *320*, 340–345. [[CrossRef](#)]
98. Voisin, T.; Monchoux, J.P.; Couret, A. Near-net shaping of titanium-aluminum jet engine turbine blades by SPS. In *Spark Plasma Sintering of Materials*; Cavaliere, P., Ed.; Springer: Cham, Switzerland, 2019; pp. 713–737.

Article

# SHS Synthesis, SPS Densification and Mechanical Properties of Nanometric Tungsten

Sarah Dine <sup>1</sup>, Elodie Bernard <sup>2</sup>, Nathalie Herlin <sup>3</sup>, Christian Grisolia <sup>2</sup>, David Tingaud <sup>1</sup> and Dominique Vrel <sup>1,\*</sup>

<sup>1</sup> Laboratoire des Sciences des Procédés et des Matériaux (LSPM), Université Sorbonne Paris Nord, UPR 3407 CNRS, 93430 Villetaneuse, France; sarah.dine@lspm.cnrs.fr (S.D.); david.tingaud@lspm.cnrs.fr (D.T.)

<sup>2</sup> CEA, Institut de Recherche sur la Fusion par Confinement Magnétique (IRFM), 13108 Saint Paul lez Durance, France; Elodie.BERNARD@cea.fr (E.B.); Christian.GRISOLIA@cea.fr (C.G.)

<sup>3</sup> CEA, Institut Rayonnement Matière de Saclay (IRAMIS) UMR Nanosciences et Innovation pour les Matériaux, la Biomédecine et l'Énergie (NIMBE), Université Paris Saclay, 91191 Gif-sur-Yvette, France; nathalie.herlin@cea.fr

\* Correspondence: dominique.vrel@lspm.cnrs.fr; Tel.: +33-1-4940-3411

**Abstract:** Recent studies have shown that low grain sizes are favorable to improve ductility and machinability in tungsten, as well as a resistance to ablation and spallation, which are key properties for the use of this material in a thermonuclear fusion environment (Tokamaks such as ITER). However, as one of the possible incidents during Tokamak operation is the leakage of air or water from the cooling system inside the chamber, resulting in the so-called loss of vacuum accident (LOVA), extensive oxidation may arise on tungsten components, and the use of an alloy with improved oxidation resistance is therefore highly desirable. As current production routes are not suitable for the fabrication of bulk nanostructured tungsten or tungsten alloys samples, we have proposed a new methodology based on powder metallurgy, including the powder synthesis, the densification procedure, and preliminary mechanical testing, which was successfully applied to pure tungsten. A similar study is hereby presented on tungsten-chromium alloys with up to 6 wt.% Cr. Results show that full tungsten densification may be obtained by SPS at a temperature lower than 1600 °C. The resulting morphology strongly depends on the amount of the alloying element, presenting a possible second phase of chromium oxide, but always keeps a partial nanostructure inherited from the synthesized powders. Such microstructure had previously been identified as being favorable to the use of these materials in fusion environments and for improved mechanical properties, including hardness, yield strength and ductility, all of which is confirmed by the present study.

**Keywords:** tungsten alloys; ductility; nanostructure; mechanical properties

**Citation:** Dine, S.; Bernard, E.; Herlin, N.; Grisolia, C.; Tingaud, D.; Vrel, D. SHS Synthesis, SPS Densification and Mechanical Properties of Nanometric Tungsten. *Metals* **2021**, *11*, 252. <https://doi.org/10.3390/met11020252>

Academic Editor: Javier S. Blázquez Gámez  
Received: 2 December 2020  
Accepted: 30 January 2021  
Published: 2 February 2021

**Publisher's Note:** MDPI stays neutral with regard to jurisdictional claims in published maps and institutional affiliations.



**Copyright:** © 2021 by the authors. Licensee MDPI, Basel, Switzerland. This article is an open access article distributed under the terms and conditions of the Creative Commons Attribution (CC BY) license (<https://creativecommons.org/licenses/by/4.0/>).

## 1. Introduction

Tungsten has been chosen as one of the principal candidates for plasma-facing components (PFC) in the construction of thermonuclear fusion tokamaks [1–6]. Indeed, among all the pure elements, it has the highest melting point while presenting a good thermal conductivity, which makes it interesting for any high-temperature application. Moreover, considering the specific conditions in tokamaks, it also presents a low activation under neutronic irradiation and low plasma sputtering. However, tungsten presents a strong drawback at room temperature for any structural application, as it is usually brittle. As a function of the preparation method used, and specifically of the presence of some impurities which may coalesce at grain boundaries [7], tungsten usually exhibit a ductile-to-brittle-transition-temperature (DBTT) within the 200–400 °C range. Indeed, due to this brittleness, cracking may pre-exist before operation due to machining, but more important, thermal cycling of PFC may also favor their formation and thus drastically reduce their life span [8,9].

In order to induce and improve ductility in tungsten, different pathways are currently being considered [6]. While in metallurgy, the use of alloying elements is usually

the first solution investigated to improve one specific property in metal, this problem is hard to circumvent for tungsten ductility, as only rhenium (Re) has such a capacity [10]. This costly element is unfortunately inadequate for the construction of large-scale pieces such as in ITER plasma-facing components, and especially because in the specific operational conditions of thermonuclear fusion, with high neutron bombardment, rhenium is transmuted into long half-life radioactive osmium, inducing waste management and safety issues [11,12]. For similar reasons, the use of niobium and molybdenum should be avoided [13]. Neutron-induced embrittlement, reducing thermal conductivity, is also a strong drawback for which these elements should not be considered.

With these considerations in mind, the list of acceptable alloying elements in tungsten is reduced to only a few, including Ta, V, Cr, Ti, Si [14–19]. Among these possible alloying elements, Cr should be specifically mentioned for its possible contribution to the improvement of tungsten oxidation resistance [20–23]. It is indeed well-known that chromium has a natural tendency to form a thin protective oxide layer that passivates the material, which is the basic principle of its use in stainless steel.

However, tungsten wires in old-fashioned light bulbs are ductile enough to be shaped as small spirals, and this is due to the fine microstructure of the material resulting from the extrusion process used to produce these wires. Unfortunately, due to the high-temperature reached during the light bulb operation, recrystallization occurs, and this ductility is lost. To avoid or limit this phenomenon, some studies have investigated the addition of dispersed phases, such as  $\text{La}_2\text{O}_3$ ,  $\text{Y}_2\text{O}_3$ ,  $\text{CeO}_2$  [6,24,25], TiC [26,27], ZrC [28] or HfC [11]. As these phases are insoluble in W, they precipitate at the grain boundaries and thus limit grain growth. As a result, the overall tungsten ductility after thermal cycling is improved, and the machinability may be preserved. Although these oxides and carbides are thermodynamically stable, their use in plasma-facing components that will be subjected to erosion should be considered cautiously. Indeed, the potential release of oxygen or carbon in the hydrogen plasma would result in detrimental pollution, with the possible formation of water or hydrocarbons. In addition, some of the metals in these compounds may form metal hydrides, resulting in large tritium retention.

For larger samples, obtaining these fine microstructures is more complex and may require processes such as equal channel angular pressing [29,30], cold rolling [31–33], surface attrition [34], or even high-pressure torsion [35]. Due to the high forces required in these processes, and the high elastic limit of tungsten, they are unfortunately not appropriate in order to obtain nanostructured plasma-facing components as large as the design of the ITER tokamak requires. Using these fine microstructures, recent investigations have shown that the DBTT can be reduced to a value as low as 77 K [31].

The use of chromium as a possible alloying element in tungsten, studied here mainly as a possible solution to increase tungsten oxidation resistance, has been previously investigated by other authors. It has been reported that the synthesis of dense W-Cr alloys is difficult due to low interdiffusion coefficients in this system [36] and that the use of a third element such as Pd would be necessary to improve interdiffusion [36–38]. However, the presence of palladium dissolves rather large amounts of tungsten and chromium, making the whole system more complex [39]. Moreover, the existence of a relatively low Cr-Pd eutectic may have a detrimental effect on the high-temperature properties of the resulting material [38,40], especially because this phase has been shown to form at grain boundaries [41]. Nanometric W-Cr alloys were also synthesized using high-energy milling from micrometric powders [22,42]. This technique, however, needing long milling times, implies a high level of energy consumption and leads inevitably to the contamination of the powders from the milling media.

## 2. Materials and Methods

In our previous works on pure W [43] and MoNbW alloys [44,45], we developed a new methodology to synthesize refractory metals nanopowders using self-propagating high-temperature synthesis (SHS). To preserve the nanostructure after densification, these

powders were sintered by spark plasma sintering (SPS) [46], which allows a full or nearly full densification in short times. A similar study is conducted here on W-Cr alloys, with up to 6 wt.% Cr. Samples will be characterized using XRD (Equinox 1000 diffractometer, Cu  $\kappa\alpha_1$  radiation, INEL, Artenay, France), SEM observations for the powders and the densified samples (ZEISS FEG-SEM Supra 40VP, Oberkochen, Germany), and these characterizations will also include electron backscattered diffraction (EBSD), and mechanical testing will be performed (hardness and compressive tests, DURAMIN 20 apparatus, STRUERS, Ballerup, Denmark) for the latter.

### 2.1. Nanopowders Synthesis

The powders were synthesized using the self-propagating high-temperature synthesis process, using the reduction of metal oxides by magnesium in thermite-like reactions, according to the protocol described in [43–45].  $\text{WO}_3$  (Alfa Aesar (Thermo Fisher GmbH, Kandel, Germany), 99.8%, ref. 11828 batch Q12F015),  $\text{Cr}_2\text{O}_3$  (Alfa Aesar, 99.8%, ref. 12285 batch D26Z027), Mg (Sigma-Aldrich (Merck KGaA, Darmstadt, Germany), 97.9%, ref. 8.18506.500 batch S7714006-901) and NaCl (VWR (Avantor, Radnor, PA, USA), 100%, ref. 27800.360 batch 17C144128), acting, respectively as an oxidizer, reducer, and moderator were first carefully weighted in order to retrieve a 20 g final mass of alloy with 2, 4 or 6 wt.% of Cr (respectively mentioned to hereunder as WCr2, WCr4 and WCr6, Table 1), then thoroughly mixed in the powder form using a 3D Turbula mixer (WAB, Muttentz, Switzerland) for 24 h, and placed in a sealed reactor, surrounded by NaCl, before the following thermite reaction was started by Joule-heating a tungsten wire placed at the bottom of the sample:



SEM micrographs of the reactants are presented in Figure 1. In order to make sure that the reaction is complete, 50% excess Mg was added from the stoichiometric proportions. As for NaCl, its introduction provides an increase of the global heat capacity of the mixture, and its amount was calculated to decrease the overall product's final temperature to 1800 °C. However, as the placement of a thermocouple proved to be difficult considering the temperatures reached, and as pyrometric measurements were not an option in our pressure sealed reactor, no temperature measurements were performed. The value of 1800 °C should therefore be considered as an estimate, allowing us to synthesize all our different samples in similar conditions. On the other hand, the introduction of NaCl in the SHS reaction is known to favor nanometric grain sizes in the resulting powders [43–45]. As magnesium has a low boiling point, these reactions were performed under confinement, for most of the gaseous magnesium to stay available for the reaction. For reference, the WCr2 experiment was also performed without confinement.

**Table 1.** Weighing of the reactants for the synthesis of 20 g of the different alloys. WCr2, WCr4 and WCr6 stand for 2, 4 and 6 weight percent chromium in the resulting tungsten alloy.

| Alloy | Cr wt.% | Cr at.% | $\text{WO}_3$ (g) | $\text{Cr}_2\text{O}_3$ (g) | Mg (g) | NaCl (g) |
|-------|---------|---------|-------------------|-----------------------------|--------|----------|
| WCr2  | 2       | 6.73    | 24.717            | 0.585                       | 12.082 | 16.13    |
| WCr4  | 4       | 12.84   | 24.213            | 1.169                       | 12.264 | 15.76    |
| WCr6  | 6       | 18.41   | 23.708            | 1.754                       | 12.447 | 15.39    |

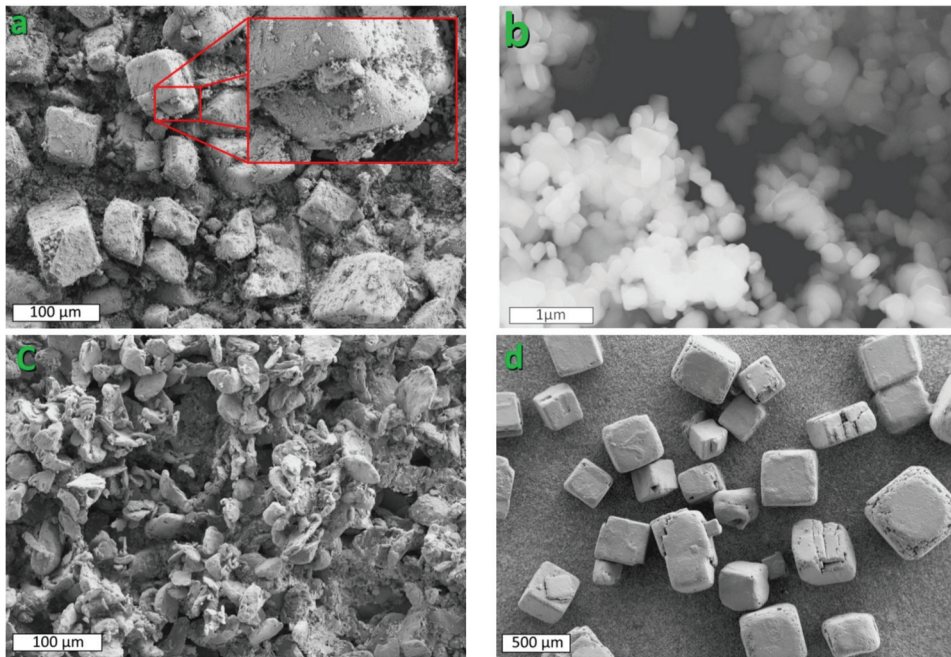


**Figure 1.** SEM observations of the reactants: (a)  $\text{WO}_3$ ; (b)  $\text{Cr}_2\text{O}_3$ ; (c) Mg; (d) NaCl. Note that tungsten trioxide particles seem to be made of large grains covered with submicronic particles (insert).

As the reaction scheme yields to the presence of MgO, residual Mg, and NaCl in the final powder mixture, these were lixiviated using 2 N hydrochloric acid for 2 h under stirring at 80 °C. The powders were then retrieved using a 0.22  $\mu\text{m}$  polyethersulfone membrane filtration (MB Express Millipore®, MERCK, Darmstadt, Germany). To ensure complete dissolution of the contaminants, this procedure was performed twice, and the retrieved powders were then rinsed before a last filtration, and finally dried in an autoclave at 50 °C for 24 h. A similar reaction was previously investigated to synthesize stoichiometric W-Cr alloys [47] using aluminum as a reducer and without a reaction moderator. However, in this case, the separation between molten alumina and the molten alloy is performed using a high gravity field, inducing a composition gradient within the alloy.

After these steps are completed, the crystal structure of the obtained powders was analyzed using X-ray diffraction. This characterization was then followed by Rietveld refinement using the Materials analysis using diffraction (MAUD) software to determine the lattice parameters of the different alloys.

## 2.2. SPS Densification

Spark plasma sintering (SPS) was performed in the “plateforme IdF de frittage flash” (Thiais, France), on a Syntec 515 S machine (Fuji Electronic Industrial Co., Ltd., Saitama, Japan). ~5 g of the as-synthesized powders were inserted in graphite mold with a 10 mm diameter. The temperature is followed with an infrared pyrometer pointing to a hole allowing temperature measurement in the direct vicinity of the sample; consequently, temperature measurements were not possible under 600 °C. Pressure and piston movement measurements were also recorded, providing all the necessary information to analyze the different steps of the sintering.

Densification experiments were performed at 1600, 1800 and 2000 °C with a plateau time of 1 to 15 min. Most cycles were made of a single ramp with a heating rate of 50 °C·min<sup>-1</sup>. However, to minimize the risk of a possible overshoot, the temperature

ramp is set to  $20\text{ }^{\circ}\text{C}\cdot\text{min}^{-1}$  when the temperature is less than  $50\text{ }^{\circ}\text{C}$  under the maximum temperature. Some more complex temperature cycles were also tested, but with no significant differences in the final density and will not be presented. The compaction pressure is always 100 MPa, set at the beginning of the heating cycle, a pre-compaction at 42 MPa being set before. This pressure is released during the quenching of the sample.

### 2.3. Densified Samples

Densified samples were polished with  $68\text{ }\mu\text{m}$ ,  $9\text{ }\mu\text{m}$  and  $3\text{ }\mu\text{m}$  cloths (P220—Struers MD-Piano 220; P2400—Struers MD-Allegro; and P4000—Struers MD-Dac, respectively, STRUERS, Ballerup, Denmark), with an OPS finishing (colloidal silica,  $40\text{ nm}$ —Struers MD-Chem). Densities have then been measured using Archimedes' method in orthoxylene.

Bulk samples were analyzed using X-ray diffraction then by Rietveld refinement. SEM observations were conducted, together with EDX local analysis and mapping. Grain sizes, preferential orientations and nature of grain boundaries were analyzed using electron backscattered diffraction (EBSD).

As for mechanical properties, Vickers hardness was measured on the plane perpendicular to the densification pressing direction using a  $1.96\text{ N}$  force applied for 10 s. In order to increase the statistical precision of the measure, this measure was repeated 10 times on each sample. Due to the small sizes of the samples ( $10\text{ mm}$  diameter and  $3\text{--}4\text{ mm}$  in thickness), we were unable to cut tensile test specimens. Instead, compression tests were performed on parallelepiped samples cut by electro-erosion, with dimensions  $2.4 \times 2.4 \times 5.0\text{ mm}^3$ , by pressing along the main axis of the sample.

## 3. Results and Discussion

### 3.1. Nanopowders Synthesis

SEM observations, Figure 2, reveal mostly rounded particle shapes, with a large polydispersity, typically ranging from 10 to 200 nm. However, in some areas, particles seem bounded together as if local melting had occurred during the reaction, whatever the composition. This morphology is significantly different from what had been obtained with pure W [46], where particle shapes were mostly in the form of platelets. Moreover, we can observe that, while keeping a wide size distribution, the average particle size seems to decrease when the amount of Cr is increased.

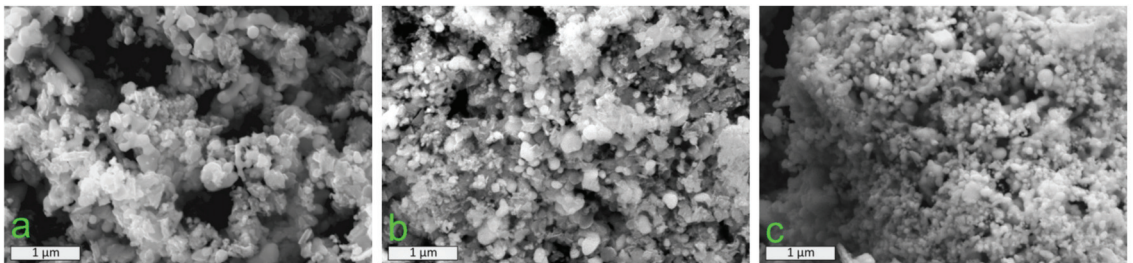


**Figure 2.** SEM micrographs of the submicrometric powders synthesized by SHS ( $\times 20,000$ ). (a) W-2 wt.% Cr (WCr2), (b) W-4 wt.% Cr (WCr4), and (c) W-6 wt.% Cr (WCr6).

X-ray diffraction patterns of the resulting powders are presented in Figure 3, and the results of the Rietveld analysis performed on these diffraction patterns are summarized in Table 2. In these patterns, the five main peaks come from the diffraction of tungsten, revealing the  $\alpha$ , Body Centered Cubic (BCC) crystal structure, as expected. However, specifically, when the reaction chamber is not sealed, some additional peaks are also observed and are the signature of the presence of  $\text{WO}_3$  and  $\text{WO}_2$ , which remain despite the excess Mg used. These residual tungsten oxide peaks are significant for the WCr2 sample synthesized without confinement and much less, but still clearly visible when

confinement was used. Indeed, the reaction temperature is  $\sim 700$  °C above the boiling point of magnesium, and, despite using a sealed reactor, this magnesium might escape away from the reaction zone and condense on the salt surrounding the sample, yielding an incompletely converted reaction product. However, we have shown that when increasing the size of the sample, the amount of oxidized tungsten present in the final powder decreases [45]. Nevertheless, it seems that the total amount of residual oxide phases decreases when the Cr amount is increased. Although the presence of chromium inside the alloy was intended to increase its oxidation resistance, it is unlikely that the residual oxides observed on WCr2 and WCr4 result from oxidation of the nanopowders; indeed, although this oxidation most likely takes place during air exposure, it should produce amorphous oxides, which would be undetected by XRD. We rather suspect that the presence of Cr<sub>2</sub>O<sub>3</sub> together with WO<sub>3</sub> modifies the reaction kinetics and improves its final yield. Finally, there is a distinct shift of the diffraction peaks when the Cr amount is increased, which could be attributed to a greater amount of Cr within the W lattice, as the Cr lattice is smaller than the one for W. Moreover, an imperfect mixing of the two elements is suspected for WCr4 and WCr6, as distinct shoulders are visible to the right of the peaks (Figure 3b).

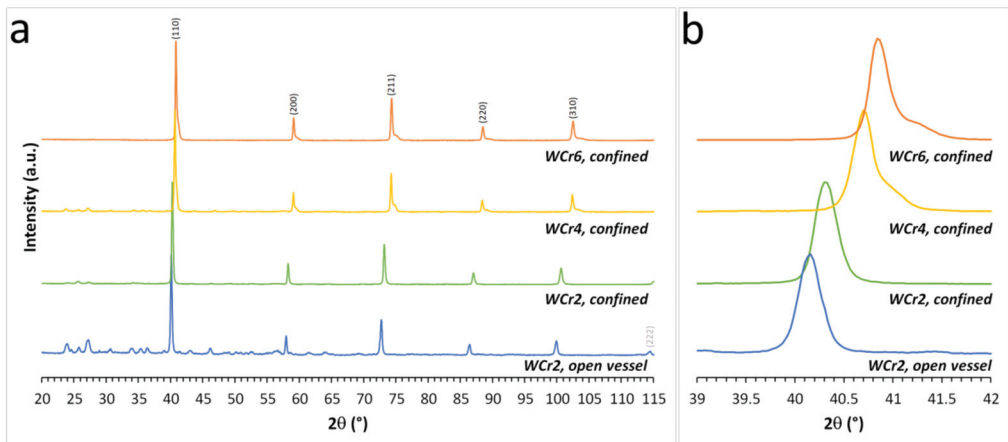


**Figure 3.** (a) X-ray diffraction pattern of the powders after synthesis, lixiviation, rinsing and drying. Miller indices represented correspond to the expected tungsten BCC crystal structure. The other peaks observed on the XRD patterns are attributed to tungsten oxides WO<sub>3</sub> and WO<sub>2</sub>. (b) Magnification of the (110) peak.

**Table 2.** Rietveld refinement of powders XRD patterns. Results shown correspond to the main BCC phase only.

| Alloy             | Lattice Parameter (nm) |
|-------------------|------------------------|
| WCr2, open vessel | 0.31814                |
| WCr2, confined    | 0.31642                |
| WCr4, confined    | 0.31241                |
| WCr6, confined    | 0.31220                |

### 3.2. SPS Densification

For the sake of clarity, as no significant differences are observed between the different cycles, we will present here the results concerning the 3 different alloys compacted at 1800 °C, Figure 4. As the mass and thicknesses of the three samples are different, the curves representing the kinetics of densification  $dz/dt$  are normalized, so their integrals are equal to 1.

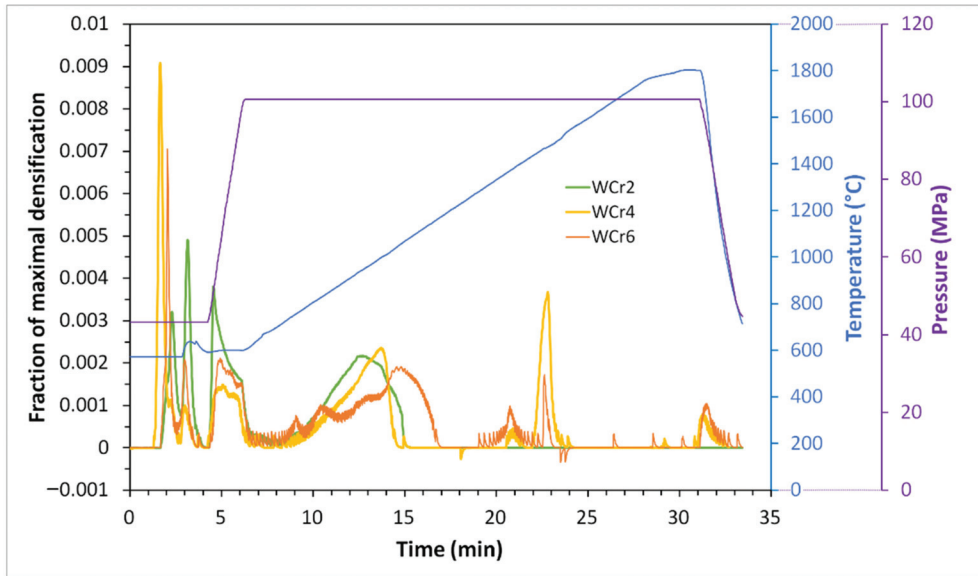


**Figure 4.** Spark plasma sintering (SPS) cycle (1800 °C—1'). Purple: pressure; blue: temperature; and green, yellow and orange: kinetics of densification as a fraction of total densification (integral of each curve is equal to 1).

A first densification peak is observed at low-temperature, below the lower pyrometer limit at 600 °C, and is due to outgassing, possibly of residual water if the drying step was incomplete. From 4 to 6.5 min, while the temperature is constant just above the detection limit of the pyrometer, the pressure on the sample is increased, and a second densification peak is observed on all three samples. After this first step, densification stops temporarily and then resumes progressively as the temperature is increased, with maximal densification kinetic at 12.4, 13.6 and 14.8 min for WCr2, WCr4 and WCr6, respectively (with corresponding temperatures of 930, 995 and 1055 °C, respectively). These low temperatures thus show the influence of the nanometric grain sizes on the sintering of tungsten. It is worth mentioning that despite chromium has a lower melting temperature, and despite the fact that powders particle sizes decrease with the increasing amount of chromium, the sintering nevertheless arises with increasing temperatures. A third, abrupt peak is observed when the temperature is in the 1465–1475 °C range. As this temperature corresponds to the tungsten trioxide melting temperature (1473 °C), we believe that a liquid phase is then present, and densification may proceed almost freely. No significant evolution in the density can be observed when the temperature is further increased to 1800 °C, nor during the 5 min plateau. Although the WCr2 yielded an incomplete reading of the densification process (saturation of the detector after 15'), it should be noted that the intensity of the shrinkage of the sample decreases when the Cr amount increases at that temperature. Indeed, the WCr6 powders had fewer residual oxides (no crystallized oxides detectable on the XRD pattern, Figure 2) and most certainly less amorphous oxides at the surface of the nanopowders after air exposure due to the Cr-induced passivation of the powders. Finally, at the end of the cycle, the temperature is abruptly decreased, yielding a shrinking of the sample due to natural thermal expansion, and an apparent densification step is observed.

A temperature of 1600 °C seems therefore sufficient to fully densify the W nanopowders produced. However, due to the melting of the oxides at or around 1473 °C, and their subsequent flowing outside of the sample, a small mass loss was observed. It is, however,

considerably smaller than what had been observed when pure tungsten samples were sintered [46].

### 3.3. Densified Samples

Measured densities using Archimedes' method were greater than 90% of the theoretical density for all samples and up to 99.91% (Table 3). Comparatively to previously published results, these densities extremely promising: Yao et al. [48] studied the densification of commercial 50 nm tungsten nanometer at a similar temperature, only limiting the pressure to 50 MPa, for a final relative density of 97.8%, and, to obtain a density of 99%, similar to the results presented here, the use of resistance sintering under ultra high-pressure (RSUHP) at 9 GPa was necessary. Comparatively, the densification of micrometric commercial tungsten powder (2  $\mu\text{m}$ ) using SPS could only provide a density of 84.3% (50 MPa, 1600  $^{\circ}\text{C}$ ) [18], and 92.16% using hot pressing (1800  $^{\circ}\text{C}$ , 2 h, 20 MPa) [49]. The specific granulometry and its polydispersity, the specific shape of the initial powder grains seem, therefore, very favorable to the densification.

**Table 3.** Relative density, Vickers hardness and Rietveld refinement results on SPS-densified samples. In bulk are the samples described more specifically in the text.

| Alloy | Sintering Temperature ( $^{\circ}\text{C}$ ) | Plateau Duration (min) | Relative Density (%) | Vickers Hardness | Lattice Parameter (nm) | Crystallite Size (nm) |
|-------|--|------------------------|----------------------|------------------|------------------------|-----------------------|
| WCr2  | 1600   | 1                      | 90.86                | 335.7            | 0.31645                | 75.9                  |
| WCr2  | 1800   | 1                      | 98.10                | 314.8            | 0.31672                | 68.4                  |
| WCr4  | 1800   | 1                      | 99.91                | 349.7            | 0.31682                | 68.5                  |
| WCr4  | 1800   | 5                      | 99.78                | 244.1            | 0.31669                | 78.0                  |
| WCr4  | 2000   | 15                     | 98.85                | 264.5            | 0.31666                | 78.3                  |
| WCr6  | 1800   | 1                      | 99.12                | 420.6            | 0.31676                | 79.6                  |

Bulk samples were analyzed using X-ray diffraction, Figure 5, then by Rietveld refinement, Figure 5 presents the X-ray diffraction patterns obtained on densified samples, and Table 3 summarizes the results of the Rietveld analysis. These diffraction patterns only display the characteristic peaks of the tungsten BCC crystal structure, and no residual (crystallized) oxide phases can be detected, accordingly to the hypothesis formulated when analyzing densification curves, attributing the third densification peak at 1473  $^{\circ}\text{C}$  to the melting of the tungsten oxides and their subsequent flowing outside of the sample. This, unfortunately, implies a small mass loss, although significantly lower than what was observed on pure W [46], but raises the possibility of obtaining pure nanostructured bulk tungsten alloys.

Contrary to what could be expected from the XRD analysis performed previously on the powders, no peak shift is observed on the different samples, and the calculated lattice parameters are very similar. Moreover, crystallites sizes are comparable, in the 68–80 nm range, despite a significant difference observed on the powder SEM images. To analyze further these diffraction patterns, we performed a magnification of the (211) peak. Whereas the positions of this peak do not seem to shift significantly, its asymmetry seems to slightly vary with the composition due to the presence of different compositional gradients as a function of the Cr content, which Rietveld analysis seems to not take correctly into account. However, this seems strongly insufficient to explain the variation of the lattice parameters from the powders to the bulk samples. As backscattered images of the three samples (not presented) show a strong increase of the Cr-rich phase (in black on Figure 6) with the Cr content, a Cr depletion cannot be the cause of the newly gained homogeneity of the lattice parameters. On the contrary, we suspect that the strong shift observed on the powders do not provide only from the addition of Cr but also from some unaccounted form of out-of-equilibria state of these powders, which disappears after densification.

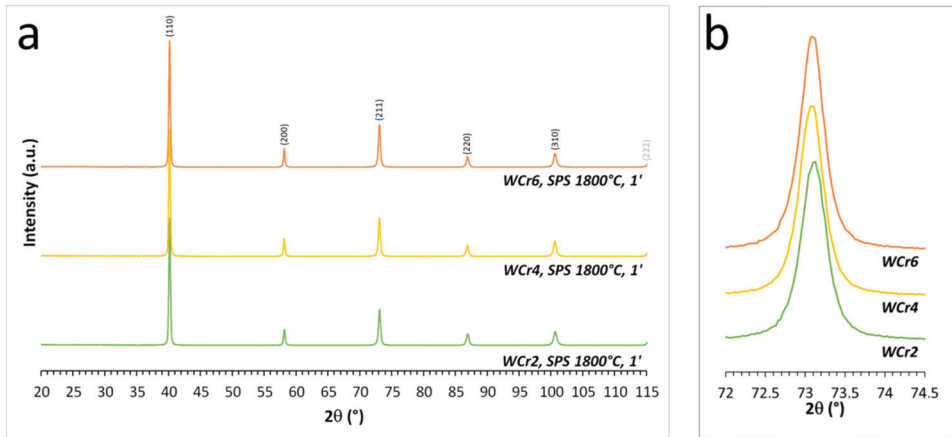


Figure 5. (a) XRD patterns of SPS sintered samples. Miller indices represented correspond to the expected tungsten BCC crystal structure. (b) magnification of the (211) peak.

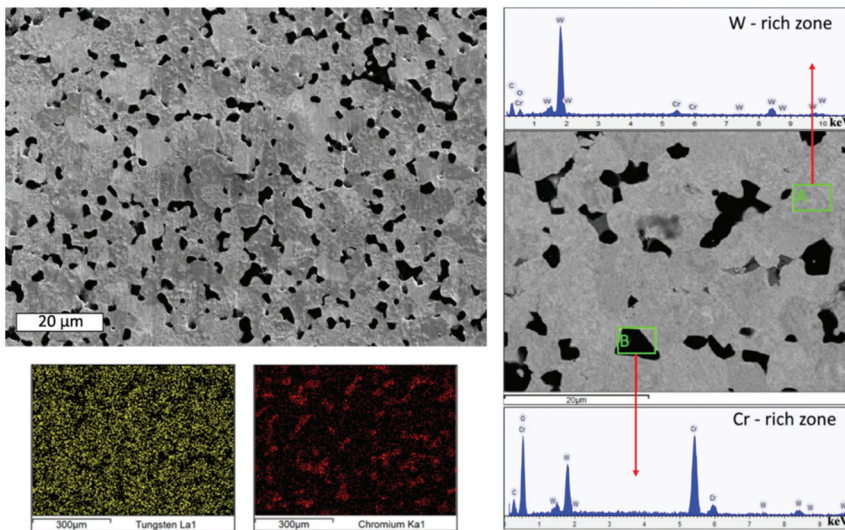


Figure 6. Upper left: SEM observation of the WCr6 sintered sample (2000 °C—5'). Right: EDX analysis of W-rich and Cr-rich regions; bottom left: EDX mapping on a large-scale of the sample.

Figure 6 shows an SEM observation of the WCr6 samples sintered at 2000 °C for 5'. On this image, the microstructure of the densified samples seems to be within a grain size range of 5 to 10 μm, and this apparent crystal growth seems more pronounced for higher W contents. Moreover, when the Cr content is 4 or 6 wt.%, dark areas appear and are naturally in greater proportions for WCr6 than for WCr4.

EDS local analysis and mapping of the sample proved these regions to also be a W-Cr alloy but significantly richer in Cr than the average of the sample. However, when performing EBSD analysis to study this apparent loss of the nanostructure, Figure 7, these micrometric grains turn out to be, for the most part, nanostructured or with a high concentration of low-angle grain boundaries (LAGB), with grain sizes consistent to the measured value obtained by Rietveld refinement (Table 3). Surprisingly, the presence

of a real nanosubstructure is the strongest for WCr2 and WCr6 and significantly less pronounced for WCr4. This nanostructuring is also of utmost importance for Plasma Facing Components as several experimental studies on metals [50,51], intermetallics [52], and ceramic materials [53,54] have shown that it would improve irradiation resistance. Dark areas in these images correspond to unresolved Kikuchi line patterns, which could be due to a different crystal structure, e.g., the presence of an oxide, or to a local loss of flatness of the sample such as a grain tear-off during polishing. In order to resolve this issue, Figure 8 presents the same magnified area of the sample observed on EBSD and SEM, where it can clearly be seen that the dark areas observed on the SEM images are properly indexed within the BCC structure, which confirms that they are made of a W-Cr alloy (and are therefore not recrystallized chromium oxide, which crystallizes with the corundum, hexagonal structure). Simultaneously, black, unindexed regions on the EBSD image due to unresolved Kikuchi lines patterns correspond to regions on the SEM image where significant irregularities are observed, seemingly from grain tear-off during polishing. This result is in good agreement with the XRD pattern, where no other phase was detected besides the BCC structure.

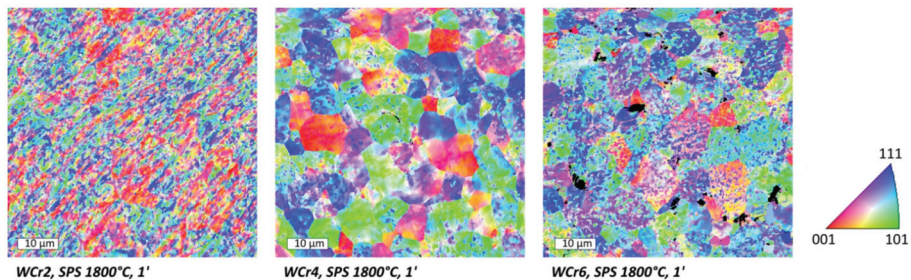


Figure 7. Electron backscattered diffraction (EBSD) images representing the grain orientations on  $60 \times 60 \mu\text{m}^2$  areas.

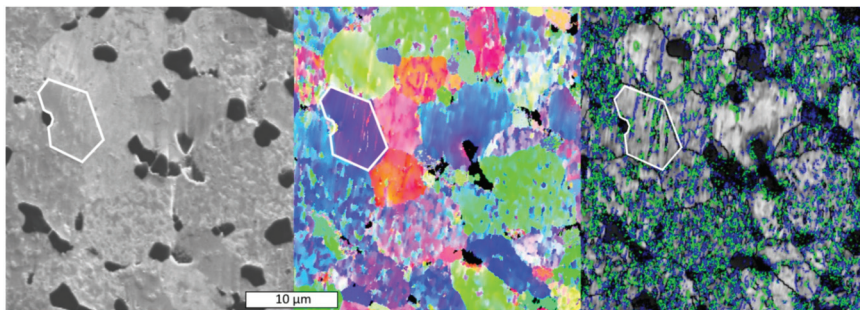


Figure 8. SEM (left) and EBSD (center) and (right) images of the same area, showing the dark SEM areas to be correctly indexed with the BCC structure, and the black EBSD areas to correspond to surface irregularities (marked grain is for the eye's guidance only); the right image shows the positions of the High-Angle Grain Boundaries (HAGB) (in black) and Low-Angle Grain Boundaries (LAGB) ( $2\text{--}5^\circ$  rotation angle in blue,  $5\text{--}15^\circ$  in green).

From the EBSD patterns in Figure 7, it is possible to retrieve the (110), (200) and (211) pole figures as shown for the WCr4 sample in Figure 9. While the symmetry of these patterns is poor, inverse pole figures calculated from these and presented in Figure 10 show a significant trend for the material towards a 111 preferential orientation. However, this analysis is performed on a small,  $60 \times 60 \mu\text{m}^2$  area, and is most certainly not statistically significant. A similar result was obtained on pure W, although in that case, grains were in the form of platelets, and a preferential orientation could be explained from an anisotropic compression behavior of the powders during SPS sintering [46]. It is much harder to

explain the origin of the preferential orientation here, as the powders were, if not spherical, at least mainly rounded (Figure 2), with only a few sharp-edged particles. A more precise analysis on a larger area, e.g., using quantitative texture analysis using XRD, would be necessary to confirm this result, but was unfortunately not performed before the samples were destroyed during mechanical testing.

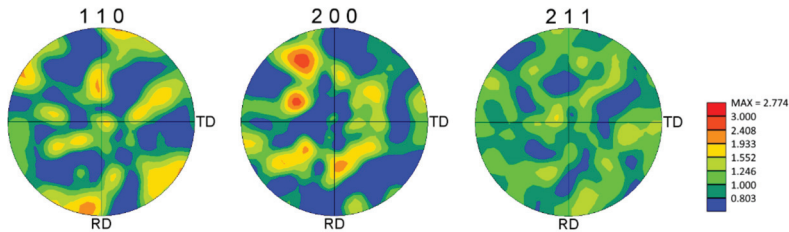


Figure 9. 110, 200 and 211 pole figures calculated from the EBSD mapping of the WCr4 sample presented in Figure 7.

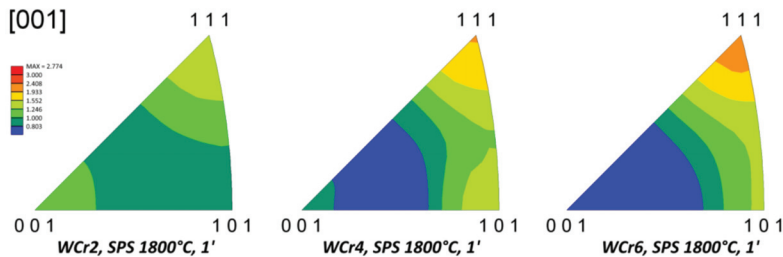
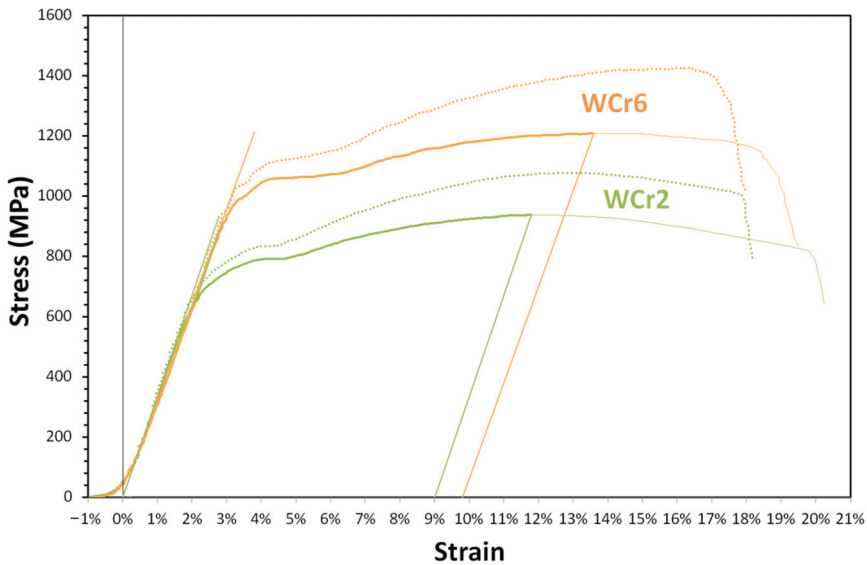


Figure 10. Inverse pole figures calculated from the three EBSD mappings (Figure 7).

Vickers hardness measurements are summarized in Table 3. The theoretical hardness for pure tungsten, as provided in the literature, is 343 HV, and, as the nanostructuring of a material is known to increase the hardness [48], increased hardnesses were expected for the samples presented here. Moreover, the hardness of 1142 HV was found in the literature for stoichiometric W-Cr alloy [47], adding another reason for an increase in hardness to be expected in our alloys. Indeed, results presented in Table 3 show an increase in hardness related to the composition: the three alloys sintered at 1800 °C for 1' have hardness values from 315 Hv for WCr2 to 420 Hv for WCr6. In the meantime, comparing the WCr2 samples sintered at 1600 °C and 1800 °C, respectively, a drop in hardness value is observed, as partial recrystallization may occur at high-temperature. A similar result is observed on the WCr4 samples, simply by increasing the plateau duration to 5'. This drop in hardness is, however, limited, and the value measured for the sample sintered at 2000 °C with a plateau duration of 15' is almost identical to the previous one. It is, however, difficult, in these conditions, to clearly identify if this increase in hardness is due to the presence of an alloying element or to the nanostructuring of the material

Results of compression tests are presented in Figure 11. They depict a ductility at room temperature in the range of 9 to 10%. Apparent mechanical properties deduced from these curves are summarized in Table 4. These results show a slight increase in the elastic limit, compared to pure, micrometric, tungsten, but is still slightly lower than the values obtained with pure, "cold rolled" (at temperatures ranging from 600 °C to 1000 °C) pure tungsten [32]. Indeed, the well-known Hall–Petch effect associates the decrease of the grain sizes to improved mechanical properties, and this result was therefore expected. However, the main improvement concerns the obtained ductility of the resulting materials, as the same study only reached a maximal engineering strain of 3–4% before rupture and <1% before the maximum stress is reached ([34], Figure 2). With values reaching 9–10% for the

strain at the maximum stress and 16–18% strain at failure at room temperature, our results are therefore very promising for the development of new refractory ductile components.



**Figure 11.** Results from the compression tests. Dotted lines: engineering strain/stress curves; full lines: true stress/strain curves, showing a ductility of 9.00% and 9.74%.

**Table 4.** Results of compression tests. Ductility is the plastic deformation only at the maximum strength.

| Alloy | Elastic Limit (MPa) | Apparent Young's Modulus (GPa) | Yield Strength (MPa) | Ductility (%) |
|-------|---------------------|--------------------------------|----------------------|---------------|
| WCr2  | 600                 | 33.8                           | 937                  | 9.00          |
| WCr6  | 950                 | 31.6                           | 1208                 | 9.74          |

#### 4. Conclusions

Magnesium-thermitic reactions were used to synthesize tungsten-chromium alloys with a morphology of nanometric to submicronic powders. Densification was then performed using SPS, with a final density of up to 99.9% of the theoretical value while preserving the nanometric substructure of the grains. Such a microstructure is thought to be favorable to increase resistance to ablation and spallation. On the other hand, the main aim of our effort to obtain this microstructure was to increase mechanical properties, and specifically ductility. Compressive testing of the samples presented an elastic limit ranging from 700 to 1000 MPa, depending on the alloy composition, while displaying a ductility greater than 9%. Future investigations will focus on slightly more complex alloys, with 2–3 alloying elements, in order not only to improve further mechanical properties but also to study the resistance of the materials to recrystallization at high-temperature.

**Author Contributions:** S.D. was the principal investigator of this study, performed under the supervision and in collaboration with D.V.; C.G., working with E.B., was the coordinator of a broader topic on Plasma Facing Materials, and brought valuable insight all along this study; N.H. provided clear information and interpretation of various analyses in this study, especially SEM. D.T. provided help during SPS synthesis and performed EBDS analyses. The paper has been mainly written by D.V. All authors have read and agreed to the published version of the manuscript.

**Funding:** This research received no external funding.

**Data Availability Statement:** No significant data in this study were created or analyzed in this study, aside from the one presented here. Additional data are available on request from the corresponding author.

**Conflicts of Interest:** The authors declare no conflict of interest.

## References

- Joachim, R.; Klaus, S. Hydrogen in tungsten as plasma-facing material. *Phys. Scr.* **2011**, *T145*, 014031.
- Bolt, H.; Barabash, V.; Krauss, W.; Linke, J.; Neu, R.; Suzuki, S.; Yoshida, N.; Team, A.U. Materials for the plasma-facing components of fusion reactors. *J. Nucl. Mater.* **2004**, *329–333*, 66–73. [[CrossRef](#)]
- Rieth, M.; Boutard, J.L.; Dudarev, S.L.; Ahlgren, T.; Antusch, S.; Baluc, N.; Barthe, M.-F.; Becquart, C.S.; Ciupinskie, L.; Correia, J.B.; et al. Review on the EFDA programme on tungsten materials technology and science. *J. Nucl. Mater.* **2011**, *417*, 463–467. [[CrossRef](#)]
- Zhou, Z.; Ma, Y.; Du, J.; Linke, J. Fabrication and characterization of ultra-fine grained tungsten by resistance sintering under ultra-high pressure. *Mater. Sci. Eng. A* **2009**, *505*, 131–135. [[CrossRef](#)]
- Cottrell, G.A. Sigma phase formation in irradiated tungsten, tantalum and molybdenum in a fusion power plant. *J. Nucl. Mater.* **2004**, *334*, 166–168. [[CrossRef](#)]
- Pintsuk, G. Tungsten as a Plasma-Facing Material, Reference Module in Materials Science and Materials Engineering—Comprehensive. *Nucl. Mater.* **2012**, *4*, 551–581.
- El-Kharbachi, A.; Chene, J.; Garcia-Argote, S.; Marchetti, L.; Martin, F.; Miserque, F.; Vrel, D.; Redolfi, M.; Malard, V.; Grisolia, C.; et al. Tritium absorption/desorption in ITER-like tungsten particles. *Int. J. Hydrogen Energy* **2014**, *39*, 10525–10536. [[CrossRef](#)]
- Pestchanyi, S.E.; Linke, J. Simulation of cracks in tungsten under ITER specific transient heat loads. *Fusion Eng. Des.* **2007**, *82*, 1657–1663. [[CrossRef](#)]
- Wittlich, K.; Hirai, T.; Compan, J.; Klimov, N.; Linke, J.; Loarte, A.; Merola, M.; Pintsuk, G.; Podkovyrov, V.; Singheiser, L.; et al. Damage structure in divertor armor materials exposed to multiple ITER relevant ELM loads. *Fusion Eng. Des.* **2009**, *84*, 1982–1986. [[CrossRef](#)]
- Mutoh, Y.; Ichikawa, K.; Nagata, K.; Takeuchi, M. Effect of rhenium addition on fracture toughness of tungsten at elevated temperatures. *J. Mater. Sci.* **1995**, *30*, 770–775. [[CrossRef](#)]
- Barabash, V.; Akiba, M.; Mazul, L.; Ulrickson, M.; Vieider, G. Selection, development and characterisation of plasma facing materials for ITER. *J. Nucl. Mater.* **1996**, *233–237*, 718–723. [[CrossRef](#)]
- El-Guebaly, L.; Kurtz, R.; Rieth, M.; Kurishita, H.; Robinson, A.; Team, A. W-based alloys for advanced divertor designs: Options and environmental impact of state-of-the-art alloys. *Fusion Sci. Technol.* **2011**, *60*, 185–189. [[CrossRef](#)]
- Wurster, S.; Baluc, N.; Battabyal, M.; Crosby, T.; Du, J.; Garcia-Rosales, C.; Hasegawa, A.; Hoffmann, A.; Kimura, A.; Kurishita, H.; et al. Recent progress in R&D on tungsten alloys for divertor structural and plasma facing materials. *J. Nucl. Mater.* **2013**, *442*, S181–S189.
- Grisolia, C.; Hodille, E.; Chene, J.; Garcia-Argote, S.; Pieters, G.; El-Kharbachi, A.; Marchetti, L.; Martin, F.; Miserque, F.; Vrel, D.; et al. Tritium absorption and desorption in ITER relevant materials: Comparative study of tungsten dust and massive samples. *J. Nucl. Mater.* **2015**, *463*, 885–888. [[CrossRef](#)]
- Coenen, J.W.; Philipps, V.; Brezinsek, S.; Pintsuk, G.; Uytendhouwen, I.; Wirtz, M.; Kreter, A.; Sugiyama, K.; Kurishita, H.; Torikai, Y.; et al. Melt-layer ejection and material changes of three different tungsten materials under high heat-flux conditions in the tokamak edge plasma of TEXTOR. *Nucl. Fusion* **2011**, *51*, 113020. [[CrossRef](#)]
- Aguirre, M.V.; Martín, A.; Pastor, J.Y.; Llorca, J.; Monge, M.A.; Pareja, R. Mechanical behavior of W-Y<sub>2</sub>O<sub>3</sub> and W-Ti alloys from 25 °C to 1000 °C. *Metall. Mater. Trans. A* **2009**, *40*, 2283–2290. [[CrossRef](#)]
- Aguirre, M.V.; Martín, A.; Pastor, J.Y.; Llorca, J.; Monge, M.A.; Pareja, R. Mechanical properties of Y<sub>2</sub>O<sub>3</sub>-doped W-Ti alloys. *J. Nucl. Mater.* **2010**, *404*, 203–209. [[CrossRef](#)]
- Arshad, K.; Guo, W.; Wang, J.; Zhao, M.Y.; Yuan, Y.; Zhang, Y.; Wang, B.; Zhou, Z.-J.; Lu, G.-H. Influence of vanadium precursor powder size on microstructures and properties of W-V alloy. *Int. J. Refract. Met. Hard Mater.* **2015**, *50*, 59–64. [[CrossRef](#)]
- Arshad, K.; Yuan, Y.; Cheng, L.; Wang, J.; Zhou, Z.J.; De Temmerman, G.; Lu, G.-H. Deuterium blistering in tungsten and tungsten vanadium alloys. *Fusion Eng. Des.* **2016**, *107*, 25–31. [[CrossRef](#)]
- López-Ruiz, P.; Koch, F.; Ordás, N.; Lindig, S.; García-Rosales, C. Manufacturing of self-passivating W-Cr-Si alloys by mechanical alloying and HIP. *Fusion Eng. Des.* **2011**, *86*, 1719–1723. [[CrossRef](#)]
- Telu, S.; Mitra, R.; Pabi, S.K. High temperature oxidation behavior of W–Cr–Nb Alloys in the Temperature Range of 800–1200 °C. *Int. J. Refract. Met. Hard Mater.* **2013**, *38*, 47–59. [[CrossRef](#)]
- Telu, S.; Patra, A.; Sankaranarayana, M.; Mitra, R.; Pabi, S.K. Microstructure and cyclic oxidation behavior of W-Cr alloys prepared by sintering of mechanically alloyed nanocrystalline powders. *Int. J. Refract. Met. Hard Mater.* **2013**, *36*, 191–203. [[CrossRef](#)]
- Zhou, Y.; Sun, Q.X.; Xie, Z.M.; Liu, R.; Wang, X.P.; Fang, Q.F.; Liu, C.S. The microstructure and microhardness of W–5wt% Cr alloy fabricated by spark plasma sintering. *J. Alloys Compd.* **2014**, *585*, 771–775. [[CrossRef](#)]

24. Veleva, L.; Oksiuta, Z.; Vogt, U.; Baluc, N. Sintering and characterization of W–Y and W–Y<sub>2</sub>O<sub>3</sub> materials. *Fusion Eng. Des.* **2009**, *84*, 1920–1924. [[CrossRef](#)]
25. Liu, R.; Xie, Z.M.; Fang, Q.F.; Zhang, T.; Wang, X.P.; Hao, T.; Liua, C.S.; Daic, Y. Nanostructured yttria dispersion-strengthened tungsten synthesized by sol-gel method. *J. Alloys Compd.* **2016**, *657*, 73–80. [[CrossRef](#)]
26. Kurishita, H.; Matsuo, S.; Arakawa, H.; Narui, M.; Yamazaki, M.; Sakamoto, T.; Kobayashi, S.; Nakaib, K.; Takidac, T.; Takebec, K.; et al. High temperature tensile properties and their application to toughness enhancement in ultra-fine grained W-(0-1.5)wt% TiC. *J. Nucl. Mater.* **2009**, *386–388*, 579–582. [[CrossRef](#)]
27. Kurishita, H.; Matsuo, S.; Arakawa, H.; Sakamoto, T.; Kobayashi, S.; Nakai, K.; Takida, T.; Kato, M.; Kawai, M.; Yoshida, N. Development of re-crystallized W-1.1%TiC with enhanced room-temperature ductility and radiation performance. *J. Nucl. Mater.* **2010**, *398*, 87–92. [[CrossRef](#)]
28. Zhang, T.; Wang, Y.; Zhou, Y.; Song, G. Effect of heat treatment on microstructure and mechanical properties of ZrC particles reinforced tungsten-matrix composites. *Mater. Sci. Eng. A* **2009**, *512*, 19–25. [[CrossRef](#)]
29. Hao, T.; Fan, Z.Q.; Zhang, T.; Luo, G.N.; Wang, X.P.; Liu, C.; Fang, Q. Strength and ductility improvement of ultrafine-grained tungsten produced by equal-channel angular pressing. *J. Nucl. Mater.* **2014**, *455*, 595–599. [[CrossRef](#)]
30. Levin, Z.S.; Hartwig, K.T. Strong ductile bulk tungsten. *Mater. Sci. Eng. A* **2017**, *707*, 602–611. [[CrossRef](#)]
31. Németh, A.A.N.; Reiser, J.; Armstrong, D.E.J.; Rieth, M. The nature of the brittle-to-ductile transition of ultrafine grained tungsten (W) foil. *Int. J. Refract. Met. Hard Mater.* **2015**, *50*, 9–15. [[CrossRef](#)]
32. Reiser, J.; Hoffmann, J.; Jäntsch, U.; Klimenkov, M.; Bonk, S.; Bonnekoh, C.; Rieth, M.; Hoffmann, A.; Mrotzek, T. Ductilisation of tungsten (W): On the shift of the brittle-to-ductile transition (BDT) to lower temperatures through cold rolling. *Int. J. Refract. Met. Hard Mater.* **2016**, *54*, 351–369. [[CrossRef](#)]
33. Reiser, J.; Hoffmann, J.; Jäntsch, U.; Klimenkov, M.; Bonk, S.; Bonnekoh, C.; Hoffmann, A.; Mrotzek, T.; Rieth, M. Ductilisation of tungsten (W): On the increase of strength AND room-temperature tensile ductility through cold-rolling. *Int. J. Refract. Met. Hard Mater.* **2017**, *64*, 261–278. [[CrossRef](#)]
34. Guo, H.Y.; Xia, M.; Wu, Z.T.; Chan, L.C.; Dai, Y.; Wang, K.; Yan, Q.-Z.; He, M.-C.; Ge, C.; Lu, J. Nanocrystalline-grained tungsten prepared by surface mechanical attrition treatment: Microstructure and mechanical properties. *J. Nucl. Mater.* **2016**, *480*, 281–288. [[CrossRef](#)]
35. Chen, L.; Ping, L.; Ye, T.; Lingfeng, L.; Kemin, X.; Meng, Z. Observations on the Ductility and Thermostability of Tungsten Processed from Micropowder by Improved High-pressure Torsion. *Rare Met. Mater. Eng.* **2016**, *45*, 3089–3094. [[CrossRef](#)]
36. Dzykovich, I.Y.; Panichkina, V.V.; Skorokhod, V.V.; Shaiderman, L.I. Effect of palladium on diffusion processes in the system tungsten-chromium. *Sov. Powder Met. Met. Ceram.* **1976**, *115*, 151–153. [[CrossRef](#)]
37. Itagaki, T.; Yoda, R. The Effect of Palladium on Oxidation Behavior of Sintered Tungsten-Chromium-Palladium Alloys. *J. Jpn. Inst. Met.* **1974**, *38*, 486–492. [[CrossRef](#)]
38. Zhang, Q.; Zhao, J.C. Impurity and interdiffusion coefficients of the Cr–X (X = Co, Fe, Mo, Nb, Ni, Pd, Pt, Ta) binary systems. *J. Alloys Compd.* **2014**, *604*, 142–150. [[CrossRef](#)]
39. Lee, D.B.; Simkovich, G. Oxidation of Mo–W–Cr–Pd alloys. *J. Less Common Met.* **1990**, *163*, 1–62. [[CrossRef](#)]
40. Waterstrat, R.M. Analysis of selected alloys in the systems Cr–Pd, Cr–Ru, V–Pd and Ta–Pt. *J. Less Common Met.* **1981**, *80*, P31–P36. [[CrossRef](#)]
41. Li, Y.; Li, P.; Bian, H.; Tang, N.; Koizumi, Y.; Chiba, A. The hot forging behaviour and its effects on the oxidation behaviour of W–Cr alloy. *Corros. Sci.* **2014**, *83*, 367–374. [[CrossRef](#)]
42. Malewar, R.; Kumar, K.S.; Murty, B.S.; Sarma, B.; Pabi, S.K. On sinterability of nanostructured W produced by high-energy ball milling. *J. Mater. Res.* **2007**, *22*, 1200–1206. [[CrossRef](#)]
43. Dine, S.; Aid, S.; Ouara, K.; Malard, V.; Odorico, M.; Herlin-Boime, N.; Habert, A.; Gerbil-Margueron, A.; Grisolia, C.; Chêne, J.; et al. Synthesis of tungsten nanopowders: Comparison of milling, SHS, MASHS and milling-induced chemical processes. *Adv. Powder Technol.* **2015**, *26*, 1300–1305. [[CrossRef](#)]
44. Kentheswaran, V.; Dine, S.; Vrel, D.; Couzinié, J.P.; Dirras, G. Synthesis of nanometric refractory alloys powders in the MoNbW system. *J. Alloys Compd.* **2016**, *679*, 80–87. [[CrossRef](#)]
45. Dine, S.; Kentheswaran, V.; Vrel, D.; Couzinié, J.P.; Dirras, G. Synthesis of nanometric MoNbW alloy using self-propagating high-temperature synthesis. *Adv. Powder Technol.* **2017**, *28*, 1739–1744. [[CrossRef](#)]
46. Dine, S.; Bernard, E.; Herlin, N.; Grisolia, C.; Tingaud, D.; Vrel, D. SHS synthesis, SPS densification and mechanical properties of nanometric tungsten. *Adv. Eng. Mater.* **2018**. [[CrossRef](#)]
47. Liu, G.; Li, J.; Chen, K.; He, G.; Yang, Z.; Guo, S. High-gravity combustion synthesis of W–Cr alloys with improved hardness. *Mater. Chem. Phys.* **2016**, *182*, 6–9. [[CrossRef](#)]
48. Yao, M.; Zhangjian, Z.; Jun, T.; Ming, L. Fabrication of Ultra-fine Grain Tungsten by Combining Spark Plasma Sintering with Resistance Sintering under Ultra High Pressure. *Rare Met. Mater. Eng.* **2011**, *40*, 0004–0008. [[CrossRef](#)]
49. Guo, W.; Arshad, K.; Yuan, Y.; Zhao, M.Y.; Shu, X.L.; Zhou, Z.-J.; Zhang, Y.; Lu, G.-H. Effects of vanadium alloying on the microstructures and mechanical properties of hot-pressed tungsten material. *Mod. Phys. Lett. B* **2016**, *30*, 1650216. [[CrossRef](#)]
50. Wurster, S.; Pippan, R. Nanostructured metals under irradiation. *Scr. Mater.* **2009**, *60*, 1083–1087. [[CrossRef](#)]
51. Nita, N.; Schaeublin, R.; Victoria, M. Impact of irradiation on the microstructure of nanocrystalline materials. *J. Nucl. Mater.* **2004**, *329–333*, 953–957. [[CrossRef](#)]

52. Kilmametov, A.R.; Gunderov, D.V.; Valiev, R.Z.; Balogh, A.G.; Hahn, H. Enhanced ion irradiation resistance of bulk nanocrystalline TiNi alloy. *Scr. Mater.* **2008**, *59*, 1027–1030. [[CrossRef](#)]
53. Shen, T.D.; Feng, S.; Tang, M.; Valdez, J.A.; Wang, Y.; Sickafus, K.E. Enhanced radiation tolerance in nanocrystalline MgGa<sub>2</sub>O<sub>4</sub>. *Appl. Phys. Lett.* **2007**, *90*, 263115. [[CrossRef](#)]
54. Yang, T.; Huang, X.; Wang, C.; Zhang, Y.; Xue, J.; Yan, S.; Wang, Y. Enhanced structural stability of nanoporous zirconia under irradiation of He. *J. Nucl. Mater.* **2012**, *427*, 225–232. [[CrossRef](#)]





Article

# Influence of Carbon Diffusion and the Presence of Oxygen on the Microstructure of Molybdenum Powders Densified by SPS

Mathias Moser <sup>1,2</sup>, Sylvain Lorand <sup>1</sup>, Florian Bussiere <sup>1</sup>, Frédéric Demoisson <sup>1</sup>, Hervé Couque <sup>2</sup> and Frédéric Bernard <sup>1,\*</sup>

<sup>1</sup> Laboratoire Interdisciplinaire Carnot de Bourgogne, UMR6303 CNRS-Université de Bourgogne-Franche-Comté, BP 47870, 21078 Dijon, France; Mathias\_Moser@etu.u-bourgogne.fr (M.M.); sylvain.lorand@live.fr (S.L.); florian.bussiere@u-bourgogne.fr (F.B.); Frederic.Demoisson@u-bourgogne.fr (F.D.)

<sup>2</sup> Nexter Munitions, 18 route de Guerry, 18000 Bourges, France; h.couque@nexter-group.fr

\* Correspondence: fbernard@u-bourgogne.fr; Tel.: +33-380-396-125

Received: 5 June 2020; Accepted: 8 July 2020; Published: 14 July 2020

**Abstract:** Due to molybdenum's Body-Centered Cubic (BCC) crystalline structure, its ductile–brittle transition temperature is sensitive to shaping, purity and microstructure. Dense molybdenum parts are usually shaped by the powder metallurgy process. The aim of this work concerns the spark plasma sintering of high-purity powders prepared by inductively coupled plasma. The influence of carbon diffusion and its interaction with oxygen on the density (i.e., the densification stage) and on the microstructure (i.e., the grain growth stage) during spark plasma sintering was investigated. The formation of carbide is usually expected for a sintering temperature above 1500 °C leading to grain growth (e.g., more than 10 times larger than the initial powder grain size after sintering at 1900 °C for 10 min). The brittleness was also affected by the segregation of molybdenum carbides at the grain boundaries (i.e., intergranular brittle fracture). Consequently, to reduce the sintering temperature to below 1500 °C, mechanically activated powders were used. From these milled powders, a dense molybdenum disc (60 mm in diameter and 10 mm in thickness) sintered at 1450 °C under a pressure of 70 MPa for 30 min was obtained. It is composed of a fine microstructure without carbide and oxide, its ductility is close to 13% with a maximum resistance of 550 MPa.

**Keywords:** molybdenum; grain growth; carbon diffusion; ball milling; spark plasma sintering

## 1. Introduction

Molybdenum is a refractory metal with a high-temperature resistance, due to its melting point of 2620 °C. Such a characteristic, along with its good mechanical properties, has motivated its use in defense [1] as well as civilian applications, such as the production of ribbons and wires for the lighting industry, electrodes for glass melting and thermal zones for high-temperature ovens. However, its high melting temperature makes the implementation of the material by traditional metallurgy (casting or forging) a complex and expensive process. That is why much research has been conducted into the powder metallurgy of molybdenum [2–4]. However, the sintering process remains complex and long. Indeed, conventional sintering of molybdenum requires temperatures between 1800 and 2000 °C for several hours. In addition, the density obtained from such a sintering process is less than 95% of the theoretical maximum density (TMD) [5,6], which is often not sufficient for target applications such as in defense. Many studies have been performed to increase the density of the end-product by using: (i) different sizes of molybdenum powder [7], (ii) heat treatment of the initial molybdenum powders before sintering [6], (iii) specific additives as densification aids [8], or (iv) alternative methods

of sintering such as explosive consolidation [9,10], microwave energy [11] or spark plasma sintering (SPS) [3,4,7,12,13].

It is well known that the presence of some impurities in molybdenum powder can modify the mechanical behavior of the sintered product. The presence of oxygen influences the mechanical properties by segregating at the grain boundaries [14–16], while other impurities, such as carbon in a reasonable proportion, increase the ductility [17,18], but have a negative effect in excess. Some studies have also investigated the relationship between impurities and the final density. For example, the addition of nickel [19,20] or silicon [21] increases the sinterability of molybdenum leading to a better density of the final product.

Apart from the direct effect of such impurities on the ductility or the density, there is a grain growth phenomenon during the sintering of molybdenum powder at high temperature with a non-negligible effect on the density of the sintered product and, consequently, on the mechanical, electrical and thermal properties. In fact, Lee et al. [22] reported that the concentration of oxygen leading to molybdenum oxide formation is an accelerator factor for grain growth during sintering.

The main objective of this study was to investigate the fabrication by SPS of dense parts starting from powders prepared using inductively coupled plasma technology (ICP). Clearly, it is essential to understand the grain growth and densification stages of such powders in order to control them. Consequently, the present work evaluated several powders and sintering conditions to observe and understand the grain growth and the effects of the presence of oxygen and carbon.

## 2. Experimental Procedure

A 99.95% pure molybdenum powder with a narrow particle size distribution (i.e., D10: 11.04  $\mu\text{m}$ , D50: 16.33  $\mu\text{m}$  and D90: 28.88  $\mu\text{m}$ ) made by the Tekna Company (Macon, France) (i.e., hereafter named Mo-45) was used. This powder was prepared using ICP, which has the advantage of having a high level of sphericity (Figure 1) and a high density ( $10.2 \text{ g} \cdot \text{cm}^{-3}$  obtained by He pycnometry) without any oxide either on the surface of or inside the particle. Scanning Electron Microscope (SEM) images highlight the spherical morphology with regularity in size and shape (Figure 1a). The presence of agglomerated clusters is certainly due to some precursor powder particles not having entirely undergone the spheroidization step because they were expelled too early from the plasma by reflux movements. However, the majority of the grains have smooth surfaces. Despite these few irregularities, two populations of particles were mainly formed: particles with smooth surfaces (Figure 1b) and particles having large facets (Figure 1c). A higher magnification observation shows that the majority of smooth particles are actually composed of large faceted grains covered with a very thin layer on the surface. The smoothing of these particles may be due to faster migration of the surface species during spheroidization than occurred on particles with well-marked facets.

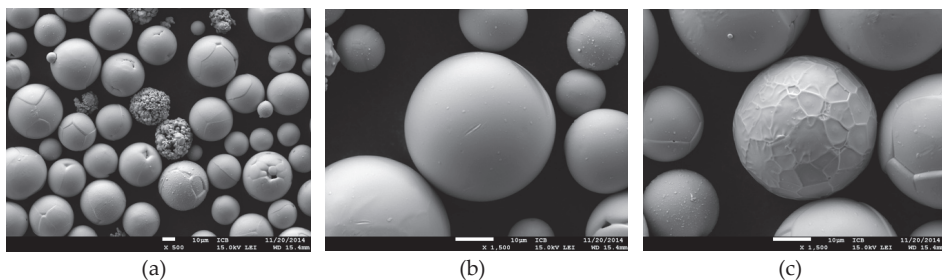


**Figure 1.** (a) SEM image of molybdenum powder Mo-45 (Tekna); (b) and (c) SEM images with a higher magnification showing different powder morphologies.

However, in addition, it is essential to verify the presence on the surface of a native molybdenum oxide. Indeed, some molybdenum oxides,  $\text{MoO}_3$  or  $\text{MoO}_2$ , are usually observed on the very surface of

the powder, due to humidity, but this thin layer can be removed by a thermal treatment at 800 °C under vacuum as proved by XPS (X-ray photoelectron spectroscopy) analysis (Figure 2) performed on Mo-45 powder. XPS spectra are presented of molybdenum powder before (green) and after (red) thermal treatment under vacuum at 800 °C. This study shows that it is not necessary to work under a reducing atmosphere since heating under vacuum at 800 °C is sufficient to remove the thin layer of oxide present on the surface of the molybdenum particles. Indeed, the  $\text{Mo}_{\text{ox}} 3d^{3/2}$  peak at 235 eV and the  $\text{Mo}_{\text{ox}} 3d^{5/2}$  peak at 232 eV associated with the presence of oxidized molybdenum disappeared in favor of metallic molybdenum after a heat treatment at 800 °C under vacuum (Figure 2). Consequently, as the SPS sintering was also carried out under vacuum, these oxides will be reduced during the heating stage, the rate of which was limited to 50 °C/min for all SPS tests.

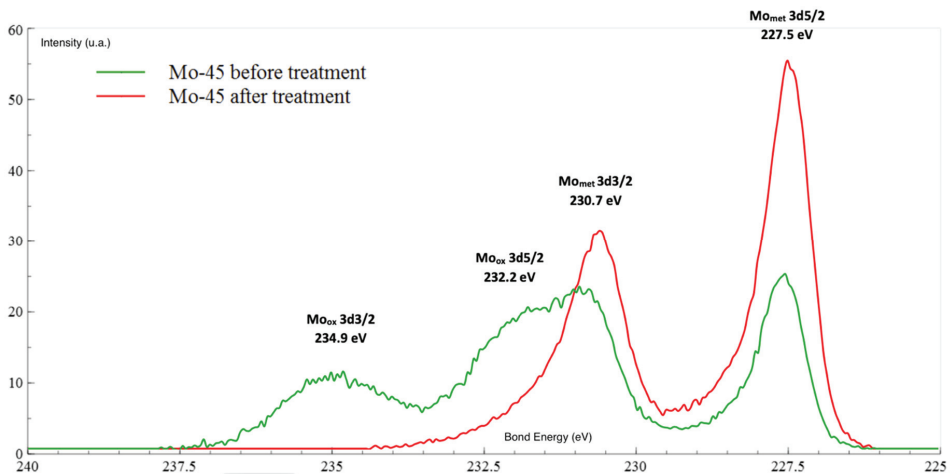


**Figure 2.** XPS spectra of molybdenum powder before (green) and after (red) thermal treatment performed under vacuum at 800 °C.

The SPS assembly used in this work is described in Figure 3a. As molybdenum is a conductive material, the current goes through the sample and, consequently, this latter is heated by Joule effect. To favor this “internal heating”, a spray of boron nitride (BN, an electrical insulating) has been deposited all around the sample (Figure 3c).

A graphite die of 60 mm inner diameter lined with a 0.35 mm thick layer of graphite foil (named Papyex®) (Mersen, Gennevilliers, France) was filled with the powder and coated with a boron nitride (BN) spray to prevent radial carbon diffusion (compare Figure 3c with the classical configuration shown in Figure 3b). An additional limit to axial carbon diffusion was provided by 3 mm thick tantalum discs placed between the punches and the powder (Figure 3d). A 3 cm thick layer of graphite felt was wrapped around the die to prevent and limit thermal gradients inside the sample during heating by reducing heat losses by radiation. Sintered samples of 60 mm in diameter and 10 mm in height were then sintered in an FCT HPD-125 spark plasma sintering machine (FCT Systeme, Rauenstein, Germany).

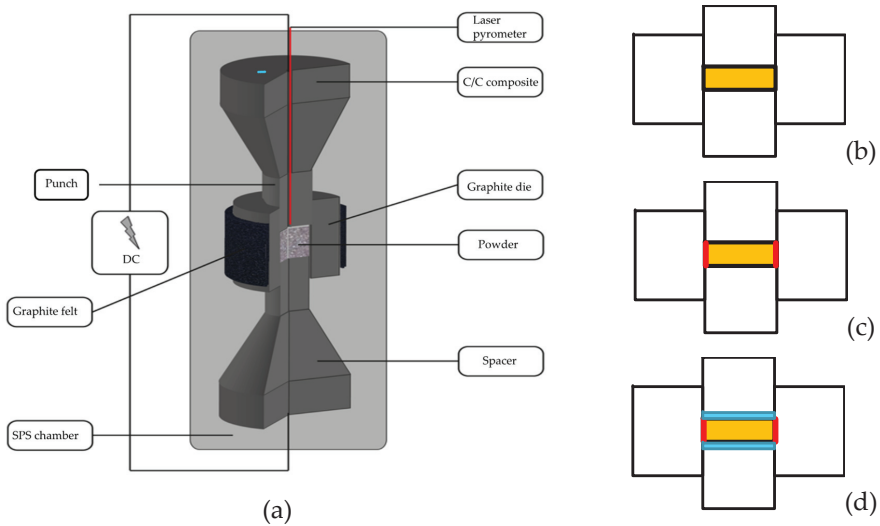


**Figure 3.** (a) General view of spark plasma sintering (SPS) assembly; (b), (c) and (d) represent different sample configurations: (b) classical assembly using graphite foil all around the sample, (c) assembly using a boron nitride (BN) spray on graphite foil around the sample to limit carbon radial diffusion, and (d) assembly with a BN barrier as previously and a tantalum disc (3 mm) on the top and bottom of the powder to limit axial carbon diffusion.

Sintering was carried out under vacuum using a DC electric current (~4000 A) and a heating rate of  $50\text{ }^{\circ}\text{C} \cdot \text{min}^{-1}$ . Above  $400\text{ }^{\circ}\text{C}$ , the temperature was measured and regulated using an optical pyrometer looking at a spot located at 7 mm on the sample top. The temperature was varied from 1750 to  $2000\text{ }^{\circ}\text{C}$  with a hold time at the maximum temperature of between 0 to 30 min. The uniaxial pressure was varied from 28 MPa (the minimum value to ensure sufficient electrical contact) to 90 MPa (the maximum value for graphite tools). The pressure was applied from RT to  $450\text{ }^{\circ}\text{C}$ , just before the activation of the laser pyrometer. To reduce thermal stresses inside the sintered part, it was cooled in a controlled manner at a rate of  $50\text{ }^{\circ}\text{C}/\text{min}$ . Simultaneously, during the cooling, the pressure was slowly decreased at a rate of 6 KN/min. In experiment 10 (see Table 1), two massive discs of tantalum (3 mm thick) located top and bottom of the powder and a BN barrier around the powder (Figure 3d) were used to avoid any carbon diffusion from the graphite into the molybdenum. The sintering conditions for each sample are listed in Table 1.

**Table 1.** Table of sintering conditions of Mo-45 powder.

| Experiment No. | Pressure (MPa)                                 | Temperature ( $^{\circ}\text{C}$ ) | Holding Time (min) | Protection |
|----------------|--|------------------------------------|--------------------|------------|
| 1              | 90   | 1750                               | 0                  | BN         |
| 2              | 90   | 1900                               | 0                  | BN         |
| 3              | 90   | 2000                               | 0                  | BN         |
| 4              | 70   | 1900                               | 0                  | BN         |
| 5              | 70   | 1900                               | 10                 | BN         |
| 6              | 70   | 1900                               | 30                 | BN         |
| 7              | 70   | 1750                               | 10                 | BN         |
| 8              | 28   | 1900                               | 0                  | BN         |
| 9              | 70 (delayed at $900\text{ }^{\circ}\text{C}$ ) | 1900                               | 0                  | BN         |
| 10             | 70   | 1900                               | 30                 | BN + Ta    |

After sintering, the graphite foil on the sample surface was removed by a sanding operation. Two types of preparation for analysis were performed on the sintered parts. First, a transverse cut was made, usually using a circular saw. The relative densities of the sintered molybdenum samples were measured using Archimedes' technique and found to have a value of 10.2. Then, the surface of this slice was mechanically polished, starting with SiC papers down to 3  $\mu\text{m}$  diamond abrasive and, finished with an alumina super-finishing solution. After ultrasonic cleaning, two types of chemical etching were then performed on the cross sections. For observation of the microstructure by optical microscopy or scanning electron microscopy, a Murakami reagent ( $\text{K}_3\text{Fe}(\text{CN})_6/\text{KOH}/\text{H}_2\text{O}$  (1:1:1)) was applied for 3 min while for the observation of carbides, Hasson's reagent ( $\text{C}_2\text{H}_5\text{OH}/\text{HCl}$  (32%)/ $\text{FeCl}_3 \cdot 6\text{H}_2\text{O}$  ( $1300 \text{ g}\cdot\text{L}^{-1}$ ) (3:1:2)) was applied for 2 min. In both cases, the samples were cleaned using distilled water and dried with ethanol.

A standard optical microscope (ZEISS) (Carl Zeiss, Jena, Germany) was used to characterize the microstructure of the SPS sintered samples. The microstructural analysis of the material was carried out using a field emission gun (FEG) scanning electron microscope (SEM JEOL JSM-7600F, Musashino, Akishima, Tokyo, Japan) coupled with a LINK OXFORD energy dispersive X-ray spectrometer (EDXS) (High Wycombe, London, UK). Tensile tests are a suitable method to determine mechanical properties such as the yield strength, the maximum tensile strength and the ductility. Three specimens were extracted from each sintered sample using electrical discharge machining (EDM) as shown in Figure 4. The gauge length and diameter of the gauge section of the samples were 16 and 4 mm, respectively. Uniaxial tensile tests were performed at a constant strain rate of  $10^{-3} \text{ s}^{-1}$  following the ASTM E8/E8M standard test method using a Testwell machine with a 1 MN load cell and a 10 mm long clip gage.

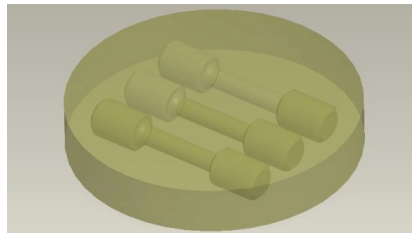


**Figure 4.** Location of the three tensile test pieces machined from within sintered discs (60 mm in diameter and 10 mm in thickness).

### 3. Experimental Results

#### 3.1. Density, Microstructure and Grain Size

Chemical etching on cross-sections of the molybdenum powder consolidated by SPS allows a description of the sintered molybdenum microstructure. Particular attention was paid to following both the evolution of the grain size and the porosity during sintering. An investigation was performed of the growth of the molybdenum grains as a function of the temperature, the holding time and the value of the uniaxial pressure. Figure 5 shows the effect of the sintering temperature (1750, 1900 and 2000  $^{\circ}\text{C}$ ) on the average molybdenum grain size (corresponding to experiments 1, 2, 3 in Table 1, respectively). Thus, a sintered sample at 1750  $^{\circ}\text{C}$  under 90 MPa pressure and without holding time (Figure 5a) has a microstructure with a grain size close to the initial size of the powder particles (i.e., 25  $\mu\text{m}$  determined by laser granulometry). At this temperature, any sign of grain growth is highlighted. By contrast at 1900  $^{\circ}\text{C}$ , grain growth starts but is not homogeneous since two different microstructures are observed: a central part composed of large grains (150  $\mu\text{m}$ , Figure 5c, right hand side) whereas the sample edge is made up of grains having a similar size as initially (i.e., 25  $\mu\text{m}$ , Figure 5c, left hand side). Such an observation is probably the result of a thermal gradient during SPS sintering. The existence of this thermal gradient is due to the absence of a holding time at the sintering temperature which does

not allow thermal homogeneization. Effectively, a thermal gradient exists (i.e., as Mo is a conductive material, the center is hotter than the periphery), this latter may be reduced by a modification of SPS tools dimensions and by the addition of graphite felt which limits the thermal losses by radiation [23]. Finally, at 2000 °C, the grain growth occurs over the whole sample (Figure 5b) and the final density is better ( $98.4 \pm 0.2\%$  TMD Theoretical Maximum Density)) in comparison with those obtained at lower temperatures for which the density is not adequate,  $96.5 \pm 0.2\%$  TMD at 1750 °C,  $97.8 \pm 0.2\%$  TMD at 1900 °C without any holding time.

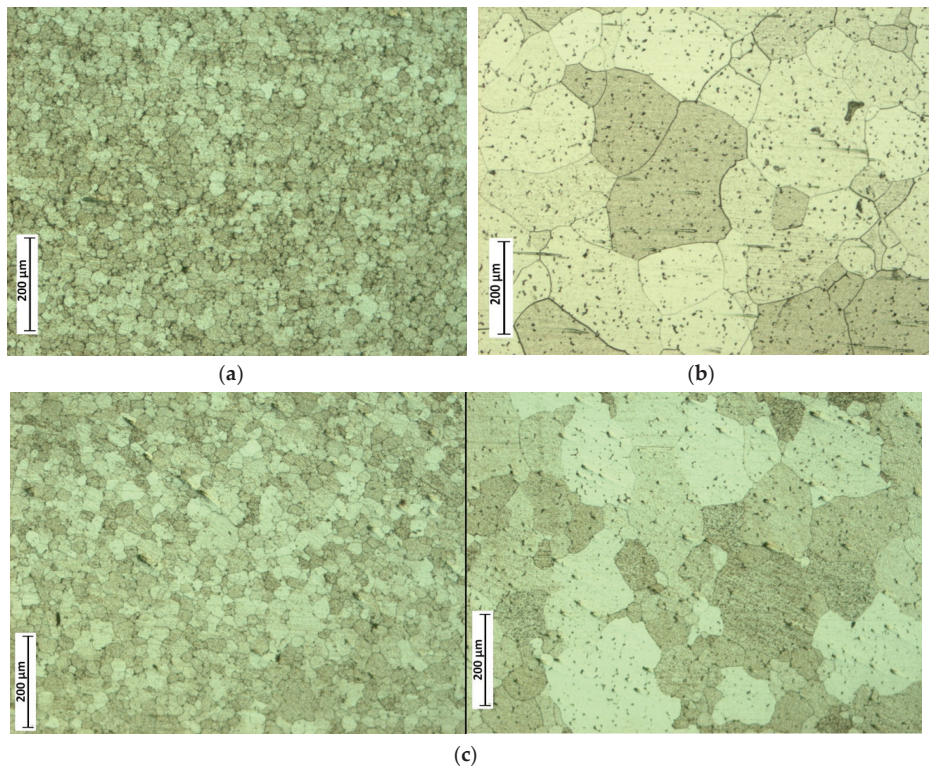


**Figure 5.** Microstructures after chemical etching of molybdenum powder (Mo-45) sintered under 90 MPa pressure without holding time at: (a) 1750, (b) 2000 and (c) 1900 °C (left: edge, right: core).

To evaluate the influence of holding time on molybdenum grain growth, studies were performed at 1900 °C for various holding times (0, 10 and 30 min) under 70 MPa pressure. These tests correspond to experiments 4, 5, 6, in Table 1. As shown in Figure 6b, after 10 min of holding time, the microstructure is different, with an irregular, but generalized grain growth compared to a sintered sample without holding time (Figure 6a). The latter has a fine microstructure on the shell but a beginning of grain growth in the core. After 30 min, the growth is total and regular in the whole sintered sample, as can be seen in Figure 6c. In reality, the grain growth starts after 2 or 3 min at temperature and it is difficult to obtain a microstructural difference between the core and shell. Because of this abrupt change in microstructure, it is possible to qualify this grain growth as exaggerated, in comparison with the phenomena usually observed in metal powders during sintering. The density is also affected by the holding time. While the density of the molybdenum powder after sintering without holding time is around  $98.2 \pm 0.2\%$  TMD, after 10 min this becomes  $99.2 \pm 0.2\%$  TMD and after 30 min, maximum densification is reached, with a density of  $99.9 \pm 0.2\%$  TMD.

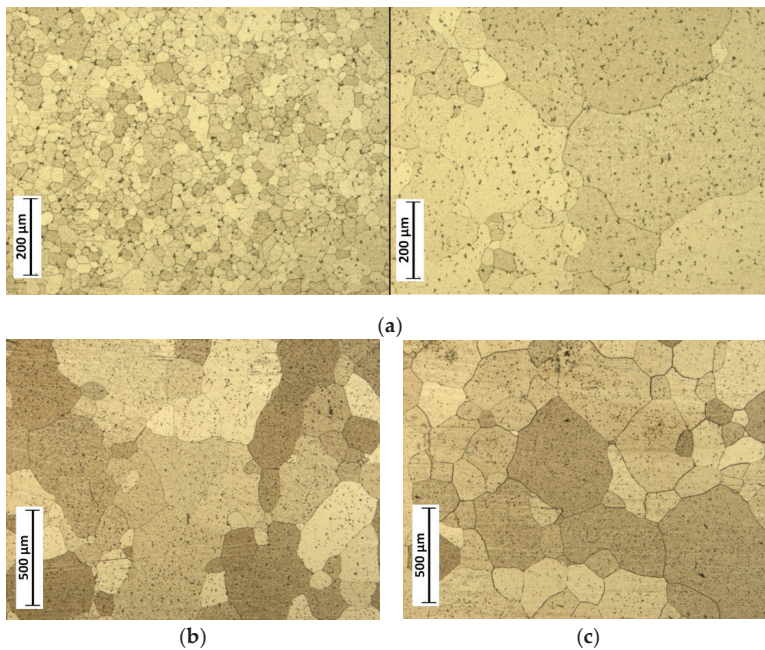


**Figure 6.** Microstructures after chemical etching of molybdenum powder (Mo-45) sintered at 1900 °C under 70 MPa pressure: (a) without holding (left: shell, right: core), (b) 10 min and (c) 30 min.

In addition (Figure 7), the Mo-45 powder, sintered at 1750 °C under 70 MPa pressure and held for 30 min (i.e., corresponding to experiment 7 in Table 1) shows a different microstructure than seen previously at 1900 °C for the same holding time (Figure 6c). The microstructure obtained is close to those obtained at 1900 °C without holding (Figure 5a). In fact, it is necessary to find a good compromise between temperature and holding time to obtain dense molybdenum with homogeneous microstructure while avoiding exaggerated grain growth.

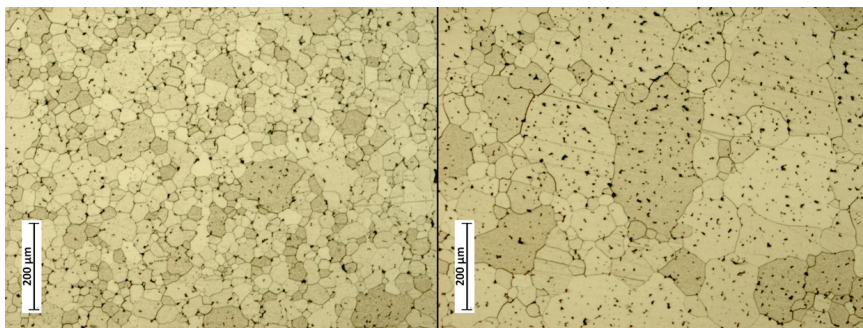


**Figure 7.** Microstructures after chemical etching of molybdenum powder (Mo-45) sintered at 1750 °C under 70 MPa pressure for 30 min (left: shell, right: core). Black dots are due colloidal silica used as reactant.

The influence of the mechanical pressure was also investigated for samples sintered at 1900 °C without holding time. Figures 5c, 6a and 8a show the evolution of molybdenum microstructure for three different pressures, 28, 70 and 90 MPa corresponding to experiments 8, 4 and 2 in Table 1, respectively.

There is no grain growth at 28 MPa even with 30 min of holding time. So at this pressure, the grain growth mechanisms are not activated and the density is limited to  $90.7 \pm 0.2\%$  TMD. But, at and above 70 MPa pressure, the grain growth is similar and seems to be governed by the same driving forces as previously since grain growth and a non-homogeneous microstructure are observed. The density of this sample was close to  $98.2 \pm 0.2\%$  TMD.

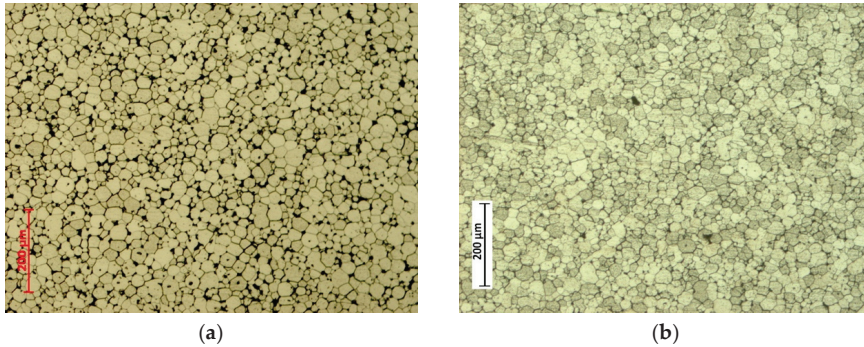


**Figure 8.** Microstructures after chemical etching of molybdenum powder (Mo-45) after sintering at 1900 °C without holding time: (a) under 28MPa and (b) under 70MPa applied at 900 °C.

However, if the pressure is not applied from the beginning of the sintering cycle but at a temperature of 900 °C, for example (i.e., corresponding to experiment 9 in Table 1), the microstructure is affected as shown in Figure 8b. Indeed, grain growth has not occurred and the microstructure is also homogeneous with a density of  $98.1 \pm 0.2\%$  TMD. Several phenomena can explain those microstructural changes, such as the effect of the mechanical pressure which induces plastic deformation (including creep) and, consequently, changes the surface contact between particles leading to a modification of the local temperature.

### 3.2. Diffusion of Carbon

During sintering at 1900 °C under 70 MPa pressure for 30 min (experiment 6 in Table 1), the presence of a carbon layer on the molybdenum surface was demonstrated (Figure 9). This phenomenon has already been highlighted by Mouawad [12]. This layer with a thickness of 100 µm was composed of molybdenum carbides, as experimentally shown by X-Ray Diffraction (XRD). These molybdenum carbides can exist in two stable forms: the  $\alpha$ -Mo<sub>2</sub>C phase and the  $\beta$ -Mo<sub>2</sub>C phase. XRD analysis confirmed that this layer was mainly composed of the hexagonal phase  $\beta$ -Mo<sub>2</sub>C (the  $\alpha$ -Mo<sub>2</sub>C phase is orthorhombic). The thickness of the carbide layers depends on how far the carbon diffuses into the molybdenum, i.e., it depends on the sintering temperature, the holding time and the pressure. However, although this layer of molybdenum carbide leads to a hardness higher than a sample without it, it has proved to be harmful since it is very brittle, which does favor some mechanical properties such as ductility.

The formation of this carbide layer is mainly due to the presence of the graphite foil in contact with the sample and of the SPS chamber environment which is super-saturated with carbon (from the dies, spacers). In order to prevent carbon diffusion, the graphite foil located on the inner part of the die was coated with a boron nitride spray to create a chemical barrier. It also enhances the passage of the electric current inside the sample. However, as it is necessary to preserve the passage of the current within the sample, it is therefore not possible to deposit boron nitride on the surface of each punch. It is difficult to find a pertinent way to protect molybdenum sample surfaces from the formation of this layer, which can be removed easily by sandblasting, but this causes cracking and then the spalling of the molybdenum carbide layer.

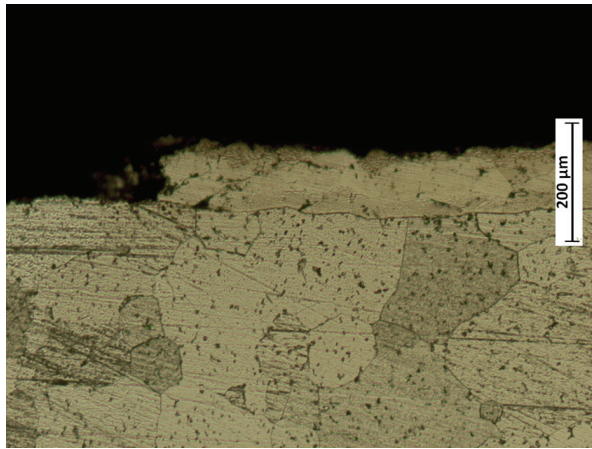


**Figure 9.** Microstructures after chemical etching of molybdenum powder after sintering at 1900 °C under 70 MPa pressure for 30 min showing the carbide layer on the surface.

Unfortunately, the diffusion of carbon is not limited to the first 200 μm of the samples. Chemical etching shows the presence of molybdenum carbides both in the bulk and at the sample periphery. A study of those carbides shows that a relationship exists between the quantity, the location and the form of those carbides and the growth of molybdenum grains during sintering. Indeed, as can be seen in Figure 10a for the case of molybdenum with no grain growth during sintering, internal diffusion of carbon from the sample surface to the bulk and the formation of carbides are not highlighted whereas when grain growth occurs (Figure 10b), carbides are present at grain boundaries.

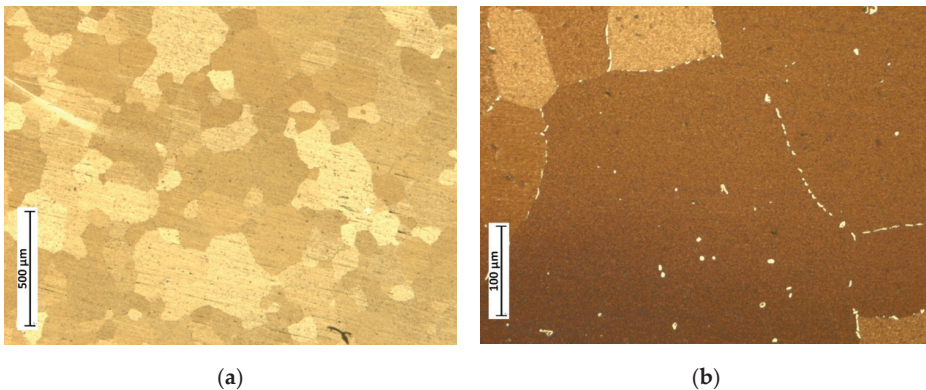


**Figure 10.** Microstructures after chemical etching of molybdenum powder sintered at 1900 °C under 70 MPa pressure: (a) without a holding time and (b) with a 30 min holding time in both cases at the sample centre.

Such carbon diffusion depends not only on the temperature, the holding time and the mechanical charge but also on the sintering environment. To reduce the presence of such carbides, it is essential either to avoid the diffusion of carbon or, if diffusion occurs, the formation of those carbides.

Our observations show that molybdenum carbides form at a high temperature, above 1500 °C, in a carbon saturated environment. At 1900 °C and without a holding time, the diffusion is minimal as is the grain growth but, in that case, the density remains low (<98% TMD ± 0.2%). A first solution is to create a barrier to the diffusion of carbon into samples. Only two materials have a melting point higher

than that of the molybdenum, namely tantalum and tungsten. Two 300 mm thick discs of tantalum were placed on either side of the powder to create a carbon diffusion barrier. This barrier enables the limitation of grain growth by reducing carbon diffusion into the molybdenum and, consequently, the formation of molybdenum carbides. This barrier is efficient because for sintering at 1900 °C under 70 MPa pressure for 30 min, there is no diffusion, no formation of carbide and no molybdenum grain growth (Figure 11).

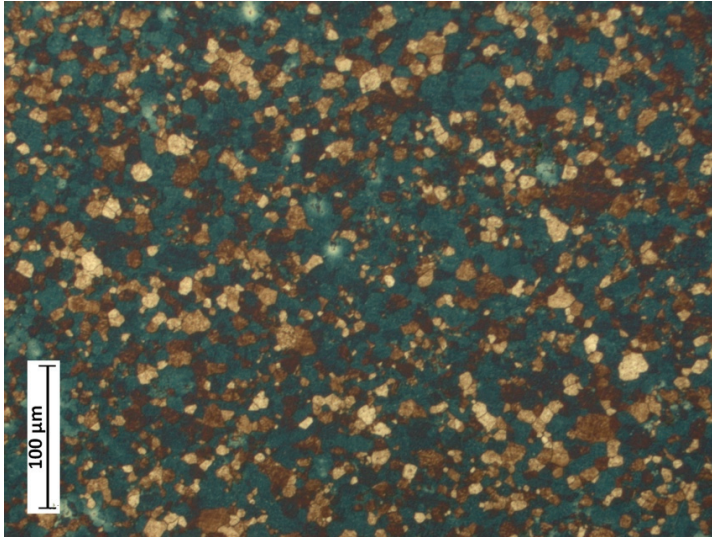


**Figure 11.** Microstructure after chemical etching of molybdenum sintered at 1900 °C under 70 MPa pressure, for a holding time of 30 min with a 3 mm tantalum barrier.

This solution shows clearly that it is essential to avoid long distance carbon diffusion. Consequently, the presence of carbon or carbides changes the grain growth mechanisms. However, this solution is expensive and non-reusable because tantalum carbides are formed, and is difficult to adapt to the sintering of complex shapes.

As the relationship between carbides and grain growth was unclear, new experiments were performed using a commercial molybdenum powder containing a high concentration of carbon. This powder is also produced by the TEKNA company (Mâcon, France) (the commercial name is Mo-45 HC) and the carbon concentration is controlled during the ICP process). This powder, which has a similar particle size as the previously studied powder (Mo-45), is composed of two phases: Mo and Mo<sub>2</sub>C. Sintering of the Mo-45HC powder at 1900 °C under 70MPa pressure for 30 min and without a tantalum diffusion barrier produces a fine microstructure (Figure 12), with a grain size close to the initial particle size of the powder grain. The molybdenum carbides do not seem to be responsible for the exaggerated grain growth but the “free” carbon plays a role in this phenomenon.



**Figure 12.** Microstructures after chemical etching of molybdenum powder with a high carbon content after sintering at 1900 °C under 70 MPa pressure for 30 min of holding.

### 3.3. Presence of Oxygen

XPS analysis performed on the molybdenum powder showed the presence of a thin layer (~4–5 nm) of molybdenum oxides at the grain surface. However, an exact measurement of the oxygen content in the bulk material after sintering remains difficult to obtain. In addition, the effect of this layer on the evolution of microstructure during sintering is uncertain. That is why, to amplify the effect of oxygen, a molybdenum powder was used with a particle size ranging from 3–7 μm (i.e., high surface area) and made without control of the oxygen concentration (produced by Alfa Aesar and named Mo-1). This powder has a smaller particle size than the previous ones, so the sintering temperature is lower. After a sintering cycle at 1750 °C under 70 MPa pressure (hold time 10 min) and using a tantalum diffusion barrier (disc of 3 mm thick), the microstructure did not show any grain growth or any molybdenum carbides. However, observation of the intergranular brittle fracture surfaces of this part (Figure 13a) shows the presence of a high concentration of spheres, composed of molybdenum oxides, i.e., MoO<sub>2</sub> and MoO<sub>3</sub>.

In order to reduce the amount of molybdenum oxides, it was decided to add a reduction stage composed of a 650 °C temperature plateau lasting 30 min in vacuum before the sintering stage. After fracture of the sample, the surfaces (Figure 13b) also are characteristic of brittle fracture but there are no oxides at the grain surface. The reduction stage in vacuum is effective since an exaggerated grain growth, with grain sizes ten times larger than the initial grain size is observed. The spherical molybdenum oxides seem to block the grain boundaries, preventing exaggerated grain growth. The elimination of these oxides releases the grain boundaries and allows grain growth to occur.

Then, in order to limit the grain growth and to avoid the use of a tantalum barrier (i.e., limit the carbon diffusion), a sintering cycle composed of an oxide reduction stage at 650 °C and sintering at a temperature lower to that relative to carbide formation (i.e., 1450 °C) was carried out. These processing conditions produce a molybdenum disc without oxides and without grain growth (Figure 13c). Even if the oxide reduction stage is efficient, the effect of temperature remains non-negligible on the grain growth and also on the density ( $95.5 \pm 0.2\%$  TMD).

At high temperature, carbon strongly reduces molybdenum oxides. The diffusion of “free” carbon from the matrix to the center of the molybdenum grains induces the reduction of the molybdenum trioxides and dioxides if these have not been eliminated during the reduction stage performed in vacuum. These reductions release the grain boundaries. Several reactions occur, as described by Hegedus and Neugebauer [24], leading to the formation of some gaseous phases (CO, CO<sub>2</sub>), which can

be observed on the fracture surfaces of the powders sintered at high temperature with a finite holding time but without a reduction stage (Figure 14).

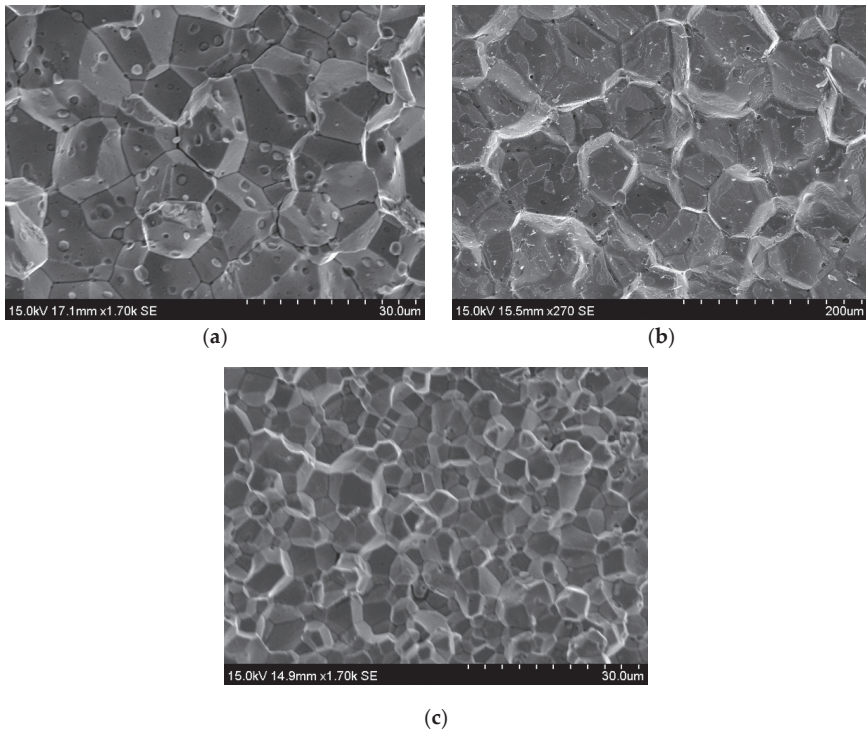


**Figure 13.** Fracture surfaces of high-oxidized sintered molybdenum: (a) at 1750 °C without reduction stage, (b) at 1750 °C and with an oxide reduction plateau at 650 °C and (c) at 1450 °C with an oxide reduction plateau at 650 °C.

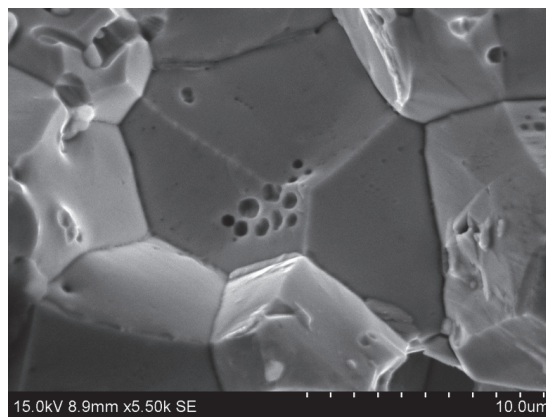


**Figure 14.** Fracture surfaces of sintered molybdenum powder at 1450 °C under 70 MPa during 30 min without reduction stage at 650 °C, showing the effect of gaseous species.

After the reduction reaction between carbon and the molybdenum oxides, the excess carbon continues to diffuse into the sample and reacts with the molybdenum to form some carbides. These carbides are responsible for the high fragility of the material. The ideal sintered molybdenum is a dense solid without oxides and carbides. For the first species, an oxide reduction stage can be implemented in the sintering cycle, but at high temperature, which is a necessary condition to obtain high density, exaggerated grain growth is observed. This heterogeneous microstructure penalizes the mechanical properties of the final product. As for the carbides, the diffusion of carbon can be limited by the use of a tantalum barrier. However, this solution is not economically or technically feasible for the production of large and complex parts. For control of both of these impurities, sintering at a temperature lower than 1500 °C seems to be a good solution but these latter are not dense ( $\sim 90\%$  TMD  $\pm 0.2\%$ ). Indeed, below this temperature, carbides do not form and if a reduction stage is implemented, the microstructure remains fine-grained without grain growth. However, it is still possible that some carbon diffusion occurs. However, the diffusion is slow, so even if it occurs, it remains limited.

In the case of the dense molybdenum produced from commercial powder made by Tekna, this sintering temperature is an interesting way of solving the carbide formation; however, its density is not sufficient (density close to  $90\%$  TMD  $\pm 0.2\%$ ), meaning another solution has to be found. Several possibilities can be envisaged, such as a powder with smaller grains or a mechanically activated powder, but in both cases, the purity of the powder remains essential.

### 3.4. Mechanical Activation

As shown previously, a sintering temperature below 1500 °C is needed to limit grain growth and carbide formation. However, a lower temperature means a lower density and usually poor mechanical properties. Mechanical activation is a means of lowering the sintering temperature by reducing the sintering activation energy.

The ball milling stage (i.e., Fritsch pulverisette 4 planetary ball mill) was carried out using hardened steel balls which are introduced inside vials made of hardened steel. Planetary ball milling is characterized by two rotations expressed in rotations per minute (rpm): (i) rotation  $\Omega$  of the plate to which the vials are fixed to obtain centrifugal acceleration, and (ii) rotation  $\omega$  of the vials in the opposite direction. Depending on the selected rotation speeds, it is possible either to promote collisions or friction (energy and frequency of shocks) [25,26]. Moreover, the vials are filled in a glove box under an argon atmosphere in order to avoid oxidation. The molybdenum powders were ground according to the condition  $\Omega/\omega/h = 250 \text{ rpm}/-250 \text{ rpm}/4 \text{ h}$  (i.e., friction mode). The size distribution of the commercial powder ranges from 10–30 to 10–75  $\mu\text{m}$  after milling confirming the formation of nanostructured agglomerates as we have seen in the case of copper [25]. On the other hand, the agglomerates are smaller because of the more fragile character of molybdenum (Figure 15).

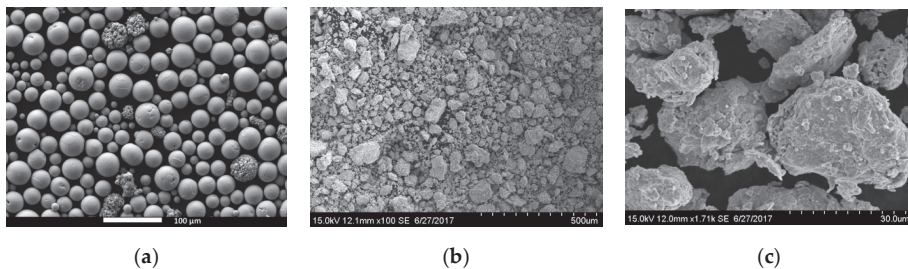


**Figure 15.** SEM microstructural analysis of commercial Mo-45 powders (a) and mechanically activated molybdenum powder agglomerates (b,c); (b) overview of the agglomerates showing that they can reach a size greater than 50  $\mu\text{m}$ , and (c) observation of mechanically activated agglomerates.

X-ray diffraction patterns of powders that were mechanically activated by milling show a significant broadening of the XRD peaks corresponding to a decrease in the size of the crystallites and an increase in structural defects when high energy milling is applied. The influence of mechanical milling on the sintering behavior is confirmed by the curves in Figure 16 which compares the shrinkage curve of unmilled commercial powder shown as a solid green line (the solid red curve corresponds to the densification speed) and that for mechanically activated powder shown as a dotted green line (the dotted red curve corresponds to the densification speed). In fact, this figure shows that sintering begins at a lower temperature, that it is more active (higher slope) and that it finishes before 1500 °C, a temperature not to be exceeded to avoid the formation of molybdenum carbides and oxides. In addition, using the master curves method Lorand [27] has shown that high-energy mechanical grinding induces a decrease in the activation energy of sintering ( $Q = 195$  kJ/mol instead of  $\sim 330$  kJ/mol) due to the presence of structural defects.

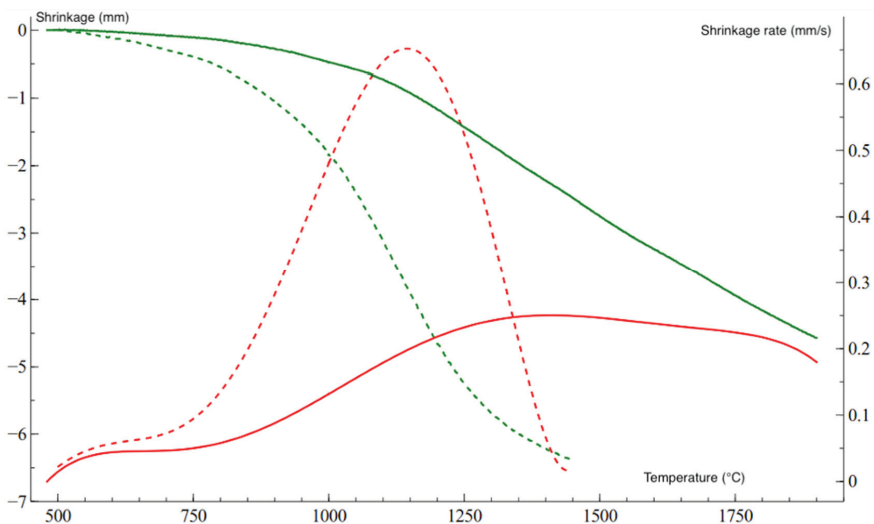


**Figure 16.** Shrinkage curves and densification speed for an unmilled Mo-45 powder (solid line, green shrinkage, red speed) and mechanically activated Mo powder (dotted line green shrinkage, speed in red). This figure clearly shows the advantage of milling to modify the sintering conditions of molybdenum powder.

SPS sintering of a mechanically activated molybdenum powder under the conditions 1450 °C, 70 MPa pressure for 30 min led to the formation of a dense molybdenum ( $98.7 \pm 0.2\%$  TMD) having a fine microstructure with no carbides or oxides. The formation of carbides is avoided if the sintering temperature is smaller than 1500 °C. However, the presence of free carbon may be interesting because this latter in low concentration enables the increasing of the Mo ductility [17,18].

Tensile tests have been carried out on samples sintered from unmilled and from mechanically activated powders (Figure 17a). The tensile test results highlight the improvement of ductility after ball milling, as a ductility of 13% was reached. We are in presence of a particular ductile failure process, encountered with BCC systems, with a cleavage fracture triggered after local plastic deformation. This cleavage process consists in plastic deformation of the crystal grains, the “ductile” aspect, followed by a transgranular failure of parallel dense atomic planes revealing facet with river appearances, the “cleavage” aspect of dense planes without dimples. This particular ductile failure process has been observed with tungsten particles, BCC as molybdenum, as reported by Lankford et al. [28]. In this work the ductile failure process has been called “transgranular shear cleavage”.

However, some pores remain after sintering (Figure 17b). These results show the efficiency of the milling process since it reduces the sintering temperature and so avoids carbide formation. This is confirmed by the ductility of the sintered molybdenum. The large difference in the elastic limit of the unmilled powder (near 500 MPa) and milled powder (about 300 MPa) compacts comes from that the grain growth during sintering of the milled powder is greater than with as received powder. Precisely, the unmilled microstructure reveals a grain size of about 10  $\mu\text{m}$ , while the grain size of the milled microstructure has been estimated at 7  $\mu\text{m}$ . Such grain size data apply to the Hall Petch relation, along with the yield stress data of Figure 17a.

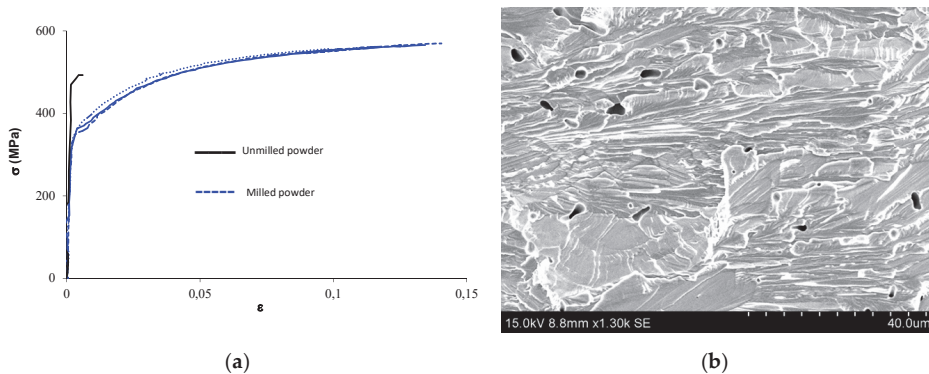


**Figure 17.** (a) True tensile stress strain curves of molybdenum samples sintered from unmilled and milled powder (b) SEM image of fracture surface of a sintered milled powder.

#### 4. Conclusions

When oxygen is present as an oxide in the bulk material, the molybdenum grain boundaries are locked, thus preventing grain growth of the molybdenum grains, an undesirable effect during sintering. In addition, this pollution is prejudicial for the purity of the final product as well as for its mechanical properties. Therefore, it is necessary to remove any trace of oxygen during sintering by application of an oxide reduction stage. This can be done by the addition of carbon via the diffusion from the graphite present in the SPS tools. However, the formation of a carbide phase is also prejudicial to molybdenum for the same reasons as the oxide. It is therefore necessary to go through an oxide reduction stage and to add protection against carbon diffusion in order to obtain dense molybdenum with a pure chemical composition. It has been shown that the solution of introducing a barrier against diffusion of carbon is not viable for SPS sintering especially in the case of complex shapes. Moreover, by eliminating oxygen, densification will inevitably lead to exaggerated grain growth. The coarser microstructure of molybdenum so formed will then affect the mechanical properties of the final part.

Sintering temperature conditions with oxide reduction and no carbon diffusion are therefore required. This can be hypothetically performed if during sintering an oxide reduction stage at 650 °C is added, and if sintering is carried out below the carbide formation temperature, i.e., at a temperature lower than 1500 °C. However, for a temperature below 1500 °C, the final product is not dense enough. The solution adopted to meet this challenge was to implement high energy mechanical milling of the molybdenum powder. SPS sintering of a mechanically activated molybdenum powder according to the conditions 1450 °C/30 min/70 MPa has been performed. This mechanical activation of molybdenum powders led to the formation of a dense product (98.7% TMD) having a fine microstructure without either carbides or oxides. A ductility close to 13% could be reached via the observation of transgranular rupture still containing a few pores resulting from mechanical activation. Our results are very encouraging, because the tensile properties  $R_m = 550$  MPa and  $A\% = 13\%$  of the raw SPS products are comparable to those obtained by Plansee for a sintered and annealed molybdenum ( $R_m = 560$  MPa and

14%). On the other hand, they are much lower than those obtained in sintered, forged and annealed products for which a ductility of 40% has been obtained [1]. Consequently, it will be essential to perform further SPS sintering investigations so as to improve the ductility, while keeping in mind that the SPS approach provides a unique advantage compared to other processes with the ability to elaborate near shape parts.

**Author Contributions:** Methodology, M.M. and F.B. (Florian Bussiere); validation, S.L. and F.D.; formal analysis, F.B. (Frédéric Bernard) and H.C.; writing—original draft preparation, M.M. and S.L.; writing—review and editing, F.D., F.B. (Frédéric Bernard) and H.C.; supervision, F.B. (Frédéric Bernard) and H.C. All authors have read and agreed to the published version of the manuscript.

**Funding:** The authors thank the Regional Council of Bourgogne Franche-Comté for funding the Ph.D. grant of Sylvain Lorand Ph-D, and the French MOD for funding the Ph.D. grant of Mathias Moser.

**Acknowledgments:** Specific thanks to Stephen Walley from Cambridge University for his valuable comments.

**Conflicts of Interest:** The authors declare no conflict of interest.

## References

1. Lichtenberger, A. Ductile behavior of some materials in the shaped charge jet. In *Metallurgical and Materials Applications of Shock-Wave and High-Strain-Rate Phenomena*; Murr, L.E., Staudhammer, K.P., Meyers, M.A., Eds.; Marcel Dekker: New York, NY, USA, 1995; pp. 463–470.
2. Kim, Y. Consolidation behavior and hardness of P/M molybdenum. *Powder Technol.* **2008**, *186*, 213–217. [[CrossRef](#)]
3. Park, H.-K.; Ryu, J.-H.; Youn, H.-J.; Yang, J.-M.; Oh, I.-H. Fabrication and property evaluation of Mo compacts for sputtering target application by spark plasma sintering process. *Mater. Trans.* **2012**, *53*, 1056–1061. [[CrossRef](#)]
4. Sakamoto, T. Sintering behavior of Mo powder compact applied SPS spark plasma sintering method. *J. Jpn. Soc. Powder Powder Metall.* **1997**, *44*, 845–850. [[CrossRef](#)]
5. Garg, P.; Park, S.-J.; German, R.M. Effect of die compaction pressure on densification behavior of molybdenum powders. *Int. J. Refract. Met. Hard Mater.* **2007**, *25*, 16–24. [[CrossRef](#)]
6. Kim, G.-S.; Kim, H.G.; Kim, D.-G.; Oh, S.-T.; Suk, M.-J.; Kim, Y.D. Densification behavior of Mo nanopowders prepared by mechanochemical processing. *J. Alloy. Compd.* **2009**, *469*, 401–405. [[CrossRef](#)]
7. Srivatsan, T.S.; Ravi, B.G.; Petraroli, M.; Sudarshan, T.S. The microhardness and microstructural characteristics of bulk molybdenum samples obtained by consolidating nanopowders by plasma pressure compaction. *Int. J. Refract. Met. Hard Mater.* **2002**, *20*, 181–186. [[CrossRef](#)]
8. Kim, Y.; Lee, S.; Noh, J.-W.; Lee, S.H.; Jeong, I.-D.; Park, S.-J. Rheological and sintering behaviors of nanostructured molybdenum powder. *Int. J. Refract. Met. Hard Mater.* **2013**, *41*, 442–448. [[CrossRef](#)]
9. Murr, L.E.; Tuominen, S.M.; Hare, A.W.; Wang, S.-H. Structure and hardness of explosively consolidated molybdenum. *Mater. Sci. Eng. A* **1983**, *57*, 107–111. [[CrossRef](#)]
10. Shankar, S.; Murr, L.E. Heat treatment of explosively consolidated molybdenum: TEM studies. *J. Mater. Sci. Lett.* **1984**, *3*, 15–17. [[CrossRef](#)]
11. Chhillar, P.; Agrawal, D.; Adair, J.H. Sintering of molybdenum metal powder using microwave energy. *Powder Metall.* **2008**, *51*, 182–187. [[CrossRef](#)]
12. Mouawad, B.; Soueidan, M.; Fabregue, D.; Buttay, C.; Bley, V.; Allard, B.; Morel, H. Full densification of Molybdenum powders using spark plasma sintering. *Metall. Mater. Trans. A* **2012**, *43*, 1–8. [[CrossRef](#)]
13. Ohser-Wiedemann, R.; Martin, U.; Seifert, H.J.; Müller, A. Densification behaviour of pure molybdenum powder by spark plasma sintering. *Int. J. Refract. Met. Hard Mater.* **2010**, *28*, 550–557. [[CrossRef](#)]
14. Huang, H.S.; Hwang, K.S. Deoxidation of molybdenum during vacuum sintering. *Metall. Mater. Trans. A* **2002**, *33*, 657–664. [[CrossRef](#)]
15. Krajnikov, A.V.; Drachinskiy, A.S.; Slyunyaev, V.N. Grain boundary segregation in recrystallized molybdenum alloys and its effect on brittle intergranular fracture. *Int. J. Refract. Met. Hard Mater.* **1992**, *11*, 175–180. [[CrossRef](#)]
16. Kumar, A.; Eyre, B.L. Grain boundary segregation and intergranular fracture in molybdenum. *Proc. R. Soc. Lond. A Math. Phys. Eng. Sci.* **1980**, *370*, 431–458.

17. Hiraoka, Y. Significant effect of carbon content in the low-temperature fracture behavior of molybdenum. *Mater. Trans. JIM* **1990**, *31*, 861–864. [[CrossRef](#)]
18. Kadokura, T.; Hiraoka, Y.; Yamamoto, Y.; Okamoto, K. Change of mechanical property and fracture mode of molybdenum by carbon addition. *Mater. Trans.* **2010**, *51*, 1296–1301. [[CrossRef](#)]
19. Hofmann, H.; Grosskopf, M.; Hofmann-Antenbrink, M.; Petzow, G. Sintering behaviour and mechanical properties of activated sintered molybdenum. *Powder Metall.* **1986**, *29*, 201–206. [[CrossRef](#)]
20. Hwang, K.S.; Huang, H.S. Identification of the segregation layer and its effects on the activated sintering and ductility of Ni-doped molybdenum. *Acta Mater.* **2003**, *51*, 3915–3926. [[CrossRef](#)]
21. Zovas, P.E.; German, R.M. Retarded grain boundary mobility in activated sintered molybdenum. *Mater. Trans. A* **1984**, *15*, 1103–1110. [[CrossRef](#)]
22. Lee, B.-K.; Oh, J.-M.; Shon, I.-J.; Kim, H.-S.; Lim, J.-W. Influence of oxygen concentration on mechanical properties of molybdenum powder during sintering. *J. Nanosci. Nanotechnol.* **2014**, *14*, 9029–9032. [[CrossRef](#)] [[PubMed](#)]
23. Naimi, F.; Ariane, M.; Barthelemy, F.; Cury, R.; Mahot, P.; Couque, H.; Bernard, F. The hybrid-SPS, an effective tool to produce large-sized parts. In *Spark Plasma Sintering: Current Status, New Developments and Challenge Dedicated to Prof. ZA. Munir*; Cao, G., Orru, R., Estournés, C., Garay, J., Eds.; Elsevier: Amsterdam, The Netherlands, 2019; pp. 301–312.
24. Hegedüs, A.J.; Neugebauer, J. Zum mechanismus der reaktion von molybdäntrioxyd mit kohlenstoff. *Z. Anorg. Allg. Chem.* **1960**, *305*, 216–226. [[CrossRef](#)]
25. Gaffet, E.; Bernard, F. Mechanically activated powder metallurgy processing: A versatile way towards nanomaterials synthesis. *Ann. Chim. Sci. Mat.* **2002**, *27*, 45–59.
26. Boytsov, O.; Gaffet, E.; Bernard, F.; Ustinov, A. Correlation between milling parameters and microstructure characteristics of nanocrystalline copper powder prepared via a high energy planetary ball mill. *J. Alloy. Compd.* **2007**, *432*, 103–110. [[CrossRef](#)]
27. Lorand, S. Maitrise De La Microstructure Du Molybdène: De La Poudre Préparée Par ICP Au Massif Fritté Par SPS. Ph.D Thesis, Université de Bourgogne, Dijon, France, November 2017.
28. Lankford, J.; Couque, H.; Bose, A.; German, R. Dynamic deformation and failure of tungsten heavy alloys. In *Tungsten and Tungsten Alloys—Recent Advances TMS Conference*; Crownson, A., Chen, E.S., Eds.; The Minerals, Metals & Materials Society: Warrendale, PA, USA, 1991; pp. 151–159.



© 2020 by the authors. Licensee MDPI, Basel, Switzerland. This article is an open access article distributed under the terms and conditions of the Creative Commons Attribution (CC BY) license (<http://creativecommons.org/licenses/by/4.0/>).



Article

# Spark Plasma Sintering as an Effective Texturing Tool for Reprocessing Recycled HDDR Nd-Fe-B Magnets with Lossless Coercivity

Awais Ikram <sup>1,2,3,\*</sup>, Muhammad Awais <sup>4</sup>, Richard Sheridan <sup>4</sup>, Allan Walton <sup>4</sup>, Spomenka Kobe <sup>2,3</sup>, Franci Pušavec <sup>1</sup> and Kristina Žužek Rožman <sup>2,3</sup>

<sup>1</sup> Faculty of Mechanical Engineering, University of Ljubljana, Aškerčeva cesta 6, SI-1000 Ljubljana, Slovenia; franci.pusavec@fs.uni-lj.si

<sup>2</sup> Department for Nanostructured Materials, Jožef Stefan Institute, Jamova 39, SI-1000 Ljubljana, Slovenia; spomenka.kobe@ijs.si (S.K.); tina.zuzek@ijs.si (K.Ž.R.)

<sup>3</sup> Jožef Stefan International Postgraduate School, Jamova 39, SI-1000 Ljubljana, Slovenia

<sup>4</sup> School of Metallurgy and Materials, University of Birmingham, Edgbaston, Birmingham B15 2TT, UK; m.awais@bham.ac.uk (M.A.); r.s.sheridan.1@bham.ac.uk (R.S.); a.walton@bham.ac.uk (A.W.)

\* Correspondence: rana.awaisikram@yahoo.com; Tel.: +386-68-67-3099

Received: 23 December 2019; Accepted: 23 March 2020; Published: 24 March 2020

**Abstract:** The low-pressure hot-deformation methodology was applied to reprocess the nanocrystalline hydrogenation–disproportionation–desorption–recombination (HDDR) Nd-Fe-B powders from end-of-life (EOL) permanent magnets’ waste to determine the mechanism of texture development and the resultant improvement in remanence (and  $BH_{max}$ ) in the recycled material. Both the hot-pressed and hot-deformed magnets produced via spark plasma sintering (SPS) were compared in terms of their magnetic properties with respect to forging pressures. Also, a comparison was established with the microstructure to cite the effectiveness of texture development at low deformation rates and pressures which is pivotal for retaining high coercivity. The hot-pressed magnets maintain the high coercivity (better than 100%) of the original recycled powder due to the control of SPS conditions. The hot deformation pressure was varied from 100–150 MPa at 750 °C processing temperature to identify the optimal texture development in the sintered HDDR Nd-Fe-B magnets. The effect of post-hot-deformation thermal treatment was also investigated, which helped in boosting the overall magnetic properties and better than the recycled feedstock. This low-pressure hot deformation process improved the remanence of the hot-pressed magnet by 11% over the starting recycled powder. The  $M_r/M_s$  ratio which was 0.5 for the hot-pressed magnets increased to 0.64 for the magnets hot-deformed at 150 MPa. Also, a 55% reduction in height of the sample was achieved with the c-axis texture, indicating approximately 23% higher remanence over the isotropic hot-pressed magnets. After hot deformation, the intrinsic coercivity ( $H_{Ci}$ ) of 960 kA/m and the remanence ( $B_r$ ) value of 1.01 T at 150 MPa is indicative that the controlled SPS reprocessing technique can prevent microstructure related losses in the magnetic properties of the recycled materials. This route also suggests that the scrap Nd-Fe-B magnets can be treated with recoverable magnetic properties subsequently via HDDR technique and controlled hot deformation with a follow-up annealing.

**Keywords:** rare earth permanent magnets; anisotropic HDDR Nd<sub>2</sub>Fe<sub>14</sub>B; recycling; spark plasma sintering; texture development; hot deformation

## 1. Introduction

The rare-earth based Nd-Fe-B permanent magnets (REPMs) are vital components for modern electronics, energy, medical imaging, and automotive industries due to their high magnetization and magnetostatic energy confined in a small volume ( $BH_{max}$ ). These excellent magnetic properties

ascend from a combination  $4f$  rare earth (RE) sublattices contributing to high magnetocrystalline anisotropy and  $3d$  transition metal (TM) sublattices return high magnetization, energy product and Curie temperature [1]. The  $BH_{max}$  is approximated to value  $J_r^2/4\mu_0$  ( $J_r$  is the remnant polarization and related to magnetic induction as:  $J = B - \mu_0 H$ , such that  $\mu_0$  is the permeability of free space), in the case when the coercivity ( $H_{Ci}$ -resistance to demagnetization) is nominally  $\frac{1}{2} J_r$  [2]. Nanocrystalline Nd-Fe-B alloys are developed to retain the high coercivity in bulk magnets by virtue of their ultrafine near single-domain sized grains. Coercivity will be very high as the reverse domains in a magnetically decoupled system will not spread easily and their movement at low external demagnetizing fields can be reduced by the pinning sites. Moreover, the probability of defects is lower in these smaller near single domain sized grains [3,4]. Nanocrystalline Nd-Fe-B alloys cannot be conventionally sintered which eludes their high coercivity exploitation because the ultrafine grain structure will undergo excessive grain coarsening at elevated sintering temperatures, resulting into coercivity losses. Due to this reason, either the bonded magnets are their primary application [5] or the rapid processing methodologies are applied, e.g., spark plasma sintering, hot deformation, and die-upsetting [1,6,7]. Previously we have demonstrated the control in SPS parameters resulted in high coercivity ( $H_{Ci} \approx 1200$  kA/m) of the recycled HDDR Nd-Fe-B-type isotropic magnets [7] and that the particle size has a critical significance on the sinterability and oxygen uptake of the recycled powder [8]. These microstructure-magnetic properties relationships were derived only for the isotropic magnets ( $M_r/M_s \leq 0.5$ ) processed by SPS, whereas the starting recycled HDDR Nd-Fe-B powder contains anisotropic powder particles. In order to enhance the remanence and the energy product, the hot deformation methodology is necessary [9] but unlike so far, the hot forging technique has not been adopted for the recycled HDDR Nd-Fe-B system. Besides oxygen content also plays an important role in the magnet reprocessing by hot deformation and since the recycled materials contain approximately two folds or higher oxygen content than the commercial grade materials, the processing route needs to be validated [8].

The deformation techniques produce a high degree of texture in the nanocrystalline Nd-Fe-B systems (melt-spun ribbons or hydrogenation–disproportionation–desorption–recombination (HDDR), making the anisotropic grains oriented towards the easy-axis of magnetization. To alter the direction of magnetization vector away from easy  $c$ -axis, a significantly larger external field is necessary in anisotropic magnets, such that the energy stored in the crystallites to work against the anisotropy increases as the elastic modulus becomes smaller in parallel direction to  $c$ -axis with more texture induced at high temperature pressure conditions [10]. The changes to the grain shape and aspect ratio alter the shape anisotropy, as the extent of magnetization due to an external field for a perfectly spherical ferromagnetic particle would be the same in any direction. However, for the non-spherical grains, the magnetization is easier in the longer direction (of higher aspect ratio) than the shorter axis. [4]. The high anisotropy is accredited mutually to the rotation and the preferred growth of  $Nd_2Fe_{14}B$  grains under pressure at elevated temperatures. Güth et al. [11] studied the anisotropy profiles of HDDR powder particles and suggested that the system demonstrated a biaxial  $\{001\}$   $(100)$  local texture (pre-dominant crystal field interactions along the  $c$ -axis  $[001]$  i.e., the easy-axis alignment and the original grains are confined along  $a$ -axis grains). This theory was later confirmed by EBSD pole figures analysis by Sepehri-Amin et al. [12] and Kim et al. [13].

In rare-earth lean systems, the stress induced crystallographic orientation of the nanocrystalline Nd-Fe-B powders by hot deformation becomes critically difficult to achieve [14]. Early work of hot deformation by Müller et al. [15] on the isotropic HDDR Nd-Fe-B powder resulted in  $B_r = 1.1$  T and  $H_{Ci} \approx 710$  kA/m. Similarly, Kirchner et al. [16] studied the effect of Nd addition during the hot deformation and reported for 14 at.% Nd in the HDDR powder, the remanence of 1.2 T and coercivity 550 kA/m can be achieved but sample cracking was still obvious after forging. Increasing the Nd content to 16 at.% prevented the HDDR samples from cracking and improved the coercivity to 750 kA/m but the  $B_r$  reduced slightly to 1 T with the higher rare-earth content. Concurrently Gopalan et al. [17] were able to increase the remanence after hot deformation from 1.07 T to 1.35 T in the precursor HDDR powder of composition  $Nd_{14.1}Fe_{78.2}Co_{1.0}B_{6.1}Cu_{0.1}Al_{0.5}$ . Likewise, Li et al. [18] obtained  $B_r = 1.09$  T

and  $BH_{max} = 114 \text{ kJ/m}^3$  after HDDR powder hot deformation through SPS, but the  $H_{Ci}$  was only 384 kA/m, due to grain shape factor and interlinked with the abnormal grain growth of  $\text{Nd}_2\text{Fe}_{14}\text{B}$  crystallites. The hot deformation temperatures were identified by Li et al. [19], achieving 69% height reduction,  $B_r = 1.22 \text{ T}$  and yet again low  $H_{Ci} = 181 \text{ kA/m}$  and  $BH_{max} = 121 \text{ kJ/m}^3$  only. This inferior coercivity in hot-deformed HDDR Nd-Fe-B magnets tends to significantly reduce the squareness of hysteresis and lowers the  $BH_{max}$  values, even after high deformation ratio; effectively rendering such magnets unsuitable for commercial applications [9,19]. Concurrently no previous report cited the hot deformation-based reprocessing of the recycled Nd-Fe-B alloys to the extent of our literature review, but the strategic task is to revitalize the recycled powders to novel magnets, retaining loop squareness, initially by gaining high  $H_{Ci}$ , and then by tackling  $B_r$  and  $BH_{max}$ .

Evidently, the hot deformation in the HDDR Nd-Fe-B system has yielded nominal improvement in texture but at the expense of coercivity. Previously, the strain rate and the degree of deformation have been considered as the controlling factors for texture development, without quantifying the terminal pressures [9]. So, in such cases, the control on resultant squareness of hysteresis loop is lost and coercivity decline is most certain [19]. The enhancement of coercivity along with  $B_r$  in hot-deformed magnets is becoming a subject of interest due to successful application of grain boundary (GB) modification of the hot deformed melt-spun ribbons yielded high  $B_r \approx 1.4 \text{ T}$  and  $H_{Ci} > 2000 \text{ kA/m}$  [20–32]. Similarly, in case of the fresh Nd-Fe-B HDDR system, Song et al. [33] utilized Pr-Cu low melting alloys to improve the coercivity of the hot-deformed HDDR Nd-Fe-B-type magnets to 1230 kA/m. Similarly, with the addition of up to 2 wt.% Nd-Cu alloys were reported to improve the coercivity of hot-deformed magnets to 1042 kA/m [34]. A significant improvement of 640 kA/m was also indicated after the grain boundary modification treatment of the HDDR-based Nd-Fe-B magnets with milled powder blend of  $\text{NdH}_x + \text{Cu}$  [35].

However, the primary argument in view of magnetic scrap reprocessing questioned the suitability of applying hot deformation techniques to the recycled HDDR Nd-Fe-B isotropic magnets. The existing literature on the commercial grade MF15P or high performance anisotropic HDDR Nd-Fe-B powders indicated a loss in coercivity and  $BH_{max}$  after texturing/forging and possible recovery attained only with the additional grain boundary modification treatments [9,19]. Thus, we imply this requirement in the recycled material, that retention of the coercivity and the squareness of the hysteresis loop is sustained as the texture is introduced. The experimental reported work in this manuscript is an effort to validate the relationship of texturing in the microstructure with the dependent properties to match commercial counterpart magnets.

This study answers these two queries: (a) can the recycled HDDR powder (with  $\approx 4800 \text{ ppm}$  oxygen content) be forged at lower pressures in view of the reduced total rare earth (TRE) content (below 30 wt.%) [7] and (b) if the process can be controlled to obtain the magnetic properties comparable to the precursor recycled powder (with the mechanism of texturing justified with the microstructure). Low forging pressures are suitable to retain texturing process control and the degree of deformation in order to retain the squareness of hysteresis loop and lossless coercivity. The SPS system and forging pressure was controlled in the terminal stages using a single step deformation to reduce the thickness of hot-pressed (SPS-ed isotropic) magnets. This low forging pressure at the terminal stage ( $750 \text{ }^\circ\text{C}$ ) prevents excessive cracking at the edges of the deformed magnet in rare-earth lean systems (like recycled HDDR nanocrystalline powder), rendering them useful for bulk applications after post-finishing and protective coating operations. Systematically, the effect of post-hot deformation thermal treatments on the magnetic properties was also established, which has not been investigated previously.

The development of textured recycled materials for the remanence enhancement is carried out in two steps: first, aligning the recycled powder in the applied magnetic field and then hot-pressing (SPS consolidation) to full density; secondly, hot-forging or deforming under higher pressures (100–150 MPa) with different dies and tooling to induce texture in the microstructure perpendicular to the pressing direction. Heating rate and pressure sequence during hot forging were optimized and the most suitable parameters are reported in this study. The pressure range was defined to factor the degree of deformation without compromising the coercivity, as the  $BH_{max}$  and remanence were enhanced by

low-pressure controlled hot forging. Taking pressure as a regulating factor helped us obtain texture in the bulk magnet, without exceptionally high strain rate or operating at very high forging temperatures. Therefore, the reported method can be adapted to sequentially tailor the magnetic properties of forged bulk magnets, which are better than the starting recycled HDDR Nd-Fe-B powder.

## 2. Contribution to the Field Statement

The bulk of the literature on the nanocrystalline Nd-Fe-B system has the vast majority of publications reporting melt-spun materials subjected to hot deformation. However, in this manuscript, we dealt only with the recycled HDDR Nd-Fe-B material. These two nanocrystalline Nd-Fe-B systems differ significantly and cannot be intermixed to devise results or a technological strategy. The progress of recycling with hydrogen-based technologies, like hydrogen decrepitation (HD) or hydrogenation–disproportionation–desorption–recombination (HDDR) processes is a widely applicable method for developing anisotropic and high coercivity bonded magnets with nanostructured Nd<sub>2</sub>Fe<sub>14</sub>B grains (≤400 nm) and has drawn significant attention for the end-of-life scrap processing. The melt-spun ribbons as produced are never anisotropic and their grain size is less than 100 nm on average, such that hot-pressing results in exceptionally good magnetic properties. On the contrary, the remanence and maximum energy products are limited due to the isotropic nature of ribbons or pressed magnets. This makes a three-step process to develop anisotropy in melt-spun ribbons. Evidently, no method has ever been reported previously on the recycled HDDR Nd-Fe-B system to develop bulk anisotropic magnets.

The microstructure—i.e., nanocrystalline grain size, phase boundaries, and particle interface—is completely different in melt-spun ribbons and HDDR Nd-Fe-B and as a general comparison commercial, MQU-F grade melt-spun ribbons have  $H_{Ci} \approx 1560$  kA/m and  $B_r = 0.6$  T (isotropic flakes) while the commercial HDDR MF-15P powder has  $H_{Ci} \approx 1100$  kA/m and  $B_r = 1.35$  T (anisotropic powder). The mechanism of sintering, grain growth kinetics, grain morphology, grain boundary structure, and derivative magnetic properties thus are very different for the melt-spun ribbons and the HDDR Nd-Fe-B.

To the best of our knowledge, to date, there is not a single report on the hot deformation of the recycled HDDR Nd-Fe-B. Previously McGuinness et al. [9] and Li et al. [19] worked on the hot deformation of fresh HDDR Nd-Fe-B alloys, but their reported magnetic properties ( $BH_{max}$  and  $H_{Ci}$ ) are comparably inferior to our recycled material system. When we compare these reports to our previous publications, the remanence values are in the range of 0.7–0.8 T, returning  $M_r/M_S$  ratio  $\approx 0.5$  which indicates the isotropic nature of high coercivity magnets. After hot forging and 55% deformation ratio, we improved the remanence to 1.01 T which is  $\geq 23\%$  better than these isotropic magnets and subsequently  $M_r/M_S$  ratio improved to 0.64, indicating the production of anisotropic magnets. Additionally, the impact of thermal treatments on the microstructure and resultant magnetic properties has never been studied after the hot deformation of either commercial or recycled HDDR Nd-Fe-B system. This study validated these principles to devise industrial recycling and reprocessing strategy of rare-earth permanent magnets. Most importantly, we proposed a model to define the mechanism behind the improvement in the magnetic properties (simultaneously) after the thermal treatment. Hence, we believe these state-of-the-art values of remanence,  $BH_{max}$  and high coercivities warrant the recycled HDDR Nd-Fe-B system as a feasible method to recycle; and controlled hot forging can be expanded to the industrial scale for developing the texture in bulk magnets.

## 3. Materials and Methods

The recycled Nd-Fe-B powder was produced from the end-of-life (EOL) scrap magnets of composition: Nd<sub>13.4</sub>Dy<sub>0.67</sub>Fe<sub>78.6</sub>B<sub>6.19</sub>Nb<sub>0.43</sub>Al<sub>0.72</sub>, pulverized and reprocessed via the well-known dynamic hydrogenation–disproportionation–desorption–recombination (d-HDDR) method (controlled hydrogen pressure for anisotropy development in nanocrystalline Nd<sub>2</sub>Fe<sub>14</sub>B grains along c-axis by texture memory effect-TME) [36,37]. The oxygen content analysis was done with the Eltra ON 900 oxygen and nitrogen analyzer (Haan, Germany). Based on the density of elements and their

weight fractions in this composition, the theoretical density of the recycled powder was calculated as  $7.57 \pm 0.01 \text{ g/cm}^3$ . The magnetic properties of the recycled HDDR Nd-Fe-B powder were measured with the Lakeshore 7400 Series (Westerville, OH, USA) Vibrating Sample Magnetometer (VSM), capable of measurements up to 2 T applied fields.

The powder handling and sample preparation was done in controlled argon (Ar) atmosphere glove box with  $\text{O}_2$  content  $< 5 \text{ ppm}$  and  $\text{H}_2\text{O}$  content  $< 1 \text{ ppm}$ . About 3 g of the recycled HDDR Nd-Fe-B powder was poured into a 10 mm graphite dies with graphite spacers in between the solid punches at the top and bottom of the same material as the die. These powder containing dies were sealed in a vacuum bag within the glove box to avoid oxidation during further sample handling before sintering. Prior magnetic alignment with a 1.5 T applied field was carried out in the direction parallel to the pressing direction. The rapid sintering or hot-pressing operation was performed under dynamic vacuum of  $2 \times 10^{-2} \text{ mbar}$ , the graphite dies containing blends were put inside the Syntex 3000 (Fuji DR. SINTER, Saitama, Japan) SPS furnace. The sintering and hot forging pressure was regulated uniaxially with a pressure controller. The hot-pressing temperature was set to  $750 \text{ }^\circ\text{C}$  with a holding time of 1 min and the heating rate of  $700 \text{ }^\circ\text{C/min}$  with a final ramp of  $50 \text{ }^\circ\text{C/min}$  was maintained for the hot pressing. The temperature measurements were controlled by a calibrated infrared pyrometer. After the hot pressing, the samples were ground with SiC papers to remove the graphite spacers and the thickness of the cylindrical sample was reduced to 3 mm.

Hot deformation (hot forging) experiments were done also at  $700\text{--}800 \text{ }^\circ\text{C}$  for 1 min, with the 16 mm WC + Co sintered cermet dies under 200 mbar Ar (99.9% purity) atmosphere and the forging die pressure was varied from 100–150 MPa. A calibrated K-type thermocouple was inserted in the cermet die to control the hot forging processing temperatures to minimize overshooting to  $<5 \text{ }^\circ\text{C}$  at peak conditions. The SPS operation was performed under  $2 \times 10^{-2} \text{ mbar}$  dynamic vacuum. A constant pressure of 40 MPa and relatively slow heating rate of  $50 \text{ }^\circ\text{C/min}$  was maintained up to the peak forging temperature in order to avoid high current density in the cermet dies, which otherwise may induce undesirable microstructural changes (grain growth, Nd-rich GB, and oxide phase transitions) [38]. Under these optimal settings, the heating rate was kept constant until the holding temperature in the range of  $700\text{--}800 \text{ }^\circ\text{C}$  was reached, but the pressure in the final  $50 \text{ }^\circ\text{C}$  step was subsequently increased to peak conditions of 100–150 MPa within one minute. A total of 3 min were given at the maximum pressure, i.e., one minute to reach the peak temperature, another one-minute holding at this hot-deformation temperature and the final one minute when the SPS current was switched off and cooling started instantly. The z-axis movement (up–down plunge of the SPS cermet dies) was recorded (as a measure against excessive cracking). The change in initial and final thickness was measured with the Vernier calipers to calculate the degree of deformation w.r.t forging pressure and temperatures.

The demagnetization measurements of bulk samples were taken on a permeameter (Magnet-Physik Dr. Steingroever, Cologne, Germany) after initially magnetizing along the c-axis. The relative density was determined with (Exelia AG DENSITEC, Zurich, Switzerland) bulk density-meter based on Archimedes principle by submerging the SPS processed samples in silicone oil.

After the hot deformation, the thermal treatment (annealing) was carried out at  $750 \text{ }^\circ\text{C}$  within the horizontal tube furnace (Carbolite Gero Limited, Hope Valley, UK) under  $> 10^{-5} \text{ mbar}$  vacuum and a heating rate of  $50 \text{ }^\circ\text{C/min}$ . The magnetic measurements were retaken after annealing. The samples were thermally demagnetized at  $450 \text{ }^\circ\text{C}$  for 10 min in the vacuum furnace ( $>10^{-5} \text{ mbar}$ ). For the microscopic examination, the demagnetized samples were grinded by 2400 and 4000 grit size SiC papers. Final polishing was done with a  $1/4 \text{ }\mu\text{m}$  diamond paste on the velvet cloth. The microstructural analysis was performed with JEOL 7600F, a Field Emission Scanning Electron Microscope (JEOL Ltd., Tokyo Japan) with an electron energy dispersive X-ray spectroscopy (EDXS) analysis fitted with a  $20 \text{ mm}^2$  Oxford X-Max detector (Oxford Instruments, High Wycombe, UK) for chemical and elemental identification, done at 20 keV.

#### 4. Results and Discussion

Summarized in Table 1, the starting EOL magnet had  $H_{Ci} = 1170$  kA/m and  $B_r = 1.19$  T which translated to the recycled HDDR powder having  $H_{Ci} = 830$  kA/m,  $J_r = 0.9$  T,  $J_S = 1.59$  T and  $BH_{max} = 124$  kJ/m<sup>3</sup> measured using a VSM with zero self-demagnetizing factor. The VSM measurements on the EOL scrap batches processed by HDDR method are shown in Figure 1, indicate the reprocessed batches are quite similar in polarization ( $J$ ) vs. applied field ( $H$ ) response, which indicates good consistency of results and recycling repeatability.

**Table 1.** Magnetic properties of the starting Nd-Fe-B materials prior to hot deformation.

| Material Class                     | Coercivity<br>$H_{Ci}$ (kA/m) | Remanence<br>$B_r$ (T) | $BH_{max}$<br>(kJ/m <sup>3</sup> ) | $M_r/M_S$ Ratio |
|------------------------------------|-------------------------------|------------------------|------------------------------------|-----------------|
| End-of-Life (EOL) Scrap Magnet     | 1170                          | 1.19                   | 250                                | 0.74            |
| Recycled HDDR Powder               | 830                           | 0.9                    | 124                                | 0.56            |
| SPS Processed (Hot Pressed) Magnet | 938                           | 0.78                   | 100                                | 0.49            |
| Post-SPS Annealed Magnets          | 1120–1160                     | 0.79–0.8               | 100–110                            | 0.5             |

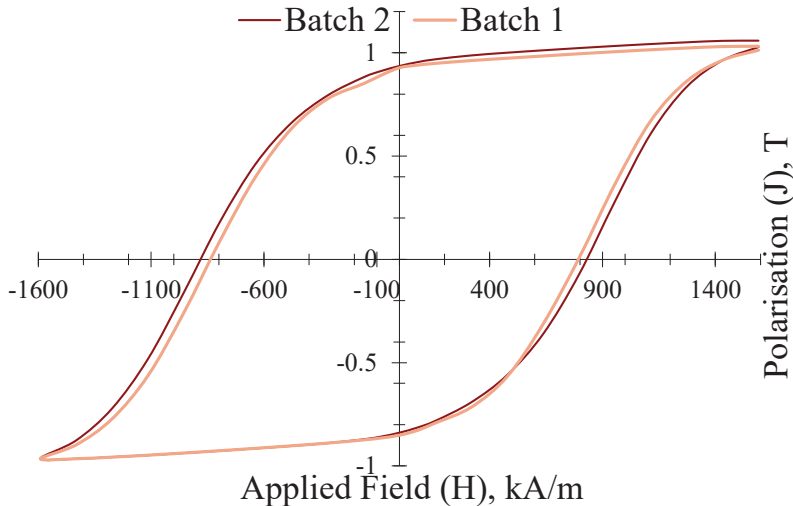


**Figure 1.** VSM analysis of recycled HDDR powder in two batches with approximately similar applied field vs. polarization response.

The oxygen content from the EOL magnet 2660 increased to 4760 ppm after the d-HDDR reprocessing in the recycled Nd-Fe-B powder [7]. Seemingly the oxygen content varies as the powder particle size is reduced below 100  $\mu\text{m}$  and it was found oxygen content nearly doubled for  $< 30$   $\mu\text{m}$  sized fractions. Therefore, the powder was not milled to prevent additional oxide phases which degrade sinterability, density, remanence (reduction in ferromagnetic phases) [8], and subsequently the texture from hot deformation [1,19]. The hot pressing conditions were kept similar to the previously reported SPS work [8] in order to achieve high coercivity and the optimal microstructure, i.e., at 750  $^{\circ}\text{C}$  for 1 min, 100 MPa uniaxial pressure and the post-SPS thermal treatment was also done for 1 h at 750  $^{\circ}\text{C}$  (above ternary transition temperature of 665  $^{\circ}\text{C}$ ) [7]. These annealed hot-pressed magnets had  $H_{Ci} \geq 1120$  kA/m and  $B_r \geq 0.79$  T, with  $M_r/M_S \approx 0.5$  indicating isotropic nature of the bulk magnets prior to hot deformation.

The average particle size of the recycled HDDR Nd-Fe-B powder (without any subsequent milling after d-HDDR) is 220  $\mu\text{m}$  and low magnification image can be seen for particles' morphology in Figure 2a. Each individually d-HDDR treated particles contains 240–400 nm sized  $\text{Nd}_2\text{Fe}_{14}\text{B}$  grains separated by thin Nd-rich phase (as in Figure 2b), which is discontinuous and non-uniformly distributed in the

microstructure of the recycled material as previously reported [7]. The effect of other elements in the composition of the HDDR powder (Dy, Nb, and Al) were also explained by Ikram et al. [7] to lower the eutectic transition temperature, such that Al is responsible for low temperature interactions (477 °C) with Nd/Dy at the Nd-rich grain boundary interface. The trace amount of Al in the composition stabilizes the  $\text{Nd}_2\text{Fe}_{14}\text{B}$  grain morphology and increasing the coercivity. The addition of Al in the HDDR powder has also been suggested to reduce the melting temperature of the RE-rich grain boundary phase [1,3]. The heavy rare-earth elements—such as Dy, Tb, Ho, etc.—are added as dopants to increase the coercivity and high temperature stability of the Nd-Fe-B magnets [2]. Whereas Nb is reported to form the  $\text{NbFe}_2$  *Laves* phase, which is finely dispersed in the nanocrystalline  $\text{Nd}_2\text{Fe}_{14}\text{B}$  matrix. The *Laves* phase does not contribute detrimentally to the magnetic properties of the HDDR Nd-Fe-B during SPS consolidation or hot pressing, as they scavenge the additional soft ferromagnetic  $\alpha$ -Fe during the recombination stage, which is necessary for retaining high coercivity in the HDDR system [7]. In a similar sense, the *Laves* phases are not anticipated to have deleterious effects during the hot deformation. The detailed phase analysis of the recycled HDDR powder is also presented in the preceding studies on explaining the oxygen content relationship to the particle size, microstructural changes, and sinterability [8].

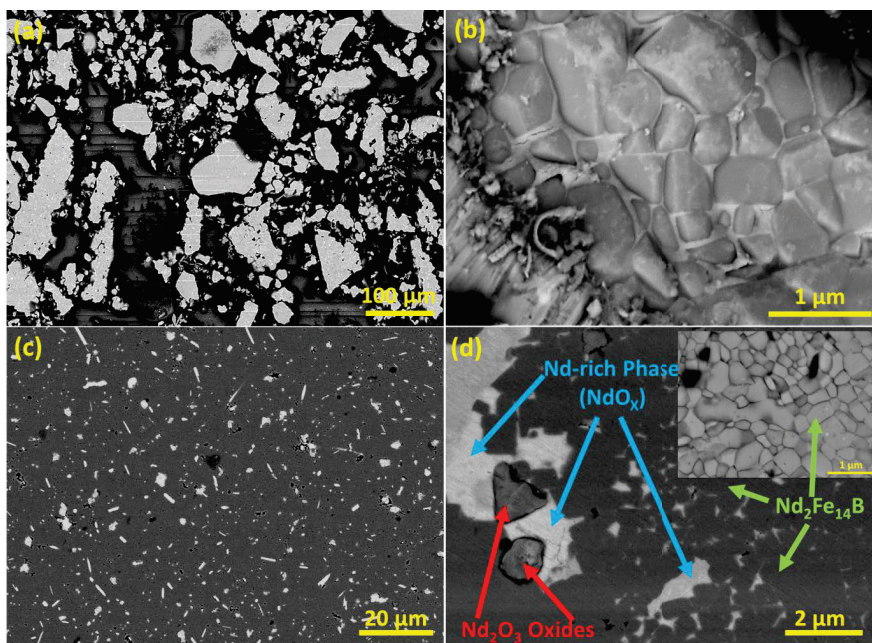


**Figure 2.** Backscattered electron (BSE) scanning electron microscope analysis of: (a) the recycled HDDR Nd-Fe-B powder particles of average 220  $\mu\text{m}$  size and (b) fractal image at 20,000 $\times$  magnification of approximately 400 nm sized  $\text{Nd}_2\text{Fe}_{14}\text{B}$  grains within each powder particle, (c) optimally hot pressed and fully dense recycled powder processed at 750 °C, (d) high magnification image of the hot pressed annealed sample showing constituent phases of different contrasts and inset showing submicron  $\text{Nd}_2\text{Fe}_{14}\text{B}$  grains exposed by etching with 3 M HCl and Cyphos ionic solution.

The microstructure of the 750 °C hot pressed sample is quite similar to the recycled HDDR powder (Figure 2c). It confirms that these conditions are suitable for attaining fully dense and high coercivity submicron sized  $\text{Nd}_2\text{Fe}_{14}\text{B}$  grains by restricting their exaggerated grain growth and avoiding unnecessary transformation of the Nd-rich phase to Nd-oxides at elevated temperatures, as observed in the inset of Figure 2d. The backscattered electron imaging (presented in Figure 2d) provides the contrast to identify different phases in the complex microstructure of HDDR Nd-Fe-B system with grey

matrix phase of submicron sized body centered tetragonal (bct)  $\text{Nd}_2\text{Fe}_{14}\text{B}$  grains,  $\text{Nd}_2\text{O}_3$  type oxides (cubic or hcp), and the bright intergranular Nd-rich phase (fcc-Nd or  $\text{NdO}_x$  type), which matches the previous reports [7,8]. The dark spots in the vicinity of matrix grains and triple pockets are pores.

The hot deformation at 100 MPa and temperature of 650 °C (below the ternary transition temperature of 665 °C [7], results not shown here) yielded  $H_{Ci} = 683$  kA/m and  $J_r = 0.64$  T ( $BH_{max} = 55$  kJ/m<sup>3</sup>) only. The remanence obtained in this case was significantly lower than the starting recycled powder. Therefore, in order to obtain better texturing in the hot-pressed samples, the temperature range was selected above this ternary transition temperature. Therefore, the hot deformation experiments were further performed at 100–150 MPa in the range of 700–800 °C. Further hot deformation temperatures higher than 800 °C, were not adapted in view of grain growth of the equiaxed and planer deformed grains which severely degrade the coercivity [14,19]. After hot deformation, these forged samples were subsequently annealed under vacuum at 750 °C for 1 h to recover the magnetic properties following strain relaxation and Nd-rich phase redistribution. Prolonging the hot forging to more than 1 min was found to have a detrimental effect on reprocessing of the HDDR Nd-Fe-B samples; therefore, further experiments were not evaluated beyond the optimized conditions.

For the hot deformation at 100 MPa pressure, the starting fully dense hot-pressed magnet after the thermal treatment had  $H_{Ci} \approx 1120$  kA/m,  $J_r = 0.8$  T and  $BH_{max} = 110$  kJ/m<sup>3</sup>. Figure 3 illustrates the polarization ( $J$ ) vs applied magnetic field ( $H$ ) results of hot deformed samples at working pressures of 100 and 150 MPa in the range of 700–800 °C, with the hold time of 1 min only. In the first case when the hot deformation pressure was 100 MPa, holding at 700 °C yielded  $J_r = 0.83$  T and  $H_{Ci} = 930$  kA/m, which indicates weak texturing for this applied pressure and low temperatures. The holding temperature of 750 °C resulted in  $J_r = 0.87$  T and  $H_{Ci} = 690$  kA/m after hot forging. The  $J_r$  increased to 0.89 T and  $H_{Ci}$  was 754 kA/m when deformed at 800 °C under 100 MPa pressure. A slightly higher temperature promotes annihilation of pores and nominal grain growth, which indicates that the optimally forged microstructure is developed in 800 °C, 100 MPa conditions (above the ternary transition temperature).

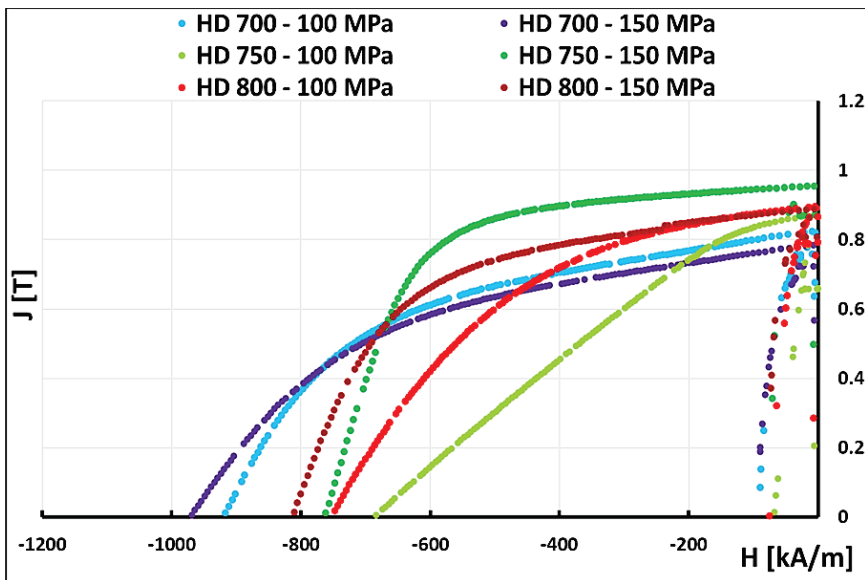


Figure 3. Comparison of the magnetic properties after hot deformation at 100 and 150 MPa.

At 700 °C, the onset of ternary transition is not complete yet, so the hot-forged samples retain the high coercivity of hot-pressed samples and the induced texture is very marginal in 100 and 150 MPa condition.

Comparing these findings with previous results on SPS processing, this slower ramp rate means low thermal stresses in the sample and  $H_{Ci}$  results are consistent with SPS reprocessing experiments [7].

As illustrated in Figure 3, by the application of higher hot deformation pressure at 150 MPa, the  $J_r$  increased in case of 750 °C sample to 0.96 T. On the contrary, at 800 °C, the remanence improvement over the 100 MPa forging was not observed with a similar value of  $J_r = 0.89$  T, possibly due to edging over the  $Nd_2Fe_{14}B$  grain growth regime at elevated temperature-pressure conditions [7,19,39]. The  $H_{Ci}$  in 150 MPa forging conditions followed a similar trend to 100 MPa samples, peaking at 990 kA/m at 700 °C to 767 kA/m at 750 °C and 817 kA/m at 800 °C. This improvement in the coercivity with temperature may be explained by the redistribution of the Nd-rich phase at the GBs and interfaces. The higher temperature and pressure conditions significantly reduce the porosity, so the Nd-rich phase achieves high wettability and transuses between the nanocrystalline grains via capillary action and compressing forces, resulting in coercivity improvement with the temperature at 150 MPa. The low forging pressure condition are appropriate to attain control in texturing and the degree of deformation, which resulted into better squareness of hysteresis loop and high coercivity. The controlled forging pressure was applied in a single step deformation in the terminal stage to reduce the thickness of hot-pressed (SPS-ed isotropic) magnets. This low pressure in the final bulk deformation stage (750 °C) prevented excessive cracking at the edges of the deformed magnet. Clearly, this approach is more suitable in rare-earth lean systems (e.g., recycled HDDR nanocrystalline powder).

The magnetic properties with post-hot deformation thermal treatment at 750 °C for 1 h in a comparative plot for all temperature regime (700–800 °C) is shown in Figure 4 and indicates the optimal results (in  $H_{Ci}$  and  $B_r$ , better than starting recycled powder) were obtained at 750 °C hot forging conditions. For the thermally treated samples forged at 100 MPa, the  $H_{Ci}$  improved for 750 and 800 °C which can be attributed to redistribution of intergranular phase and relaxation of deformation stresses. At 800 °C, 100 MPa, the range of improvement is lower than 750 °C, which can be explained with a possible grain growth in parallel and perpendicular directions as not enough room for redistribution may be available in the former case. For hot deformation at 700 °C, 100 MPa, the sample was characterized with surface cracking which may generate voids and dislocations under deformation. The hot-pressed sample had  $H_{Ci} > 1120$  kA/m which dropped to 930 kA/m after hot forging and slightly more to  $\approx 900$  kA/m with annealing. The slight decline in  $H_{Ci}$  after annealing can be attributed to inadequate redistribution of the Nd-rich phase below 746 °C (completion of ternary transition) into isolated voids that will not fully consolidate [7]. However, the remanence for all samples forged at 100 MPa pressure increased with the thermal treatments, as illustrated in Figure 4.

In the case of 150 MPa samples annealed at 750 °C, 1 h, the  $H_{Ci}$  increased subsequently for all the samples: 700 °C ( $H_{Ci} = 1007$  kA/m), 750 °C ( $H_{Ci} = 960$  kA/m), and very marginal for 800 °C sample ( $H_{Ci} = 820$  kA/m). This is due to the Nd-rich phase experiencing prominent wettability and high compressing forces during the forging stage at 800 °C, 150 MPa. Therefore, the liquid phase has already diffused (redistributed) along the grain boundary of the particles and between the nanocrystalline grains via pressure-assisted capillary action. Whereas, the 750 °C in both pressure ranges gained 200–350 kA/m coercivity improvement by thermal treatment because the Nd-rich phase was not uniformly redistributed during the slower ramp rate of 50 °C/min during the forging stage. The pressure assisted coalescence of microstructure at 50 °C/min effectively diffused the Nd-rich phase to the grain boundary regions, but at higher temperatures, it assists in grain growth [7]. The  $J_r$  of 150 MPa forging condition increased subsequently for the lower temperature samples, i.e., 700 °C (0.9 T) and 750 °C (1.01 T) after the thermal treatment. However, the remanence improvement was insignificant after the thermal treatment for 800 °C sample (0.89  $\rightarrow$  0.9 T), which as previously explained is due to the completion of pressure-assisted coalescence and Nd-rich phase diffusion during forging at elevated temperatures [19]. This mild increment in  $J_r$  can be related to the relaxation of the processing stresses [7].

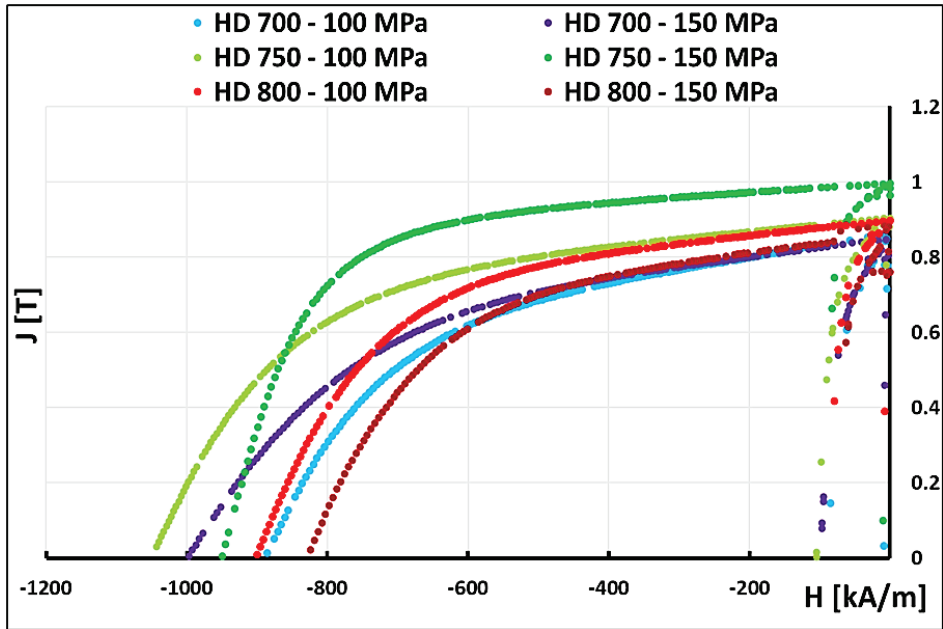


**Figure 4.** Comparative augmentation of magnetic properties of hot forged HDDR Nd-Fe-B magnets after vacuum post-processing thermal treatment at 750 °C for 1 h.

In short under low temperatures forging, the induced texture and  $J_r$  values are low, however the coercivity is high as the microstructure may correspond to hot-pressed magnets. As the temperature is increased at 100 MPa, texture development is better as  $J_r$  tends to increase and the annealing retains higher magnetic properties. With higher pressure—i.e., 150 MPa—the texture begins to develop at lower temperatures and the recovery of properties after the thermal treatment is mild since the hot deformation has already yielded the optimal microstructure. The thermal treatment for high temperature and pressure conditions correspond to stress relieving [7,8].

Moreover, under higher temperature–pressure conditions, the larger HDDR particles are prone to rupture and cracking, which could be associated with the 800 °C, 150 MPa sample not achieving high remanence as compared to 750 °C, 150 MPa [8]. These hot deformation-annealing results are in-line with the SPS study performed on the recycled HDDR Nd-Fe-B powders [8].

The 100 MPa hot-deformation process yielded  $\approx 40\%$  height reduction at 750 °C in the sample and the magnetic properties were:  $H_{Ci} = 690$  kA/m,  $J_r = 0.87$  T, and  $BH_{max} = 99$  kJ/m<sup>3</sup>. The hot deformation is a high strain process and therefore the stresses induced during the deformation can be considered to reduce the coercivity apart from the grain elongation [15,16,19,40]. The thermal treatment subsequently was performed at 750 °C for 1 h to release the microstructure of processing stresses and to also achieve the improvement in the magnetic properties due to the redistribution of the Nd-rich phase and the restructuring the surfaces of Nd<sub>2</sub>Fe<sub>14</sub>B matrix grain to accommodate the intergranular phase upon solidification [7]. Thus, after the heat treatment, the magnetic properties of 100 MPa hot forged sample improved to  $H_{Ci} \approx 1060$  kA/m,  $J_r = 0.91$  T, and  $BH_{max} = 144$  kJ/m<sup>3</sup>, as shown in Figure 5a and indicates a 12% improvement in remanence over the hot-pressed magnet at 0.79 T.

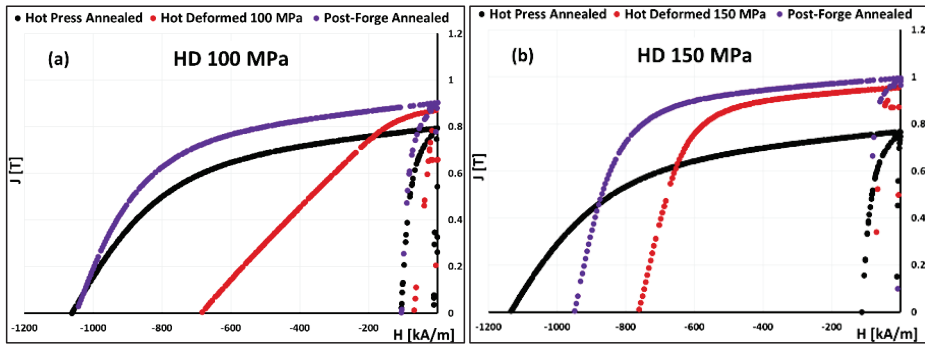


**Figure 5.** Comparison of the magnetic properties of recycled HDDR Nd-Fe-B based magnets optimally hot deformed at 750 °C under different forging pressures: (a) at 100 MPa and (b) 150 MPa. Plot legend: hot-pressing (black), hot-deformation (red), and post hot-deformation thermal treatment (purple).

Similarly, the hot-deformation experiments repeated at higher pressures resulted in better remanence than 100 MPa samples or hot-pressed magnets. The measured magnetic properties for the 750 °C, 150 MPa hot-deformed sample are illustrated in Figure 5b which gives ≈23% higher remanence with post-forging thermal treatment than isotropic hot-pressed magnets and 11% over the starting recycled anisotropic HDDR Nd-Fe-B powder. The heating rate was kept constant to 50 °C/min and during the final 3 min, the pressure was consequently maintained at 150 MPa in the second instance. The hot deformation pressure was increased rapidly from 40 MPa at 700 °C to 150 MPa at 750 °C within one minute to maximize the strain rate since a lower strain rate at high temperatures can cause grain coarsening as the deformation time is extended and the degree of alignment of the fine grains gets disturbed from the available Gibbs surface free (thermal) energy to undergo coarsening [14]. The magnetic properties of the starting hot-pressed magnet were:  $H_{Ci} \approx 1157$  kA/m,  $J_r = 0.79$  T, and  $BH_{max} = 103$  kJ/m<sup>3</sup>. The hot deformation at 150 MPa resulted in remanence enhancement and up to 55% height reduction. Therefore, the magnetic properties were measured to be:  $H_{Ci} \approx 770$  kA/m,  $J_r = 0.96$  T and  $BH_{max} = 165$  kJ/m<sup>3</sup>. Subsequently, the thermal treatment improved the overall magnetic properties and squareness of the loop in the hot-deformed magnet forged at 150 MPa, which were:  $H_{Ci} = 960$  kA/m,  $J_r = 1.01$  T, and  $BH_{max} = 180$  kJ/m<sup>3</sup>. In comparison, Li et al. [19] attained up to 69% height reduction with  $B_r = 1.22$  T and  $H_{Ci} = 181$  kA/m only from the fresh HDDR powder (possibly high degree of grain growth or hot forging stresses), measured parallel to the pressing direction.

In order to explain the behavior of remanence enhancement after annealing, we can systematically relate it according to the relationship of remanent magnetization [41]

$$M_r = A(1 - \beta) \frac{d}{d_0} \cos \theta M_s \tag{1}$$

In Equation (1),  $A$  denotes the positive parallel domains prior to the magnetic alignment,  $(1 - \beta)$  represents the volume fraction of hard magnetic phase (Nd<sub>2</sub>Fe<sub>14</sub>B in this case),  $d_0$  is theoretical density,  $d$  shows experimental density, the degree of orientation or texture is indicated by  $\cos \theta$  and  $M_s$  is the saturation magnetization. Therefore, a higher  $A$  factor indicates a low number of reverse magnetized domains in the system after annealing, as the  $H_{Ci}$  tends to increase as well due to microstructural factors (grain shape, morphology, stress relief, non-ferromagnetic grain boundary widening/decoupling effect, pinning field enhancement, and redistribution of Nd-rich phase). Moreover, no additional non-ferromagnetic additives were made part of hot-forging experiments, so  $A$  and  $\beta$  are not the influencing factors in hot deformation from Equation (1). Similarly, the densities of hot-forged and hot-pressed samples are nearly the same (99% of theoretical values, i.e., 7.57 g/cm<sup>3</sup>), so they are not affecting the remanence after thermal treatments either. The saturation magnetization ( $M_s$ ) remains largely unchanged before the HDDR reprocessing, hot pressing/deformation and subsequently annealing at 750 °C, 1 h. Therefore,

a 5% improvement in remanence from 0.96 to 1.01 T is invariably linked to the degree of texturing perpendicular to the pressing direction which tends to get reduced subsequently after the thermal treatment. The microstructure composed of highly textured Nd<sub>2</sub>Fe<sub>14</sub>B grains is beneficial for preferential grain growth during hot deformation and which will impart favorable remanence enhancement. In the case of nanocrystalline melt-spun ribbons, Wang et al. [41] identified with EBSD that the texture in platelet shaped layers on the basal plane was enhanced by increasing the annealing time. Moreover, the oriented platelet grains, although followed inhomogeneous grain growth pattern but suppressed the abnormal grain growth of non-aligned coarse grains and the number of mis-oriented grains decreased after annealing. Although EBSD was out of the scope of this research but the model from Equation (1) advocate the degree of orientation  $\overline{\cos \theta}$  of Nd<sub>2</sub>Fe<sub>14</sub>B hard phase grain tends to increase after the thermal treatment due to grain surface restructuring (both aligned and coarse non-aligned grains), besides relaxation of the forging stresses is also a contributing factor. Since the thermal treatments were performed above the ternary transition temperature of 665 °C, it may also be expected that the intergranular phases experience non-ferromagnetic transformations, which effectively improves the localized exchange decoupling behavior [41–44], however, such a study has not been proven on the HDDR Nd-Fe-B system.

In Nd-lean HDDR powder (e.g., recycled), the stress induced crystallographic orientation of the nanocrystalline grains by hot deformation is difficult and can only be achieved by critically controlling the forging parameters coupled with stress-relief thermal treatments. The applicable pressure of 150 MPa was in a sense limit for the operation mode and a further increase was not possible on this system. Therefore, from the comparison of 100 and 150 MPa range, the improvement (10%) is evident at 0.1 T approximately for 50 MPa increase. Thereby, if the system allowed hot deformation up to 500 MPa, the recycled HDDR powder is capable of reaching the remanence values much higher than these obtained but at a severe toll on coercivity as previous studies have shown for height reductions greater than 50% [17,45,46].

The cross sections of hot deformed magnets prepared at 750 °C were characterized for their microstructure by HR-SEM in backscattered electron imaging mode as shown in Figure 6. The pressing direction in each case is indicated by the arrows. As clearly seen from Figure 6a, when the hot deformation pressure is low at 100 MPa only, the microstructure is similar to the initial recycled HDDR Nd-Fe-B powder or the hot-pressed (optimally SPS-ed) samples in Figure 2. The equiaxed and the platelet-shaped grains both coexist with a poor degree of alignment due to inadequate deformation as marked with the red arrows in Figure 6a. Apart from only a few grains, the majority of the Nd<sub>2</sub>Fe<sub>14</sub>B grains are not aligned after hot deformation with the pressing direction, as represented in Figure 6b. This suggests incomplete hot-deformation or the lack of uniform texture in the sample. The matrix grains are also not excessively deformed (Figure 6b), which is the reason for higher coercivity than the starting material. After the thermal treatment, we can expect the relaxation of deformation stresses, which improved the overall magnetic properties.

In the case of hot deformation at 150 MPa pressure, the microstructure in Figure 6c is more appropriately textured and several grains are deformed perpendicular to the pressing direction which resulted in higher  $B_r$ . In this case, the two-zone microstructure is not distinguishable as clearly the grains are suitably deformed when magnified in Figure 6d with the pressing direction. At 750 °C forging temperature, overall limited grain growth in equiaxed manner or perpendicular to the pressing direction was observed which is suitable to conserve the magnetic properties of the starting recycled powder. Higher forging pressure resulted in a larger degree of deformation and thereby improvement in the texture is apparent. The very high degree of deformation (above 80%) results in nanocrystalline grains elongated beyond > 1 μm size [14,15]. The elongation of matrix grains is also considered as grain growth and consequently, the demagnetizing field will be higher on severely deformed grain surfaces, so the coercivity starts to decrease as grains begin to grow, but more importantly with higher percentage reduction in height, the deformation stresses on the microstructure are higher, which degrade the  $H_{Cj}$  [15,16,19,40]. The in-homogeneities in the crystal structure, as well as the surface imperfections generated after hot deformation, are apparently the local sites for initiating demagnetization. The defects

like irregularly shaped grains, non-ferromagnetic inclusions/grain boundaries, surface or geometric defects, etc. become the sites for local nucleation fields  $H_N$  (regions favoring magnetization reversal). These defects reduce the coercivity to

$$H_{Ci} = \alpha H_a - N_{\text{eff}} M_S \quad (2)$$

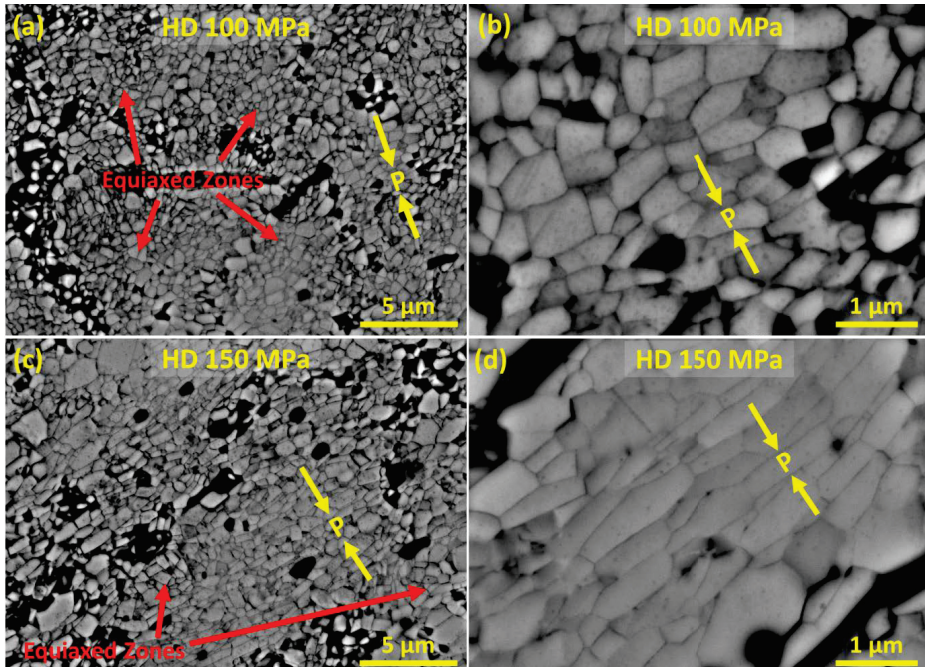


**Figure 6.** BSE micrographs of (non-annealed) hot deformed samples at (a) 100 MPa with two zone microstructure, (b) 100 MPa at high magnification indicating the pressing direction, and (c) 150 MPa with minimal equiaxed grains; and (d) 20,000× magnification of hot deformed  $\text{Nd}_2\text{Fe}_{14}\text{B}$  grains; the arrows indicate the direction of pressing with “P” during SPS hot deformation.

Here in Equation (2),  $H_a$  is the anisotropy field, the Kronmüller’s factor  $\alpha \approx 0.2\text{--}0.5$  and the effective demagnetizing factor ( $N_{\text{eff}} \approx 0.8\text{--}1.7$ ) [10]. The deformed platelet-shaped grains largely increase the  $N_{\text{eff}}$  value and the possible accelerated grain growth above 800 °C is reasoned to degrade the coercivity [14]. During the hot deformation, it has been advocated that the liquid grain boundary phase is squeezed out above the ternary transition temperature of 665 °C as it rotates and gets redistributed along with the smaller aspect ratio grain facets [47]. Therefore, the Nd-rich phase perpendicular to the pressing direction is forced out of the intergranular regions where textured parallel facing grains get into intermittent contact with each other. Therefore, the localized exchange coupling effects at these regions without the Nd-rich phase contribute to the lowering of the coercivity [17]. With the release of interfacial energy from the liquid Nd-rich phase during hot deformation, the stress concentration gets developed in the contact points and triple pockets which can lead to the formation of non-aligned grains in the vicinity thereby necessitates the annealing treatment [14]. In regions where the grain boundaries are absent, the nanocrystalline  $\text{Nd}_2\text{Fe}_{14}\text{B}$  grains can rapidly grow above the ternary transition temperature and the lattice mismatch is gradually truncated, which will also release lattice from distortion under reprocessing (thermally induced) stresses [41]. This study verified that potential is very high for the HDDR Nd-Fe-B based commercial as well as recycled materials and provides the

fundamental understanding of hot deformation application on the recycled HDDR Nd-Fe-B alloys, defining the limits for coercivity, processing conditions, annealing, and controlled texture development.

Henceforth, with the application of higher deformation pressures and the subsequent addition of low melting eutectic alloys or RE-rich nanoparticles blends, not only the remanence enhancement and  $BH_{max}$  are possible but coercivity can also be improved in low grade recycled materials. This scope of simultaneous improvement of  $H_{Ci}$  after hot deformation on the recycled HDDR Nd-Fe-B is currently under investigation and further results shall be explained in an alternate report.

## 5. Conclusions

This short study determines that the SPS hot pressed recycled HDDR Nd-Fe-B powder has coercivity values slightly higher than the commercial HDDR MF-15P powder because of the initial HDDR grain-size, microstructure preservation, and the SPS processing control. The achieved magnetic properties imply that the recycled HDDR Nd-Fe-B system can still achieve an optimal level of magnetic properties after hot deformation and without the addition of excessive Nd content, by controlling the forging parameters and supplementary thermal treatments. The application of higher pressures during hot deformation can develop texture in these originally isotropic magnets. The hot deformation pressure of 150 MPa resulted in 55% reduction in height and improvement in  $J_r$  to 0.96 T which is subsequently improved to 1.01 T ( $BH_{max} = 180 \text{ kJ/m}^3$ ) after the thermal treatment at 750 °C for 1 h, i.e.,  $\approx 11\%$  improvement over the recycled magnetic powder. This reduced pressure optimal hot deformation suitably retains high coercivity and imparts texture, which evidentially yields magnetic properties better than the starting recycled HDDR Nd-Fe-B powder.

**Author Contributions:** Conceptualization, A.I.; Methodology, A.I.; Software, A.I.; Validation, A.I. and M.A.; Formal analysis, A.I.; Investigation, A.I.; Resources, M.A., R.S. and A.W.; Data curation, A.I.; Writing—original draft preparation, A.I.; Writing—review and editing, A.I., M.A. and F.P.; Visualization, A.I.; Supervision, S.K., A.W., K.Ž.R. and F.P.; Project administration, K.Ž.R., S.K. and A.W.; Funding acquisition, S.K., A.W. and K.Ž.R. All authors have read and agreed to the published version of the manuscript.

**Funding:** The study leading to these results has received the funding from the European Community's Horizon 2020 Program (H2020/2014-2019) under grant agreement no. 674973 (MSCA-ETN DEMETER). Project website: <http://etn-demeter.eu/>. This publication reflects only the authors' research findings, which are targeted to contribute to the betterment of the global community

**Acknowledgments:** The authors aptly acknowledge the Department for Nanostructured Materials (K7 Nano) for provisioning the magnet synthesis/measurement facilities and the Center for Electron Microscopy & Microanalysis (CEMM) for scanning electron microscopy support at the Jožef Stefan Institute, Slovenia.

**Conflicts of Interest:** The authors declare no conflict of interest.

## References

1. Sugimoto, S. Current status and recent topics of rare-earth permanent magnets. *J. Phys. D Appl. Phys.* **2011**, *44*, 6. [[CrossRef](#)]
2. Gutfleisch, O. Controlling the properties of high energy density permanent magnetic materials by different processing routes. *J. Phys. D Appl. Phys.* **2000**, *33*, 16. [[CrossRef](#)]
3. Morimoto, K.; Katayama, N.; Akamine, H.; Itakura, M. Coercivity enhancement of anisotropic Dy-free Nd-Fe-B powders by conventional HDDR process. *J. Magn. Magn. Mater.* **2012**, *324*, 3723–3726. [[CrossRef](#)]
4. Coey, J.M.D. *Magnetism and Magnetic Materials*; Cambridge University Press: New York, NY, USA, 2010.
5. Kimiabeigi, M.; Sheridan, R.S.; Widmer, J.D.; Walton, A.; Farr, M.; Scholes, B.; Harris, I.R. Production and Application of HPMS Recycled Bonded Permanent Magnets for a Traction Motor Application. *IEEE Trans. Ind. Electron.* **2018**, *65*, 3795–3804. [[CrossRef](#)]
6. Nakamura, H. The current and future status of rare earth permanent magnets. *Scr. Mater.* **2018**, *154*, 273–276. [[CrossRef](#)]

7. Ikram, A.; Mehmood, M.F.; Podlogar, M.; Eldosouky, A.; Sheridan, R.S.; Awais, M.; Walton, A.; Kržmanc, M.M.; Tomše, T.; Kobe, S.; et al. The sintering mechanism of fully dense and highly coercive Nd-Fe-B magnets from the recycled HDDR powders reprocessed by spark plasma sintering. *J. Alloys Compd.* **2019**, *774*, 1195–1206. [[CrossRef](#)]
8. Ikram, A.; Mehmood, F.; Sheridan, R.S.; Awais, M.; Walton, A.; Eldosouky, A.; Šturm, S.; Kobe, S.; Rožman, K.Ž. Particle size dependent sinterability and magnetic properties of recycled HDDR Nd-Fe-B powders consolidated with spark plasma sintering. *J. Rare Earths* **2020**, *38*, 90–99. [[CrossRef](#)]
9. McGuinness, P.J.; Short, C.; Wilson, A.F.; Harris, I.R. The production and characterization of bonded, hot-pressed and die-upset HDDR magnets. *J. Alloys Compd.* **1992**, *184*, 243–255. [[CrossRef](#)]
10. Cullity, B.D.; Graham, C.D. *Introduction to Magnetic Materials*, 2nd ed.; IEEE/Wiley: Hoboken, NJ, USA, 2009.
11. Güth, K.; Woodcock, T.G.; Thielsch, J.; Schultz, L.; Gutfleisch, O. Local orientation analysis by electron backscatter diffraction in highly textured sintered, die-upset, and hydrogenation disproportionation desorption and recombination Nd-Fe-B magnets. *J. Appl. Phys.* **2011**, *109*, 07A764. [[CrossRef](#)]
12. Sepehri-Amin, H.; Ohkubo, T.; Hono, K.; Güth, K.; Gutfleisch, O. Anisotropy inducement mechanism in hydrogen disproportionation (HDDR) processed Nd-Fe-B powders. *J. Magn. Soc. Jpn.* **2014**, *38*, 37–44.
13. Kim, T.-H.; Oh, J.-S.; Cha, H.-R.; Lee, J.-G.; Kwon, H.-W.; Yang, C.-W. Direct observation of texture memory in hydrogenation-disproportionation-desorption-recombination processed Nd-Fe-B magnets using electron backscatter diffraction. *Scr. Mater.* **2016**, *115*, 6–9. [[CrossRef](#)]
14. Chen, R.J.; Wang, Z.X.; Tang, X.; Yin, W.Z.; Jin, C.X.; Ju, J.Y.; Lee, D.; Yan, A.R. Rare earth permanent magnets prepared by hot deformation process. *Chin. Phys. B* **2018**, *27*, 117504. [[CrossRef](#)]
15. Müller, K.H.; Grünberger, W.; Hinz, D.; Gebel, B.; Eckert, D.; Handstein, A. Hot deformed HDDR Nd-Fe-B permanent magnets. *Mater. Lett.* **1998**, *34*, 50–54. [[CrossRef](#)]
16. Liesert, S.; Kirchner, A.; Grünberger, W.; Handstein, A.; de Rango, P.; Fruchart, D.; Schultz, L.; Müller, K.H. Preparation of anisotropic NdFeB magnets with different Nd contents by hot deformation (die-upsetting) using hot-pressed HDDR powders. *J. Alloys Compd.* **1998**, *266*, 260–265. [[CrossRef](#)]
17. Gopalan, R.; Sepehri-Amin, H.; Suresh, K.; Ohkubo, T.; Hono, K.; Nishiuchi, T.; Nozawa, N.; Hirosawa, S. Anisotropic Nd-Fe-B nanocrystalline magnets processed by spark plasma sintering and in situ hot pressing of hydrogenation-decomposition-desorption-recombination powder. *Scr. Mater.* **2009**, *61*, 978–981. [[CrossRef](#)]
18. Li, X.; Chen, Z.; Yang, C.; Qu, S. NdFeB Magnets Prepared by Spark Plasma Sintering and Hot Deformation, Xiyou Jinshu Cailiao Yu Gongcheng/Rare. *Met. Mater. Eng.* **2013**, *42*, 194–199.
19. Li, X.-Q.; Li, L.; Hu, K.; Chen, Z.-C.; Qu, S.-G.; Yang, C. Microstructure and magnetic properties of anisotropic Nd-Fe-B magnets prepared by spark plasma sintering and hot deformation. *Trans. Nonferrous Met. Soc. China* **2014**, *24*, 3142–3151. [[CrossRef](#)]
20. Xu, X.D.; Sepehri-Amin, H.; Sasaki, T.T.; Soderžnik, M.; Tang, X.; Ohkubo, T.; Hono, K. Comparison of coercivity and squareness in hot-deformed and sintered magnets produced from a Nd-Fe-B-Cu-Ga alloy. *Scr. Mater.* **2019**, *160*, 9–14. [[CrossRef](#)]
21. Song, J.; Guo, S.; Ding, G.F.; Chen, K.; Chen, R.J.; Lee, D.; Yan, A. Boundary structure modification and coercivity enhancement of the Nd-Fe-B magnets with TbCu doping by the process of pre-sintering and hot-pressing. *J. Magn. Magn. Mater.* **2019**, *469*, 613–617. [[CrossRef](#)]
22. Soderžnik, M.; Li, J.; Liu, L.H.; Sepehri-Amin, H.; Ohkubo, T.; Sakuma, N.; Shoji, T.; Kato, A.; Schrefl, T.; Hono, K. Magnetization reversal process of anisotropic hot-deformed magnets observed by magneto-optical Kerr effect microscopy. *J. Alloys Compd.* **2019**, *771*, 51–59. [[CrossRef](#)]
23. Li, J.; Liu, L.H.; Sepehri-Amin, H.; Tang, X.; Ohkubo, T.; Sakuma, N.; Shoji, T.; Kato, A.; Schrefl, T.; Hono, K. Coercivity and its thermal stability of Nd-Fe-B hot-deformed magnets enhanced by the eutectic grain boundary diffusion process. *Acta Mater.* **2018**, *161*, 171–181. [[CrossRef](#)]
24. Castle, E.; Sheridan, R.; Zhou, W.; Grasso, S.; Walton, A.; Reece, M.J. High coercivity, anisotropic, heavy rare earth-free Nd-Fe-B by Flash Spark Plasma Sintering. *Sci. Rep.* **2017**, *7*, 11134. [[CrossRef](#)] [[PubMed](#)]
25. Kim, T.-H.; Lee, S.-R.; Yun, S.J.; Lim, S.H.; Kim, H.-J.; Lee, M.-W.; Jang, T.-S. Anisotropic diffusion mechanism in grain boundary diffusion processed Nd-Fe-B sintered magnet. *Acta Mater.* **2016**, *112*, 59–66. [[CrossRef](#)]
26. Castle, E.; Sheridan, R.; Grasso, S.; Walton, A.; Reece, M. Rapid sintering of anisotropic, nanograined Nd-Fe-B by flash-spark plasma sintering. *J. Magn. Magn. Mater.* **2016**, *417*, 279–283. [[CrossRef](#)]

27. Sepehri-Amin, H.; Liu, L.H.; Ohkubo, T.; Yano, M.; Shoji, T.; Kato, A.; Schrefl, T.; Hono, K. Microstructure and temperature dependent of coercivity of hot-deformed Nd-Fe-B magnets diffusion processed with Pr-Cu alloy. *Acta Mater.* **2015**, *99*, 297–306. [[CrossRef](#)]
28. Liu, J.; Sepehri-Amin, H.; Ohkubo, T.; Hioki, K.; Hattori, A.; Schrefl, T.; Hono, K. Grain size dependence of coercivity of hot-deformed Nd-Fe-B anisotropic magnets. *Acta Mater.* **2015**, *82*, 336–343. [[CrossRef](#)]
29. Sepehri-Amin, H.; Liu, J.; Ohkubo, T.; Hioki, K.; Hattori, A.; Hono, K. Enhancement of coercivity of hot-deformed Nd-Fe-B anisotropic magnet by low-temperature grain boundary diffusion of Nd<sub>60</sub>Dy<sub>20</sub>Cu<sub>20</sub> eutectic alloy. *Scr. Mater.* **2013**, *69*, 647–650. [[CrossRef](#)]
30. Liu, L.H.; Sepehri-Amin, H.; Ohkubo, T.; Yano, M.; Kato, A.; Sakuma, N.; Shoji, T.; Hono, K. Coercivity enhancement of hot-deformed Nd-Fe-B magnets by the eutectic grain boundary diffusion process using Nd<sub>62</sub>Dy<sub>20</sub>Al<sub>18</sub> alloy. *Scr. Mater.* **2017**, *129*, 44–47. [[CrossRef](#)]
31. Seelam, U.M.R.; Liu, L.H.; Akiya, T.; Sepehri-Amin, H.; Ohkubo, T.; Sakuma, N.; Yano, M.; Kato, A.; Hono, K. Coercivity of the Nd-Fe-B hot-deformed magnets diffusion-processed with low melting temperature glass forming alloys. *J. Magn. Magn. Mater.* **2016**, *412*, 234–242. [[CrossRef](#)]
32. Akiya, T.; Liu, J.; Sepehri-Amin, H.; Ohkubo, T.; Hioki, K.; Hattori, A.; Hono, K. High-coercivity hot-deformed Nd-Fe-B permanent magnets processed by Nd-Cu eutectic diffusion under expansion constraint. *Scr. Mater.* **2014**, *81*, 48–51. [[CrossRef](#)]
33. Song, T.; Tang, X.; Yin, W.; Chen, R.; Yan, A. Coercivity enhancement of hot-pressed magnet prepared by HDDR Nd-Fe-B powders using Pr-Cu eutectic alloys diffusion. *J. Magn. Magn. Mater.* **2019**, *471*, 105–109. [[CrossRef](#)]
34. Wang, H.H.; Chen, R.J.; Yin, W.Z.; Zhu, M.Y.; Tang, X.; Wang, Z.X.; Jin, C.X.; Ju, J.Y.; Lee, D.; Yan, A. The effect of Nd-Cu diffusion during hot pressing and hot deformation on the coercivity and the deformation ability of Nd-Fe-B HDDR magnets. *J. Magn. Magn. Mater.* **2017**, *438*, 35–40. [[CrossRef](#)]
35. Cha, H.R.; Jeon, K.W.; Yu, J.H.; Kwon, H.W.; Kim, Y.D.; Lee, J.G. Coercivity enhancement of hot-deformed Nd-Fe-B magnet by grain boundary diffusion process using the reaction of NdHX and Cu nanopowders. *J. Alloys Compd.* **2017**, *693*, 744–748. [[CrossRef](#)]
36. Sheridan, R.S.; Sillitoe, R.; Zakotnik, M.; Harris, I.R.; Williams, A. Anisotropic powder from sintered NdFeB magnets by the HDDR processing route. *J. Magn. Magn. Mater.* **2012**, *324*, 63–67. [[CrossRef](#)]
37. Sheridan, R.S.; Williams, A.J.; Harris, I.R.; Walton, A. Improved HDDR processing route for production of anisotropic powder from sintered NdFeB type magnets. *J. Magn. Magn. Mater.* **2014**, *350*, 114–118. [[CrossRef](#)]
38. Ikram, A.; Mehmood, M.F.; Samardzija, Z.; Sheridan, R.S.; Awais, M.; Walton, A.; Šturm, S.; Kobe, S.; Žužek, R.K. Coercivity Increase of the Recycled HDDR Nd-Fe-B Powders Doped with DyF<sub>3</sub> and Processed via Spark Plasma Sintering & the Effect of Thermal Treatments. *Materials (Basel)* **2019**, *12*, 1498.
39. Seelam, U.M.R.; Ohkubo, T.; Abe, T.; Hirose, S.; Hono, K. Faceted shell structure in grain boundary diffusion-processed sintered Nd-Fe-B magnets. *J. Alloys Compd.* **2014**, *617*, 884–892. [[CrossRef](#)]
40. Kirchner, A.; Grünberger, W.; Gutfleisch, O.; Neu, V.; Müller, K.H.; Schultz, L. A comparison of the magnetic properties and deformation behaviour of Nd-Fe-B magnets made from melt-spun, mechanically alloyed and HDDR powders. *J. Phys. D Appl. Phys.* **1998**, *31*, 1660–1666. [[CrossRef](#)]
41. Wang, Z.; Ju, J.; Wang, J.; Yin, W.; Chen, R.; Li, M.; Jin, C.; Tang, X.; Lee, D.; Yan, A. Magnetic Properties Improvement of Die-upset Nd-Fe-B Magnets by Dy-Cu Press Injection and Subsequent Heat Treatment. *Sci. Rep.* **2016**, *6*, 38335. [[CrossRef](#)]
42. Hono, K.; Sepehri-Amin, H. Strategy for high-coercivity Nd-Fe-B magnets. *Scr. Mater.* **2012**, *67*, 530–535. [[CrossRef](#)]
43. Kim, T.-H.; Lee, S.-R.; Lee, M.-W.; Jang, T.-S.; Kim, J.W.; Kim, Y.D.; Kim, H.-J. Dependence of magnetic, phase-transformation and microstructural characteristics on the Cu content of Nd-Fe-B sintered magnet. *Acta Mater.* **2014**, *66*, 12–21. [[CrossRef](#)]
44. Mouri, T.; Kumano, M.; Yasuda, H.Y.; Nagase, T.; Kato, R.; Nakazawa, Y.; Shimizu, H. Effect of two-stage deformation on magnetic properties of hot-deformed Nd-Fe-B permanent magnets. *Scr. Mater.* **2014**, *78–79*, 37–40. [[CrossRef](#)]
45. Sadullahoğlu, G.; Altuncvahir, B.; Okan, A.A. Investigation of Grain Boundary Compositions and Magnetic Properties of Hot-Worked Nd<sub>18</sub>Tb<sub>1</sub>Fe<sub>66.5</sub>Co<sub>5</sub>Al<sub>1.5</sub>B<sub>8</sub> Magnets. *Acta Phys. Pol. A* **2013**, *123*, 233–234. [[CrossRef](#)]

46. Liu, Z.W.; Huang, Y.L.; Hu, S.L.; Zhong, X.C.; Yu, H.Y.; Gao, X.X. Properties enhancement and recoil loop characteristics for hot deformed nanocrystalline NdFeB permanent magnets. *IOP Conf. Ser. Mater. Sci. Eng.* **2014**, *60*, 012013. [[CrossRef](#)]
47. Bance, S.; Seebacher, B.; Schrefl, T.; Exl, L.; Winklhofer, M.; Hrkac, G.; Zimanyi, G.; Shoji, T.; Yano, M.; Sakuma, N.; et al. Grain-size dependent demagnetizing factors in permanent magnets. *J. Appl. Phys.* **2014**, *116*, 233903. [[CrossRef](#)]



© 2020 by the authors. Licensee MDPI, Basel, Switzerland. This article is an open access article distributed under the terms and conditions of the Creative Commons Attribution (CC BY) license (<http://creativecommons.org/licenses/by/4.0/>).



Review

# Spark Plasma Sintering of Titanium Aluminides: A Progress Review on Processing, Structure-Property Relations, Alloy Development and Challenges

Ntebogeng F. Mogale \* and Wallace R. Matizamhuka

Department of Metallurgical Engineering, Vaal University of Technology, Vanderbijlpark 1911, South Africa; wallace@vut.ac.za

\* Correspondence: ntebogeng.mogale@yahoo.co.za

Received: 1 May 2020; Accepted: 5 June 2020; Published: 11 August 2020

**Abstract:** Titanium aluminides (TiAl) have the potential of substituting nickel-based superalloys (NBSAs) in the aerospace industries owing to their lightweight, good mechanical and oxidation properties. Functional simplicity, control of sintering parameters, exceptional sintering speeds, high reproducibility, consistency and safety are the main benefits of spark plasma sintering (SPS) over conventional methods. Though TiAl exhibit excellent high temperature properties, SPS has been employed to improve on the poor ductility at room temperature. Powder metallurgical processing techniques used to promote the formation of refined, homogeneous and contaminant-free structures, favouring improvements in ductility and other properties are discussed. This article further reviews published work on phase constituents, microstructures, alloy developments and mechanical properties of TiAl alloys produced by SPS. Finally, an overview of challenges in as far as the implementation of TiAl in industries of interest are highlighted.

**Keywords:** titanium aluminide; spark plasma sintering; microstructure; mechanical properties; alloy development

## 1. Introduction

Titanium-based intermetallics can be defined as metallic materials consisting of approximate stoichiometric ratios in ordered crystal structures [1]. These have properties such as low densities and high melting points, good high-temperature strength, resistance to oxidation and creep [2]. The research interest in intermetallics for at least the past 30 years according to Muktinutalapati & Nageswara [3] has been due to the need to replace the previously used NBSAs (8–8.5 g/cm<sup>3</sup> in density) with lower density (4–7 g/cm<sup>3</sup>) materials, saving about 55% of the weight gain of turbine engines [4].

Much attention was given to titanium (Ti) and nickel-based aluminides amongst many others. Of interest for this research work is titanium aluminides (TiAl). According to Muktinutalapati and Nageswara, intermetallics around TiAl can be classified into two-alpha ( $\alpha_2$ -Ti<sub>3</sub>Al and gamma ( $\gamma$ )-TiAl phase. The greatest disadvantage of  $\alpha_2$ -Ti<sub>3</sub>Al is poor toughness and fatigue crack growth, shifting much research and development more on  $\gamma$ -TiAl. These possess properties which include good creep and oxidation properties at elevated temperature applications, low densities (3.9–4.2 g/cm<sup>3</sup> varying with composition), high stiffness and yield strength [5].

It has been over 20 years since the successful implementation of gamma titanium aluminide ( $\gamma$ -TiAl) alloys in aerospace components produced by companies such as General Electric Aircraft Engines, Pratt and Whitney and Rolls Royce [6–8]. The alloys have been employed in various aerospace components such as rotating and static engine components used in turbines, compressors, combustors, and nozzles. Research development of such alloys over the years primarily focused on the refinement

of microstructure and improvement of properties, particularly ductility and formability, through compositional optimisations and application of various processing technologies.

Compositional variations including controlling gaseous impurities such as oxygen (O) and nitrogen (N), and the addition of chromium (Cr) and manganese (Mn) to TiAl alloys have been previously addressed with the aim of ductility improvement [9–11]. Furthermore, employing wrought processing techniques followed by post-treatments have also been extensively experimented [12–14]. However, microstructural inconsistencies resulting from solidification and phase transformations further deteriorate and scatter the mechanical properties of the alloys [15,16]. Spark plasma sintering (SPS) presents an opportunity to consolidate metallic powder materials without the deviations mentioned above. The process employs DC pulses of high intensity and pressure to achieve the required sintering temperature under a specified time. The SPS technique has been used in a large number of investigations and has advantages compared to traditional techniques such as shorter holding times, lower sintering temperatures and marked increases on the properties of materials [17–19]. This work is a summary of the progress, advances and challenges in the production and implementation of spark plasma sintered  $\gamma$ -TiAl alloys.

## 2. Powder Metallurgical Processing of $\gamma$ -TiAl Alloys

### 2.1. Gas Atomization (GA)

The current preferred method for mass production of metallic powders consolidated using various methods including SPS is GA [20,21]. Although GA is said [21] to be more costly compared to water atomization, improved yields of spherical powders are achieved aiding flowability. The conventional basic operation of gas atomisation (GA) is illustrated in Figure 1. During GA, the metal or alloy is melted inside a crucible, followed by pouring the stream of hot metal liquid and finally pulverizing using a pressurized gas jet. The solidified metal droplets are then accumulated at the powder collection chamber for collection. According to Martín et al. [21], processing parameters such as the melt temperature and flow, nozzle type and gas purity and pressure affect the powder size and quality.

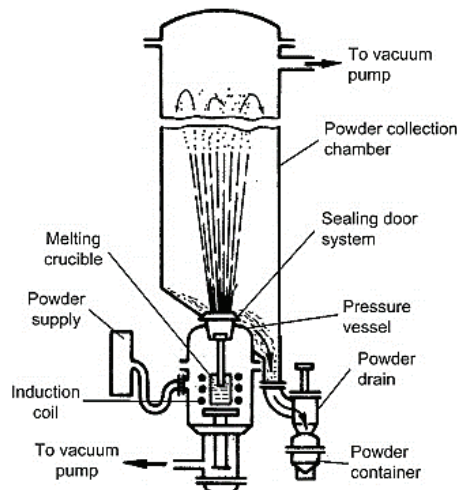


**Figure 1.** Gas atomisation (GA) schematic, reproduced from [22], with permission from Elsevier, 2019.

The production of  $\gamma$ -TiAl powders using GA is rather challenging. This can be ascribed to the high reactivity of the melt with the crucible lining material and the high impurity gas pick-up of the melt, atomized droplets and the hot powder particles [23]. As a result, cold-crucible or crucible-free

techniques such as electrode induction melting gas atomization (EIGA) and plasma melting induction guiding gas atomization (PIGA) can be employed. For further reading on these techniques, the reader is referred to [24–26].

Powder characteristics of concern during the GA production of  $\gamma$ -TiAl affecting powder quality are particle size distributions, gaseous impurity levels and cooling rates [23]. The morphology of powders produced using GA, as shown in Figure 2, is spherical despite the particle size. Spherical powders are beneficial to subsequent PM processes, promoting flowability and packing density. The level of impurity gases such as O and N in GA produced powders can impair the mechanical properties after consolidation. Furthermore, oxide or nitride layers on powder surfaces may hinder compaction [23]. Minimal gas entrapment can be achieved by using an inert gas atmosphere during powder alloy atomization and handling. Finally, GA employs high cooling rates enhancing microstructural and compositional uniformity.

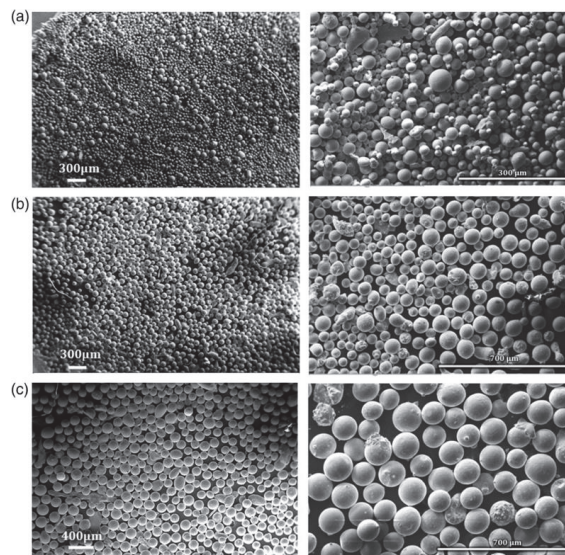


**Figure 2.** Scanning electron microscope (SEM) images of GA produced Ti4522XD powders with sizes: (a)  $d < 45 \mu\text{m}$ ; (b)  $45 \mu\text{m} < d < 100 \mu\text{m}$ ; and (c)  $100 \mu\text{m} < d < 150 \mu\text{m}$ , reproduced from [21], with permission from John Wiley and Sons, 2020.

Several studies involving the use of GA and SPS have been carried out to date [27–30]. Gu et al. [27] fabricated pre-alloyed (PA) Ti–43Al–5Nb–2V–Y (at. %) powders utilizing the PIGA technique and densified the powders at different temperatures by SPS. The morphology of the varying particle size (50–120  $\mu\text{m}$ ) PA powders was reported as spherical with satellite particles. Moreover, a cellular dendritic interior microstructure was observed, a characteristic microstructure of rapidly solidified metal droplets. In a related study, Liu and associates [28] studied the size-dependency on structural properties of a Ti–48Al–2Cr–8Nb (at. %) powder alloy produced using EIGA for PM and additive manufacturing technologies. It was found that decreasing the powder particle size decreased the content of the  $\gamma$  and increased that of  $\alpha_2$ -phase.

## 2.2. Mechanical Milling (MM)

PA powder can be effectively manufactured using MM [31]. As stated by Xiao et al., MM aids solid diffusion and rapid compound formation. In work done by Hadeif [32]; it is stated that milling includes grinding through impact, compression and attrition. During MM experiments, powders are

introduced in required proportions into hardened steel (typically tungsten carbide, stainless steel and zirconia) vial along with milling balls of a selected size. Voluntarily, a process control agent (PCA) is also added to aid in minimising cold welding and lump formation. Collisions between the wall of the vial and the contents thereof exist at high frequencies and velocities, effectively milling the powder contained [33]. Milling time and speed, vial type, milling media, ball-to-powder weight ratio (BPR), milling atmosphere and the level of vial filling are parameters affecting the ultimate powder mix constituents.

Extensive research has been devoted over the years to study the effect of the various milling parameters on the constitution of the ultimate powder mix [34,35]. Oehring et al. [36], investigated the milling process of elemental Ti–Al powder blends using detailed X-ray diffraction (XRD) analysis and found that a dual mixture of hcp solid solution and an amorphous phase in alloy Ti<sub>50</sub>Al<sub>50</sub> exist at lower milling intensities. Oehring et al. also found that energetic destabilisation of present phases occurring during milling results in the final observed intermetallic compounds. Zhang et al. [37] studied phase formation during milling of Ti–75Al powder mixtures using XRD analysis and concluded that a solid solution of Al(Ti) formed as a result diffusion of Ti into Al during the early milling stages. In addition to the study findings, an L1<sub>2</sub> ordered Al<sub>3</sub>Ti phase with an average phase grain size of 18 nm was formed with extended milling time.

Wang et al. [38] studied the effects of SPS temperature and mechanical milling treatment parameters on the phase constitution and microstructure. The as-atomised powder following SPS at 1200 °C showed microstructural inhomogeneities consisting of  $\alpha_2$  and  $\gamma$  and some lamella colonies as compared to the homogeneous, fully dense MM powder. Additionally, it was found that extended milling times and speeds during MM attribute to the uniform distribution of the phases present.

Double mechanical milling (DMM) has recently gained attention [39,40] and involves two milling stages. The initial stage normally entails mixing of the elemental powders at low speeds, followed by high-energy ball milling at higher speeds for a shorter interval. Optionally, the powder mix is removed from the vial and heat-treated in a controlled atmosphere before the final milling stage at higher speeds and longer intervals. In a study employing DMM on TiAl alloys [40], the authors reported the formation of a regular shaped powder with a particle size decrease from a maximum of 80 to 40  $\mu\text{m}$  after the final milling stage. Consequently, peak broadening was observed and can be attributed to the reactions and interdiffusion occurring between phases. In a similar study Shulong et al. [39] obtained an ultrafine regular powder morphology after DMM with sizes in the range of 20–40  $\mu\text{m}$ .

### 2.3. Mechanical Alloying (MA)

The process of mechanical alloying (MA) involves loading of PA or elemental powders inside a high energy ball mill and the usage of grinding media to repeatedly cold weld, fracture and reweld powder particles [41]. Parameters including time, speed and BPR [42] are optimised to control and balance the resultant powder particle sizes. PCA are inorganic compounds [43] often used in MA of ductile metals to prevent agglomeration of powder particles. According to Suryanarayana [41], adding 1–2 wt. % of PCA can prevent excessive cold welding or agglomeration of the individual powders on the grinding media and the milling vessel. The working principles of MA involve the excessive deformation of powder particles through work hardening and flattening of colliding or contacting ductile particles using grinding media. In addition, intermetallic compounds are refined and fractured, while oxide dispersoids comminuted.

MA has proven to be effective in the production of non-equilibrium and nanostructured TiAl alloys [44–46]. Some of the successful developments in TiAl research through MA include the ability to produce fine-grained alloys [47], although some shortcomings, such as gas contamination [48] still need to be overcome. Sim et al. [46] found that alloys sintered from a 40 h MA powder showed promising yielding and ultimate strength in compression. The reported yielding and ultimate strength values from the previous study were as high as 1644 and 2542 MPa, respectively. Failure strains at both ambient temperatures and 650 °C were 31.3% and 55.3%. Forouzanmehr and colleagues [45]

found that the milling of Ti–50Al (at. %) powder mixture formed a Ti(Al) solid solution earlier in milling, followed by a transformation of the amorphous structure to a Ti(Al) that is supersaturated with longer milling durations. Additionally, further annealing treatment for the amorphous and the supersaturated Ti(Al), formed a nanocrystalline TiAl intermetallic compound with an ultrafine grain size of ~50 nm and a microhardness value of ~11.67 GPa.

To limit elevated temperature grain growth in  $\gamma$ -TiAl and other PA powders, Bohn et al. [47] found that the addition of Si to Ti powders (resulting in precipitates of  $Ti_5(Si,Al)_3$  embedding on grain boundaries of  $\gamma$ -TiAl matrix) gave refined microstructures with a grain size ranging from 160–480 nm for the matrix and 80–190 nm for the precipitates. To produce low contaminated TiAl powder, Bhattacharya et al. [48] found planetary ball milling to have to increase O contents. At the same time, insignificant impurity levels (O pick-up of  $\approx 0.014$  wt. % and N pick-up of 0.031 wt. %) were observed in attrition milled powders. However, in both cases, the powders used were handled in a glovebox with purified Ar atmosphere.

#### 2.4. Cryomilling (CM)

Another interesting PM technique that evolved as a modification of the conventional high energy ball milling is cryomilling (CM). The process involves soaking grinding media in a cryogenic liquid (such as N) while optimising processing parameters to minimise recovery and recrystallisation, resulting in ultra-refined grain structures [49]. According to Lavernia et al., benefits of employing CM over traditional milling include the reduction of cold welding and powder agglomeration to the grinding media producing effective milling outcomes, limited powder oxidation occurrences and reduced milling times. Consolidation is required after CM processing, allowing the exploration of studies on phase and microstructural evolutions as a function of properties, comparable to those produced using conventional ball milling.

Figure 3 shows the basic setup used for CM. The apparatus involves thermocouples used to monitor the mill and ensure a constant cryogenic liquid level, thus maintaining a constant milling environment [50]. Additionally, the cryogenic liquid is in constant circulation into the mill with excess liquid drained through a particle filtering blower, enabling powder particle entrainment in the gas flow. Compatibly, the setup comprises of opening and closing valves to ease the flow of the cryogenic liquid and are monitored by temperature fluctuations above the slurry level. Some of the implemented configurations, according to Witkin & Lavernia, are 101 attritor mills used at the University of California in Davis, charging up to 1 kg of powder and the commercialised 35 kg capacity attritor mill sponsored by" Boeing's Rocketdyne division.

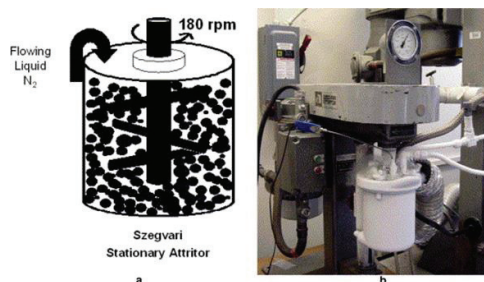


**Figure 3.** (a) Cryomilling (CM) apparatus representation; (b) a customised 500 g capacity mill in operation, reproduced from [50], with permission from Elsevier, 2006.

Several recent studies [51–54] have been devoted to understanding the processing and behaviour of nanostructured TiAl alloys produced using CM and SPS. Shanmugasundaram et al. [52], investigated the densification and microstructure of a  $\gamma$ -TiAl alloy produced using gas atomised CM powder and consolidated using SPS at 1050 and 1200 °C. CM resulted in a 100% powder yield, reduced particle

(2–50  $\mu\text{m}$ ) and crystalline sizes (40 nm). Although the alloy fully densified at 1200  $^{\circ}\text{C}$ , 8 h of CM resulted in a decrease in the sintering temperature. The obtained refined microstructure (with grain sizes of 0.9 and 0.6  $\mu\text{m}$  at 1200 and 1050  $^{\circ}\text{C}$ ) consisted of  $\gamma$  and  $\alpha_2$ , with volume fraction of the later found to be dependent on the sintering temperature and O content. Deng et al. [51] obtained an ultrafine-grained FL and near  $\gamma$  microstructure promoted by CM and varying sintering temperatures of 900, 1000 and 1100  $^{\circ}\text{C}$ , respectively. The authors found that sintering at 1000  $^{\circ}\text{C}$  produced excellent compression properties, with yield strengths as high as 1575 MPa RT and 955 MPa at 850  $^{\circ}\text{C}$ .

### 3. Powder Consolidation by SPS

#### 3.1. Basic Operating Principles

SPS, also referred to as field assisted sintering technique is a powder metallurgy (PM) method used to consolidate powders subjected to applied current and pressure [17]. As stated by Munir et al., the practice (schematically shown in Figure 4) employs uniaxial pressure and pulsed high direct current to consolidate powders. The science behind the successful consolidation of the powders is attributed to the sufficient generation of Joule heating [55], employing voltages below 10V and currents as high as 10 kA in conjunction with the electrically conductive tool materials used in the set-up. The widely used SPS technique has advantages compared to conventional manufacturing techniques such as hot-pressing, pressureless sintering, laser sintering and hot isostatic pressing (HIP). These advantages include shorter holding times, lower sintering temperatures and marked increases in the properties of materials [18,19,56].

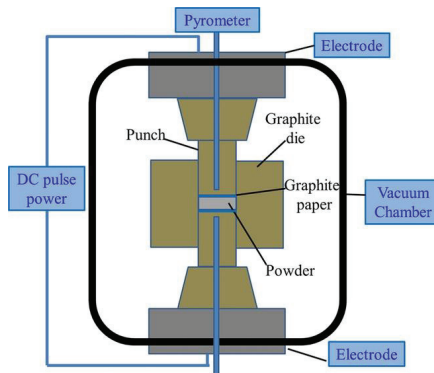


**Figure 4.** Spark plasma sintering (SPS) process representation, reproduced from [57], with permission from John Wiley and Sons, 2014.

#### 3.2. Mechanisms of Sintering in SPS

The complex mechanisms and theories involved in SPS are as a result of electrical, thermal and mechanical effects [55]. Of the vast available models and theories, the standard and accepted involves effects due to joule heating, plasma generation and electroplasticity [58,59]. According to Matizanhuka [58], the electrical effects are related to the electrical properties of the powders. Furthermore, electrically conductive powders allow smooth current flow and are heated by the “Joule effect” and transferred to the bulk of the powder by conduction. The formation of necks between the powder particles through cleaning of powder surfaces, welding and vaporization is enhanced by the electric current flow through particles when pressure is applied [60]. Additionally, the electric current pulses produced during SPS are said to accelerate the densification kinetics existing between powder particle necks. The formation of arcs and plasma between powder particles promotes localized

melting in amorphous material jet-form between spherical nanosized ceramic particles [61], through liquid wetting [62] and partial melting in W and ZrB<sub>2</sub> ceramic particles [63].

The mechanical effects promoting densification are related to the quasi-static compressive stress applied in SPS [55]. This results in better particle contact, altering the morphology and amount of contacting particles and further enhancing the existing densification kinetics related to viscous flow, lattice, and grain boundary diffusion. Alternatively, new mechanisms like grain boundary sliding or deformation plastically can be activated [64]. The most common thermal factor promoting densification during SPS is the heating rate. In the study conducted by Olevsky and colleagues [65], high heating rates reduced noncontributing surface diffusion, favoring sinterability and intensifying densification by grain boundary diffusion. Furthermore, high rates of heating were found to retard grain growth.

### 3.3. SPS Modeling for Complex-Net Shaping

Advanced nanomaterials can potentially be manufactured using SPS owing to the impressive characteristics offered by the process. These include pressures as high as 100 MPa, temperatures of up to 2500 °C, heating rates ranging up to 1000 K.min<sup>-1</sup> and pulsed electric current readings of a few thousand amperes [66]. Despite these benefits, the challenge of manufacturing complex shapes beyond the traditional 2-D parts remains. This is due to the homogeneity variations experienced during the densification of components having high thickness regions, wherein the thicker regions require more shrinkage compared to the rest of the component [66,67]. To date, various models have been employed in SPS to overcome those, as mentioned earlier. These include modified punch designs [68], controlling punch displacement through the usage of sacrificial materials [69], deformed interface approach [70], finite element method (FEM) [67,71], and the controllable interface approach [66].

Voisin et al. [68], produced two GA  $\gamma$ -TiAl alloys to the nominal composition of Ti<sub>49.92</sub>Al<sub>48</sub>W<sub>2</sub>B<sub>0.08</sub> and Ti<sub>48</sub>Al<sub>48</sub>Cr<sub>2</sub>Nb<sub>2</sub> using SPS. Difficulty was experienced in as far as shaping a blade with a thick root and a thin foil, raising the need to design a mold of graphite (in Figure 5) consisting of a multiple punch assembly, the matrix and cylindrical pieces. The FEM was later employed to control the temperature at each point in the sample [72]. An 80 mm long blade was obtained by employing models in Figure 5 and FEM. The FEM was proven [71] to be reliable for qualitative predictions of powder sample grain growth and densification kinetics in SPS with a given temperature regime.

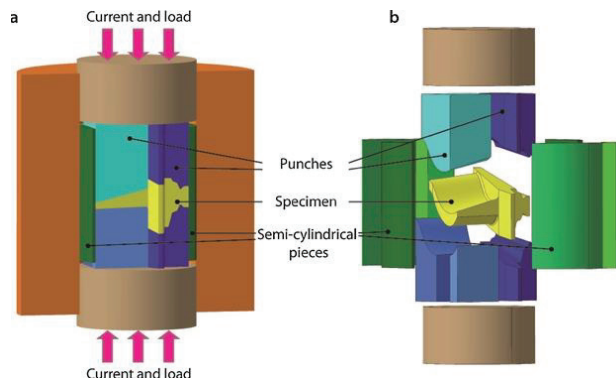


**Figure 5.** Representation of the graphite mold assembly with (a) punches in position and (b) side view of the mold, reproduced from [68], with permission from John Wiley and Sons, 2015.

Alternatively, a sacrificial material (such as in Figure 6) can be used to achieve complex part homogeneity. According to Manière and colleagues [69], this approach presents advantages such as possibilities of fully densifying parts of varying thickness complexities, even stress distributions as a result of shrinkage uniformity at all points on the sample and control over the final part shape.

Unfortunately, this approach has shortcomings related to material losses of the sacrificial component and the limitations of the number of thickness variations.

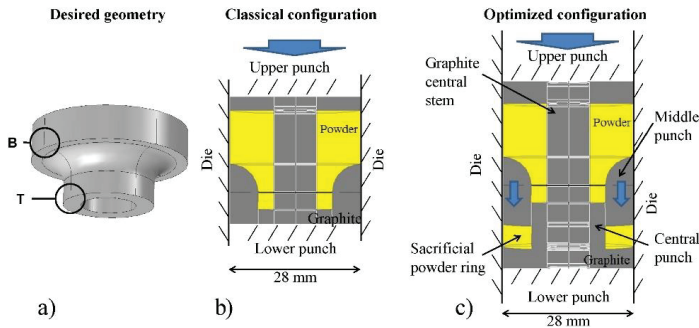


**Figure 6.** An illustration of the sacrificial material approach with (a) showing the desired geometry, (b) presenting the traditional configuration and (c) displaying the sacrificial material configuration reproduced from [69], with permission from Elsevier, 2016.

Commonly known as the "DEFORMINT" approach, the deformed interfaces method involves assembling a minimum of two porous materials (i.e., porous bodies or powder beds) separated by single or multiple interfaces [70]. Manière et al. described that the simple geometry on the outside (i.e., often cylindrical) is obtained by assembling a porous complex shape that is covered by a separation material and surrounded by an additional porous sacrificial material, that is the reverse of the initial shape. The detailed process steps for the deformed interfaces method are shown in Figure 7, and consists of the reproduction of porous assembly materials, densification of the assembly materials and sacrificial parts removal. Successful implementation of this method includes a 98% densification of a highly complex CoNiCrAlY alloy turbine blade developed by Manière et al. [70].

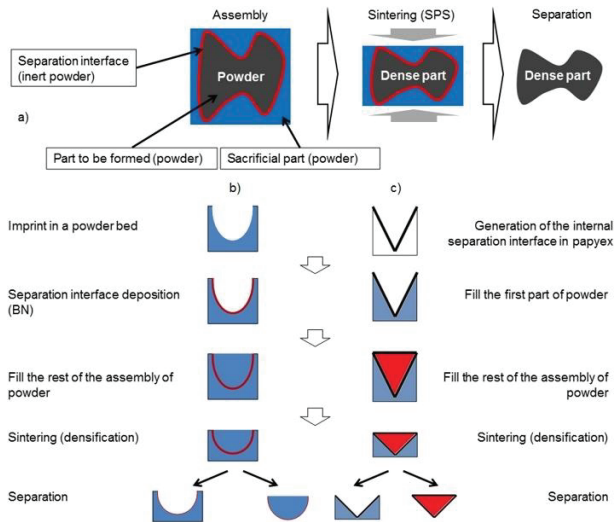


**Figure 7.** Deformed interfaces method process steps, (a) three main method steps comprising of: assembly, sintering, and the separation of the sacrificial tools, (b) imprint in powder bed approach, (c) graphite foil approach. reproduced from [70], with permission from Elsevier, 2017.

Finally, the recent controllable interface approach combines the adjustable interface thermal/electrical fluxes and the DEFORMINT approach. The controllable interface approach has been successfully used to manufacture 40 mm nickel gears [66], and the process steps (in Figure 8) for this consisted of powder loading into the assembly, SPS densification, removal of densified gear and polishing. SPS is modified by this approach through multiple die tooling, improving on the production number of complex shapes.

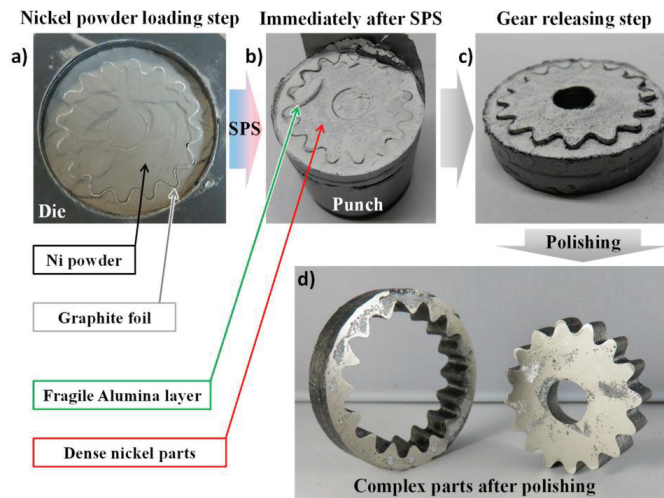


**Figure 8.** Controllable interface approach process steps for SPS densification of 40 mm nickel gears; where (a) shows loading; (b) following SPS; (c) gear releasing; and (d) polished parts [66].

### 3.4. Carburization at High Temperature during SPS

One of the major challenges during the processing of materials using SPS is carbon (C) contamination experienced at high temperatures, also known as carburization. For this reason, caution should be taken when selecting tooling materials. Pressing tools are generally covered with graphite foils/sheets to ease sample removal subsequent to SPS [73,74]. Therefore, at temperatures above 600 °C, reactions between the graphite covered tools and the O present in the sample may occur. Excess O, as stated by Franceschin et al. [73], can arise from the gaseous sintering atmosphere or moisture. The vigorous gaseous transportation occurring between the sample and the graphite mold may encourage the precipitation of C or carbides [55].

The effects of carburization on SPS manufactured materials are numerous. Waseem et al. [75] characterized a  $Ti_xW_yTa_zVCr$  alloy synthesized using SPS and detected up to 0.83 wt. % of C during gas fusion analysis. The presence of C was ascribed to the diffusion of graphite into the samples during SPS. Furthermore, the presence of a TiC phase was observed during XRD analysis resulting in a ~30  $\mu\text{m}$  thick layer on the surface of the samples. Moreover, the availability of TiC may be beneficial, improving on the resistance to irradiation and high heat fluxes. Meir et al. [76] showed that during the SPS densification of a magnesia–aluminate spinel, carbide precipitation was enhanced by the C containing atmosphere from the SPS apparatus. Carbide precipitation was found to impair light transmittance and even opacity in LiF-free samples. Additionally, volatile  $(CF)_n$  species were formed at high temperatures due to the interaction between C and LiF vapor.

Of much interest to this paper is carburization in TiAl alloys manufactured using SPS. Martin et al. [77] fully densified a commercial 48-2-2 TiAl powder by SPS and developed a two-fold protocol to obtain the desired microstructure and avoid TiC formation. Firstly, 8 and 10 mm samples were densified at 1200 °C below 50 MPa to obtain fully densified compacts with minimal (less than 1  $\mu\text{m}$ ) growth of the

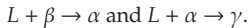
TiC layer. Secondly, the sample was introduced into a 36 mm inner diameter graphite mold, avoiding any contact between the sample and mold walls. Lastly, an annealing treatment for 5 min at 1360 °C was carried out with minimal load application to promote current conduction. TiC layer formation was achieved through avoiding mutual contact between the mold walls and the sample.

To avoid carburization, graphite pressing tools can be reinforced with C fibers to improve on the mechanical strength [78]. Additionally, double-walled tools with inner ceramic die and an outer graphite covering may be employed. Tooling material made from refractories and steel such as silica, alumina, concrete, TNZ molybdenum and copper-beryllium alloys may be such employed at sintering temperatures below 1000 °C [79,80]. Finally, the graphite tools can be separated from the sample by using foil layers such as hexagonal boron nitride [81] or alumina [82].

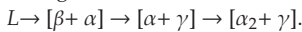
#### 4. Crystallographic Phases and Microstructures

##### 4.1. Crystallographic Phases

The characteristic phases existing in SPS produced  $\gamma$ -TiAl alloys are TiAl ( $\gamma$ ),  $\text{Ti}_3\text{Al}$  ( $\alpha_2$ ) or dual ( $\gamma + \alpha_2$ ). The  $\gamma$ -phase has an  $L1_0$  type face-centred tetragonal structure [83] consisting of atomic layers at 90° to the  $c$ -axis [84] with lattice parameters  $a = 0.4005$  nm,  $c = 0.4070$  nm and a tetragonality ratio ( $c/a$ ) of 1.02 [85,86]. Two peritectic reactions exist near the equiatomic composition [87]:



The prime phase that crystallises in Ti-base alloys from the liquid is  $\beta$ . According to McCullough et al. [87] the solidification path is as follows:



On cooling, the phase becomes unstable and transforms into the  $\gamma$ -phase. With further solid-state cooling, the phase becomes unstable and orders into the two-phase around 1117 °C [88,89].

The  $\alpha_2$ - $\text{Ti}_3\text{Al}$  phase has a hexagonal symmetry of a  $D0_{19}$  (Figure 9) structure with lattice parameters  $a_{\text{ord}} = 2a_{\text{disor}} = 0.58$  nm;  $c_{\text{ord}} = 0.48$  nm. In a review by Djanarthany et al. [90], the last parameter is said to resemble that of an A3 type structure with a long-range ordering only in the direction perpendicular to the  $c$ -axis. Phase transformation according to  $\beta \rightarrow \alpha \rightarrow \alpha_2$  resulting from cooling forms the  $\alpha_2$ -phase, and orders between 1125 and 1150 °C [91]. As shown in Figure 10, the  $\gamma$  phase exists at a composition of ~48.5–60,  $\alpha_2$  at ~24–34 and ( $\gamma + \alpha_2$ ) at ~34–49 at. % Al. Although the  $\alpha_2$ -phase shows good strength at high temperatures, it has been found to be very brittle, much related to the high absorption level of O and hydrogen [85,92]. Contrarily, the  $\gamma$ -phase exhibits excellent resistance to oxidation with low-level O and hydrogen absorption and poor ductility at room temperature (RT). In recent studies [51,52,93], TiAl powders were consolidated using SPS and the phases mentioned above were obtained.

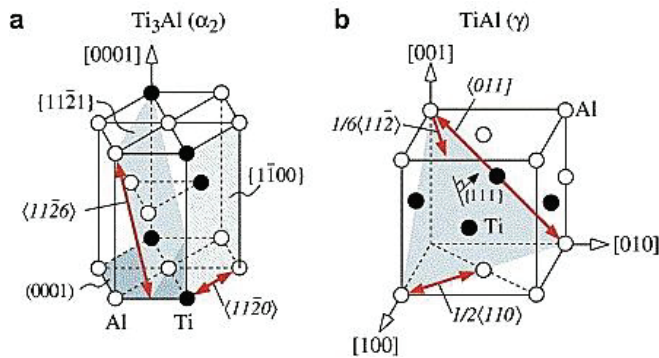


Figure 9. Titanium aluminide (TiAl) crystal structures, reproduced from [94], with permission from Elsevier, 2007.

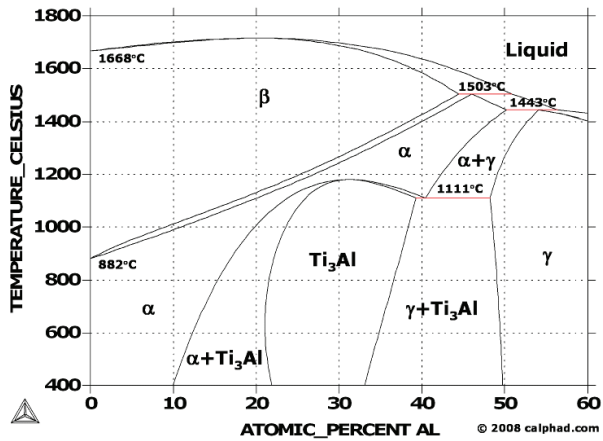


Figure 10. Ti-Al binary phase diagram.

A high performance Ti-48Al-2Cr-2Nb alloy was produced by employing SPS to consolidate spherical pre-alloyed (SP powder) and ball milled pre-alloyed powders (MP powder). In this work, Wang et al. [93] carried out an analysis of the variations in density, microstructure and mechanical properties at different sintering temperatures. Similar phases as mentioned above ( $\gamma$ -TiAl,  $\alpha_2$ -Ti<sub>3</sub>Al) were achieved with additional TiAl<sub>2</sub>, TiAl<sub>3</sub> for both the SP and MP powders. Additionally, the MP powder showed the presence of a Ti<sub>2</sub>Al phase. At sintering temperatures between 1200 and 1350 °C, the authors obtained  $\gamma$ -TiAl, TiAl<sub>3</sub> and TiAl<sub>2</sub> (see Figure 11).

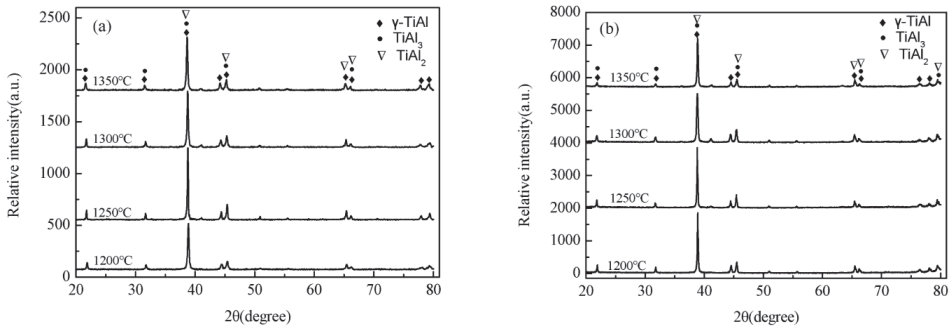


Figure 11. (a) XRD patterns of Ti-48Al-2Cr-8Nb alloys produced by SPS at different temperatures using spherical pre-alloyed (SP); and (b) milled ore-alloyed (MP) powders [93].

In a similar study, Deng et al. [51] demonstrated a novel avenue for the manufacturing of Ti-45Al-8Nb alloys using CM and SPS. To prevent cold welding and promote powder homogeneity, elemental powders were ball milled for 16 h at a rotating speed of 200 rpm. Subsequently, the blended powders were cryomilled for 40 h at a speed of 350 rpm. The alloys were sintered using a heating rate of 100 °C/min up to sintering temperatures of 900, 1000 and 1100 °C, respectively. XRD analysis showed the presence of the much dominant  $\gamma$ -TiAl phase with minor amounts of the  $\alpha_2$ -Ti<sub>3</sub>Al phase.

#### 4.2. Microstructures of TiAl

With a composition ranging from ~46–52 at. % of Al; the general microstructure is either a dual  $\alpha_2/\gamma$  or single pure  $\gamma$ -phase microstructure [95]. From the previously mentioned phases, with further

processing and treatment characteristic microstructures referred to as equiaxed, duplex (DP), nearly lamellar (NL) and fully lamellar (FL) can be achieved [4]. The equiaxed structure contains a single phase  $\gamma$ -TiAl. The phase is stable in the region of the phase diagram above 50 at. %Al. Combined phase microstructure (commonly referred to as DP) made up of both  $\alpha_2$  and  $\gamma$  is formed in the dual-phase section where the at. % of Al is between 46 and 50, depending on the heat treatment employed.

The single-phase  $\gamma$  consists of a continuous built-up of smaller equiaxed grains [83], and is formed in the  $\gamma + \alpha_2$  phase field resulting in grain coarsening of existing  $\gamma$  grains [96]. This microstructure possesses good properties at high temperatures. This microstructure is very brittle and, therefore, not desired in structural or engineering applications [96,97]. The disadvantages are its poor room-temperature properties such as fracture toughness and ductility [95].

Heating in the two-phase region, followed by cooling results in a DP microstructure consisting of  $\gamma$  and lamella grains [98]. Grain refined DP microstructures have ambient strength and ductility with poor response to creep and fatigue at elevated temperatures [99]. A NL microstructure is formed in the  $\alpha_2 + \gamma$  phase region where the  $\alpha/\gamma$  ratio is greater than 1 whereas a FL microstructure is obtained in the pure  $\alpha$ -phase field, followed by air-cooling to ambient temperature [96]. Optimum tensile strengths with superior low-cycle fatigue performance are observed in fine-grained NL microstructures, while a coarse microstructure significantly affects the fatigue performance at low-cycles [100]. Improved hardness and toughness is mostly observed in FL structures [101,102].

## 5. Microstructure-Property Relations

Fully densified  $\gamma$ -TiAl alloys with less residual porosity can be successfully produced using SPS. It has been proved countlessly [27,103–106] that the superior properties of these alloys can also be achieved by optimising SPS parameters. A fully densified  $\gamma$ -TiAl by SPS will have three distinctive microstructures namely, equiaxed  $\gamma$  grains, DP and lamella colonies having alternating layers of  $\alpha_2$  and  $\gamma$  phase [9,103,107]. The lamella microstructure with ( $\gamma + \alpha_2$ ) phase is the preferred in structural applications [85,108] due to the ease of controlling the distributions and amounts of the  $\alpha_2$  and  $\gamma$  formed [109].

In a recent study, Gu and associates [27] produced a PA TiAl alloy with added yttrium using SPS. The microstructures (in Figure 12) obtained were DP, NL and FL by employing varying sintering temperatures ranging from 100 up to 1250 °C at a sintering pressure of 40 MPa. The compression results (Figure 13) obtained from the study showed that the compressive strength of the samples decreases with increasing sintering temperature. Furthermore, DP microstructure exhibited excellent yield, fracture strength and ultimate strain as compared to the samples with NL and FL microstructures. Wang et al. [103] investigated the effect of stresses and sintering temperature on the microstructural evolution and mechanical properties of a Ti–Al–Cr–Nb alloy produced by SPS. The authors reported that mechanical properties were reliant on the microstructures produced by the varied SPS conditions. An optimal true fracture strength of 1820 MPa and a plastic true strain of 32.6% were obtained for the alloy sintered at 1150 °C, consisting of a double phased and lamellar microstructure.

A NL microstructure has restricted RT ductility. According to a recent study, this effect can be defined by the difficult plastic deformation in  $\gamma/\alpha_2$  colonies due high-volume percent of  $\alpha_2$  present [106].  $\gamma + \alpha_2$  and DP microstructures offer enhanced yield strength, ductility and ultimate tensile strength at RT [18]. According to Couret and colleagues [18], these are governed by SPS parameter optimisation and addition of grain growth inhibitors such as boron. In the very same study, it was found that the poor strength and limited ductility in lamella microstructures can be attributed to the large grain size and lack of texture inhibiting propagation of dislocations in a preferred mode.

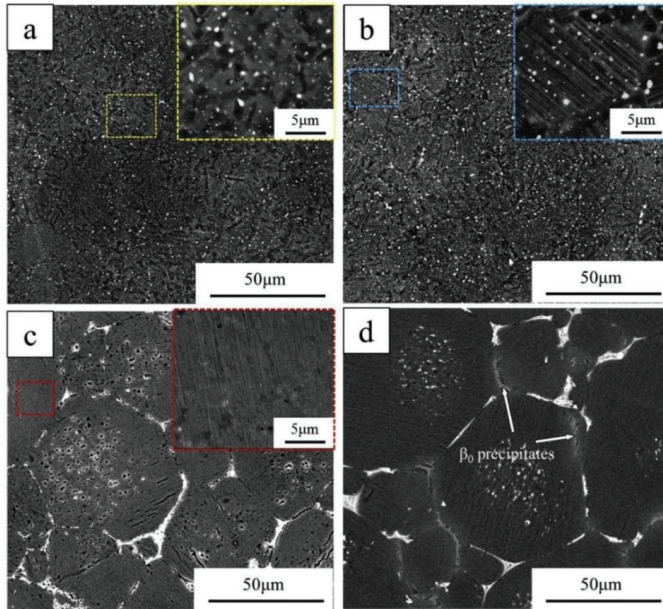


**Figure 12.** Scanning electron microscope (SEM) images of yttrium added TiAl alloys produced by SPS with (a) outer part of sample sintered at 1100 °C; (b) center of sample sintered at 1150 °C; (c) sample sintered at 1200 °C; and (d) 1250 °C (reproduced from [27], with permission from Elsevier, 2020).

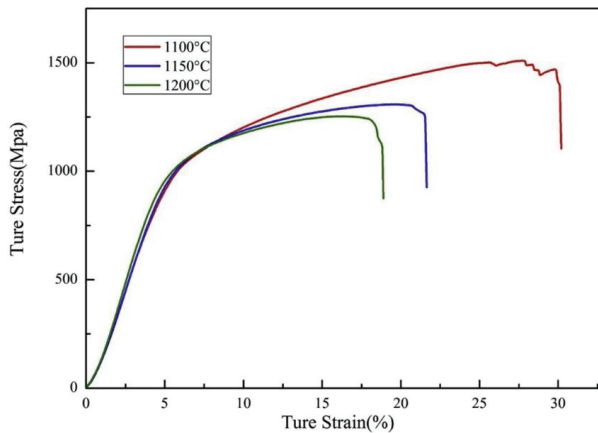


**Figure 13.** Stress-strain plots at room temperature (RT) of yttrium added TiAl alloys produced by SPS, reproduced from [27], with permission from Elsevier, 2020.

Voisin et al. [106], consolidated a TNM ( $\gamma$ -TiAl with Nb and Mo additions) alloy with chemical composition Ti-43.9Al-4Nb-0.95Mo-0.1B using SPS by varying sintering temperature of 1237–1429 °C. In addition, experiments on RT tensile deformation and creep at 700 °C employing stress of 300 MPa were conducted. A NL microstructure (in Figure 14a) was attained at sintering temperatures ranging from 1262 to 1336 °C. The highest ductility obtained from the results exhibited a fracture elongation of 0.86–0.9% for the specimen sintered at 1336 °C. TEM fractography also showed that the NL microstructure deformed using ordinary dislocation pileups and twinning (Figure 14c). Excellent creep

resistance (Figure 14b) was obtained with lifetimes >2000 h at creep rates of  $<10^{-8} \text{ s}^{-1}$ , with the highest attained at a lifetime of ~4000 h for the alloy is that sintered at 1304 °C.

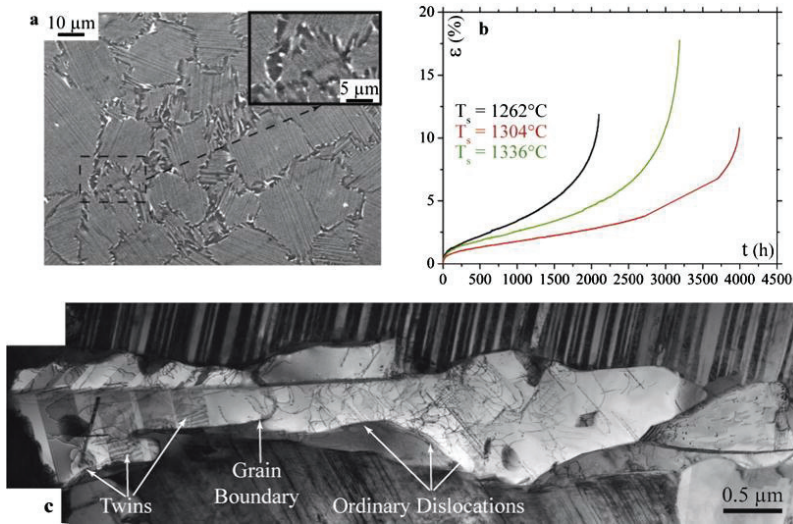


**Figure 14.** (a) Near lamella (NL) microstructure, (b) creep curves at 700 °C using stress of 300 MPa, (c) RT tensile deformation microstructure for SPS consolidated TNM alloy, reproduced from [106], with permission from Elsevier, 2014.

Another property of interest for TiAl alloys is oxidation. Resistance to oxidation, commonly known to as the resistance to corrosion at high temperatures, of  $\gamma$ -TiAl is said to be generally good at temperatures below 850 °C [110]. The kinetics of oxidation includes the formation of a non-protective mixed oxide scale of alumina ( $\text{Al}_2\text{O}_3$ ) and titania ( $\text{TiO}_2$ ) on the surface of bare  $\gamma$ -TiAl alloys in a favourable condition and environment [111]. Simultaneous formation of  $\text{Al}_2\text{O}_3$  and  $\text{TiO}_2$  occurs during the initial state of oxidation and thrive in the optimal growth direction [112]. Furthermore,  $\text{TiO}_2$  grows at a higher velocity compared to  $\text{Al}_2\text{O}_3$  attributable to the low growth activation energy of  $\text{TiO}_2$  as compared to  $\text{Al}_2\text{O}_3$ . Additionally, the subsequent series of reactions are described as rapid and favour the formation of  $\text{TiO}_2$ . However, below the  $\text{TiO}_2$  layer, an aluminium (Al)-rich layer exists because of Ti depletion. The oxide scale in TiAl consists of multi-layers of both  $\text{TiO}_2$  and  $\text{Al}_2\text{O}_3$ . A decrease in the oxidation resistance of  $\gamma$ -TiAl as mentioned by Dai et al. [112] can be as a result of the thickening of the multi-layered oxide film due to mass transportation, weakening the bond existing between the oxide layer and the substrate.

A FL microstructure seems to be the most preferred as far as oxidation resistance is concerned. However, the average lamella grain size and compositional variations are to be considered. A lamella grain size of 25–20  $\mu\text{m}$  with Nb additions was reported to suppress diffusion activity in TiAl alloys [113,114]. The kinetics of oxidation involves the simultaneous formation of a non-protective mixed oxide scale of alumina ( $\text{Al}_2\text{O}_3$ ) and titania ( $\text{TiO}_2$ ) on the surface of bare  $\gamma$ -TiAl alloys in a favourable condition and environment [111,112].

Several recent studies [113,115,116] aimed at improving the oxidation resistance of SPS produced TiAl alloys. Cobbinah and colleagues [115] investigated the effect of Ta additions (0.8, 4, and 8 at. %) on the isothermal oxidation resistance of a Ti–46.5Al (at. %) alloy produced by SPS. The results indicate that the superior resistance of the TiAl alloys is related to the formation of a non-porous and interconnected layer of  $\text{Al}_2\text{O}_3$  at the interface of the metal-oxide. In works by Lu et al. [113], isothermal resistance at 1000 °C of SPS produced alloys of nominal composition Ti–45Al–8.5Nb–0.2B–0.2W–0.1Y

and Ti-47.5Al-2.0V-1.0Cr were studied. A mixed oxide scale consisting of  $\text{Al}_2\text{O}_3/\text{TiO}_2$  was formed next to the spalled  $\text{TiO}_2$  layer for the Ti-47.5Al-2.5V-1.0Cr. Furthermore, the mixed scale produced proved to have no protective effect, resulting in high rates of oxidation (with mass gains of  $51.06 \text{ mg/cm}^2$ ) as compared to alloy Ti-45Al-8.5Nb-0.2B-0.2W-0.1Y (with only  $2.27 \text{ mg/cm}^2$  mass gain) tested under the same conditions. Relatively, the inner oxide scale of alloy Ti-45Al-8.5Nb-0.2B-0.2W-0.1Y exhibited an outer  $\text{TiO}_2$ -rich layer with traces of  $\text{Al}_2\text{O}_3$  and TiN. The addition of 8.5% Nb promoted the formation of a Nb-rich diffusion layer between the substrate and the oxide layer, further enhancing the oxidation resistance of the alloy.

## 6. Alloy Development

During the initial advances in two-phase binary alloys, it was acknowledged that these alloys cannot be utilised owing to their poor oxidation and creep resistance [43]. Consequently, this resulted in a vast number of investigations aimed at understanding the effect of alloy additions in binary TiAl on the microstructure-property relations. To date, four generations [97,117] of TiAl alloys have been developed.

### 6.1. 1st and 2nd Generation of TiAl alloys

In this generation of alloys, elements such as Cr, V, Mn were added to Ti-(42–48)Al (at. %) to produce ternary alloys. These alloys were further processed using heat and thermomechanical treatments to improve ductility measures. In a previous study of interest [118], it was reported that additions of up to 4 at. % of Cr to binary Ti-(44–54)Al alloys consisting of DP microstructures led to partial ductilization due to the occupancy of Cr in Al lattice sites. Cr additions also modified the Al partitioning and the thermal stabilisation of transformed  $\alpha_2$  laths comparable to findings made when 0.4 at. % of V was added [119].

The 2nd generation of TiAl is based on the following composition [43]:

$$\text{Ti-(45-48)Al-(1-3)X-(2-5)Y-(<1)Z} \quad (1)$$

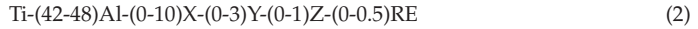
where X = Cr, Mn, Y = Nb, Ta, W, Mo; Z = Si, B, C.

The additions of the elements, as mentioned above, shift the position of the phase boundaries in the Ti–Al binary phase diagram [43,96]. Additions of element X improve the mechanical properties of TiAl alloys by increasing flow stress [120], reducing the stacking fault energy and thus enhancing the susceptibility of twinning [96]. Zhu et al. [121] studied the effect of Cr additions on the microstructure and nanohardness of Ti-48Al binary alloy produced using a single roller melt spinning and arc melting processing routes. With 2 at. % Cr, the microstructure of the alloy ribbons was lamella with equiaxed  $\alpha_2$  and small B2 phase particles. Additions of up to 4 at. % Cr increases the B2 phase grain sizes and the lamella structure disappears. The nanohardness of the alloys increased also with additions of up to 4 at. % of Cr. Additions of V and Mn have been reported [122] to increase the fracture and yield stresses much related to grain refinement and solid solution strengthening (particularly for V additions).

Adding elements like Ta, Mo and W (Y additions) improve the oxidation and creep properties at elevated temperatures. Recently [115], additions of 4 and 8 at. % of Ta to an SPS produced Ti-46.5Al alloy promoted the formation of an  $\text{Al}_2\text{O}_3$  layer severing as a diffusion barrier on the metal-oxide interface, hence, resulting in outstanding resistance to oxidation. For further reading on the effect Ta on the oxidation performance of TiAl, the reader is referred to [123–126]. Remarkable creep properties were obtained in some research work [127–129] when Ta and W were added to TiAl alloys. Z additions such as B promote grain refinement utilising retarding grain growth in the  $\alpha$ -phase field [96]. Moreover, the strength and resistance to creep is improved through the formation of  $\text{Ti}_3\text{AlC}$  perovskite precipitates when C is added. Numerous work has been conducted to date [130–134] on the effect B and C have on the microstructure and mechanical properties of TiAl, attesting to the above alloy addition benefits.

6.2. 3rd and 4th Generation of TiAl Alloys

This generation of alloys contains high Mo and or Nb contents to promote precipitation hardening and were developed for applications at elevated temperatures. The third generation of TiAl alloys follow the constitution below [43]:



where X = Ta, Nb, Mn, Cr; Y = Zr, Hf, W, Mo; Z = C, B, Si and RE designates rare earth metals.

The additions of Zr is a known  $\beta$ -stabilizer, promoting occupancy of the Ti sites in the lattice of Ti–Al systems [135]. Furthermore, adding Zr to binary TiAl alloys improves compression strength. However, when added in the presence of Cr, the strength decreases with increasing elongation. Finally, phase evolutions occurring as a result of the existence of both Cr and Zr in Ti–43Al–4Nb–1Mo–0.1B (TNM-B1) alloy include the formation of  $\omega$ , reduction of  $\alpha_2$  and increments in the amount of  $\beta$  phases. Y rare earth metal additions promote grain refinement, thus improving ductility [136,137], elevated temperature deformability [138] and heat resistance [139]. The oxidation rate of TNM alloys can be reduced by ~0.1 at. % RE metal additions such as La or Er [140]. Conversely, additions of ~0.2 at. % of aforementioned RE metals can impair the resistance to oxidation through the formation of hillocks in the oxide scale.

The fourth generation of TiAl, commonly referred to as TNM alloys, exhibit excellent oxidation resistance through Nb and or Ta additions and outstanding creep properties promoted by Mo additions. In addition, these alloys are said to have excellent workability making them universally applicable for various processing routes other than casting and hot forming such as additive manufacturing and SPS [141]. Some of the alloys developed to date include the  $\beta$ -solidifying Ti–43.5Al–4Nb–1Mo–0.1B [141], Ti–46Al–8Nb and Ti–46Al–8Ta [142]. Wimler et al. [141] studied the capabilities of SPS coupled with subsequent heat treatments to produce a Ti–43.5Al–4Nb–1Mo–0.1B alloy with strength and creep performance at 750 °C comparable to those produced by conventional processing techniques. After SPS consolidation of the gas atomised powder alloy at 1300 °C, the microstructure produced consisted of a refined and homogeneous NL  $\gamma$  and  $\beta_0$ . Subsequent two-step heat treatments resulted in the formation of NL  $\gamma$ , FL and NL  $\beta_0$  structures (in Figure 15) decreasing the lamella spacing from  $83 \pm 7$  in the as-sintered condition to  $10 \pm 3$  nm. It was concluded that the strength and creep properties at 750 °C (in Figure 16) obtained can keep up with that of the conventional routes of processing.

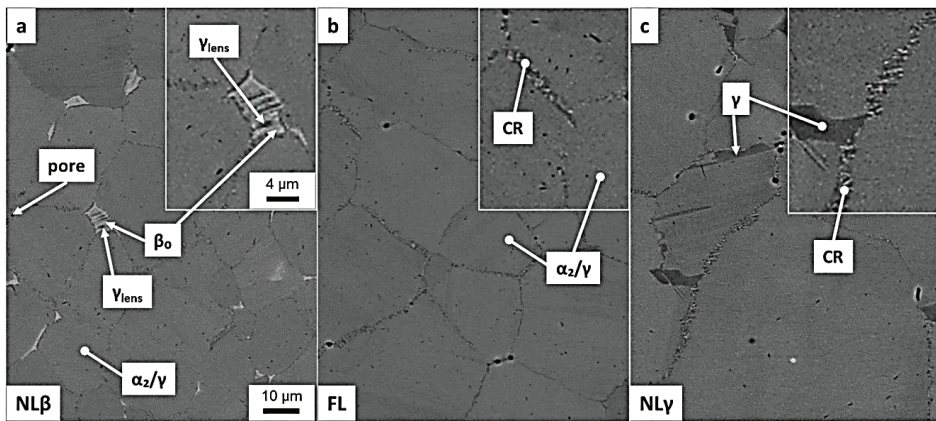
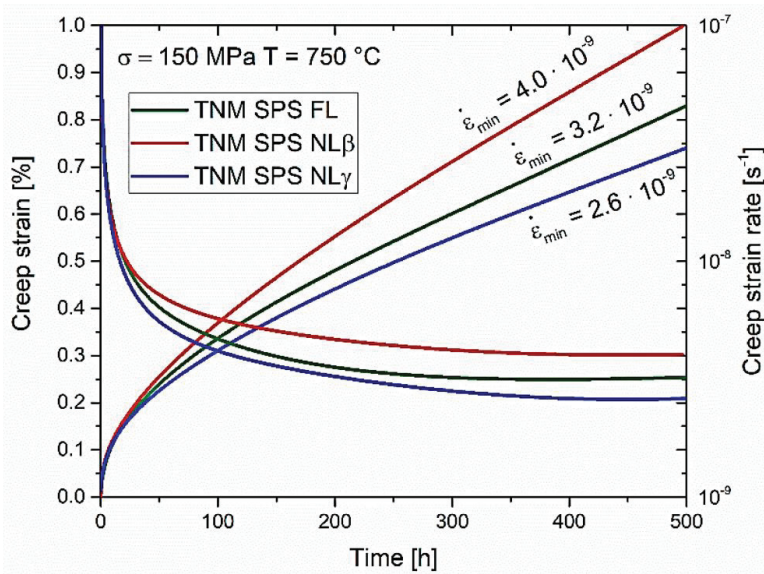


Figure 15. SEM images showing (a) NL beta ( $\beta$ ); (b) fully lamella (FL); and (c) NL gamma ( $\gamma$ ) microstructures after two-step heat treatment [141].



**Figure 16.** Plots of creep stress and strain versus time of the heat-treated microstructures tested at 750 °C and 150 MPa [141].

## 7. Perspectives and Conclusions

The realisation of the process has been highlighted by remarkable accomplishments in the production of a refined microstructure of  $\gamma$ -TiAl since it offers prompt rates of both heating and cooling. Currently, research and development have shifted attention to TiAl powder forming techniques such as DMM, GA, and, amongst others, pre-alloying. MA and SPS can be coupled in the production of nanocrystalline intermetallic TiAl owing to the advantages of obtaining non-equilibrium and amorphous phases, ultrafine grain sizes and, at the same time, retaining the grain size during consolidation. As an added advantage, SPS uses shorter holding times to obtain fully densified material as compared to conventional processes such as HIP. Consolidation methods aimed at balancing microstructure and properties have also been explored.

However, SPS shows an impressive balance of microstructure and mechanical properties.

A significant challenge in as far as TiAl alloys are concerned is commercialisation and costs. Although limited applications have been achieved, the reality is that implementation of TiAl alloys in both the automobile and aerospace industries is an on-going challenge. Although TiAl were designed as candidates to replace the Ni-based superalloys, the gap existing between the two is quite recognisable from both the properties and production costs perspective. Much research has been dedicated to improving the ductility at RT for TiAl alloys through compositional variations, opting for manufacturing technologies and thermomechanical treatments. These attempts aimed at refining and altering the microstructures and morphologies of the produced alloys. Advanced PM techniques present the opportunity to manufacture near-net-shape components with improved mechanical properties. However, challenges exist concerning methods that can be employed to characterise PM produced TiAl alloys effectively. Although the future seems exciting for TiAl alloys produced using PM, implementation on an industrial scale seems to lag far behind.

**Author Contributions:** Writing—original draft preparation, N.F.M.; writing—review and editing, W.R.M. All authors have read and agreed to the published version of the manuscript.

**Funding:** This research was funded by National Research Foundation of South Africa, grant number 116368.

**Conflicts of Interest:** The authors declare no conflict of interest.

## References

1. Taub, A.I.; Fleischer, R.L. Intermetallic compounds for high-temperature structural use. *Science* **1989**, *243*, 616–621. [CrossRef] [PubMed]
2. Wolff, I.M.; Hill, P.J. Platinum metals-based intermetallics for high-temperature service. *Platin. Met. Rev.* **2000**, *44*, 158–166.
3. Mukhtinalapati, N.R. Materials for gas turbines—an overview. In *Advances in Gas Turbine Technology*; IntechOpen: London, UK, 2011; Available online: <https://www.intechopen.com/books/advances-in-gas-turbine-technology/materials-for-gas-turbines-an-overview> (accessed on 1 May 2020).
4. Leyens, C.; Peters, M. *Titanium and Titanium Alloys: Fundamentals and Applications*; John Wiley & Sons: Hoboken, NJ, USA, 2003.
5. Clemens, H.; Smarsly, W. Light-weight intermetallic titanium aluminides—status of research and development. *Adv. Mater. Res.* **2011**, *278*, 551–556. [CrossRef]
6. Voice, W. The future use of gamma titanium aluminides by Rolls-Royce. *Aircr. Eng. Aerosp. Technol.* **1999**, *71*, 337–340. [CrossRef]
7. Bewlay, B.P.; Weimer, M.; Kelly, T.; Suzuki, A.; Subramanian, P.R. The science, technology, and implementation of TiAl alloys in commercial aircraft engines. *MRS Online Proc. Libr. Arch.* **2013**, *1516*, 49–58. [CrossRef]
8. Loria, E.A. Quo vadis gamma titanium aluminide. *Intermetallics* **2001**, *9*, 997–1001. [CrossRef]
9. Liu, B.; Liu, Y. 27-Powder metallurgy titanium aluminide alloys. In *Titanium Powder Metallurgy*; Elsevier Inc.: Amsterdam, The Netherlands, 2015; pp. 515–531.
10. Lamirand, M.; Bonnetien, J.L.; Ferrière, G.; Guérin, S.; Chevalier, J.P. Relative effects of chromium and niobium on microstructure and mechanical properties as a function of oxygen content in TiAl alloys. *Scr. Mater.* **2007**, *56*, 325–328. [CrossRef]
11. Wang, Q.; Ding, H.; Zhang, H.; Chen, R.; Guo, J.; Fu, H. Influence of Mn addition on the microstructure and mechanical properties of a directionally solidified  $\gamma$ -TiAl alloy. *Mater. Charact.* **2018**, *137*, 133–141. [CrossRef]
12. Imayev, V.; Oleneva, T.; Imayev, R.; Christ, H.J.; Fecht, H.J. Microstructure and mechanical properties of low and heavy alloyed  $\gamma$ -TiAl +  $\alpha$ 2-Ti3Al based alloys subjected to different treatments. *Intermetallics* **2012**, *26*, 91–97. [CrossRef]
13. Larsen, J.M.; Worth, B.D.; Balsone, S.J.; Jones, J.W. *An Overview of the Structural Capability of Available Gamma Titanium Aluminide Alloys*; U.S. Department of Energy Office of Scientific and Technical Information: Oak Ridge, TN, USA, 1995.
14. Tang, J.; Huang, B.; Liu, W.; He, Y.; Zhou, K.; Wu, A.; Peng, K.; Qin, W.; Du, Y. A high ductility TiAl alloy made by two-step heat treatment. *Mater. Res. Bull.* **2003**, *38*, 2019–2024. [CrossRef]
15. Lasalmonie, A. Intermetallics: Why is it so difficult to introduce them in gas turbine engines? *Intermetallics* **2006**, *14*, 1123–1129. [CrossRef]
16. Lagos, M.A.; Agote, I. SPS synthesis and consolidation of TiAl alloys from elemental powders: Microstructure evolution. *Intermetallics* **2013**, *36*, 51–56. [CrossRef]
17. Munir, Z.A.; Anselmi-Tamburini, U.; Ohyanagi, M. The effect of electric field and pressure on the synthesis and consolidation of materials: A review of the spark plasma sintering method. *J. Mater. Sci.* **2006**, *41*, 763–777. [CrossRef]
18. Couret, A.; Molénat, G.; Galy, J.; Thomas, M. Microstructures and mechanical properties of TiAl alloys consolidated by spark plasma sintering. *Intermetallics* **2008**, *16*, 1134–1141. [CrossRef]
19. Jaramillo, D.; Cuenca, R.; Juárez, F. Sintering comparison of NiCoCrAl-Ta powder processed by hot pressing and spark plasma. *Powder Technol.* **2012**, *221*, 264–270.
20. Chang, I.; Zhao, Y. *Advances in Powder Metallurgy: Properties, Processing and Applications*; Elsevier: Amsterdam, The Netherlands, 2013.
21. Martin, A.; Cepeda-Jiménez, C.M.; Pérez-Prado, M.T. Gas atomization of  $\gamma$ -TiAl Alloy Powder for Additive Manufacturing. *Adv. Eng. Mater.* **2020**, *22*, 1900594. [CrossRef]
22. Neikov, O.D. Chapter 4-Atomization and Granulation. In *Handbook of Non-Ferrous Metal Powders: Technologies and Applications*; Neikov, O.D., Naboychenko, S.S., Yefimov, N.A., Second, E., Eds.; Elsevier: Oxford, UK, 2019; pp. 125–185.
23. Gerling, R.; Clemens, H.; Schimansky, F.P. Powder Metallurgical Processing of Intermetallic Gamma Titanium Aluminides. *Adv. Eng. Mater.* **2004**, *6*, 23–38. [CrossRef]

24. Sun, P.; Fang, Z.Z.; Zhang, Y.; Xia, Y. Review of the methods for production of spherical Ti and Ti alloy powder. *JOM* **2017**, *69*, 1853–1860. [[CrossRef](#)]
25. Antony, L.V.M.; Reddy, R.G. Processes for production of high-purity metal powders. *JOM* **2003**, *55*, 14–18. [[CrossRef](#)]
26. Franz, H.; Plochl, L.; Schimansky, F.P. Recent advances of titanium alloy powder production by ceramic-free inert gas atomization. In Proceedings of the Titanium 2008, Las Vegas, NV, USA, 21–24 September 2008.
27. Gu, X.; Cao, F.; Liu, N.; Zhang, G.; Yang, D.; Shen, H.; Zhang, D.; Song, H.; Sun, J. Microstructural evolution and mechanical properties of a high yttrium containing TiAl based alloy densified by spark plasma sintering. *J. Alloy. Compd.* **2020**, *819*, 153264. [[CrossRef](#)]
28. Liu, B.; Wang, M.; Du, Y.; Li, J. Size-Dependent Structural Properties of a High-Nb TiAl Alloy Powder. *Materials* **2020**, *13*, 161. [[CrossRef](#)] [[PubMed](#)]
29. Xia, Y.; Zhao, J.L.; Qian, M. Spark Plasma Sintering of Ti-48Al-2Cr-2Nb Alloy Powder and Characterization of an Unexpected Phase. *JOM* **2019**, *71*, 2556–2563. [[CrossRef](#)]
30. Wang, J.; Wang, Y.; Liu, Y.; Li, J.; He, L.; Zhang, C. Densification and microstructural evolution of a high niobium containing TiAl alloy consolidated by spark plasma sintering. *Intermetallics* **2015**, *64*, 70–77. [[CrossRef](#)]
31. Xiao, S.L.; Jing, T.; Xu, L.J.; Chen, Y.Y.; Yu, H.B.; Han, J.C. Microstructures and mechanical properties of TiAl alloy prepared by spark plasma sintering. *Trans. Nonferrous Met. Soc. China* **2009**, *19*, 1423–1427. [[CrossRef](#)]
32. Hadeif, F. Synthesis and disordering of B2 TM-Al (TM=Fe, Ni, Co) intermetallic alloys by high energy ball milling: A review. *Powder Technol.* **2017**, *311*, 556–578. [[CrossRef](#)]
33. Aliofkhaezrai, M. *Handbook of Mechanical Nanostructuring*; John Wiley & Sons: Hoboken, NJ, USA, 2015.
34. Suryanarayana, C.; Ivanov, E.; Boldyrev, V.V. The science and technology of mechanical alloying. *Mater. Sci. Eng. A* **2001**, *304*, 151–158. [[CrossRef](#)]
35. Yadav, T.P.; Yadav, R.M.; Singh, D.P. Mechanical milling: A top down approach for the synthesis of nanomaterials and nanocomposites. *Nanosci. Nanotechnol.* **2012**, *2*, 22–48. [[CrossRef](#)]
36. Oehring, M.; Klassen, T.; Bormann, R. The formation of metastable Ti–Al solid solutions by mechanical alloying and ball milling. *J. Mater. Res.* **1993**, *8*, 2819–2829. [[CrossRef](#)]
37. Zhang, F.; Lu, L.; Lai, M.O. Study of thermal stability of mechanically alloyed Ti–75% Al powders. *J. Alloy. Compd.* **2000**, *297*, 211–218. [[CrossRef](#)]
38. Wang, Y.; Zhang, C.; Liu, Y.; Zhao, S.; Li, J. Microstructure characterization and mechanical properties of TiAl-based alloys prepared by mechanical milling and spark plasma sintering. *Mater. Charact.* **2017**, *128*, 75–84. [[CrossRef](#)]
39. Shulong, X.; Lijuan, X.; Hongbao, Y.; Yuyong, C. Effect of Y Addition on Microstructure and Mechanical Properties of TiAl-based Alloys Prepared by SPS. *Rare Met. Mater. Eng.* **2013**, *42*, 23–27. [[CrossRef](#)]
40. Xiao, S.; Xu, L.; Chen, Y.; Yu, H. Microstructure and mechanical properties of TiAl-based alloy prepared by double mechanical milling and spark plasma sintering. *Trans. Nonferrous Met. Soc. China* **2012**, *22*, 1086–1091. [[CrossRef](#)]
41. Suryanarayana, C. Mechanical Alloying: A Novel Technique to Synthesize Advanced Materials. *Research* **2019**, *2019*, 4219812. [[CrossRef](#)] [[PubMed](#)]
42. Suryanarayana, C. Mechanical alloying and milling. *Prog. Mater. Sci.* **2001**, *46*, 1–184. [[CrossRef](#)]
43. Clemens, H.; Mayer, S. Design, Processing, Microstructure, Properties, and Applications of Advanced Intermetallic TiAl Alloys. *Adv. Eng. Mater.* **2013**, *15*, 191–215. [[CrossRef](#)]
44. Lu, L.; Lai, M.O.; Froes, F.H. The mechanical alloying of titanium aluminides. *JOM* **2002**, *54*, 62–64. [[CrossRef](#)]
45. Forouzanmehr, N.; Karimzadeh, F.; Enayati, M.H. Study on solid-state reactions of nanocrystalline TiAl synthesized by mechanical alloying. *J. Alloy. Compd.* **2009**, *471*, 93–97. [[CrossRef](#)]
46. Sim, K.H.; Wang, G.; Son, R.C.; Choe, S.L. Influence of mechanical alloying on the microstructure and mechanical properties of powder metallurgy Ti<sub>2</sub>AlNb-based alloy. *Powder Technol.* **2017**, *317*, 133–141. [[CrossRef](#)]
47. Bohn, R.; Klassen, T.; Bormann, R. Mechanical behavior of submicron-grained  $\gamma$ -TiAl-based alloys at elevated temperatures. *Intermetallics* **2001**, *9*, 559–569. [[CrossRef](#)]
48. Bhattacharya, P.; Bellon, P.; Averbach, R.S.; Hales, S.J. Nanocrystalline TiAl powders synthesized by high-energy ball milling: Effects of milling parameters on yield and contamination. *J. Alloy. Compd.* **2004**, *368*, 187–196. [[CrossRef](#)]

49. Lavernia, E.J.; Han, B.Q.; Schoenung, J.M. Cryomilled nanostructured materials: Processing and properties. *Mater. Sci. Eng.* **2008**, *493*, 207–214. [[CrossRef](#)]
50. Witkin, D.B.; Lavernia, E.J. Synthesis and mechanical behavior of nanostructured materials via cryomilling. *Prog. Mater. Sci.* **2006**, *51*, 1–60. [[CrossRef](#)]
51. Deng, H.; Chen, A.; Chen, L.; Wei, Y.; Xia, Z.; Tang, J. Bulk nanostructured Ti-45Al-8Nb alloy fabricated by cryomilling and spark plasma sintering. *J. Alloy. Compd.* **2019**, *772*, 140–149. [[CrossRef](#)]
52. Shanmugasundaram, T.; Guyon, J.; Monchoux, J.P.; Hazotte, A.; Bouzy, E. On grain refinement of a  $\gamma$ -TiAl alloy using cryo-milling followed by spark plasma sintering. *Intermetallics* **2015**, *66*, 141–148. [[CrossRef](#)]
53. Sun, Y.; Kulkarni, K.; Sachdev, A.K.; Lavernia, E.J. Synthesis of  $\gamma$ -TiAl by reactive spark plasma sintering of cryomilled Ti and Al powder blend, part I: Influence of processing and microstructural evolution. *Met. Mater. Trans. A* **2014**, *45*, 2750–2758. [[CrossRef](#)]
54. Sun, Y.; Kulkarni, K.; Sachdev, A.K.; Lavernia, E.J. Synthesis of  $\gamma$ -TiAl by reactive spark plasma sintering of cryomilled Ti and Al powder blend: Part II: Effects of electric field and microstructure on sintering kinetics. *Met. Mater. Trans. A* **2014**, *45*, 2759–2767. [[CrossRef](#)]
55. Guillon, O.; Gonzalez-Julian, J.; Dargatz, B.; Kessel, T.; Schierning, G.; Räthel, J.; Herrmann, M. Field-assisted sintering technology/spark plasma sintering: Mechanisms, materials, and technology developments. *Adv. Eng. Mater.* **2014**, *16*, 830–849. [[CrossRef](#)]
56. Guyon, J.; Hazotte, A.; Monchoux, J.P.; Bouzy, E. Effect of powder state on spark plasma sintering of TiAl alloys. *Intermetallics* **2013**, *34*, 94–100. [[CrossRef](#)]
57. Chen, F.; Yang, S.; Wu, J.; Galaviz Perez, J.A.; Shen, Q.; Schoenung, J.M.; Lavernia, E.J.; Zhang, L. Spark plasma sintering and densification mechanisms of conductive ceramics under coupled thermal/electric fields. *J. Am. Ceram. Soc.* **2015**, *98*, 732–740. [[CrossRef](#)]
58. Matizanhuka, W.R. Fabrication of Fine-Grained Functional Ceramics by Two-Step Sintering or Spark Plasma Sintering (SPS). In *Sintering [Working Title]*; IntechOpen: London, UK, 2019.
59. Matizanhuka, W.R. Spark plasma sintering (SPS)-an advanced sintering technique for structural nanocomposite materials. *J. South. African Inst. Min. Met.* **2016**, *116*, 1171–1180. [[CrossRef](#)]
60. Suárez, M.; Fernández, A.; Menéndez, J.L.; Torrecillas, R.; Kessel, H.U.; Hennicke, J.; Kirchner, R.; Kessel, T. Challenges and opportunities for spark plasma sintering: A key technology for a new generation of materials. *Sinter. Appl.* **2013**, *13*, 319–342.
61. Marder, R.; Estournès, C.; Chevallier, G.; Chaim, R. Spark and plasma in spark plasma sintering of rigid ceramic nanoparticles: A model system of YAG. *J. Eur. Ceram. Soc.* **2015**, *35*, 211–218. [[CrossRef](#)]
62. Marder, R.; Estournès, C.; Chevallier, G.; Chaim, R. Plasma in spark plasma sintering of ceramic particle compacts. *Scr. Mater.* **2014**, *82*, 57–60. [[CrossRef](#)]
63. Saunders, T.; Grasso, S.; Reece, M.J. Plasma formation during electric discharge (50V) through conductive powder compacts. *J. Eur. Ceram. Soc.* **2015**, *35*, 871–877. [[CrossRef](#)]
64. Rahaman, M.N. *Ceramic Processing and Sintering*; CRC press: Boca Raton, FL, USA, 2003.
65. Olevsky, E.A.; Kandukuri, S.; Froyen, L. Consolidation enhancement in spark-plasma sintering: Impact of high heating rates. *J. Appl. Phys.* **2007**, *102*, 114913. [[CrossRef](#)]
66. Manière, C.; Torresani, E.; Olevsky, E.A. Simultaneous spark plasma sintering of multiple complex shapes. *Materials* **2019**, *12*, 557. [[CrossRef](#)]
67. Manière, C.; Durand, L.; Weibel, A.; Estournès, C. Spark-plasma-sintering and finite element method: From the identification of the sintering parameters of a submicronic  $\alpha$ -alumina powder to the development of complex shapes. *Acta Mater.* **2016**, *102*, 169–175. [[CrossRef](#)]
68. Voisin, T.; Monchoux, J.P.; Durand, L.; Karnatak, N.; Thomas, M.; Couret, A. An Innovative Way to Produce  $\gamma$ -TiAl Blades: Spark Plasma Sintering. *Adv. Eng. Mater.* **2015**, *17*, 1408–1413. [[CrossRef](#)]
69. Manière, C.; Durand, L.; Weibel, A.; Chevallier, G.; Estournès, C. A sacrificial material approach for spark plasma sintering of complex shapes. *Scr. Mater.* **2016**, *124*, 126–128. [[CrossRef](#)]
70. Manière, C.; Nigito, E.; Durand, L.; Weibel, A.; Beynet, Y.; Estournès, C. Spark plasma sintering and complex shapes: The deformed interfaces approach. *Powder Technol.* **2017**, *320*, 340–345. [[CrossRef](#)]
71. Olevsky, E.A.; Garcia-Cardona, C.; Bradbury, W.L.; Haines, C.D.; Martin, D.G.; Kapoor, D. Fundamental Aspects of Spark Plasma Sintering: II. Finite Element Analysis of Scalability. *J. Am. Ceram. Soc.* **2012**, *95*, 2414–2422. [[CrossRef](#)]

72. Voisin, T.; Durand, L.; Karnatak, N.; Le Gallet, S.; Thomas, M.; Le Berre, Y.; Castagné, J.F.; Couret, A. Temperature control during Spark Plasma Sintering and application to up-scaling and complex shaping. *J. Mater. Process. Technol.* **2013**, *213*, 269–278. [[CrossRef](#)]
73. Franceschin, G.; Flores-Martínez, N.; Vázquez-Victorio, G.; Ammar, S.; Valenzuela, R. Sintering and reactive sintering by spark plasma sintering (SPS). In *Sintering of Functional Materials*; IntechOpen: London, UK, 2017; Available online: <https://www.intechopen.com/books/sintering-of-functional-materials/sintering-and-reactive-sintering-by-spark-plasma-sintering-sps> (accessed on 1 May 2020).
74. Isobe, T.; Daimon, K.; Sato, T.; Matsubara, T.; Hikichi, Y.; Ota, T. Spark plasma sintering technique for reaction sintering of Al<sub>2</sub>O<sub>3</sub>/Ni nanocomposite and its mechanical properties. *Ceram. Int.* **2008**, *34*, 213–217. [[CrossRef](#)]
75. Waseem, O.A.; Lee, J.; Lee, H.M.; Ryu, H.J. The effect of Ti on the sintering and mechanical properties of refractory high-entropy alloy Ti<sub>x</sub>W<sub>1-x</sub>TaVCr fabricated via spark plasma sintering for fusion plasma-facing materials. *Mater. Chem. Phys.* **2018**, *210*, 87–94. [[CrossRef](#)]
76. Meir, S.; Kalabukhov, S.; Froumin, N.; Dariel, M.P.; Frage, N. Synthesis and densification of transparent magnesium aluminate spinel by SPS processing. *J. Am. Ceram. Soc.* **2009**, *92*, 358–364. [[CrossRef](#)]
77. Martins, D.; Grumbach, F.; Simoulin, A.; Sallot, P.; Mocellin, K.; Bellet, M.; Estournès, C. Spark plasma sintering of a commercial TiAl 48-2-2 powder: Densification and creep analysis. *Mater. Sci. Eng. A* **2018**, *711*, 313–316. [[CrossRef](#)]
78. Anselmi-Tamburini, U.; Garay, J.E.; Munir, Z.A. Fast low-temperature consolidation of bulk nanometric ceramic materials. *Scr. Mater.* **2006**, *54*, 823–828. [[CrossRef](#)]
79. Lenel, F. Resistance sintering under pressure. *JOM* **1955**, *7*, 158–167. [[CrossRef](#)]
80. Weissler, G.A. Resistance sintering with alumina dies. *Int. J. Powder Met. Powder Technol.* **1981**, *17*, 107–118.
81. Herrmann, M.; Schulz, I.; Bales, A.; Sempf, K.; Hoehn, S. “Snow flake” structures in silicon nitride ceramics—Reasons for large scale optical inhomogeneities. *J. Eur. Ceram. Soc.* **2008**, *28*, 1049–1056. [[CrossRef](#)]
82. Langer, J.; Hoffmann, M.J.; Guillon, O. Electric Field-Assisted Sintering in Comparison with the Hot Pressing of Ytria-Stabilized Zirconia. *J. Am. Ceram. Soc.* **2011**, *94*, 24–31. [[CrossRef](#)]
83. Westbrook, J.H.; Fleischer, R.L. *Crystal Structures of Intermetallic Compounds*; John Wiley & Sons: Hoboken, NJ, USA, 2000.
84. Paufler, P.J.H. *Westbrook, R.L. Intermetallic Compounds Principles and Practice*; John Wiley & Sons: Hoboken, NJ, USA, 1995.
85. Cobbinah, P.V.; Matizamhuka, W.R. Solid-State Processing Route, Mechanical Behaviour, and Oxidation Resistance of TiAl Alloys. *Adv. Mater. Sci. Eng.* **2019**, *2019*, 1–21. [[CrossRef](#)]
86. Froes, F.H.; Suryanarayana, C.; Eliezer, D. Synthesis, properties and applications of titanium aluminides. *J. Mater. Sci.* **1992**, *27*, 5113–5140. [[CrossRef](#)]
87. McCullough, C.; Valencia, J.J.; Levi, C.G.; Mehrabian, R. Phase equilibria and solidification in Ti-Al alloys. *Acta Met.* **1989**, *37*, 1321–1336. [[CrossRef](#)]
88. Jones, S.A.; Shull, R.D.; McAlister, A.J.; Kaufman, M.J. Microstructural studies of Ti-Al alloys in the vicinity of the “eutectoid” reaction ( $\alpha \rightarrow \alpha_2 \gamma$ ). *Scr. Met.* **1988**, *22*, 1235–1240. [[CrossRef](#)]
89. JH, P. Phase Reactions and Processing in the Ti-Al Based Intermetallics. *ISI Int.* **1991**, *31*, 1080–1087.
90. Djanarthany, S.; Viala, J.C.; Bouix, J. An overview of monolithic titanium aluminides based on Ti<sub>3</sub>Al and TiAl. *Mater. Chem. Phys.* **2001**, *72*, 301–319. [[CrossRef](#)]
91. Sastry, S.M.L.; Lipsitt, H.A. Ordering transformations and mechanical properties of Ti 3 Al and Ti 3 Al-Nb alloys. *Met. Trans. A* **1977**, *8*, 1543–1552. [[CrossRef](#)]
92. Sarkar, S.; Datta, S.; Das, S.; Basu, D. Oxidation protection of gamma-titanium aluminide using glass–ceramic coatings. *Surf. Coat. Technol.* **2009**, *203*, 1797–1805. [[CrossRef](#)]
93. Wang, Z.; Sun, H.; Du, Y.; Yuan, J. Effects of Powder Preparation and Sintering Temperature on Properties of Spark Plasma Sintered Ti-48Al-2Cr-8Nb Alloy. *Metals* **2019**, *9*, 861. [[CrossRef](#)]
94. Werwer, M.; Kabir, R.; Cornec, A.; Schwalbe, K.H. Fracture in lamellar TiAl simulated with the cohesive model. *Eng. Fract. Mech.* **2007**, *74*, 2615–2638. [[CrossRef](#)]
95. Stoloff, N.S.; Sikka, V.K. *Physical Metallurgy and Processing of Intermetallic Compounds*; Springer Science & Business Media: Berlin/Heidelberg, Germany, 2012.
96. Kothari, K.; Radhakrishnan, R.; Wereley, N.M. Advances in gamma titanium aluminides and their manufacturing techniques. *Prog. Aerosp. Sci.* **2012**, *55*, 1–16. [[CrossRef](#)]

97. Kim, Y.W.; Dimiduk, D.M. Progress in the understanding of gamma titanium aluminides. *JOM* **1991**, *43*, 40–47. [[CrossRef](#)]
98. Wu, X. Review of alloy and process development of TiAl alloys. *Eur. Congr. Adv. Mater. Process.* **2006**, *14*, 1114–1122. [[CrossRef](#)]
99. Hernandez, J.; Murr, L.E.; Gaytan, S.M.; Martinez, E.; Medina, F.; Wicker, R.B. Microstructures for two-phase gamma titanium aluminide fabricated by electron beam melting. *Met. Microstruct Anal.* **2012**, *1*, 14–27. [[CrossRef](#)]
100. Recina, V. *Mechanical Properties of Gamma Titanium Aluminides*; Chalmers University of Technology: Gothenburg, Sweden, 2000.
101. Wang, G.X.; Dahms, M. Influence of heat treatment on microstructure of Ti-35wt%Al prepared by elemental powder metallurgy. *Scr. Met. Mater.* **1992**, *26*, 717–722. [[CrossRef](#)]
102. Gupta, R.K.; Pant, B.; Sinha, P.P. Theory and practice of  $\gamma$   $\alpha$  2 Ti aluminide: A review. *Trans. Indian Inst. Met.* **2014**, *67*, 143–165. [[CrossRef](#)]
103. Wang, D.; Yuan, H.; Qiang, J. The microstructure evolution, mechanical properties and densification mechanism of TiAl-based alloys prepared by spark plasma sintering. *Metals* **2017**, *7*, 201. [[CrossRef](#)]
104. Wang, D.; Zhao, H.; Zheng, W. Effect of temperature-related factors on densification, microstructure and mechanical properties of powder metallurgy TiAl-based alloys. *Adv. Powder Technol.* **2019**, *30*, 2555–2563. [[CrossRef](#)]
105. Liu, J.; Li, Z.; Yan, H.; Jiang, K. Spark Plasma Sintering of Alumina Composites with Graphene Platelets and Silicon Carbide Nanoparticles. *Adv. Eng. Mater.* **2014**, *16*, 1111–1118. [[CrossRef](#)]
106. Voisin, T.; Monchoux, J.P.; Hantcherli, M.; Mayer, S.; Clemens, H.; Couret, A. Microstructures and mechanical properties of a multi-phase  $\beta$ -solidifying TiAl alloy densified by spark plasma sintering. *Acta Mater.* **2014**, *73*, 107–115. [[CrossRef](#)]
107. Zhang, C.; Zhang, K.; Wang, G. Dependence of heating rate in PCAS on microstructures and high temperature deformation properties of  $\gamma$ -TiAl intermetallic alloys. *Intermetallics* **2010**, *18*, 834–840. [[CrossRef](#)]
108. Mphahlele, M.R.; Olevsky, E.A.; Olubambi, P.A. Chapter 12-Spark plasma sintering of near net shape titanium aluminide: A review. In *Spark Plasma Sinter*; Elsevier Inc.: Amsterdam, The Netherlands, 2019; pp. 281–299.
109. Appel, F.; Clemens, H.; Fischer, F.D. Modeling concepts for intermetallic titanium aluminides. *Prog. Mater. Sci.* **2016**, *81*, 55–124. [[CrossRef](#)]
110. Bewlay, B.P.; Nag, S.; Suzuki, A.; Weimer, M.J. TiAl alloys in commercial aircraft engines. *Mater. High Temp.* **2016**, *33*, 549–559. [[CrossRef](#)]
111. Pflumm, R.; Friedle, S.; Schütze, M. Oxidation protection of  $\gamma$ -TiAl-based alloys—A review. *Intermetallics* **2015**, *56*, 1–14. [[CrossRef](#)]
112. Dai, J.; Zhu, J.; Chen, C.; Weng, F. High temperature oxidation behavior and research status of modifications on improving high temperature oxidation resistance of titanium alloys and titanium aluminides: A review. *J. Alloy. Compd.* **2016**, *685*, 784–798. [[CrossRef](#)]
113. Lu, X.; He, X.B.; Zhang, B.; Qu, X.H.; Zhang, L.; Guo, Z.X.; Tian, J.J. High-temperature oxidation behavior of TiAl-based alloys fabricated by spark plasma sintering. *J. Alloy. Compd.* **2009**, *478*, 220–225. [[CrossRef](#)]
114. Kumpfert, J.; Kim, Y.W.; Dimiduk, D.M. Effect of microstructure on fatigue and tensile properties of the gamma TiAl alloy Ti-46.5Al-3.0Nb-2.1Cr-0.2W. *Mater. Sci. Eng. A* **1995**, *192*, 465–473. [[CrossRef](#)]
115. Cobbinah, P.V.; Matizamhuka, W.; Machaka, R.; Shongwe, M.B.; Yamabe-Mitarai, Y. The effect of Ta additions on the oxidation resistance of SPS-produced TiAl alloys. *Int. J. Adv. Manuf. Technol.* **2020**, *106*, 3203–3215. [[CrossRef](#)]
116. Kenel, C.; Lis, A.; Dawson, K.; Stiefel, M.; Pecnik, C.; Barras, J.; Colella, A.; Hauser, C.; Tatlock, G.J.; Leinenbach, C.; et al. Mechanical performance and oxidation resistance of an ODS  $\gamma$ -TiAl alloy processed by spark plasma sintering and laser additive manufacturing. *Intermetallics* **2017**, *91*, 169–180. [[CrossRef](#)]
117. Kim, Y.W. Ordered intermetallic alloys, part III: Gamma titanium aluminides. *JOM* **1994**, *46*, 30–39. [[CrossRef](#)]
118. Huang, S.C.; Hall, E.L. The effects of Cr additions to binary TiAl-base alloys. *Met. Trans. A* **1991**, *22*, 2619–2627. [[CrossRef](#)]
119. Huang, S.C.; Hall, E.L. Characterization of the effect of vanadium additions to TiAl base alloys. *Acta Met. Mater.* **1991**, *39*, 1053–1060. [[CrossRef](#)]
120. Hashimoto, K. High-Temperature Tensile Properties of Ti-Al-X (X=Cr,W) Consisting of  $\hat{1} \pm 2$ ,  $\hat{1}^2$  and  $\hat{1}^3$  in Three Phases. *Mater. Sci. Forum* **2012**, *706–709*, 1066–1070. [[CrossRef](#)]

121. Zhu, D.D.; Wang, H.W.; Qi, J.Q.; Zou, C.M.; Wei, Z.J. Effect of Cr addition on microstructures and nanohardness of rapidly solidified Ti–48Al alloy. *Mater. Sci. Technol.* **2012**, *28*, 1385–1390. [\[CrossRef\]](#)
122. Kawabata, T.; Fukai, H.; Izumi, O. Effect of ternary additions on mechanical properties of TiAl. *Acta Mater.* **1998**, *46*, 2185–2194. [\[CrossRef\]](#)
123. Pelachová, T.; Lapin, J. Cyclic oxidation behaviour of intermetallic Ti-46Al-8Ta alloy in air. *Kov. Mater* **2015**, *53*, 415–422. [\[CrossRef\]](#)
124. Yuanyuan, L.; Weidong, Z.; Zhengping, X.; Xiaonan, M.; Yingli, Y.; Jinping, W.; Hangbiao, S. Microstructure, mechanical properties and oxidation behavior of a hot-extruded TiAl containing Ta. *Rare Met. Mater. Eng.* **2015**, *44*, 282–287. [\[CrossRef\]](#)
125. Mitoraj, M.; Godlewska, E.M. Oxidation of Ti–46Al–8Ta in air at 700 °C and 800 °C under thermal cycling conditions. *Intermetallics* **2013**, *34*, 112–121. [\[CrossRef\]](#)
126. Popela, T.; Vojtěch, D.; Novák, P.; Knotek, V.; Průša, F.; Michalcová, A.; Novák, M.; Šerák, J. High-temperature oxidation of Ti-Al-Ta and Ti-Al-Nb alloys. *Metal* **2010**, *18*, 1–4.
127. Lapin, J.; Pelachová, T.; Dománková, M. Long-term creep behaviour of cast TiAl-Ta alloy. *Intermetallics* **2018**, *95*, 24–32. [\[CrossRef\]](#)
128. Lapin, J.; Pelachová, T.; Dománková, M. Creep behaviour of a new air-hardenable intermetallic Ti–46Al–8Ta alloy. *Intermetallics* **2011**, *19*, 814–819. [\[CrossRef\]](#)
129. Hodge, A.M.; Hsiung, L.M.; Nieh, T.G. Creep of nearly lamellar TiAl alloy containing W. *Scr. Mater.* **2004**, *51*, 411–415. [\[CrossRef\]](#)
130. Fang, H.; Chen, R.; Yang, Y.; Tan, Y.; Su, Y.; Ding, H.; Guo, J. Effects of Boron On Microstructure Evolution and Mechanical Properties in Ti46Al8Nb2.6C0.8Ta Alloys. *Adv. Eng. Mater.* **2019**, *21*, 1900143. [\[CrossRef\]](#)
131. Li, M.; Xiao, S.; Xiao, L.; Xu, L.; Tian, J.; Chen, Y. Effects of carbon and boron addition on microstructure and mechanical properties of TiAl alloys. *J. Alloy. Compd.* **2017**, *728*, 206–221. [\[CrossRef\]](#)
132. Čegan, T.; Szurman, I. Thermal stability and precipitation strengthening of fully lamellar Ti-45Al-5Nb-0.2 B-0.75 C alloy. *Met. Mater.* **2018**, *55*, 421–430.
133. Wang, Q.; Ding, H.; Zhang, H.; Chen, R.; Guo, J.; Fu, H. Variations of microstructure and tensile property of  $\gamma$ -TiAl alloys with 0–0.5at% C additives. *Mater. Sci. Eng. A* **2017**, *700*, 198–208. [\[CrossRef\]](#)
134. Li, M.; Xiao, S.; Chen, Y.; Xu, L.; Tian, J. The effect of boron addition on the high-temperature properties and microstructure evolution of high Nb containing TiAl alloys. *Mater. Sci. Eng. A* **2018**, *733*, 190–198. [\[CrossRef\]](#)
135. Bazhenov, V.E.; Kuprienko, V.S.; Fadeev, A.V.; Bazlov, A.I.; Belov, V.D.; Titov, A.Y.; Koltzgin, A.V.; Komissarov, A.A.; Plisetskaya, I.V.; Logachev, I.A. Influence of Y and Zr on TiAl43Nb4Mo1B0. 1 titanium aluminide microstructure and properties. *Mater. Sci. Technol.* **2020**, *36*, 548–555. [\[CrossRef\]](#)
136. Xu, W.; Huang, K.; Wu, S.; Zong, Y.; Shan, D. Influence of Mo content on microstructure and mechanical properties of  $\beta$ -containing TiAl alloy. *Trans. Nonferrous Met. Soc. China* **2017**, *27*, 820–828. [\[CrossRef\]](#)
137. Wu, Y.; Hwang, S.K. Microstructural refinement and improvement of mechanical properties and oxidation resistance in EPM TiAl-based intermetallics with yttrium addition. *Acta Mater.* **2002**, *50*, 1479–1493. [\[CrossRef\]](#)
138. Kong, F.T.; Chen, Y.Y.; Li, B.H. Influence of yttrium on the high temperature deformability of TiAl alloys. *Mater. Sci. Eng. A* **2009**, *499*, 53–57. [\[CrossRef\]](#)
139. Stringer, J. The reactive element effect in high-temperature corrosion. *Mater. Sci. Eng. A* **1989**, *120*, 129–137. [\[CrossRef\]](#)
140. Hadi, M.; Bayat, O.; Meratian, M.; Shafyei, A.; Ebrahimzadeh, I. Oxidation Properties of a Beta-Stabilized TiAl Alloy Modified by Rare Earth Elements. *Oxid. Met.* **2018**, *90*, 421–434. [\[CrossRef\]](#)
141. Wimler, D.; Lindemann, J.; Clemens, H.; Mayer, S. Microstructural Evolution and Mechanical Properties of an Advanced  $\gamma$ -TiAl Based Alloy Processed by Spark Plasma Sintering. *Materials* **2019**, *12*, 1523. [\[CrossRef\]](#)
142. Saage, H.; Huang, A.J.; Hu, D.; Loretto, M.H.; Wu, X. Microstructures and tensile properties of massively transformed and aged Ti46Al8Nb and Ti46Al8Ta alloys. *Intermetallics* **2009**, *17*, 32–38. [\[CrossRef\]](#)







Article

# Joining of Oxide Dispersion-Strengthened Steel Using Spark Plasma Sintering

Foad Naimi <sup>1</sup>, Jean-Claude Niepce <sup>1</sup>, Mostapha Ariane <sup>2</sup>, Cyril Cayron <sup>3</sup>, José Calapez <sup>3</sup>, Jean-Marie Gentzbittel <sup>3</sup> and Frédéric Bernard <sup>2,\*</sup>

<sup>1</sup> SINTERmat, 7 Avenue Maréchal Leclerc, 21500 Montbard, France; foad.naimi@sinter-mat.com (F.N.); jc.niepce@sinter-mat.com (J.-C.N.)

<sup>2</sup> ICB UMR 6303 CNRS/ UBFC, 9 Av. A. Savary BP47078, 21078 Dijon, France; moustapha.ariane@u-bourgogne.fr

<sup>3</sup> GRENOBLE-ALPES-CEA-LITEN, 38054 Grenoble CEDEX 9, France; cyril.cayron@epfl.ch (C.C.); jose.calapez@cea.fr (J.C.); jean-marie.gentzbittel@cea.fr (J.-M.G.)

\* Correspondence: fbernard@u-bourgogne.fr; Tel.: +33-3-80-39-61-25

Received: 5 June 2020; Accepted: 30 July 2020; Published: 2 August 2020

**Abstract:** Difficulties with joining oxide dispersion-strengthened (ODS) steels using classical welding processes have led to the development of alternative joining techniques such as spark plasma sintering (SPS). SPS, which is classically employed for performing sintering, may also be used to join relatively large components due to the simultaneous application of electrical pulsed current and uniaxial charge. SPS technology was tested by joining two ODS steel disks. The preliminary tests showed that it is necessary to control surface roughness before joining. Furthermore, the use of ground and lapped surfaces seemed to improve the quality of the interface. Tensile tests on two ODS cylinders joined using SPS were performed at 750 °C without any additives. Failure occurred away from the interface with a total elongation close to 50% and an ultimate stress of 110 MPa.

**Keywords:** ODS steel; SPS joining; interface; tensile tests

## 1. Introduction

Generation IV nuclear power plants need to increase efficiency and produce less radioactive material. Compared to current thermal-neutron reactors, the new generation of fast-neutron reactors can reduce the total radiotoxicity of nuclear waste by using all or almost all of the waste as fuel. Due to their excellent creep strength, corrosion resistance, and radiation resistance, ODS (oxide dispersion-strengthened) ferritic steels are good structural candidates for cladding and fuel applications in fast-neutron reactors [1–3]. The strengthening of these materials is due to the homogeneous distribution of nanosized oxide particles, which inhibits dislocation movement and stabilizes the grain boundary microstructure [4–6]. However, the joining of ODS alloys proves to be challenging. The classical fusion welding techniques such as electric arc welding or high energy fusion such as laser welding or electron beam welding, results in the agglomeration as well as coarsening of dispersed nanoparticles and a loss of strength in the joined material [7]. Solid-state welding processes such as inertia friction welding, friction stir welding, and pressure resistance welding have already been explored [8–10]. Mechanical testing and microstructure observation of ODS steels joined using solid-state diffusion bonding have also obtained encouraging results [11,12]. The SPS (spark plasma sintering) technique was employed in this study to join bulk ODS ferritic steel to itself without disrupting both the fine uniform dispersion of nanosized oxide particles and the grain structure. Joining was achieved by supplying an electrical pulsed current to the samples in order to cause rapid heating via the Joule effect, while simultaneously applying uniaxial pressure. The two cylindrical ODS steel samples were encapsulated in a graphite tool, formed by a die and two punches used

to transmit the applied load. The electrical pulsed current flows through the setup formed by the graphite assembly and the bulk sample. This leads to direct heating via the Joule effect in a very short time [13,14]. Recently, SPS was used as an alternative consolidation technique of ODS steel powder [15,16]. A few studies have dealt with bulk metallic material joined using SPS [16] and only one of them has been performed on an extruded 20 wt.% chromium ODS PM2000 sample (PM2000 is a commercial product of the Plansee Company), which exhibits a fine microstructure [17]. The use of SPS technology as a means of joining two recrystallized large grain ODS PM2000 disks is the subject of the present article.

## 2. Materials and Methods

SPS joining was performed on an FCT HPD-25 spark plasma sintering machine (FCT Systeme, Rauenstein, Germany), located in the MATEIS laboratory at INSA Lyon using an on/off pulse sequence of 10:10 ms. Two joining configurations were tested: one with and one without a graphite die (Figure 1a,b), for which two thermal distributions were simulated (Figure 1c,d) using a thermo-electrical Abaqus model. In Figure 1a, the temperature was monitored using a radial pyrometer that determines the temperature at the centre of the graphite die wall 2 mm from the sample. SPS-joining was performed using a graphite foil of 0.2 mm thickness inserted between the various system components. Addition of the graphite foil helps to preserve the SPS tools as well as improve the electrical contact between each SPS component. In Figure 1b, the IR pyrometer is placed in contact with the joining area. This latter configuration was selected in order to eliminate any contamination of the material with graphite. Moreover, the temperature measurement via the radial pyrometer was performed at the contact zone between the two disks, which is un-joined at the beginning of the SPS cycle.

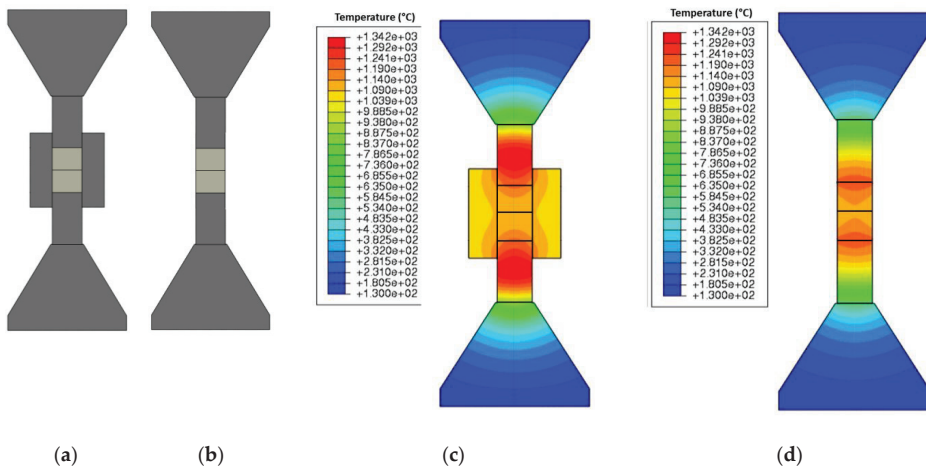


**Figure 1.** SPS configurations investigated in this study where (a) uses a die and (b) does not use a die. Numerical thermal mapping for both configurations where (c) represents the experimental setup with a die and (d) is without a die.

The thermal mappings for the two configurations previously described (Figure 1c,d) do not show a real difference regardless of the presence or absence of the SPS graphite die. Indeed, both thermal and electrical contact resistance between each component is assumed as perfect. Consequently, only the material properties can affect the flow of current. In our case, the sample and the die were both electrical conductors, therefore, a small proportion of current was diverted to the die, but the majority flowed through the sample (Figure 2).

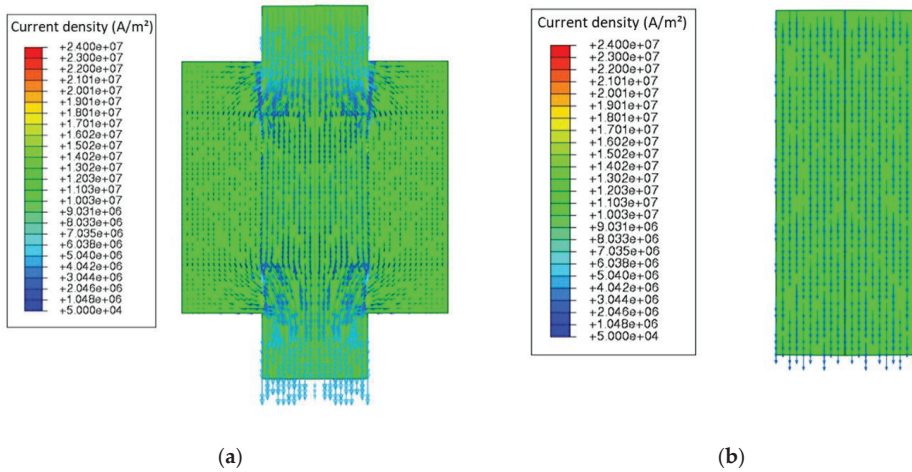


Figure 2. Current vector field for a sample (a) with a die and (b) without a die.

A recrystallized ODS PM2000 steel bar was delivered from Plansee AG, with a cylindrical diameter of 100 mm. PM2000 is a ferritic 19 wt.%, Cr–5.5 wt.%, Al–0.5 wt.%, Ti–0.5 wt.%, Y<sub>2</sub>O<sub>3</sub> steel. The as-received microstructure was composed of large elongated grains (~few mm) parallel to the bar axis orientation, as shown in Figure 3.

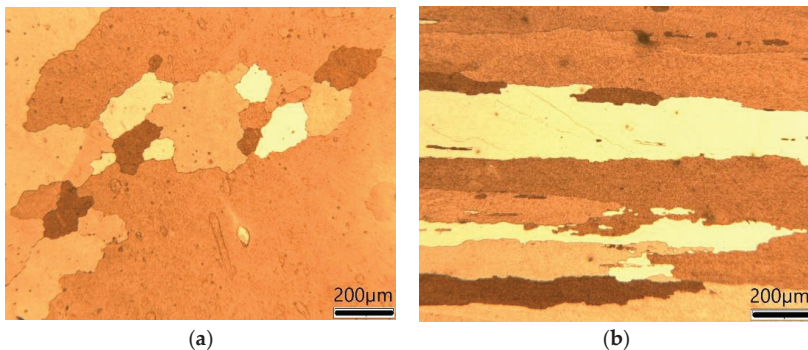
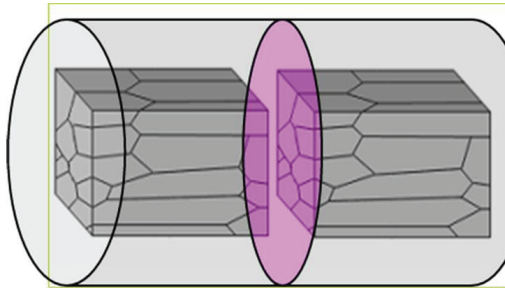


Figure 3. Optical micrographs of a PM2000 sample where (a) shows a transverse section and (b) depicts a longitudinal section.

Cylindrical samples of 10 mm diameter and 5 mm height were machined in the axis parallel to the bar axis. Only the orientation “transverse–transverse” of the joint, shown in Figure 4, was tested.

In order to evaluate the SPS joining technology, a similar SPS procedure involving surface preparation, SPS environment, and thermal conditions was carried out without an additional interlayer (i.e., direct contact between parts to be assembled). SPS diffusion bonding of samples with varying surface roughness was investigated. Three levels of surface finish were tested corresponding to the following surface roughness values:

- Rough machined surface (Ra ~1.2 microns).
- Ground surface (Ra ~0.17 microns).
- Lapped surface (Ra ~0.04 microns).



**Figure 4.** Diagram of the SPS joining orientation according to the sample orientation.

Several experimental SPS conditions, summarized in Table 1, were tested.

**Table 1.** Experimental conditions for SPS joining of ODS steel disks.

| 3 Sample Preparations                                | Heating Rate | Pressure                                  | Temperature       | Holding Time |
|--|--------------|---|-------------------|--------------|
| Machined surface<br>Ground surface<br>Lapped surface | 150 °C/min   | 20 MPa without a die to 64 MPa a with die | 950 °C to 1100 °C | 0 to 30 min  |

In order to evaluate the possibility of performing a SPS-joining on ODS steel, two sample dimensions were investigated:

(i) On small disks (two disks with a 10 mm diameter and 5 mm thickness) to determine the best SPS-joining conditions. In this case, the classical SPS environment (graphite die and graphite foil called papyex<sup>®</sup>) was used. The main objective of these preliminary tests was to study the influence of the surface roughness on the quality of the interface. The quality of SPS welding, especially the quality of the SPS interface, was evaluated by studying the metallographic micrographs obtained after cutting the samples in the longitudinal orientation. Then, the samples were polished and chemically etched with a solution (20 mL HF + 50 mL HCl + 10 mL HNO<sub>3</sub> + 30 mL water).

(ii) On larger samples (two cylinders with a 20 mm diameter and 15 mm length) for the purpose of performing tensile tests at room temperature and at 750 °C in order to evaluate the mechanical resistance of the interface. Moreover, to achieve a clean interface without graphite contamination, SPS-joining was performed without a die using the lowest possible applied load of 16 MPa.

### 3. Results and Discussion

#### 3.1. Small Disks: Influence of Surface Roughness

The optical micrograph shown in Figure 5, relative to the sample prepared with a machined surface and joined using SPS at 975 °C for 10 min, revealed large voids corresponding to the initial surface roughness ( $R_a = 1.2 \mu\text{m}$ ) and large unbounded areas measuring up to 150  $\mu\text{m}$ . Additional experiments showed that time and temperature did not remove the pores or reduce the size of defects at the joining interface.

Metallographic observations showed that SPS-joining of samples with a lapped surface were more encouraging. Only some areas remained un-joined or contained pores (Figure 6a). In addition, some cracks were observed at lower temperatures (950 °C, Figure 6a) and remained after joining at higher temperatures (1025 °C and 1050 °C, Figure 6b). However, some joints seemed perfect, as shown in Figure 6b. The observed interface was clean, without cavities, and with few small grains at the interface.

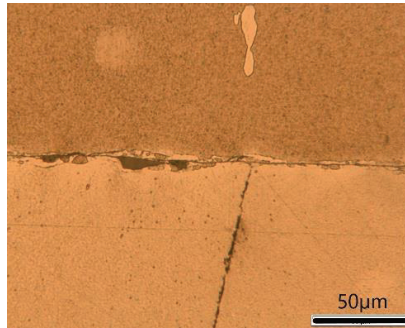


**Figure 5.** Micrograph of the bonding interface. SPS joined at 975 °C for 10 min from a sample with a rough machined surface.

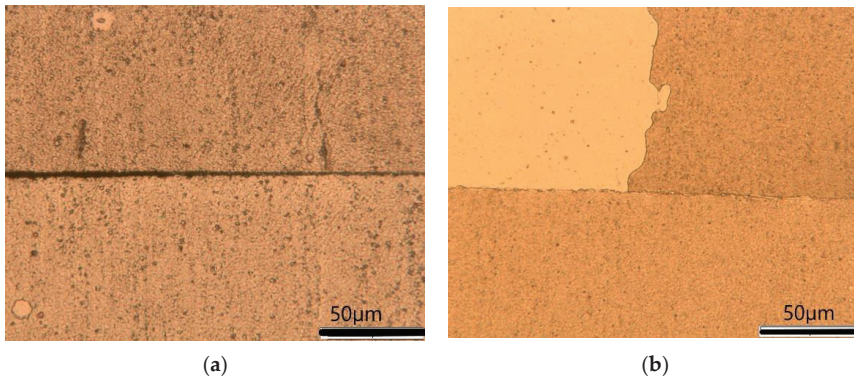


**Figure 6.** Metallographic observations of the interface in a joint made from two pieces with lapped surfaces, showing: (a) a poor-quality joint at lower temperature (950 °C) and (b) a good quality joint at higher temperatures (1025 °C and 1050 °C).

Metallographic results of the samples prepared with a ground surface were quite similar to those obtained using the SPS of a lapped surface. A satisfactory joint was obtained at 975 °C for 10 min although some large defects appeared. The initially large elongated grains did not cross the interface. Moreover, a strong crystal lattice distortion in the interfacial zone was observed in a 10 µm wide area on both sides of the interface using backscattered electron (BSE) imaging under a scanning electron microscope (SEM) (Figure 7). The presence of micron-sized grains at the interface could be observed.

Electron backscatter diffraction (EBSD) images (Figure 8a–c) revealed new micron-sized grains that were randomly oriented and are highlighted at the joining interface. These small grains were formed via recrystallization at the joining interface during SPS operation at 975 °C. Such small grains have also been observed on lapped surfaces, but their number and size were relatively small.

Consequently, the preliminary results confirmed the possibility of joining PM 2000 small disks using SPS. From previous tests, successful joining was only achieved with samples that had their surfaces lapped or ground. In contrast, SPS joining of samples with a machined surface did not lead to satisfactory joining. Too many defects (non-welded areas and cavities) remained, despite an increase in the SPS temperature or holding time. Distortion along the interface combined with the application of a high SPS temperature resulted in the recrystallization of new micrometric grains. In conclusion, these preliminary tests, despite the observed defects, have demonstrated the potential to join PM2000 samples using SPS. This work shows that the SPS temperature and the holding time have a slight

effect on the microstructure of the bonding interface. Bonding coarse grain to coarse grain is known to be difficult [18], however, the micrographic observations revealed some very clean joining areas. SEM and EBSD imaging of the well-bonded interface revealed recrystallized small micron-sized grains that were randomly oriented.

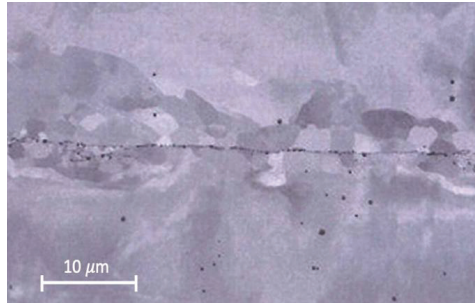


**Figure 7.** Scanning electron microscopy (SEM) image in backscattered electron (BSE) imaging of the interface between two joined disks with ground surfaces.

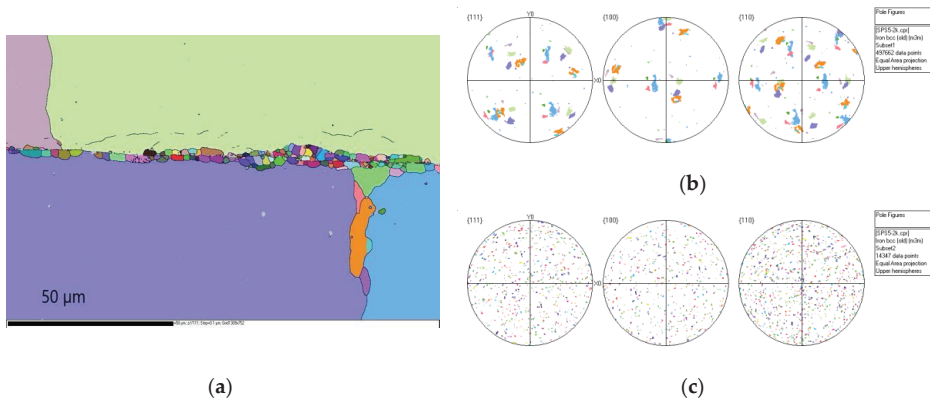


**Figure 8.** Interface between two joined disks where (a) shows the associated electron backscatter diffraction (EBSD) image, (b) reveals the pole figures of the large millimetric grains, and (c) represents the pole figures of the small micron-size grains at the interface. The same colour code is used in (a), (b), and (c).

3.2. Large Disks: Evaluation of the Mechanical Properties

Five large-size samples were joined with SPS using the welding conditions reported in Table 2. An example of a joined block obtained using SPS is shown in Figure 9.

**Table 2.** Summary of the SPS-joining conditions.

| Samples | Surface Preparation | SPS Conditions |
|---------|---------------------|----------------|
| 1       | Ground              | 975 °C/20 min  |
| 2       | Ground              | 1050 °C/20 min |
| 3       | Ground              | 1100 °C/10 min |
| 4       | Lapped              | 1100 °C/3 min  |
| 5       | Lapped              | 1100 °C/10 min |

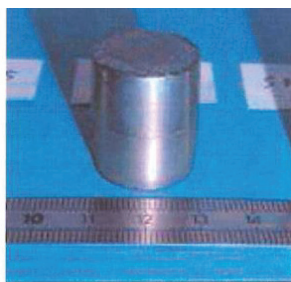


**Figure 9.** Example of a block joined using SPS.

The sampling of tensile specimens in each block was made using electrical discharge machining (EDM), according to the orientation defined in Figure 10. Two small-sized cylindrical tensile samples with a gauge length of 10.2 mm and a gauge diameter of 2.6 mm, along with two additional flat tensile specimens ( $2 \times 2 \text{ mm}^2$  section and 10 mm gauge length) were machined in each block. The welding bond failed during the machining of numerous tensile test specimens and thus a limited number of tensile specimens were available. Tensile tests were performed at room temperature and at  $750 \text{ }^\circ\text{C}$  in air using an initial strain rate of  $5 \times 10^{-4} \text{ s}^{-1}$ , according to the NF-EN6892-1 and NF-EN6892-2 standards, respectively. At  $750 \text{ }^\circ\text{C}$ , the tensile specimens were heated with a radiant furnace for 30 min prior to testing.

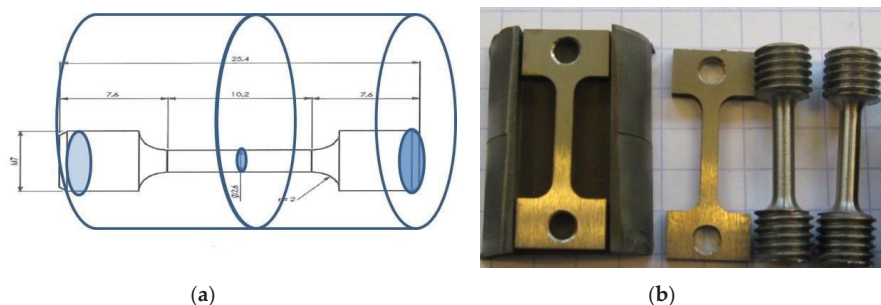


**Figure 10.** (a) Tensile testing samples were fabricated using electrical discharge machining (EDM) from the joined blocks. (b) Examples of flat and cylindrical tensile testing samples.

Only one tensile specimen from sample 1 could be tested at room temperature. The tensile specimen broke at the welded interface at a stress value of 282 MPa, a value much lower than the elastic yield strength of the parent material (Table 3). At room temperature, due to the anisotropic tensile behaviour of large textured grain, the strain mismatch at the bonding interface in such a small-sized tensile specimen induced high stress concentration at the welding interface.

At  $750 \text{ }^\circ\text{C}$ , the PM2000 tensile behaviour was much more ductile and both tensile specimens extracted from Sample 1 failed at the interface and resulted in an ultimate tensile strength (UTS) of 110 MPa and 114 MPa associated with a total elongation of 6% and 8%, respectively. Sample 2 also demonstrated promising mechanical strength ( $\sim 112 \text{ MPa}$ ), however, too many cracks were generated, leading to failure at the joined interface. The tensile rupture properties of all SPS-joined samples are listed in Table 3.

**Table 3.** Results of the tensile tests performed at 20 °C and 750 °C for the PM2000 SPS-joined disks

| Temperature | At 20 °C |                                 |                      | At 750 °C |                                 |                      |           |
|-------------|----------|---------------------------------|----------------------|-----------|---------------------------------|----------------------|-----------|
|             | Samples  | Ultimate Tensile Strength (MPa) | Total Elongation (%) | Failure   | Ultimate tensile strength (MPa) | Total Elongation (%) | Failure   |
|             | 1a       | 282                             | 0                    | interface | 110                             | 6.6                  | Interface |
|             | 1b       |                                 |                      |           | 114                             | 8.4                  | Interface |
|             | 2        | No tensile specimen available   |                      |           | 112                             | 0.4                  | Interface |
|             | 3        | No tensile specimen available   |                      |           | No tensile specimen available   |                      |           |
|             | 4a       | 200                             | 0                    |           | 101                             | 53.0                 | PM 2000   |
|             | 4b       | 534                             | 2.9                  |           | 116                             | 44.0                 | PM 2000   |
|             | 5        | No tensile specimen available   |                      |           | No tensile specimen available   |                      |           |

From these results, a higher temperature of 1100 °C and lapped surface preparation was chosen to perform SPS-joining of Sample 4 and Sample 5 (Table 2). Four tensile specimens could be machined from Sample 4, while the entire specimen from Sample 5 broke during final machining. Improved mechanical results compared to the previous were obtained at 20 °C and 750 °C (Table 3). The bonding strength at room temperature of one tensile specimen reached a value of 534 Ma, associated with an elongation of 2.9% of the base material and rupture was located at the welding interface. The second specimen broke at a lower value (200 MPa) and without plastic deformation. After a tensile test at 750 °C, specimens achieved an ultimate tensile strength of 101 and 116 MPa and a total elongation of 53% and 44%, respectively, and they fractured in the bulk material rather than at the joint (Figure 11a,b). In addition, Figure 11b presents the stress–strain curves for the specimens taken from Sample 4 and the as-received PM2000 alloy.

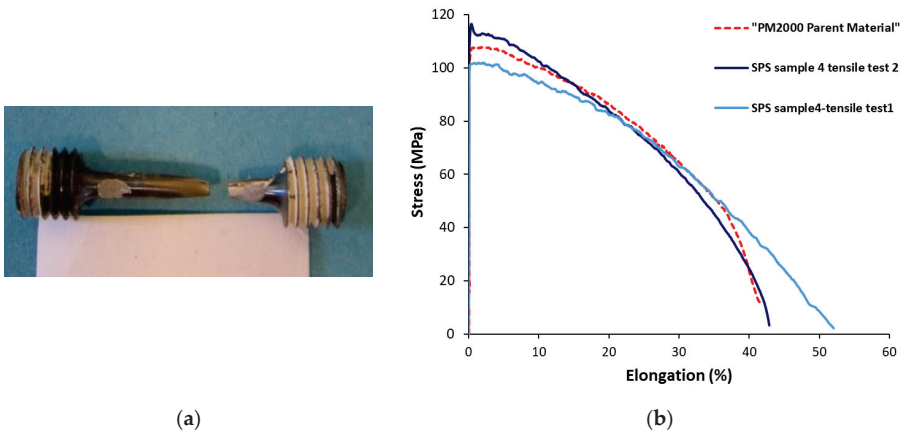


**Figure 11.** (a) Feature photographs of cylindrical tensile specimen (Sample 4-tensile test 2) following mechanical testing alongside (b) stress–strain curves at 750 °C for Sample 4 (cylindrical and flat samples) and the base PM2000 alloy in the as-received state.

Consequently, Sample 4, joined at 1100 °C with a very short dwell time, exhibited an interface that appeared clean, straight, and undamaged, even after the tensile test at 750 °C, as shown in the micrograph (Figure 12a) of the joint of the flat specimen seen in Figure 12a,b.

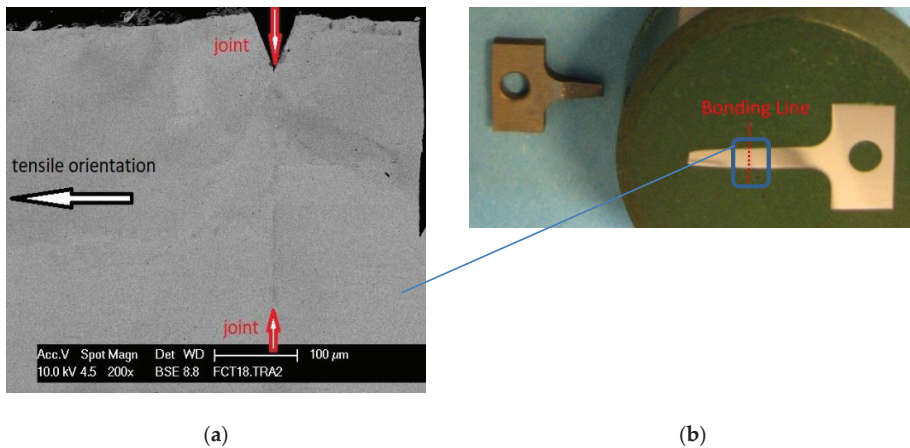


**Figure 12.** (a) Micrograph obtained by SEM of the bonding interface of a flat specimen from Sample 4 tested at 750 °C, (b) Location of the assembly area on the tensile specimen which is observed by SEM.

Nevertheless, the tensile tests conducted at 20 °C and 750 °C indicate that this joint achieved an interesting value of maximum strength. This study clearly demonstrates the potential to join ODS PM2000 steel to itself using a SPS technique.

#### 4. Conclusions

Twenty wt.% chromium ODS steel PM2000 exhibiting a microstructure of coarse grain was joined to itself via SPS. Different surface preparation techniques, joining temperature, and dwell times were tested. Microstructural observations of the bonding interface were carried out and tensile tests were performed on various samples at room temperature and at 750 °C. The main results are as follows:

- Successful joining was achieved with samples that had lapped joining surfaces.
- Micrographic observations revealed some very clean joining areas. SEM and EBSD imaging of the well-bonded interface revealed recrystallized small micron-sized grains that were randomly oriented.
- The sample prepared with a lapped surface and joined by SPS at 11,000 °C during 3 min exhibited nearly the same tensile behaviour as the base material at elevated temperatures and did not fracture at the joint, but rather failure occurred in the bulk material.

This shows the importance of surface roughness and surface preparation. Indeed, the joining of ODS steel involving the raw machining of its surfaces did not result in a junction free of defects and unassembled areas. The ODS steel joined using SPS with ground surfaces did not exhibit sufficient mechanical strength. The tensile strength at 750 °C reached the nominal values (i.e., 114 MPa) of the base material, but its ductility did not exceed 8% despite the presence of many defects. However, SPS-joining of ODS steel with lapped surfaces demonstrated good performance during tensile testing at 750 °C with failure occurring in the base metal and not at the interface (i.e., an ultimate tensile strength of 101 MPa and a total elongation of 53%). The results of the mechanical tests clearly indicate that these samples joined using SPS gives rise to satisfactory mechanical strength.

**Author Contributions:** Methodology F.N., J.C.; Modelling, M.A.; Formal analysis, F.N., J.-C.N., J.C. and C.C.; Writing—original draft preparation, F.N., J.-C.N. and C.C.; Writing—review and editing, J.-M.G., M.A. and F.B.; Supervision, F.B. and J.-M.G. All authors have read and agreed to the published version of the manuscript.

**Funding:** The direction of the Nuclear Energy Department of the CEA is acknowledged for their financial support through the ASTRID project.

**Acknowledgments:** The authors would like to thank the MATEIS laboratory in INSA Lyon. We would also like to acknowledge the advice provided by G. Bonnefont (INSA Lyon) and G. Fantozzi (INSA Lyon). Specific thanks to N. Al-Mufachi from AEC for his valuable comments.

**Conflicts of Interest:** The authors declare no conflicts of interest.

## References

1. Yvon, P.; Carré, F. Structural materials challenges for advanced reactor systems. *J. Nucl. Mater.* **2009**, *385*, 217–222. [[CrossRef](#)]
2. De Carlan, Y.; Béchade, J.-L.; Dubuisson, P.; Seran, J.-L.; Billot, P.; Bougault, A.; Cozzika, T.; Hamon, J.; Doriot, S.; Henry, J.; et al. CEA developments of new ferritic ODS alloys for nuclear applications. *J. Nucl. Mater.* **2009**, *386*, 430–432. [[CrossRef](#)]
3. Klueh, R.L.; Maziasz, P.J.; Kim, I.S.; Heatherly, L.; Hoelzer, D.T.; Hashimoto, N.; Kenik, E.A.; Miyahara, K. Tensile and creep properties of an oxide dispersion-strengthened ferritic steel. *J. Nucl. Mater.* **2002**, *307*, 773–777. [[CrossRef](#)]
4. Ukai, S.; Okuda, T.; Fujiwara, M.; Kobayashi, T.; Mizuta, S.; Nakashima, H. Characterization of High Temperature Creep Properties in Recrystallized 12Cr-ODS Ferritic Steel Claddings. *J. Nucl. Sci. Technol.* **2002**, *39*, 872–879. [[CrossRef](#)]
5. Steckmeyer, A.; Vargas Hideroa, R.; Gentzbitel, J.M.; Rabeau, V.; Fournier, B. Tensile anisotropy and creep properties of a Fe–14CrWTi ODS ferritic steel. *J. Nucl. Mater.* **2012**, *426*, 182–188. [[CrossRef](#)]
6. Inoue, M.; Kaito, T.; Ohtsuka, S. Research and Development of Oxide Dispersion Strengthened Ferritic Steels for Sodium Cooled Fast Breeder Reactor Fuels. In *Materials Issues for Generation IV Systems*; Springer: Dordrecht, The Netherlands, 2008; p. 311.
7. Sketchley, P.; Threadgill, P.L.; Wright, I.G. Rotary friction welding of an Fe<sub>3</sub>Al based ODS alloy. *Mater. Sci. Eng. A* **2002**, *329*, 756–762. [[CrossRef](#)]
8. Mathon, M.H.; Klosek, V.; De Carlan, Y.; Forest, L. Study of PM2000 microstructure evolution following FSW process. *J. Nucl. Mater.* **2009**, *386*, 475–478. [[CrossRef](#)]
9. Corpacce, F.; Monnier, A.; Poulon Quintin, A.; Manaud, J.-P. Resistance upset welding of an ODS steel fuel cladding—Identification of the thermal and mechanical phenomena using a numerical simulation. *Matériaux Tech.* **2012**, *100*, 291–298. [[CrossRef](#)]
10. Krishnardula, V.G.; Aluru, R.; Sofrijon, N.I.; Fergus, J.W.; Gale, W.F. Transient liquid phase bonding of ferritic oxide-dispersion-strengthened alloys. *Mater. Trans. A* **2006**, *37A*, 497–504. [[CrossRef](#)]
11. Noel, D. *Les Nanomatériaux et Leurs Applications Pour L'énergie Nucléaire*; Lavoisier: Paris, France, 2014; pp. 73–76.
12. Orru, R.; Licheri, R.; Locci, A.M.; Cincotti, A.; Cao, G.C. Consolidation/synthesis of materials by electric current activated/assisted sintering. *Mater. Sci. Eng. R-Rep.* **2009**, *63*, 127–287. [[CrossRef](#)]
13. Minier, L.; Le Gallet, S.; Grin Yu Bernard, F. A comparative study of nickel and alumina sintering using Spark Plasma Sintering (SPS). *Mat. Chem. Phys.* **2012**, *134*, 243–253. [[CrossRef](#)]
14. Boulnat, X.; Perez, M.; Fabregue, D.; Douillard, T.; Mathon, M.-H.; De Carlan, Y. Microstructure Evolution in Nano-reinforced Ferritic Steel Processed by Mechanical Alloying and Spark Plasma Sintering. *Metall. Mater. Trans. A* **2014**, *45A*, 1485–1497. [[CrossRef](#)]
15. Auger, M.A.; De Castro, V.; Leguey, T.; Muñoz, A.; Pareja, R. Microstructure and mechanical behavior of ODS and non-ODS Fe–14Cr model alloys produced by spark plasma sintering. *J. Nucl. Mater.* **2013**, *436*, 68–75. [[CrossRef](#)]
16. Naimi, F. *Approches Scientifiques et Technologiques du frittage et de L'assemblage de Matériaux Métalliques par Frittage Flash*. Ph.D. Thesis, Université de Bourgogne, Dijon, France, 26 November 2013.
17. Tatlock, G.; Dyadko, E.; Dryenpondt, S.; Wright, I. Pulsed Plasma-Assisted Diffusion Bonding of Oxide Dispersion-Strengthened FeCrAl Alloys. *Metall. Mater. Trans. A* **2007**, *38A*, 1663–1665. [[CrossRef](#)]
18. Krishnardula, V.G.; Aluru, R.; Sofyan NB, I.; Fergus, J.W.; Gale, W.F. Solid-state diffusion bonding of MA956 and PM2000. In *Proceedings of the 7th International Conference, Pine Mountain, GA, USA, 16–20 May 2005*; Volume 2005, pp. 885–888.



© 2020 by the authors. Licensee MDPI, Basel, Switzerland. This article is an open access article distributed under the terms and conditions of the Creative Commons Attribution (CC BY) license (<http://creativecommons.org/licenses/by/4.0/>).

Article

# Processing and Characterization of Bilayer Materials by Solid State Sintering for Orthopedic Applications

Jorge Sergio Téllez-Martínez<sup>1</sup>, Luis Olmos<sup>2</sup>, Víctor Manuel Solorio-García<sup>1</sup>, Héctor Javier Vergara-Hernández<sup>1,\*</sup>, Jorge Chávez<sup>2</sup> and Dante Artega<sup>3</sup>

- <sup>1</sup> Tecnológico Nacional de México/ITMorelia, Av. Tecnológico # 1500, Colonia Lomas de Santiaguito, Morelia C.P. 58120, Mexico; D16121682@morelia.tecnm.mx (J.S.T.-M.); v\_ms\_g@hotmail.com (V.M.S.-G.)
- <sup>2</sup> INICIT, Universidad Michoacana de San Nicolás de Hidalgo, Fco. J. Mujica S/N, Morelia C.P. 58060, Mexico; luisra24@gmail.com (L.O.); jomachag@gmail.com (J.C.)
- <sup>3</sup> Centro de Geociencias, Universidad Nacional Autónoma de México, Blvd. Juriquilla No. 3001, Querétaro C.P. 76230, Mexico; dartega@geociencias.unam.mx
- \* Correspondence: hector.vh@morelia.tecnm.mx; Tel.: +52-443-335-7888

**Abstract:** A new processing route is proposed to produce graded porous materials by placing particles of Ti6Al4V with different sizes in different configurations to obtain bilayer samples that can be used as bone implants. The sintering behavior is studied by dilatometry and the effect of the layers' configuration is established. To determine pore features, SEM and computed microtomography were used. Permeability is evaluated by numerical simulations in the 3D real microstructures and the mechanical properties are evaluated by compression tests. The results show that a graded porosity is obtained as a function of the size of the particle used. The mechanical anisotropy due to the pore size distribution and the sintering kinetics, can be changed by the particle layer arrangements. The Young modulus and yield stress depend on the relative density of the samples and can be roughly predicted by a power law, considering the layers' configuration on the compression behavior. Permeability is intimately related to the median pore size that leads to anisotropy due to the layers' configuration with smaller and coarser particles. It is concluded that the proposed processing route can produce materials with specific and graded characteristics, with the radial configuration being the most promising for biomedical applications.

**Keywords:** Functional Graded Materials; sintering; porosity; permeability; mechanical properties

**Citation:** Téllez-Martínez, J.S.; Olmos, L.; Solorio-García, V.M.; Vergara-Hernández, H.J.; Chávez, J.; Artega, D. Processing and Characterization of Bilayer Materials by Solid State Sintering for Orthopedic Applications. *Metals* **2021**, *11*, 207. <https://doi.org/10.3390/met11020207>

Received: 31 December 2020

Accepted: 19 January 2021

Published: 23 January 2021

**Publisher's Note:** MDPI stays neutral with regard to jurisdictional claims in published maps and institutional affiliations.



**Copyright:** © 2021 by the authors. Licensee MDPI, Basel, Switzerland. This article is an open access article distributed under the terms and conditions of the Creative Commons Attribution (CC BY) license (<https://creativecommons.org/licenses/by/4.0/>).

## 1. Introduction

Nowadays, industrial processes demand materials with specific properties and localized microstructures to improve material performance. To satisfy particular needs, the development of materials with changing mechanical properties and/or microstructures along a preferential direction has been developed. These are called Functional Graded Materials (FGMs). Among these materials, a variation on the porosity along the part is very useful for different industrial applications, such as microfiltration [1], biomedical applications [2–5] and microelectronic devices [6]. Research into materials that can be used as bone implants has received a lot of attention in the past decade due to their capacity to improve human health. Some earlier investigations focused on solving the mismatch stiffness between metallic implants and human bones [6]. Therefore, there is a need to develop porous materials by using different techniques showing that the stiffness of Ti and its alloys can be reduced to close to that of human bones [7–10]. Nevertheless, it is worth noting that bones have anisotropic mechanical properties and that stiffness will change depending on the direction of analysis in the structure [11,12]. Thus, it is necessary for the design of FGMs to satisfy the requirements to produce an improved and specialized bone implant.

The powder metallurgy route is better suited to producing materials with graded properties. It allows for control over the sintering parameters and/or the introduction of space-holder particles; with that, it is possible to design the pore characteristics needed in a sample. Processes oriented toward the elaboration of FGMs with a graded porosity of Ti and its alloys have been reported [4,13–16]. M. Dewidar and Kim [13] and Lee et al. [14] produced Ti compacts consisting of a solid core and a porous outer shell and studied the compression behavior of such components. On the other hand, Ahmadi and Sadrnezhad [15] elaborated on a component with a bonelike configuration, composed of foamy cores of different diameters surrounded by compact shells. The porous core diameter varied from 6 to 14 mm, whereas the outer diameter remained constant to 16 mm, with a linear relation found between Young’s modulus and the porous core diameter. Recently, Trueba et al. [16] concocted a device to produce materials with graded porosity in the radial direction that was used to produce FGMs of Ti by varying the quantity and pore size in the radial direction, from the core to the surface or vice versa. These works focused mainly on the mechanical response of the FGMs obtaining materials with stiffness and strength close to that of human bones. Nevertheless, biocompatibility and osteoconductivity are very important to producing a successful bone implant. The first one refers to the acceptance of the material inside the human body, which is related to the release of dangerous ions. For acceptance of materials in the body, after Ta, Ti and its alloys have superior biocompatibility [17]. Osteoconductivity, on the other hand, is the ability of a porous implant to facilitate bone growth through itself. Permeability plays a major role, as it favors the pass of nutrients and minerals to the osteocytes while removing metabolic waste as they are carried out through the porosity of the bones; this is associated with enhanced bone adaptation and regeneration [18]. Also, interconnected pores enhance anchoring and vascularization, obtaining better mechanical adhesion between bone and implant [19–22].

This work aims to develop Ti6Al4V materials with graded porosity by sintering particles with different sizes and distributions located in two main configurations: axial and radial directions. The sintering kinetic of each configuration is evaluated by dilatometry tests. To determine the pore size distribution of the sintered materials, characterization by scanning electronic microscopy (SEM) and computed microtomography is performed. The mechanical properties for graded porous materials are evaluated by compression tests, while permeability is estimated by numerical simulations in the different axes of the sample to determine the anisotropy created by the distribution of the pore sizes.

## 2. Materials and Methods

### 2.1. Sample Fabrication

Spherical Ti6Al4V powders furnished by Raymor (Boisbriand, QC, Canada) were used to develop this work. The powder was sieved into two different particle size distributions: 20–45  $\mu\text{m}$  (Figure 1a) and 75–106  $\mu\text{m}$  (Figure 1b). The chemical composition of powders furnished by the fabricant is as follows: 6.35% Al, 4% V, 0.21% Fe, 0.0045% H, 0.02% N, 0.02% O, 0.01% C and the balance of Ti.

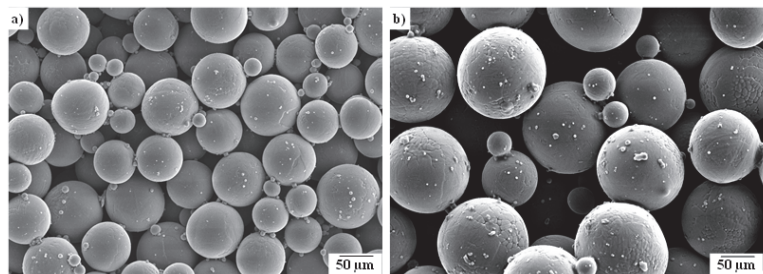


**Figure 1.** Scanning electronic microscopy (SEM) micrographs of Ti6Al4V powders sieved into two different particle size distributions: (a) 20–45  $\mu\text{m}$  and (b) 45–75  $\mu\text{m}$ .

To fabricate the samples, the powder’s mass was estimated, to obtain samples of 12 mm in height and 10 mm in diameter. The main objective of this study is to obtain porous materials. The powders were poured into a zirconia crucible which was lightly tapped. Four different samples were sintered in a L75 Linseis vertical dilatometer (Linseis Messgeraete GmbH, Selb, Germany) at 1260 °C with 5 min of holding under high purity Ar (99.999%) atmosphere. The cooling rate was the same for all samples 20 °C/min. Sample composition and sintering schedules are detailed in Table 1, as is the nomenclature for each sample.

**Table 1.** Characteristics and nomenclature of samples used for SEM and compression analysis with dimensions of 10 mm in diameter and 12 mm in height.

| Sample Type  | Particle Size (µm)                      | Heating Rate °C/min | Nomenclature | Fabrication Methodology   |
|--|---|---------------------|--------------|---|
|   | 20–45                                   | 5                   | MSP-5        | Monolithic samples were elaborated by pouring the particles into the crucible; then they were flattened by hand pressing with zirconia punch.   |
|  | (Volume Fraction Particles:1)           | 15                  | MSP-15       |   |
|  |   | 25                  | MSP-25       |   |
|  | 75–106                                  | 5                   | MCP-25       |   |
|  | (Volume Fraction Particles: 1)          | 15                  | MCP-25       |   |
|   | 20–45                                   | 5                   | BA-5         | To create a gradient of porosity in the axial direction, the sample was prepared by first pouring the smaller particles into a zirconia crucible. Then the surface was flattened by hand pressing with zirconia punch. The coarser particles were poured onto the smaller ones and the surface was again flattened.   |
|  | (Up Volume Fraction Particles: 0.5)     | 15                  | BA-15        |   |
|  | 75–106                                  | 25                  | BA-25        |   |
|  | 75–106                                  | 5                   | BR-5         | To create a gradient of porosity in the radial direction, this sample was fabricated by using a quartz tube of 5 mm inner diameter that was placed in the center of the zirconia crucible, where the coarser powders were poured. Then the smaller powders were poured around the quartz tube. Finally, the quartz tube was pulled out and the surface was flattened. |
|  | (Core Volume Fraction Particles: 0.25)  | 15                  | BR-15        |   |
|  | 20–45                                   |                     |              |   |
|  | (Shell Volume Fraction Particles: 0.75) | 25                  | BR-25        |   |

Two additional samples of 1 and 2 mm in diameter were prepared to achieve the computed tomography analysis. The characteristics and composition of the samples are detailed in Table 2.

**Table 2.** Characteristics and nomenclature of the samples used for computed microtomography analysis with dimensions of 1 and 2 mm in diameter.

| Sample Type   | Particle Size (µm)                      | Heating Rate °C/min | Nomenclature | Fabrication Methodology  |
|---|---|---------------------|--------------|--|
|  | 75–106                                  | 25                  | TBA-25       | This sample is fabricated by first pouring the smaller particles into a quartz crucible of 1 mm in diameter. Then the surface is flattened by hand pressing with a glass rod. Next, the coarser particles are poured over the smaller ones and the surface is again flattened.   |
|   | (Up Volume Fraction Particles: 0.5)     |                     |              |  |
|  | 20–45                                   | 25                  | TBR-25       | This sample was prepared by using two quartz capillaries. The first one, with a 1 mm diameter, was used for the coarser powders. Then it was carefully introduced and placed on the center of a 2-mm-diameter capillary, where the smaller particles were poured around it. Finally, the smaller capillary was pulled out. |
|   | (Down Volume Fraction Particles: 0.5)   |                     |              |  |
|  | 75–106                                  | 25                  | TBR-25       | This sample was prepared by using two quartz capillaries. The first one, with a 1 mm diameter, was used for the coarser powders. Then it was carefully introduced and placed on the center of a 2-mm-diameter capillary, where the smaller particles were poured around it. Finally, the smaller capillary was pulled out. |
|   | (Core Volume Fraction Particles: 0.25)  |                     |              |  |
|  | 20–45                                   | 25                  | TBR-25       | This sample was prepared by using two quartz capillaries. The first one, with a 1 mm diameter, was used for the coarser powders. Then it was carefully introduced and placed on the center of a 2-mm-diameter capillary, where the smaller particles were poured around it. Finally, the smaller capillary was pulled out. |
|   | (Shell Volume Fraction Particles: 0.75) |                     |              |  |

## 2.2. Sample Characterization

### 2.2.1. Scan Electronic Microscopy (SEM) Observation

Samples used for SEM observation were cut in half. Roughing was carried out with different SiC papers and polishing was performed by using alumina powders with a final size of 50 nm. After surface preparation, samples were cleaned in an ultrasonic bath for 30 min to remove alumina particles. The microstructure was observed with a Tescan MIRA 3 LMU field emission scanning electron microscope (FE-SEM, TESCAN ORSAY HOLDING, a.s., Brno-Kohoutovice, Czech Republic).

### 2.2.2. X-ray Microtomography (microCT)

To obtain detailed information about the porosity and its tridimensional distribution inside the samples, 3D images were acquired with a Zeiss Xradia 510 Versa 3D X-ray microscope (ZEISS, Oberkochen, Germany). The beam intensity was set at 120 kV, which was enough to pass through the 1- and 2-mm-diameter Ti6Al4V samples. Nearly 1600 projections were recorded around all 360° of the sample with a CCD camera (ZEISS, Oberkochen, Germany) of 1024 × 1024 pixels with a voxel size of 1 and 2 μm, respectively. The voxel size depends on the diameter of the samples, although it is possible to acquire inner volumes without destroying the sample. Those kinds of acquisitions take more time when the exposure time to radiation is longer. Because this work is aimed at analyzing the interparticle pores left between the particles after sintering, a 2 μm voxel size is needed to accurately assess the microstructure features.

### 2.3. Mechanical Property Evaluation

To obtain the mechanical properties, simple compression tests were performed on the 12-mm-height samples. For that, the bottom and top surfaces of the samples were polished and compression tests were performed following ASTM D695-02 with an Instron 1150 universal mechanical testing machine (INSTRON, Norwood, MA., USA) at a strain rate of 0.5 mm/min. From the stress-strain curves, the Young modulus and the yield strength were estimated in the elastic zone. The stress is measured by correcting the contact surface area of the sample, assuming that the volume was constant during compression. The axial strain is calculated as the ratio of the real axial displacement (after machine stiffness correction) to the initial height of samples.

### 2.4. Numerical Simulation Permeability

The flow properties of porous samples were estimated by numerical simulations of permeability performed using Avizo® software (V8.0, ThermoFisher SCIENTIFIC, Waltham, MA, USA) on the 3D binary images containing porosity. Before the numerical simulations were run, the minimum representative volume (MRV) was estimated by cropping the image in small volume cubes (20 × 20 × 20 voxels) at the center of the image. Then the pore volume fraction for that volume was calculated. These operations were repeated by increasing the cube volume by 20 voxels per side until constant relative density was reached. The optimal minimal volume to obtain enough accuracy in our results had to be calculated considering computational limitations, to save time for the numerical simulations. It was found that the volume at which the pore volume fraction reached a constant value was near 300<sup>3</sup> voxels<sup>3</sup>. Therefore, a volume of 300 × 300 × 300 voxels was used for the numerical simulation in the three main directions of the cube, where x and y represent the horizontal plane and z the vertical axis.

Simulations on Avizo are based on the Darcy law by solving Navier-Stokes equations with a finite volume method. The simulation considered a single-phase incompressible Newtonian fluid with a steady-state laminar flow and a viscosity of 0.0045 Pa s, which represents the viscosity of the blood. The boundary conditions used were the inlet and outlet pressure, with values of 130 and 100 kPa, respectively.

### 3. Results and Discussion

#### 3.1. Sintering Kinetics

The axial strain for the different samples studied, as a function of the time and temperature during the entire thermal cycle, is depicted in Figure 2a. All samples show the same behavior. First, a positive deformation is due to the thermal dilation of the samples. Then a sharp negative deformation is found, which corresponds to the pore elimination by sintering. Finally, when the temperature reaches the sintering plateau, the axial deformation continues to be negative but with an exponential behavior. It is observed that smaller powders shrank at lower temperatures than coarser ones, which indicates that sintering was activated before. This is explained due to the smaller particles that show a higher surface energy that promotes the atomic diffusion during solid-state sintering [23]. The final deformation is 2.5 times larger for the sample with smaller particles in comparison to that reached by the coarser ones. A similar effect was reported for yttria-stabilized zirconia powder consolidated by flash sintering [24]. The behavior of bilayer samples falls between both monolith samples. However, the onset of sintering is driven by the coarser layer in both bilayers' samples, as the shrinkage generated by the sintering is activated at the same temperature as that of the sample with coarser powders. Despite the fact that sintering is activated at the same time, a clear effect of the position of the layer is noted because the final deformation is larger when the radial configuration is used. This indicates that smaller powders induce stress at the interphase between both layers, which accelerates the shrinkage. On the other hand, each layer sinters more independently, although the axial strain is driven by the layer with the coarser powders.

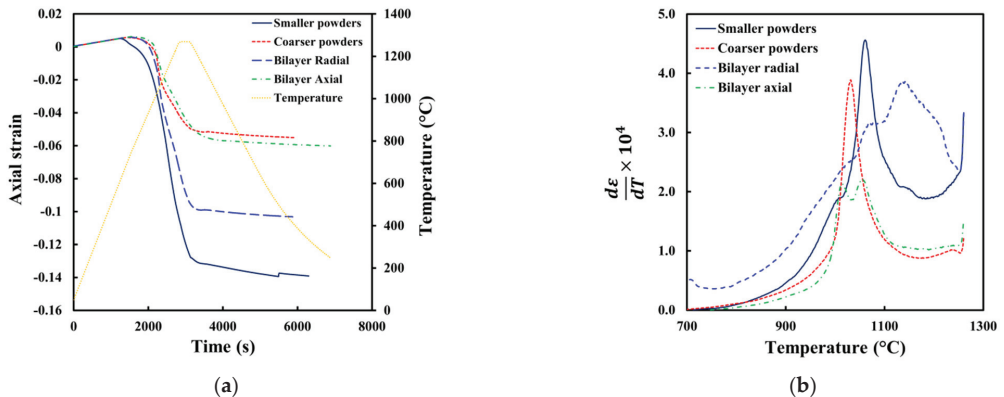


**Figure 2.** (a) Axial strain as a function of time and temperature during the whole sintering cycle and (b) deformation rate as a function of the temperature during heating with a rate of 25 °C/min. Samples MSP-25, MCP-25, BA-25, BR-25.

The deformation rate as a function of the temperature during the heating stage is presented in Figure 2b for all samples heated at 25 °C/min. It is found that a maximum value of deformation rate is reached for the monolithic samples, which is higher for the sample with smaller particles, confirming the results discussed above. The bilayer samples show maximum values of the deformation rate, which correspond with the maximal ones of monolithic samples. For the axial configuration, the two peaks on the curve correspond approximately with the temperature of the peaks of the monolithic samples, indicating that each layer sinters independently with a low effect of the interphase. On the other hand, for the radial configuration, the maximal values of the deformation rate are reached later than the monolithic samples and the values are higher than those found in the axial configuration. This suggests that sintering is affected by the interphase along the vertical axis, though the maximal values of the deformation rate are retarded and the final deformation reached is larger than that of the bilayer with the axial configuration.

The effect of the heating rate on the axial strain is shown in Figure 3. As was expected, a slower heating rate increases the final strain and as has been discussed, the bilayers in the radial configuration show larger strains. However, the ratio between the maximal values of the strain diminishes from 2.5 to 1.9 times as the heating rate decreases from 25 to 5 °C/min.

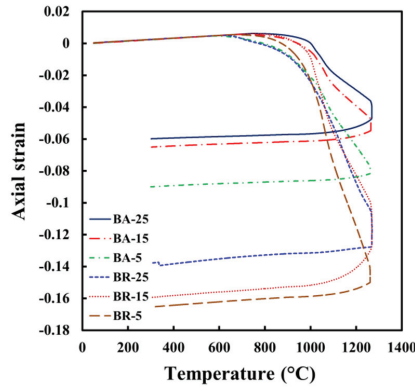


Figure 3. Axial strain as a function of the temperature during the whole sintering cycle of bilayer samples sintered at 1260 °C with different heating rates from 5 to 25 °C/min.

The green and sintered relative densities of all samples studied were estimated by weighing the mass and measuring the volume of cylinders. The obtained values are listed in Table 3. The MSP-25 sample shows a lower green density than the MCP-25 sample, which is expected because smaller particles are more difficult to pack than coarser ones. However, the sintered density is 8% higher for the MSP-25 because sintering advances rapidly as the particle size diminishes. This confirms the findings about the axial strain. The bilayer samples have lower green relative densities than those obtained for monolithic samples, which indicates that packing is affected by the interphase of layers. Nonetheless, the green density of all bilayer samples has the same value, which is not expected because differences in packing between each layer should affect the final packing. The numeric values on the Table 3 show that the samples with the axial configuration (BA-X) have lower densities by sintered process respect at the samples with radial configuration (BR-X); independent of the heating rate. It can be noticed that the lower heating rates produce high densification but BA-5’s density is still less than BR-25. The highest value of the sintered relative density is obtained for the BR-5 sample, with a value of 78.59%. It is established that relative densities of bilayer samples BA-25 and BR-25 are close to the monolithic ones MCP-25 and MSP-25, respectively. The results confirm that volumetric densification has a strong relationship with the axial strain measured by dilatometry as is observed in Figure 2a.

Table 3. Green and sintered relative densities of the different samples consolidated at different heating rates.

| Sample | Green Density ( $D_0$ ) | Sintered Density ( $D_f$ ) |
|--------|-------------------------|----------------------------|
| MSP-25 | 0.6121                  | 0.7413                     |
| MCP-25 | 0.6257                  | 0.6902                     |
| BA-25  | 0.6008                  | 0.6949                     |
| BA-15  | 0.6033                  | 0.7003                     |
| BA-5   | 0.6004                  | 0.7178                     |
| BR-25  | 0.6000                  | 0.7308                     |
| BR-15  | 0.6016                  | 0.7516                     |
| BR-5   | 0.6021                  | 0.7859                     |

### 3.2. Microstructural Characterization

#### 3.2.1. Scan Electronic Microscopy Observation

Microstructures of the bilayer samples are presented in Figure 4. The sample BA-25, Figure 4a,b, shows a clear division between both layers (interphase). The top layer is composed of coarser particles with a higher pore density. Despite this definition, through these 2D images, it is not possible to clearly establish the difference in the pore characteristics. Figure 4b is an approach of the interphase between both layers and it can be noticed that necks between particles are better developed for the smaller particles and the larger pores in the top layer between coarser particles. Because of surface preparation by cutting and polishing with alumina particles, some pores seem to be closed. Figure 4c,d show the polished surface of the BR-25 sample. The picture of Figure 4c shows a higher density of pores in the core composed of coarser particles; a more detailed difference about this observation will be exposed in the next section by using digital cutting planes (X-ray microtomography analysis). Figure 4d shows a section of the upper outline of the sample between the exterior edge and the core. On this borderline, it is possible to notice that the layer of smaller particles has undergone larger shrinkage in the axial direction compared to the core of the sample. From these images, we can determine that no fractures at the interphases were formed during sintering, despite the large difference in the deformation and deformation rate of both layers. This could be attributed to the lower densification required for the possible biomedical application.

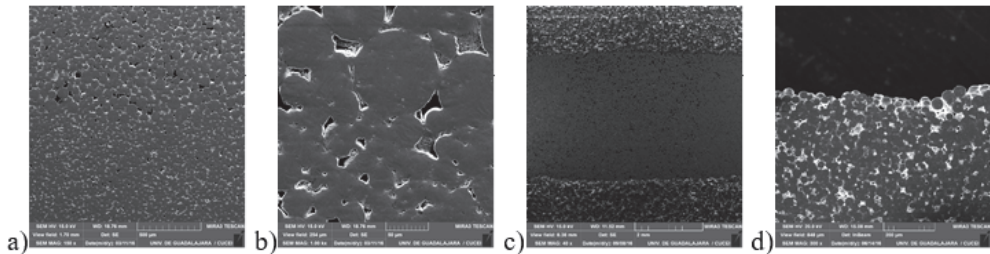


**Figure 4.** SEM micrographs of bilayer samples sintered at 1260 °C with a heating rate of 25 °C/min; (a) and (b) BA-25 and (c) and (d) BR-25.

Thus, the constraint stresses generated at the interphase between layers are weaker than those reported for bilayer ceramic processes by sintering [25].

#### 3.2.2. X-ray Microtomography Analysis

To obtain a deep analysis of the porosity generated by the radial and axial configuration of the bilayers, 3D images of the TBA-25 and TBR-25 samples were acquired using the Median and Unsharp mask filters with the open-source software Image J. Figure 5 shows a 3D and 2D virtual slice of both samples after reconstruction. Figure 5a shows the TBA-25 3D sample; it can be observed that the top layer is composed of coarser particles and the bottom layer of smaller particles. It can be seen that the interphase is not completely flat due to the fragile nature of the quartz capillary. Besides it is possible to better observe the porosity without surface modifications as the ones needed for SEM observation. The TBR-25 2D sample is shown in Figure 5b. We can observe that coarser particles are found in the core of the sample and that interphases are almost vertical. This indicates that the process method is optimal for elaboration of this type of configuration.



**Figure 5.** 3D and 2D virtual slices of samples of 1 and 2 mm in diameter, respectively, sintered at 1260 °C with a holding time of 5 min and a heating rate of 25 °C/min; (a) TBA-25 and (b) TBR-25.

To enhance the contrast between the solid and void phases, 3D images were filtered with median and unsharp mask filters, obtaining good quality in the images, as we can observe in Figure 6a. The greyscale images were transformed into binary images to obtain quantitative information. A thresholding method was applied, separating the solid from the void spaces, in which the solid phase gets a value of 1 and void of 0, as can be observed in Figure 6b. This method allowed us to measure the pore volume fraction and size distribution and to run the permeability simulations. Finally, to obtain information like coordination number, neck size and distribution on the volume, a segmentation process was performed by following the watershed method used by Olmos et al. [26,27]. After this process, the particles are considered individual objects in the volume analyzed, as is shown in Figure 6c.

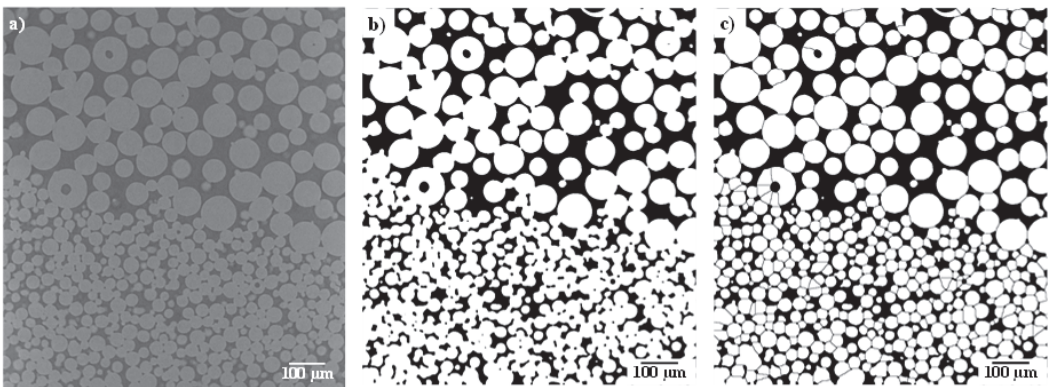


**Figure 6.** 2D slice of the TBA-25 sample; (a) filtered image, (b) binary, (c) binary segmented.

A 3D rendering of both samples TBA-25 and TBR-25 is shown in Figure 7a,b. Inner volumes were reconstructed due to the size of the sample. However, from these volumes, it can be observed that large particles are located at the bottom of Figure 7a and at the center of Figure 7b. Additional quantitative information will be presented from 3D images. Through this method, a coarse particle located at the interphase of the TBR-25 sample and the smaller particles that are in contact with it can be observed, as can be seen in Figure 7c. This helps to illustrate information at the particle level.

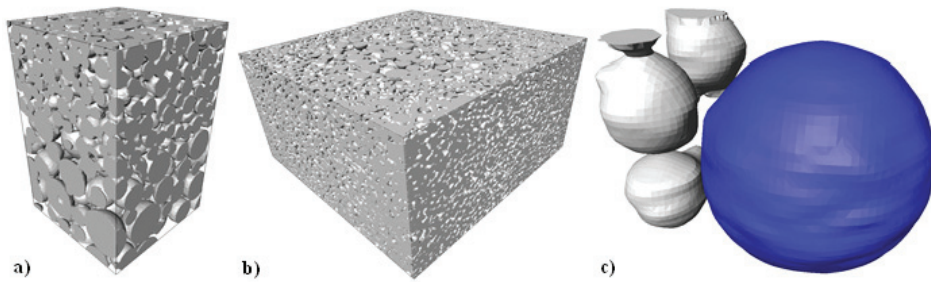


**Figure 7.** Representation of the tridimensional internal volumes of the samples; (a) TBA-25 and (b) TBR-25 and (c) 3D particles at the interphase of TBR-25 after particle segmentation.

The quantitative data of the packing of particles is separated by layers; taking the whole sample into account, the 3D images allowed us to virtually select and crop the volume of interest inside the sample. The objective of this procedure was to establish the differences obtained after each layer of the bilayer samples was sintered. Table 4 lists the results involving particles and their environment, such as relative density, neck size ( $a/R$ ), coordination number and particle sphericity. The relative density values calculated from the 3D images for TBA-25 and TBR-25 correspond to those measured from the volume and dimensions of the samples; see Table 3. The local values for each layer in both samples show that the layer with smaller particles is denser than the one with coarser particles. It is observed that the relative density for each layer in the TBA-25 sample is lower than that obtained in the monolithic samples for the same sintering conditions; see Table 3. This suggests that the stresses developed at the interphase reduce the densification in the corresponding layer, as was reported for sintering on solid substrates [28]. On the other hand, the values of the density measured in each layer of the TBR-25 sample correspond with those obtained for the monolithic samples, which indicates that radial configuration reduces the effect of interphase during densification.

**Table 4.** Quantitative data of the packing of particles of the two bilayer samples.

| Nomenclature | Layer    | Relative Density | $\frac{a}{R}$ | Z    | Sphericity |
|--------------|----------|------------------|---------------|------|------------|
| TBA-25       | Smaller  | 0.7221           | 0.43          | 7.52 | 0.7484     |
|              | Coarser  | 0.6564           | 0.25          | 5.83 | 0.8847     |
|              | Complete | 0.6909           | -             | 6.77 | -          |
| TBR-25       | Smaller  | 0.7494           | 0.48          | 7.95 | 0.7088     |
|              | Coarser  | 0.7063           | 0.39          | 6.46 | 0.7927     |
|              | Complete | 0.7315           | -             | 7.54 | -          |

The average ( $\frac{a}{R}$ ) ratio measured from the 3D data for each layer in both TBA-25 and TBR-25 samples increases as the relative density of the layer does, which is expected because the neck size is responsible for the densification. To validate the values obtained from the 3D images, the ( $\frac{a}{R}$ ) can be estimated from the geometrical relationship between axial shrinkage and the neck ratio proposed by German [29] as follows:

$$\frac{a}{R} = \left( \frac{\Delta l}{l_0} b \right)^{\frac{1}{2}}, \tag{1}$$

where:

( $\frac{a}{R}$ ), relationship between the neck’s radius and the particle’s diameter; ( $\frac{\Delta l}{l_0}$ ), sample axial shrinkage; ( $b$ ), a parameter determined by experimental procedures with a value of 3.6.

Likewise, with the assumption that the volume changes are isotropic during sintering ( $\frac{\Delta V}{V_0}$ ) and because the mass remains constant during sintering, the relative density value reach ( $D$ ) depends on the initial green density and the shrinkage as follows [29]:

$$D = \frac{D_0}{\left(1 + \frac{\Delta l}{l_0}\right)^3}, \tag{2}$$

where:

( $D_0$ ), is the initial relative density or green value.

Thus, an estimation of the neck size and the particle’s radius ratio can be calculated if one knows the relative density values by combining Equations (1) and (2), respectively. To estimate the ( $\frac{r}{R}$ ) ratio from Equations (1) and (2), the values of the ( $D_0$ ) for each layer were the ones measured for the MSP-25 and MCP-25 samples and the ( $D$ ) values listed in Table 4. The ( $\frac{r}{R}$ ) obtained for the BA-25 smaller and coarser layers are 0.44 and 0.24. Meanwhile, the BR-25 smaller and coarser layers are 0.49 and 0.38, respectively. This demonstrates that the geometrical relationship of Equation (1) is a good approximation for lower values of relative densities, which is represented at early sintering stages.

The particle coordination number was calculated for each layer of both TBA-25 and TBR-25 samples after sintering by following the methodology used for Vagnon et al. [30]. The Z values increase as the relative density does for each layer, no matter their configuration. The Z value for the complete samples follows the same tendency.

The particles’ sphericity is another indicator of the sintering advance because, the lower the particle sphericity is, the higher the relative density, as is shown in Table 4, where the lower average value of sphericity is found for the layer that shows the highest densification.

The pore size distribution of both TBA-25 and TBR-25 samples is shown in Figure 8. To show the differences in the porosity that remained after sintering in each layer, the pore size distributions are estimated in subvolumes that contain only the characteristics of the smaller and coarser layers for both samples. As was expected, the smaller pore sizes are found in the layers with smaller particles and the pore size distribution of the complete sample falls in between both layers. To get a proper comparison of the porosity after sintering on both samples, the pore volume fraction, the median pore size ( $d_{50}$ ) and the tortuosity were measured from the 3D volumes, which are listed in Table 5.

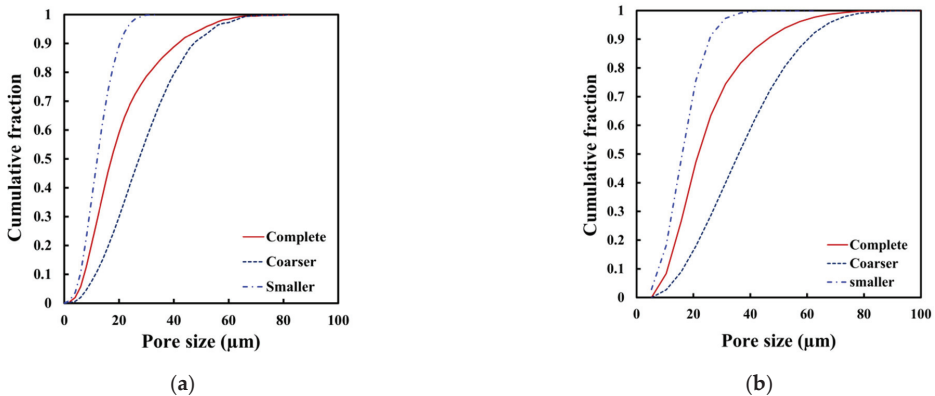


Figure 8. Pore size distribution of bilayer samples, (a) TBA-25 and (b) TBR-25.

Table 5. Porosity characteristics and properties.

| Layer    | Pore Volume Fraction (%) | Median Pore Size ( $\mu\text{m}$ ) | Tortuosity | Axial Permeability ( $1 \times 10^{-12} \text{ m}^2$ ) | Radial Permeability ( $1 \times 10^{-12} \text{ m}^2$ ) |
|----------|--------------------------|------------------------------------|------------|--|---|
| TBA-25   |                          |                                    |            |  |   |
| Smaller  | 27.78                    | 14.01                              | 1.13       | 0.4233   | 0.4380  |
| Coarser  | 34.36                    | 29.27                              | 1.22       | 2.2956   | 2.5903  |
| Complete | 30.90                    | 17.24                              | 1.18       | 0.8110   | 1.3368  |
| TBR-25   |                          |                                    |            |  |   |
| Smaller  | 25.05                    | 16.03                              | 1.27       | 0.4814   | 0.3985  |
| Coarser  | 29.39                    | 35.86                              | 1.08       | 3.0523   | 2.9721  |
| Complete | 26.84                    | 21.77                              | 1.17       | 2.0911   | 0.4854  |

The highest values for the pore volume fraction are found in the TBA-25 sample. Nevertheless, the larger median pore size was found for the TBR-25 sample, which indicates that the packing of particles in such a configuration is more complicated compared to the axial configuration. Qualitatively, the pore size distribution of the TBR-25 is slightly larger than that of the TBA-25, as can be noticed from Figure 8. The  $d_{50}$  obtained for the layer with smaller particles ranges between 14–16  $\mu\text{m}$  and the  $d_{50}$  of particles is 36  $\mu\text{m}$ , which means that the  $d_{50}$  pore size is close to 38% of the particle size. Similarly, the  $d_{50}$  pore size for the coarser particles ranges between 29–35  $\mu\text{m}$ . Meanwhile, the particle size of  $d_{50}$  is 76  $\mu\text{m}$ . The same ratio was found for the pore size, which represents 38% of the particle size. This indicates that the median pore size can be predicted from the initial particle size distribution when sintering takes place only in the early stages, as was also mentioned [26]. The values of tortuosity are very close for all layers ranging from 1.08–1.27, indicating that porosity shows a similar path in each layer. This happens because the particles are spherical and the sintering is in the early stage, which means that porosity is completely interconnected, as can be confirmed in the 3D rendering shown in Figure 9a,c.

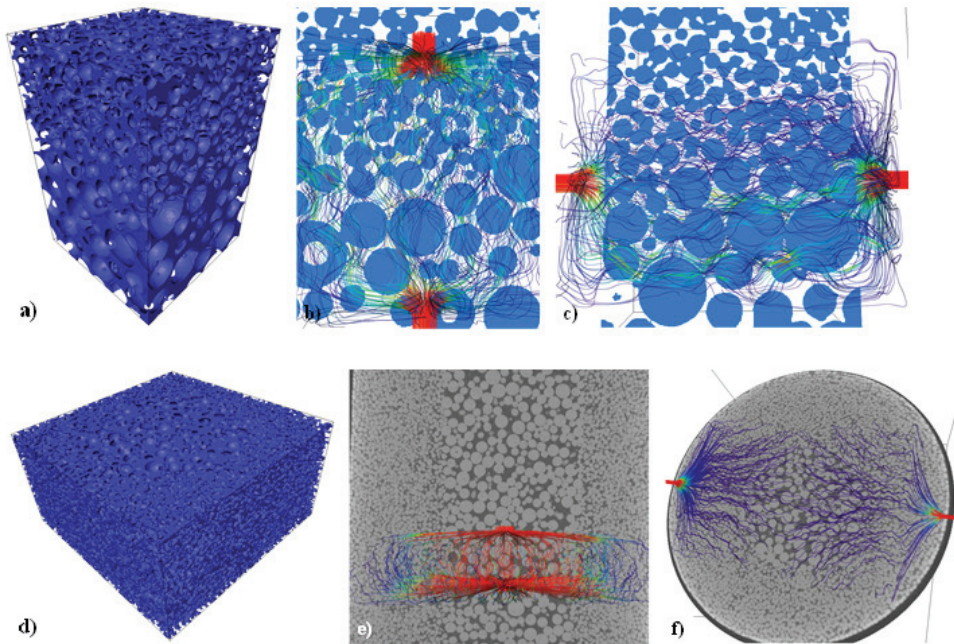


Figure 9. 3D volume rendering of the porosity and streamlines for the fluid flow through pores in the axial and radial directions for TBA-25, (a–c) and TBR-25, (d–f).

### 3.3. Permeability Evaluation

Figure 9 is a representation of a 3D rendering of the porosity found in the TBA-25 (Figure 9a) and TBR-25 (Figure 9d) samples, where it is possible to distinguish larger pores in the bottom and center of the samples as a consequence of the configuration of the layers, axial and radial, respectively. A pseudo color code to identify the connectivity of pores was used, obtaining only one color, which means that porosity is fully connected in both samples. Figure 9b,c show the flow path lines throughout the TBA-25 sample obtained from the numerical simulations in the axial and radial directions, respectively. The color code indicates the velocity of the fluid at any point in the volume, with red representing the highest velocity and blue the slowest. It is found that permeability in the radial direction is higher than in the axial one, for the TBA-25 sample, when the simulation is carried out in the whole sample. See Table 5.

To understand the behavior of the permeability, simulations were carried out in subvolumes containing only characteristics of each layer in both directions, axial and radial. The value of permeability in the layer with coarser particles is five times higher than the one with smaller particles. However, the permeability values estimated in the axial and radial directions are barely the same for each layer, which indicates a homogeneous porosity distribution in the sample. Therefore, when the fluid passes through the sample in the axial direction, the permeability is driven by the layer with the lowest permeability, as the fluid is forced to pass through that layer. For the radial direction, most of the fluid passes through the layer with the largest pores and the permeability is higher than in the axial direction. Qualitatively, the above mentioned can be deduced from the flow path lines shown in Figure 9b,c, where it can be noticed that the fluid can achieve a more tortuous and slower velocity when it is passing throughout the layer with smaller pores. In the radial direction, Figure 9c allows us to see more path lines in the bottom layer.

The values of permeability for the TBR-25 sample are slightly higher than those estimated for the TBA-25 sample but are in the same range. As was discussed above, the permeability shows a higher anisotropy when the complete sample is evaluated. For this case, the permeability higher values are obtained when the axial direction is evaluated. This is due to the fluid passing throughout the layer with larger pores that are located in the center of the sample, as can be noticed in Figure 9e. The permeability value in the axial direction is reduced by one-third of the value obtained for the layer with coarser particles. Figure 9f shows the flow path lines in the radial direction. As was mentioned, the paths become more tortuous in the layer with smaller particles. In that case, as the flow must pass twice throughout the layer with smaller particles, the permeability is close to the estimated value for that layer.

The values of permeability measured for the samples fabricated in this work are underestimated by three orders of magnitude compared to those measured by Grimm and Williams [31] for the human trabecular bone ( $0.4\text{--}11 \times 10^{-9} \text{ m}^2$ ) and those experimentally measured by Nauman et al. [11] in human vertebral and proximal femur bones, which have a large range of permeability values for human bones ( $2.68 \times 10^{-11}\text{--}2 \times 10^{-8} \text{ m}^2$ ). On the other hand, the permeability values are in good agreement with the range measured for the natural cancellous bone ( $3 \times 10^{-13}\text{--}7.4 \times 10^{-12} \text{ m}^2$ ) [32], which also has a maximal anisotropy in the permeability (axial/radial) of five times, similar to what was obtained by the radial configuration of layers. This is in agreement with that reported by Nauman et al. [11], who pointed out that permeability in human bones can reach high anisotropy in the permeability values, as much 22 times of difference between axial and radial directions.

### 3.4. Mechanical Properties

The compression behavior of the bilayer samples is shown in Figure 10. Stress-strain curves of the MSP-25, MCP-25, BA-25 and BR-25 samples are plotted in Figure 10a. All samples show similar behavior, a linear increase in the stress as the strain increases, elastic zone and then a maximum value of the stress is reached until failure. The MSP-25

sample is the strongest among the others and the MCP-25 is the weakest. This is mainly because the relative density is higher for the MSP-25 sample, as well as the a/R ratio, which indicates that necks have a stronger connection between particles. The BA-25 and BR-25 samples show resistance in between the monolithic samples, which was expected. Qualitative analysis indicates that the BA-25 sample behaves as the MCP-25 one and the BR-25 shows similar behavior to the MSP-25 one. For the case of the axial configuration of layers, it is clear that the mechanical resistance is driven by the weakest layer with a small increment in the resistance due to the combination of both layers. Nevertheless, the mechanical values are closer to those of the MCP-25 sample. For the radial configuration of layers, it can be noticed that the resistance of the BR-25 is influenced by both layers and the values are closer to those of the MSP-25 sample. This indicates that the strongest layer can support more load during the compression test, as the weakest layer is in the core of the sample. These results show a similar trend to that reported by Ahmadi and Sadrnezhad [15] for the compression behavior of foamy core samples, in which they suggest that mechanical resistance is linked to the foamy core diameter.

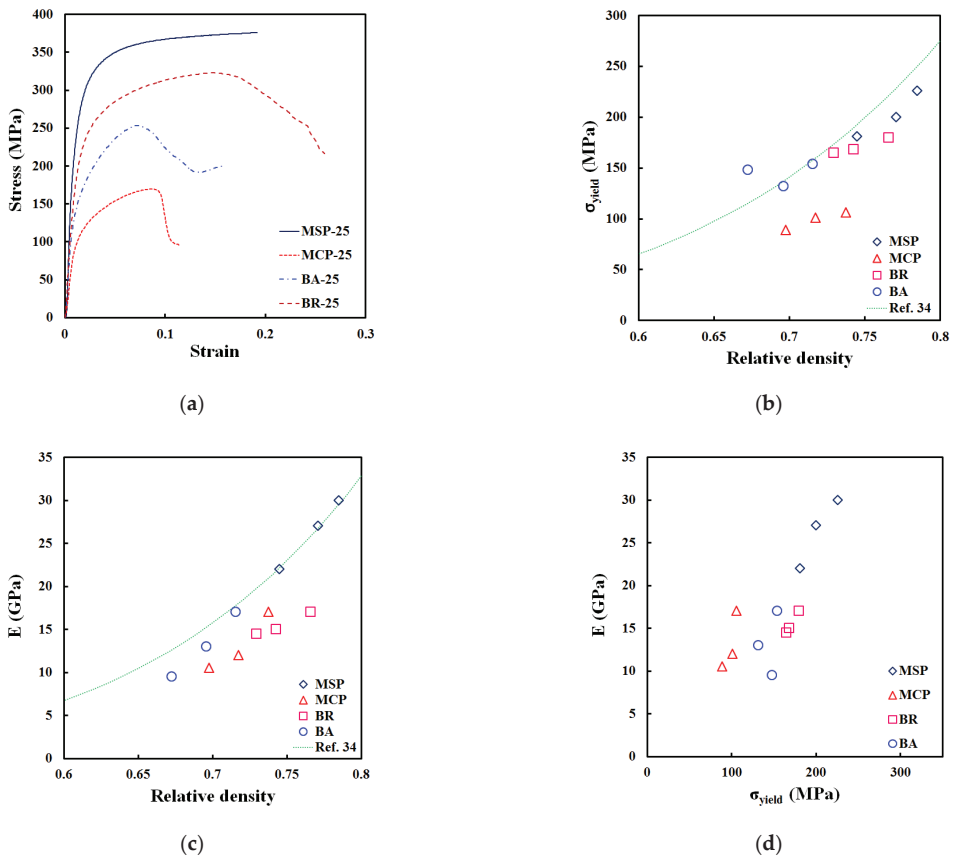


**Figure 10.** Compression behavior of the different samples tested; (a) stress-strain curves, (b) Young’s modulus as a function of the relative density, (c) yield stress as a function of the relative density and (d) Young’s modulus as a function of the yield stress.

The Young’s modulus is estimated from the elastic zone of the stress-strain curves for all samples by fitting a slope in the zone mentioned. The results are depicted as a function

of the relative density for the sample, Figure 10b. The higher value of  $E$  is 30 GPa and corresponds to the MSP-5 sample, which is the one with the highest relative density. We obtained a reduction of the  $E$  values for the monolithic samples when the relative density diminishes, which has been previously reported. However, the  $E$  values follow a power law as a function of the relative density that could be associated with that proposed by Gibson and Ashby [33] and modified by Cabezas et al. [34]. The  $E$  values calculated for the BA-X samples show a good agreement with the power law, which indicates that the mechanical response of the bilayer samples with axial configuration corresponds to the microstructure of the sample, with a normal effect of porosity. Also, the values of  $E$  for BR-X samples are lower than those calculated by the power law, with respect to the relative density of the whole sample. This suggests that stiffness is controlled by the sample with higher porosity. The  $E$  values obtained for the bilayer samples ranged between 9–17 GPa, agreeing with those reported for the compact bone [9].

The compressive strength is determined by the yield stress of samples and the values obtained from the stress-strain curves are plotted as a function of the samples' relative density, Figure 10c. The values for the monolithic samples show a similar trend to  $E$ , which means the  $\sigma_{\text{yield}}$  diminishes as the relative density does. Nevertheless, it can be observed that samples with smaller particles have a better fit with the power law proposed by Cabezas et al. [34]. Meanwhile, the samples with coarser particles are overestimated by the power law. This can be attributed to the advance in the sintering because the  $a/R$  ratio is about two times smaller for coarser particles, for an increment of 3% on the relative density. This suggests that necks between particles are weaker and the failure of such samples is due to the necks breaking, which is shown in Figure 10a. Bilayer samples show good agreement with respect to the power law. It can be determined that BR-X samples with around the same relative density as MSP-X samples show a lower  $\sigma_{\text{yield}}$ , a result of the combination of layers that has an effect associated with either the  $a/R$  ratio or interphase wall effect.

To establish whether this kind of sample could perform well in orthopedic applications, the  $E$  values are depicted as a function of the  $\sigma_{\text{yield}}$ , Figure 10d. The combination of Young's modulus and mechanical strength called "admissible strain" is defined as the strength-to-modulus ratio and the numerical study of the effect of several metallic elements was performed by Song et al. [35]. In this case, the higher the admissible strain, the more desirable the materials are for implant applications. It is found that stiffness and strength engage in near-linear behavior, in which the  $E$  increases as  $\sigma_{\text{yield}}$  does. The admissible strain values for all samples range from 6 to  $15 \times 10^{-3}$ . Those values are higher than the ones reported by Zhou and Niinomi [36] for casting Ti-Ta alloys. On the other hand, those values are lower than those reported for porous materials [8], mainly because the addition of large pores reduces the stiffness of materials but the solid phase is more stable, which reduces the effect of porosity in the strength of the porous material. The highest value of the admissible strain was obtained for the BA-25 sample ( $15 \times 10^{-3}$ ) and the second one with  $11 \times 10^{-3}$  is the BR-25 sample.

#### 4. Conclusions

A novel experimental methodology to fabricate porous gradient materials with controlled porosity by powder metallurgy was proposed. The pore size distribution is determined by the initial particle size of powders and the sintering parameters of monolithic samples. Ti6Al4V bilayer components with two main configurations, axial and radial, were designed by placing particles with different size distributions in a determined place in the sample but any desired configuration can be achieved following this methodology. It was found that no cracks are developed at the interphase of bilayers components because the neck formation between particles is strong enough to support the stresses generated by different densification rates of layers.

It was assessed that mechanical properties and permeability are highly influenced by the configuration of layers, radial or axial one. The radial configuration of the layers

is most suitable for bone implants because it is the natural configuration of bone and the Young's modulus, yield stress and permeability values obtained are in good agreement with those reported for human bones. To reduce the E values, additional pores could be added to mimic the real porosity included in bones. This work is in progress by controlling the quantity and pore characteristics.

**Author Contributions:** J.S.T.-M.: conceptualization, formal analysis, investigation, writing—original draft preparation, writing-review and editing. L.O.: methodology, investigation, supervision, validation, writing-review and editing. V.M.S.-G.: methodology and investigation. H.J.V.-H.: advisor to graduate students, financial administration of the project and supervision as group head of the dilatometry laboratory. J.C.: methodology and investigation. D.A.: methodology, investigation, resources, software, visualization. All authors have read and agreed to the published version of the manuscript.

**Funding:** This research was funded by Tecnológico Nacional de México (TecNM)/Instituto Tecnológico de Morelia (ITM), through the Doctoral Program in Engineering Sciences. This support allowed the obtaining of J.S. Téllez-Martínez and V.M. Solorio-García. Additional funding was obtained by the CIC of the UMSNH and the Laboratorio Nacional SEDEAM. The Consejo Nacional de Ciencia y Tecnología (CONACyT) supported the postdoctoral program of J. Chávez (postdoctoral fellow, 000614).

**Institutional Review Board Statement:** Not applicable.

**Informed Consent Statement:** Not applicable.

**Data Availability Statement:** The manuscript “Processing and characterization of bilayer materials by solid state sintering for orthopedic applications” is an original work and has not been sent elsewhere. All the results are part of the research of the doctoral student (J.S. Téllez-Martínez), and the master's degree student (V.M. Solorio-García). The experiments reported in this work focus on obtaining mechanical properties and permeability data in novel samples with a concentric bilayer structure of sintered particles. These data will be the basis for future works in the authors' field of research.

**Acknowledgments:** The authors like to thank to the Laboratory “LUMIR” Geosciences of the UNAM, Juriquilla, for the 3D image acquisition and processing with microCT technology, and for the use of the Avizo®software. Finally, thank CONACyT for the support given to graduate students.

**Conflicts of Interest:** The authors declare no conflict of interest.

## References

1. Meulenberg, W.A.; Mertens, J.; Bram, M.; Buchkremer, H.-P.; Stöver, D. Graded porous TiO<sub>2</sub> membranes for microfiltration. *J. Eur. Ceram. Soc.* **2006**, *26*, 449–454. [[CrossRef](#)]
2. Reig, L.; Amigó, V.; Busquets, D.J.; Calero, J.A. Development of porous Ti6Al4V samples by microsphere sintering. *J. Mater. Process. Technol.* **2012**, *212*, 3–7. [[CrossRef](#)]
3. Bender, S.; Chalivendra, V.; Rahbar, N.; el Wakil, S. Mechanical characterization and modeling of graded porous stainless steel specimens for possible bone implant applications. *Int. J. Eng. Sci.* **2012**, *53*, 67–73. [[CrossRef](#)]
4. Torres, Y.; Trueba, P.; Pavón, J.J.; Chicardi, E.; Kamm, P.; García-Moreno, F.; Rodríguez-Ortiz, J.A. Design, processing and characterization of titanium with radial graded porosity for bone implants. *Mater. Des.* **2016**, *110*, 179–187. [[CrossRef](#)]
5. Miao, X.; Sun, D. Graded/gradient porous biomaterials. *Materials* **2010**, *3*, 26–47. [[CrossRef](#)]
6. Bahraminasab, M.; Sahari, B.B.; Edwards, K.L.; Farahmand, F.; Arumugam, M.; Hong, T.S. Aseptic loosening of femoral components—A review of current and future trends in materials used. *Mater. Des.* **2012**, *42*, 459–470. [[CrossRef](#)]
7. Tirta, A.; Baek, E.R.; Chang, S.S.; Kim, J.H. Fabrication of porous material for micro component application by direct X-ray lithography and sintering. *Microelectron Eng.* **2012**, *98*, 297–300. [[CrossRef](#)]
8. Cabezas-Villa, J.L.; Olmos, L.; Bouvard, D.; Lemus-Ruiz, J.; Jiménez, O. Processing and properties of highly porous Ti6Al4V mimicking human bones. *J. Mater. Res.* **2018**, *33*, 650–661. [[CrossRef](#)]
9. Wang, X.; Xu, S.; Zhou, S.; Xu, W.; Leary, M.; Choong, P.; Xie, Y.M. Topological design and additive manufacturing of porous metals for bone scaffolds and orthopaedic implants: A review. *Biomaterials* **2016**, *83*, 127–141. [[CrossRef](#)]
10. Torres, Y.; Rodríguez, J.A.; Arias, S.; Echeverry, M.; Robledo, S.; Amigo, V.; Pavón, J.J. Processing, characterization and biological testing of porous titanium obtained by space-holder technique. *J. Mater. Sci.* **2012**, *47*, 6565–6576. [[CrossRef](#)]
11. Nauman, E.; Fong, K.; Keaveny, T. Dependence of intertrabecular permeability on flow direction and anatomic site. *Ann. Biomed. Eng.* **1999**, *27*, 517–524. [[CrossRef](#)] [[PubMed](#)]

12. Daish, C.; Blanchard, R.; Gulati, K.; Losic, D.; Findlay, D.; Harvie, D.J.E.; Pivonka, P. Estimation of anisotropic permeability in trabecular bone based on microCT imaging and pore-scale fluid dynamics simulations. *Bone Rep.* **2017**, *6*, 129–139. [[CrossRef](#)] [[PubMed](#)]
13. Dewidar, M.M.; Lim, J.K. Properties of solid core and porous surface Ti–6Al–4V implants manufactured by powder metallurgy. *J. Alloys Compd.* **2008**, *454*, 442–446. [[CrossRef](#)]
14. Lee, J.H.; Park, H.J.; Hong, S.H.; Kim, J.T.; Lee, W.H.; Park, J.M.; Kim, K.B. Characterization and deformation behavior of Ti hybrid compacts with solid-to-porous gradient structure. *Mater. Des.* **2014**, *60*, 66–71. [[CrossRef](#)]
15. Ahmadi, S.; Sadmezhaad, S.K. A novel method for production of foamy core@ compact shell Ti6Al4V bone-like composite. *J. Alloys Compd.* **2016**, *656*, 416–422. [[CrossRef](#)]
16. Trueba, P.; Chicardi, E.; Rodríguez-Ortiz, J.A.; Torres, Y. Development and implementation of a sequential compaction device to obtain radial graded porosity cylinders. *J. Manuf. Process.* **2020**, *50*, 142–153. [[CrossRef](#)]
17. Matsuno, H.; Yokoyama, A.; Watari, F.; Uo, M.; Kawasaki, T. Biocompatibility and osteogenesis of refractory metal implants, titanium, hafnium, niobium, tantalum and rhenium. *Biomaterials* **2001**. [[CrossRef](#)]
18. Woodard, J.R.; Hilldore, A.J.; Lan, S.K.; Park, C.J.; Morgan, A.W.; Eurell, J.A.C.; Clark, S.G.; Wheeler, M.B.; Jamison, R.D.; Johnson, A.J.W. The mechanical properties and osteoconductivity of hydroxyapatite bone scaffolds with multi-scale porosity. *Biomaterials* **2007**. [[CrossRef](#)]
19. Takemoto, M.; Fujibayashi, S.; Neo, M.; Suzuki, J.; Kokubo, T.; Nakamura, T. Mechanical properties and osteoconductivity of porous bioactive titanium. *Biomaterials* **2005**, *26*, 6014–6023. [[CrossRef](#)]
20. Dabrowski, B.; Swieszkowski, W.; Godlinski, D.; Kurzydowski, K.J. Highly porous titanium scaffolds for orthopaedic applications. *J. Biomed. Mater. Res. B Appl. Biomater.* **2010**, *95*, 53–61. [[CrossRef](#)]
21. Le, H.; Wang, C.A.; Huang, Y. *Biomimetics Learning from Nature*; InTechOpen: London, UK, 2010. [[CrossRef](#)]
22. Kienapfel, H.; Sprey, C.; Wilke, A.; Griss, P. Implant fixation by bone ingrowth. *J. Arthroplasty* **1999**, *14*, 355–368. [[CrossRef](#)]
23. Coble, R.L. Effects of particle-size distribution in initial-stage sintering. *J. Am. Ceram. Soc.* **1973**, *56*, 461–466. [[CrossRef](#)]
24. Francis, J.S.; Cologna, M.; Raj, R. Particle size effects in flash sintering. *J. Eur. Ceram. Soc.* **2012**, *32*, 3129–3136. [[CrossRef](#)]
25. Morsi, K.; Keshavan, H.; Bal, S. Processing of grain-size functionally gradient bioceramics for implant applications. *J. Mater. Sci. Mater. Med.* **2004**, *15*, 191–197. [[CrossRef](#)] [[PubMed](#)]
26. Olmos, L.; Takahashi, T.; Bouvard, D.; Martin, C.L.; Salvo, L.; Bellet, D.; di Michiel, M. Analysing the sintering of heterogeneous powder structures by in situ microtomography. *Philos. Mag.* **2009**. [[CrossRef](#)]
27. Olmos, L.; Bouvard, D.; Cabezas-Villa, J.L.; Lemus-Ruiz, J.; Jiménez, O.; Arteaga, D. Analysis of compression and permeability behavior of porous Ti6Al4V by computed microtomography. *Met. Mater. Int.* **2019**, *25*, 669–682. [[CrossRef](#)]
28. Martin, C.L.; Bordia, R.K. The effect of a substrate on the sintering of constrained films. *Acta Mater.* **2009**, *57*, 549–558. [[CrossRef](#)]
29. German, R.M. Sintering theory and practice. *Sol.-Terr. Phys.* **1996**, 568.
30. Vagnon, A.; Rivière, J.P.; Missiaen, J.M.; Bellet, D.; Di Michiel, M.; Josserond, C.; Bouvard, D. 3D statistical analysis of a copper powder sintering observed in situ by synchrotron microtomography. *Acta Mater.* **2008**, *56*, 1084–1093. [[CrossRef](#)]
31. Grimm, M.J.; Williams, J.L. Measurements of permeability in human calcaneal trabecular bone. *J. Biomech.* **1997**, *30*, 743–745. [[CrossRef](#)]
32. Syahrom, A.; Kadir, M.R.A.; Harun, M.N.; Öchsner, A. Permeability study of cancellous bone and its idealised structures. *Med. Eng. Phys.* **2015**, *37*, 77–86. [[CrossRef](#)] [[PubMed](#)]
33. Gibson, L.J.; Ashby, M.F. *Cellular Solids: Structure and Properties*; Cambridge University Press: Cambridge, UK, 1999; p. 52.
34. Cabezas-Villa, J.L.; Lemus-Ruiz, J.; Bouvard, D.; Jiménez, O.; Vergara-Hernández, H.J.; Olmos, L. Sintering study of Ti6Al4V powders with different particle sizes and their mechanical properties. *Int. J. Miner. Metall. Mater.* **2018**, *25*, 1389–1401. [[CrossRef](#)]
35. Song, Y.; Xu, D.S.; Yang, R.; Li, D.; Wu, W.T.; Guo, Z.X. Theoretical study of the effects of alloying elements on the strength and modulus of  $\beta$ -type bio-titanium alloys. *Mater. Sci. Eng. A* **1999**, *260*, 269–274. [[CrossRef](#)]
36. Zhou, Y.L.; Niinomi, M. Ti–25Ta alloy with the best mechanical compatibility in Ti–Ta alloys for biomedical applications. *Mater. Sci. Eng. C* **2009**, *29*, 1061–1065. [[CrossRef](#)]

Article

# Influence of Successive Chemical and Thermochemical Treatments on Surface Features of Ti6Al4V Samples Manufactured by SLM

Jesús E. González <sup>1,\*</sup>, Gabriela de Armas <sup>1</sup>, Jeidy Negrin <sup>1</sup>, Ana M. Beltrán <sup>2</sup>, Paloma Trueba <sup>2</sup>, Francisco J. Gotor <sup>3</sup>, Eduardo Peón <sup>1</sup> and Yadir Torres <sup>2</sup>

<sup>1</sup> Departamento de Biomateriales Cerámicos y Metálicos, Centro de Biomateriales, Universidad de La Habana, La Habana 6323, Cuba; gdearmasortiz@gmail.com (G.d.A.); jeidy930924@gmail.com (J.N.); epeon@biomat.uh.cu (E.P.)

<sup>2</sup> Departamento de Ingeniería y Ciencia de los Materiales y el Transporte, Escuela Politécnica Superior, Universidad de Sevilla, 41011 Sevilla, Spain; abeltran3@us.es (A.M.B.); ptrueba@us.es (P.T.); ytorres@us.es (Y.T.)

<sup>3</sup> Instituto de Ciencia de Materiales de Sevilla (CSIC-US), 41011 Sevilla, Spain; francisco.gotor@icmse.csic.es

\* Correspondence: jgonzalezr1961@gmail.com; Tel.: +53-58454530

**Abstract:** Ti6Al4V samples, obtained by selective laser melting (SLM), were subjected to successive treatments: acid etching, chemical oxidation in hydrogen peroxide solution and thermochemical processing. The effect of temperature and time of acid etching on the surface roughness, morphology, topography and chemical and phase composition after the thermochemical treatment was studied. The surfaces were characterized by scanning electron microscopy, energy dispersive X-ray spectroscopy, X-ray diffraction and contact profilometry. The temperature used in the acid etching had a greater influence on the surface features of the samples than the time. Acid etching provided the original SLM surface with a new topography prior to oxidation and thermochemical treatments. A nanostructure was observed on the surfaces after the full process, both on their protrusions and pores previously formed during the acid etching. After the thermochemical treatment, the samples etched at 40 °C showed macrostructures with additional submicro and nanoscale topographies. When a temperature of 80 °C was used, the presence of micropores and a thicker anatase layer, detectable by X-ray diffraction, were also observed. These surfaces are expected to generate greater levels of bioactivity and high biomechanics fixation of implants as well as better resistance to fatigue.

**Keywords:** selective laser melting; Ti6Al4V; acid etching; chemical oxidation; thermochemical treatment; surface features

**Citation:** González, J.E.; Armas, G.d.; Negrin, J.; Beltrán, A.M.; Trueba, P.; Gotor, F.J.; Peón, E.; Torres, Y. Influence of Successive Chemical and Thermochemical Treatments on Surface Features of Ti6Al4V Samples Manufactured by SLM. *Metals* **2021**, *11*, 313. <https://doi.org/10.3390/met11020313>

Academic Editor: Eric Hug

Received: 24 January 2021

Accepted: 8 February 2021

Published: 11 February 2021

**Publisher's Note:** MDPI stays neutral with regard to jurisdictional claims in published maps and institutional affiliations.



**Copyright:** © 2021 by the authors. Licensee MDPI, Basel, Switzerland. This article is an open access article distributed under the terms and conditions of the Creative Commons Attribution (CC BY) license (<https://creativecommons.org/licenses/by/4.0/>).

## 1. Introduction

Titanium and its alloys are widely used in the manufacturing of biomedical devices, especially dental and orthopedic implants, which operate under high biomechanical loads [1–3]. Titanium has a moderate capacity to osseointegrate, excellent mechanical characteristics and great resistance to corrosion in biological fluids [4–6]. However, there are significant differences between the chemical and phase composition presented by these materials and those of bone tissues. Therefore, their insertion into the human skeleton may result in the absence of strong bonds between the bone and implant. Commonly, the Ti6Al4V alloy is one of the most widely used in the medical world, since it significantly increases the strength, ductility and fatigue resistance of the implants, which could prevent their fracture [2,7,8].

In the last two decades, a kind of technological revolution involving advanced biomaterials, structure designs and new manufacturing methods for implantable medical devices has notably improved the clinical success of surgical operations for the treatment of hard tissue affections [9]. Additive manufacturing (AM) is a new concept involving

the industrial production of objects through which the material is deposited layer by layer [10,11]. Using this technique, which is also known as three-dimensional (3D) printing, custom geometric shapes can be produced depending on the needs of each patient [11]. This process is suitable for producing low-volume parts with great shape complexity. AM has beneficial features, such as high precision, freedom of design, minimization of waste, production of components directly from digital files, as well as lightweight parts with complex scales. It also reduces the cost of product development and cycle time [12].

One of the advantages of AM, is that it provides extensive customization for medical applications based on individual patient data and requirements, and enables the design and manufacture of patient-specific implants [12–14], which are modeled in 3D sections. For this reason, in recent years there has been notable progress in the implementation of AM in the field of biofabrication. Selective laser melting (SLM) and electron beam melting (EBM) have been selected in most research studies as suitable methods for fabricating scaffolds for bone tissue engineering (BTE), due to their good controllability and high level of precision [11,15]. The SLM technique is used in biomedicine to print complex geometries and lightweight structures and, since printed components can have thin walls, deep cavities, and hidden channels, it has a high potential for being used for the manufacturing of porous objects, such as metal scaffolds. For instance, by SLM, it is possible to manufacture implants with porous 3D structures known as lattice structures [12].

In the last 30 years, a great deal of effort has been devoted to obtaining a biological answer related to the topology and chemistry of the surface of implants [16]. Increasing cellular activity on the implant surface is of great importance to accelerate the growth of bone tissue. The relationship between surface topography and cell viability has drawn increasing attention to a wide variety of surface modification approaches [16,17]. Nanoscale profiles may play an important role in the adsorption of extracellular matrix (ECM) proteins and in cell adhesion properties [2,18]. Micro/nanoscale surface topography has been confirmed to modulate cellular functions and have positive effects on the differentiation, orientation, adhesion of osteoblasts and implant osseointegration [19,20]. In different studies, human osteoblasts were found to prefer surfaces with nanometric topologies [6].

Some works have addressed the manufacturing and characterization of specimens of the commercially pure (c.p.) titanium and Ti6Al4V alloys, made by SLM [21–23]. SLM titanium and SLM Ti6Al4V samples have shown good biocompatibility both *in vitro* and *in vivo* [24]. However, their topography and surface chemistry are not the most appropriate for achieving rapid osseointegration [17,25]. In this context, to improve the biocompatibility and osseointegration of SLM Ti6Al4V implants, several surface modification treatments have been proposed in the literature [26–30], obtaining roughness surface at submicro and nanoscale level. However, no studies have been found in which these surface treatments were able to obtain and control roughness features ranging from the macroscale to the nanoscale. Therefore, the main goal of this investigation is to evaluate the role of different consecutive surface treatments: acid etching (influence of temperature and time), chemical oxidation and thermochemical treatment on the surface features of SLM Ti6Al4V samples.

## 2. Materials and Methods

### 2.1. Fabrication of Ti6Al4V Samples

The samples were designed with Inventor Professional three dimensional computer-aided design (3D CAD) Inventor software (Autodesk Inc, Mill Valle, CA, USA). Plates with a size of around 10 mm × 5 mm × 5 mm were made on the SLM250 selective laser melting machine (SLM 250<sup>HL</sup>, SLM solutions GmbH, Lübeck, Germany). The samples were printed in the z-direction (parallel to the longitudinal direction of the plates) in an argon atmosphere. A Ti6Al4V alloy powder (grade 5 supplied by SLM Solutions GmbH) with spherical morphology and an average diameter of 31 ± 12 µm, with dimensions between 10 and 65 µm, was used. Details of the raw powder have already been reported in a previous work [31]. An ytterbium fiber laser, with a power of 200 W, line scanning

strategy using antiparallel stripes, hatch distance of 120 μm and thickness of the powder layer of 50 μm, were used.

2.2. Surface Modification Treatments

The surface modification process of the Ti6Al4V samples used during the development of this research can be summarized as described in Figure 1. First, the samples were subjected to an acid etching (AE) treatment. A mixture of HCl/H<sub>2</sub>SO<sub>4</sub> at 67% with a v/v 1:1 ratio was prepared according to the procedure described by Zhang et al. [32] and the samples were immersed in this mixture using one of the four treatment regimens shown in Table 1. Then, they were washed using distilled water in an ultrasonic bath for 10 min and dried in an oven at 90 °C for 1 h. Later, the chemical oxidation (C) treatment of samples in a mixture of H<sub>2</sub>O<sub>2</sub> and HCl was carried out according to the procedure reported by Wang et al. [33,34]. Test tubes, with 5 mL of a mixture of H<sub>2</sub>O<sub>2</sub> with a concentration of 8.8 mol/L and 0.1 mol/L of HCl with a v/v 1:1, were placed in a thermostatic water bath at 80 °C and the samples were submerged in the oxidizing mixture for 30 min. The specimens were then washed again with distilled water and dried in an oven at 90 °C for 1 h. Finally, a thermochemical (T) treatment was carried out in a furnace at 400 °C for 1 h, using a heating regime of 10 °C/min. The successive chemical oxidation and thermochemical treatments were applied to the samples obtained with the four AE regimens shown in Figure 1. Table 1 summarizes the label of the samples and the successive superficial treatment of each of them (AE+C+T, AECT). For instance, AECT-1 means this substrate was subjected to a sequential acid etching (AE) a 40 °C during 8 min, followed by a chemical oxidation (C) and, then, thermochemical treatment (T).

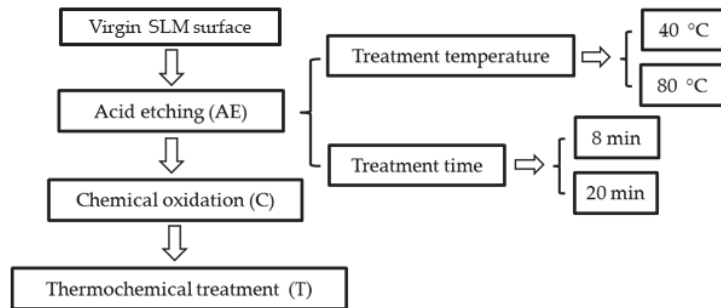


Figure 1. Schematic representation of the surface treatments used. SLM: selective laser melting.

Table 1. Acid etching treatments. All samples were superficially modified with successive chemical oxidation treatment (at 80 °C for 30 min) and thermochemical treatment (at 400 °C for 1 h).

| Sample Denomination | Acid Etching (AE) |         |
|---------------------|-------------------|---------|
|                     | T (°C)            | t (min) |
| AECT-1              | 40                | 8       |
| AECT-2              |                   | 20      |
| AECT-3              | 80                | 8       |
| AECT-4              |                   | 20      |

2.3. Surface Characterization

Surface morphology of different samples was studied by field emission scanning electron microscopy (FE-SEM) (S-4800, Hitachi, Japan). The semi-quantitative elemental composition was measured using energy dispersive X-ray spectroscopy coupled with scanning electron microscopy (EDX-SEM) (Quantax EDS, Bruker Corporation, Mannheim, Germany). Surface topographical features (i.e., protuberances, size of the pores) were

measured using the software ImageJ version 1.44. The X-ray diffraction (XRD) patterns of the surfaces were acquired with a PANalytical X'Pert Pro diffractometer, using Cu K $\alpha$  radiation ( $\lambda = 0.1542$  nm) with 40 kV and 40 mA, a step size of  $0.05^\circ$ , a counting time of 80 s/step and a diffraction angle  $2\theta$  between  $20^\circ$  and  $80^\circ$ . The surface roughness ( $R_a$ ) of the samples before and after the thermochemical treatment was measured using a contact profilometer (SurfTest SJ-210, Mitutoyo, Japan) at 0.5 mm/s, using the standard UNE-EN-ISO 4287:1999 [35]. Two replicas of each surface were used, and data were acquired five times on each sample.

#### 2.4. Statistical Analysis

All experimental measurements are presented as the mean value  $\pm$  standard deviation (SD). At least one replica of each experimental run was used, with more than 50 measurements of the micropore, sub micropore and protrusion sizes. In addition, more than 5 measurements of the  $R_a$  of each sample were performed. The data were analyzed using StatGraphics Centurion XV software (Statpoint Technologies, Warrenton, VA, USA). Multiple-sample comparison tests (multiple range tests, Tukey HSD) were used to determine significant differences among groups. A value of  $p < 0.05$  was taken as a statistically significant difference.

### 3. Results

#### 3.1. Acid Etching of SLM Surface

Different AE regimens (Table 1) were performed to determine the influence of the temperature and time on the topographical surface features of Ti6Al4V samples after the full surface modification process (Figure 1). As an example, the SEM images of the Ti6Al4V sample before and after the acid etching at  $80^\circ\text{C}$  for 20 min are displayed in Figure 2. The as-prepared SLM samples showed surface morphological features according to those reported in previous studies (Figure 2a) [25,36]. Residual partially melted powder particles (protrusions) were found on the surface of the native SLM samples that showed a rough wavy surface without nano-topographic characteristics. On the surfaces subjected to the AE process, a significant variation of the topography and morphology (Figure 2a,b) was observed in comparison with the SLM surfaces. In samples etched at  $80^\circ\text{C}$ , micropores were revealed on the surfaces, which were not observed when etched at  $40^\circ\text{C}$ . Higher micropores content was noticed on the surfaces of samples etched at  $80^\circ\text{C}$  for 20 min with an average size of  $6.1 \pm 3.2$   $\mu\text{m}$ . Furthermore, some grooves with a width of around 9  $\mu\text{m}$  and parallel orientation between them were observed. On the other hand, the mean size of the protrusions on the AE surface decreased from  $31 \pm 12$   $\mu\text{m}$  to  $28 \pm 10$   $\mu\text{m}$  according to the dimensional losses observed in Figure 2.

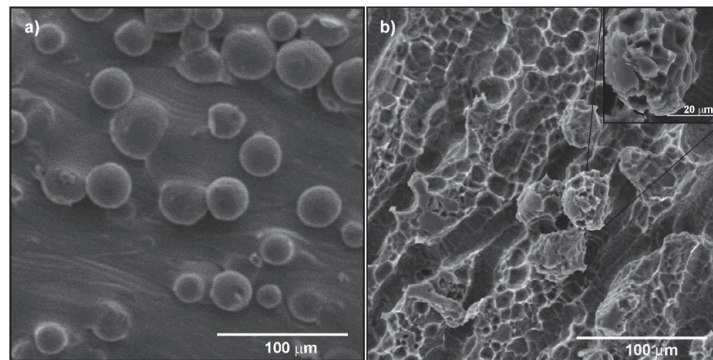


**Figure 2.** SEM micrographs of the surface of the Ti6Al4V alloy samples obtained by SLM before and after the acid etching (AE). (a) SLM surface, (b) AE surface (etched at  $80^\circ\text{C}$  for 20 min). Inset: higher magnification image.

The superficial elemental composition of the SLM and AE surfaces was determined by EDX-SEM (Figure 3). In general, the spectra acquired after etching are similar to those observed on the surface of the SLM samples without treatment. Peaks associated with Ti, Al and V were identified. Only a slightly higher Al content was observed on the AE surfaces. Moreover, a new peak was detected on these surfaces, which was assigned to S. The presence of this element must be related to the existence of  $H_2SO_4$  in the acid mixture.

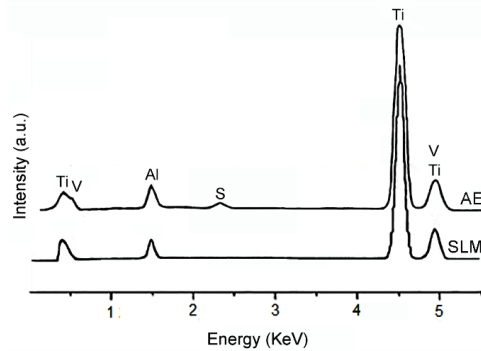


**Figure 3.** EDX-SEM spectra of the surface of SLM and AE samples.

### 3.2. Successive Chemical Oxidation and Thermochemical Treatments of the Acid Etched Ti6Al4V Surfaces

Figure 4 shows the SEM images of the surface of the Ti6Al4V samples subjected to successive acid etching, chemical oxidation (in  $H_2O_2/HCl$  mixture) and thermochemical ( $400\text{ }^\circ\text{C}$  for 1 h) treatments (AECT surfaces). AECT surfaces differed by the AE regimen used (Table 1) and two surface topographies were observed. The AECT-1 and AECT-2 samples presented a similar topography to the SLM samples, while the surface of the AECT-3 and AECT-4 samples additionally showed micropores. In Figure 4, it is possible to appreciate the size and the size distribution of the spheroidal protrusions present on the surfaces of these samples.

The AECT surfaces showed protrusions with diameters between 6 and  $60\text{ }\mu\text{m}$  and an average diameter of about  $30\text{ }\mu\text{m}$ , as could be observed in the histograms (insets Figure 4). In general, no statistically significant differences were found when comparing the diameter of the protrusions of the AECT surfaces with the AE surfaces. However, a slight increase in this parameter was observed in the AECT surfaces. Neither statistically significant differences were found between the diameter of the protrusions on the four AECT evaluated surfaces. On the other hand, on AECT-3 and AECT-4 surfaces, the presence of micropores can be observed with an average diameter of  $4.8 \pm 2.8\text{ }\mu\text{m}$  and  $5.2 \pm 2.0\text{ }\mu\text{m}$ , respectively. This parameter decreased in about  $1\text{ }\mu\text{m}$  compared to that presented by the AE surfaces and, furthermore, statistically significant differences were found when the micropore diameter on AECT-3 and AECT-4 surfaces was compared with AE surfaces. The micropores appeared not only on the protrusions, but also on the rest of the surface and had a concave configuration with the tendency to adopt a spheroidal shape. Note that the pores cover a greater surface area in the sample subjected to the treatment at  $80\text{ }^\circ\text{C}$ –20 min (AECT-4), while this was not observed in the samples treated at  $40\text{ }^\circ\text{C}$  (AECT-1 and AECT-2). Porous surfaces on implants provide high frictional resistance between the host bones and high primary stability. After implantation, the bone tissues can grow into the pores, and biological fixation is achieved [26].

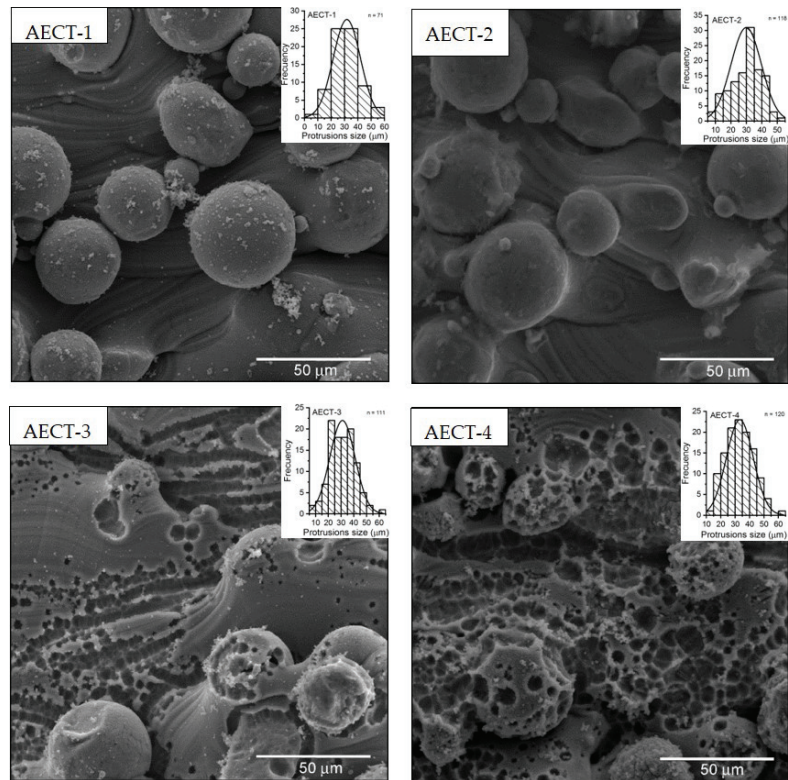


**Figure 4.** SEM micrographs AECT surfaces at low magnification and protrusions size distribution on AECT surfaces.

The SEM images at higher magnification of the AECT samples show the presence of structures at the submicrometric and nanometric scale (Figure 5), as a result of the chemical reaction between the titanium and the  $H_2O_2/HCl$  mixture [34]. Specifically, on all surfaces, a three-dimensional interconnected network with an open porous structure, formed by nanosheets that surround nano-submicropores was observed. The aforementioned network structure could be seen both on the surface of the protrusions and inside the pores previously formed in the AE process. The nano-submicropores (dark areas, while lighter areas were the sheets; see Figure 5) exhibited an irregular shape with an average size of around 130 nm. No statistically significant differences were found when comparing the average size of these pores for all studied surfaces. Some microcracks were also observed, which probably originated during the heating and cooling steps of the thermochemical treatment of the samples. In addition, structures with spheroidal shape and size of about one micrometer were detected.

In general, two multiscale topographies were observed after the successive chemical and thermochemical oxidation treatments. These topographies are related to the time and temperature used during acid etching. In the samples with acid etching at 40 °C (AECT-1 and AECT-2), macro, submicro and nanoscale structures were observed, while in the samples treated at 80 °C (AECT-3 and AECT-4), micropores were additionally seen. In recent years, the combination of micro- and nano-features has attracted the attention of researchers [14,18,19,37]. Xu et al. have reported that the presence of micro-nano topography in SLM titanium allowed significantly higher osteoblast proliferation, total protein contents, bone-implant contact (BIC) and bone-bonding force than in as-

built SLM [25]. In this sense, the nanotopographical features increase the surface area of biomaterials and may contribute to increased protein adsorption [18], the adhesion of osteoblasts and the osseointegration of the implant surface [17]. Therefore, it is expected that the surfaces could improve the cell response and the osseointegration of the implants.

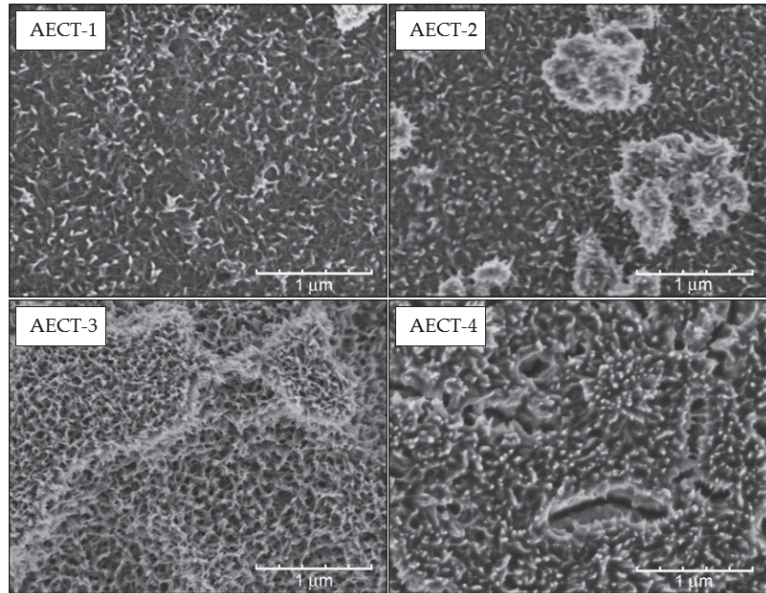


Figure 5. SEM micrographs of the surface of AECT samples at high magnification.

EDX-SEM spectra of the surfaces subjected to the chemical oxidation and thermochemical treatments are shown in Figure 6. Peaks of Ti, Al and V corresponding to the starting composition and additional O were observed. The presence of high oxygen content (around 40%) must be related to the formation of an oxide scale layer. The spectra did not show the peak corresponding to S detected on the AE surfaces that was probably eliminated during the H<sub>2</sub>O<sub>2</sub>/HCl chemical oxidation. In general, the Al, V and Ti contents on these surfaces remained lower than on the SLM and AE surfaces, but the Ti/Al/V ratio was similar to that of the AE surfaces.

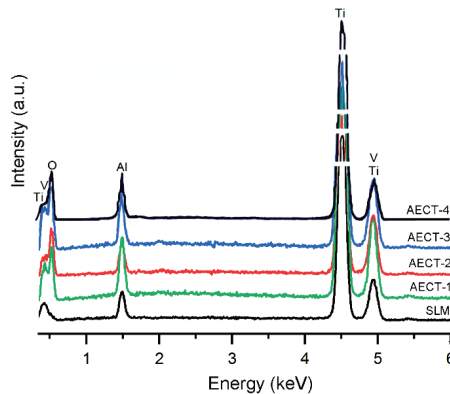
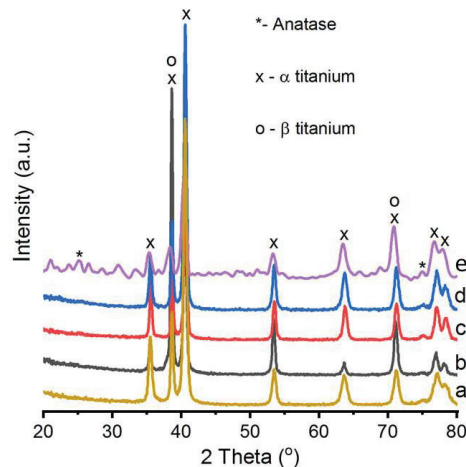


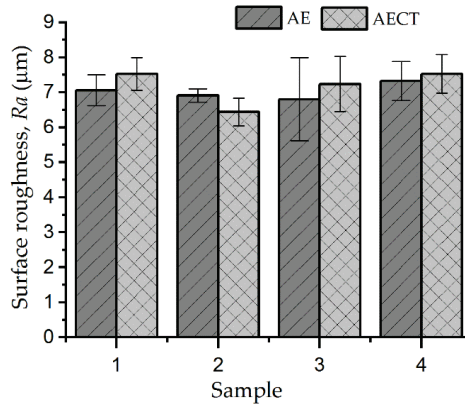
Figure 6. EDX-SEM spectra of SLM and AECT surfaces.

Figure 7 shows the XRD patterns of the surface of the SLM samples before and after the successive surface modification treatments evaluated in this work. The presence of the  $\alpha$  phase, with hcp crystal structure, was clearly observed. The existence of a small amount of the cubic  $\beta$  phase cannot be excluded. The low intensity XRD peaks also observed in Figure 7 were assigned to anatase  $\text{TiO}_2$  (2 Theta = 25.28 and 75.03). The low intensity of these peaks was related to the small thickness of the oxide layer (according with the results of Wang et al., the anatase layer thickness was estimated to be about 30 nm [33]). The titania gel obtained during the treatment of Ti in  $\text{H}_2\text{O}_2$  solution was transformed into an anatase crystal structure after heating between 400 and 500 °C [34]. Su et al. reported that protein adsorption and subsequent cellular responses could be also affected by the surface functional groups [38]. Specifically, anatase has excellent bioactivity and significant differences have been found in the percentage of BIC between the anatase layer and control implants during the early stages of bone regeneration [39]. On the other hand, the formation of a titanium oxide layer increases the corrosion resistance of the titanium alloy and prevents the release of ions into the body fluid [40]. In this sense, accumulation of aluminum has been observed around Ti6Al4V implants, which could be harmful; therefore, a proper passivating layer would reduce the risk of aluminum release [41].



**Figure 7.** XRD patterns of SLM and AECT surfaces. (a) SLM, (b) AECT-1, (c) AECT-2, (d) AECT-3 and (e) AECT-4.

Figure 8 shows  $R_a$  values of the AE and AECT surfaces. In general, rough surfaces were observed in all the samples ( $R_a$  average between 6.8 and 7.5  $\mu\text{m}$ ). These  $R_a$  values were slightly lower than those obtained for the SLM surfaces ( $R_a = 9.35 \pm 0.47 \mu\text{m}$ ) and were like those reported by Benedetti et al. [42]. On the other hand, different studies have reported  $R_a$  values in the range of 6 and 40  $\mu\text{m}$  on as built SLM Ti6Al4V parts [42–45]. The surface roughness of samples manufactured by SLM depends on several factors: material, processing parameters, laser inclination angle to the build platform, build direction, particle size distribution and parts spacing [46–50]. Both the transition boundaries between layers and partially melted powder particles contribute to the overall roughness of the top surfaces. In the top surface, the roughness differs strongly from the roughness of side surfaces [43]. The influence of the partially melted particles on the surface roughness increases as the inclination angle increases, and it is the primary cause of surface roughness when the inclination angle is close to 90° [50]. In this sense, it has been reported that specimens built in the 45° direction show higher levels of roughness than the vertically built specimens.



**Figure 8.** Surface roughness in AE and AECT samples. (1) AECT-1, (2) AECT-2, (3) AECT-3, (4) AECT-4.

In general, larger  $R_a$  values were observed in AECT surfaces compared to the AE surfaces. Nevertheless, no statistically significant differences were found between the  $R_a$  values of the AE and AECT surfaces ( $p > 0.005$ ). On the other hand, the AECT surfaces only showed slight differences between their  $R_a$  values. Several studies have demonstrated the influence of the surface roughness of titanium implants on their osseointegration rate and biomechanical fixation [3]. The rough surface could increase the anchorage possibility of the bone cells and, according to Bose et al., the intrinsic roughness of the AM surfaces can increase tissue integration, implant fixation and, also, the mechanical adherence of coatings [16]. Benedetti et al. investigated the effect of shot peening and electropolishing in SLM Ti6Al4V samples on cell growth at different times [51]. The surface roughness decreased because of these treatments, but they found no influence of these surfaces on cell growth at 90 h of incubation. Additionally, Tsukanaka et al. stated that a rough surface was beneficial for early mechanical stability, but for osteoblast differentiation and bone formation, the surface must undergo a bioactive treatment [26].

Endosseous implants under load bearing must maintain high mechanical properties, biocompatibility and osseointegration over a time scale exceeding at least two decades [51]. The multiscale topography, chemical and phase composition obtained in the AECT-3 and AECT-4 surfaces must generate adequate biocompatibility and fast osseointegration of the implants. Although the mechanical properties of SLM Ti6Al4V samples are superior, compared to conventionally manufactured parts, this is not the case in the high-cycle fatigue regime [52,53]. The fatigue performance of as built SLM Ti6Al4V components is over 75% lower than wrought materials, due to their surface finish, porosity and residual stresses [54]. In this sense, it was reported that as built Ti6Al4V parts manufactured by SLM after a stress relief treatment have a fatigue resistance of 240 MPa at  $5 \times 10^6$  cycles [51]. The fatigue crack initiation life depends on different factors, such as residual stresses, surface roughness, internal defects, microstructure and microstructural inhomogeneities. For built SLM specimens, surface roughness has been found to be the most influential factor in reducing fatigue life [55,56]. The mean fatigue life of SLM Ti6Al4V parts decreases with increasing surface roughness due to the stress concentration at the surface [52,57]. Different post-melting treatments, such as heat treatment, machining, acid etching, polishing, shot peening, hot isostatic pressing (HIP) and electropolishing, were used to increase the resistance of SLM Ti6Al4V parts to fatigue [44,51,52,58]. The best results were obtained when stress-relief treatments were used, followed by at least one of the following processes: machining, shot peening or HIP [44,51,59]. The machining processes reduce surface roughness and subsurface defects, but its use in complex geometries is difficult. On the other hand, shot peening and HIP reduce surface defects and create a surface compressive residual stress layer [51].

Porous coatings have also been associated with decreases in the fatigue life of medical devices [60]. Smith considered that the decrease in endurance limited, to sintered porous coatings, was related to pores and cracks in the layer [61]. Apachitei et al. found a significant increase in fatigue resistance by decreasing the thickness of porous coatings by plasma electrolytic oxidation (PEO) on titanium alloys [60]. They also observed that, in the coatings in which anatase prevails over rutile, the fatigue strength values were increased. According to Khan et al., the anatase coatings induced compressive stresses [62], which must improve the fatigue performance of the treated implant.

As previously stated, it is expected that the surfaces acid etched at 80 °C (AECT-3 and AECT-4), which present macro-micro-submicro and nanoscale structures and, in addition, an anatase layer, would generate greater levels of bioactivity and high biomechanic fixation of implants to the bone. However, these surfaces had greater porosity, which could also affect their resistance to fatigue. Thus, future research should determine the influence of the two topographies obtained on the biological behavior of the endosseous implants, using in vitro and in vivo tests. In addition, the influence of the surface features obtained in the AECT samples on the fatigue resistance of SLM biomedical devices should be evaluated.

#### 4. Conclusions

In this work, the effect of successive processes of acid etching, chemical oxidation and thermochemical treatment of Ti6Al4V samples (AECT surfaces) manufactured by selective laser melting was evaluated. It was found that AECT surfaces showed significant differences in their topography and elemental composition in comparison with the AE surfaces. The temperature used in the AE process had a greater influence on the surface features of the samples. Two topographies were obtained on the AECT surfaces as a function of the temperature used during acid etching. After the thermochemical treatment at 400 °C for 1 h, the samples subjected to acid etching at 40 °C (AECT-1 and AECT-2 samples) showed macro structures combined with submicro and nano scale topographies, characterized by the absence of micropores. The samples with acid etching at a temperature of 80 °C (AECT-3 and AECT-4 samples) also showed a multiscale topography in which additionally micropores were observed. A network shape structure was observed on all surfaces, both on their protrusions and inside their pores previously formed in the acid etching. In addition, thermochemical treatment caused an increase in oxygen content on the Ti6Al4V surface, the formation of an anatase thin layer and a micropore size decrease.

**Author Contributions:** Conceptualization, project administration, supervision, methodology, J.E.G., E.P., F.J.G. and Y.T., investigation, formal analysis, validation, G.d.A., J.N., A.M.B. and P.T., discussion and writing—original draft preparation, all the authors. All authors have read and agreed to the published version of the manuscript.

**Funding:** This work was supported by the Ministry of Science and Innovation of Spain under the grant PID2019-109371GB-I00, by the Junta de Andalucía–FEDER (Spain) through the Project Ref. US-1259771.

**Institutional Review Board Statement:** Not applicable.

**Informed Consent Statement:** Not applicable.

**Data Availability Statement:** Not applicable.

**Acknowledgments:** The authors are sincerely grateful to the to the “Luces” project of IMRE, University of Havana for its collaboration in conducting tests.

**Conflicts of Interest:** The authors declare no conflict of interest.

#### References

1. Gagg, G.; Ghassemieh, E.; Wiria, F.E. Effects of sintering temperature on morphology and mechanical characteristics of 3D printed porous titanium used as dental implant. *Mater. Sci. Eng. C* **2013**, *33*, 3858–3864. [[CrossRef](#)]
2. Tsai, P.-I.; Lam, T.-N.; Wu, M.-H.; Tseng, K.-Y.; Chang, Y.-W.; Sun, J.-S.; Li, Y.-Y.; Lee, M.-H.; Chen, S.-Y.; Chang, C.-K. Multi-scale mapping for collagen-regulated mineralization in bone remodeling of additive manufacturing porous implants. *Mater. Chem. Phys.* **2019**, *230*, 83–92. [[CrossRef](#)]

3. Shibata, Y.; Tanimoto, Y. A review of improved fixation methods for dental implants. Part I: Surface optimization for rapid osseointegration. *J. Prosthodont. Res.* **2015**, *59*, 20–33. [[CrossRef](#)] [[PubMed](#)]
4. Bai, L.; Gong, C.; Chen, X.; Sun, Y.; Zhang, J.; Cai, L.; Zhu, S.; Xie, S.Q. Additive manufacturing of customized metallic orthopedic implants: Materials, structures, and surface modifications. *Metals* **2019**, *9*, 1004. [[CrossRef](#)]
5. Yadroitsava, I.; du Plessis, A.; Yadroitsev, I. Bone regeneration on implants of titanium alloys produced by laser powder bed fusion: A review. In *Titanium for Consumer Applications*, 1st ed.; Elsevier: Amsterdam, The Netherlands, 2019; pp. 197–233.
6. Miranda, G.; Sousa, F.; Costa, M.; Bartolomeu, F.; Silva, F.; Carvalho, O. Surface design using laser technology for Ti6Al4V-hydroxyapatite implants. *Opt. Laser Technol.* **2019**, *109*, 488–495. [[CrossRef](#)]
7. Chang, J.; Tsai, P.-I.; Kuo, M.; Sun, J.-S.; Chen, S.-Y.; Shen, H.-H. Augmentation of DMLS Biomimetic Dental Implants with Weight-Bearing Strut to Balance of Biologic and Mechanical Demands: From Bench to Animal. *Materials* **2019**, *12*, 164. [[CrossRef](#)]
8. Sui, Q.; Li, P.; Wang, K.; Yin, X.; Liu, L.; Zhang, Y.; Zhang, Q.; Wang, S.; Wang, L. Effect of Build Orientation on the Corrosion Behavior and Mechanical Properties of Selective Laser Melted Ti-6Al-4V. *Metals* **2019**, *9*, 976. [[CrossRef](#)]
9. Yuan, L.; Ding, S.; Wen, C. Additive manufacturing technology for porous metal implant applications and triple minimal surface structures: A review. *Bioact. Mater.* **2019**, *4*, 56–70. [[CrossRef](#)]
10. Bartolomeu, F.; Dourado, N.; Pereira, F.; Alves, N.; Miranda, G.; Silva, F. Additive manufactured porous biomaterials targeting orthopedic implants: A suitable combination of mechanical, physical and topological properties. *Mater. Sci. Eng. C* **2020**, *107*, 110342. [[CrossRef](#)]
11. Zhang, X.-Y.; Fang, G.; Zhou, J. Additively manufactured scaffolds for bone tissue engineering and the prediction of their mechanical behavior: A review. *Materials* **2017**, *10*, 50. [[CrossRef](#)]
12. Dhiman, S.; Sidhu, S.S.; Bains, P.S.; Bahraminasab, M. Mechanobiological assessment of Ti-6Al-4V fabricated via selective laser melting technique: A review. *Rapid Prototyp. J.* **2019**, *25*, 1266–1284. [[CrossRef](#)]
13. Javaid, M.; Haleem, A. Additive manufacturing applications in medical cases: A literature based review. *Alex. J. Med.* **2018**, *54*, 411–422. [[CrossRef](#)]
14. Bouet, G.; Cabanettes, F.; Bidron, G.; Guignandon, A.; Peyroche, S.; Bertrand, P.; Vico, L.; Dumas, V. Laser-Based Hybrid Manufacturing of Endosseous Implants: Optimized Titanium Surfaces for Enhancing Osteogenic Differentiation of Human Mesenchymal Stem Cells. *ACS Biomater. Sci. Eng.* **2019**, *5*, 4376–4385. [[CrossRef](#)]
15. Oliveira, T.T.; Reis, A.C. Fabrication of dental implants by the additive manufacturing method: A systematic review. *J. Prosthet. Dent.* **2019**, *122*, 270–274. [[CrossRef](#)]
16. Bose, S.; Robertson, S.F.; Bandyopadhyay, A. Surface modification of biomaterials and biomedical devices using additive manufacturing. *Acta Biomater.* **2018**, *66*, 6–22. [[CrossRef](#)] [[PubMed](#)]
17. Xiong, Y.; Gao, R.; Zhang, H.; Li, X. Design and fabrication of a novel porous titanium dental implant with micro/nano surface. *Int. J. Appl. Electromagn. Mech.* **2019**, *59*, 1097–1102. [[CrossRef](#)]
18. Wang, G.; Moya, S.; Lu, Z.; Gregurec, D.; Zreiqat, H. Enhancing orthopedic implant bioactivity: Refining the nanotopography. *Nanomedicine* **2015**, *10*, 1327–1341. [[CrossRef](#)] [[PubMed](#)]
19. Ferraris, S.; Bobbiob, A.; Miola, M.; Spriano, S. Micro- and nano-textured, hydrophilic and bioactive titanium dental implants. *Surf. Coat. Technol.* **2015**, *276*, 374–383. [[CrossRef](#)]
20. Cohen, D.J.; Cheng, A.; Sahingur, K.; Clohessy, R.M.; Hopkins, L.B.; Boyan, B.D.; Schwartz, Z. Performance of laser sintered Ti-6Al-4V implants with bone-inspired porosity and micro/nanoscale surface roughness in the rabbit femur. *Biomed. Mater.* **2017**, *12*, 025021. [[CrossRef](#)] [[PubMed](#)]
21. Bartolomeu, F.; Costa, M.; Gomes, J.; Alves, N.; Abreu, C.; Silva, F.; Miranda, G. Implant surface design for improved implant stability—A study on Ti6Al4V dense and cellular structures produced by Selective Laser Melting. *Tribol. Int.* **2019**, *129*, 272–282. [[CrossRef](#)]
22. Wysocki, B.; Idaszek, J.; Zdunek, J.; Roźniatowski, K.; Pisarek, M.; Yamamoto, A.; Świąszkowski, W. The influence of selective laser melting (SLM) process parameters on in-vitro cell response. *Int. J. Mol. Sci.* **2018**, *19*, 1619. [[CrossRef](#)] [[PubMed](#)]
23. Wally, Z.J.; Haque, A.M.; Feteira, A.; Claeysens, F.; Goodall, R.; Reilly, G.C. Selective laser melting processed Ti6Al4V lattices with graded porosities for dental applications. *J. Mech. Behav. Biomed. Mater.* **2019**, *90*, 20–29. [[CrossRef](#)] [[PubMed](#)]
24. Wang, H.; Zhao, B.; Liu, C.; Wang, C.; Tan, X.; Hu, M. A comparison of biocompatibility of a titanium alloy fabricated by electron beam melting and selective laser melting. *PLoS ONE* **2016**, *11*, e0158513. [[CrossRef](#)] [[PubMed](#)]
25. Xu, J.-Y.; Chen, X.-S.; Zhang, C.-Y.; Liu, Y.; Wang, J.; Deng, F.-L. Improved bioactivity of selective laser melting titanium: Surface modification with micro-/nano-textured hierarchical topography and bone regeneration performance evaluation. *Mater. Sci. Eng. C* **2016**, *68*, 229–240. [[CrossRef](#)] [[PubMed](#)]
26. Tsukanaka, M.; Fujibayashi, S.; Takemoto, M.; Matsushita, T.; Kokubo, T.; Nakamura, T.; Sasaki, K.; Matsuda, S. Bioactive treatment promotes osteoblast differentiation on titanium materials fabricated by selective laser melting technology. *Dent. Mater. J.* **2016**, *35*, 118–125. [[CrossRef](#)] [[PubMed](#)]
27. Chen, Z.; Yan, X.; Chang, Y.; Xie, S.; Ma, W.; Zhao, G.; Liao, H.; Fang, H.; Liu, M.; Cai, D. Effect of polarization voltage on the surface componentization and biocompatibility of micro-arc oxidation modified selective laser melted Ti6Al4V. *Mater. Res. Express* **2019**, *6*, 086425. [[CrossRef](#)]
28. Zhao, D.-P.; Tang, J.-C.; Nie, H.-M.; Zhang, Y.; Chen, Y.-K.; Zhang, X.; Li, H.-X.; Yan, M. Macro-micron-nano-featured surface topography of Ti-6Al-4V alloy for biomedical applications. *Rare Met.* **2018**, *37*, 1055–1063. [[CrossRef](#)]

29. Luo, Y.; Jiang, Y.; Zhu, J.; Tu, J.; Jiao, S. Surface treatment functionalization of sodium hydroxide onto 3D printed porous Ti6Al4V for improved biological activities and osteogenic potencies. *J. Mater. Res. Technol.* **2020**, *9*, 13661–13670. [[CrossRef](#)]
30. Torres, Y.; Sarria, P.; Gotor, F.J.; Gutiérrez, E.; Peon, E.; Beltrán, A.M.; González, J.E. Surface modification of Ti-6Al-4V alloys manufactured by selective laser melting: Microstructural and tribo-mechanical characterization. *Surf. Coat. Technol.* **2018**, *348*, 31–40. [[CrossRef](#)]
31. Sarria, P.; Torres, Y.; Gotor, F.J.; Gutiérrez, E.; Rodríguez, M.; González, R.; Hernández, L.; Peón, E.; Guerra, H.; González, J.E. Processing and characterization of Ti-6Al-4V samples manufactured by selective laser melting. *Key Eng. Mater.* **2016**, *704*, 260–268. [[CrossRef](#)]
32. Zhang, E.; Wang, Y.; Gao, F.; Wei, S.; Zheng, Y. Enhanced bioactivity of sandblasted and acid-etched titanium surfaces. *Adv. Mater. Res.* **2009**, *79–82*, 393–396. [[CrossRef](#)]
33. Wang, X.X.; Hayakawa, S.; Tsuru, K.; Osaka, A. A comparative study of in vitro apatite deposition on heat-, H<sub>2</sub>O<sub>2</sub>-, and NaOH-treated titanium surfaces. *J. Biomed. Mater. Res.* **2001**, *54*, 172–178. [[CrossRef](#)]
34. Wang, X.-X.; Hayakawa, S.; Tsuru, K.; Osaka, A. Bioactive titania gel layers formed by chemical treatment of Ti substrate with a H<sub>2</sub>O<sub>2</sub>/HCl solution. *Biomaterials* **2002**, *23*, 1353–1357. [[CrossRef](#)]
35. ISO. ISO 4287; ISO: Geneva, Switzerland.
36. Wu, F.; Xu, R.; Yu, X.; Yang, J.; Liu, Y.; Ouyang, J.; Zhang, C.; Deng, F. Enhanced Biocompatibility and Antibacterial Activity of Selective Laser Melting Titanium with Zinc-Doped Micro-Nano Topography. *J. Nanomater.* **2019**, *2019*, 1–14. [[CrossRef](#)]
37. Xu, R.; Hu, X.; Yu, X.; Wan, S.; Wu, F.; Ouyang, J.; Deng, F. Micro-/nano-topography of selective laser melting titanium enhances adhesion and proliferation and regulates adhesion-related gene expressions of human gingival fibroblasts and human gingival epithelial cells. *Int. J. Nanomed.* **2018**, *13*, 5045. [[CrossRef](#)]
38. Su, Y.; Luo, C.; Zhang, Z.; Hermawan, H.; Zhu, D.; Huang, J.; Liang, Y.; Li, G.; Ren, L. Bioinspired surface functionalization of metallic biomaterials. *J. Mech. Behav. Biomed. Mater.* **2018**, *77*, 90–105. [[CrossRef](#)] [[PubMed](#)]
39. He, F.M.; Yang, G.L.; Li, Y.N.; Wang, X.X.; Zhao, S.F. Early bone response to sandblasted, dual acid-etched and H<sub>2</sub>O<sub>2</sub>/HCl treated titanium implants: An experimental study in. *Int. J. Oral Maxillofac. Surg.* **2009**, *38*, 677–681. [[CrossRef](#)]
40. Cao, H.; Liu, X. Activating titanium oxide coatings for orthopedic implants. *Surf. Coat. Technol.* **2013**, *233*, 57–64. [[CrossRef](#)]
41. Zaffe, D.; Bertoldi, C.; Consolo, U. Accumulation of aluminium in lamellar bone after implantation of titanium plates, Ti-6Al-4V screws, hydroxyapatite granules. *Biomaterials* **2004**, *25*, 3837–3844. [[CrossRef](#)] [[PubMed](#)]
42. Benedetti, M.; Fontanari, V.; Bandini, M.; Zanini, F.; Carmignato, S. Low-and high-cycle fatigue resistance of Ti-6Al-4V ELI additively manufactured via selective laser melting: Mean stress and defect sensitivity. *Int. J. Fatigue* **2018**, *107*, 96–109. [[CrossRef](#)]
43. Bagehorn, S.; Wehr, J.; Maier, H. Application of mechanical surface finishing processes for roughness reduction and fatigue improvement of additively manufactured Ti-6Al-4V parts. *Int. J. Fatigue* **2017**, *102*, 135–142. [[CrossRef](#)]
44. Cao, F.; Zhang, T.; Ryder, M.A.; Lados, D.A. A review of the fatigue properties of additively manufactured Ti-6Al-4V. *JOM* **2018**, *70*, 349–357. [[CrossRef](#)]
45. Vayssette, B.; Saintier, N.; Brugger, C.; El May, M. Surface roughness effect of SLM and EBM Ti-6Al-4V on multiaxial high cycle fatigue. *Theor. Appl. Fract. Mech.* **2020**, *108*, 102581. [[CrossRef](#)]
46. Bourell, D.; Stucker, B.; Spierings, A.; Herres, N.; Levy, G. Influence of the particle size distribution on surface quality and mechanical properties in AM steel parts. *Rapid Prototyp. J.* **2011**, *17*, 195–202.
47. Günther, J.; Leuders, S.; Koppa, P.; Tröster, T.; Henkel, S.; Biermann, H.; Niendorf, T. On the effect of internal channels and surface roughness on the high-cycle fatigue performance of Ti-6Al-4V processed by SLM. *Mater. Des.* **2018**, *143*, 1–11. [[CrossRef](#)]
48. Vandembroucke, B.; Kruth, J.P. Selective laser melting of biocompatible metals for rapid manufacturing of medical parts. *Rapid Prototyp. J.* **2007**, *13*, 196–203. [[CrossRef](#)]
49. Krol, M.; Tański, T. Surface quality research for selective laser melting of Ti-6Al-4V alloy. *Arch. Metall. Mater.* **2016**, *61*, 1291–1296. [[CrossRef](#)]
50. Strano, G.; Hao, L.; Everson, R.M.; Evans, K.E. Surface roughness analysis, modelling and prediction in selective laser melting. *J. Mater. Process. Technol.* **2013**, *213*, 589–597. [[CrossRef](#)]
51. Benedetti, M.; Torresani, E.; Leoni, M.; Fontanari, V.; Bandini, M.; Pederzoli, C.; Potrich, C. The effect of post-sintering treatments on the fatigue and biological behavior of Ti-6Al-4V ELI parts made by selective laser melting. *J. Mech. Behav. Biomed. Mater.* **2017**, *71*, 295–306. [[CrossRef](#)]
52. Fotovvati, B.; Namdari, N.; Dehghanhadikolaei, A. Fatigue performance of selective laser melted Ti6Al4V components: State of the art. *Mater. Res. Express* **2018**, *6*, 012002. [[CrossRef](#)]
53. Leuders, S.; Meiners, S.; Wu, L.; Taube, A.; Tröster, T.; Niendorf, T. Structural components manufactured by selective laser melting and investment casting—impact of the process route on the damage mechanism under cyclic loading. *J. Mater. Process. Technol.* **2017**, *248*, 130–142. [[CrossRef](#)]
54. Edwards, P.; Ramulu, M. Fatigue performance evaluation of selective laser melted Ti-6Al-4V. *Mater. Sci. Eng. A* **2014**, *598*, 327–337. [[CrossRef](#)]
55. Kahlin, M.; Ansell, H.; Moverare, J. Fatigue behaviour of notched additive manufactured Ti6Al4V with as-built surfaces. *Int. J. Fatigue* **2017**, *101*, 51–60. [[CrossRef](#)]
56. Zhang, J.; Fatemi, A. Surface roughness effect on multiaxial fatigue behavior of additive manufactured metals and its modeling. *Theor. Appl. Fract. Mech.* **2019**, *103*, 102260. [[CrossRef](#)]

57. Chan, K.S.; Koike, M.; Mason, R.L.; Okabe, T. Fatigue life of titanium alloys fabricated by additive layer manufacturing techniques for dental implants. *Metall. Mater. Trans. A* **2013**, *44*, 1010–1022. [[CrossRef](#)]
58. Vayssette, B.; Saintier, N.; Brugger, C.; El May, M.; Pessard, E. Numerical modelling of surface roughness effect on the fatigue behavior of Ti-6Al-4V obtained by additive manufacturing. *Int. J. Fatigue* **2019**, *123*, 180–195. [[CrossRef](#)]
59. Witkin, D.B.; Patel, D.N.; Helvajian, H.; Steffaney, L.; Diaz, A. Surface treatment of powder-bed fusion additive manufactured metals for improved fatigue life. *J. Mater. Eng. Perform.* **2019**, *28*, 681–692. [[CrossRef](#)]
60. Apachitei, I.; Lonyuk, B.; Fratila-Apachitei, L.; Zhou, J.; Duszczyk, J. Fatigue response of porous coated titanium biomedical alloys. *Scr. Mater.* **2009**, *61*, 113–116. [[CrossRef](#)]
61. Smith, T. The effect of plasma-sprayed coatings on the fatigue of titanium alloy implants. *JOM* **1994**, *46*, 54–56. [[CrossRef](#)]
62. Khan, R.H.; Yerokhin, A.; Matthews, A. Structural characteristics and residual stresses in oxide films produced on Ti by pulsed unipolar plasma electrolytic oxidation. *Philos. Mag.* **2008**, *88*, 795–807. [[CrossRef](#)]



MDPI  
St. Alban-Anlage 66  
4052 Basel  
Switzerland  
Tel. +41 61 683 77 34  
Fax +41 61 302 89 18  
[www.mdpi.com](http://www.mdpi.com)

*Metals* Editorial Office  
E-mail: [metals@mdpi.com](mailto:metals@mdpi.com)  
[www.mdpi.com/journal/metals](http://www.mdpi.com/journal/metals)





MDPI  
St. Alban-Anlage 66  
4052 Basel  
Switzerland

Tel: +41 61 683 77 34  
Fax: +41 61 302 89 18

[www.mdpi.com](http://www.mdpi.com)



ISBN 978-3-0365-1781-0